A Study on the Selective Laser Melting of Scalmalloy and the Influence of Cold Rolling, Heat Treatment and Gas Tungsten Arc Welding on its Mechanical Properties and Microstructure

Celine Turangi

A thesis submitted to

Auckland University of Technology

in fulfilment of the requirements for the degree of

Doctor of Philosophy (PhD)

2023

School of Engineering, Computer and

Mathematical Sciences

Auckland University of Technology

I hereby declare that this submission is my work and that, to the best of my knowledge and belief, it contains no material previously published or written by another person (except where explicitly defined in the acknowledgements), nor material which to a substantial extent has been submitted for the award of any other degree or diploma of a university or other institution of higher learning.

Signed _____ **Date:** 25/09/2023

Acknowledgement

I would like to thank my supervisors – Dr. Marcel Schaefer, Dr. Junior Nomani and Dr. Tim Pasang, and Dr. Maziar Ramezani - for their guidance and knowledge in assisting me in this research. I am very appreciative of all the constructive feedback I have received on my research in order to produce this complete thesis. I am also very appreciative of the guidance they have provided me over the years.

I would also like to thank the following people:

- Mark Masterton for helping with the metallographic preparation, heat treatment and tensile testing of my samples.
- Yuan Tao for her assistance with the SEM data analysis
- Professor Zhan Chen for assisting me with EBSD sample preparation and EBSD analysis,
- Florian Häslich for his work in the research of selective laser melting process parameters
- Dr. Burghart Klöeden, Ben Smuda, Ulrike Jehrig and Dr. Thomas Weißgärbe for their help with tensile testing with DIC Imaging.
- Professor Pai-Chen Lin and Shih-Jie Gao for their assistance in tensile testing the post processed and welded samples with DIC Imaging
- Tianping Zhu, Peter Buchanan and Professor Steve Matthews for assisting in etching my samples.

These individuals have been a huge help in my research, and I am very grateful to them.

Lastly, I'd like to thank my family as this has been a very long academic journey and I wouldn't have made it this far without their continued support and encouragement.

Publications

Turangi, C., Haslich, F., & Pasang, T. (2020). An Investigation of the Influence of Changing Energy Volume Densities to Produce a Complete Process Parameter Window for Selective Laser Melting of Scalmalloy. *Nusantara Science and Technology Proceedings*, 21-33.

Turangi, C., Häslich, F., Schaefer, M., Nomani, J., Pasang, T., Jehring, U., & Weißgärber, T. (2022, September). Mechanical properties and microstructure of cold-rolled Scalmalloy®(Al-4.5 Mg-0.6 Sc-0.3 Zr alloy) at a low reduction in thickness. In *Journal of Physics: Conference Series* (Vol. 2345, No. 1, p. 012028). IOP Publishing.

Accepted publication (to be published) - Turangi, C., Schaefer, M., Nomani, J., Häslich, F., Pasang, T., Gao, S., & Lin, P. (2024). Mechanical Properties and Microstructural Evolution of GTAW Welded Joints on Additively Manufactured Scalmalloy® and Extruded Aluminium Alloys. *中國機械工程學刊（Journal of the Chinese Society of Mechanical Engineers)*.

Table of Contents

List of Figures

List of Tables

Abstract

Scalmalloy is an Al-Mg-Sc-Zr modified aluminium alloy specifically designed for the laser powder bed fusion (LPBF) additive manufacturing process of Selective Laser Melting (SLM). This thesis investigates the processing and manufacture of Scalmalloy in an *Additive Manufacturing (AM) 400 Renishaw* laser beam melting (LBM) machine and the effect post processing treatments (heat treatment, cold rolling and a combination of heat treatment and cold rolling) and gas tungsten arc welding (GTAW) has on the mechanical properties and microstructures of Scalmalloy when compared to its as-built structure. Heat treatment is well reported in the literature, however there is opportunity to explore different heat treatment conditions. Cold rolling has not been widely reported for Scalmalloy and offers a novel area to study its effect on Scalmalloy. Lastly, GTAW of Scalmalloy has not been reported in the literature and offers solutions to join complex additively manufactured parts together and to join Scalmalloy parts to pre-existing structures. Hence, this thesis is comprised of three main studies:

1. Experimental works were carried out to determine optimal SLM parameters for Scalmalloy using an AM Renishaw LBM machine with constant parameters of 400W laser power, layer thickness of 30µm and hatch distance of 150µm. Energy volume densities were then modified to establish an optimum range. Findings showed that samples manufactured with an energy volume density between 70J/mm^3 and 110J/mm^3 resulted in samples with >99% relative densities. Furthermore, it was shown that the influence of the layout position of each sample on the build platform had very little impact on relative densities. Therefore, optimal processing parameters were found with 400W laser power, allowing productivity to be increased when compared to current literature employing 200W laser power.
2. Scalmalloy samples manufactured using the optimal SLM process parameters from the first study were subjected to cold rolling, heat treatment and a combination of both. Scalmalloy in its as built condition can possess reasonably high tensile strengths, which can be further increased by heat treatment, and, in turn, the microstructure is also refined. When heat treatment was applied an immediate increase of 14.6% occurred, while subsequent heat treatment had slightly lower values due to slight over ageing but remained higher than the as built condition. Once cold rolling was applied to the as built condition almost no increase was evident thought to be due to the low rolling reduction, however when cold rolling and heat treatment was applied an immediate increase of 28.4% occurred. The grain size distribution was consistent with literature for the as built condition, however, it was increased by the cold rolling due to elongation of the grains. Overall, the application of heat treatment and cold rolling had a positive effect on the microstructure of Scalmalloy reflected in its increased mechanical properties.
3. GTAW was performed to join Scalmalloy to itself and to extruded aluminium alloys using standard welding parameters employed to weld conventionally manufactured aluminium alloys. High porosity and defects were found in the welded joint leading to poor mechanical

properties likely due to release of hydrogen content within the Scalmalloy base metal. Hence, standard welding parameters are feasible to be used for GTAW of Scalmalloy, but only as a starting point, highlighting that parameters cannot be simply transferred from one alloy to another, but rather have to be modified in order to achieve optimum results.

The main output of this thesis is that the academic community would have a better understanding of the effect that different heat treatment methods, cold rolling, and GTAW have on the microstructure and mechanical properties of Scalmalloy. Hence, providing a modified heat treatment than the typical heat treatment reported in the literature, and providing info on cold rolling of additively manufactured components, which has not been widely reported. In addition, to evaluating the feasibility of welding Scalmalloy using standard welding parameters for conventionally manufactured aluminium alloys, consequently, aiming to eliminate size limitations in additive manufacturing and reduce manufacturing costs.

Chapter 1 Introduction

Aluminium is often used as an alloy with elements such as magnesium, zinc, and silicon, as these increase its mechanical and physical properties. Aluminium alloys are one of the most common metal alloys used within society today due to their good mechanical properties, corrosion resistance and high strength to density ratio (Glazoff, Khvan, Zolotorevsky, Belov, & Dinsdale, 2019b; Rabinovich, 2013). Aluminium alloys are used in conventional manufacturing processes, such as extrusion and casting. However, it has recently been introduced into the additive manufacturing process of laser powder bed fusion (LPBF), where components are manufactured in a closed vacuum chamber where metal powder is melted and solidified to build the component according to its predefined geometry in a layer-by-layer fashion (Aboulkhair et al., 2019). Although, it has proven difficult to hone the properties of aluminium alloys to be suitable for laser powder bed fusion (LPBF) processes due to solidification cracking tendencies and its high reflectivity (Aversa et al., 2019), Scalmalloy was developed by *Airbus Group Innovation* over a period of 20 years specifically for the LPBF process of selective laser melting (SLM) and have exhibited enhanced mechanical properties compared to conventionally manufactured aluminium alloys due to the addition of scandium and zirconium (R. Li et al., 2017). This LPBF process requires specific parameters to successfully manufacture Scalmalloy, hence, there are various studies that have reported the processing parameters for specific machines and different compositions of Scalmalloy (R. Li et al., 2019; R. Li et al., 2017; A. B. Spierings, Dawson, Dumitraschkewitz, Pogatscher, & Wegener, 2018; A. B. Spierings, Dawson, Heeling, et al., 2017) . However, it was necessary to carry out a study to manufacture Scalmalloy in *AM 400 Renishaw LBM machine*, the machine used in this research, as it has not been widely reported.

Heat treatment is often used as a post processing treatment to further increase and refine Scalmalloy mechanical properties and microstructure (Schmidtke, Palm, Hawkins, & Emmelmann, 2011; A. B. Spierings, Dawson, Kern, Palm, & Wegener, 2017). Although, heat treatment of Scalmalloy has been reported well, there is further room to explore different heat temperature ranges and holding times. Cold rolling is another post processing treatment used to increase mechanical properties and improve the microstructure of some aluminium alloys, especially for the Al-Mg alloys, the type of aluminium alloy group that Scalmalloy belong to (B. Wang, Chen, Pan, Mao, & Fang, 2015). This is a topic of interest for Scalmalloy, however, there is no application yet, for this to be applied to additively manufactured parts, but the effect it may have on the mechanical properties and microstructure of Scalmalloy may prove interesting, hence, these will be observed and reported in addition to comparing the findings to extruded aluminium alloys.

The size of additively manufactured components is hugely dictated by the size of the build chamber of the additive manufacturing machines, especially for components manufactured by

LPBF (Matilainen, Pekkarinen, & Salminen, 2016). Fusion welding of Scalmalloy can eliminate the size limitations of additively manufactured components as several smaller components may be joined together through welding. In addition, additively manufactured parts can also be joined to pre-existing structural elements and conventionally manufactured aluminium alloys to further compensate for sizing limitations. Potential cost reductions may also be a by-product of this as it can eliminate the need to re-manufacture a whole component using LPBF processes, which can be costly (Braun et al., 2023). Although, welding of Scalmalloy is seldom reported in the literature, welding of aluminium alloys is very common and often used (Hakem, Lebaili, Miroud, Bentaleb, & Toukali, 2012; Shanavas & Dhas, 2017; G. Xu et al., 2016). Hence, these topics will be studied in greater depth and detail in the following chapters.

1.1 Objectives/ Aim of study

This thesis builds on the existing literature and is aimed at developing Scalmalloy processing parameters to manufacture full (>99%) density samples with acceptable dimensional accuracy and surface roughness of the as-built structure in an *AM400 Renishaw* LBM machine and attempting to provide a comprehensive investigation and analysis on the effect that post processing treatments and GTAW welding have on the microstructural characterisation and mechanical properties of Scalmalloy. At present, the literature does not fully explain the effect of heat treating at various temperatures and holding times, cold rolling, nor a combination of these. It also does not state the feasibility of using GTAW in the welding of Scalmalloy to join structural components to one another and to conventionally manufactured components, therefore the research questions are as follows:

- ***Post Processing Treatments for Scalmalloy –*** *What effect does different heat treatment conditions (temperature, holding times) have on the microstructure and mechanical properties of Scalmalloy compared to the standard 325^{o}C/4h reported in literature? What are the effects that heat treatment (with differing conditions) only, cold rolling only, and cold rolling with heat treatment have on the microstructure and mechanical properties of Scalmalloy?*
- ***Welding of Scalmalloy*** *- Is it feasible to use GTAW to join Scalmalloy to itself and to extruded aluminium alloys using standard GTAW welding parameters for conventionally manufactured aluminium alloys? What is the effect of GTAW standard welding parameters on the microstructure and mechanical properties of the welded joints, and how does the welded joint perform in terms of structural integrity?*

This thesis will attempt to answer the above research questions with full analysis and discussion of the results.

1.2 Layout

This thesis follows a traditional layout in the following order: Chapter 2 consists of an in-depth literature review, Chapter 3 consists of the design of study (experimental procedure), Chapters 4 to 6 consist of the results and discussion, and, finally, Chapter 7 consists of the summary, conclusions and future recommendations of the work on hand. It is comprised of three main research topics. Firstly, a selective laser melting parameter study conducted to determine suitable process parameters for Scalmalloy in an *AM400 Renishaw* LBM machine using 400W laser power. This involved necessary steps such as powder characterisation, verification of several SLM process parameters from literature, and then an evaluation of the SLM parameters through mechanical testing. Once these were verified, the SLM parameters were chosen based on findings and then three additional build jobs were performed to observe sample reproducibility and influence of layout position on the build platform. Secondly, Scalmalloy underwent post processing treatment such as heat treatment and cold rolling. Heat treatment conditions were based on literature, and cold rolling was performed according to literature recommendations for extruded aluminium alloys as there is little to no published research on this for Scalmalloy. Thirdly, gas tungsten arc welding (GTAW) of Scalmalloy was performed using typical welding parameters for conventionally manufactured aluminium alloys. Finally, subsequent testing and analysis were performed on all Scalmalloy samples to observe microstructural evolution and changes in mechanical properties. Additionally, extruded aluminium alloys were used as comparison and a baseline for the research on hand.

Chapter 2 Background/ Literature review

2.1 Aluminium

This section provides an introduction of Aluminium. Its history, classification, material properties, and applications are discussed, particularly the Al-Mg group as this is the aluminium alloy group this research is based upon.

2.1.1 History and classification

Aluminium has the symbol "Al", atomic number of 13 and is the third most common metallic element used globally. Al is a non-ferrous metallic substance having a silver-white appearance and makes up about 8% of the Earth's crust (Santos Junior, Machado, Falco Sales, Barrozo, & Ezugwu, 2016). Aluminium was first discovered and named in 1807 by Sir Humphry Davy. Its name comes from the Latin word "alum" which refers to a white mineral used in dyeing during ancient times and the Greek word "alumen" which refers to a bitter substance. Although, Sir Humphry Davy first named the metal "aluminum", it was later changed to aluminium, however "aluminum" is still used in the US today (Kvande, 2008).

Aluminium is a highly reactive material that oxidises quickly and proved difficult to isolate in its elemental form. Hans Christian Orsted extracted a very small amount of impure aluminium using potassium amalgam in 1825. Two years later, Friedrich Wohler built on Christian's method and was the first to isolate aluminium in its pure form. Aluminium possessed valuable properties such as corrosion resistance, high strength to density ratio and excellent electrical properties. However, Wohler's and Christian's methods' only produced small amounts and it was expensive due to the needed potassium (Rabinovich, 2013). With its favourable properties and expensive extraction process, aluminium became one of the world's most sought after and expensive metals during the 1800's (Kvande, 2008; Santos Junior et al., 2016). In 1886, Charles Martin Hall, an American engineer, and Paul Heroult, a French engineer, both developed separately the Hall-Heroult process in which electrolysis of alumina in molten cryolite was used to separate aluminium. Another method was developed based upon the Hall-Heroult Process, called the Bayer method, where aluminium was extracted from bauxite. Both processes are still used today to extract aluminium. Now that the Hall-Heroult and Bayer method has allowed aluminium to be extracted easily and more cost efficient, the price plummeted as production of aluminium soared from 45,000 tonnes in 1933 to 17.3 million tonnes in 1988 and rose even further to 58.3 million tonnes in 2016, making aluminium one of the most available metals in the world (Ashkenazi, 2019; Rabinovich, 2013; Santos Junior et al., 2016).

2.1.2 Material properties and physical metallurgy

Aluminium, in its purest form, has very low hardness and is very ductile. It has a face-centred cubic unit cell (FCC) structure, a melting temperature of 660°C, a low density of 2,700kg/m^3 at room temperature and tensile strengths as low as 10MPa. Pure aluminium is typically used in electrical and chemical applications. Commercial aluminium alloys were developed with increased strengths by adding elements such as zinc (Zn), copper (Cu), silicon (Si), magnesium (Mg) and manganese (Mn). These elements are usually known as "basic" or "primary" elements as these are added to influence microstructure and properties (Ashkenazi, 2019; Glazoff, Khvan, Zolotorevsky, Belov, & Dinsdale, 2019a). Fig. 2.1 shows that these elements possess solid solubility in aluminium and this solubility increases with temperature known as either ancillary additions (dopants) or impurities (Glazoff et al., 2019a). Eutectic phase diagrams are formed from the basic alloying elements used in aluminium, shown in Fig. 2.2a shows an aluminium binary phase diagram with eutectic alloying additions, while Fig. 2.2b shows the phase diagram of aluminium alloys with the addition of typical alloying elements. Fig. 2.3a shows the typical microstructure of solid solution alloys such as Al-Cu and Al-Mg exemplified by a nonequilibrium eutectic reaction that vanishes after T6 heat treatment. Fig. 2.3b shows hypoeutectic alloys with two-phase structures like Al-Si alloys. Fig. 2.3c typically represent eutectic alloys where basic elements are the primary microstructural components and finally Fig. 2.3d represent alloys containing many phases with crystals (Ashkenazi, 2019; Glazoff et al., 2019a).

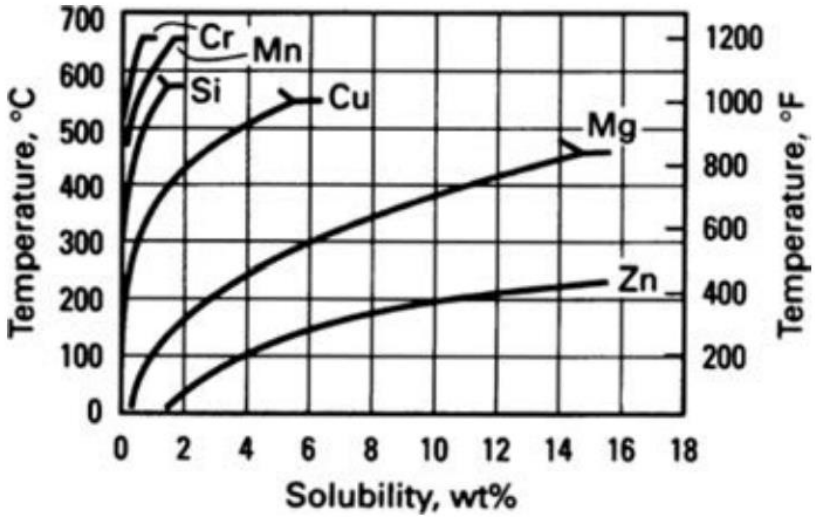

Fig. 2.1 Binary solid solubility as a function of temperature for basic alloying elements for aluminium (Callister, 2014)

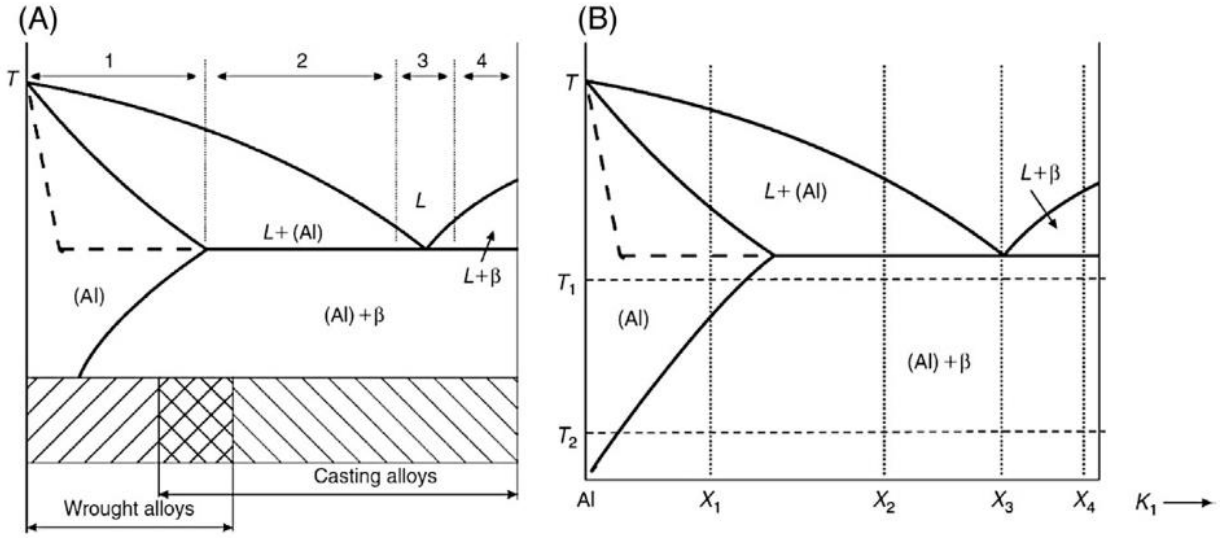

Fig. 2.2 a) Al-binary phase diagram with eutectic alloys, b) Al-binary phase diagram for typical alloys (Glazoff et al., 2019a)

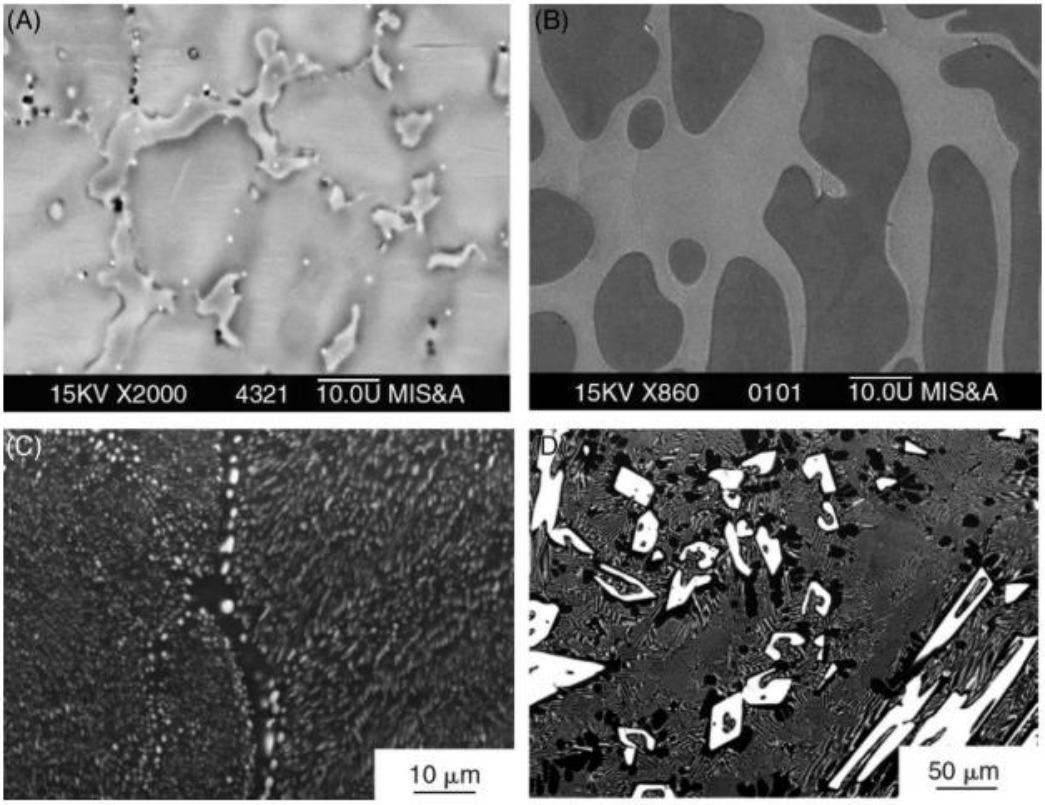

Fig. 2.3 Typical microstructures of basic binary aluminium alloys for the phases presented in Fig. 2.2 at X1, X2, X3 and X4 points - a) X1, b) X2, c) X3, d) X4 from Fig. 2.2 (Glazoff et al., 2019a)

2.1.3 Classification, strengthening methods, and application

The first aluminium alloy developed was the Al-Si-Mg heat treatable alloy used in railroad and automotive applications with many more being developed later (Ashkenazi, 2019). Aluminium alloys are classified into heat treatable (cast) and non-heat treatable (wrought). The heat-treatable

alloys are those whose strength and hardness can be manipulated through heat, while the non-heat treatable (wrought) aluminium alloys are those whose strength and hardness can be manipulated by plastic deformation such as rolling stretching and pressing (Callister, 2014; Hornbogen & Starkejr, 1993; Rao, Vasu, Govindaraju, & Srinadh, 2014; Westermann, Pedersen, Furu, Børvik, & Hopperstad, 2014). A typical heat treatment used for aluminium alloys is T6 heat treatment. This process is graphically explained in Fig. 2.4 using an example of both the solution treatment and ageing treatments for a 6061 Al alloy. The 6061 Al alloy is heated up to a high temperature (585ºC) and held there for a short time (30 mins) where this is called solutionising (solution treatment), then water quenching immediately follows and suppresses any precipitation during cooling. Precipitates that occur after quenching from a solutionised state are called primary precipitates. Next, the material is heated up to a low temperature for a designated time, then air cooled. The remaining solutes are in a supersaturated state to allow for precipitation hardening. In this hardening step, secondary phase particles are formed called secondary precipitates that are normally only nanometres in size. (Jägle et al., 2016).

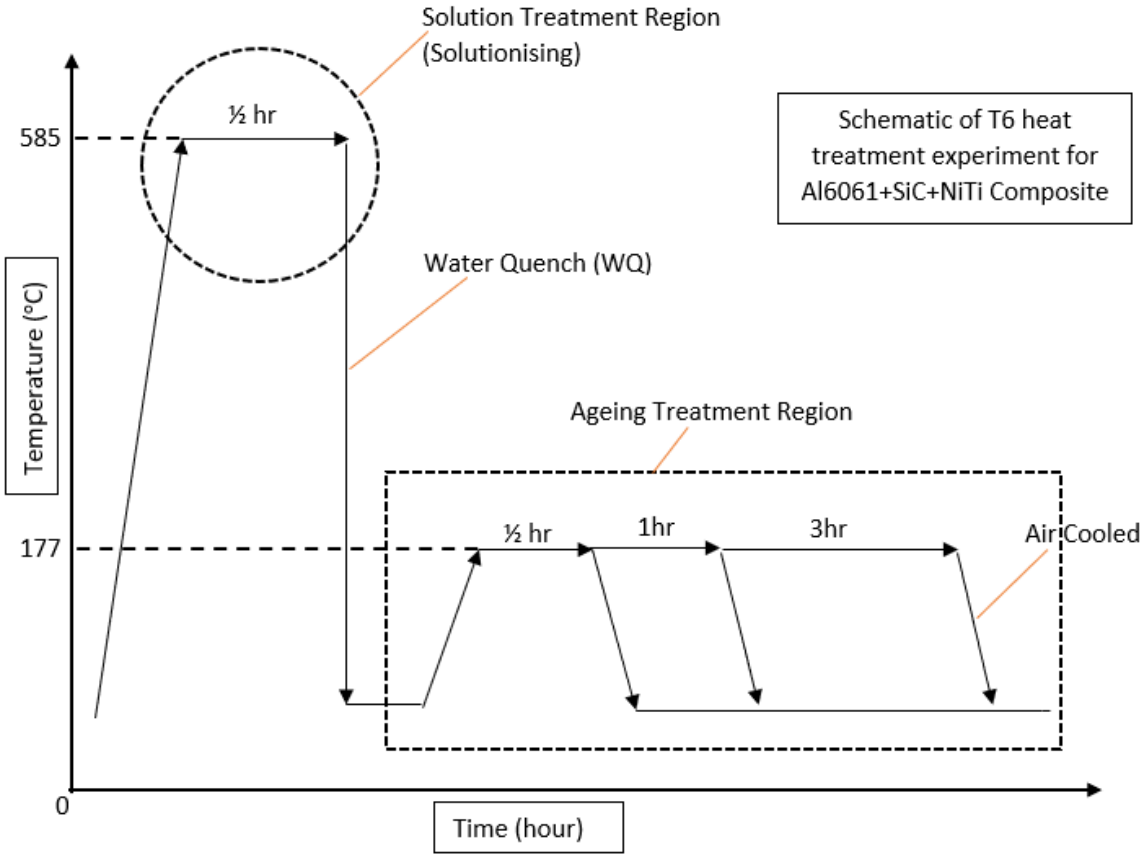

Fig. 2.4 Schematic showing the stages of solution treatment and ageing treatment for a 6061 aluminium alloy adapted from (Chaudhury, Hailat, Liu, & Newaz, 2010)

The non-heat-treatable alloys are strengthened by strain hardening induced by cold working or some form of plastic deformation. This increases dislocation density impeding dislocation movement and is normally performed at ambient temperatures (Callister, 2014; Hornbogen &

Starkejr, 1993; Rao et al., 2014; Westermann et al., 2014). The amount of cold work that has been applied to a material can be expressed as:

$$\%CW = \left(\frac{A_0 - A_d}{A_0}\right) \times 100 \qquad \textit{Equation 2.1}$$

where CW = the amount of cold work performed on the material, A_0 = the original cross-sectional area before cold working, and A_d = the decreased cross-sectional area of the material after cold work. Cold work increases strength dramatically; however, this is at the expense of ductility and elongation represented in Fig. 2.5. Fig. 2.6 shows a graphical representation of the elements used to produce the basic aluminium alloys. According to the American Society for Testing Materials (ASTM), these groups are classified as 1000, 2000, 3000, 4000, 5000, 6000, 7000 and 8000 series aluminium alloys. The first digit represents the alloy group, the second and third digits indicate aluminium purity and the last digit indicates the Al form either ingot or casting (Sivaramakrishnan, 1995). Table 2-1 shows the aluminium classification and common alloying elements, properties and applications for each series (Polmear, Qian, StJohn, & Nie, 2017; Zahner, 2019). Aluminium is very versatile and can be used in various fields such as weaponry, construction, aerospace, automotive and marine applications (Polmear et al., 2017).

2.1.4 Al-Mg alloys

The Al-Mg alloys also known as the 5000 series will be the main Al alloy group of interest in this research as Scalmalloy, is derived from this group of Al alloys. The second major alloying element, Mg, is responsible for solid solution hardening in these alloys (B. Wang et al., 2015). Three intermetallic phases exist for Al-Mg alloys - β-Al_3Mg_2 with composition range 38.5 - 40.3 at%, ε-phase with the composition of 42 at% Mg and γ-$Al_{12}Mg_{17}$ with a composition range 45-60.5 at% Mg. These are represented in the Al-Mg phase diagram shown in Fig. 2.7. All Al-Mg alloys are in the single-phase (α) region and the FCC structure continues to increase with increasing Mg content. Al-Mg alloys cannot be age hardened as the increased Mg content increases its response to cold working rate, which leads to intercrystalline failure at the slip band due to formation of Al_8Mg_5 phase resulting in strength reduction of the alloy. On the other hand, cold work causes an increase in the distortion of the crystal lattice as the Mg atoms in the FCC lattice position increase Al-Mg alloys' as-received condition.

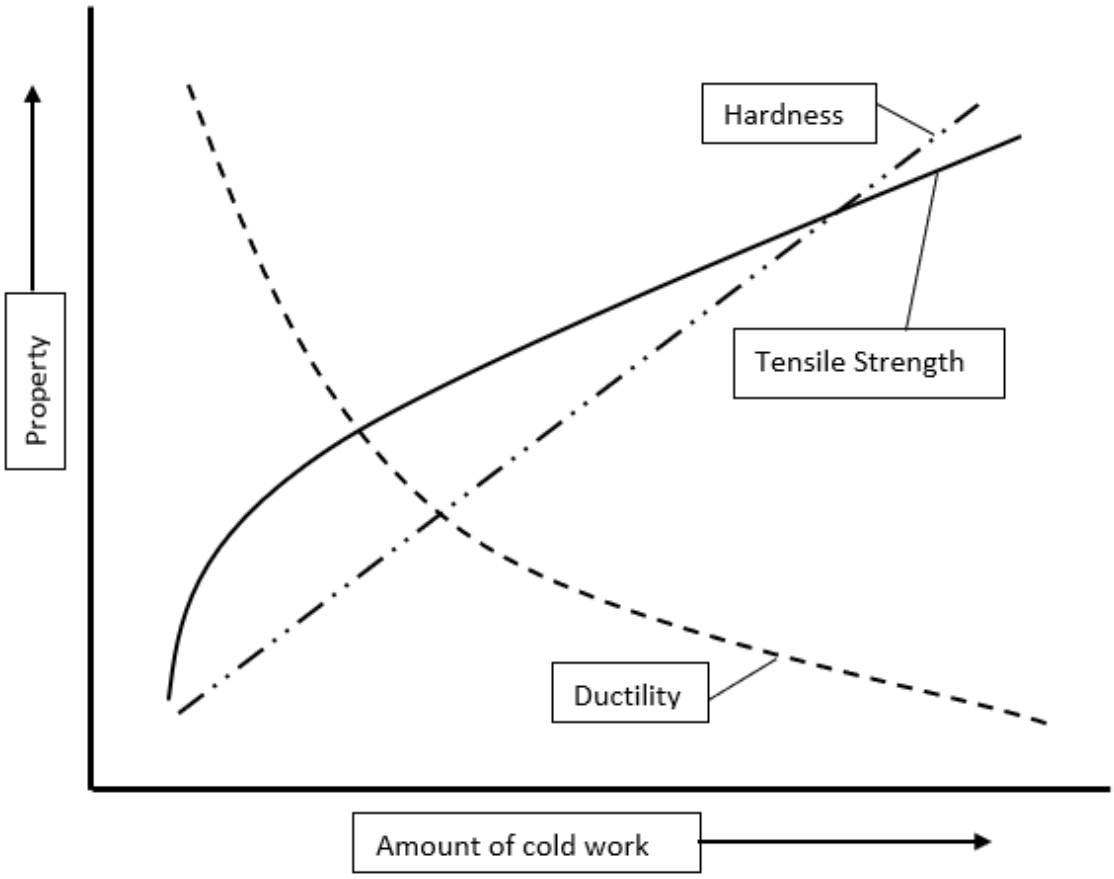

Fig. 2.5 Schematic showing amount of cold work in relation to strength, hardness and ductility (Chaudhury et al., 2010; Olaru, 2011)

Table 2-1 Aluminium Classification (Zahner, 2019)

Heat treatable alloys	Non-heat treatable alloys
2000 – Al-Cu-Mg, used for pipes, plates, and profiles, aircraft industry, usually needs corrosion protection	**1000** – < 99% Aluminium, soft and ductile, used for electrical and chemical applications
6000 – Al-Mg-Si, extrusion, welded and bolted and riveted connections	**3000** – Al-Mn, somewhat higher strength than 1xxx series, high ductility, used for roofing
7000 – Al-Zn-Mg & Al-Zn-Mg-Cu, rolled and extruded profiles, good corrosion resistance, used in structural applications	**4000** – Al-Si-Cu & Al-Si, similar to 3xxx series, good heat and wear resistance used as welding and building materials
8000 – Al-Fe-Si, used for packaging processes, aircraft and military applications, high strength	**5000** – Al-Mg-Mn & Al-Mg, similar to 4xxx & 3xxx series, but has higher strength and responds better to cold working (moderate strength)

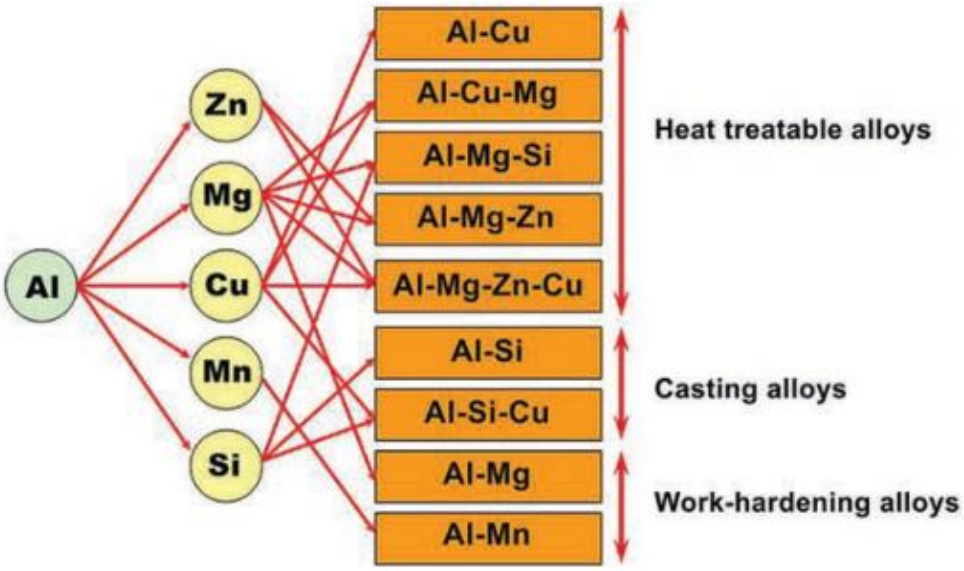

Fig. 2.6 Classification of Aluminium Alloys (Callister, 2014)

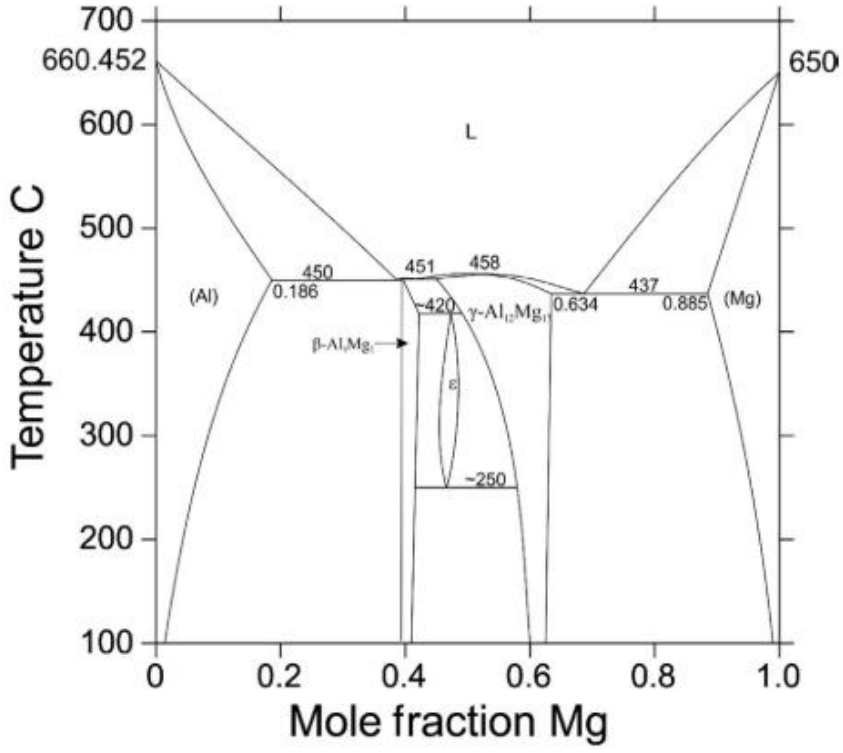

Fig. 2.7 Al-Mg phase diagram (Glazoff et al., 2019a)

These conditions are characterised by a coarse grain microstructure due to a small addition of the second component to the Al matrix which often contains intermetallic phases with different compositions such as β-, ϵ-, γ- and metastable phases. The coarse grain microstructure can be significantly improved by severe plastic deformation (cold work) and induces an ultra-fine-grained microstructure, hence why Al-Mg alloys are strengthened by strain hardening (Kaiser, Datta, Roychowdhury, & Banerjee, 2014; Kogtenkova, Straumal, Mazilkin, Czeppe, & Zieba).

As 5052Al and 5083Al are two Al alloys belonging to the Al-Mg alloys, these will be experimented as a comparison to Scalmalloy. These two alloys can be processed by either casting or extrusion. 5083Al is one of the most commercially used alloys and is mainly utilised in ship structures, pressure vessels and vehicle building as these have good strength and superior corrosion resistance. It has a nominal composition of Mg, Mn, Si, Cr and Fe. Scandium, in particular, has been used in 5083Al alloys since the 1970s to enhance grain refinement and result in an equiaxed grain structure to prevent recrystallization up to high temperatures (Aiura, Sugawara, & Miura, 2000; Jaya Prasad, Rao, Kamaluddin, & Surya, 2018). 5052Al has relatively low strength and is strengthened through severe plastic deformation, where it is mostly used as flat plates and sheets. It also has a nominal composition of Mg, Fe, Cu, Si and Mn (B. Wang et al., 2015).

2.2 Laser Powder Bed Fusion Process - Selective laser melting

This section will discuss the subjects of additive manufacturing (AM), a specific AM laser powder bed fusion (LPBF) process of selective laser melting (SLM), and defects caused by this process. This section is necessary to include before discussing Scalmalloy, since Scalmalloy was specifically developed for LPBF. LPBF process parameters are also discussed here as this directly correlates to the size, number and type of defects that could occur affecting the quality of components being manufactured.

2.2.1 Selective laser melting process

Aluminium is most commonly used in traditional manufacturing methods like casting, extrusion, and forging, but recently it has been introduced into Additive Manufacturing (AM). AM produces 3D-components from 3D-computer model data. A computer model is produced using computer aided design (CAD) software, then converted into an STL (stereolithography) file to be sliced up into layers called g-code data and loaded into the AM machine, where the component is manufactured subsequently in a layer by layer fashion, shown in Fig. 2.8 (Olakanmi, Cochrane, & Dalgarno, 2015). AM is a rapidly evolving area of manufacturing that can manufacture components with reduced weight and increased geometrical complexity (S. Singh, Ramakrishna, & Singh, 2017). AM is used in many industrial fields like aviation, automotive and medical components. There are several different categories of AM one of which is selective laser melting (SLM), which is a part of the AM laser powder bed fusion (LPBF) technologies, and is most commonly used to process metallic alloys, especially Al alloys (Aversa et al., 2019). The LPBF manufacturing process, shown in Fig. 2.9, involves a component built inside an inert chamber where a layer of metal powder is spread onto the build platform. A laser within the chamber is reflected onto the powder, where the laser light melts the powder, but then rapidly solidifies to form a layer. Melting and solidifying of the material consecutively takes place until the component is built according to its computer model data in a layer-by-layer fashion (Aboulkhair et al., 2019). This rapid melting and solidification that occurs when the laser light interacts with

the powdered material is depicted in Fig. 2.10, where heat transfer and changes in the melt pool are shown (Gibson, Rosen, & Stucker, 2010; J. Zhang, Song, Wei, Bourell, & Shi, 2019). When the material begins to melt, epitaxial solidification occurs in the direction of the welding line and crystallisation occurs in the direction of the interior melt to form columnar crystals. The high cooling rates allow for grain growth to be more refined, increasing its strength, while slower rates of cooling can increase grain size causing a weaker structure.

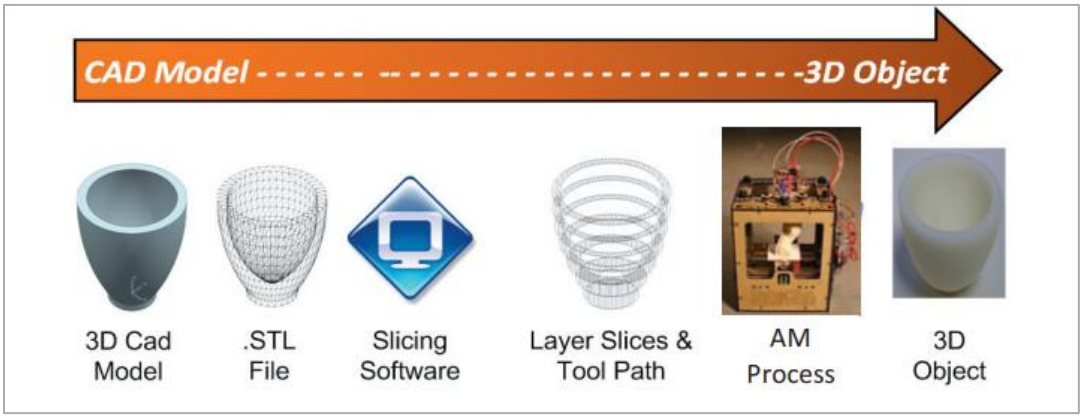

Fig. 2.8 Schematic of additive manufacturing process (Azlin et al., 2022)

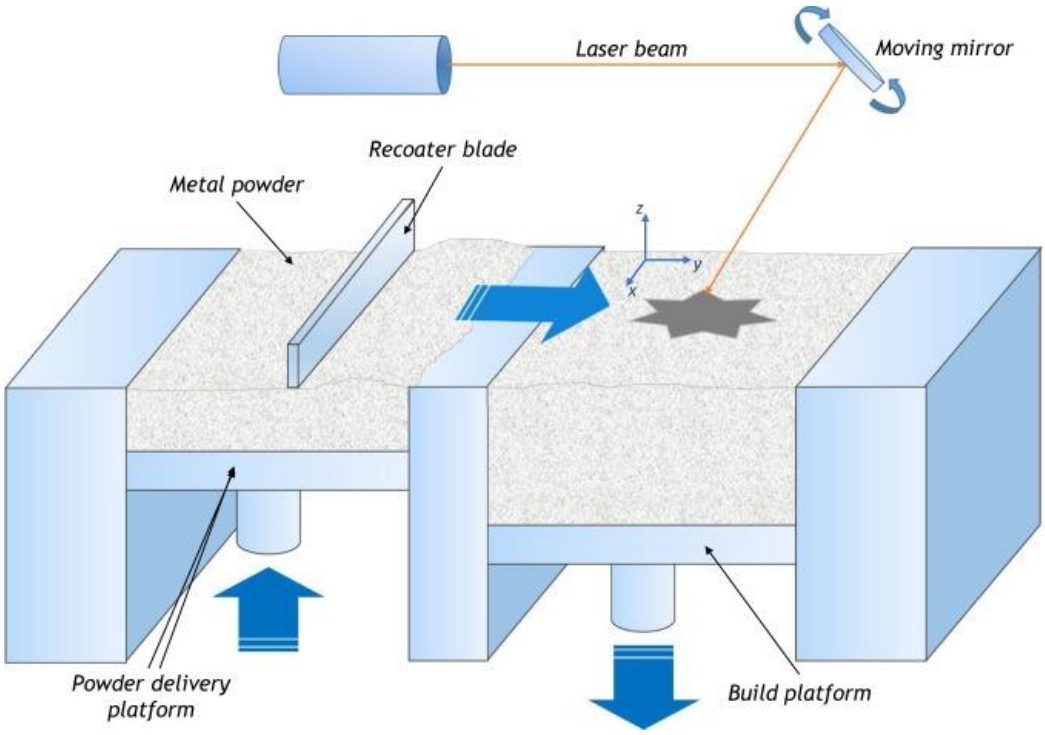

Fig. 2.9 Diagram showing the typical process of LPBF (Griffiths, Scanlan, Eres, Martinez-Sykora, & Chinchapatnam, 2019)

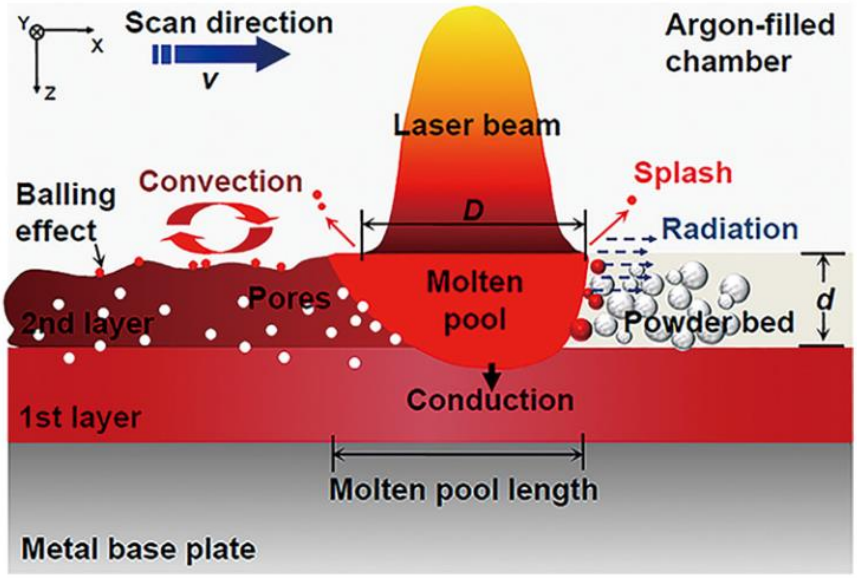

Fig. 2.10 Diagram showing the internal interactions during LPBF process (J. Zhang et al., 2019)

The temperature gradient, *G*, that affects this grain growth is represented as,

$$G = \frac{dT}{dx}$$

Where solidification rate, *R*, is,

$$R = \frac{dx}{dt}$$

And cooling rate can be represented as,

$$\frac{dT}{dt} = G \cdot R$$

Grain size and type are dependent upon $G \cdot R$ and $\frac{G}{R}$ so when $G \cdot R$ increases, crystal morphology will change from dendritic to cellular and from cellular to planar and vice versa. Smooth planar crystal grains will form if the temperature gradient is high (G_1), while a slightly lowered temperature gradient (G_2) may cause constitutional supercooling (shown in Fig. 2.11). This is when a liquid is cooled to below its freezing point without solidifying or crystallising. From this cooling, planar crystals can transform into cellular crystals. A further reduction in the temperature gradient (G_3) will cause a cellular dendritic grain formation and an even further decrease in the temperature gradient (G_4) will cause a dendritic grain formation. It is also possible during this time for new grains to form and become equiaxed. Although, planar growth is the most common grain type within LPBF products, many different grain types may also occur in the microstructure (S. Liu, Zhu, Peng, Yin, & Zeng, 2018; J. Zhang et al., 2019).

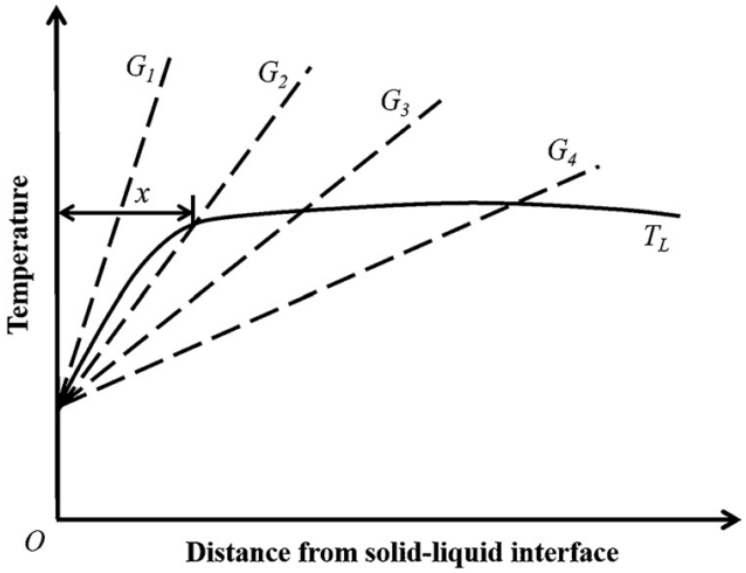

Fig. 2.11 Criteria to induce constitutional supercooling (J. Zhang et al., 2019)

LPBF process parameters control the conditions produced within the machine. These are predetermined by the operator of the machine. The primary process parameters are scanning speed (mm/s), laser power (W), build direction/orientation, hatching distance/ spacing, hatch angle and layer thickness shown in Fig. 2.12. Scanning speed and laser power influence the amount of liquid phase present during the LPBF process and the energy volume density. Energy volume density and the material are important factors as these can affect surface roughness, surface defects, performance, and relative density of the fabricated part (Hanzl, Zetek, Bakša, & Kroupa, 2015; Maamoun, Xue, Elbestawi, & Veldhuis, 2018). Energy volume density is represented by the Equation 2.2 (Wong & Hernandez, 2012),

$$E_d = \frac{P}{V_s \cdot D_h \cdot T_1} \qquad \textit{Equation 2.2}$$

where E_d is energy density (J/mm^3), P is laser power (W), D_h is hatch spacing (mm), T_1 is layer thickness and V_s is scanning speed (mm/s). This equation shows the relationship between scan speed, laser power and energy density (Maamoun et al., 2018). Build direction is the orientation in which a given sample is built with respect to the longitudinal axis and vertical axis of the sample during LPBF. For example, a sample may be printed in an orientation of 0^o, 45^o, 90^o and 180^o with respect to the given axes. Build direction affects the anisotropic behaviour of the material such that it may determine the direction in which elongated grain growth may occur and changes in tensile properties(Hanzl et al., 2015; B. Zhang, Li, & Bai, 2017). Hatch angle is the angle between laser scanning directions and layers. As with build direction, this also influences anisotropic behaviour and affects mechanical properties (Hanzl et al., 2015). Hatch spacing, shown in Fig. 2.12, can affect dimensional accuracy, surface flatness and incur defects (Yap et al., 2015). Finally, layer thickness affects mechanical properties such as strength and plasticity, whereby if layer thickness is thicker than 30µm, than strength can be compromised (Sufiiarov et al., 2017). The magnitude of the affect for each processing parameter depends upon the material,

hence various tests must be carried out to determine the optimal parameters for a material and to ensure reproducibility (Hanzl et al., 2015; Maamoun et al., 2018; Yap et al., 2015).

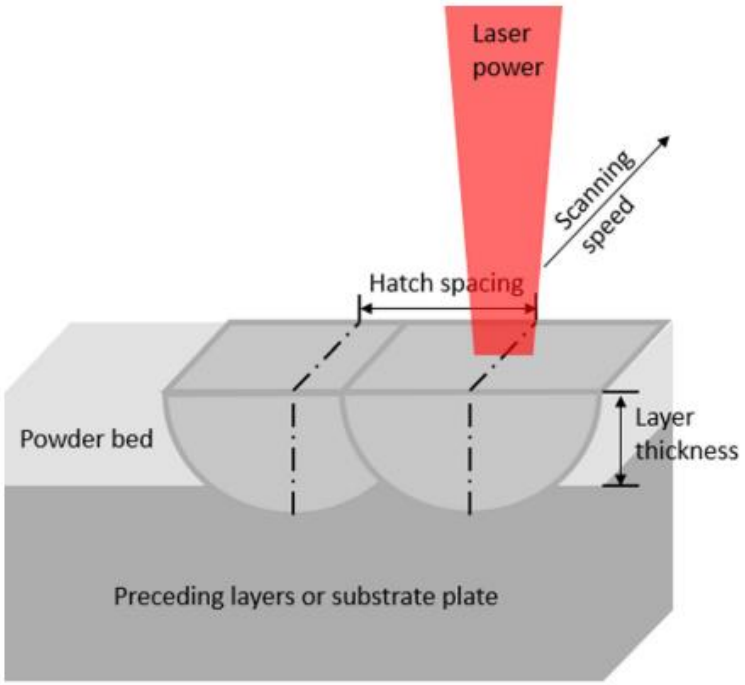

Fig. 2.12 Schematic representation of LPBF process parameters (Yap et al., 2015)

Characteristics and properties of the powdered material, such as flowability, particle size, surface morphology, size distribution and composition, can also affect densities and mechanical properties of the fabricated part. These characteristics are dependent on powder manufacturing process performed by AM companies such as Renishaw, EOS and ReLizer (Chituc, 2017; DebRoy et al., 2018). Flowability describes the behaviour of a powder between each particle when exposed to stress or some disturbance. Good flowability is desirable and correlates to the size morphology of the powder. Smooth spherical morphology allows for good flowability and an ideal packing density. Spherical particle shape and narrower size distribution are optimal with a typical powder size usually within 10μm to 60μm for powder bed fusion (PBF) processes. A small particle size and regular morphology yields a finer microstructure with better surface finish, thinner layers, better performance and better manufacturing capability (N. Li et al., 2019; Vock, Klöden, Kirchner, Weißgärber, & Kieback, 2019).

LPBF is very efficient in its use of material as any leftover powder can be re used and recycled and the powder size does not require moulds, welding or riveting, whereby decreasing production cost and design time. (Olakanmi et al., 2015) These factors along with shorter lead times, smaller operational footprints, customisation, and direct translation of designs due to computer model data are factors that may make it more favourable to use over traditional manufacturing methods. However, LPBF parts can develop defects during this process such as porosity, balling and cracking leading to low density and defective components.

2.2.2 Selective laser melting defects

Porosity is one of the most common defects to occur in LPBF parts, where metallurgical pores and parameter-based pores are the two types of porosity. Metallurgical pores develop from absorption of the shielding gas within the chamber or evaporation of elements, while parameter-based pores are formed by process errors such as incompatible process parameters and material issues. These are identified by mostly spherical morphology and occur on both a microscopic and macroscopic scale. Some may also have sharp edges which can lead to cracking (Galy, Guen, Lacoste, & Arvieu, 2018). Lack of fusion or incomplete fusion holes may also occur due to insufficient laser energy causing a poor re-melting of layers and a poor bond between layers. The shapes of these are not usually spherical, but more jagged and abstract and contain numerous un-melted metal powders within the defect as shown in Fig 2.13. Keyhole pores, shown in Fig. 2.14, are a combination of both parameter-based pores and lack of fusion where insufficient energy and gas entrapment has occurred between layers (Galy, Guen, et al., 2018; Maamoun et al., 2018; B. Zhang et al., 2017). Inner porosity, such as gas pores, shown in Fig. 2.15, may also develop due to entrapped gas within powder particles, which can escape and interrupt the scanning path, while shrinkage porosity can develop due to the inadequate supply of molten metal during solidification (Cherry et al., 2014; B. Zhang et al., 2017).

Balling, shown in Fig. 2.16, may occur due to liquid metal transforming into a ball-like shape due to surface energy (tension) from poor contact with a substrate (J. Zhang et al., 2019). It may also occur from partial melting and complete melting. Partial melting occurs when the melted and un-melted material are heated together resulting in coarse small balls forming on the surface of the component. Complete melting leaves molten metal tracks along the surface and can also occur in the form of lines where they eventually split into small beads upon the surface (Cherry et al., 2014; Hanzl et al., 2015).

Cracking is another common defect and may result from high residual stresses caused by huge temperature gradients present during the rapid melting and solidification in the LPBF process (B. Zhang et al., 2017). Two types of cracks may occur - liquation cracking and solidification cracking. Liquation cracking occurs in materials with many alloying elements due to tensile stresses. Solidification cracking, shown in Fig. 2.17, develops in the last stage of solidification and is initiated by residual liquid between crystals in the mushy zones of the melt pool. Cracking may appear on the surface or within the finished part (B. Zhang et al., 2017).

High porosity, lack of fusion and cracking result in poor mechanical properties and low-density parts, while balling results in a poor surface finish and surface defects. Defects can require additional processing and machining to correct and for some parts, consequently increasing production time and cost. Minimization of defects should be a high priority as these are solely dependent upon LPBF process parameters, process and the powdered material (Galy, Le Guen, Lacoste, & Arvieu, 2018; B. Zhang et al., 2017).

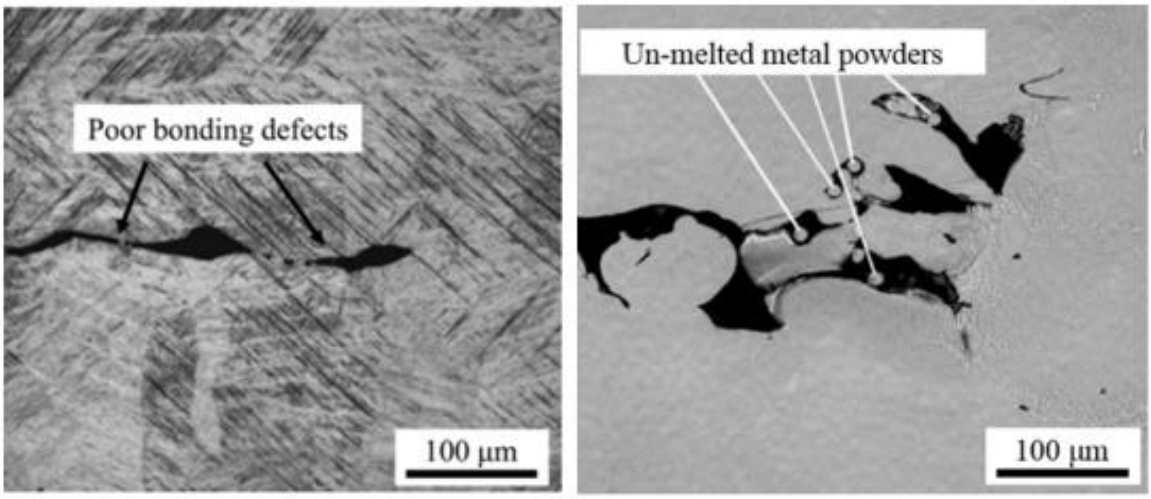

Fig. 2.13 Lack of fusion and incomplete fusion holes on LPBF fabricated parts (B. Zhang et al., 2017)

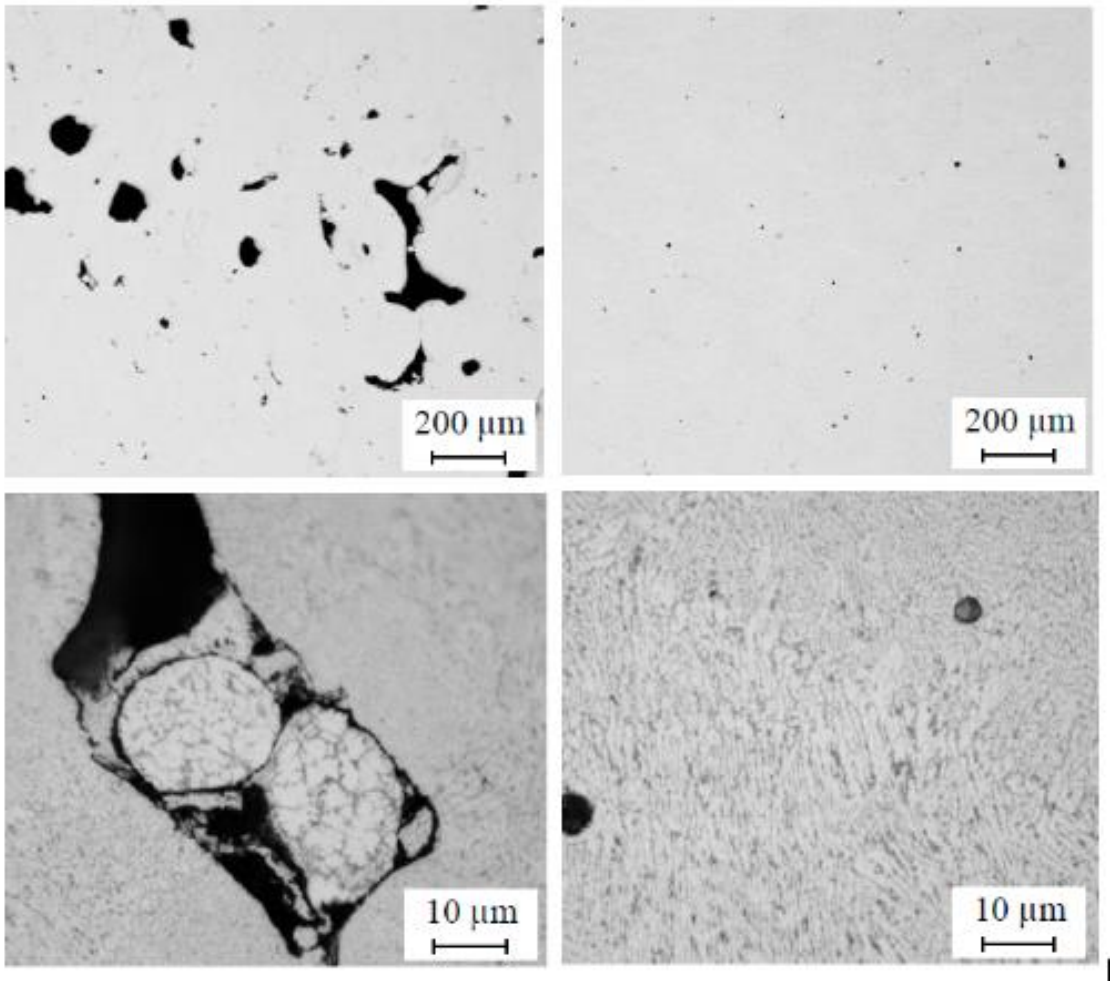

Fig. 2.14 Examples of keyhole pores present on AlSi10Mg LPBF fabricated parts (Maamoun et al., 2018)

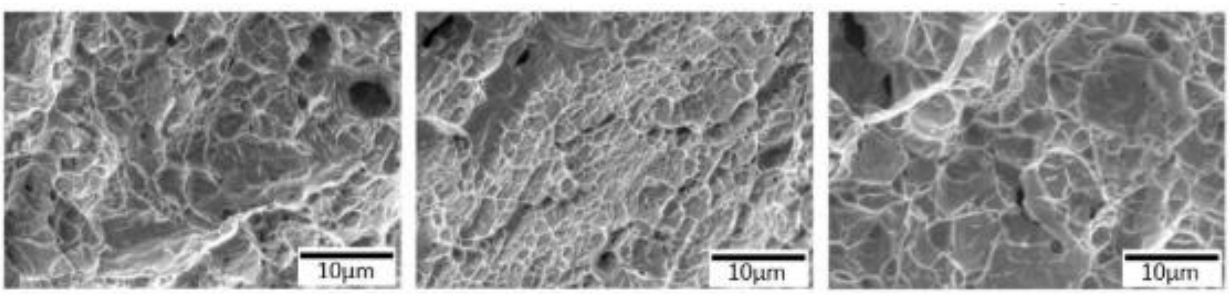

Fig. 2.15 Microporosities -gas pores on LPBF processed parts (Pasang et al., 2021)

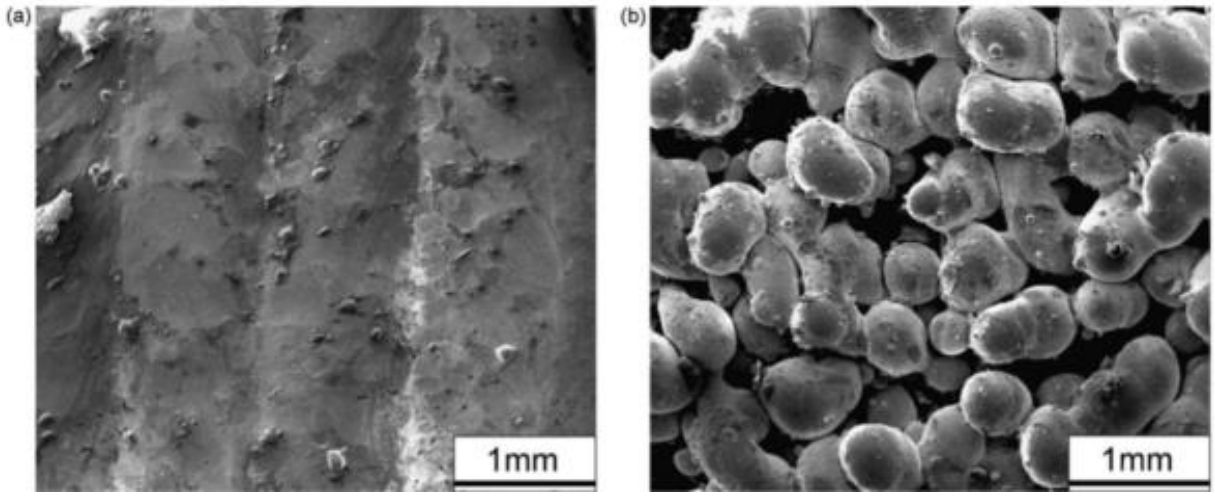

Fig. 2.16 Balling defect present on surface of LPBF fabricated parts (Hanzl et al., 2015)

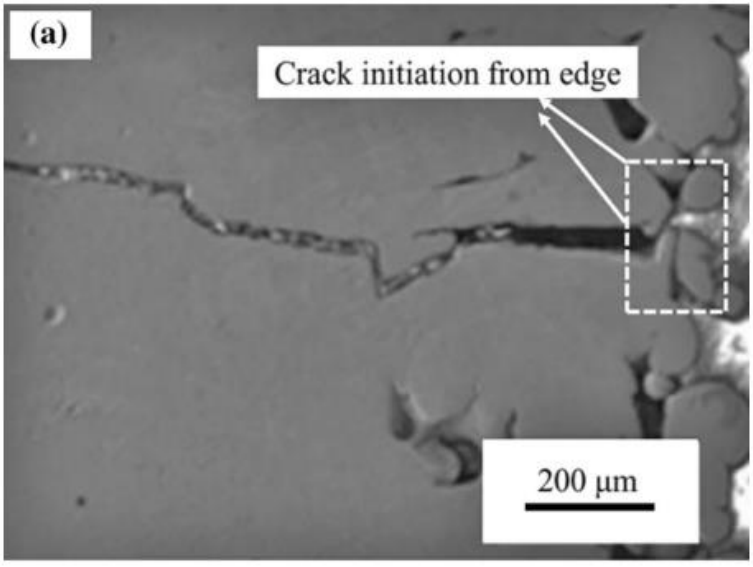

Fig. 2.17 Crack Initiation on LPBF fabricated part (B. Zhang et al., 2017)

2.3 Scalmalloy

This section is solely focused on Scalmalloy. The development, material properties, applications, and physical metallurgy are discussed in the following sections.

2.3.1 Development, material properties and applications

The interest to develop new high strength aluminium alloys for LPBF had grown in more recent years with the growing interest in AM processes and the need for lightweight and geometrically complex components increased. Unfortunately, the use of aluminium in LPBF has eluded many manufacturers for years as the majority of aluminium alloys available today are incompatible with LPBF proesses. The 2000, 6000, and 7000 series of aluminium alloys have solidification cracking tendencies and possess Zn, Mg and Lithium (Li) that tend to evaporate during the LPBF process. Al-Si alloys are commonly processed for use in LPBF due to their ability to withstand these conditions (Aversa et al., 2019), however, challenges to control the high reflectivity, oxidation tendencies, poor spreading of powder, freezing range and thermal conductivity properties of these alloys have proven difficult to hone (Aversa et al., 2019; R. Li et al., 2017). Scalmalloy is an aluminium alloy specifically designed for the LPBF process of SLM by *Airbus Group Innovation* and has been in development for the last 20 years. It is a modified Al-Mg alloy with added scandium and traces of zirconium and manganese. Its composition is given by the manufacturer safety data sheet listed in Table 2-2 (Awd et al., 2017; R. Li et al., 2017). Al alloys can only be processed using SLM in LPBF processes, as opposed to electron beam melting (EBM), since EBM exceeds the nominal melting temperature of aluminium (approx. 660^{o}C) (Awd et al., 2017). Scalmalloy has various applications usually is used in the aerospace, automotive, and medical industries. Although, scandium is expensive with a high buy-to-fly ratio, it's addition to the Al-Mg alloy is necessary and the benefits far outweigh the drawbacks. Therefore, Scalmalloy possesses high strength, ductility and elongation in the as built state and low anisotropic behaviour (Adriaan B. Spierings, Dawson, Voegtlin, Palm, & Uggowitzer, 2016).

Table 2-2 Chemical Composition of Scalmalloy by Specification and Analysis (From SDS Material Sheet given Appendix A)

wt%	**Al**	**Mg**	**Sc**	**Zr**	**Mn**	**Si**	**Fe**	**Zn**	**Ti**	**Cu**	**V**	**O**
Max.	bal.	4.90	0.80	0.50	0.80	0.40	0.40	0.25	0.15	0.10	0.05	0.05
Analysis.	bal.	4.55	0.65	0.30	0.51	0.16	0.14	0.02	0.01	0.01	0.01	0.04
Min.	---	4.00	0.60	0.20	0.03	---	---	---	---	---	---	---

Scandium has been a viable candidate used in doping aluminium alloys since the 1970s originating in Russia with the first recorded effects showing increased mechanical properties and, consequently, further research of this soared in the following decades (Zakharov, 2003).

Fig. 2.18 shows the Al-Sc phase diagram is typically used to describe Scalmalloy. As shown in Fig. 2.18, there are several intermetallic phases that exist such as Al_3Sc, Al_2Sc, AlSc, and $AlSc_2$.

The aluminium to scandium weight ratio for the work on hand (given in Table 2-1) would be 6.6%, indicating that the equilibrium microstructure would consist of α-Al matrix and the intermetallic phase of Al_3Sc in a eutectic reaction that typically occurs at either 0.5w% scandium from the liquid at 660ºC or at 0.55wt% at 655ºC showing the narrow gap between the melting point and eutectic reaction (Murray, 1998; Zakharov, 2003). The narrow range can be attributed to similar liquidus and solidus temperature ranges as scandium has a low coefficient of diffusion for both solid and liquid aluminium. This results in the likelihood of a supersaturated solid solution and at the eutectic temperature the maximum solid solution solubility of Sc in the α-Al matrix is reported to be 0.38%, however this can be increased to between 0.4% and 0.6% for higher cooling rates. The formation of a supersaturated solid solution enables effectiveness of heat treatments like age hardening(Jostein Røyset & N. Ryum, 2005).

Davydov, Rostova, Zakharov, Filatov, and Yelagin (2000) reported scandium had three positive effects in aluminium – the recrystallisation temperature could be positively altered, increased mechanical strength due to the precipitation of Al_3Sc particles induced through age hardening, and the modification of the microstructure. Scandium alters the recrystallisation temperature, shown in Fig. 2.19, by the formation of Al_3Sc precipitates through Zener pinning whereby aluminium's solidification microstructure remains. For instance, the recrystallisation temperature is increased up to 300ºK by 0.5wt% scandium addition (Davydov et al., 2000). Al_3Sc precipitates are highly coherent with aluminium solid solution which increases precipitates and evenly distributes these throughout the matrix due to a low lattice mismatch in the FCC structure of aluminium and the Ll2 lattice structure of the Al_3Sc precipitates. However, if precipitates grow to sizes of 21-40μm, then coherency is lost by Ostwald Ripening. The modification of the microstructure is initiated by seeding of primary Al_3Sc precipitates that are highly coherent with a stable globular structure in hypereutectic Al-Sc alloys, as opposed to the typically dendritic structure, resulting in better mechanical properties. Additionally, scandium improves the weldability of Al to prevent such defects as hot cracking and delamination during high temperature processes such as LPBF (Jostein Røyset & N. Ryum, 2005; A. B. Spierings, Dawson, Kern, et al., 2017).

As with Scalmalloy, scandium is often added to Al-Mg alloys as magnesium can act as a solid solution strengthener. While at times, it can also substitute scandium in the Al_3Sc phase and- it has been reported that magnesium and scandium can reduce each other's solubility in the α-Al matrix. Lastly, the Al_3Sc particles tend to nucleate on Mg-oxides. The addition of just 0.1wt% zirconium can reduce needed scandium content from 0.55wt% to 0.18wt%, and forms the $Al_3(Sc_{1-x}Zr_{-x})$ precipitate which can slow down Ostwald Ripening (Davydov et al., 2000; Zakharov, 2003), while further increasing its strength. Zirconium can also lessen the potential of over-ageing and stabilises the alloy at higher temperatures (Davydov et al., 2000; Marquis & Seidman, 2001; Zakharov, 2003).

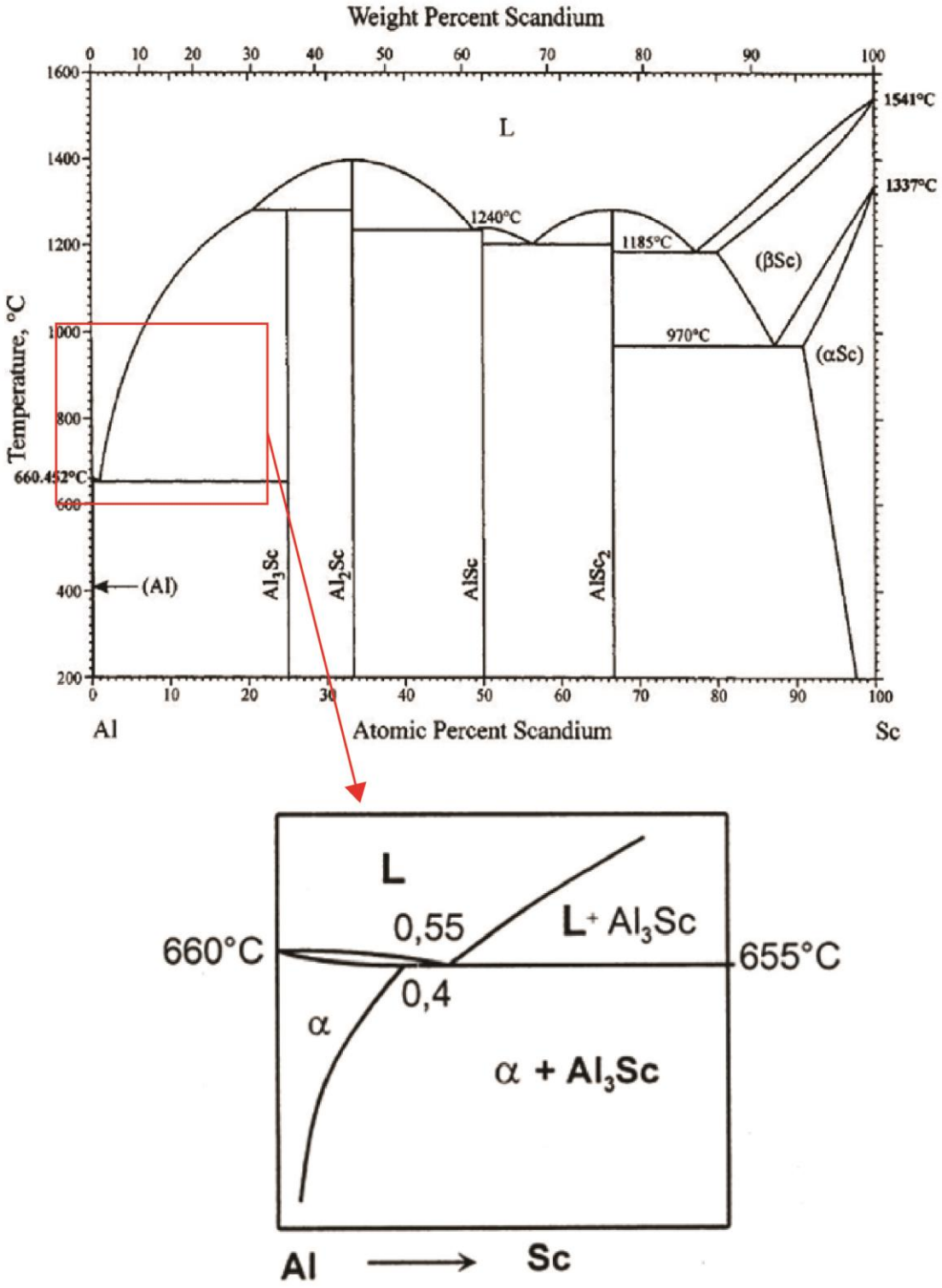

Fig. 2.18 Full Al-Sc phase diagram describing Scalmalloy with the Al-Sc Binary phase diagram on the aluminium rich section of the Al-Sc binary phase diagram enlarged (Davydov et al., 2000; Jostein Røyset & N. Ryum, 2005)

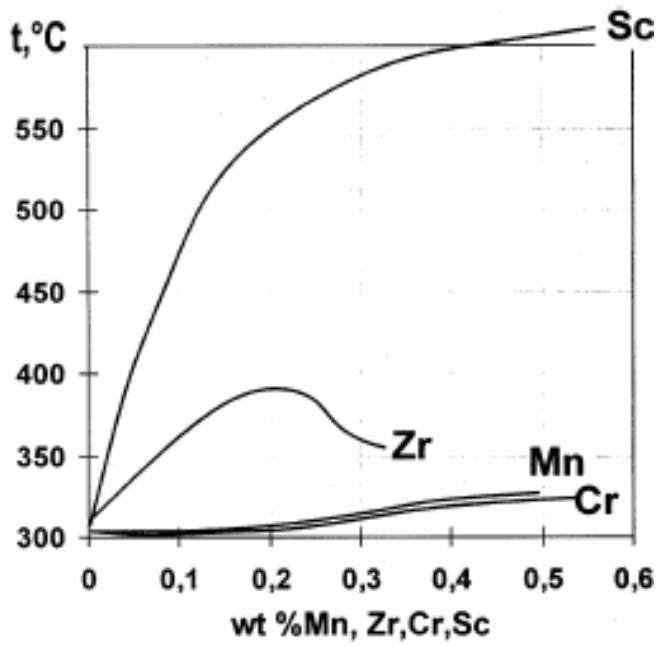

Fig. 2.19 Recrystallization temperature for cold worked binary AL-Transition metals vs Transition Metal Content (Davydov et al., 2000)

Al-Mg alloy and Al-Mg-Sc microstructures are compared in Fig. 2.20 and 2.21. The microstructure of the Al-Mg-Sc alloy has finer grains than the Al-Mg alloy (R. Li et al., 2017). These characteristic effects of scandium in aluminium alloys have led to the successful development of Scalmalloy.

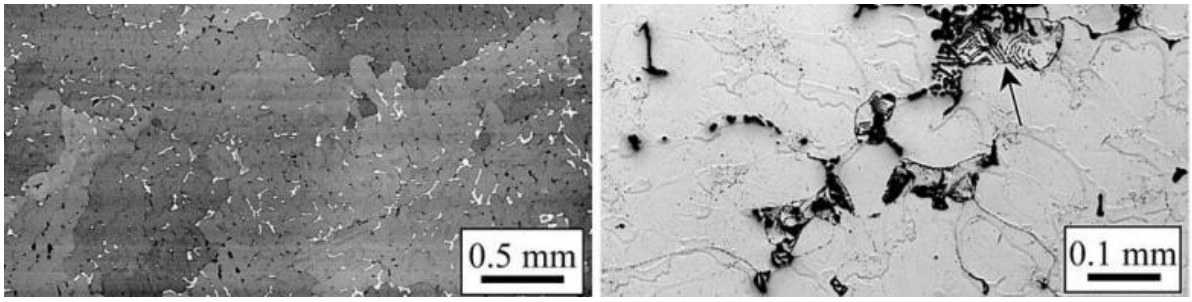

Fig. 2.20 Left- BSE image of cast Al-Mg-Sc alloy microstructure; Right- Magnified optical micrograph of left image (R. Li et al., 2017)

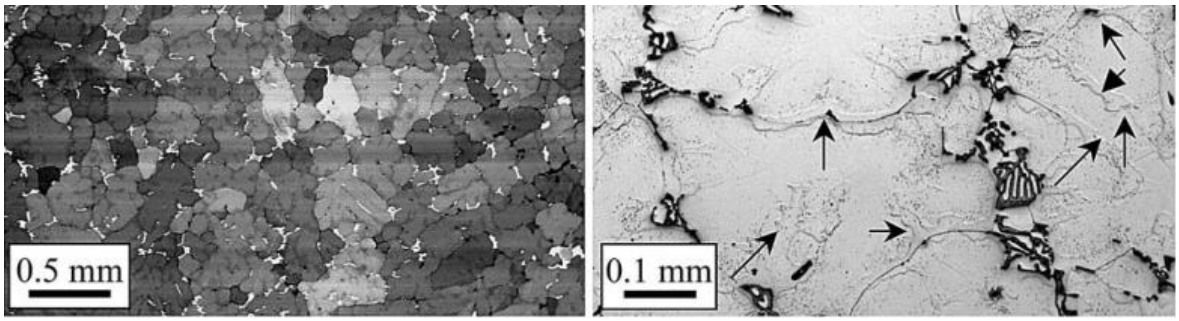

Fig. 2.21 Left- BSE image of cast Al-Mg alloy microstructure; Right- Magnified optical micrograph of left image (R. Li et al., 2017)

2.3.2 Selective laser melting of Scalmalloy

Processing of Scalmalloy has been explored and showed that it can be well processed using SLM. Adriaan B. Spierings et al. (2016) explored energy volume densities (EVDs) between 75 and 240J/mm^3 for hatch distances of 135-165µm with a laser power of 200W. Densities of more than 99% were achieved and reproducibility was sufficient with a mean deviation of 0.09% for varying hatch distances. EVD did not exhibit significant effect on the microstructure and density of samples, except that lower EVD induced further grain refinement. A. B. Spierings, Dawson, Uggowitzer, and Wegener (2018) also studied the influence of scan speed on mechanical properties of as-built samples of Scalmalloy. A 200W laser power and layer thickness of 30µm, with varying hatch distances (135 µm, 150 µm, 165 µm), scan speed (170mm/s, 750mm/s) and EVD (54J/mm^3, 290J/mm^3) were used. Samples produced using 115J/mm^3, had a density of 99.3%, while samples produced using 135J/mm^3 had densities of 99.57% showing no significant changes here. Ideal hatch distances were between 35 and 65% of the laser spot diameter. The microstructure remains unaffected by the varying EVD and scan speeds, except that the fine-grained regions show finer grains (1µm-600nm) for higher scan speeds attributed to formation of Al_3Sc seed crystals. Smaller grain sizes are evident using scan speed of 350mm/s as there is faster cooling rate as compared to 170mm/s. Additionally, structural and mechanical anisotropy remain unaffected by the parameter window (A. B. Spierings, Dawson, Uggowitzer, et al., 2018). R. Li et al. (2017) reported that relative densities appeared to increase with increasing laser power, and scan strategy such that island scanning produced a more consistent powder bed than rotary scanning. Higher EVD reduced defects as it increased temperature, lowering dynamic viscosity. This enables micropores to be filled more easily allowing for a denser microstructure, however too high a temperature led to induced balling phenomena. Visual inspection of the surfaces of samples with changing EVD, shown in Fig. 2.22, appeared to be dense with no signs of any pores, and a low EVD increased balling phenomena detrimentally affecting surface quality. When EVD was increased from 81J/mm^3 to 97J/mm^3, the latter samples showed fewer balling effects and at very high EVDs the sample surface was smooth with almost no balling at all. Some crack initiation was apparent along the molten tracks usually caused by high tensile residual stresses generated by the large temperature gradient from rapid melting and solidification during SLM.

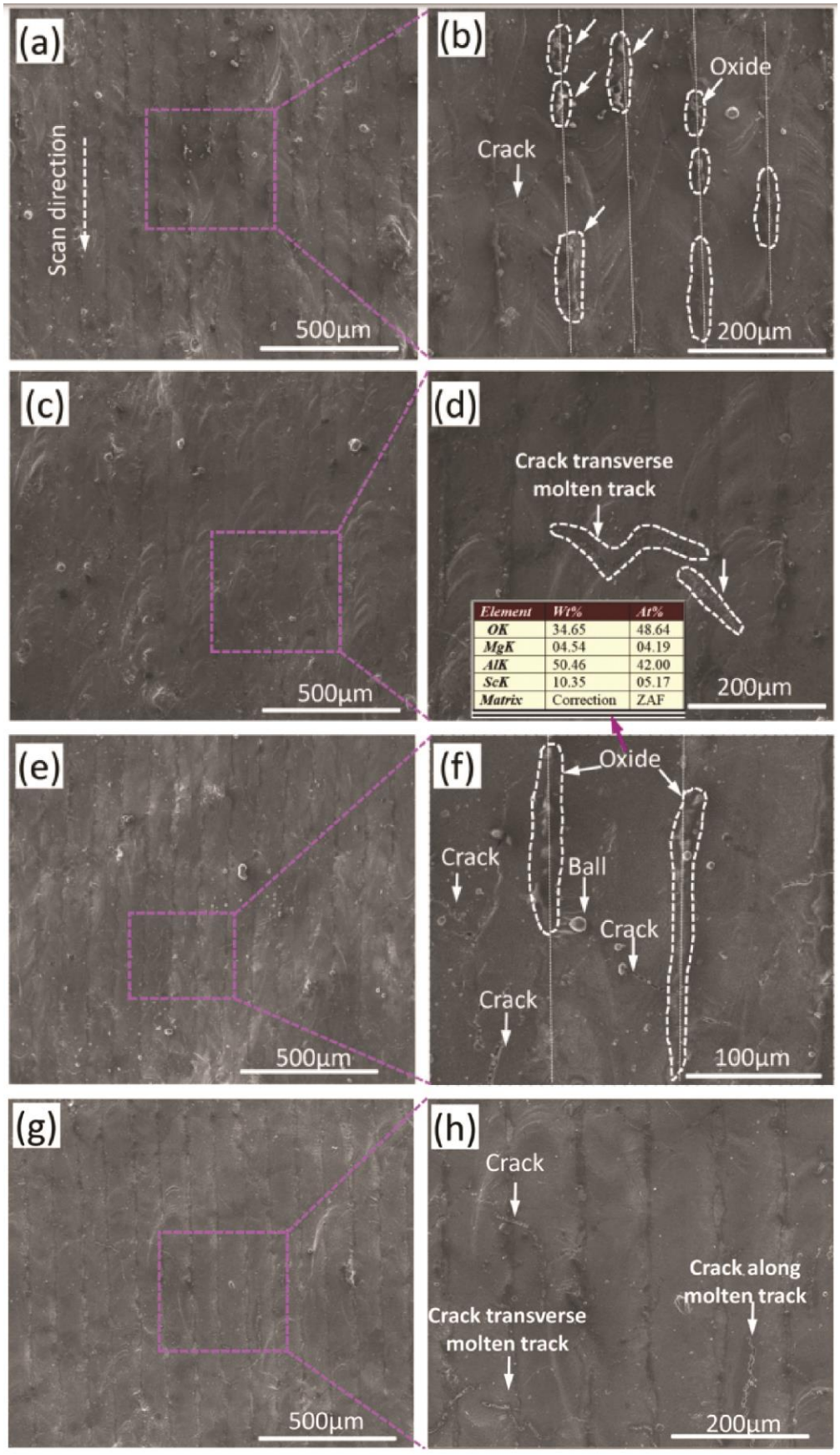

Fig. 2.22 SEM images showing surface morphology of Scalmalloy processed using various EVDs a) 81J/mm^3, c) 97J/mm^3, g) 111J/mm^3, e) 139J/mm^3 with magnified sections indicated by b), d), f) & h), respectively (R. Li et al., 2017)

The phases for different EVD showed no major changes with primarily an Al phase matrix and minor Al_3(Sc, Zr) phase. The weld pool of the samples is shown in Fig. 2.23 with different scan strategies and presented a fine-grained band with a thickness of about 10µm and has columnar grains growing epitaxially along the fine grains. In another study, Koutny et al. (2018) explored a processing window for Scalmalloy with low scandium content, laser power of 325W to 400W, scan speeds between 100-1400mm/s, hatch distance of 100 µm and layer thickness of 30µm. From Fig. 2.24, the optimal EVD was between 60J/mm^3 to 70J/mm^3 and scan speeds between 800mm/s to 1000mm/s. Optimal results with highest density of 98.3% were observed with laser power between 325W to 375W and scan speed of 900mm/s. Large pores appeared in samples produced using 100-500mm/s scan speeds, while scan speeds of up to 100mm/s (55J/mm^3 EVD) produced fusion defects caused by rapid solidification without filling pores completely as discussed by R. Li et al. (2017). Through reproducibility tests, the majority of samples yielded densities of 99.5% with optimal parameters of a laser power of 375W, scan speed of 900mm/s, hatch distance of 100µm. In a study by Awd et al. (2017) the mechanical strength of Scalmalloy was studied in a slow constant fatigue mode. A laser power of 500W to 700W and scan speed between 1200mm/s to 1700mm/s was used, and samples were built perpendicular to the build platform. Keyhole pores were present, which could have been due to too high an energy density, however, relative densities were found to be 99.96%. Additionally, an ultra-fine-grained microstructure occurred due to high cooling rates and rapid solidification with an average (dendrite) grain size of 0.4µm.

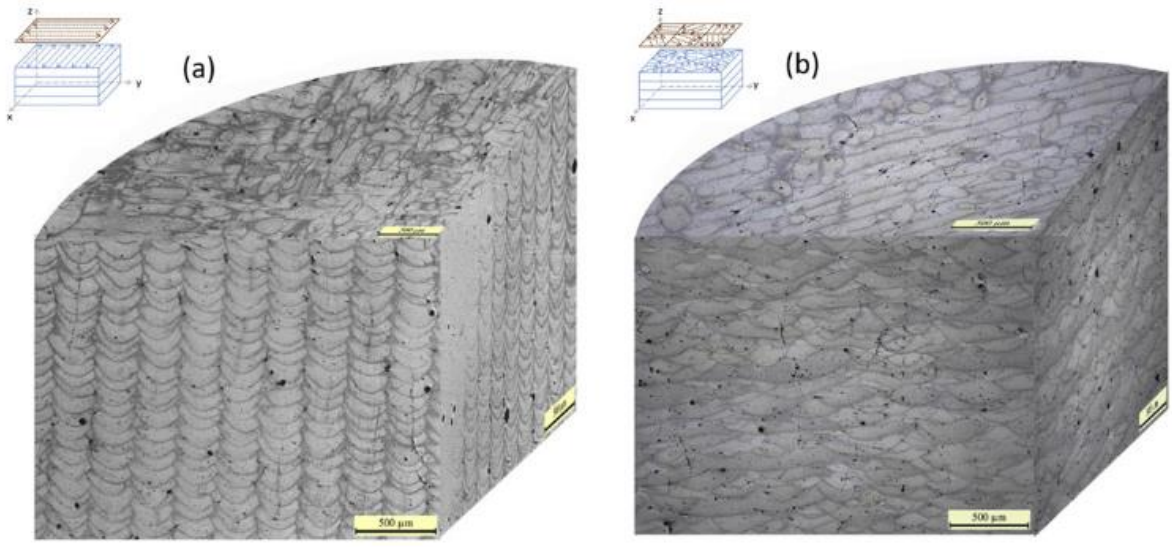

Fig. 2.23 3-D Optical Micrograph showing weld pool in the build plane direction and scan track in horizontal direction with a) 90^o rotary scanning, b) island scanning (R. Li et al., 2017)

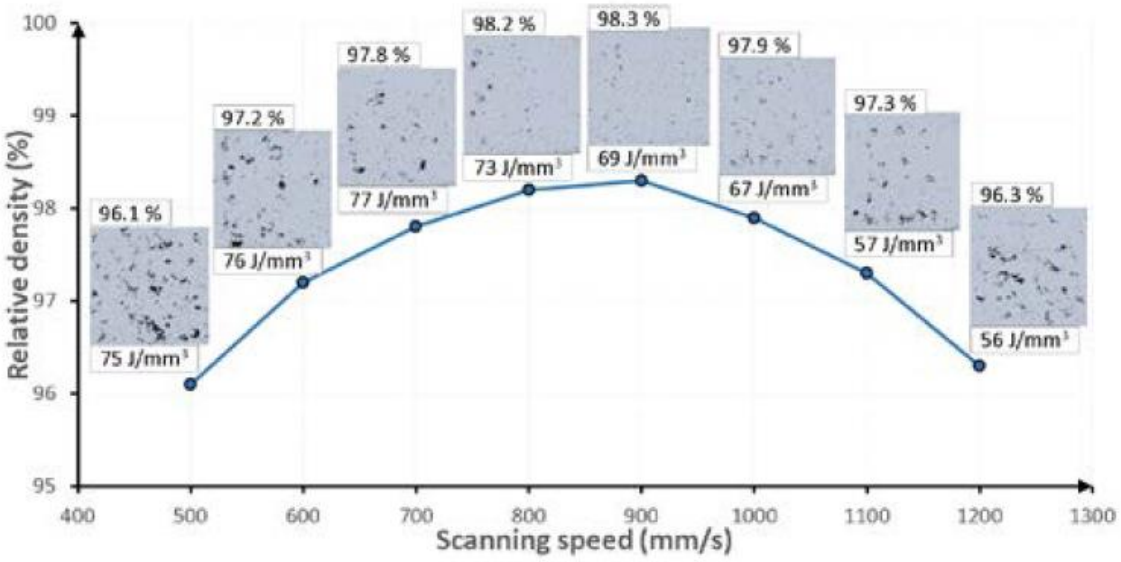

Fig. 2.24 Relative densities and optical micrographs showing defects of samples are compared according to varying scan speeds (Koutny et al., 2018)

In another study by Li et al (R. Li et al., 2019), relative densities were reported to be affected by the change in scan speed and EVD. Increasing laser power with fixed scan speed increased density, while fixed laser power with increasing scan speed reduced density. Irregular shaped micropores occurred with a laser power of 200W and scan speed of 800mm/s attributed to insufficient melting and poor flowability due to low energy input. When laser power, increased to 300W and to a scan speed of 500mm/s, the micropores decline and were rounder as the higher laser power trapped hydrogen and evaporated Mg during the SLM process. When using a laser power of 400W and scan speed of 800mm/s even fewer micropores occurred and full density was achieved.

2.3.3 Microstructure of Scalmalloy

Scalmalloy was developed to be compatible with SLM and offer a microstructure retaining maximum relative density and able to form a supersaturated solid solution in liquid form. Its microstructure is characterized by a unique bi-modal grain structure. The region of fine equiaxed grains are typically known as the FG region, and are located next to coarser columnar grains, also known as the CG region, shown in Fig. 2.25a and 2.25b. A layered microstructure is also evident here which is expected from the additive manufacturing method (R. Li et al., 2017; Schmidtke et al., 2011; A. B. Spierings, Dawson, Dumitraschkewitz, et al., 2018; A. B. Spierings, Dawson, Heeling, et al., 2017; A. B. Spierings, Dawson, Uggowitzer, et al., 2018; Adriaan B. Spierings et al., 2016). The smallest grain size in the FG regions, reported by A. B. Spierings, Dawson, Heeling, et al. (2017), were typically between 150nm-1µm and exhibited no texture, while the largest grain size in the CG region were typically between 2µm to 15µm with typical grain orientation in the build direction and the <100> crystal direction. The CG regions are attributed to the high temperature differences and low density of Al-Mg oxide seed crystals giving rise to

columnar and coarse grain structure (A. B. Spierings, Dawson, Heeling, et al., 2017) . Microstructure of samples cut perpendicular to the build direction, are shown in Fig. 2.25c and 2.25d, where the scan direction showed large weld line cross-sections and weld pool dimensions significantly larger than the laser beam diameter which may be attributed to aluminium's good thermal conductivity. In Fig. 2.26, EDS scans of the microstructure showed $Al_3(Sc, Zr)$ particles pinned grain boundaries prohibiting grain growth shown in the homogenous distribution of Sc, Zr and O distributed throughout the CG region with no Mg build up unlike the FG regions where Mg build up had occurred. Additionally, distinct areas in the melt pool of the transition of FG to CG, shown in Fig. 2.27, with high concentration of particles located in the FG regions, occur along the grain boundary in both grain regions (A. B. Spierings, Dawson, Heeling, et al., 2017). From here, a hypereutectic Al-Sc solid solution was formed and decomposed during cooling to form finely dispersed coherent intermetallic Al_3Sc particles of the cubic LI_2 crystal structure. $Al_3(Sc_xZr_{1-x})$ and mixed particles of Al and Mg directly affect the formation of the FG region caused by the outstanding lattice match to the Al matrix (A. B. Spierings, Dawson, Dumitraschkewitz, et al., 2018; A. B. Spierings, Dawson, Heeling, et al., 2017).

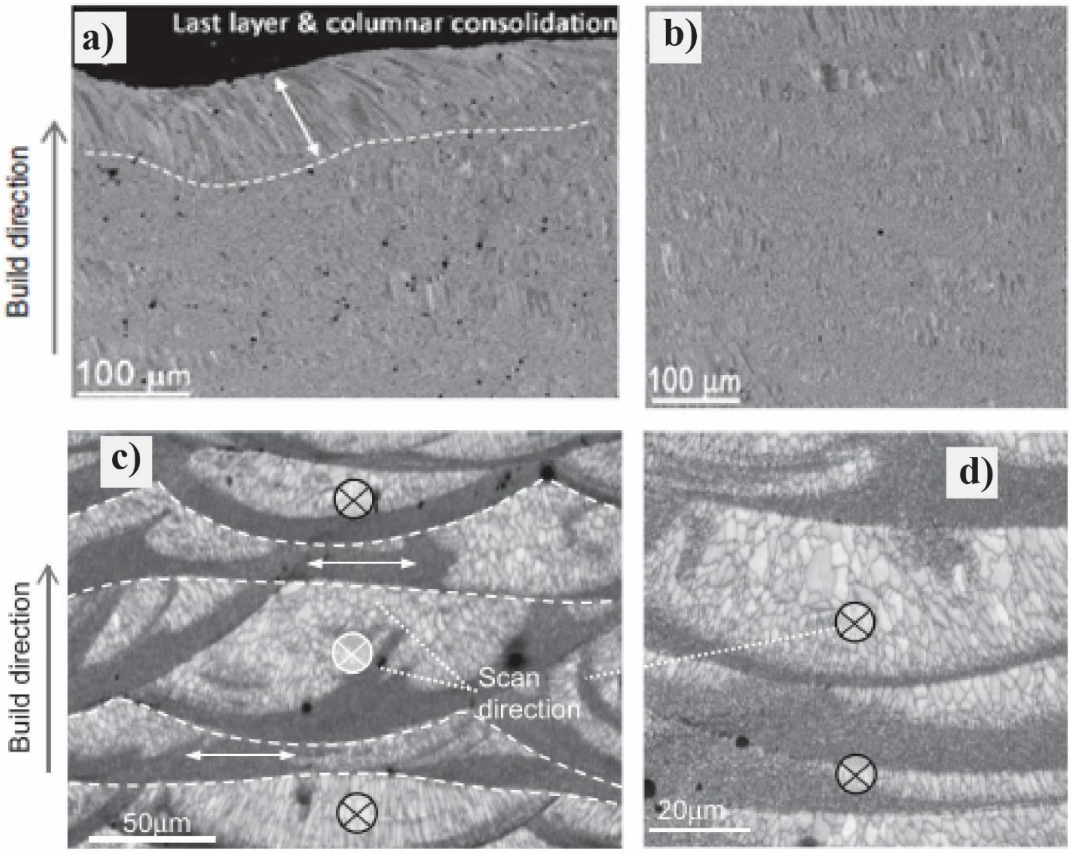

Fig. 2.25 Typical microstructure of as-built Scalmalloy a) upper region on longitudinal axis showing scan tracks, b) mid area built from top to bottom, c) microstructure of 115J/mm^3 sample showing scan direction and alternating layers, d) magnification of c) (A. B. Spierings, Dawson, Heeling, et al., 2017)

R. Li et al. (2017) reported the $Al_3(Sc, Zr)$ particles were separated from the weld pool boundary causing grain refinement and are either square or triangular, shown in Fig. 2.28. Furthermore,

lamellar eutectic lattice had a layer thickness of 20nm and the nano particles Al_3(Sc, Zr) were on average 100nm. In the <001> crystal direction (horizontal plane), equiaxed grains were evident. The weld track boundary resulted in fine grains (less than 5µm), while the central weld track resulted in coarse grains (10µm to 40µm) and parallel to the build direction, grains are columnar. Hence, the microstructure is very different to other Al alloys processed using SLM and traditional manufacturing methods due to this bi-modal grain size distribution (R. Li et al., 2017).

A. B. Spierings, Dawson, Dumitraschkewitz, et al. (2018) investigated the microstructure of selective laser melted Scalmalloy samples that were heat treated and Hot Isostatic Pressing (HIP) treated. The samples were processed using a ConceptLaser M2 machine at 200W and a laser spot diameter of 100µm, 30 µm layer thickness and EVD range of 135J/mm^3 to 238J/mm^3. For the HIPed samples, the usual bi-modal microstructure remains. There is almost no change in the microstructures for these samples compared to the as-built samples, except that the HIPed treatment tends to cause grain growth in the coarse-grained region. The coarsening of the grains by HIPed samples described earlier was due to the inability for denser grain boundaries to form, like that in the fine-grained region. Heat treatment allows the remaining Sc and Zr trapped in solid solution due to high cool rates during SLM to precipitate coherent Al_3Sc and $Al_3(Sc_xZr_{1-x})$ particles – density of precipitates increased from 0.5-1.0 x 10^{23} to between $3x10^{23}$ m^{-3} and $5x10^{23}$ m^{-3}.

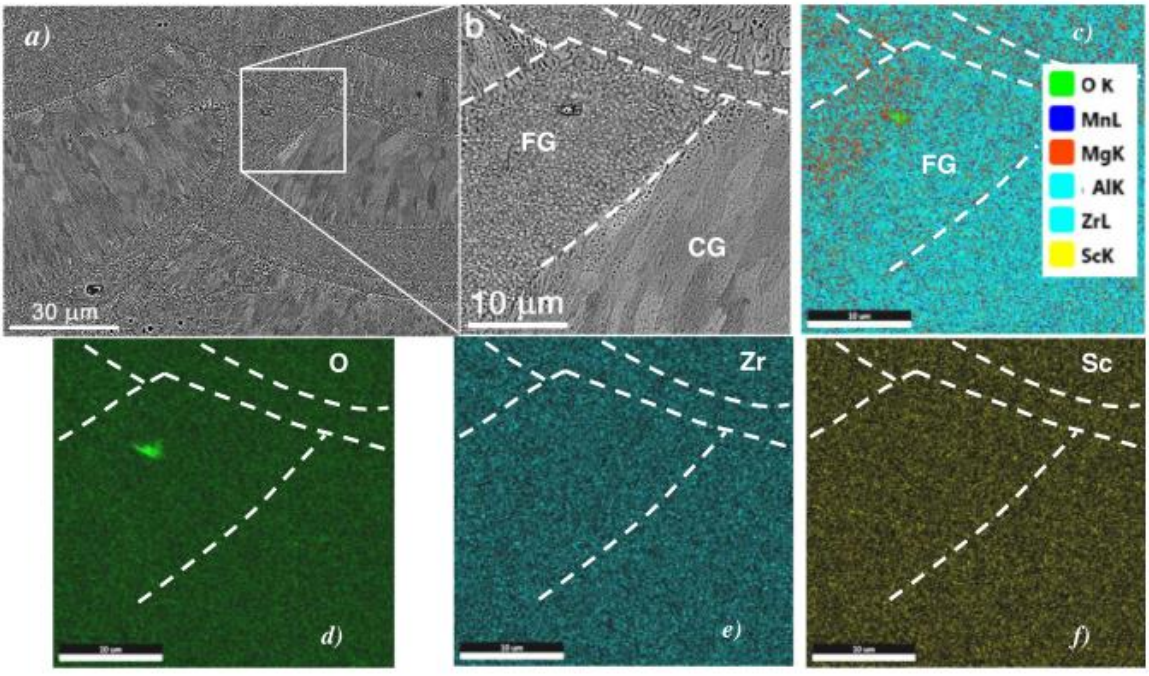

Fig. 2.26 EDS scans of FG and CG regions: a) microstructure of FG and CG region, b) a) magnified, c), d),e) EDS mapping showing highlighted elements (A. B. Spierings, Dawson, Heeling, et al., 2017)

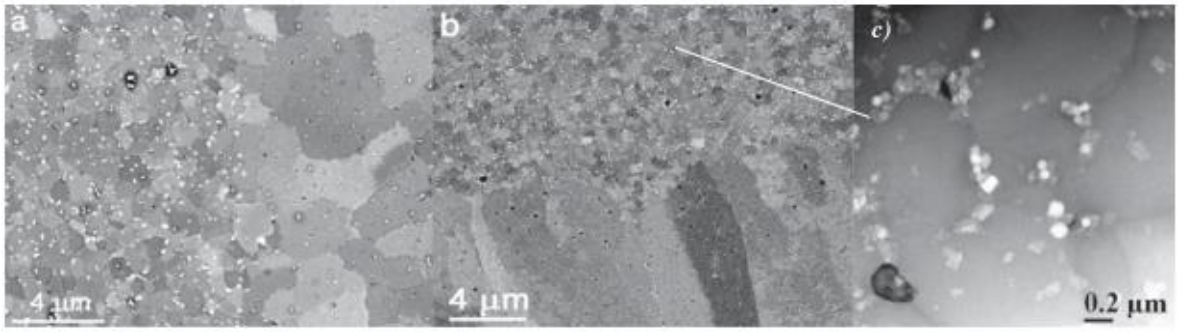

Fig. 2.27 SEM Images of bi-modal grain structure and grain boundaries with precipitates (A. B. Spierings, Dawson, Heeling, et al., 2017)

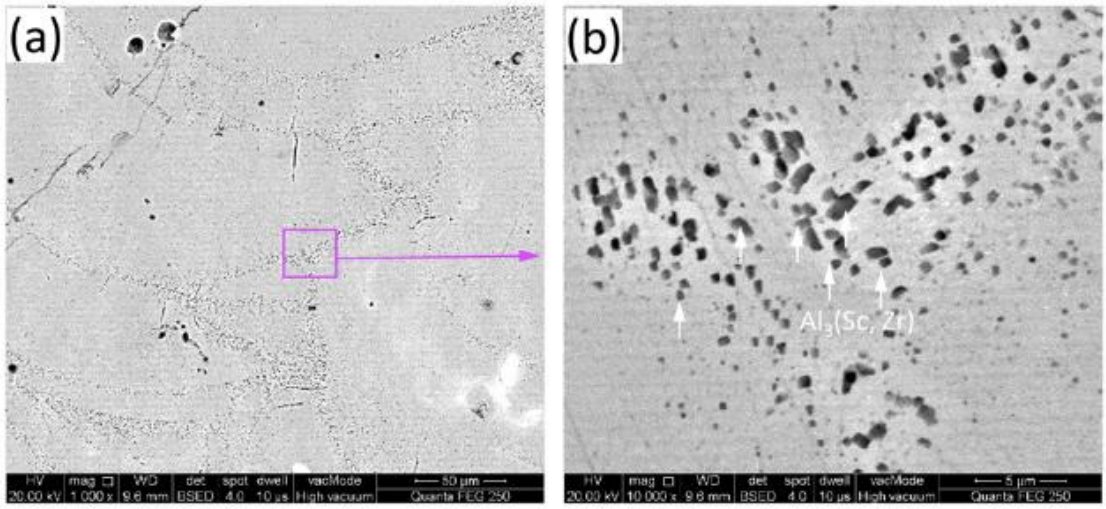

Fig. 2.28 SEM image of cross sections of SLM processed samples showing distribution of $Al_3(Sc,Zr)$ particles a) & b) perpendicular to build direction (R. Li et al., 2017)

2.3.4 Mechanical properties and heat treatment of Scalmalloy

Scalmalloy is normally heat treated for precipitation hardening after being built, however at times precipitation may occur during the SLM process (Jägle et al., 2016). Fig. 2.29 show the 4 stages of possible heat treatment (precipitation) a component undergoes during SLM. Stage 1 is material atomization, stage 2 is intrinsic heat treatment occurring during the SLM process, stage 3 is through high temperature peaks and stage 4 is by regular heat treatment of the final component.

The risk of precipitation hardening occurring for the first three stages are unlikely as precipitation should be supressed due to the rapid cooling rates, but there is possibility. A study by Jägle et al. (2016) reported no premature precipitation occurred during gas atomization of the Scalmalloy powder further confirming high temperatures and rapid cooling rates are high enough to induce a supersaturated solid solution within Scalmalloy. Typical cooling rates in the SLM process is similar to that of gas atomisation (10^6 K/s) (A. B. Spierings, Dawson, Heeling, et al., 2017), whereby suppression of precipitation can be assumed. Hence, if premature precipitation were to occur during the SLM process, it would be due to the intrinsic heat treatment, shown in Fig. 2.29.

Schmidtke et al. (2011) reported tensile (>520MPa) and yield strengths (>500MPa) of Scalmalloy samples after heat treatment of 325ºC, according to build direction and can be observed in Fig. 2.30. The average elongation was 14% and reduction in area was 20%. Variation between strengths of samples built in different directions was less than 5%, hence anisotropic behaviour was low. Variation in area and elongation for both build directions was also negligibly low. Ductile and fast fracture occurred as samples broke at 45º angles. Additionally, a significant increase in hardness from 105 to 177HV (Fig. 2.31) was reported due to the artificial ageing process of 325ºC/4h that enabled the formation of Al_3Sc precipitates. Although, Schmidtke used 325ºC/4h as ageing temperature and holding time, other authors (explained in the following) explored other ageing temperature ranges and holding times and observed their effects.

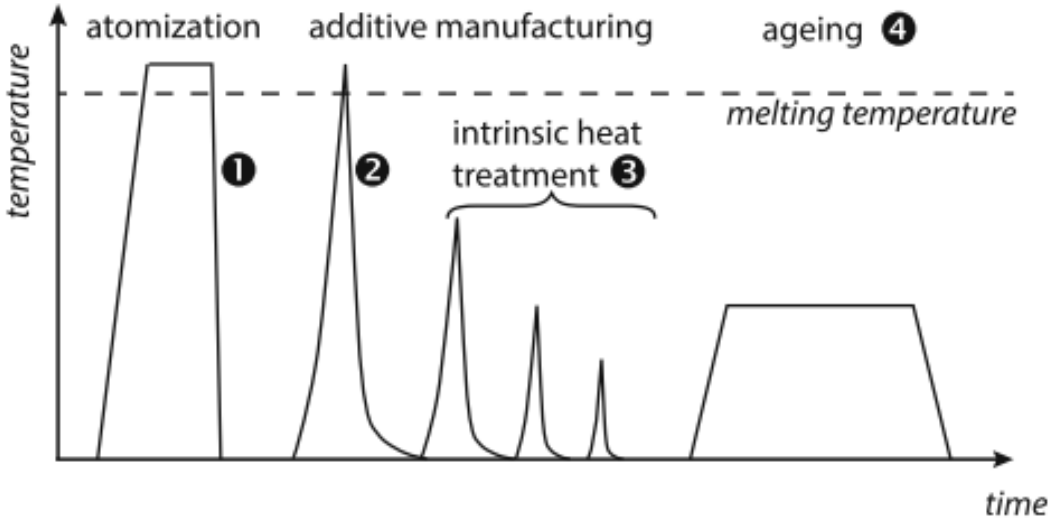

Fig. 2.29 Temperature-time profile of the process that an additively manufactured component is subject to during manufacturing. Each number represents the different stages within the process and when precipitation may occur (Jägle et al., 2016)

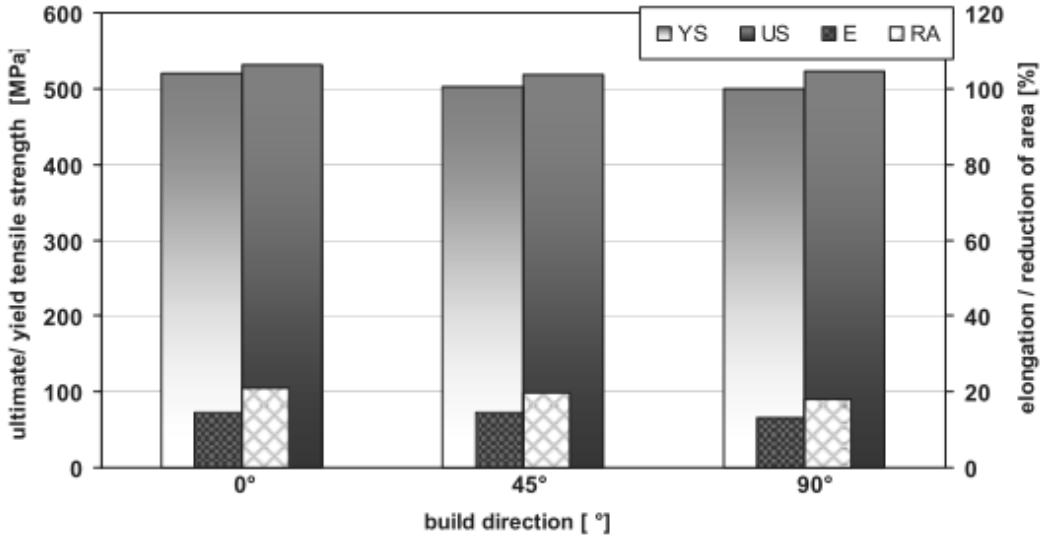

Fig. 2.30 Mechanical properties of samples built in the 0º, 45º, and 90º directions. Yield stress, UTS and elongation are compared with heat treatment of 325ºC/4h (Schmidtke et al., 2011)

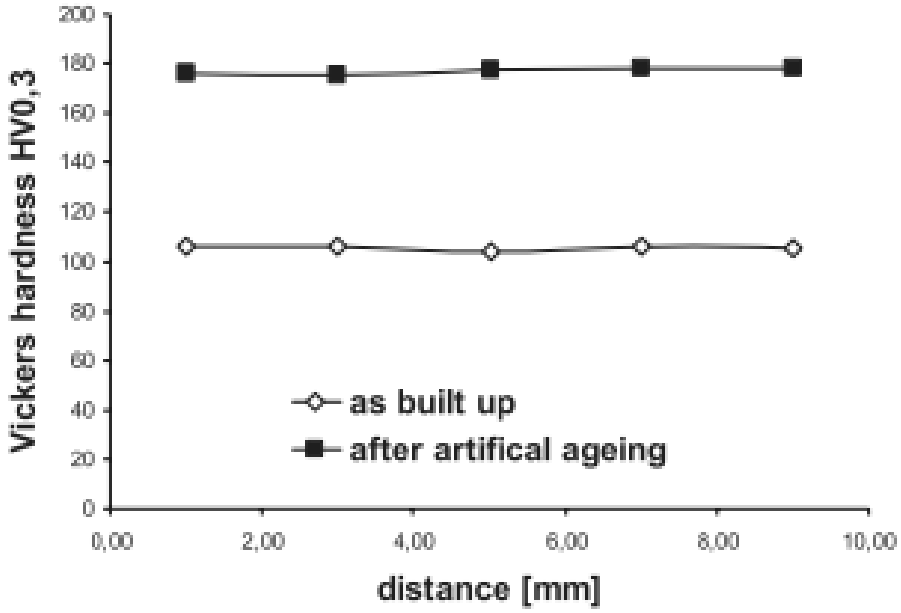

Fig. 2.31 Microhardness curves of test cubes on as built and artificially aged at 325°C/4h samples (Schmidtke et al., 2011)

R. Li et al. (2017) performed microhardness testing on the densest samples and found it to be higher than a typical Al-Mg-Sc-Zr alloy cast part, yet lower than a solutionised annealed alloy. Corrosion resistance was also higher than the cast alloy with a maximum compression strength of 390.25MPa. Best, Maeder, Michler, and Spierings (2018), found that precipitation hardening induced by annealing was evident in both the FG and CG regions. Near-isotropic behaviour was reported for macroscopic samples in both regions of the microstructure, further confirming claims by Schmidtke et al. (Schmidtke et al., 2011) of near-isotropic behaviour of Scalmalloy in their work. As reported by previous authors (A. B. Spierings, Dawson, Dumitraschkewitz, et al., 2018; A. B. Spierings, Dawson, Kern, et al., 2017; Adriaan B. Spierings et al., 2016), Scalmalloy samples processed in SLM result in the Al matrix being supersaturated with fine Al_3Sc and Si precipitates which provide optimum plastic flow properties. A. B. Spierings, Dawson, Kern, et al. (2017) reported the effects of heat treatment on SLM processed Scalmalloy observing temperatures ranging between 250 to 500°C/4h. Hardness increased for temperatures up to 400°C, but any higher temperatures resulted in reduced hardness, thought to be caused by loss of coherency of $Al_3(S_{cx}Zr_{1-x})$ particles. Hardness was observed at annealing temperatures of 275, 325 and 375 °C with holding times between 0.5h and 24h. An ageing temperature of 325 °C with a holding time of less than 4h proved to achieve high hardness than other combinations. Ageing at temperatures below 300°C slowed precipitation and lengthened holding times. For instance, hardness values achieved at ageing conditions of 325°C/1h equalled that of 275°C/24h. Preferred ageing temperature was found to be between 325°C to 350°C showing that some variations in temperature are not significant. Tensile strengths of both vertically and horizontally built samples were reported and showed very little anisotropy with differences of 2.6% for vertically built and

2.7% for horizontally built. Yield strength, however, is slightly higher with 3.8% for the vertical built and 10.8% for the horizontal built samples.

A study conducted by R. Li et al. (2019) observed the effects of aging heat treatment on the microstructure and mechanical properties of Scalmalloy. Annealed samples with varying laser power, but constant scan speed of 800mm/s resulted in higher hardness than as-built samples (approx. 85HV). Hardness increased with temperature during ageing until it reached maximum hardness of 125HV, then it decreased with increasing temperature. They found ideal ageing parameters for their experiments were between 300ºC and 350ºC for aging times between 4 and 12h and are consistent with ageing temperatures reported by various authors (R. Li et al., 2019; Schmidtke et al., 2011; A. B. Spierings, Dawson, Kern, et al., 2017). Stress-strain curves were observed at different ageing temperatures. As-built samples had a yield strength of 166MPa, a tensile strength of 222MPa and elongation to failure of 10%. After ageing for 2h, yield strength increased to 289MPa, tensile strength to 373MPa and elongation to failure to 32.5%. After 12h of aging the elongation to failure dropped sharply, yet the strength increased slightly. Optimal aging condition was at a temperature of 325ºC with an ageing time between 2h and 6h. Al_3(Sc, Zr) precipitates, shown in Fig. 2.32, occur mainly at the grain boundaries, while the number and size of the precipitates increased with increasing ageing times. No evidence of high dislocation density was found in the columnar grain regions, but dislocation density can be observed in the original phase matrix. Fracture micrographs, shown in Fig. 2.33, of the samples show cleavage facets and few dimples leading to the poor strength and low ductility in the as-built samples. Large amounts of dimples (2-5µm in size) can be seen on the fracture surface of the sample aged at 325ºC/4h, showing that strength and ductility were improved. The sample aged for 16h at 325ºC had dimple sizes of about 4µm, where pores can be seen throughout causing a lower ductility seen in all the samples, but higher tensile strength (R. Li et al., 2019). .

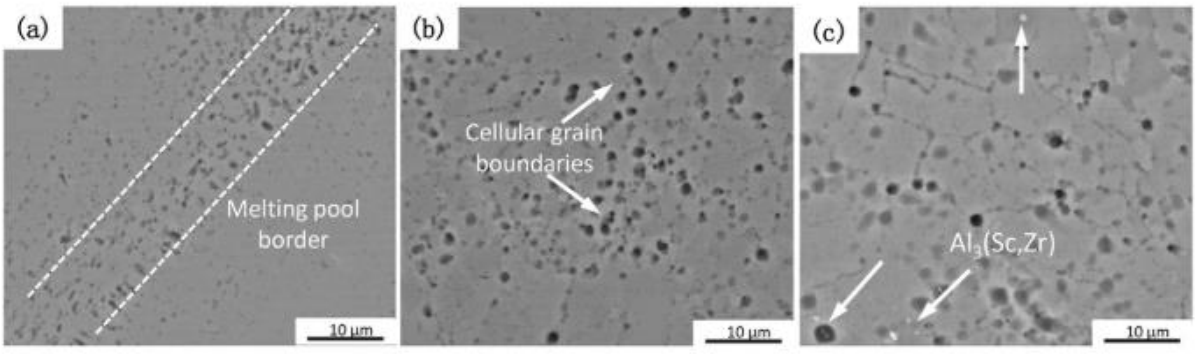

Fig. 2.32 SEM images of the distribution of Al_3(Sc, Zr) particles at 83 J/mm^3: (a) as-built (b) 325 °C/4 h, (c) 325 °C/12 h. [49] (R. Li et al., 2019)

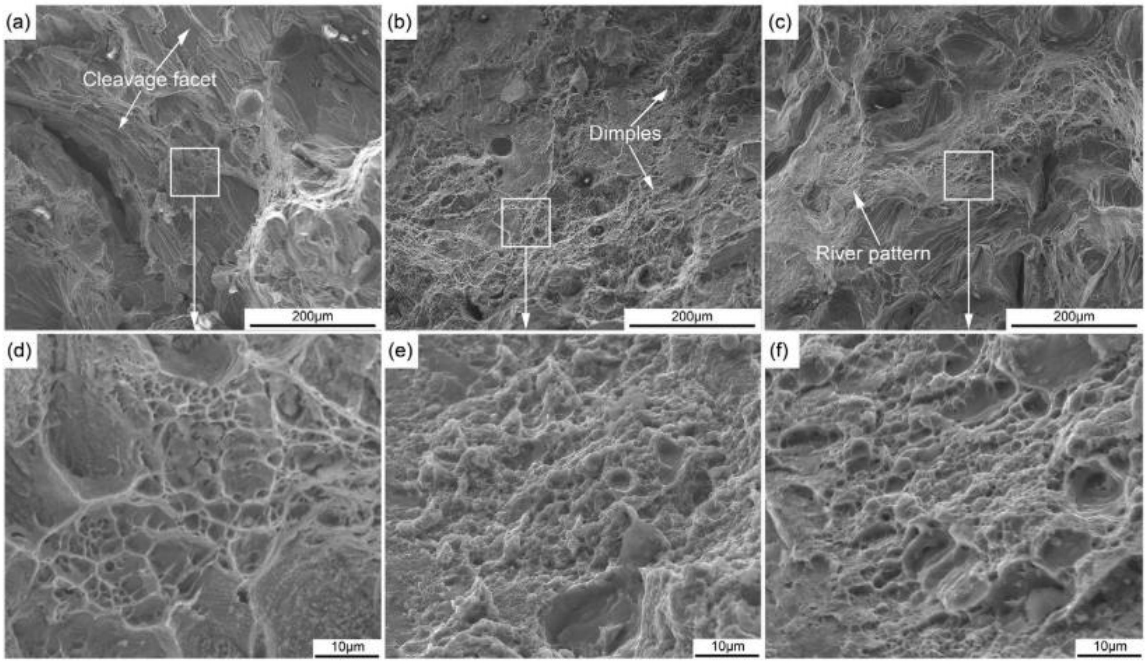

Fig. 2.33 SEM fracture images showing fracture surfaces a&d) as-built, b&e) 325ºC/4h, c&f) 325º/16h (R. Li et al., 2019)

Ageing temperatures between 200ºC and 500ºC and holding times between 1h and 24h have been explored, yet the ideal ageing conditions for Scalmalloy is 325ºC/4h. Spierings et al. (A. B. Spierings, Dawson, Dumitraschkewitz, et al., 2018) showed for this ageing condition, Scalmalloy yielded high hardness and tensile strengths by sufficient precipitation of Al_3Sc and $Al_3(Sc_xZr_{1-x})$ particles. Additionally, grain size distribution and microstructural features for the samples heat treated at 325ºC/4h were not significantly altered. This extremely stable microstructure was attributed to the combination of intergranular particles of $Al_3(Sc_xZr_{1-x})$.

Fatigue strength of Scalmalloy is also important as this can occur due to crack propagation, which is the crack initiation stage where premature propagation of a crack originates from its material micro-defects. The progressive propagation of a short crack will determine the fatigue life of the component. The fatigue limit can be defined as the maximum stress level below where a crack or an existing crack will not propagate into failure within a set life span of the component (Curtis, de los Rios, Rodopoulos, & Levers, 2003). Awd et al. (2017) investigated the fatigue strength of additively manufactured Scalmalloy and AlSi10Mg in a stable fatigue mode of loading. Findings showed that both failed at (approx.) 10^5cycles under stress amplitude range between 120 and 140MPa. A study by Schneller et al. (2021) studied the fatigue life of Scalmalloy using R=-1. Findings showed that heat treatment should be applied before fatigue tests as the stress amplitude increased from 51.6MPa to 126.4MPa after heat treatment of 325ºC/4h attributed to the formation of Al_3(Sc, Zr) increasing strength and further grain refinement. Qin et al. (2021) reported the effect of defects on the fatigue behaviour of a selectively laser melted Al-Mg-Sc-Zr alloy. A stress amplitude of 90MPa and 144MPa, with a decrement of 54MPa, yielded a fatigue life (R=0.1) between 10^4 to 10^7 cycles. For samples that did not fail at 10^7 cycles, fatigue strengths were

100.5MPa (19% of UTS) and almost a 50% survival rate. Also, defects did affect the fatigue strength as presence of these lead to crack initiation and propagation evident as fatigue strength of Scalmalloy was lower when compared to cast Al7075-T65 alloy. Chernyshova, Guraya, Singamneni, Zhu, and Chen (2021) also studied the fatigue crack growth behaviour regarding stress intensity factor threshold. They found that stress intensity factor was not dependent on orientation of crack growth and build direction in as built and heat-treated conditions due to as crack propagation tends to follow the bi-modal grain structure regarding equiaxed grain and columnar grains.

2.3.5 Summary

Scalmalloy has high reflectivity tendencies consistent with typical aluminium alloys. In the SLM process, a laser power of 200W or greater is required to counter this, and relative densities appear to increase with increasing laser power. Hatch distances should also be larger than the laser diameter (as given by machine specifications) as scan track width areas tend to expand due to the high thermal conductivity of aluminium. However, too large a hatch distance can lead to a loss of density. Energy volume density was the primary parameter that affected grain refinement and apparent defects. Hence, these factors need to be considered when processing Scalmalloy and determining a suitable process parameter window. Furthermore, the inherent bi-modal microstructure in Scalmalloy is not affected by processing parameters and remains constant. However, grain size, type and precipitates are affected by the SLM process parameters and so these should be optimised to obtain smallest grain size and development of precipitates to produce optimum mechanical properties. Additionally, the mechanical properties of as-built Scalmalloy are reasonable but can be positively affected when heat treated. The optimum heat treatment time was found to be at 325^{o}C/4h, however the heat treatment conditions can be further explored. There is a current gap in the literature in exploration of various heat treatment conditions to optimise strength, hardness, and ductility and to determine the effect of heat treatments on cold rolled samples of Scalmalloy, where cold rolling is discussed in the next section.

2.4 Cold rolling process

Cold Rolling is a type of cold working method, where a metal is wedged between two rollers and pushed through at a certain velocity reducing in material thickness, and usually performed at ambient temperatures or a point below the recrystallisation temperature of the material. A typical cold rolling process is shown in Fig. 2.34, where the material passes through the rolls with an initial velocity (V_i) and the roll gap is maintained on the desired final thickness (h_f). Initial thickness of material is h_i, radius of the rolls is r, the contact length is L, the reduction in thickness after the rolling operation is s, and the frictional force on the surface of the rolls is F_f (M. Singh & Singh, 2019). Cold rolling changes the initial microstructure of a metal to one with a reduced grain size (more fine-grained), elongated grains and high dislocation density that improves

mechanical properties, such as strength and hardness, but reduces ductility (M. Singh & Singh, 2019; B. B. Wang et al., 2021).

2.4.1 Effect of cold rolling of aluminium alloys

Cold rolling is usually performed on the non-heat-treatable aluminium alloys as this induces strain hardening, but can also be performed on the heat treatable aluminium alloys in conjunction with heat treatment. Panagopoulos and Georgiou (2010) studied the effect of cold rolling on the lubricated wear of a 5083-aluminium alloy. 30mm thick sheets were used and reduced in thickness by 7% and 15%. According to Fig. 2.35, the microstructure after 7% and 15% reduction by rolling shows reduction in grain size attributed to the recrystallisation of grains caused by stress of rolling as an aluminium solid solution and intermetallic phases of Mg_2Si were induced after rolling.

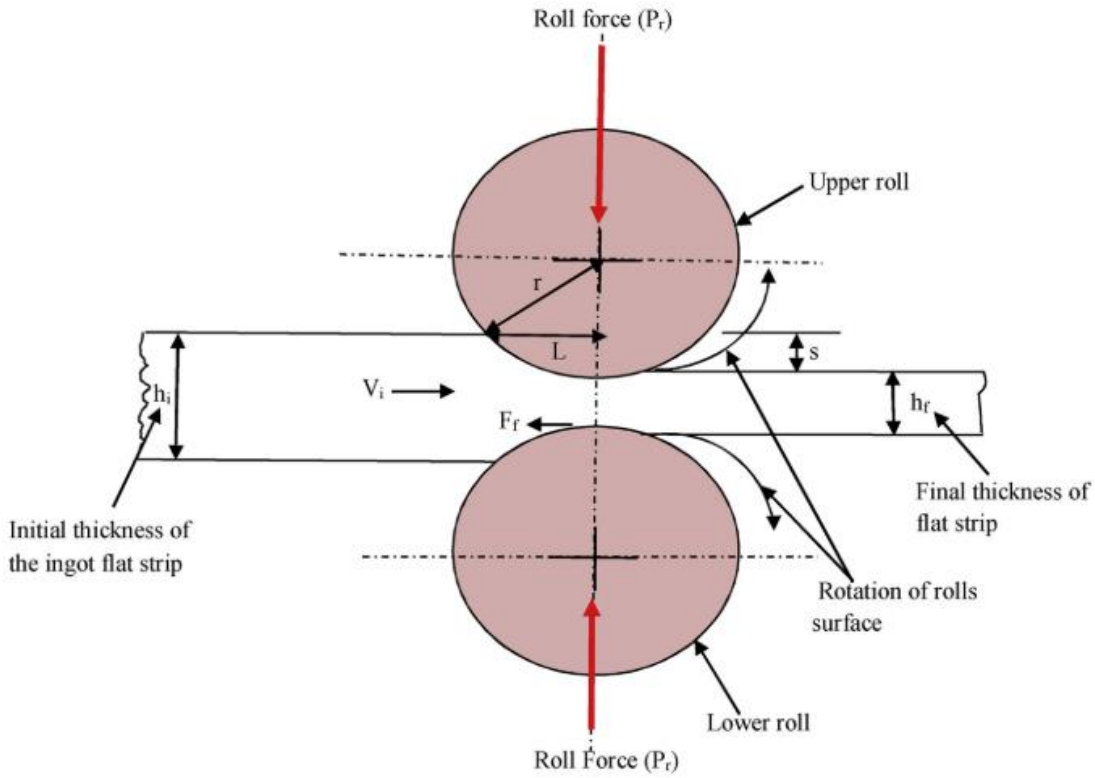

Fig. 2.34 Cold Rolling Process Schematic also showing force representation (M. Singh & Singh, 2019)

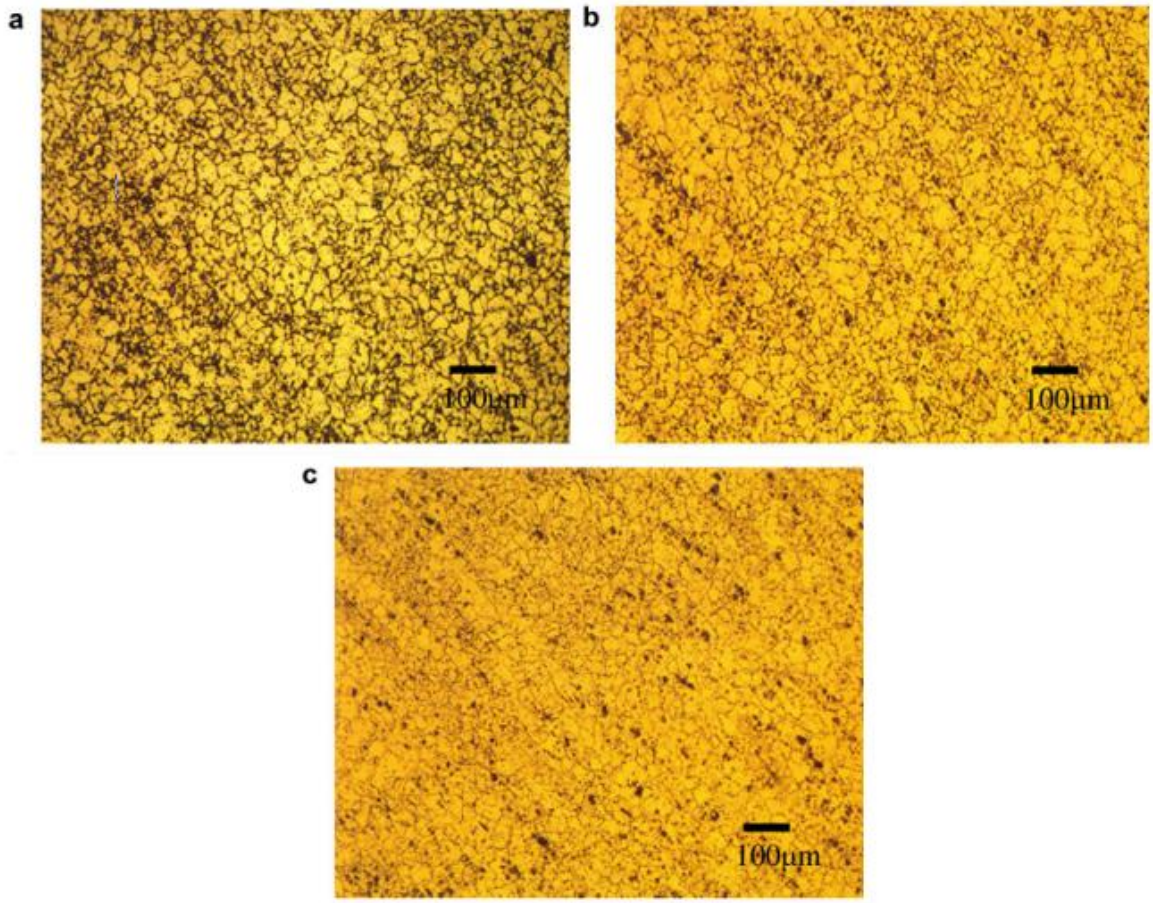

Fig. 2.35 Microstructure of 5083Al alloy. a) as-received, b) cold rolled to 7% reduction in thickness, c) cold rolled to 15% reduction in thickness (Panagopoulos & Georgiou, 2010)

Hardness increased from 74HV (as-received) to 84HV (7% roll reduction) to 88HV (15% roll reduction) caused by reduction in grain size elucidated by the Hall-Petch Equation that shows the relationship between increasing yield strength of a metal with decreasing grain size:

$$\sigma_y = \sigma_o + \frac{K}{\sqrt{d}} \qquad \textit{Equation 2.2}$$

K = strengthening coefficient, σ_0 = material constant of starting stress for dislocation movement and d = grain diameter. Although, yield strength can also be related to hardness in the following equation:

$$HV \approx 2.9\sigma \qquad \textit{Equation. 2.3}$$

Through the relationships represented by Equation 2.3 and 2.4, it can be said that increasing hardness is related to decreasing grain size. Additionally, cold working increases the number of dislocations within the material's volume and the development and movement of new dislocations are inhibited by existing dislocations and the occurrence of texture orientation, hence hardness is increased (Panagopoulos & Georgiou, 2010). T. Wang et al. (2021) studied a powder metallurgy manufactured (sintered and hot pressed) 2024 aluminium alloy subjected to cold rolling and annealing to study its microstructure and mechanical properties. The as-sintered microstructure

features a typical equiaxed grain structure and clear powder particle grain boundary. Cold rolled samples showed elongated ellipsoidal grains in the rolling direction and were more stretched with increasing rolling reduction. Precipitates for as-sintered samples were distributed along powder particle boundaries and were typically coarse and irregularly shaped, but precipitates distributed in the Al matrix within the cold rolled samples were more spherical and evenly distributed. This redistribution and change in morphology of precipitates were attributed to shear stress between the matrix and precipitates, movement of dislocations, and nucleation of precipitates from the dissolution of precipitate phases due to the blend of both cold rolling and annealing. Relative densities were also positively affected by cold rolling porosity within the matrix, reduced as the compactness of the microstructure increased due to cold rolling. Hardness also increased due to work hardening effect during deformation. Tensile strength eventually increased due to the blend of both phase precipitation and work hardening. Hence, mechanical properties improved due to intense cold rolling and second phase precipitation occurred due to the blend of annealing treatments and cold rolling.

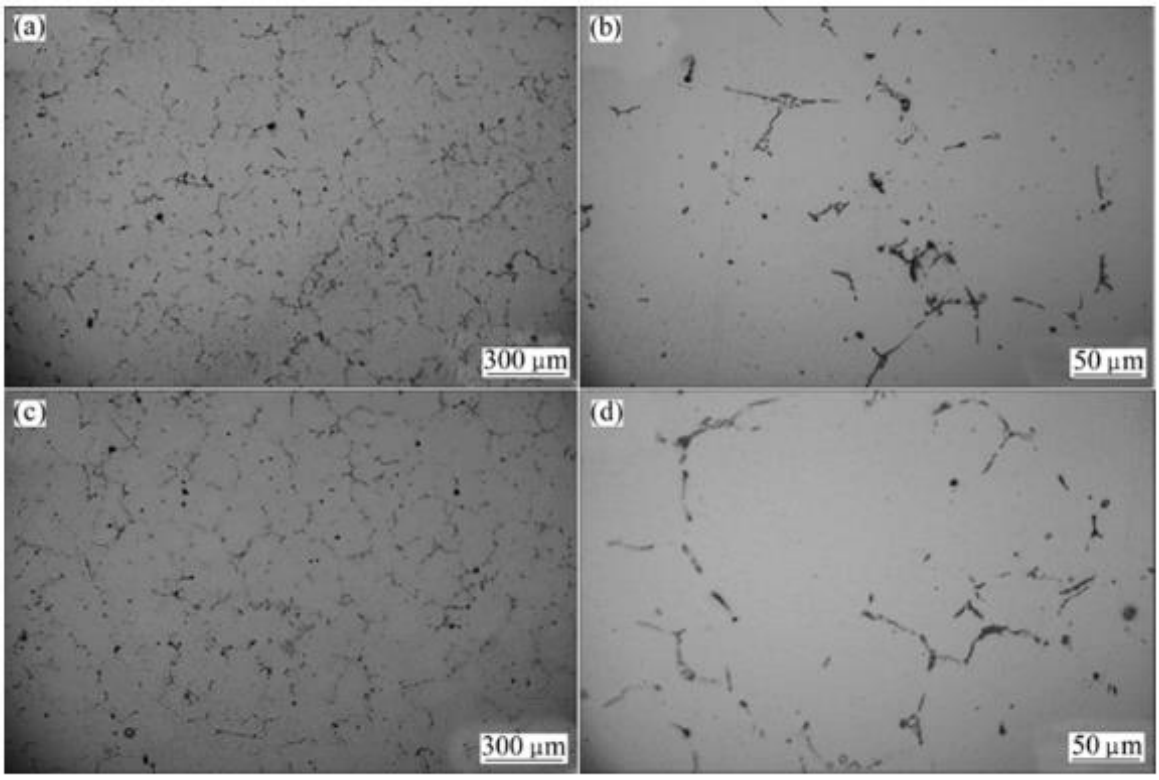

Fig. 2.36 Microstructure of as received 5052Al alloy - a &b) as cast, c &d) solutionised (B. Wang et al., 2015)

The refined grains developed during cold rolling inhibit dislocation movement that consequently increases resistance and reduces ductility; thus, annealing can be beneficial in reducing these effects.

Another study by B. Wang et al. (2015) observed the effects of heat treatment and cold rolling of a 5052Al alloy. Rolling reductions of the alloy were 15%, 33% 46%, 60%, 75% and 87%. The

75% reduction in rolling was also annealed at temperatures of 220ºC/4h, 250ºC/4h, 300ºC/4h, 350ºC/4h, and 380ºC/4h. Fig. 2.36 shows dendritic structure with large Al matrix phase and second phases located along the boundary of the dendritic grains for the as received alloy, and obvious grain growth for the solutionised alloy where typical grain size increased from 118µm to 136µm. Additionally, solutionised alloys show the grain structure dissolved with little obvious grain boundaries, structure and second phase particles - typical features in solutionising. Fig. 2.37 show obvious elongated grains in rolling direction and a strained structure with increasing elongated grain size with increasing rolling reduction. Typical grain size lengthening for the rolling reductions from least to greatest were 148µm, 156µm, 180µm, 467µm, 701µm, and 732µm showing that rolling reductions between 46% and 87% result in very coarse grains. Al matrix, Mg_2Si and Al_3Fe were the phases identified in all samples showing that the kind of phases are unaffected by cold rolling, however secondary phase increases with increasing rolling reduction. Samples of annealed and 75% roll reduction exhibited different phases to that of only cold rolled - Mg_2Al_3, Al, Mg_2Al_3, Mg_2Si, Al_3Fe and Mg_2Al_3, where the Mg_2Al_3 phase is known to be induced through annealing. Hardness increased from 61HV to 99HV from as received to the highest roll reduction of 87% due to the increase of dislocation density. Hardness reduced from 61HV to 57HV after solutionising as the microstructure is mostly dissolved. Samples that were annealed with a roll reduction of 75% reduced in hardness from 83HV to 58HV with rising annealing temperature attributed to recovery and recrystallisation and shows work hardening decreases due to annealing. As received ultimate tensile strength (UTS) increased from 69MPa to 325MPa, yield strength (YS) from 69MPa to 320MPa, however ductility reduced drastically from 25% to 2.5%. Increase in tensile strengths are attributed to the intense roll reduction and elongated grains in the rolling direction and second phase particles being more numerous after cold rolling inducing precipitation hardening. Consequently, the increased work hardening reduces ductility and elongation. Samples that had been cold rolled and annealed had highest UTS value of 311MPa, but with subsequent annealing treatments, it decreased to 212MPa, YS decreased from 201MPa to 75MPa, while max elongation increased from 2.8% to 25.2% and final grain size was 516µm. These tensile strengths were synonymous to that of the solutionised and cold rolled then annealed at 300ºC to 380ºC for 4h samples. This increase in elongation was thought to be due to the annealing temperature increasing grain size and precipitates according to Equation 2.3. Hence, smaller refined grain improved mechanical properties through increased dislocation density that changed slip systems within the metal. Finally, the recrystallisation occurred at 300ºC leading to loss in density of dislocations and corresponding mechanical properties (B. Wang et al., 2015).

Mansourinejad and Mirzakhani (2012) investigated the influence of age hardening and cold working in a 6061Al (Al-Mg-Si) alloy. Samples were subjected to a series of heat treatment and cold work. Cold working reductions were 20%, 40% and 60%, and all samples were homogenised at 520ºC/1h then quenched in water. In cold worked samples, the samples are subjected to heavy strain providing numerous nucleation sites for precipitation to take place increasing hardness and

strength. Reduced area and elongation is attributed to high dislocation density impeding the flow of the material. When cold worked samples were aged, elongation (ductility) was improved by the annihilation of dislocations, strain hardening effect is reduced and work softening in the material exceeded the detrimental effects of dislocation pinning by precipitates. The potential for precipitates to nucleate and form increases with the increasing reduction in area as precipitates lock in dislocations and hinder gliding dislocations. Final ageing for samples showed strength was constant or decreased slightly, while elongation improved.

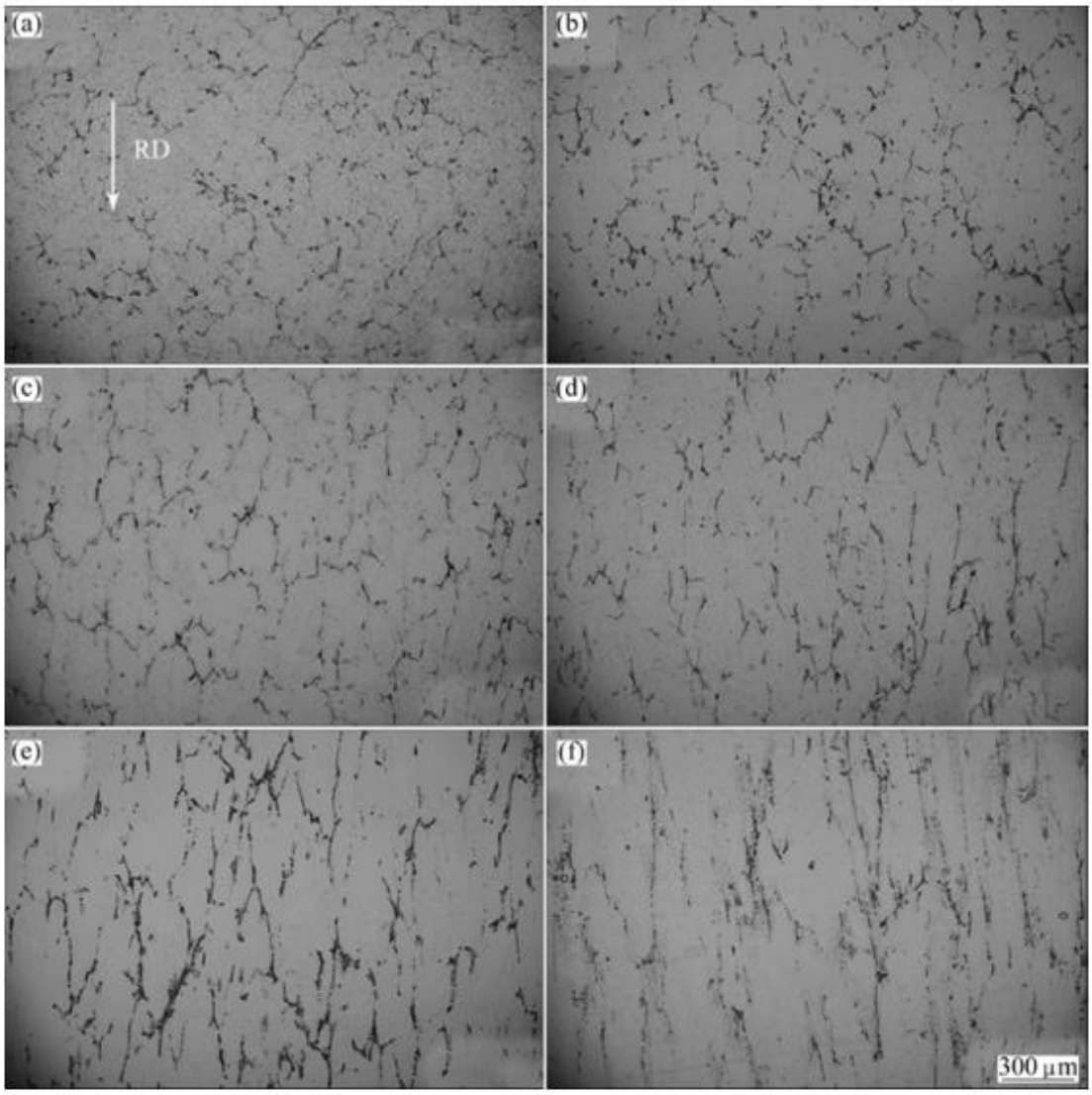

Fig. 2.37 Optical images of microstructure of cold rolled 5052Al alloy. a)15%, b)33%, c)46%, d)60% e)75% f)87% (B. Wang et al., 2015)

Solution treatment on the alloy showed that recovery and recrystallisation had taken place due to cold work expanding defect density in the microstructure, thus internal energy causes the recrystallisation and recovery process to accelerate and the high solution temperature caused grain growth.

2.4.2 Effect of cold rolling on additively manufactured metals

Little to no literature is provided on the cold rolling of additively manufactured alloys as this is not typically performed for lack of application, however observation of the effects of cold rolling on mechanical properties, microstructure and density may be beneficial. A study by Natali, Brotzu, and Pilone (2019) made a comparison between thin sheets of 316L stainless steel produced using additive manufacturing and cold rolling. The microstructures, shown in Fig. 2.38, exhibit very fine grains in both samples, while shear bands were reported in the cold rolled samples due to the deformation induced in cold rolling centrally located in the sheet. TS, YS, and elongation were examined and showed that UTS and elongation for additively manufactured samples are lower, than cold rolled samples, but have a higher YS. These were attributed to a non-heterogenous microstructure and mechanical properties, and complicated thermal cycles induced during the additive manufacturing process. Furthermore, defects such as lack of fusion and micrporosity resulted in crack propagation leading to failure and lowered strength. Both samples exhibited a ductile fracture with many dimples, where increased dimples were visible on the cold rolled samples.

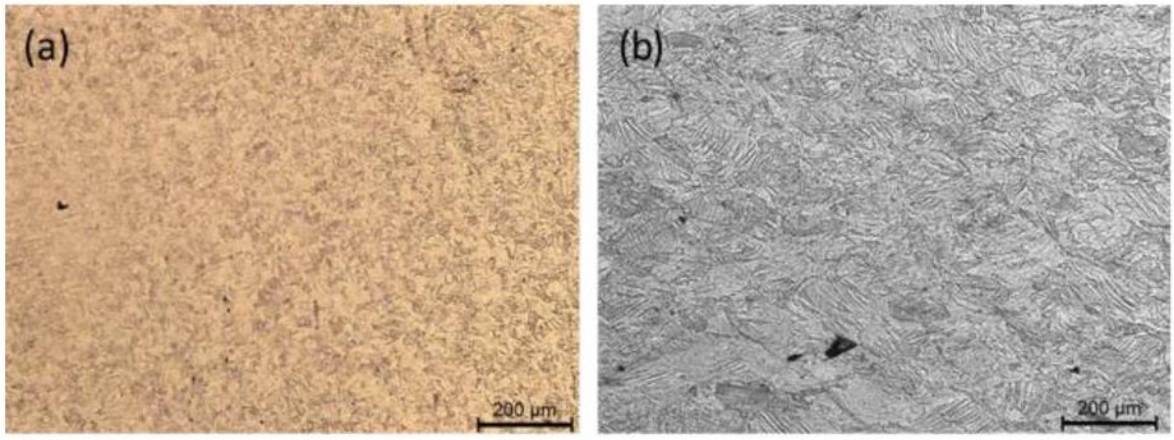

Fig. 2.38 Planar view of the microstructure of 316L stainless steel - a) rolled, b) additively manufactured (Natali et al., 2019)

Additionally, the effect of rolling direction on samples and sample thickness showed that mechanical properties remained independent of these. A study by Ma et al. (2020a) investigated the enhanced mechanical properties of a selectively laser melted Al-Mg-Sc-Zr alloy by cold rolling and annealing. It was found that the coarse-grained regions in the alloy were refined by as much as 30%. This is thought to be due to the Al_3(Sc, Zr) precipitates prevention of grain growth and promotion of thermal stability. Mechanical properties of samples cold rolled to 80% reduction in thickness had YS and TS of 573MPa and 612MPa, respectively, attributed to the high dislocation density and induced point defects to inhibit dislocation movement. Hence, improved tensile properties of the alloy were apparent.

2.4.3 Summary

Cold rolling can improve the hardness and tensile strengths of Al-Mg alloys through increasing dislocation density, inducing changes in microstructure, solid solution hardening and precipitation hardening. This shows that Scalmalloy could benefit from cold rolling in terms of refinement in microstructure and improved mechanical properties. However, very little to no literature has been reported on cold rolling of Scalmalloy. As cold rolling is not typically performed on additively manufactured alloys, a valid comparison can be made between the cold rolled microstructure of the additively manufactured Scalmalloy, and conventionally extruded aluminium alloys. Furthermore, the effect of cold rolling and cold rolling and heat treatment on the microstructure and mechanical properties of Scalmalloy can be observed and reported.

2.5 Gas tungsten arc welding

This section will provide background on Gas Tungsten Arc welding (GTAW) method and studies of GTAW on aluminium alloys. GTAW and other types of welding of additively manufactured metals will also be discussed.

2.5.1 Definition and characteristics of gas tungsten arc welding process

Welding is a common joining method for metals and plastics. There are different types of welding processes, the most common of which is fusion welding. Fusion welding joins two pieces of metal by heating both to melting point and then having them solidify together to fuse into one piece (Subbaiah, 2019) . GTAW is a fusion welding method that can weld both ferrous and non-ferrous metals. It is extremely economical, easy to use, and welded joints are have good quality, making it the most commonly used fusion welding process (Varshney & Kumar, 2021). GTAW consists of various components shown in Fig. 2.39. The power source supplies a constant current to the non-consumable tungsten electrode to produce the energy needed to melt the metals. A filler metal is usually used to aid in the fusion process. An inert shielding gas, usually argon or helium to protect the welding environment from oxidation, is distributed around the weld through the nozzle (Błachnio, Kułaszka, Chalimoniuk, & Woźny, 2016). Macroscopically, the weld joint is affected by the welding parameters such as power input, weld speed, filler material, welding angle, electrode diameter, shielding gas, electric current type, and welding voltage. These may be pre-determined by the welder (Messler Jr, 2008).

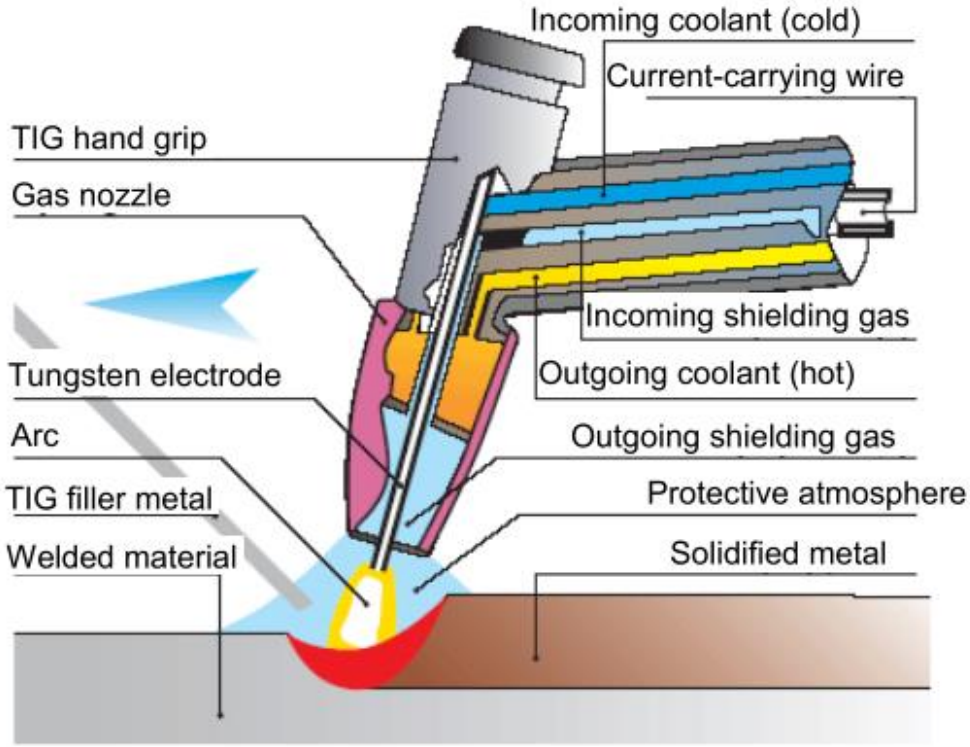

Fig. 2.39 Schematic of GTAW Process (Błachnio et al., 2016)

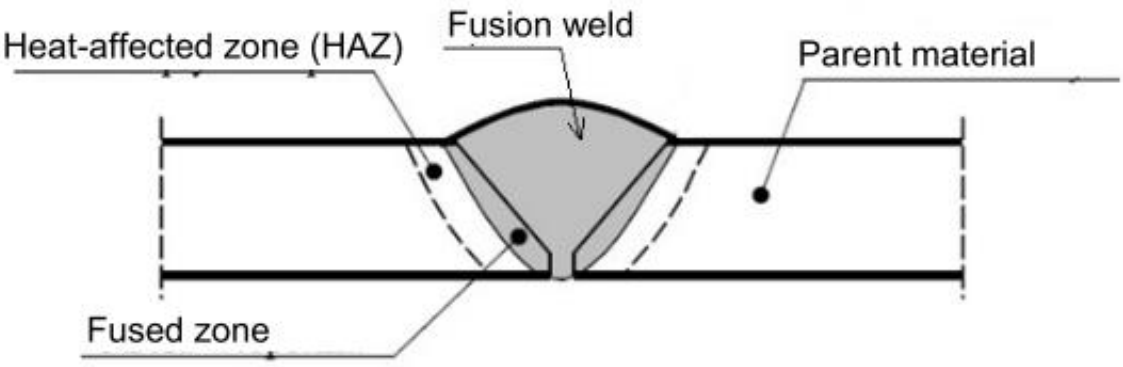

Fig. 2.40 Profile of single groove butt joint showing main areas of interest (Błachnio et al., 2016)

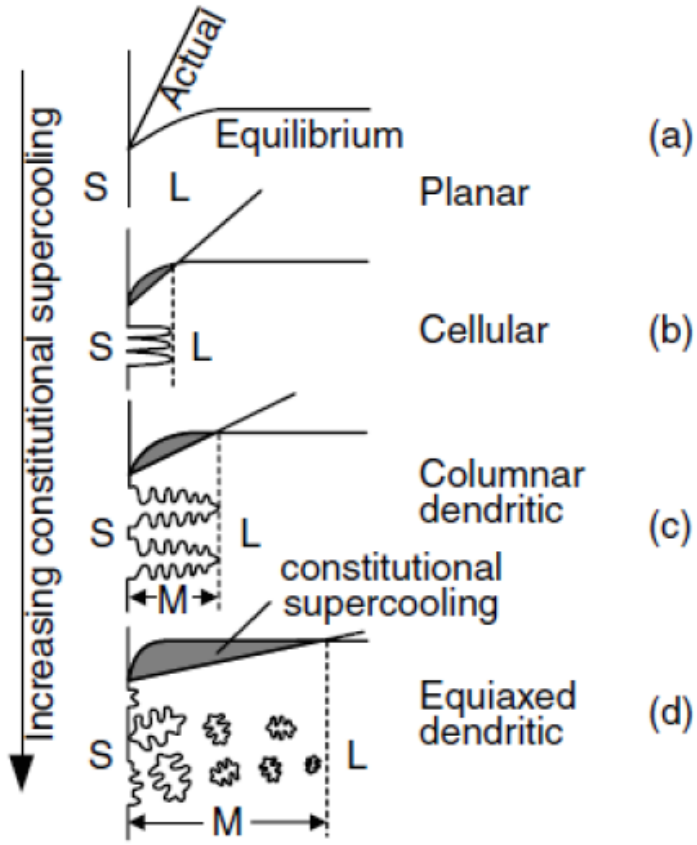

Fig. 2.41 Different solidification modes affected by constitutional supercooling (Kou, 2003)

During the welding process, three distinct areas emerge across the weld profile, shown in Fig. 2.40. The main areas are the fusion zone (FZ) - the area that is in direct contact with the tungsten electrode and metals being melted; the true heat-affected zone (HAZ) - the zone thermally affected by the heat from the welding process; and the parent material or base metal (BM) which remains unchanged. A partially melted zone (PMZ) may be seen in the fused zone indicated in Fig. 2.40, however this may not be observed at all for alloys with very short solidification temperature ranges (Li, Zou, Yao, & Peng, 2017; Messler Jr, 2008).

After welding has ceased, different types of grain structures may occur after solidification. Quality of the welded joint and its mechanical properties, such as strength, hardness, and

elongation, are dependent on this grain structure. The thermodynamic aspect affecting solidification is the location of the solid liquid interface depicted in Fig. 2.41 as a phase diagram. Constitutional supercooling is the cooling of a liquid to its freezing point without solidifying and affects the solidification mode of the weld. Fig. 2.41 also shows the four typical grain formations – planar, cellular, columnar dendritic, and equiaxed dendritic, affected by constitutional supercooling, whereby the degree of constitutional supercooling corresponds to the grain structure (Kou, 2003).

2.5.2 Gas tungsten arc welding of aluminium alloys

Aluminium has high thermal conductivity, possesses some excellent weldability and good heat efficiency making it very responsive to the high-power input experienced during GTAW and other higher power welding (Varshney & Kumar, 2021). The lifecycle (strength) of a weld joint is dependent upon the mechanical properties of the weld and upon the number of defects present within the weld mainly focusing on the FZ, but fracture can occur at the HAZ due to coarser grains forming here attributed to elevated temperatures. Lack of fusion, lack of weld penetration, porosity, inclusions, and cracks can be the prevailing defects and should be minimized where possible as this can facilitate component failure (D.-k. Zhang et al., 2019). A good balance of welding parameters is necessary to ensure mechanical properties are optimized, while defects are minimized. GTAW weld parameters have been researched well. Shanavas and Dhas (2017) investigated the effect of weld current and shielding gas flow on the tensile strength of welds using GTAW welding and friction stir welding (FSW), where FSW is a type of solid-state welding, and these results were compared. They found that the welding current increased tensile strengths slightly as weld penetration is increased improving weld properties. Shielding gas flow rate also influenced strength, whereby a moderate level was beneficial. Additionally, grain growth occurred in the weld, especially the HAZ, due to the elevated temperatures during welding. Çetkin, Çelik, and Temiz (2019) compared effects of GTAW and MIG welding parameters on the microstructure and mechanical properties of an AA7075 and AA5182 Al alloy. Again, a higher welding current induced sufficient weld penetration resulting in less porosity. All round, the GTAW weldments exhibited better mechanical properties in terms of tensile strength, hardness, and fatigue than the MIG samples. The effects of weld penetration on the tensile properties of a 2219Al alloy was investigated by D.-k. Zhang et al. (2019) and it was reported that weld penetration does have some effect on the tensile properties. Hence, it was found that weld penetration can be controlled by the welding current and welding voltage, although all welding parameters should be considered to achieve suitable weld penetration. Hence, weld parameters are important in achieving a good, welded joint.

Apart from welding parameters, the overall effect of GTAW on aluminium alloy mechanical properties and microstructures has been observed. In a study by Y. Liu et al. (2012) the microstructures and mechanical properties of GTAW and GMAW (Mig welding) were studied. They found that GTAW welds were visually better and less defective than the GMAW

weldments. Slower welding speeds and arc cleaning from the shielding gas reduced pores resulting in higher tensile strengths. A homogenous equiaxed grain structure developed in the centre of the weld, and these were more ductile showing dimpled fracture with coalescence. In another study by D. Zhang et al. (2019) observed the inconsistencies of mechanical properties for the same alloy. It was found that these were due to the differing shapes of the weld joints and the presence of a coarse eutectic microstructure. Additionally, parameters such as welding heat input and wire feeding speed affected tensile strength and microhardness. Hence, it was important to consider the geometrical and metallurgical attributes during the welding process. A study by Arunkumar and Subbaiah (2019) conducted welding trials using GTAW on cast Al-Mg-Sc alloys. GTAW welded joints exhibited good hardness, but hardness profile was constant until it reached HAZ and FZ where a sharp drop occurred but then rose again until it reached BM hardness. Tensile strengths were reasonable as magnesium seemed to evaporate fully in the weld. The microstructure of the FZ, shown in Fig. 2.42a consists of fine homogenously distributed Al_3Sc recrystallising from solutionsing and heat treatment. BM to HAZ is shown in Fig. 2.42b and shows recrystallisation of Al_3Sc precipitates and no shrinkage voids are apparent. Small gas pores (<50µm) can also be seen here due to melting and solidification in GTAW process. Additionally, fracture occurred in the HAZ zone due to coarsening of grains in this region. G. Xu et al. (2016) studied whether a new Al-Mg-Mn-Sc-Zr alloy could be joined using GTAW welding and the mechanical properties and microstructure were examined. It was possible to join this alloy by GTAW and mechanical properties, such as strength and hardness, reached acceptable levels, and some were higher than the as-cast alloy. Microstructures of this weld is shown in Fig. 2.43 consisted of a cast dendritic and super saturated solid solution in FZ and some gas pores are evident here, HAZ consists of coarsened elongated grains due to heat from welding, and the BM remains unaffected as welding does not affect this area. Microhardness was also reported to have a downward trend as it transitioned from BM to HAZ and then drops sharply in the FZ before rising again to BM hardness, which is consistent with the relevant microstructures in each zone.

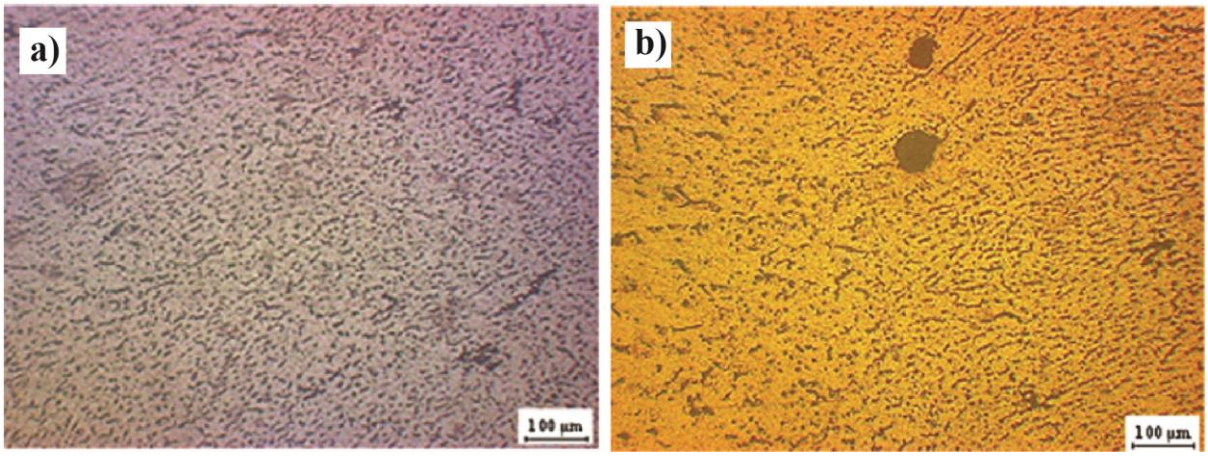

Fig. 2.42 a) Microstructure of FZ and b) microstructure of BM and HAZ for GTAW cast Al-Mg-Sc alloy adapted from (Arunkumar & Subbaiah, 2019)

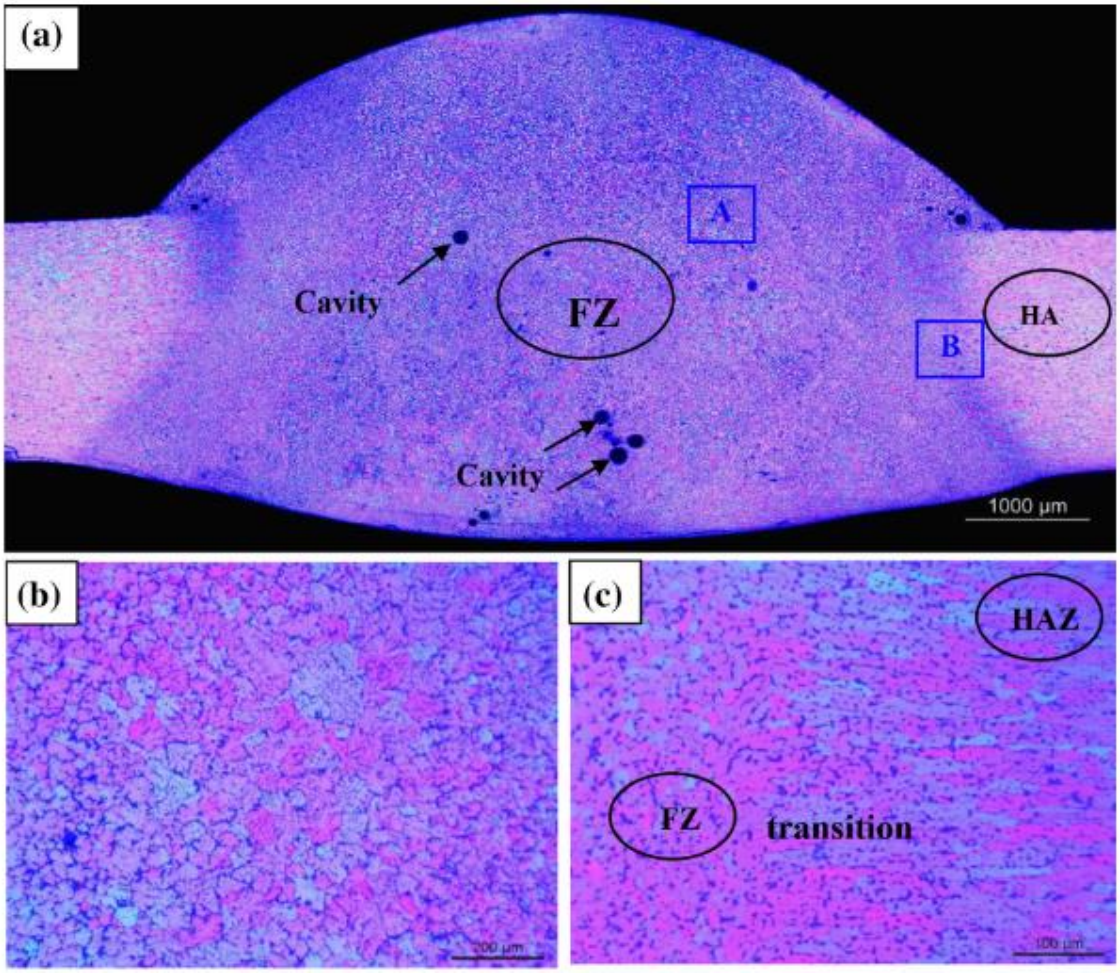

Fig. 2.43 Microstructure of GTAW joints of Al-Mg-Sc-Zr alloy. a) macrostructure, b) FZ, c) HAZ (G. Xu et al., 2016)

2.5.3 Welding of additively manufactured metals

Welding of additively manufactured metals is beneficial as geometrically complex additively manufactured parts can be joined to existing structures or other components. Component size limitations in AM is a common problem due to a restricted build chamber size and footprint. GTAW can be particularly advantageous as it offers an inexpensive and easy way of joining costly additively manufactured metal components (Matilainen et al., 2016; Shanavas & Dhas, 2017). However, there are very few studies conducted using GTAW on additively manufactured parts; hence, the following studies are based upon both GTAW and laser beam welding, where laser beam welding studies offer observations of the influence of welding on additively manufactured components that could occur during GTAW.

Mäkikangas, Rautio, Mustakangas, and Mäntyjärvi (2019) investigated the suitability of laser welding on a selectively laser melted AlSi10Mg based alloy. This alloy was successfully joined by laser welding. Average tensile strength was found to be 63% lower than the as built specimen and pores as large as 0.7mm were found in the FZ of the weld, but the weld shape was good with

minimum welding spatters. However, more research needed to be done to minimize porosity. Matilainen et al. (2016) studied the weldability of powder bed fusion (PBF) stainless steel. It was found that PBF exhibited good weldability when energy input was low as this led to full weld penetration. However, when energy input was high, large pores generated within the weld. Also, crack tendencies were apparent and thought to be due to residual stresses within PBF components, but more research was needed to conclusively determine the root causes of these. In another study involving laser beam welding, Wits and Becker (2015) investigated joining a selective laser melted titanium part with similar laser welding process parameters as that for conventional titanium parts. However, the conventional process settings could not be transferred from one to another as the weld geometry became irregular. A higher energy and slightly different process settings were suggested. A study by Pasang et al. (2019) investigated the mechanical properties, strain distribution and microstructure of the additively manufactured SS316L following GTAW welding. This alloy was easily welded through GTAW, and precipitates were apparent in FZ and BM, but lacking in HAZ as these dissolved due to elevated temperatures during GTAW. Hardness remained at original BM values and was consistent throughout the weld profile as this alloy is non heat treatable. Additionally, tensile strengths were higher than the as-built condition with primarily ductile fracture occurring.

A study by Xu (P. Xu et al., 2018) reported the effects Variable Polarity Plasma Arc welding had on an Al-Mg-Sc-Zr alloy. Microhardness was consistent across the BM but dropped sharply across HAZ and FZ and then slowly rose to the original BM values. Fig. 2.44 shows the macrostructure and the microstructures of the weld zone. The FZ consists of equiaxed dendritic grains (20µm to 40µm in size), HAZ consists of coarser grains than BM due to heat input from welding, and some recrystallised grains near the bond. Tensile strengths are also slightly lower than BM due to the high heat suppressing Al_3Sc precipitates from forming.

C. Zhang et al. (2019) compared GTAW and laser welding for an AlSi10Mg cast and a selective laser melted alloy. The selective laser melted alloy had very high pore susceptibility due to pre-existing high hydrogen content compared to the cast alloy. Tensile strength was also inferior to the cast alloy, while all samples had very low elongation. Furthermore, a study by Cui et al. (2022) compared welding methods that would reduce hydrogen pore susceptibility of AlSi10Mg in both the cast and selective laser melted form. Autogenous, single pass and laser melting deposition (LMD) welding were compared resulting in LMD having the highest mechanical properties due to a smaller melting zone resulting in less hydrogen entering the weld pool.

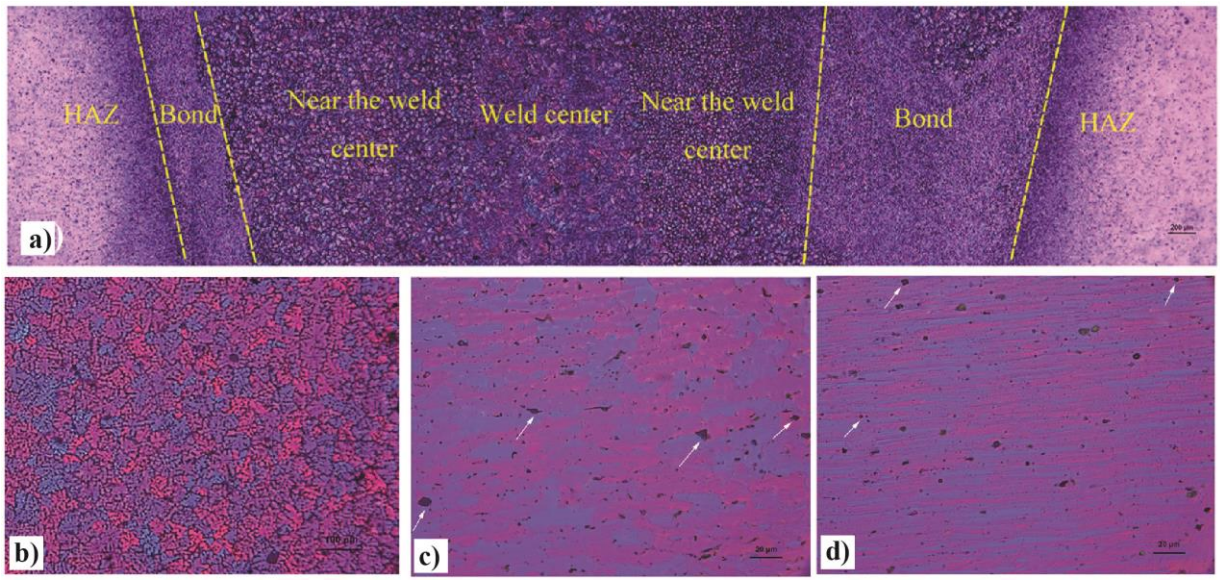

Fig. 2.44 Microstructure of Al-Mg-Sc-Zr alloy a) Macrostructure of weld, b)FZ, c) HAZ, d) BM (P. Xu et al., 2018)

2.5.4 Summary

Welding of metal parts is very beneficial, especially additively manufactured parts, as this eliminates sizing issues and can be done cheaply. It is also clear that aluminium alloys are highly compatible with GTAW and can be used on additively manufactured alloys in a satisfactory manner, especially those produced using PBF. Furthermore, parameters often need to be optimized for these parts and fusion welding has proven to be difficult for aluminium additively manufactured alloys due to their hydrogen susceptibility. However, GTAW (welding) of Scalmalloy has not been reported, therefore, the effect and processing of GTAW on Scalmalloy can be explored to determine whether it is feasible to weld Scalmalloy using GTAW with standard GTAW parameters often used on aluminium alloys. The effects on the resulting microstructures across the weld and the prevailing mechanical properties will also be observed and reported.

Chapter 3 Design of study

This chapter will discuss the design of study for each research topic and incorporates the necessary steps of manufacturing, testing, and analysing microstructures and mechanical properties, both qualitatively and quantitively. There are three main studies in this research each having slightly different methods to one another: the SLM parameter study (Chapter 4), cold rolling and heat treatment study (Chapter 5) and GTAW Welding study (Chapter 6). A schematic outline for the design of each study is shown in Fig. 3.1 and the subsequent sections explain each in detail.

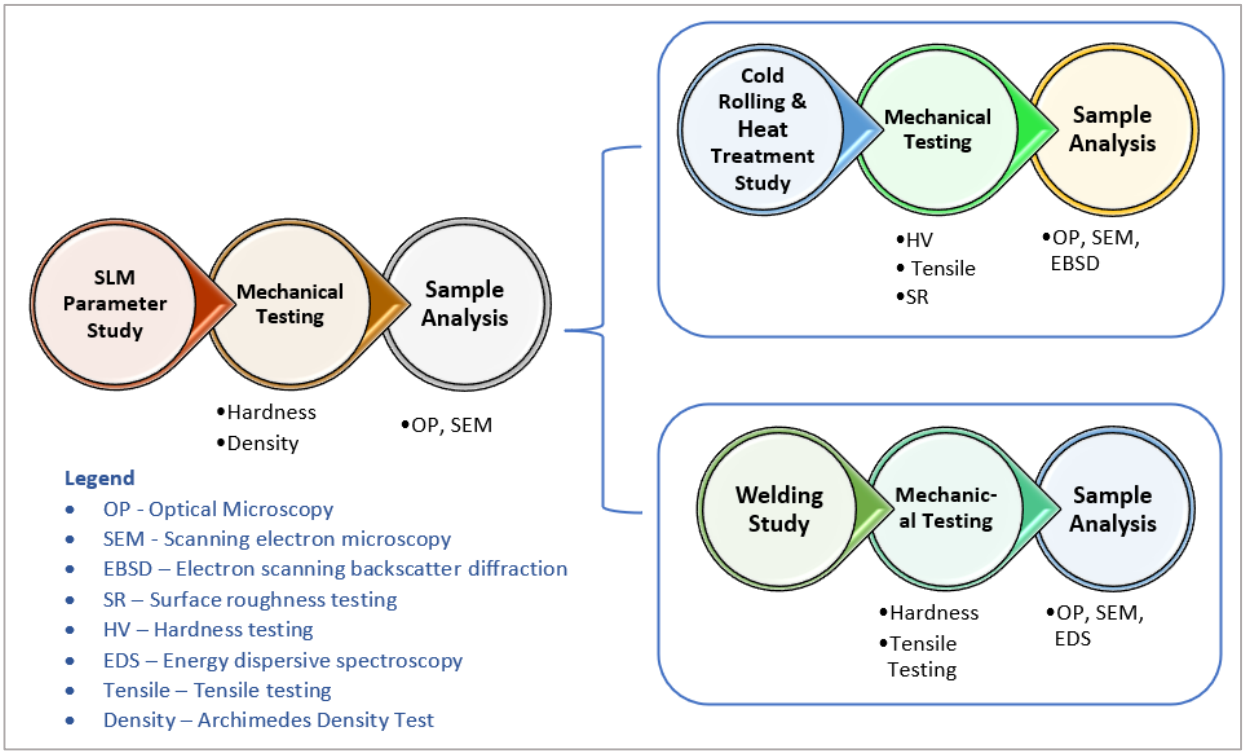

Fig. 3.1 Design of study schematic

3.1 Sample preparation

The following section outlines the method of preparation of the samples for each topic of study in this research.

3.1.1 Selective laser melting parameter study

It was necessary to develop SLM process parameters to manufacture Scalmalloy samples of >99% relative densities using a *Renishaw AM 400* LBM. This section will include the method of obtaining these optimal SLM parameters. Please note that the experimental method explained in this section has similar elements to the experimental method reported in Celine Turangi, Haslich, and Pasang (2020) as this is earlier published research of the work on hand.

3.1.1.1 Selective laser melting machine

A *Renishaw AM 400* SLM machine was outfitted with a pulsed laser having a maximum power of 400W and a laser focus diameter of 70µm. The build chamber was 250mm x 250mm x 300mm in size and used an argon shielding gas flow. Samples were built on a stainless-steel build platform and the surface of the build platform was either milled or sandblasted before each use. Standard software was used with each layer being hatched bi-directionally first and then two single scan tracks of contour and alternating hatch direction of 67° layer-wise.

3.1.1.2 Scalmalloy powder characterisation

Scalmalloy powder was obtained from LPW Technology and chemical composition can be seen in Table 3-1. From the material data sheet provided by LPW Technology, 0 wt% of the particles were larger than 63µm according to sieve analysis and 6 vol% particles were found to be smaller than 20µm according to the laser size diffraction analysis. For accuracy, powder morphology was assessed using a Hitachi SU-70 SEM (section 3.5.3) according to the standard VDI 3405 Part 2. A minimal amount of powder was distributed onto a carbon adhesive strip to ensure electric conductivity and 5kV voltage was used with the Hitachi SU-70 SEM. Gas porosity was also investigated where samples were cold mounted using Struers EpoFix epoxy resin and hardener. Metallography (section 3.5.1) was carried out upon these powder samples an examined using an Olympus BX51M optical microscope (section 3.5.2). Three different optical micrographs at 100x magnification were taken of all cut particles with visible inner pores where the total number of these pores were analysed and counted using *Image J* software. Microhardness testing was carried out upon the cut cross-section powder particle samples according to section 3.4.3. Only spherical powder particles having similar diameters with the edge at least 2.5x distances away from indentation diagonal length were tested. In addition, samples were coated with a thin film of nm platinum for electric conductivity for the SEM system which is thought to be negligible during microhardness testing.

Table 3-1 Chemical composition of Scalmalloy from data sheet (refer to Fig. A.1 in Appendix A)

/wt%	**Al**	**Mg**	**Sc**	**Zr**	**Mn**	**Si**	**Fe**	**Zn**	**Ti**	**Cu**	**V**	**O**
Max.	bal.	4.90	0.80	0.50	0.80	0.40	0.40	0.25	0.15	0.10	0.05	0.05
Analysis.	bal.	4.55	0.65	0.30	0.51	0.16	0.14	0.02	0.01	0.01	0.01	0.04
Min.	---	4.00	0.60	0.20	0.03	---	---	---	---	---	---	---

3.1.1.3 Initial verification of selective laser melting process parameters

Spierings et al. (A. B. Spierings, Dawson, Dumitraschkewitz, et al., 2018; A. B. Spierings, Dawson, Heeling, et al., 2017; A. B. Spierings, Dawson, Kern, et al., 2017; A. B. Spierings, Dawson, Uggowitzer, et al., 2018; Adriaan B. Spierings et al., 2016) have researched Scalmalloy heavily in regards to processing, mechanical properties and microstructure in recent years. Adriaan B. Spierings et al. (2016) developed process parameters that manufactured >99% relative density Scalmalloy samples and was used as a starting point for the work on hand.

Table 3-2 lists the process parameters developed by Spierings et al. (Adriaan B. Spierings et al., 2016) and the process parameters used in this work. There are differences in elemental composition of Scalmalloy, scan strategy, SLM machine and laser focus diameter between Adriaan B. Spierings et al. (2016) and the work on hand, which may cause some differences in the results.

Table 3-2 Comparison of process parameters from Spierings et al. (Adriaan B. Spierings et al., 2016) and process parameters used in this work

Process Parameters	**Adriaan B. Spierings et al. (2016) Process Parameters**	**Process Parameters used for the work on hand**
SLM Machine	*Concept Laser M2*	*Am Renishaw 400*
Laser Power	200W	400W
Laser focus diameter	100µm	70µm
Layer thickness	30µm	30µm
Scan strategy	Bi-directional and alternating by 90° layer-wise	Bi-directional and alternating by 67° layer-wise
Hatch distance	135…165µm	135…165µm
Energy volume density	120…240 J/mm^3	120…240 J/mm^3
Chemical Composition	Al-Mg4.6-Sc0.66-Zr0.42-Mn0.49	Al-4.5Mg-0.6Sc-0.3Zr

Due to this, an initial verification of parameters was necessary consisting of one build job of five 10mm x 10mm x 10mm size cubes spaced 20mm apart, supported by 3mm high structures, built in the centre of the build platform (Fig. 3.2). In addition, a laser power of 400W was used in this research to substantially increase productivity and employ the full potential of the SLM machine. Each cube sample was subjected to a different energy volume density and Equation 2.1 was used to calculate energy volume densities of 80J/mm^3, 120J/mm^3, 150J/mm^3, 240J/mm^3 and 280J/mm^3 when hatch distance of 150µm and layer thickness of 30µm remained constant. Corresponding scan speeds were 1111mm/s, 741mm/s, 593mm/s, 370mm/s and 317mm/s. Expected findings from Spierings et al.(Adriaan B. Spierings et al., 2016) are shown in Fig 3.3 in relation to relative density changing with varying energy volume density. Furthermore, each cube was visually inspected, and dimensional accuracy of opposing cube faces and lengths of upper cube edges were measured with a micrometre.

3.1.1.4 Evaluation of relative densities, microhardness and defects

Relative densities were assessed for each cube sample using the Archimedes density measurement test conducted according to section 3.4.1 to determine the level of inner porosity. Samples underwent metallography, optical microscopy (OP) and scanning electron microscopy (SEM) according to sections 3.5.1, 3.5.2 and 3.5.3, respectively. SEM was used to investigate porosity and surface topology and SEM and OP was used to observe the microstructure.

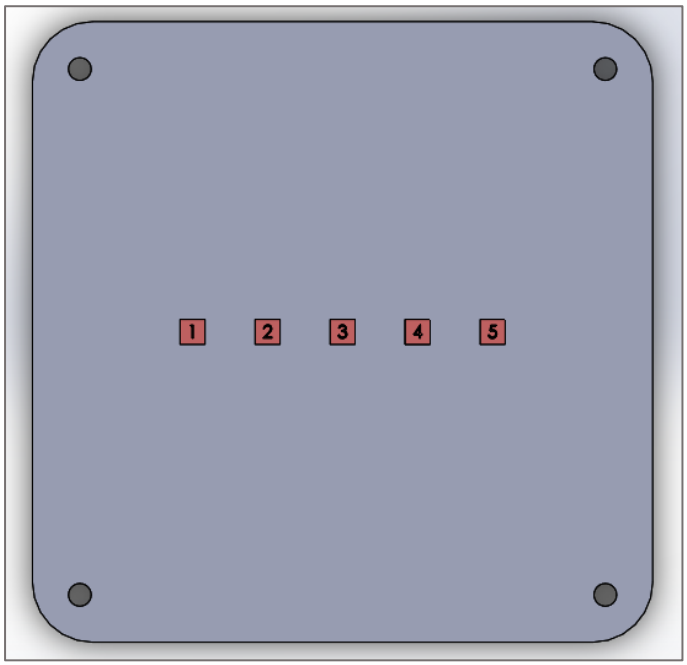

Fig. 3.2 Build Job Layout on Renishaw AM 400 LBM steel platform for first build job with cubes numbered from 1-5

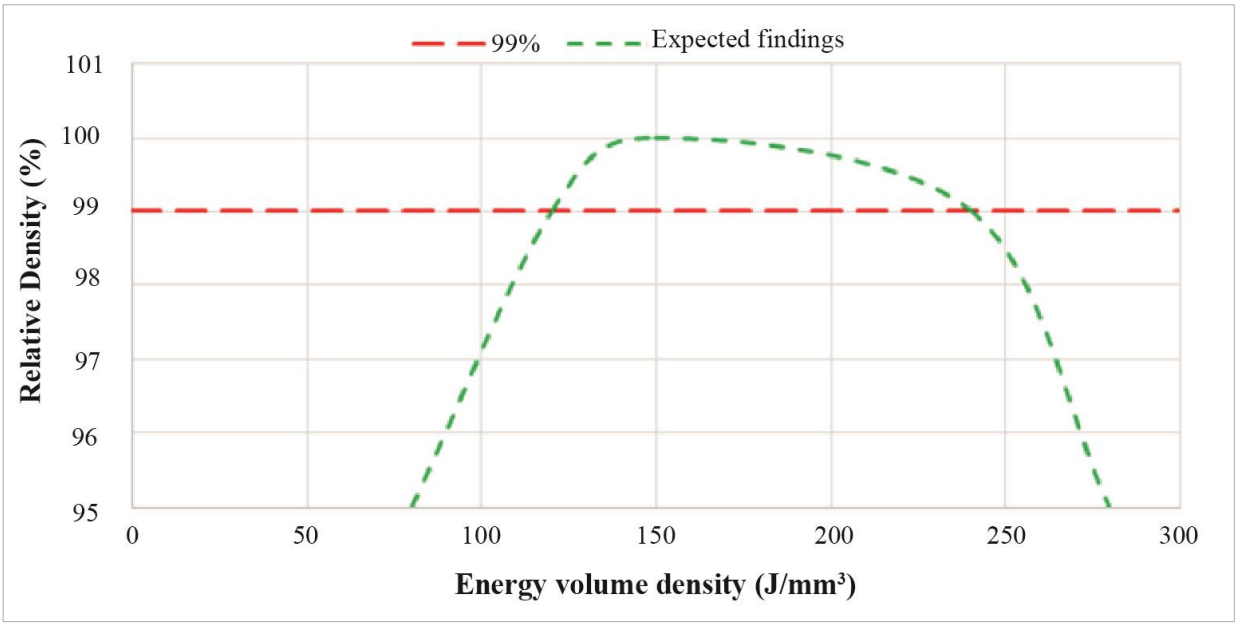

Fig. 3.3 Expected findings of relative density for chosen energy volume densities from results of (Adriaan B. Spierings et al., 2016)

Microhardness testing was carried out according to section 3.4.3 on each metallographic sample and compared with powder particle microhardness (refer to Chapter 4).

3.1.1.5 Investigation of selective laser melting parameter window

Findings from the initial build job (refer to Chapter 4) showed the expected findings from the work on hand (Fig 4.4), had shifted to the right due to laser power of 400W compared to expected findings from Spierings et al. (Adriaan B. Spierings et al., 2016) using laser power of 200W (Fig 3.3). Therefore, corresponding results from this work do not show the full parameter window, but

only part of it, when compared to Spierings et al (Adriaan B. Spierings et al., 2016). Hence, a second build job was necessary. The second build job was identical to the first build job (according to section 3.1.1.3); however, the energy volume densities were changed to 30J/mm^3, 45J/mm^3, 60J/mm^3, 80J/mm^3, and 100J/mm^3 with corresponding scan speeds of 2962mm/s, 1975mm/s 1481mm/s, 1111mm/s and 889mm/s. The newly calculated scan speeds and energy volume densities ensured a full SLM parameter process window was explored for the work on hand in comparison to expected findings from Spierings et al. (Adriaan B. Spierings et al., 2016). Similar to the first build job, all samples from this second build job were analysed according to the methods and equipment outlined in section 3.1.1.4.

3.1.1.6 Reproducibility and influence of layout position

Reproducibility of samples was assessed to ensure as-built samples yielded >99% relative densities using optimum SLM parameters regardless of the number of build jobs (refer to Chapter 4). Influence of layout position on the build platform was also investigated to determine its effect on the as-built samples. Therefore, to inspect intra- and inter- build reproducibility of samples, the following experimental procedure was established. Three build jobs were carried out consecutively using optimal SLM parameter (refer to Chapter 4). A total of 75 cubes (10mm x10mm x10mm) were built with 25 samples per a build job. These were arranged in a 5x5 array 200mm in length and width, within the mounting holes of the build platform shown in Fig. 3.4. Each cube sample was assigned a number to track its position on the build platform and determine influence of layout position regarding relative densities. Archimedes density tests (section 3.4.1) were carried out to determine and compare relative densities of all 75 cube samples.

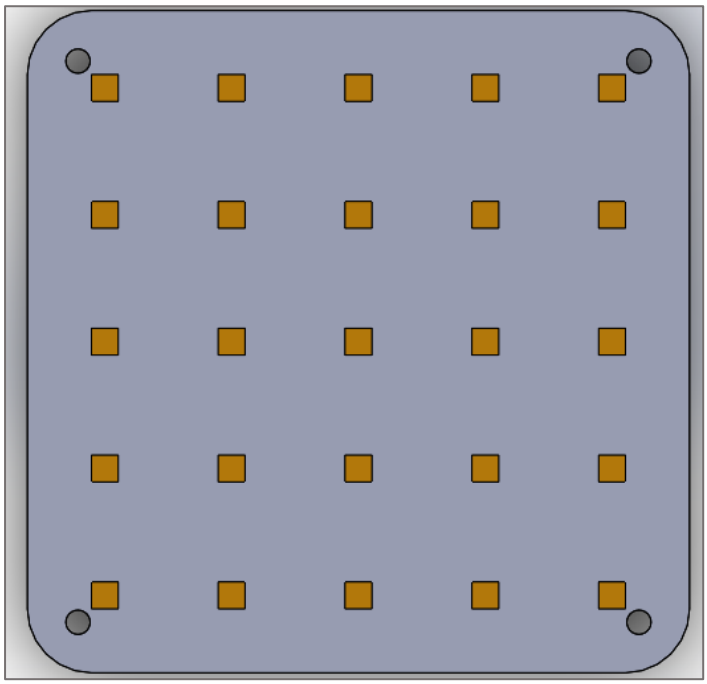

Fig. 3.4 Layout of cube samples on build platform in a 5x5 array to assess reproducibility and influence of layout position

3.2.1 Cold rolling and heat treatment of Scalmalloy study

The experimental procedure for the cold rolling and heat treatment study is outlined in the following sections. Please note that elements of the experimental procedure discussed here are the same as those reported in Celine Turangi et al. (2020) as this earlier published research of the work on hand.

3.2.1.1 Sample manufacturing and preparation

Scalmalloy samples were manufactured using optimal SLM parameters obtained during the SLM parameter study explained in section 3.1.1. As established earlier, build direction bears no measurable effect upon the finished component, hence, samples were built horizontally (XY direction) to minimise build time and material usage. Scalmalloy samples were manufactured in two geometries - tensile sample geometry shown in Fig. 3.5a and square sample geometry shown in Fig. 3.5b, as these will be subject to different heat treatment and cold rolling conditions before testing.

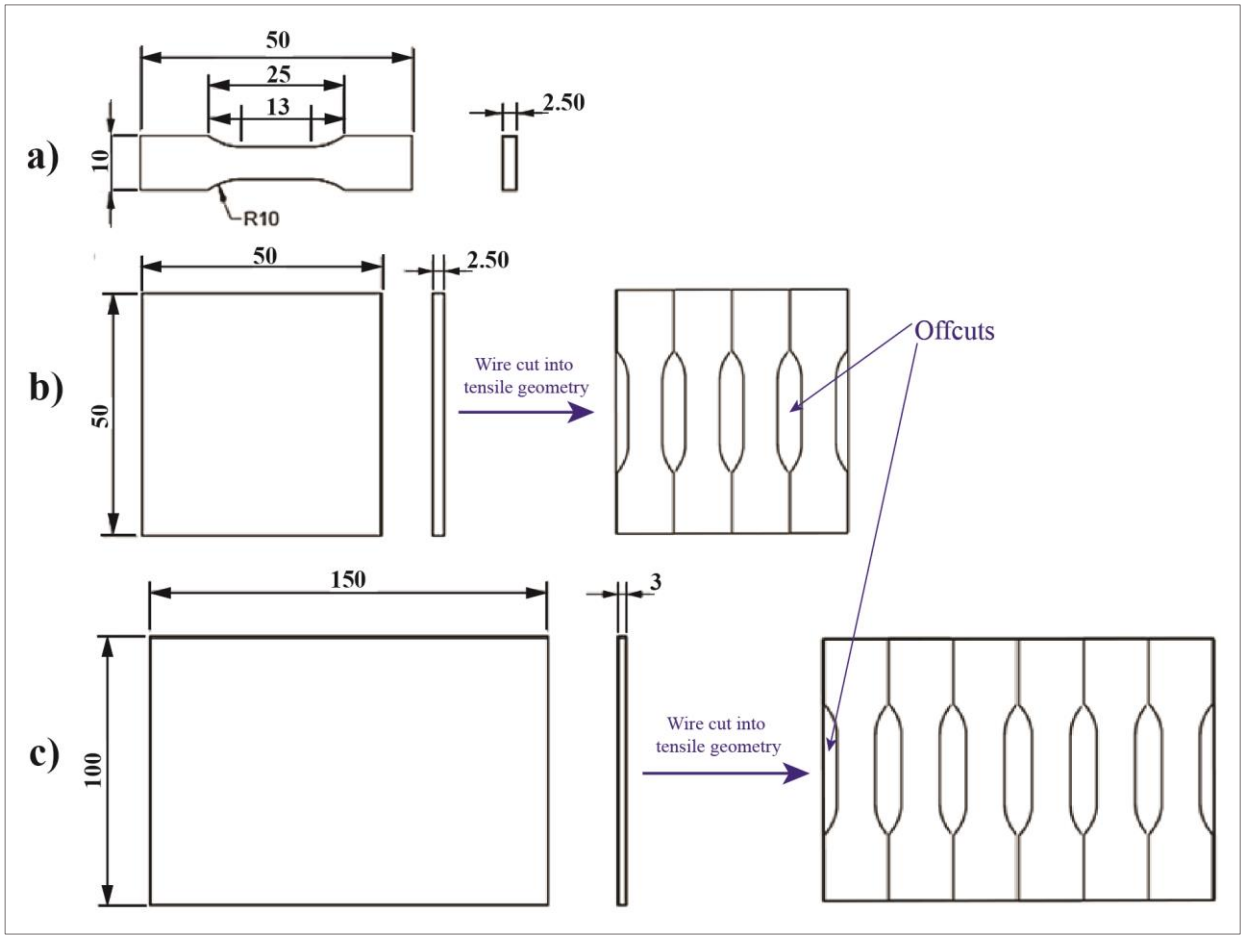

Fig. 3.5 Dimensioned drawing (a) tensile specimen, (b) square specimen - only for Scalmalloy to be additively manufactured for cold rolling, (c) extruded plates wire cut for cold rolling (units are in mm)

Table 3-3 Composition of 5052Al and 5083Al

Base Metal	Al	Mg	Mn	Si	Fe	Cu	Cr	
5052Al	Bal.	2.70	0.07	0.43	0.36	0.04	---	%wt
5083Al	Bal.	3.5	0.50	0.30	0.25	---	0.26	%wt

5052Al and 5083Al alloy extruded plates having a thickness of 3mm were obtained from *Ullrich Aluminium* to be compared with Scalmalloy. Their composition is given in Table 3-3. As mentioned earlier in section 2.1.4, 5052Al and 5083Al were chosen as comparison to Scalmalloy samples as these belong to the same alloying group of Al-Mg 5000 series alloys. Similarly, to Scalmalloy samples, tensile samples were wire cut from the extruded plates according to Fig. 3.5a, while 150mm x 100mm rectangles were wire cut from the extruded plates shown in Fig. 3.5c as these also were subject to different conditioning. It must be noted that the extruded aluminium alloys are 0.5mm thicker than the Scalmalloy samples, as it was necessary to test sample in the as-received state. This will not affect the observation of microstructure and microhardness, but only tensile strength, which is not significant as this data is only used as a baseline for the work on hand.

3.2.1.2 Cold rolling method

Scalmalloy square samples, shown in Fig. 3.5b, and 5083Al and 5052Al rectangular samples, shown in Fig.3.5c, were subjected to cold rolling. Each one was reduced in thickness by 10% and 30% (from a thickness of 2.5mm to 2.25mm and 1.75mm, respectively). Similarly, 5052Al and 5083Al rectangular samples, shown in Fig.3.5c, were reduced in thickness by 10% and 30% (from a thickness of 3mm to 2.7mm and 2.1mm, respectively). These samples were then wire cut into tensile sample shapes shown in Fig. 3.5a and referred to as the 'cold rolled' samples. These were cold rolled at ambient temperature and passed through the rollers as many times as needed to achieve final intended reduction in thickness. These were wire cut into the tensile sample geometry shown in Fig 3.5a. All offcuts were preserved for later testing and sample analysis.

3.2.1.3 Heat treatment conditions

Preliminary tests were conducted to test suitable heat treatment temperatures and showed that heat treatments with temperatures exceeding 540^{o}C resulted in melting within the sample, hence, melting occurred below the expected melting point of 660^{o}C (as per the data sheet in Appendix A). A thermogravimetric (TGA) test was performed on one manufactured Scalmalloy sample to determine the exact melting point of Scalmalloy used in this work and ensured the chosen heat treatment conditions did not cause local melting or other undesirable occurrences. The TGA graph can be seen in Fig. 3.6. Two more samples were tested (shown in Fig. A.2 and A.3 in Appendix A) resulting in an average melting point for Scalmalloy for the work on hand as 618^{o}C. Therefore, this has been the heat treatment limit in selecting heat treatment conditions. Heat treatment was carried out on the Scalmalloy samples only, as the 5052Al and 5083Al are non-heat treatable. Heat treatment conditions are listed in Table 3-4. Heat treatment 1 (HT1) was chosen based on the Al-Sc phase diagram, shown in Fig. 2.19, as the $Al_3(Sc_xZr_{1-x})$ second phase particles are expected to precipitate at this temperature during heat treatment. This is also below the melting temperature given in Fig. 3.6, ensuring there is no melting (liquid) occurring within the sample. Heat treatment 2 (HT2) is a mixture of HT1 and the typical heat treatment of 325^{o}C as given in the literature (A. B. Spierings, Dawson, Kern, et al., 2017). while heat treatment 3 (HT3) is based on the Al-Mg phase diagram. Furthermore, these heat treatment conditions were selected on the basis that they have not been reported in the literature.

T6 heat treatment process was used as this is a typical heat treatment process for aluminum alloys (Yu & Wang, 2018), where the thermomechanical diagrams for the different heat treatment conditions are shown in Fig. 3.7 – Fig. 3.9, and three different heat treatments were applied to the as built and cold rolled Scalmalloy samples.

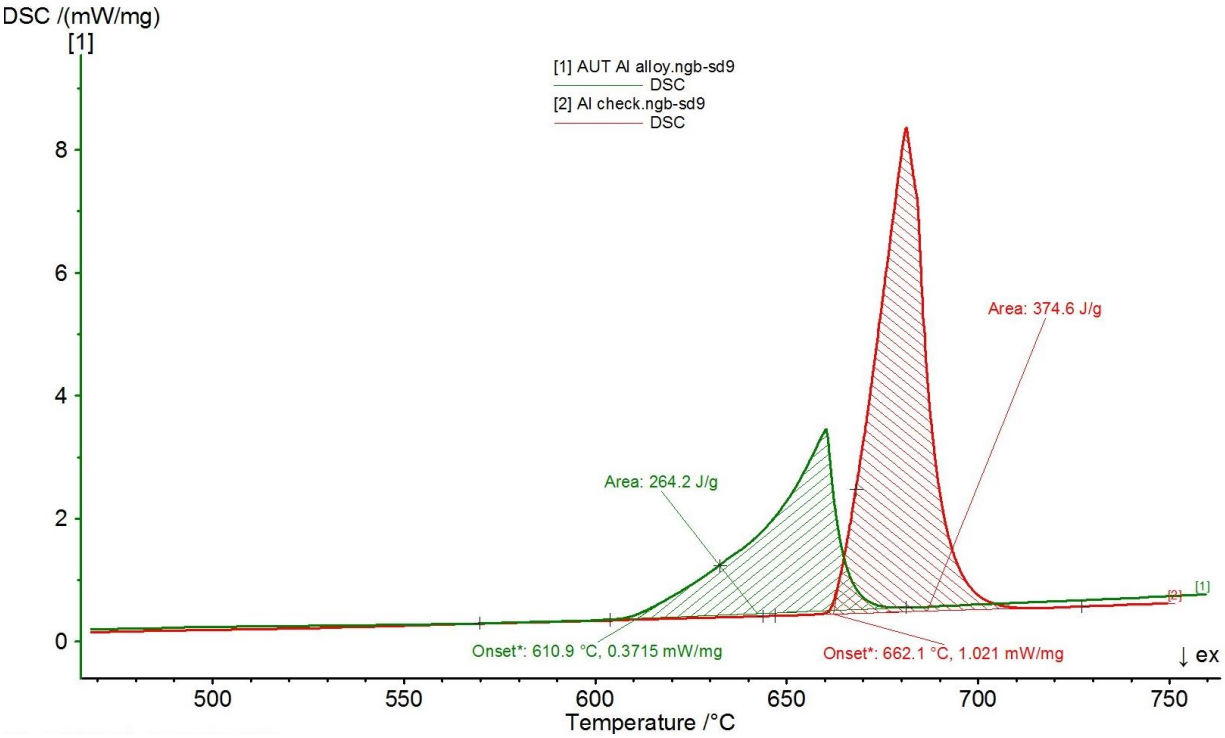

Fig. 3.6 Thermogavimetric graph showing the actual melting temperature of Scalmalloy used in this work

Table 3-4 Selected heat treatment conditions

Heat Treatment Conditions
HT1 - 450ºC /1h – selected based upon Al-Sc Phase Diagram given in section 2.1 and melting temperature of Scalmalloy
HT2 - 450ºC /1h, water quenched (WQ), heat treated at 325ºC /4h, WQ - selected based upon multiple authors (Koutny et al., 2018; R. Li et al., 2019; Schmidtke et al., 2011; A. B. Spierings, Dawson, Kern, et al., 2017; Zhao et al., 2021)
HT3 - 450ºC /1h, WQ, heat treated at175ºC /8h, selected based on Al-Mg Phase Diagram

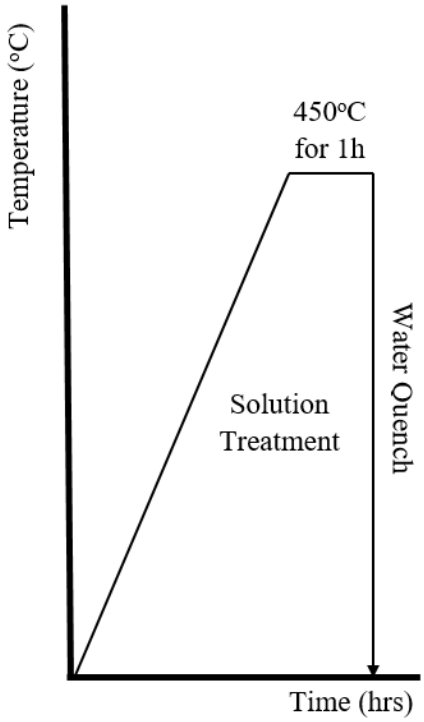

Fig. 3.7 Thermomechanical diagram of HT1 (450°C/1h, WQ)

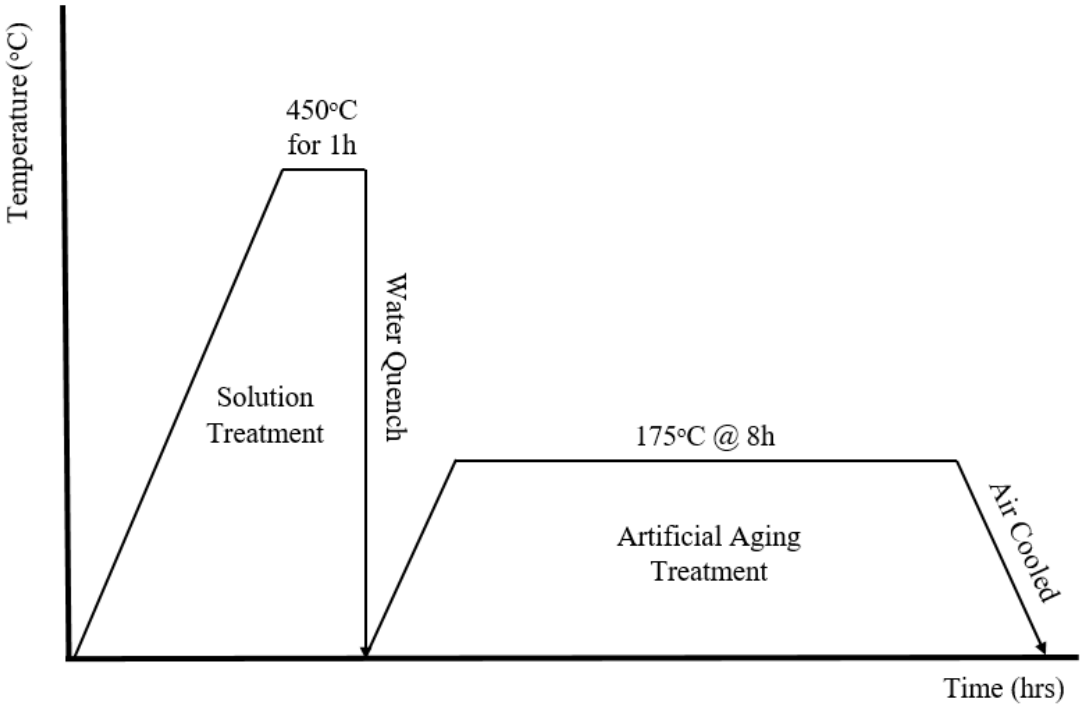

Fig. 3.8 Thermomechanical diagram of HT2 (450°/1h, WQ, then heat treated at 175°C/8h)

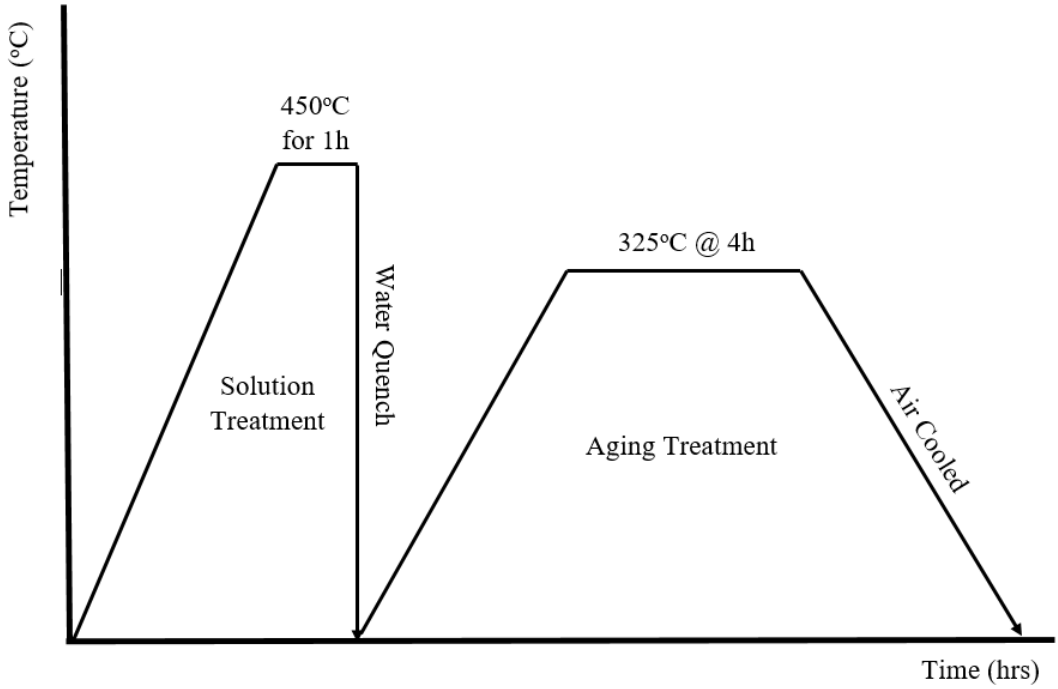

Fig. 3.9 Thermomechanical Diagram of HT3 (450°/1h, WQ, then heat treated at then heat treated at 325°C/4h)

Fig. 3.10 and 3.11 show schematic sequences of how samples were conditioned as there are different combinations of heat treatment and cold working conditions applied to a single sample. Once all samples were conditioned (cold rolled, heat treated), they were set aside to be prepared for testing and sample analysis. As built or as received samples are considered non-conditioned. Table 3-5 shows the abbreviations for the different heat treatment and cold rolled conditions for the samples of Scalmalloy, 5052Al and 5083Al, which will be used through the remainder of this thesis.

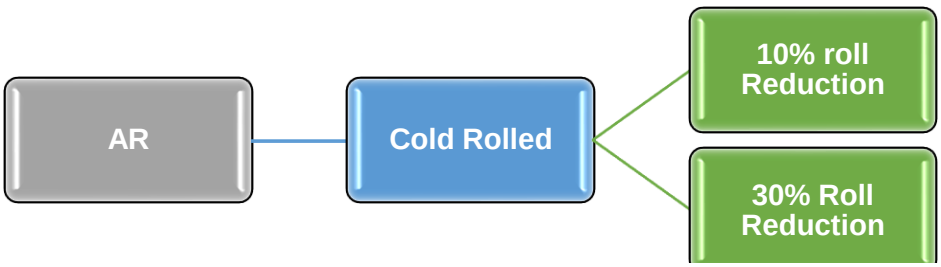

Fig. 3.10 Sample Conditioning diagram for extruded aluminium alloys

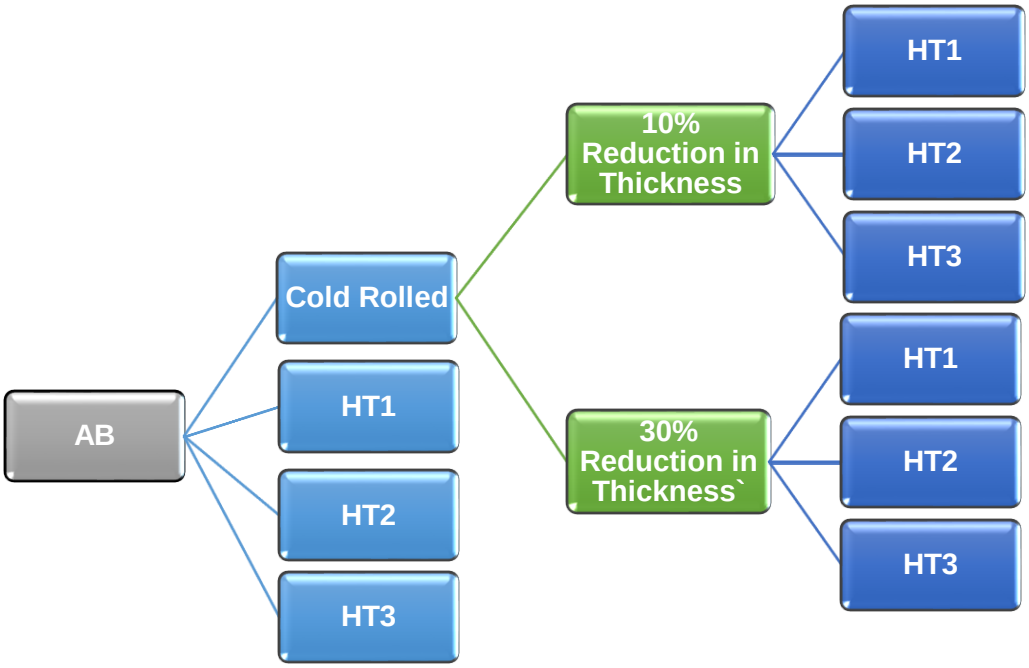

Fig. 3.11 Sample conditioning diagram for Scalmalloy

Table 3-5 Abbreviations for samples to indicate condition for non-conditioned, cold rolled, and heat-treated samples

Abbreviation	Description
AR	As Received – in the condition from which it was received and **only** refers to 5052Al and 5083Al alloys
AB	As built – in the condition immediately after manufacturing process and **only** refers to Scalmalloy
10% CR	As built or as received condition cold rolled to 10% reduction in thickness. Can refer to both Scalmalloy and the extruded aluminium alloys
30% CR	As built or as received condition cold rolled to 30% reduction in thickness. Can refer to both Scalmalloy and the extruded aluminium alloys
AB+HT1	As built condition heat treated at 450°C/1h, then WQ. **Only** refers to Scalmalloy
AB+HT2	As built condition heat treated at 450°C/1h, WQ, heat treated at 175°C/8h, then air cooled to room temperature. **Only** refers to Scalmalloy
AB+HT3	As Built condition heat treated at 450°C/1h, WQ, heat treated at 325°C/4h, then air cooled to room temperature. **Only** refers to Scalmalloy
10%CR+HT1	As built condition cold rolled to 10% reduction in thickness and heat treated at 450°C/1h, then WQ. **Only** refers to Scalmalloy
10%CR+HT2	As built condition cold rolled to 10% reduction in thickness and heat treated at 450°C/1h, WQ, heat treated at 175°C/8h, then air cooled to room temperature. **Only** refers to Scalmalloy
10%CR+HT3	As built condition cold rolled to 10% reduction in thickness heat treated at 450°C/1h, WQ, heat treated at 325°C/4h, then air cooled to room temperature. **Only** refers to Scalmalloy
30%CR+HT1	As built condition cold rolled to 30% reduction in thickness and heat treated at 450°C/1h, then WQ. **Only** refers to Scalmalloy
30%CR+HT2	As built sample cold rolled to 30% reduction in thickness heat treated at 450°C/1h, WQ, heat treated at 175°C/8h, then air cooled to room temperature. **Only** refers to Scalmalloy
30%CR+HT3	As built condition cold rolled to 30% reduction in thickness heat treated at 450°C/1h, WQ, heat treated at 325°C/4h, then air cooled to room temperature. **Only** refers to Scalmalloy

3.3.1 Welding of Scalmalloy study

This section outlines the Gas Tungsten Arc Welding method used on Scalmalloy, 5052Al and 5083Al samples. Sample building and procurement, the welding machine used on the experiment, and the welding parameters are discussed in the following section.

3.3.1.1 Sample manufacturing and preparation

Scalmalloy samples for welding were built using the optimal SLM process parameters established in Chapter 4 and were 60mm x 27mm x 2mm in size (Fig. 3.12). A layout of the Scalmalloy samples on the build platform is shown in Fig. 3.13, where samples are built in the XY direction. Extruded aluminium samples for welding, like the Scalmalloy samples, were wire cut into the geometry shown in Fig. 3.12. Samples were then welded together and then wire cut into the geometry shown in Fig. 3.15a.

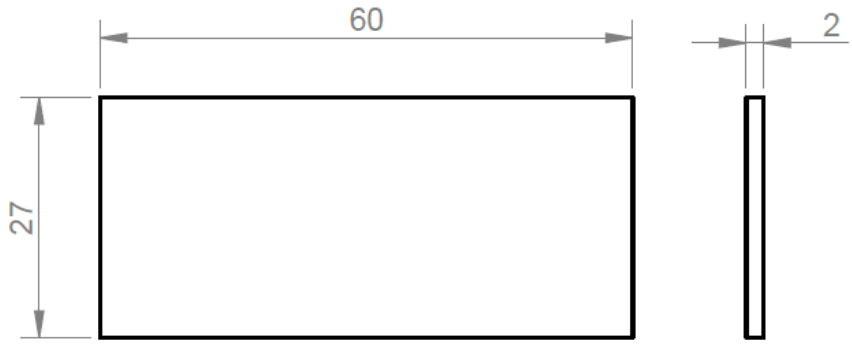

Fig. 3.12 Dimensioned drawing of samples for welding – units are in mm

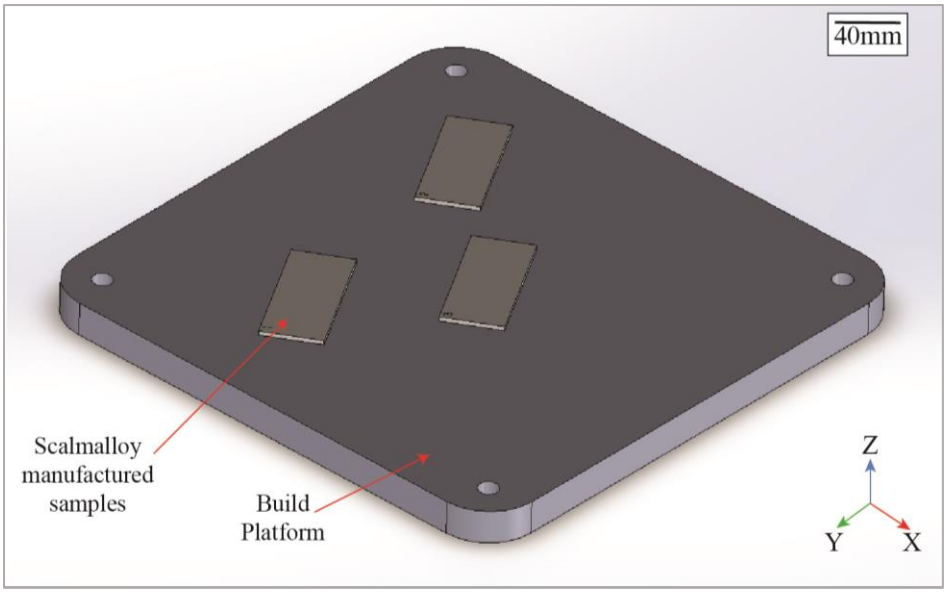

Fig. 3.13 Scalmalloy samples for welding on build platform – units are in mm

3.3.1.2 Gas tungsten arc welding machine

A *Hobart Tigwave 250 AC/DC Arc Welder*, shown in Fig. 3.14, was employed to weld Scalmalloy, 5052Al and 5083Al samples together to form one rectangle 60mm x 54mm in size with a thickness of 2mm via a butt weld.

Fig. 3.14 Hobart Tigwave 250 AC/DC Arc Welder

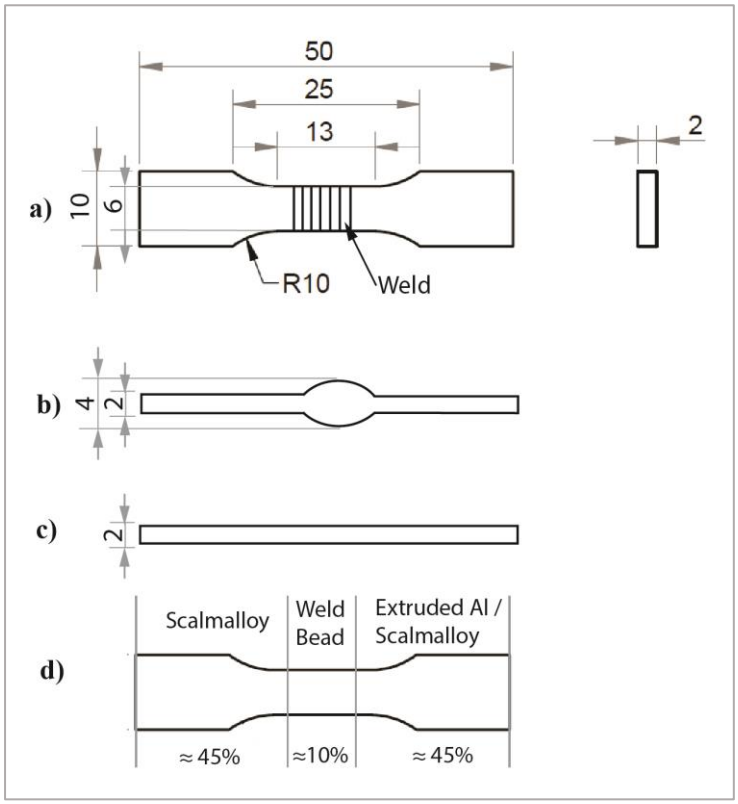

Fig. 3.15 Geometry of tensile test specimen showing dimensions. Side view of b) as welded cross-sectional view and c) post machined cross-sectional view and d) proportions of Scalmalloy, extruded Al alloy and welded metal over the entire length of the sample, where the percentages refer to the approximate proportions of each material contained in the sample - (units are in mm)

3.3.1.3 Gas tungsten arc welding parameters

The GTAW welding parameters are introduced in this section. Table 3-6 summarises the welding parameters that remained constant based on available literature for welding 5083Al and 5052Al alloys (Lei, Deng, Peng, Yin, & Xu, 2013; Y. Liu et al., 2012; Messler Jr, 2008; Shanavas & Dhas, 2017; Subbaiah, 2019). Samples were welded in the following method: Scalmalloy to Scalmalloy, Scalmalloy to 5052Al and Scalmalloy to 5083Al in the 'as welded (AW)' condition and 'post machined (PM)' condition. PM condition refers to samples where the weld nugget was removed by wire cutting to suit the original thickness of 2mm. The AW condition refers to the weld nugget being left intact on the sample. Welding current was the only varying welding parameter among the three aluminium alloys as weld penetration and deposition rate can affect the quality of the weld, where a low welding current can result in lack of penetration and lack of fusion, while a high welding current can cause premature hot cracking. Hence, the welding current varies due to the varying composition of each alloy being welded and is whereby determined based upon preliminary welding tests (Shanavas & Dhas, 2017; Shankar & Wu, 2002; W. Wang et al., 2018). Optimal currents are listed in Table 3-7. These are consistent with the typical welding currents for the 5xxx aluminium alloys reported to be between 70-90A according to literature (Shanavas & Dhas, 2017; Shankar & Wu, 2002; W. Wang et al., 2018). Additionally, the composition of the filler wire of 5356Al is listed in Table 3-8.

Table 3-6 Constant Welding Parameters

Parameters	**Values**
Electrode Material	Tungsten
Welding Angle (º)	≈ 45
Filler Wire	5356Al
Electrode diameter (mm)	2
Weld Speed (mm/s)	3.6
Shielding Gas	Argon
Welding/Gas Flow (l/min)	81
Electric Current Type	AC – High Frequency, Continuous
Welding Voltage (V)	9

Table 3-7 Selected Welding Currents based upon preliminary weld tests

Parameters	**Values**
Scalmalloy - 5083Al Welding Current (A)	85
Scalmalloy - 5052Al Welding Current (A)	88
Scalmalloy Welding Current (A)	81

Table 3-8 Composition of Filler Wire 5356Al

Filler Metal	Al	Mg	Mn	Si	Fe	Cu	Zn	Cr	
5356Al	Bal.	5.0	0.07	0.22	0.38	0.1	0.1	0.45	%wt

The PM samples ensured that the area for tensile testing was uniform and tensile results were not influenced by a variable cross section by the weld bead remaining intact. AW samples were included for information since it is not always possible or practical to remove the weld bead in real life applications. The tensile strength of each sample was calculated individually using their nominal cross sections given in Fig 3.15. Fig. 3.15a shows the tensile geometry for the welded samples with the welded region located in the centre of the sample. The AW samples had a nominal cross section of 6mm (gauge length size) and 4mm due to the size of the weld bead (Fig. 3.15b). PM samples had a nominal cross section of 6mm and 2mm (Fig. 3.15c). The approximate proportions for the base metal substrates to the welded zone is given in Fig. 3.15d for information as the elongation will be measured along the overall length of the sample.

3.4 Mechanical testing

This section outlines and describes the mechanical tests used in this experiment. Tensile testing, hardness testing, fatigue testing, Archimedes density measurement and surface roughness testing are included here.

3.4.1 Relative density evaluation by Archimedes Principle

Archimedes density measurement test was used to determine the relative densities of each sample as this is one of the simplest and most efficient ways in determining relative densities of a part. The samples were weighed in air and then in ethanol while being attached to a thin metallic wire supported by a metal frame, shown in Fig 3.16. A *BSM220.4* electronic balance with accuracy of 0.1mg was used to weigh the samples. Each sample in both air and ethanol were weighed three times to account for temperature differences and other possible errors. Absolute densities were calculated using Equation 3.1 taking the theoretical density of Scalmalloy as 2.67g/cm^3.

$$\rho_{abs} = \frac{m_{air}}{m_{eth}} \cdot \rho_{eth}(T) \qquad \textit{Equation 3.1}$$

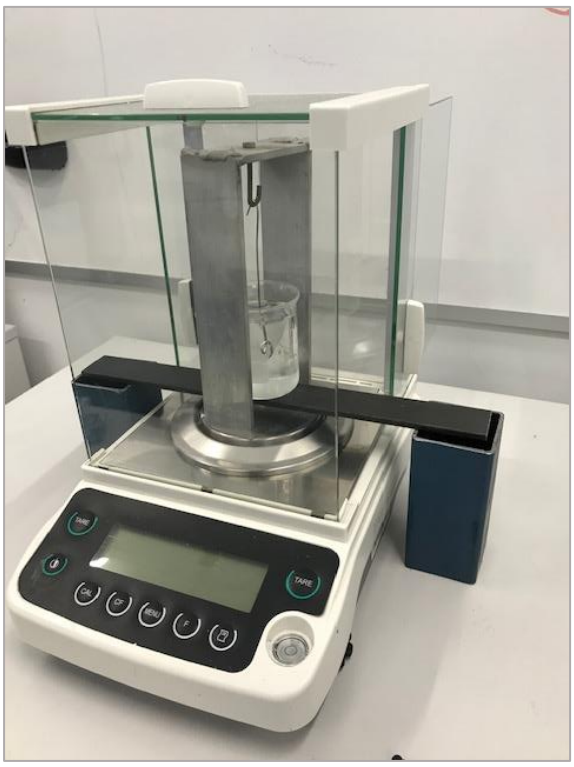

Fig. 3.16 Archimedes Density Measurement Experimental Setup

3.4.2 Strength analysis by tensile testing with digital image correlation

Tensile testing was carried out using three systems. The *Tinius Olesen Tensile Testing System, Zwick 1476 Universal Testing Machine Limess VERTSS position measuring system* with Digital Image Correlation (DIC) and the *Autograph Universal Testing Machine Ag-Is* also equipped with DIC. A position rate of 3mm/min and a 10kN load cell was used for all tests. A minimum of three samples per condition were tested and the mean value was calculated for all tensile properties. One sample of each condition were either tensile tested with the *Zwick 1476 Universal Testing*

Machine Limess VERTSS position measuring system and *an Autograph Universal Testing Machine Ag-Is* with DIC Imaging, while the remaining samples were tested with the *Tinius Olesen Tensile Testing System*.

3.4.3 Microhardness assessment by hardness testing

Vickers microhardness testing was carried out upon samples using an *LM800AT* tester. A dwell time of 10 seconds and a load of 100fg was used. This test was used to compare hardness among the samples subjected to different conditions and was also used to compare hardness among powder samples for determining optimal SLM parameters in Chapter 4. Ten indents were made along the sample in the horizontal (x), transverse (y) and longitudinal (z) planes, and the mean value was calculated. The microhardness of the welded samples was recorded slightly differently, where readings were taken from left to right starting at the Scalmalloy base metal side and continuing through heat affected zone and welded region until finally reaching the next base metal substrate along the transverse plane perpendicular to the weld plane. This was done to illustrate the varying microhardness through each region.

3.4.4 Surface topology inspection by profilometer

Surface roughness was measured using a *Taylor Hobson Ultra 2006 version*, where ten readings were taken per a sample upon each surface in the horizontal (x), transverse (y) and longitudinal (z) directions, shown in Fig. 3.17. This was done to illustrate the effect of post processing treatments of heat treatment and cold rolling on the surface topology (roughness) of Scalmalloy samples compared to the as built condition and the as received condition of the extruded aluminium alloys.

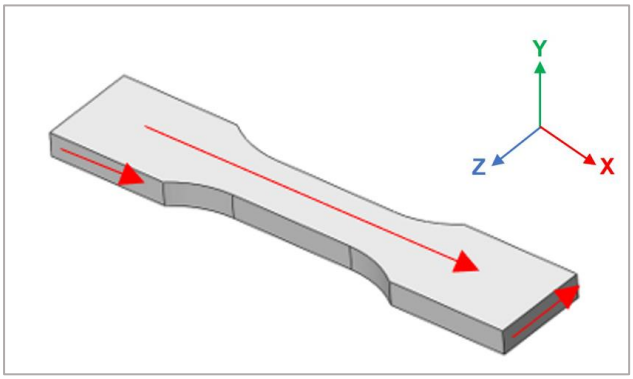

Fig. 3.17 Depiction of surface roughness test

3.5 Sample analysis

This section details methods used to prepare samples for analysis and describes the different equipment used in analysing samples. Metallography, optical microscopy (OP), scanning electron microscopy (SEM), electron backscatter diffraction (EBSD) is employed to analyse mechanical properties, microstructural features, and material characterization of all samples.

3.5.1 Sample preparation by metallography

Samples were metallographically prepared to undergo microhardness testing, fracture and defect analysis, and microstructural analysis. A *Stuers Labotom-3* cutter was used to cut samples. These were then hot mounted using *PolyFast* and a Struers Labo-Press 3 at 150°C at 25kN. Each sample was ground using *Struers* silicon carbide grinding papers with 180, 500, 1200, and 2400µm mesh on a *Buehler MetaServ* rotary grinding machine. Then, manually polished with *Struers* diamond paste on a 6µm on *MD-Dac* fabric on a *Struers LaboPol-2* polishing machine. Lastly, a *Struers TegraPol-25* automatic polisher with a 3µm diamond suspension on *MD-ol* fabric for 3min and 0.04µm colloidal silica suspension n *MD-Chem* fabric for 1min. Samples were cleaned with ethanol between each polishing step. For examination of microstructure, cross sectioned mounted samples were etched using Keller's agent, a solution of 2.5% HNO3, 1.5% HCl, 1% HF and the balance is distilled water.

3.5.2 Microstructural characterisation by optical microscopy

Olympus *BX51M* was used to observe the microstructure of the samples. Images were captured and then *ScopePhoto* system was used to record the micrographs. Micrographs were taken at magnifications of x5, x10, x20, x100 and x1000. Fig. 3.18 shows the correct orientation for the planes and axes that will be used in this study especially when presenting micrographs.

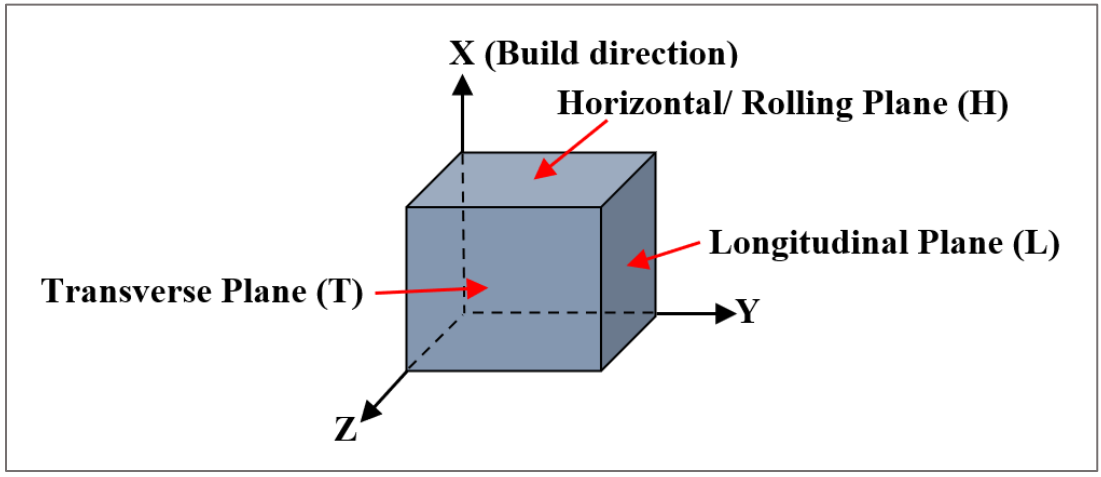

Fig. 3.18 Orientation cube showing reference planes and axes

3.5.3 Fracture, defect, and microstructural analysis by scanning electron microscopy

Hitachi SU-70 Schottky field emission scanning electron microscope (SEM) was used in fracture analysis and defect observation of samples. SEM was also used to obtain high magnification

images of the microstructure. Micrographs were taken at several magnifications, in a range between x100 and x5000 depending upon the sample under investigation. *Energy Dispersive Spectrometer* (EDS) was used to observe elemental composition of samples by the incorporation of the Noran System 7 (NSS) especially for the welded samples.

3.5.4 Microstructural–crystallographic characterization by electron backscatter diffraction

Electron Backscatter Diffraction (EBSD) is a powerful technology often coupled with an SEM machine to obtain microstructural information of a material by mapping the microstructure of the surface area to obtain crystallographic and grain information. The EBSD process, shown in Fig.3.19a, consists of an electron beam probing the surface of a sample within an SEM machine. Electrons that backscattered from the sample are collected by a detector and displayed on a monitor to show the electron backscatter diffraction pattern, where the sample is tilted to an angle between 60^{o} and 70^{o} towards the detector to increase the definition of the pattern. This pattern that is obtained is called the Kikuchi pattern (Wilkinson & Britton, 2012). The EBSD maps produced through this process are then used to determine crystal orientation, grain size, grain size distribution and grain type. Crystal orientation is often described using Miller indices. This is a reference convention used to describe the orientation of a cubic crystal with reference to the overall material axes - (x, y, z), which are also known as directions of the crystal. Some common directions are (1 0 0), (1 0 1), and (0 0 1), where <1 0 0> signing convention can also be used, described in Fig. 3.19a, noting that the crystal orientation is worth knowing as it can indicate whether a material has anisotropic tendencies (Waeselmann, 2012; Wilkinson & Britton, 2012).

EBSD was carried out using the *Hitachi SU-70 Schottky* SEM and only performed on the Scalmalloy AB condition and the Scalmalloy cold rolled and heat-treated conditions that possessed the highest tensile properties. Samples were prepared according to section 3.5.1 but with a mixture of Struers Polyfast and Condufast due to their conductive properties to perform electropolishing. The mounted sample thickness was between 15-17mm for higher accuracy during the EBSD process. Struers electrolytic machine was used for electropolishing for 10s at 23V in an electrolytic solution of 10% perchloric acid and 90% ethanol solution. Lastly, samples were rinsed with 99.8%+ (pure) ethanol, and immediately stored in the ethanol until EBSD could be performed ensuring the smallest time period between polishing and performing EBSD to minimise oxidation. A diagram of the EBSD camera and mounted sample is shown in Fig. 3.19b, where the sample is tilted at between 60^{o} and 70^{o} to observe the Taguchi pattern and begin the EBSD scan. Furthermore, the grain size and grain size distribution information from the EBSD maps were analysed using *ImageJ* software.

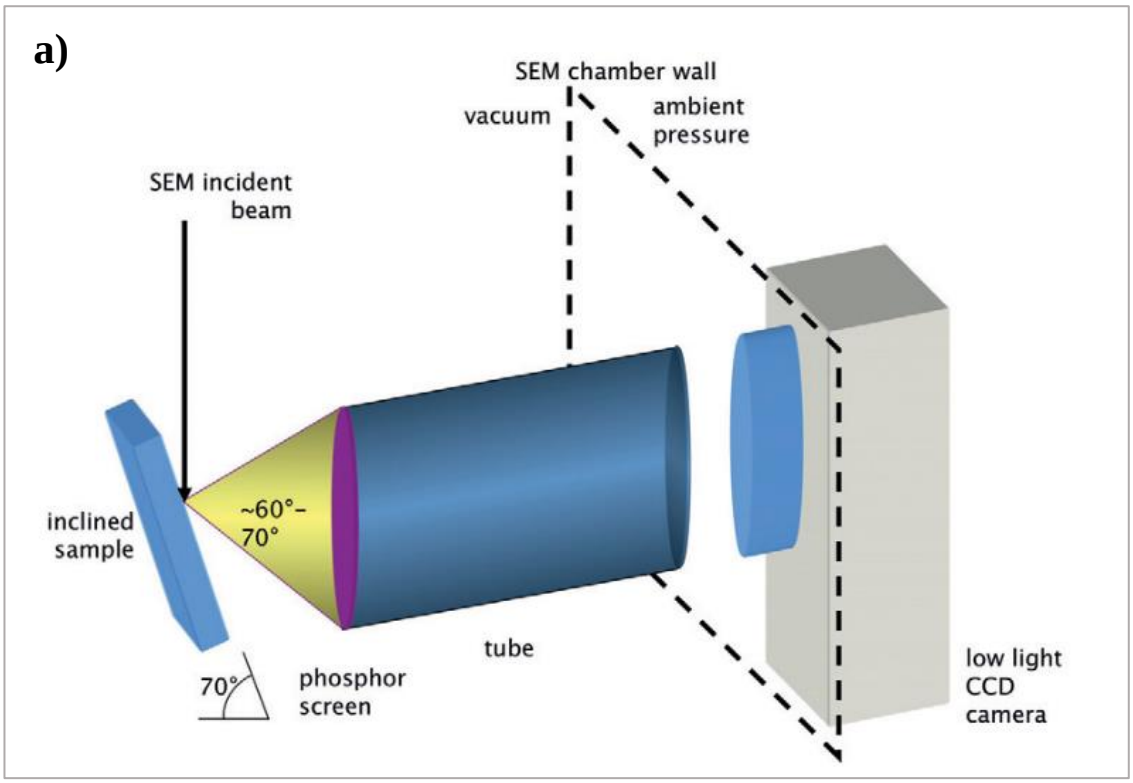

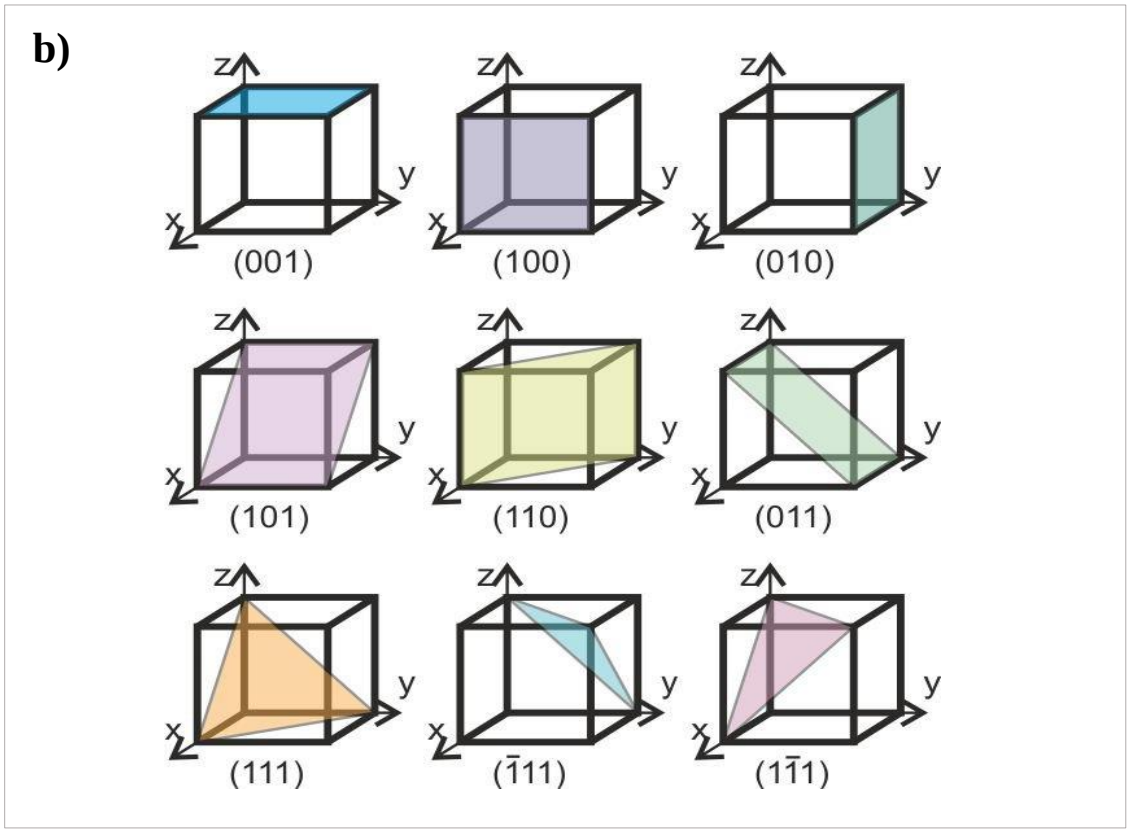

Fig. 3.19 a) Miller indices directions on a cubic crystal structure adapted from (Waeselmann, 2012). b) Graphical representation of the EBSD process adapted from(Wilkinson & Britton, 2012)

Chapter 4 Results and discussion of selective laser melting process parameter study

This section will include powder characterisation, verification of SLM parameters, investigation of SLM process parameters, reproducibility, and the influence of layout position. These factors determined the optimum set of SLM process parameters to produce Scalmalloy samples for this work. It is worth noting that the results discussed in this chapter are also reported in Celine Turangi et al. (2020), as this is earlier published research for the work on hand. Having said that, the final conclusive results for the Archimedes relative density measurements achieved a higher accuracy, as the experimental apparatus for the Archimedes density test was refined. Hence, the published results may differ slightly to the results reported in the work on hand.

4.1. Powder characterisation

SEM micrographs, shown in Fig. 4.1, were taken of the supplied Scalmalloy powder and show powder particles had mostly spherical morphology with an average diameter distribution size between 5µm and 40µm. A small number of irregular-shaped elongated particles with lengthwise dimensions between 60µm and 80µm were observed, along with satellites having diameters as low as 2 µm. At higher magnifications, all particles displayed a rough surface structure.

The supplied material data sheet, shown in Fig. A.1 in Appendix A, for the Scalmalloy powder shows a sieve analysis with 0wt% particles larger than 63µm. As discussed above, a small number of particles have dimensions larger than 63µm with the majority of these being elongated suggesting that at least one of their dimensions is smaller than 60µm. Hence, they can pass the sieve analysis, which is one disadvantage of this analysis method. This is why powder particles were also analysed optically to ensure accuracy in powder characterisation. Fig. 4.2 shows optical micrographs of powder particle cross sections showing inner porosity in 7.1% of 966 optically evaluated powder particle cross sections.

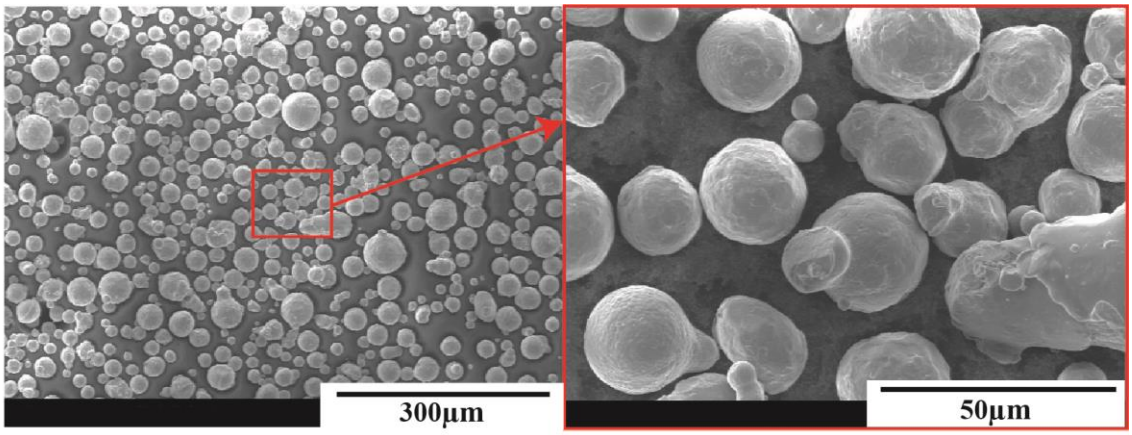

Fig. 4.1 SEM micrographs of powder morphology at different magnifications

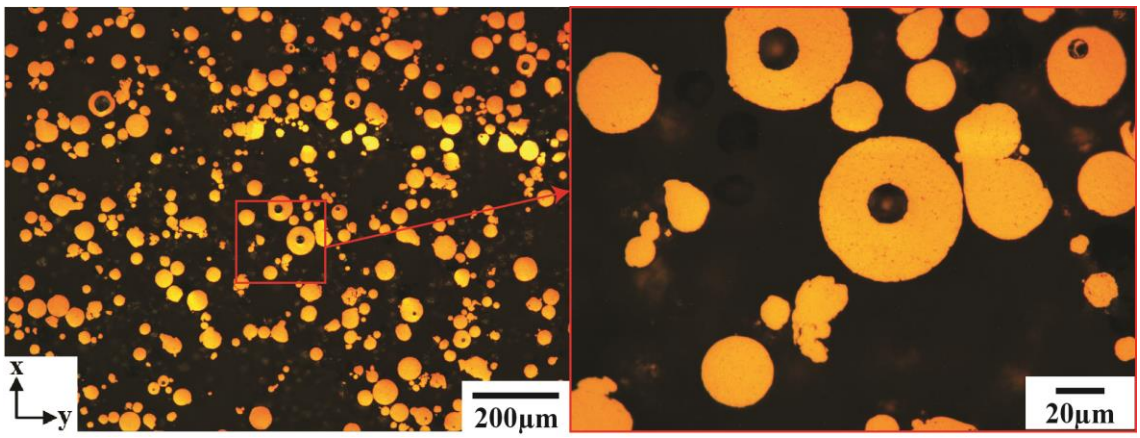

Fig. 4.2 Optical Micrographs of Scalmalloy powder particle cross sections

Inner porosity had mostly spherical morphology likely due to gas entrapment during solidification similar to findings in Galy, Guen, et al. (2018) (Galy, Guen, et al., 2018). Inner porosities were either much smaller than the powder particle cross section size or as large as their powder particle size. Hence, it is worth noting that the likelihood of a metallographic cross section to cut an inner pore is lower than to cut a powder particle cross section so the number of powder particles with inner pores was assumed to be slightly higher than 7.1%. Microhardness testing was carried out on 30 different powder particle cross sections resulting in an average value of (91.4±9.7) HV0.005. This is in agreement with findings reported by Palm, Leuschner, Schubert, and Kieback (2010) where it was reported that microhardness values ranged from 120 to 175HV.0.005 for a different Scalmalloy composition than the one used in this work, processed by melt spinning. According to Palm et al. (2010), the lower microhardness readings in the range of 120HV were thought to be due to the increasing suppression of $Al_3(Sc_{1-x},Zr_x)$ due to increased cooling rates and thicker ribbon thicknesses. This is likely the reason for the lower microhardness in the Scalmalloy powder particles in this work as cooling rates for gas atomisation processes are between 10^5-10^7K/s for aluminium alloys, exceeding cooling rates experienced in melt spinning processes

Powder morphology must be uniform and a standard size between 20µm to 100µm for the powder particles sizes to achieve better flowability of the powder. Smaller powder particles will have low flowability as Van der Waals forces would result in agglomeration, while larger powder particles would result in poor build tolerance and resolution (Yap et al., 2015). Hence, good SLM processability of the Scalmalloy powder used in this work is expected as powder particles showed mostly spherical powder morphology and typical powder particle size distribution suitable for SLM processes allowing for the formation of homogenous powder layers. Additionally, suppression and absence of $Al_3(Sc_{1-x}Zr_x)$ precipitates increase powder processability as these do not need to be melted during the SLM process and formation of a supersaturated solid solution is also more likely to occur. However, inner porosity found in powder particles may lead to increased porosity of the manufactured parts detrimentally affecting mechanical properties.

4.2 Verification of selective laser melting process parameters

The first five manufactured Scalmalloy cube samples are shown in Fig 4.3, and were processed using SLM process parameters (Table 3-2 given in section 3) reported by A. B. Spierings, Dawson, Dumitraschkewitz, et al. (2018). By visual inspection, it appears that the swelling on the top surfaces increases with increasing EVD.

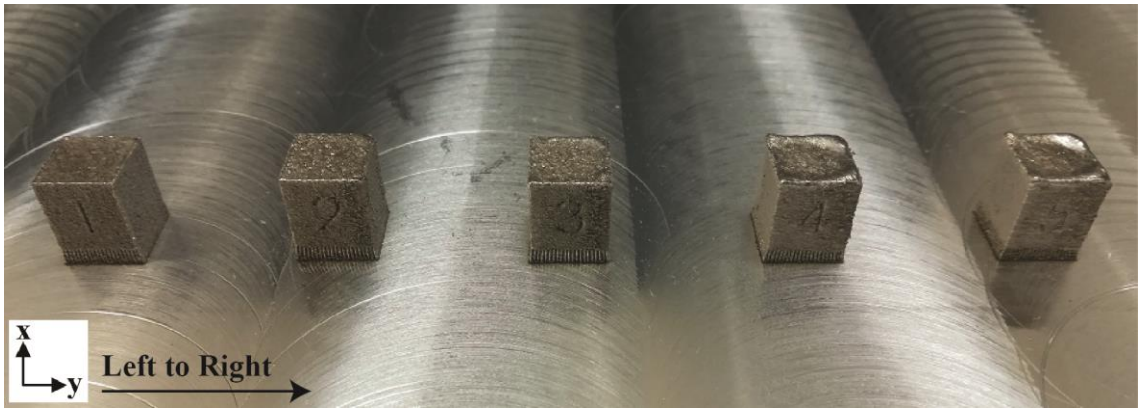

Fig. 4.3 As-built cube samples from first build job showing swelling on top surface with 3mm bottom support structures. From left to right: 80J/mm^3, 120J/mm^3, 150J/mm^3, 240J/mm^3, 280J/mm^3 energy volume density.

Dimensional accuracy of each sample is compared to changing EVD (energy volume density) in Fig 4.4. Low influence from EVD is evident as all samples were ±0.1mm to 0.2mm larger than the CAD model. Distances between opposing surfaces in y-direction are slightly larger than in the x-direction as each sample was marked with a sample number in y-direction (to identify each sample) which may negatively influence the results. Standard VDI3405 Part 3 (VDI, 2014) suggested a tolerance of ±0.1mm for dimensional accuracy which has been slightly exceeded here. The swelling on the top surfaces and varying dimensional accuracy is thought to be due to the attraction and melting of adjacent powder particles next to actual laser scan tracks from the surface tension of the melt pool and melt pool motion with laser scan speed (Yadroitsev, Gusarov, Yadroitsava, & Smurov, 2010).

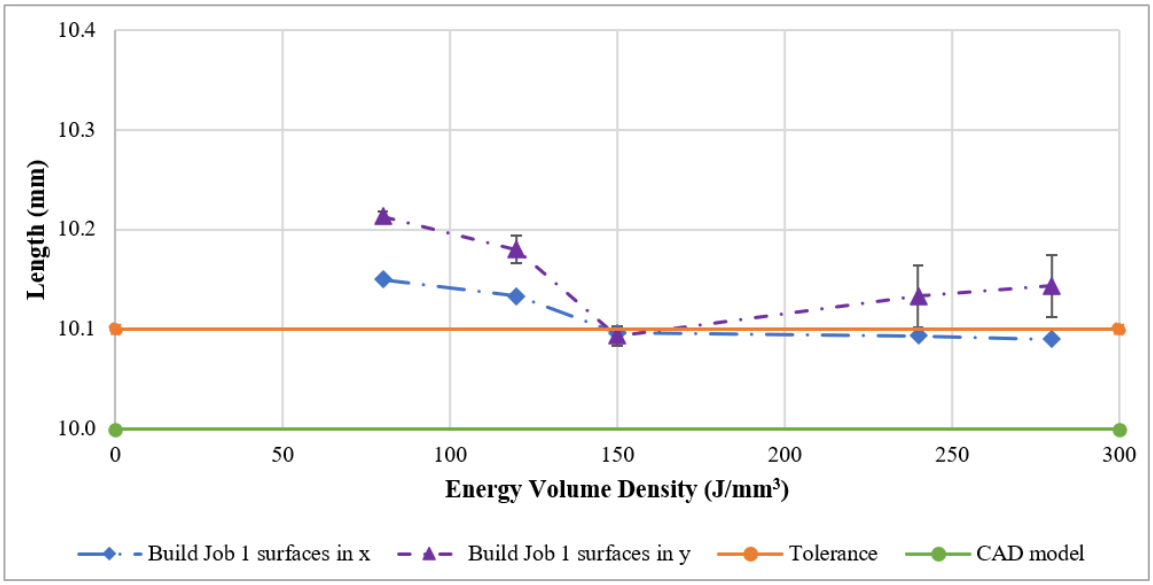

Fig. 4.4 As-built dimensional accuracy of first build job for all five cube samples in x and y directions with changing energy volume density. CAD model and suggested tolerance of ±0.1mm is included

Fig. 4.5 compares the surface quality of as-built samples processed with 80J/mm^3 and 280J/mm^3 EVD. The top surfaces for the samples show visible hatch and contour scan directions of the finally built metal layer. Visual inspection detected partially melted powder particles appearing on the surface of both samples. The 280J/mm^3 samples observed visible swelling and side surfaces have open porosity. The apparent surface roughness on the side surfaces and top surfaces are likely due to differing surface tension in the melt pool causing Marangoni convection, balling and partially melted particles to stick to the surfaces like results reported by Strano, Hao, Everson, and Evans (2013).

Relative densities of the five cube samples from the first build job were evaluated to determine the level of inner porosity. Fig. 4.6 shows results of Archimedes and metallographic relative densities with changing EVD. The 120J/mm^3 and 80J/mm^3 samples reached relative densities of more than 99%, while other samples reached values between 95% and 98%. The differences between Archimedes and metallographic relative densities were significantly small almost less than 2%, where this discrepancy can be attributed to a smaller section of the sample being evaluated in the estimation of metallographic density compared to the Archimedes density method that involves the entire sample in its calculation of relative density. The standard deviations of samples with lower EVD were much higher. When compared to expected findings shown in Fig 3.3 (section 3.1.1.4), the curve has shifted to lower EVDs consistent with findings reported in A. B. Spierings, Schneider, and Eggenberger (2011) where Archimedes density measurements showed lower standard deviation than metallographic densities.

Fig 4.7 shows optical micrographs of innner porosity for samples processed with 80J/mm^3 and 280J/mm^3 EVD. Hot cracks did not occur for any of the samples, and the three samples with lower relative densities (150J/mm^3, 240J/mm^3, 280J/mm^3) showed uneven lateral pore distribution and

a wider range of pore size distribution consistent with higher standard deviations for metallographic relative densities. The porosity shown in Fig 4.7a for the 80J/mm^3 are randomly distributed mostly spherical micro pores with diameters smaller than the powder particle size likely caused by powder derived gas porosity (Galy, Le Guen, et al., 2018). The larger pore sizes are likely due to insufficent melting of powder and low flowability due to lower energy input consistent with the literature (R. Li et al., 2019). While Fig. 4.7b with high EVD of 280J/mm^3 features large mettalurgical pores and irregular sized pores with a higher pore size distribution likely related to high energy input resulting in rapid solidification of the metal without completely filling all gaps with molten metal (Koutny et al., 2018). Hence, the sharp drop in relative densities (Fig. 4.6) for samples manufactured with 150J/mm^3, 240J/mm^3 and 280J/mm^3 is attributed to the higher level of inner porosity shown in Fig 4.7. Differences in the measured shifted SLM process parameter window compared to expected findings (Fig 3.3), from Adriaan B. Spierings et al. (2016) are explained by the differences between SLM machines, laser focus diameter, lasers, scanning direction and Scalmalloy powder. Additionally, doubling laser power does not result in the same relative densities even when EVDs remained constant. Yadroitsev et al. (2010) reported decreasing scan track width, while increasing scan speed for single scan tracks seemed to incur gas entrapment porosity as the hatch distance was too high for SLM parts. However, the influence of scan speed on scan track width with increasing laser power decreased.

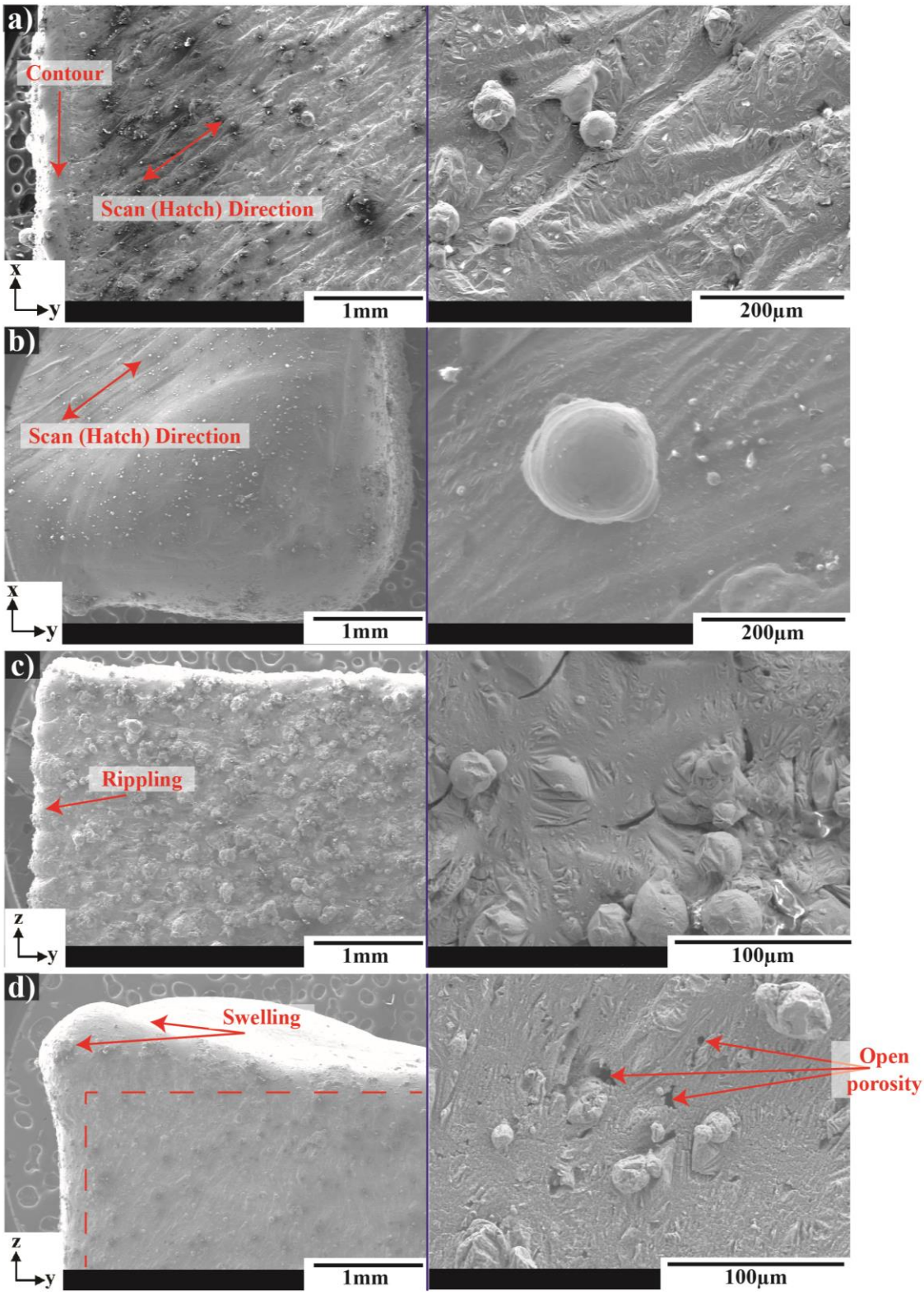

Fig. 4.5 SEM micrographs of as-built cube samples showing surface quality: top view (a,b) and side view (c, d). (a, c)80J/mm^3, (b, d) 280J/mm^3 samples. Hatch direction, scan direction contour, rippling and swelling as indicated

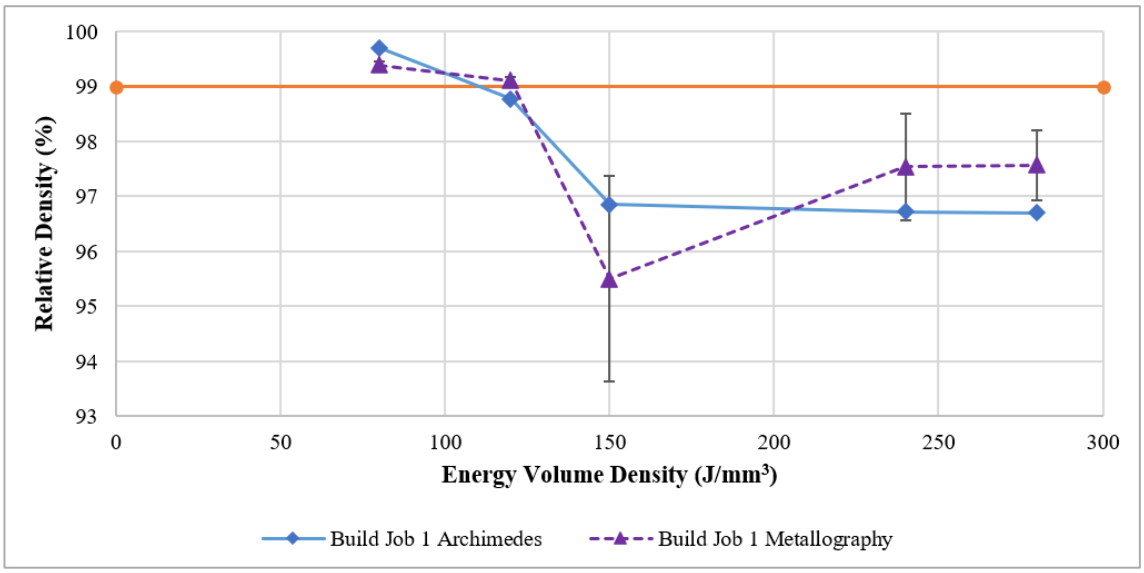

Fig. 4.6 Relative densities, both Archimedes and metallographic, are compared with changing EVD. Ideal density (99%) as indicated for reference

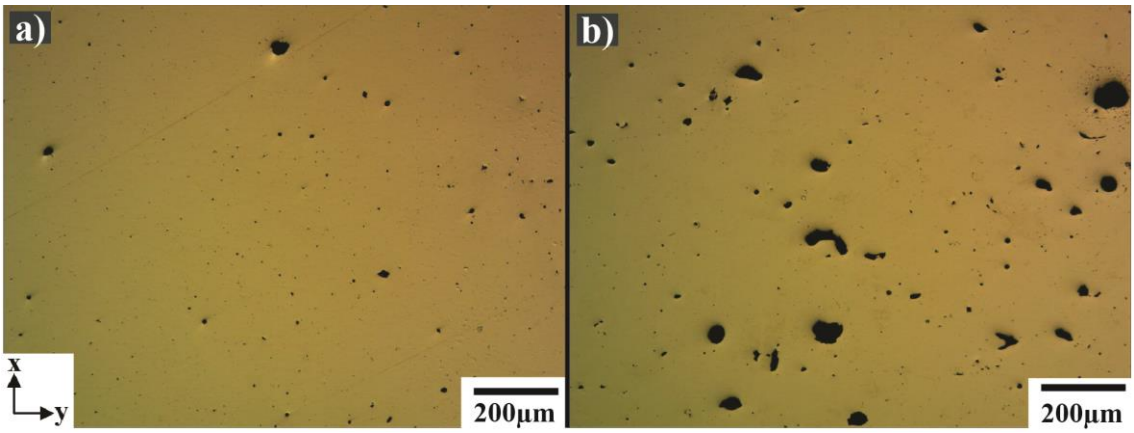

Fig. 4.7 Optical micrograph showing cube sample cross sections with morphology, lateral and size distribution of inner porosity for a) 80J/mm³ and b) 280J/mm³ energy volume density

Fig. 4.8 shows the microhardness results for the five cube samples, where an increase in microhardness is visible as EVD increases. Low microhardness corresponded to the suppression of precipitates $Al_3(Sc_{1-x}Zr_x)$ by rapid solidification. Hence, low EVDs result in less heat in the melt pool and the high thermal conductivity of Scalmalloy solidified layers underneath caused higher cooling rates. Fig. 4.8 also compares microhardness of the cube samples to the microhardness of the initial metal powder particle cross sections. Standard deviations for all average values are identical and the cube samples processed using 80J/mm³ and 280J/mm³ EVD exhibit similar microhardness readings to the powder particles. Hence, parts produced with a laser power of 400W and EVDs lower than 120J/mm³ result in high suppression of $Al_3(Sc_{1-x}Zr_x)$ particles and high supersaturation of aluminium solid solution leading to optimum conditions for post heat treatment of Scalmalloy (B. Zhang et al., 2017). Fig. 4.9 shows etched cross sections of cube samples processed using 80J/mm³ and 280J/mm³ EVD. These show similar microstructures as those discussed in the literature (Best et al., 2018; A. B. Spierings, Dawson, Dumitraschkewitz,

et al., 2018; A. B. Spierings, Dawson, Heeling, et al., 2017; A. B. Spierings, Dawson, Kern, et al., 2017) where scan track depth increases with increasing EVD.

In summary, a partial optimal SLM processing window with relative densities exceeding 99% was found for a laser power of 400W in an *AM 400 Renishaw SLM* machine. Findings were confirmed using Archimedes density method and metallographically prepared cross sections of samples. This partial processing window also resulted in lowest microhardness of samples comparable to microhardness of powder particles. Further investigations were made in the following section to explore the full SLM parameter window and as no maximum in relative densities were found yet.

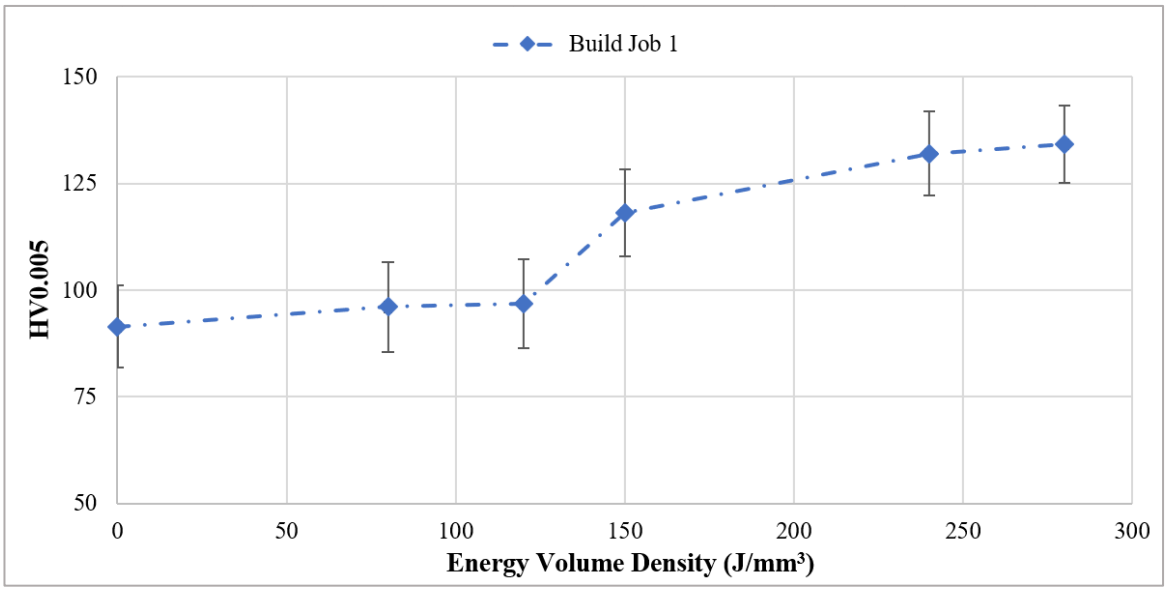

Fig. 4.8 Microhardness results of cube samples dependent on energy volume density, where 0 J/mm³ refers to powder particle cross sections.

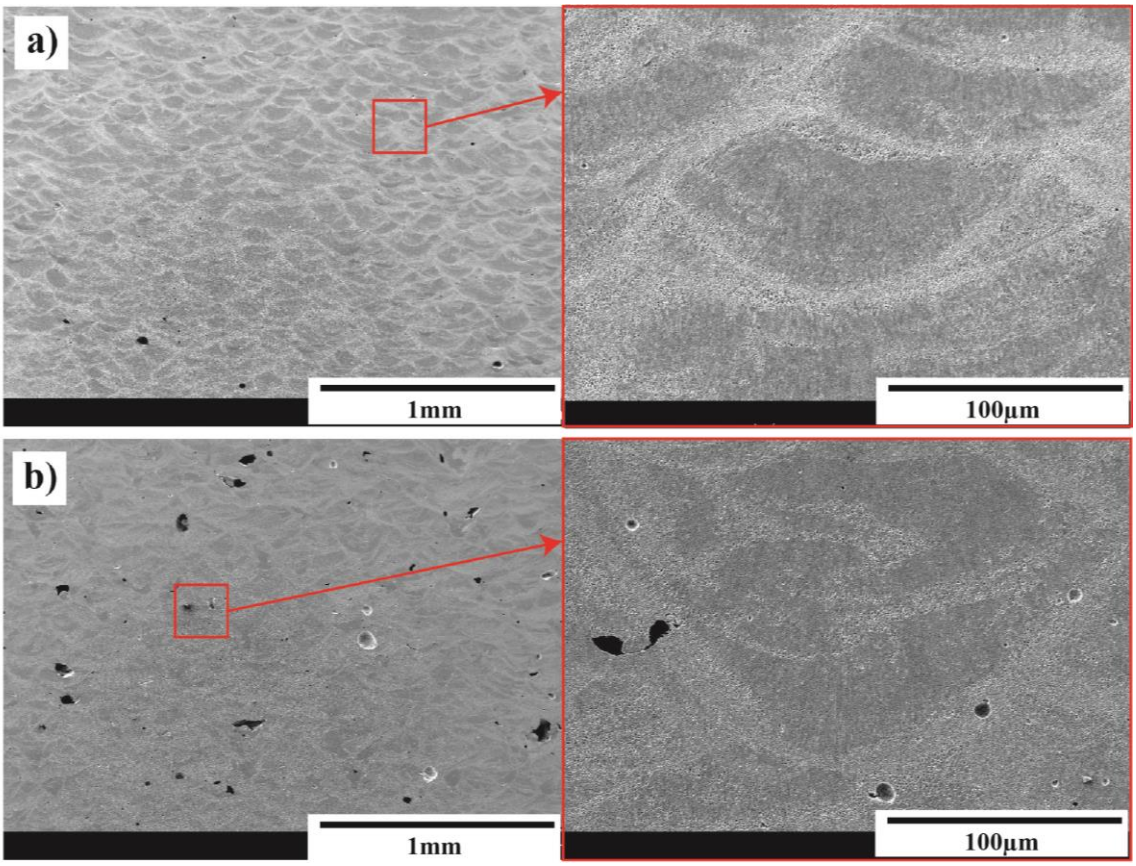

Fig. 4.9 SEM micrographs of etched microstructures for cube samples produced using a) 80J/mm^3 and b) 280J/mm^3

4.3 Investigation of selective laser melting process parameters

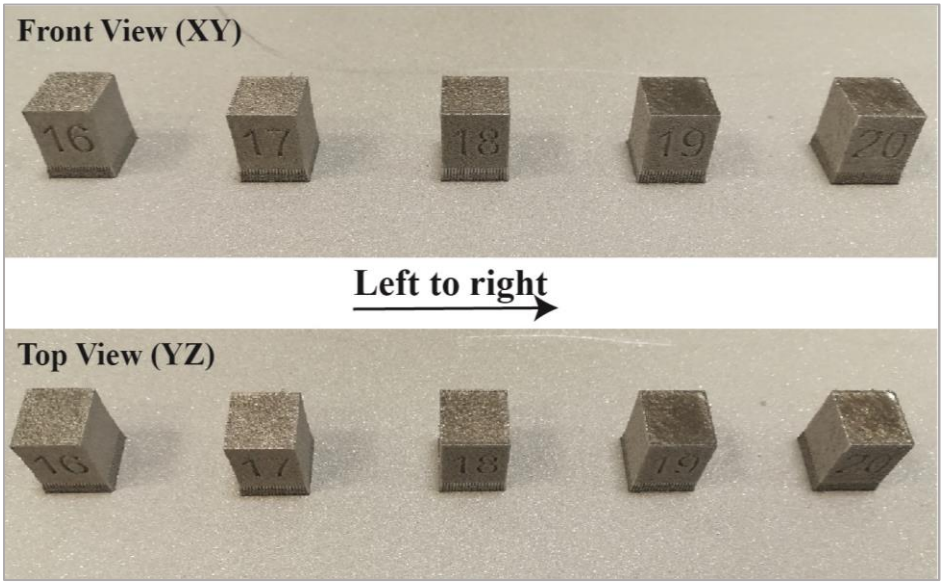

Fig. 4.10 As-built cubes showing surface quality in both the front and top views. Cubes are built on 3mm high supports. Left to right: 30J/mm^3, 45J/mm^3, 60J/mm^3, 80J/mm^3, 100J/mm^3.

Identical experiments and methods were performed, but with modified EVDs. The second build job consisted of five cube samples, shown in Fig. 4.10. These samples were produced using 30J/mm^3, 45J/mm^3, 60J/mm^3, 80J/mm^3 and 100 J/mm^3, lower EVDs than the first build job. By

visual inspection, swelling was less evident compared to the first build job, but surface roughness appears to have increased with decreasing EVD.

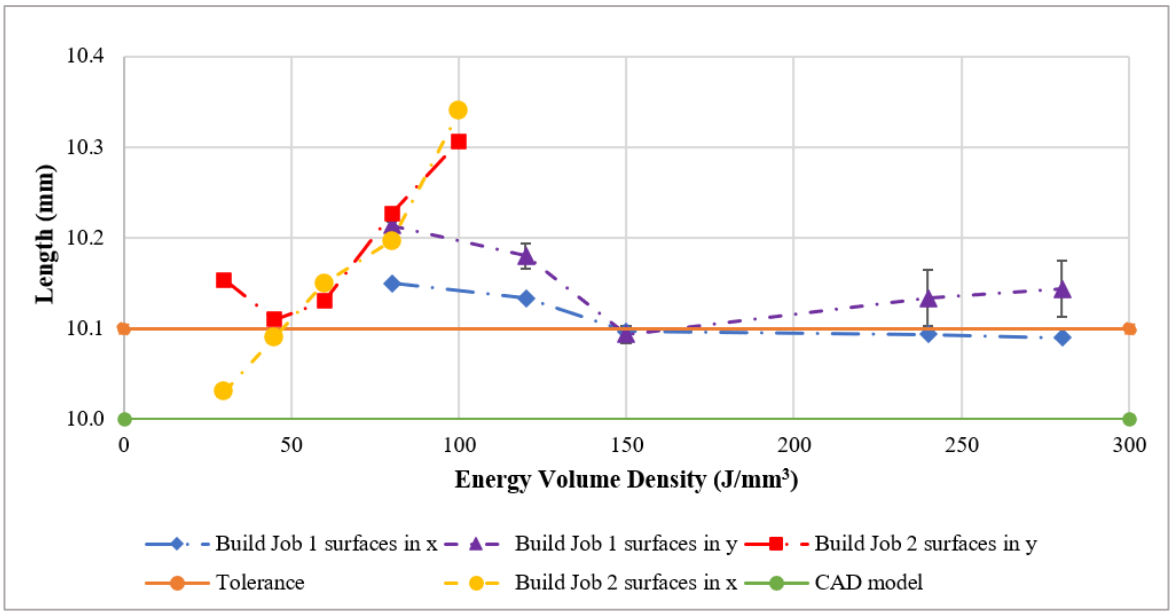

Fig. 4.11 Comparison of dimensional accuracy for as-built cube samples for both build jobs in different surface directions with changing energy volume density. Tolerance of 0.1mm is indicated here as suggested by VDI 3405 Part 3 for SLM process (VDI, 2014)

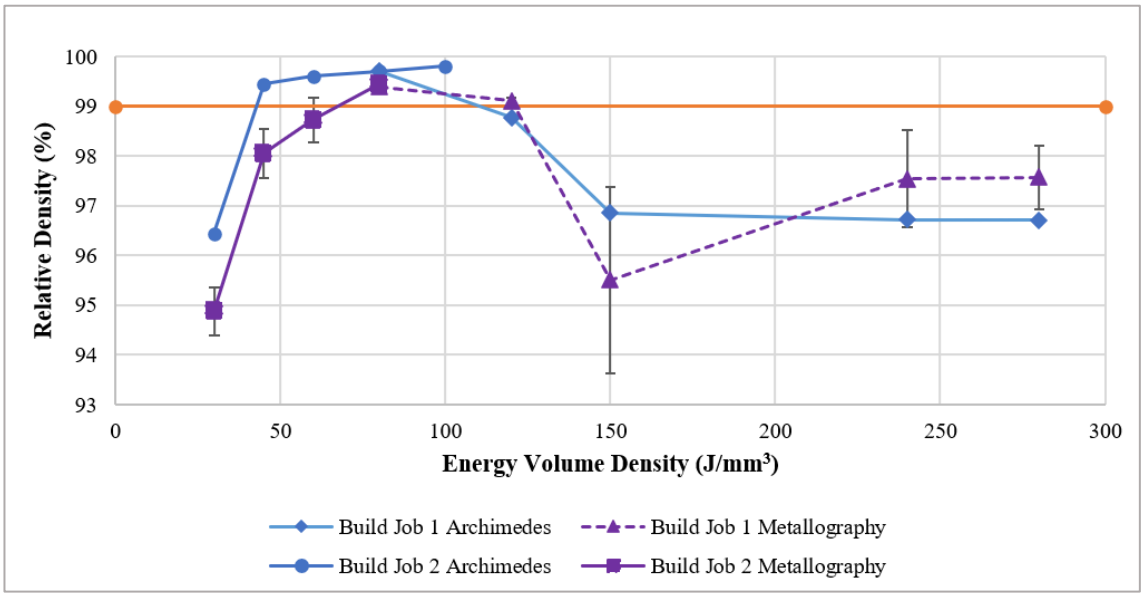

Fig. 4.12 Comparison of Archimedes and Metallographic relative densities for as-built cube samples for both build jobs. 99% relative density desired value is as indicated.

Fig. 4.11 compares the dimensional accuracy in the x- and y- directions of all samples from both build jobs according to changing EVD. The 80J/mm^3 sample indicates a high inter-reproducibility, while the 30J/mm^3 sample deviates by >0.1mm in the y-direction, yet in the x-direction it is almost equal to the exact dimension of 10mm. On the other hand, the 100J/mm^3

sample was >0.3mm than the 10mm sample cube in both directions. It should also be noted that cube faces in the y direction were marked with sample numbers, which may have a negative effect on dimensional accuracy.

Fig.4.12 compares Archimedes and metallographic relative densities of all cube samples for both build jobs according to changing EVDs. For 40J/mm^3 to 110J/mm^3 samples, Archimedes relative densities were equal to or slightly more than 99%, while the 70J/mm^3 to 120J/mm^3 cube samples showed optimum values for metallographic densities. All standard deviations for the Archimedes average values are far lower than metallographic average values. The 80J/mm^3 cube samples for both build jobs are almost identical with relative density slightly higher than 99%, further confirming its high reproducibility.

Fig. 4.13 compares porosity for the 30J/mm^3 and 80J/mm^3 cube sample. Each show irregular-shaped pores between 20µm to 100µm and micro porosity likely due to lack of fusion from the low EVD range consistent with finding from A. B. Spierings, Dawson, Dumitraschkewitz, et al. (2018). Fig. 4.14 shows the presence of unmelted powder particles further supporting the assumption of lack of fusion. Koutny et al. (2018) also investigated SLM processing of a variant of Scalmalloy with much lower levels of scandium, magnesium, and zirconium than the Scalmalloy composition used in this work. Laser powers were between 325W to 400W and yielded samples with less than 98% relative densities. Optimum laser power and EVD was found to be 375W and 69J/mm^3, respectively, consistent with the work on hand. It should be noted that, we did not model the work on hand after the findings from Koutny et al. (2018) as it did not use Scalmalloy, but a variant.

Fig. 4.15 compares microhardness results for both build jobs with changing energy volume density. The 80J/mm^3 cube sample and their standard deviations are identical for both build jobs confirming high inter-reproducibility of Scalmalloy and the *AM 400 Renishaw SLM* machine. All microhardness data of build job 2 are consistent with data of build job 1. Although, microhardness average value for 30J/mm^3 cube sample is decreased slightly and standard deviation is higher assumed to be caused by the high levels of inner porosity as shown in Fig. 4.13.

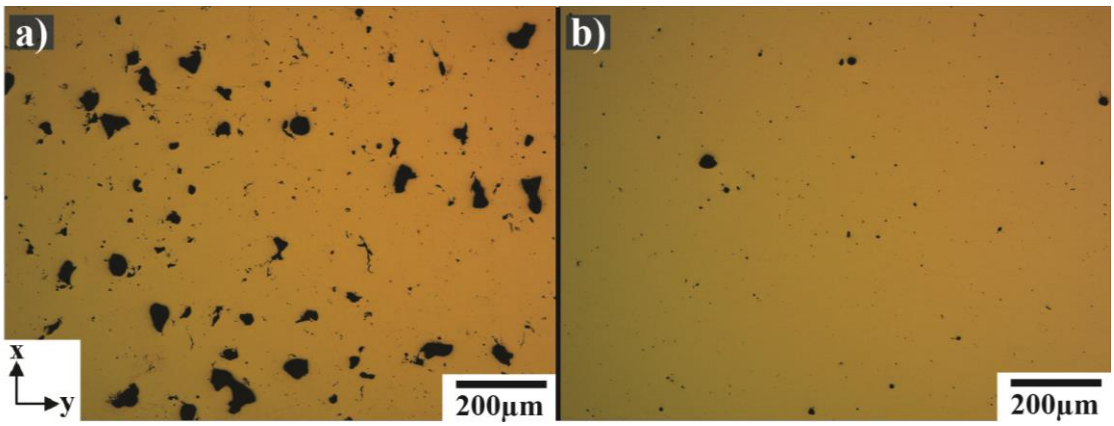

Fig. 4.13 Optical micrographs of cube cross sections showing size morphology, size distribution and lateral distribution of porosity for a) 30J/mm³ and b) 80J/mm³ cube samples

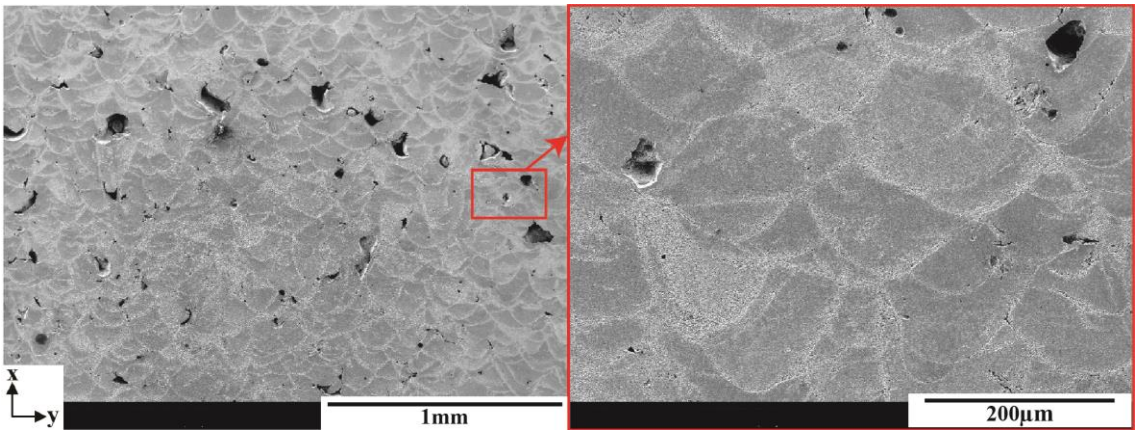

Fig. 4.14 SEM micrographs of etched cube cross sections for 30J/mm³ cube sample

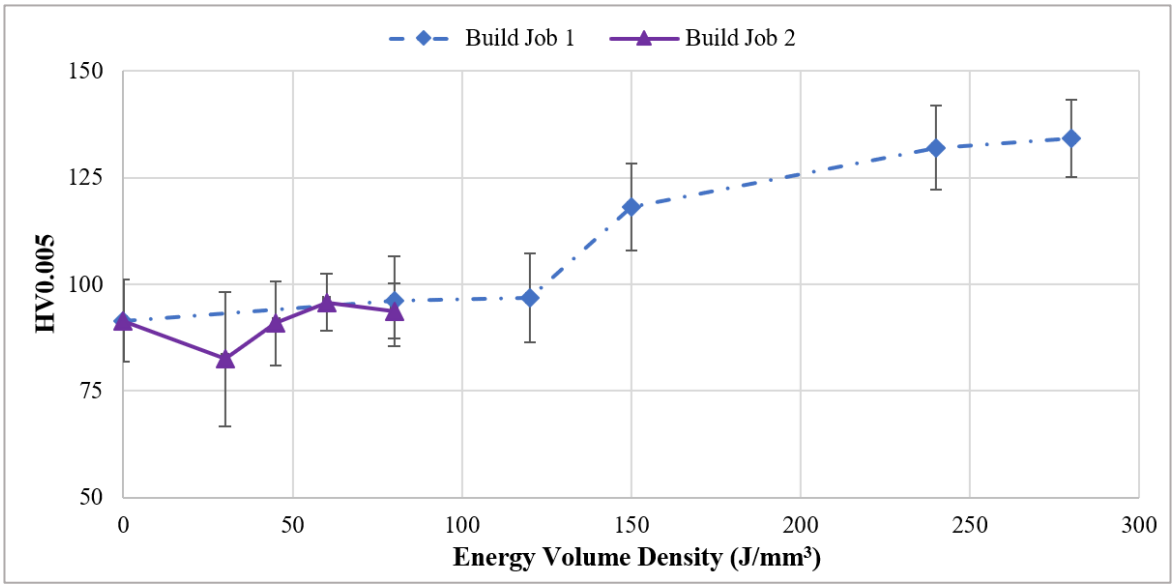

Fig. 4.15 Microhardness results for all cube sample cross sections with changing energy volume density. 0J/mm³ corresponds to powder particle cross sections

In conclusion, the full SLM processing window considering relative densities exceeding 99% for chosen laser power of 400W, layer thickness of 30µm and hatch distance of 150µm for processing

Scalmalloy was found to be between 70J/mm^3 to 110J/mm^3 EVD. Microhardness of samples manufactured with these EVDs showed high potential for subsequent post heat treatment and good mechanical properties for Scalmalloy parts. SLM inter-build reproducibility is presumably high, based on relative density, dimensional accuracy, and microhardness of two cube samples built in subsequent build jobs.

4.4 Reproducibility and influence of layout position

Fig. 4.16 shows contour plots of the average relative densities mapped in the build platform according to the method outlined in section 3.1.1.6. The contour plots for each build job (25 cube samples) compare Archimedes relative densities to their position on the build platform with standard deviations shown in Fig. A.4 and Fig. A.5 in Appendix A. The highest Archimedes average relative density was 99.8% and no values are lower than 99.4%. Standard deviations were between ±0.2%, which is considered low. The discrepancies in average relative densities seen between the different positions on the build platform for SLM are influenced by many factors such as homogeneity of powder layers, shielding gas flow and laser properties. However, the average values are consistent and overall standard deviations are low. Hence, it is proven that the Scalmalloy samples processed in an *AM 400 Renishaw SLM* machine with optimal processing parameters (section 4.3) for laser power of 400W exhibited high intra- and inter-build reproducibility regarding relative density. These may be indicative of the SLM machine, and cannot be recommended for a different SLM machine, Scalmalloy powder, or metallic powder.

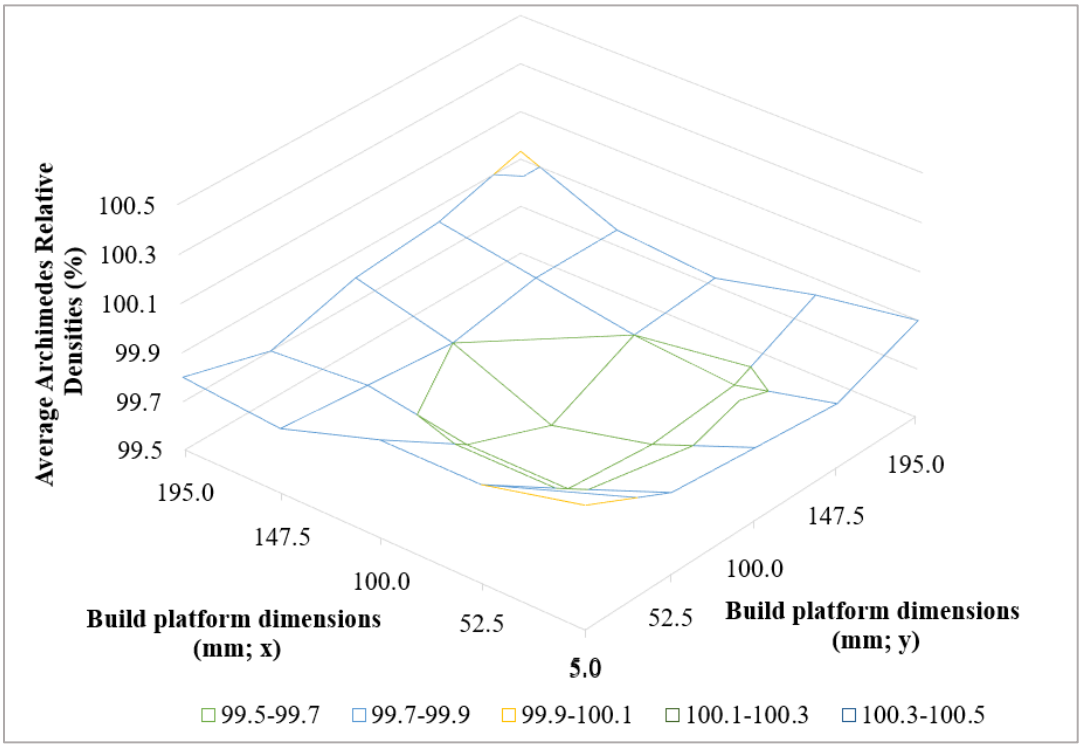

Fig. 4.16 Contour plots of the build platform mapping the average values for Archimedes relative densities

4.5 Summary

In this chapter, processing parameters were developed to manufacture Scalmalloy samples in a *Renishaw 400 LBM Machine* using 400W laser power which has not been widely reported as most of the literature generally reported the use of 200W laser power. Powder characterisation was carried out and overall results showed that the powder on hand had good processability. Two build jobs were carried out with adjustments to the energy volume density for the samples, where Archimedes method was used to measure each sample's relative densities. It was found that the parameter window that was explored showed a shift to lower energy volume densities when compared to literature, where the optimal parameter window occurred between 70J/mm^3 and 110J/mm^3. Therefore, Scalmalloy can be manufactured with a high laser power to greatly improve productivity. Microhardness testing shows that $Al_3(Sc_{1-x}Zr_x)$ precipitates were suppressed so subsequent heat treatment has a higher potential of increasing the mechanical properties. In addition, anisotropy is apparent in the x direction and should be considered when manufacturing thin-walled and complex components. The influence of the layout position on the build chamber was also observed but showed no significant impact on the relative densities of the samples.

Chapter 5 Results and discussion of the heat treatment and cold rolling of Scalmalloy

This result section will include tensile and hardness properties, microstructural characterisation, fracture, and defect analysis for all as-built, heat treated, cold rolled, and heat treated and cold rolled samples of Scalmalloy. Tensile, hardness, surface roughness and microstructural characterisation of 5052Al and 5083Al extruded aluminium alloys are also included for comparison to Scalmalloy samples and to use as a base line for the reported findings. The optimal SLM parameters from Chapter 4 will be used to manufacture the Scalmalloy samples used in this section. It is worth noting that the results of the cold rolled (10%CR, 30%CR) and AB condition discussed in the following sections are also published in C Turangi et al. (2022) as this is an earlier published paper of the work on hand. Having said that, the published results of the cold rolled samples may differ slightly to the results reported in the work on hand as the tensile testing procedure was refined since slight slippage may have occurred during testing. Hence, the final conclusive results for the cold rolled samples reported in the work on hand achieved a higher accuracy. Furthermore, additional optical and SEM micrographs for each sample condition are provided for further information in Appendix B and C, respectively.

5.1 Microstructural characterisation

The microstructure for heat treated and cold rolled samples were investigated through optical microscopy, SEM and EBSD. Fig. 5.1 and Fig. 5.2 show optical and SEM micrographs of the 5052Al as received (AR) microstructure in the horizontal, longitudinal, and transverse planes, respectively. In a similar manner, Fig. 5.3 and Fig. 5.4 shows optical and SEM micrographs of the 5083Al AR microstructure in the horizontal, longitudinal, and transverse planes, respectively. Fig. 5.1 and Fig. 5.3 both show visible magnesium silica distributed evenly over the entire surface with no pores or defects visible typical of the extrusion process. Additionally, Fig. 5.2 and 5.4 show visible lines indicating the direction of extrusion and small voids on the surface is indicative of phase dissolution of Al_6Mn common in the 5000 aluminium alloy series (Sivaramakrishnan, 1995; Varshney & Kumar, 2021).

Fig. 5.5 shows optical micrographs of the SLM-processed Scalmalloy AB microstructure in the horizontal, longitudinal, and transverse planes. All additive manufactured components, including Scalmalloy, have a unique layer-by-layer microstructure perpendicular to the build direction (transverse and longitudinal planes). A bi-modal grain size distribution was observed in Scalmalloy consisting of a coarse columnar grain (CG) and a fine equiaxed grain region (FG). The conditions within the SLM process such as high cooling rates ($\approx 1.5\times10^6$ K/s), direction of heat, and reactions within the melt-pool pre- and post-solidification are the driving factors behind the mechanism for its microstructure. Particularly for Scalmalloy, the grain structure is mostly dependent upon different aspects such as formation of precipitates and their behaviour within the

as-built material. The darker shaded areas in Fig. 5.5 represent the FG regions and the lighter shaded areas represent the CG regions. The grain size and shape can be seen at higher magnification in Fig. 5.5 along with the transition from the CG region into the FG region. The numerous small are assumed to be $AlSc_3$ particles formed during the SLM process as reported by (Davydov et al., 2000). These general features of Scalmalloy are consistent with findings reported by A. B. Spierings, Dawson, Heeling, et al. (2017). The CG and FG regions of the horizontal plane are randomly distributed throughout the surface of the cross section.

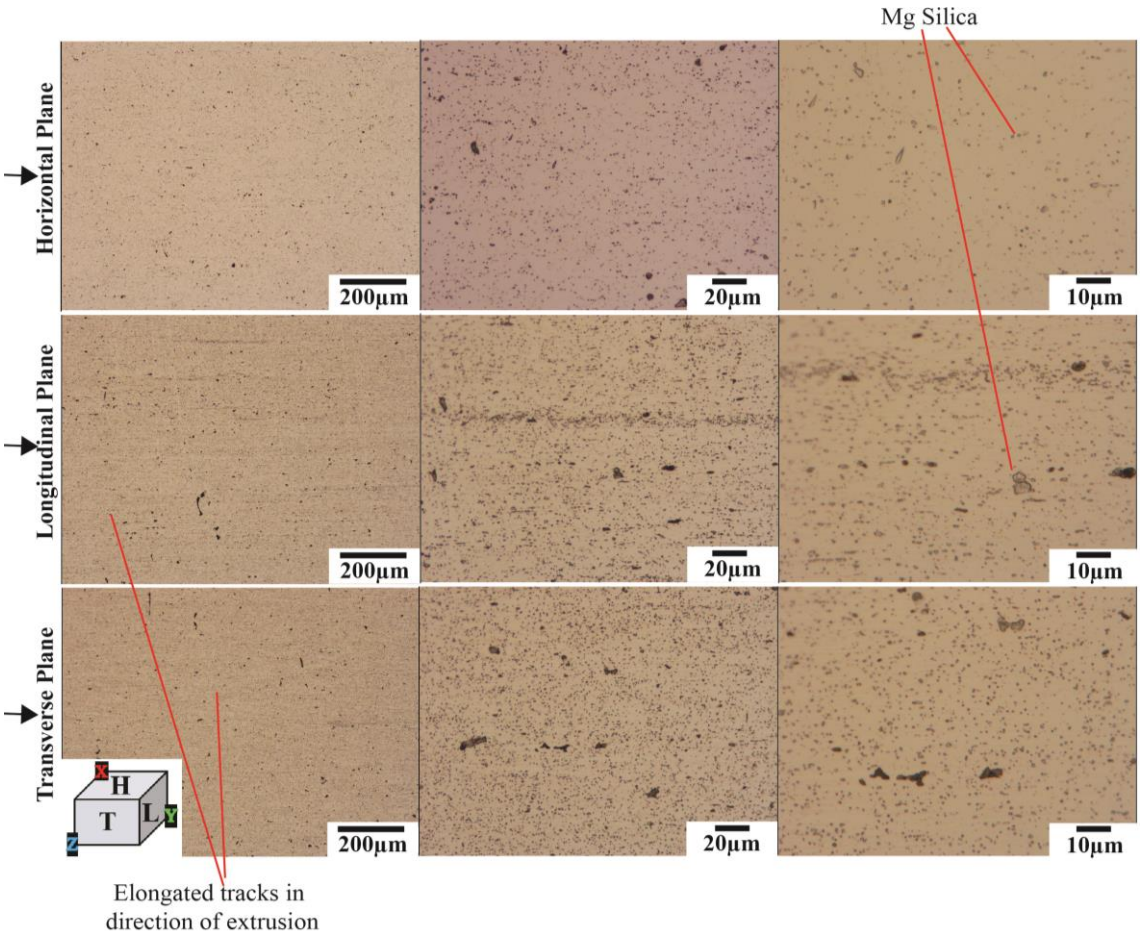

Fig. 5.1 Optical micrograph of the microstructure of AR 5052Al alloy in the horizontal, longitudinal, and transverse planes

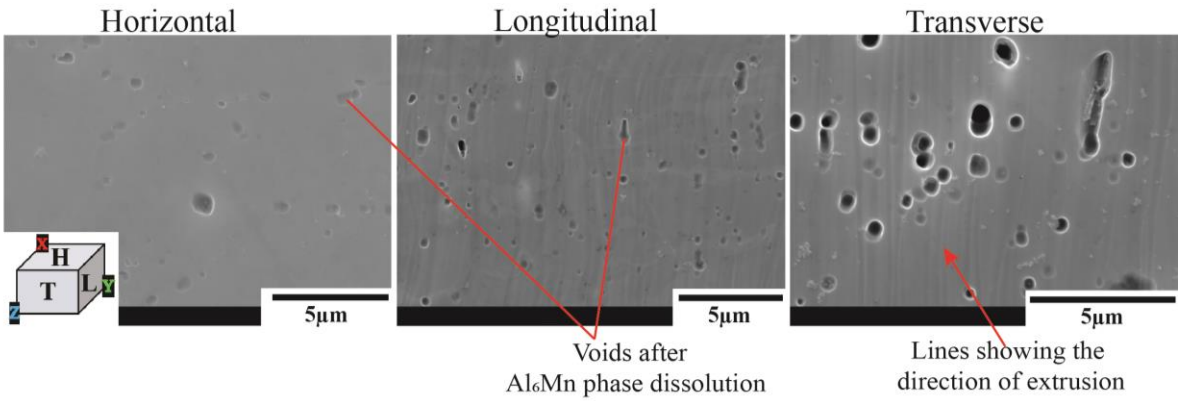

Fig. 5.2 SEM micrographs of the microstructure of AR 5052Al in the horizontal, longitudinal, and transverse planes

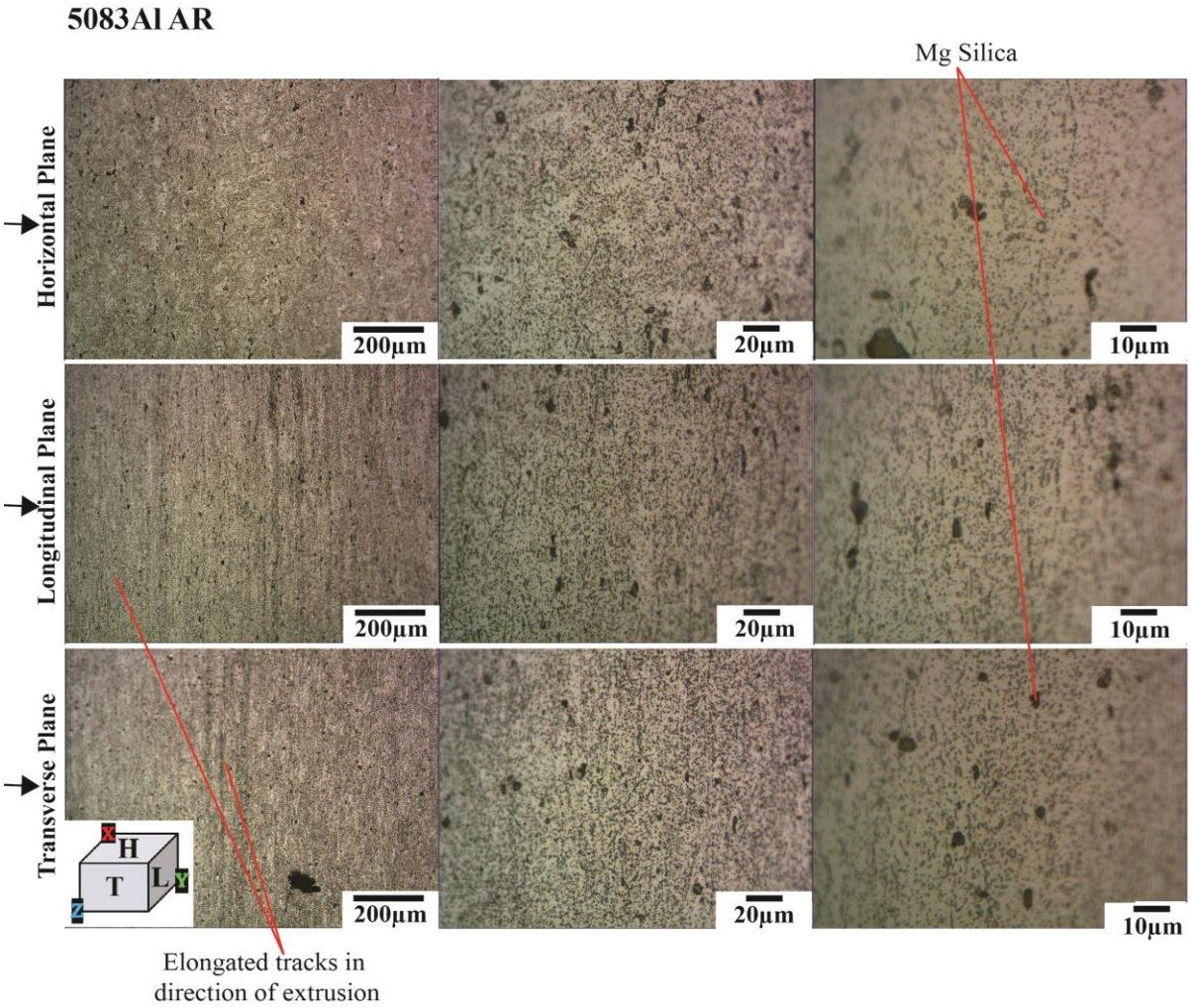

Fig. 5.3 Optical micrograph of the microstructure of AR 5083Al alloy in the horizontal, longitudinal, and transverse planes

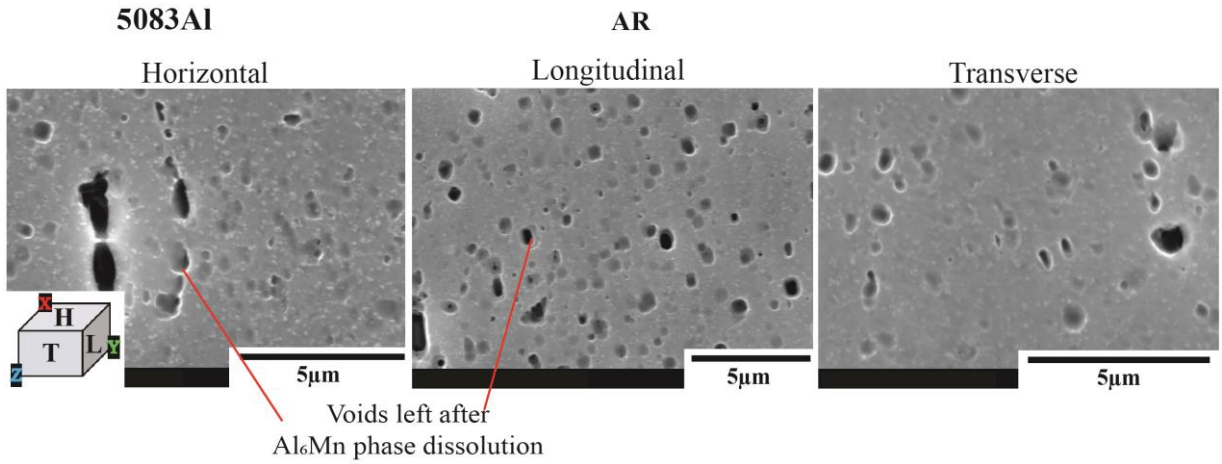

Fig. 5.4 SEM micrographs of the microstructure of AR 5083Al alloy in the horizontal, longitudinal, and transverse planes

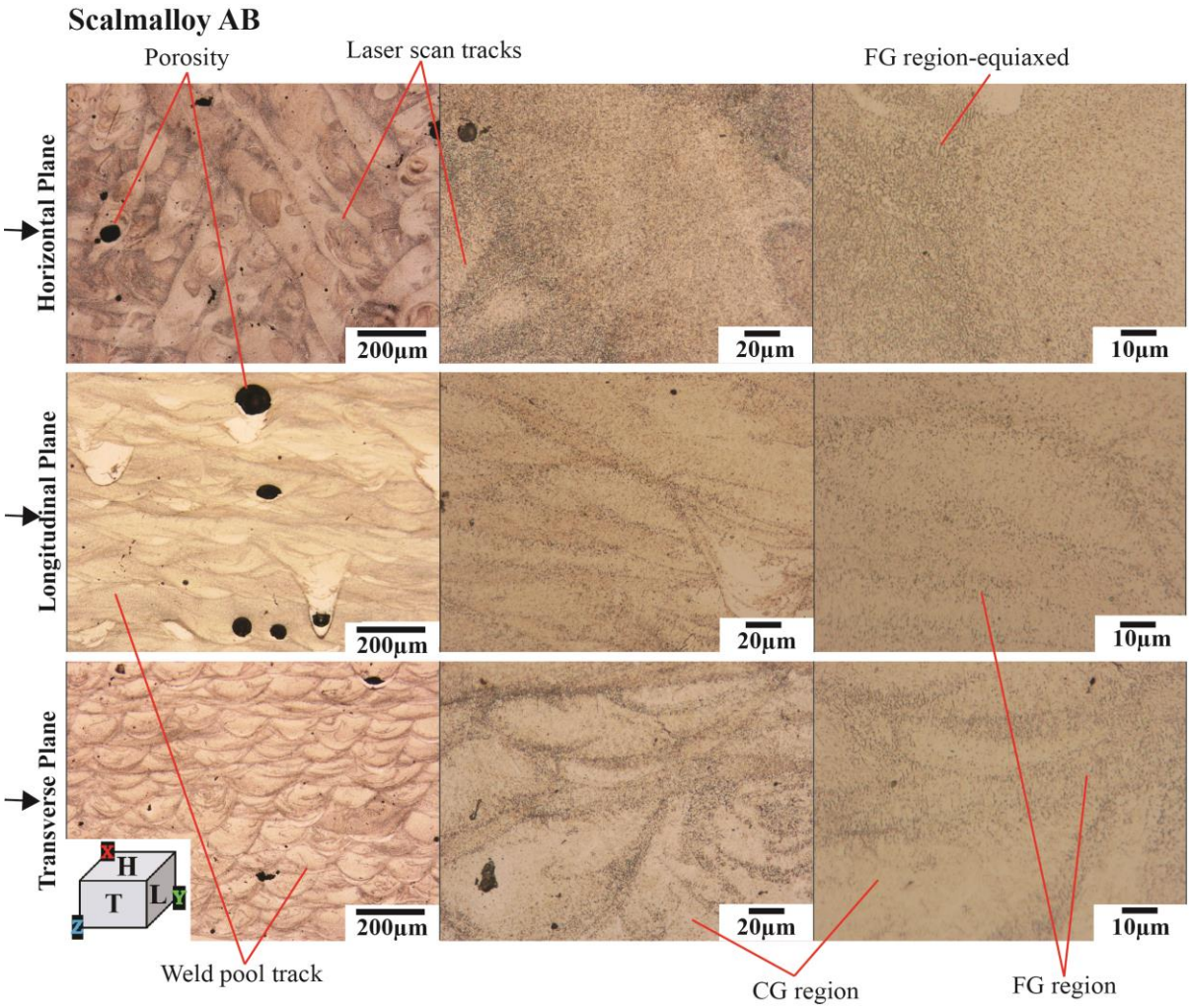

Fig. 5.5 Optical micrograph of Scalmalloy AB microstructure in horizontal, longitudinal, and transverse planes

However, it shows a different microstructural pattern, compared to the longitudinal and transverse planes, as the 67° bi-directional laser scanning pattern is obvious here. The weld pool size for the longitudinal and transverse planes varied between 150µm to 200µm in width and about 50µm to 150µm in depth. This is much larger than the laser focus diameter of 70µm indicative of good

thermal conductivity of most aluminium alloys. Additionally, the size of the melt pool (width and depth) varies depending on the melt pool flow and energy effects in the localized area of the cross section. As the melt pool depth was between 50µm to 150µm (shown in Fig. 5.5), and the layer thickness is 30µm, it shows that with each new layer the previous layers are remelted between 2 to 5 times as the laser power was high. The alternating CG and FG regions are visible, where the average thickness of the darker band of FG regions is approximately 10µm in size, while the CG regions are much larger showing about 20 µm to 40µm wide. Fan-like shaped irregularities were evident as the FG region merged into the CG region suggesting significant heat transfer occurring in the weld pool.

EBSD mapping of the AB condition perpendicular to the build direction is shown in Fig. 5.6. A range of different colors in the FG region indicated there was no preferred crystal orientation for the grain growth. The FG region was thought to result from a large number of seed crystals present in the shell around the melt pool base, which A. B. Spierings, Dawson, Heeling, et al. (2017) demonstrated through an SLM simulation. It was found that the Al_3(Sc, Zr) particles dissolved at temperatures close to 800^{o}C, while temperatures less than 800^{o}C existed, but within a very small band (≈10µm) around the shell of the melt pool (FG region). Scandium and zirconium usually form $Al_3(Sc_xZr_{1-x})$ second phase particles to refine microstructure and improve mechanical properties during heat treatment (age hardening). According to A. B. Spierings, Dawson, Heeling, et al. (2017) and Jostein Røyset and N. Ryum (2005), Scalmalloy is a hypereutectic alloy that has the ability to form additional primary Al_3Sc during amalgamation as the non-equilibrium conditions allow the solubility of scandium to increase from 0.55%wt to 0.6%wt for cooling rates of 100K/s. The SLM processing window and melt-pool lifetime influences the formation of Al-Sc precipitates seed crystals in the melt pool and result in significant grain refinement in the Al-alloy.

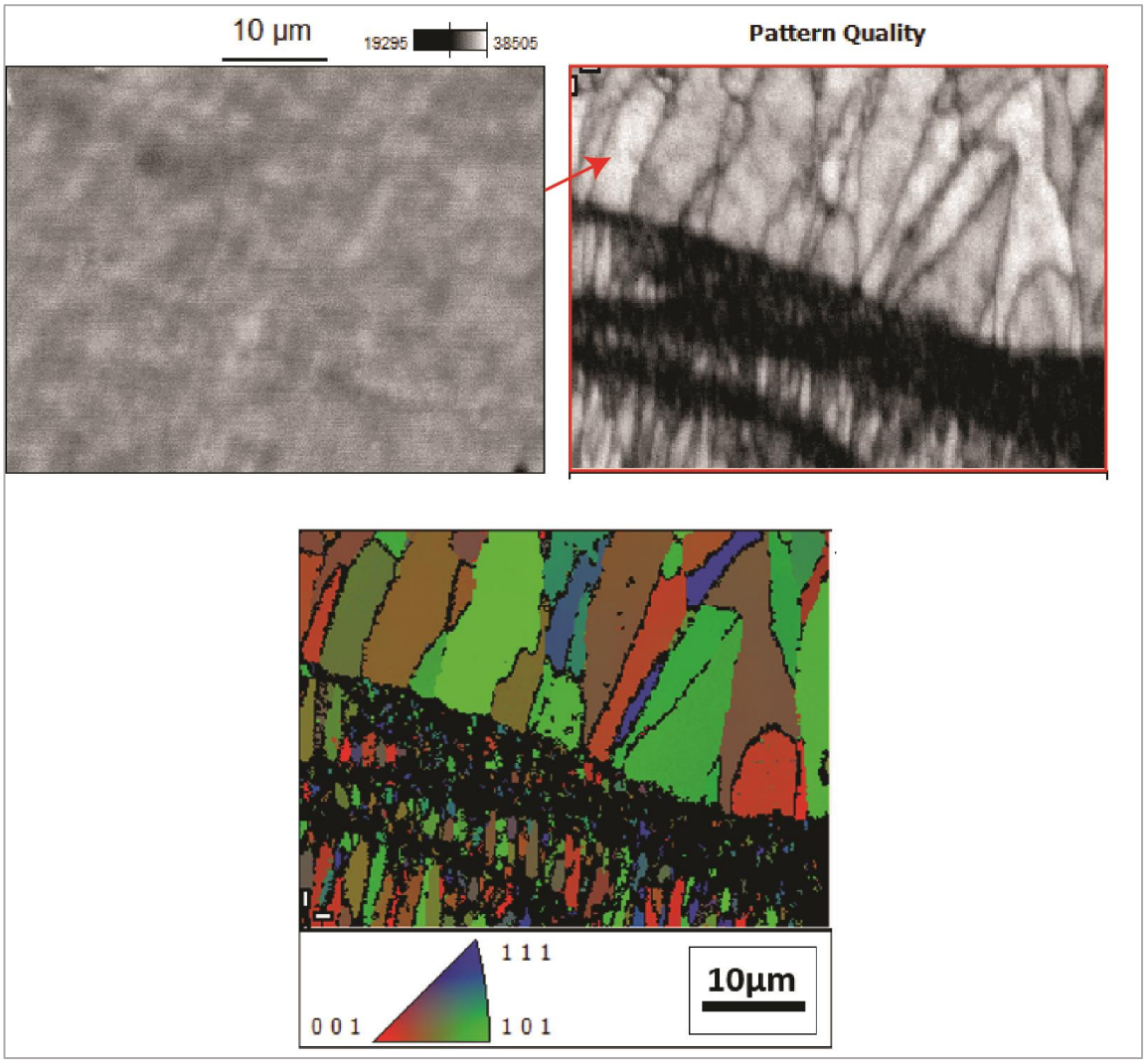

Fig. 5.6 EBSD Orientation Map of AB condition in the transverse direction perpendicular to the build direction. Pattern quality is also shown here.

The metal powder is, inevitably, exposed to air leaving the powder particles covered in a very thin Al-oxide. The oxygen content is, therefore, sufficient to precipitate numerous oxide particles during the SLM process. Hence, numerous types of intermetallic phases such as $Al_3(Sc_xZr_{1-x})$ particles, Al-Mg oxides, and other oxides were assumed to be present in within this region as reported by (A. B. Spierings, Dawson, Heeling, et al., 2017). These are also ideal nucleation sites since most have good lattice matches within the aluminium matrix. Additionally, Al-Mg oxides were found to exist densely within the FG region leading to higher potential of nucleation sites. Some $Al_3(Sc_xZr_{1-x})$ particles may also remain after the stringent heat cycle from the SLM process if a dissolution temperature is not met. These particles act as inoculants to promote the quick formation and growth of FCC-aluminium grains, while also pinning and stabilising grain boundaries resulting in the fine-grained microstructure.

The CG region microstructure mechanism is different to that of the FG region as both regions have different solidification behaviour. Coarse columnar grains nucleate, first, in the FG region and grow in the direction of the temperature gradient and build direction (usually radially)

continuing until the top of the melt pool. The CG region has significantly less Al-Mg oxides and almost no detection of $Al_3(Sc, Zr)$ particles as it was assumed they had dissolved towards the top of the melt pool and, hence, very low potential for nucleation sites. As these grains grow in the direction of the temperature gradient and the build direction, anisotropic behaviour is confirmed by a strong <100> crystal texture from the EBSD mapping in Fig. 5.6, also in line with current literature (Awd et al., 2017; Koutny et al., 2018; Musekamp et al., 2021; A. B. Spierings, Dawson, Heeling, et al., 2017).

Fig. 5.7 shows the overall grain size distribution, where the average grain size is ≈1.76µm. The FG region consisted of equiaxed grains between 0.2µm and 1µm, and the CG region consisted of elongated columnar grains with sizes close to 12µm in length. In both Fig. 5.5 and Fig 5.8, defects are apparent in the as-built structure. The longitudinal plane and the horizontal plane show pores with some as large as 50µm in size, and their spherical shape indicate these are likely caused by gas entrapment around the melt pool during the SLM process. The porosity seen in the transverse plane consisted more of microporosity and one small irregular shaped pore. Judging by the shape and location of the irregular shaped pore, this was likely caused by incomplete melting of the last solidified layer due to insufficient energy supply during the SLM process. Hence, the porosity seen in these planes are parameter-based pores (Galy, Guen, et al., 2018). Microporosity (<2µm) is present in all the planes in Fig. 5.8, which is common within most additively manufactured metals as small amounts of hydrogen ever present on the metal powders used in the SLM process remain.

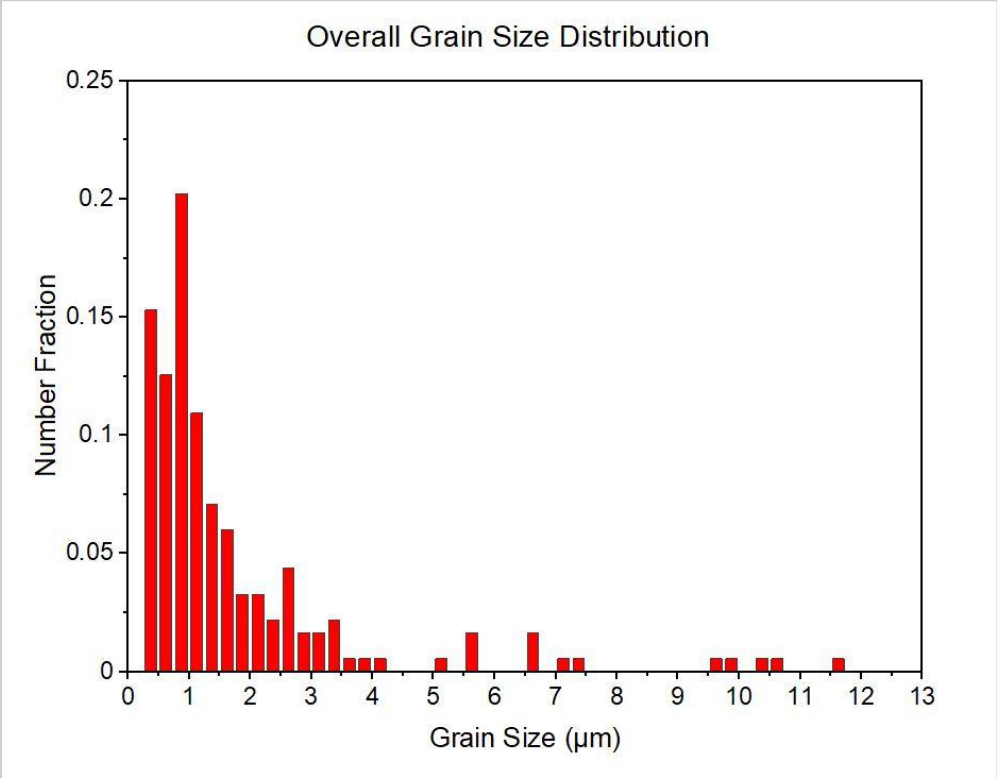

Fig. 5.7 Overall grain size distribution of the AB condition

However, as these pores are tiny, they usually do not cause any detrimental effects unless they were to coalesce or a numerous amount of these existed in the components wherein at least 96% relative density was not achieved. Spherical porosity with sizes between 5μm and 150μm is also visible at higher magnification likely due to gas entrapment during the SLM process consistent with literature (Aboulkhair et al., 2019; Galy, Guen, et al., 2018; Olakanmi et al., 2015). Fig. 5.9 shows optical micrographs of the SLM-processed Scalmalloy AB+HT1 microstructure in the horizontal, longitudinal, and transverse planes. Both the AB and AB+HT1 microstructures are very similar. From the EBSD mapping, no preferential grain growth is apparent in the FG region, but the CG region has a strong preference in the <100> direction in line with the build direction and the thermal gradient. It appears that the AB+HT1 has more darker shaded bands of FG regions assumed to be due to a large number of second phase particles $Al_3(Sc_xZr_{1-x})$ precipitated during heat treatment as described in Ma et al. (2020b) and A. B. Spierings, Dawson, Kern, et al. (2017).

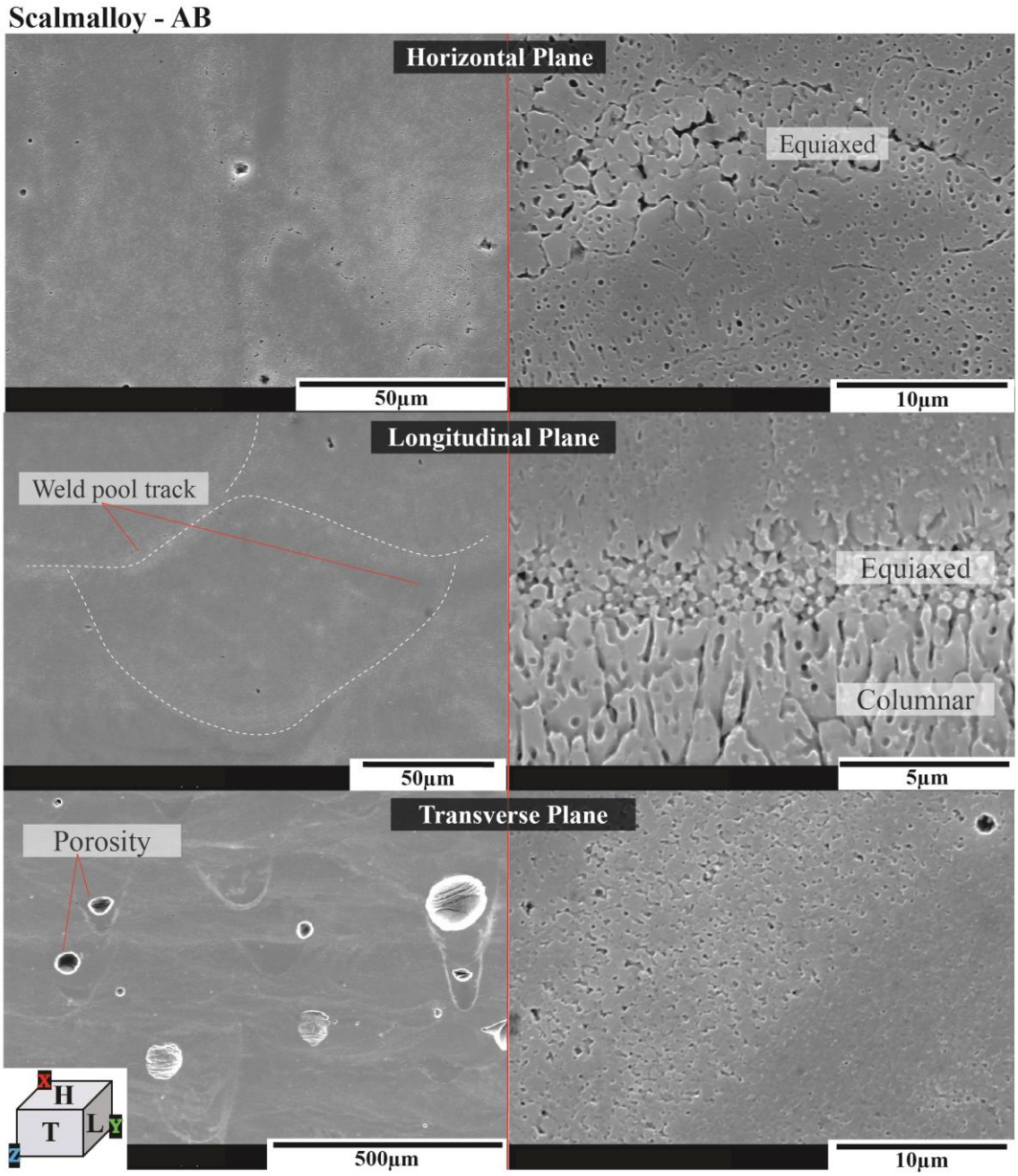

Fig. 5.8 SEM micrographs of the AB microstructure in the horizontal, longitudinal, and transverse planes

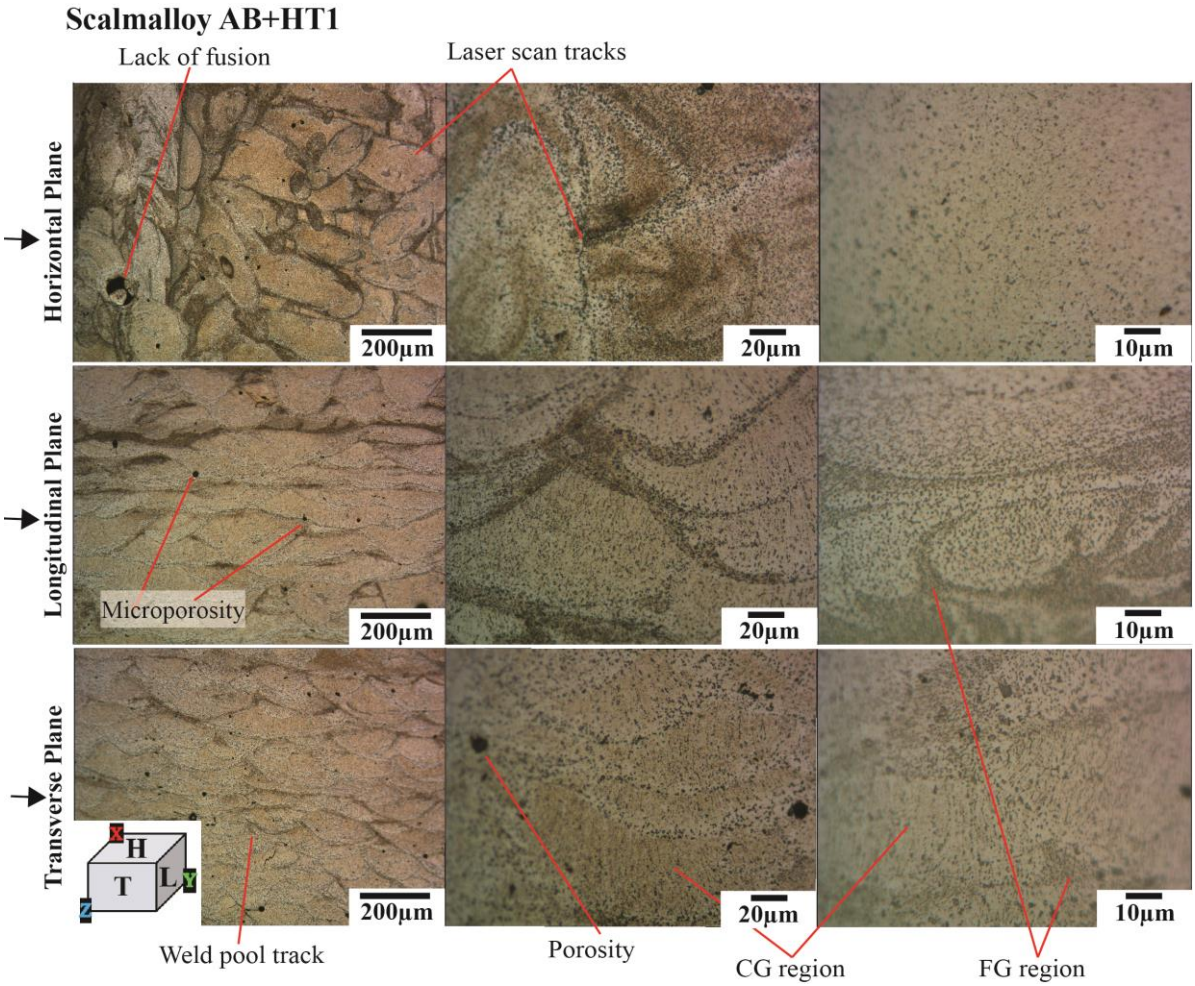

Fig. 5.9 Optical micrograph o1f the AB+HT1 microstructure in horizontal, longitudinal, and transverse planes

Microstructural features and grain size distribution are very similar to the AB condition. The preferential grain growth still remains in the CG regions indicated by the conglomerate of red grains showing a strong <100> direction in Fig. 5.10. and the range of colours in the FG region shows it has almost no anisotropy or preferential grain growth The overall grain size distribution, shown in Fig 5.11 for the AB+HT1 sample was comparable to the AB sample, but with a similar grain size distribution. Although gas porosity and some defects exist after this heat treatment, they are comparable to the AB condition and, hence, the heat treatment has not caused any detrimental effects. Grains in the FG region are still ≈1µm, but the largest grain size was ≈8µm, while the overall average grain size was 1.2µm. As reported by Ma et al. (2020a), the microstructure does not change much as it was assumed that grain boundary particles prevent such growth of grains.

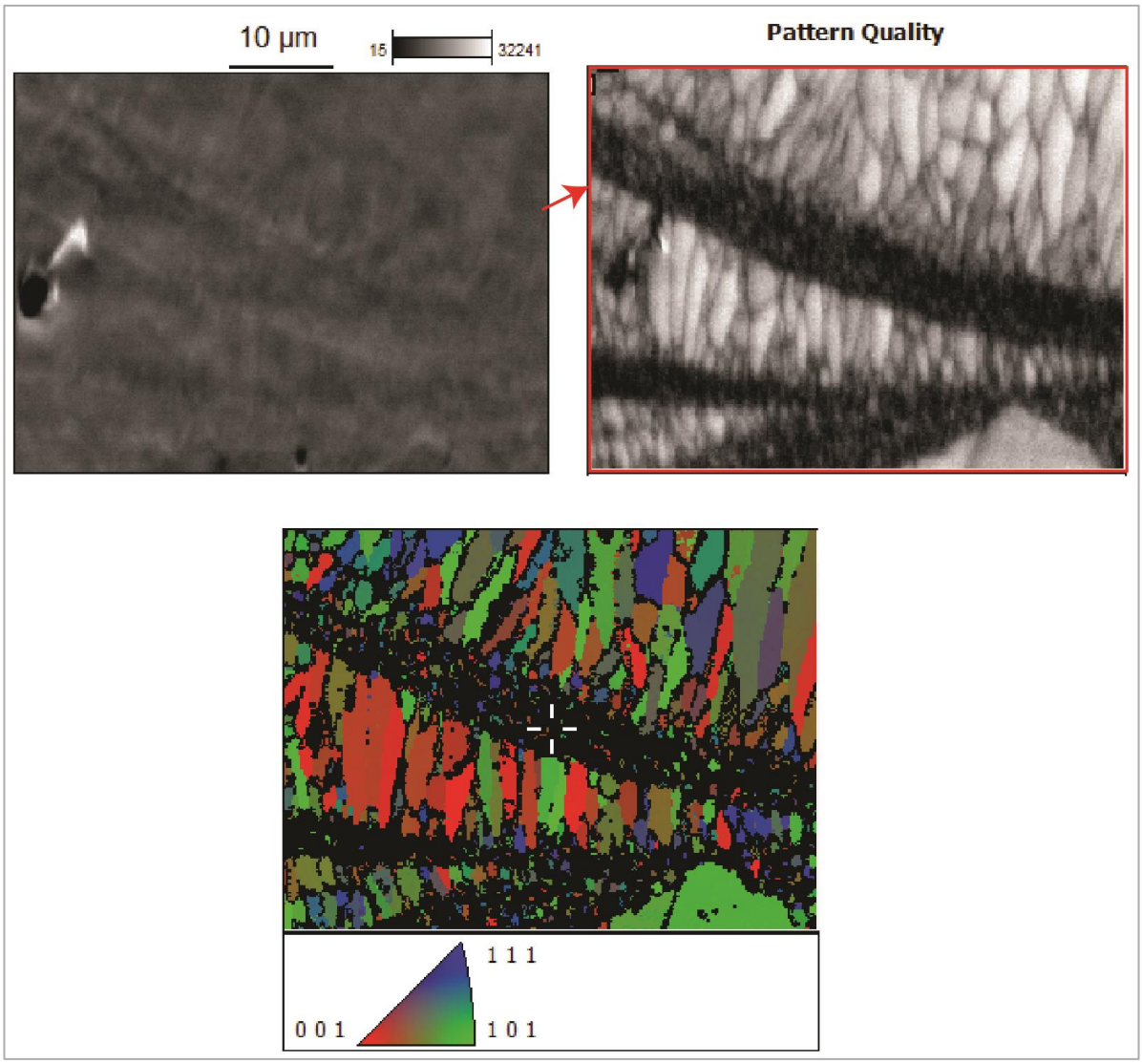

Fig. 5.10 EBSD Orientation Map of AB+HT1 condition in the transverse direction perpendicular to the build direction. Pattern quality is also shown here

Fig. 5.12 show SEM micrographs of the AB+HT1 microstructure. Here, the FG and CG regions and the grain size are very distinct. Defects such as cracking and porosity are also visible. Similar to the AB sample, the visible porosity are likely gas porosity judging from their spherical and round shape. The small cracks are likely due to insufficient solidification during the SLM process and the microporosity are probably caused by exposure to hydrogen from the atmosphere according to literature (Beckmann & Emmelmann, 2019; Cui et al., 2022; Weingarten et al., 2015). The HT1 has allowed rapid cooling to occur and coherent $Al_3(Sc_xZr_{1-x})$ second phase particles to exist within the solid solution indicated by the dark bands of FG region and consistent with reports from A. B. Spierings, Dawson, Kern, et al. (2017) (Fig. 5.10).

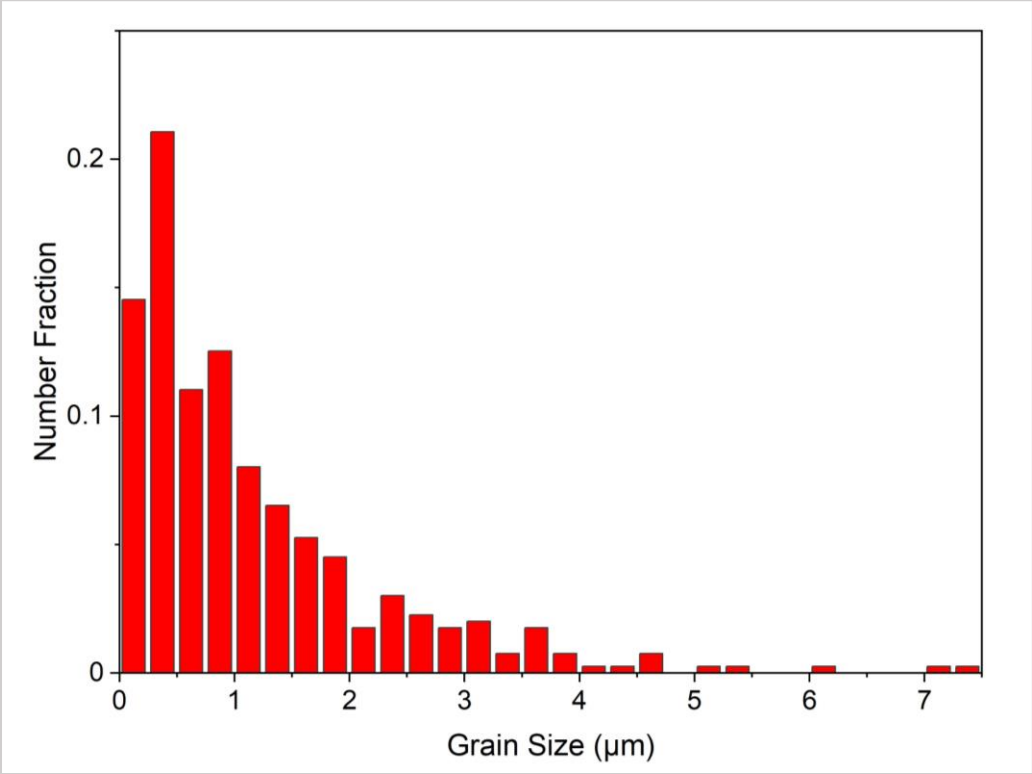

Fig. 5.11 Overall grain size distribution of the AB+HT1 condition

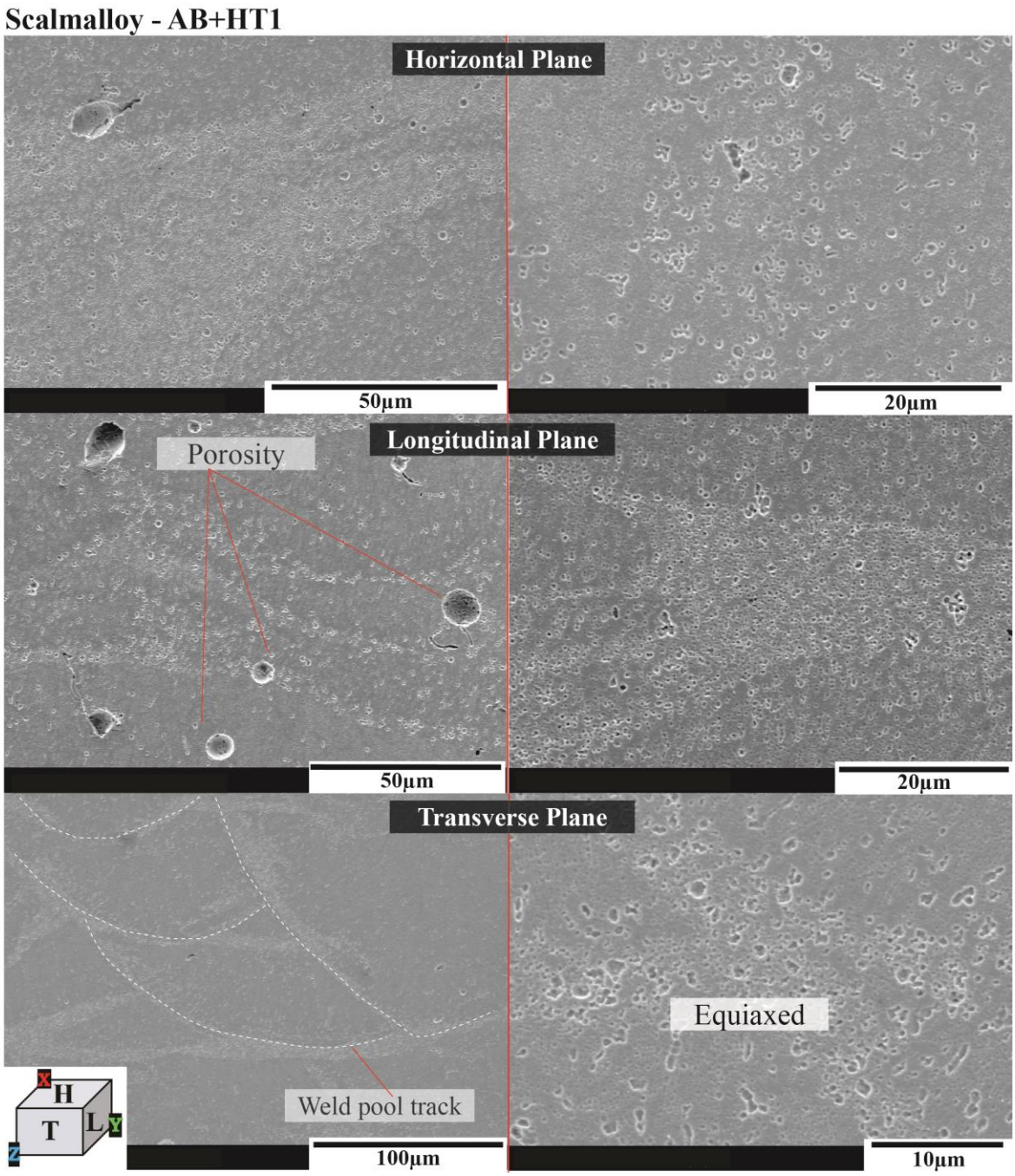

Fig. 5.12 SEM micrographs of the AB+HT1 microstructure in the horizontal, longitudinal, and transverse planes

Fig. 5.13 and 5.14 show the optical micrographs and SEM micrographs in the horizontal, longitudinal, and transverse planes of the AB+HT2 conditions, respectively. Fig. 5.15 and 5.16 show the optical micrographs and SEM micrographs in the horizontal, longitudinal, and transverse planes of the AB+HT3 conditions, respectively. Fig 5.13 and Fig. 5.15 show that the $Al_3(Sc_xZr_{1-x})$ precipitates appear to have coarsened compared to the AB and AB+HT1 condition assumed to be caused by overageing, where a key cause is prolonged heat treatment times consistent with literature (Fuller, Seidman, & Dunand, 2003; R. Li et al., 2019). Fig. 5.14 and Fig. 5.16 show similar microstructural features to both the AB and AB+HT1 conditions including visible metallurgical defects such as cracking, lack of fusion and gas porosity likely occurring

during the SLM process as reported by B. Zhang et al. (2017). It is also worth noting that although the AB+HT3 condition shows a significant amount of visible porosity with pore sizes ranging from 5µm to 100µm and where some seemed to have coalesced, the shape of the porosity indicates they are also likely process induced as well, hence are not caused by the heat treatment conditions.

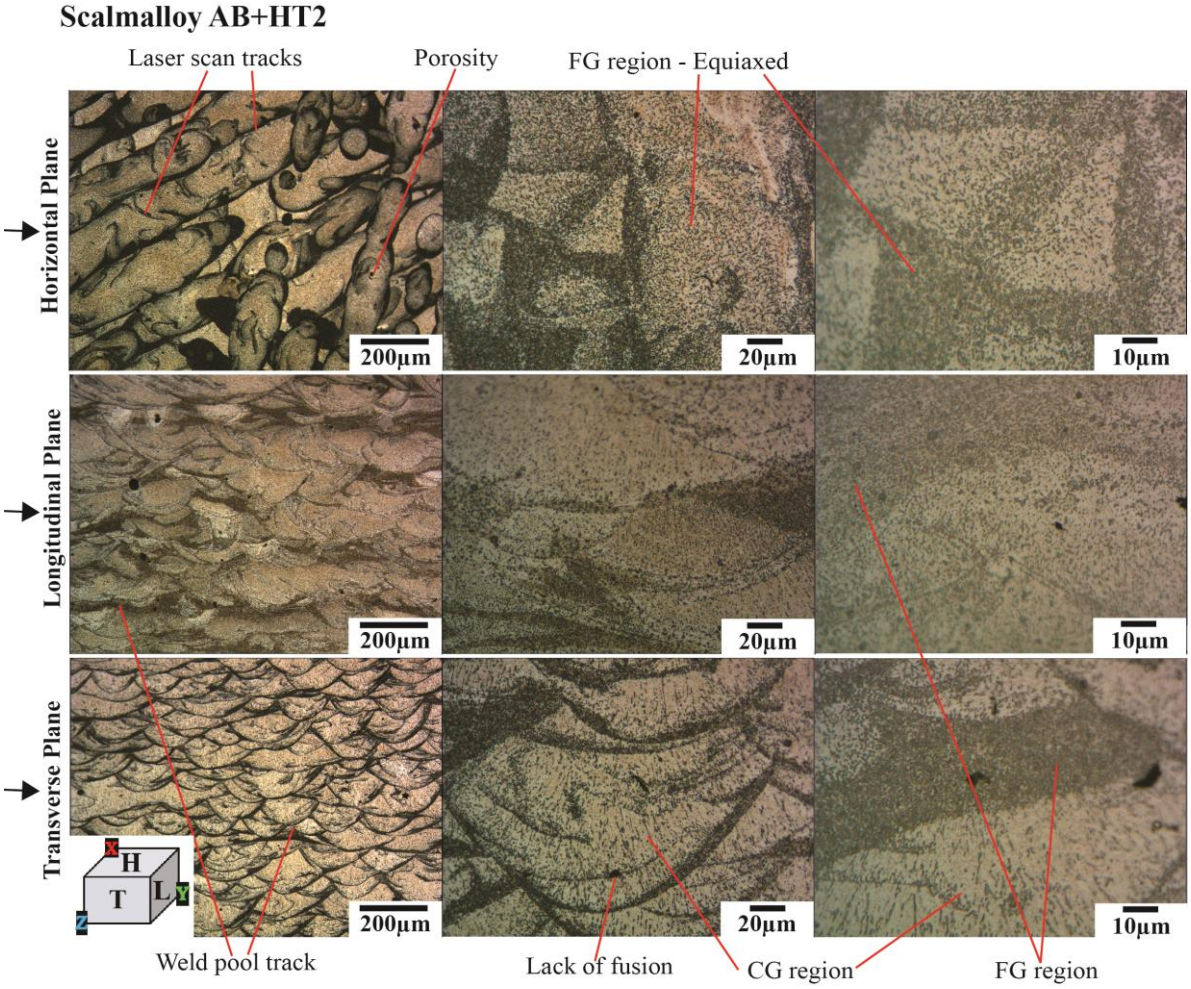

Fig. 5.13 Optical micrograph of AB+HT2 microstructure in horizontal, longitudinal, and transverse planes

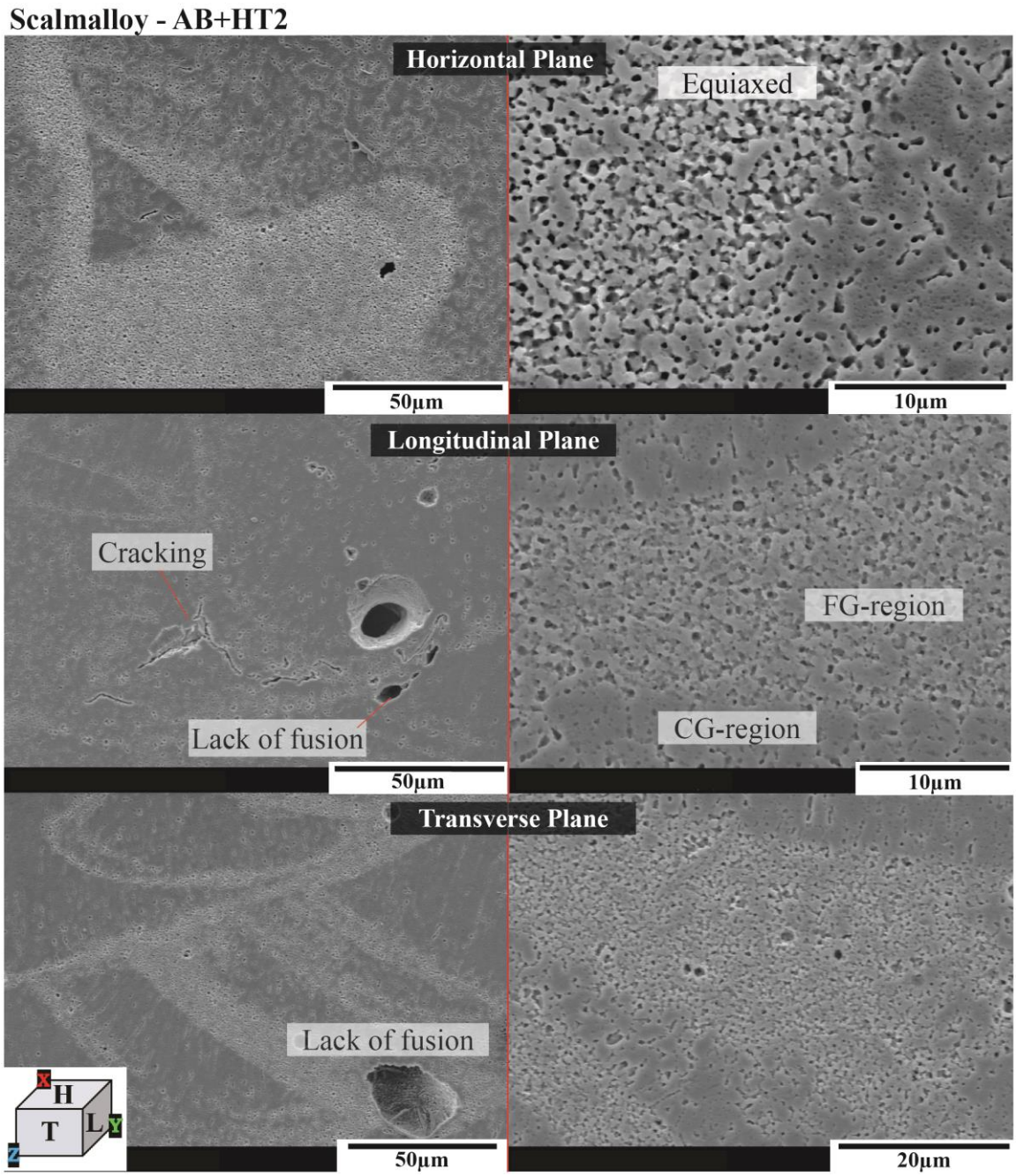

Fig. 5.14 SEM micrographs of AB+HT2 microstructure in the horizontal, longitudinal, and transverse planes

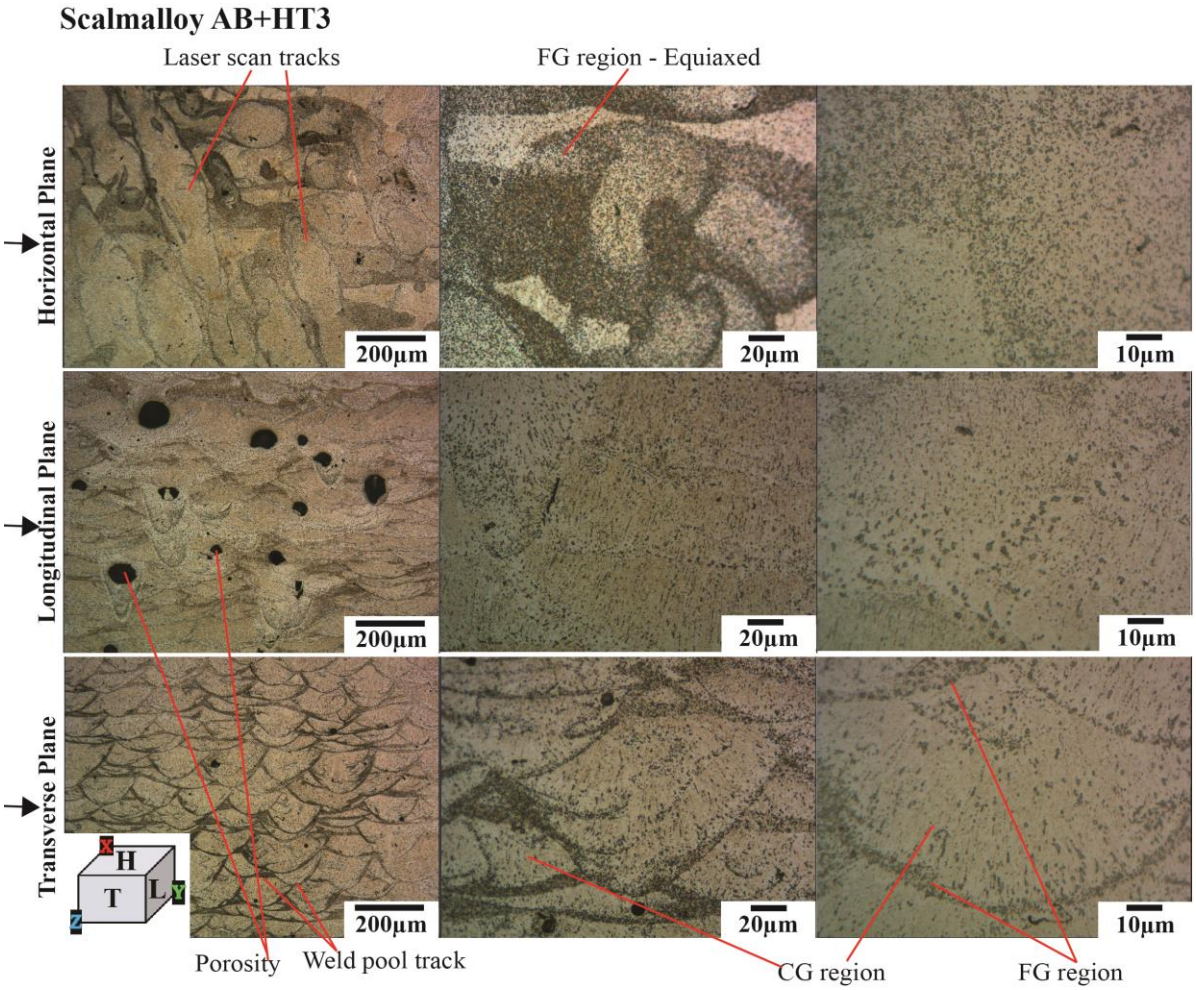

Fig. 5.15 Optical micrograph of AB+HT3 microstructure in the horizontal, longitudinal, and transverse planes

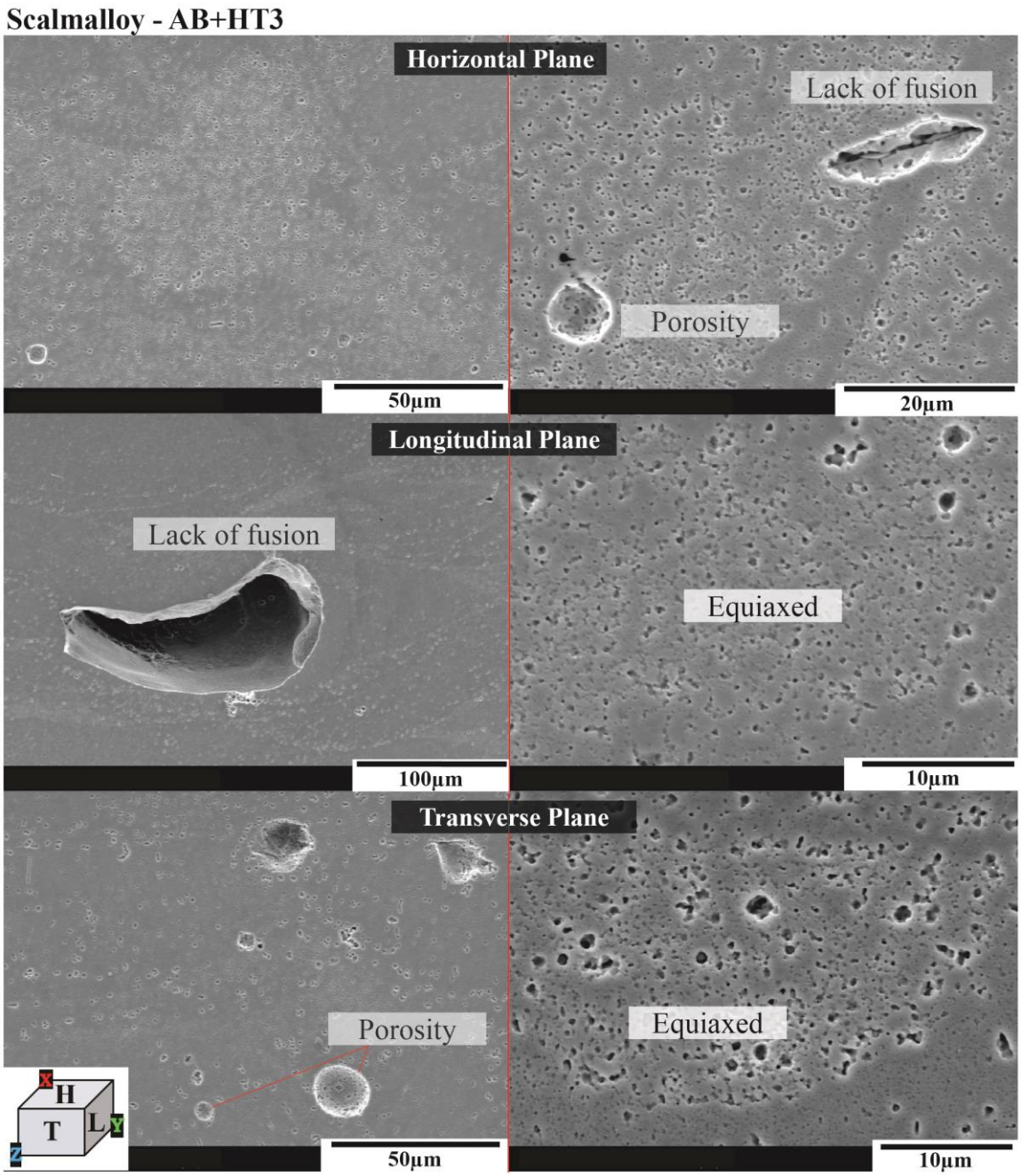

Fig. 5.16 SEM micrographs of the AB+HT3 microstructure in the horizontal, longitudinal, and transverse planes

Fig. 5.17 and Fig. 5.18 show optical and SEM micrographs of the 5052Al 10%CR microstructure in the horizontal, longitudinal, and transverse planes, respectively. In a similar manner, Fig. 5.19 and Fig. 5.20 shows optical and SEM micrographs of the 5083Al 10%CR microstructure in the horizontal, longitudinal, and transverse planes, respectively. The microstructure there is almost no change between the microstructure of the 10%CR and AR conditions of the extruded aluminium alloys, except more magnesium silica particles are visible on the surfaces due to the plastic deformation induced through cold rolling (Akhtar, Afzal, Khan, Hussain, & Ali, 2017).

Fig. 5.21 shows the microstructure of the Scalmalloy condition cold rolled to a reduction in thickness of 10% (10% CR condition). In comparison to the AB structure (Fig. 5.5), the

microstructure of the 10%CR condition changes slightly. The weld pool dimensions have changed with a length between 100µm to 200µm and a depth of 40µm to 50µm. Although defects are still evident here, they seem to be reduced in size. It was reported by T. Wang et al. (2021), that the relative densities of a powder metallurgy 2024 Al alloy increased after the cold rolling process due to the pores either being eliminated or reduced in size as the compactness of the microstructure increased. This could explain the changes seen in Fig. 5.21, where the defects seem to be minimised in size and the weld pools are further deformed and elongated attributed to the compacted microstructure.

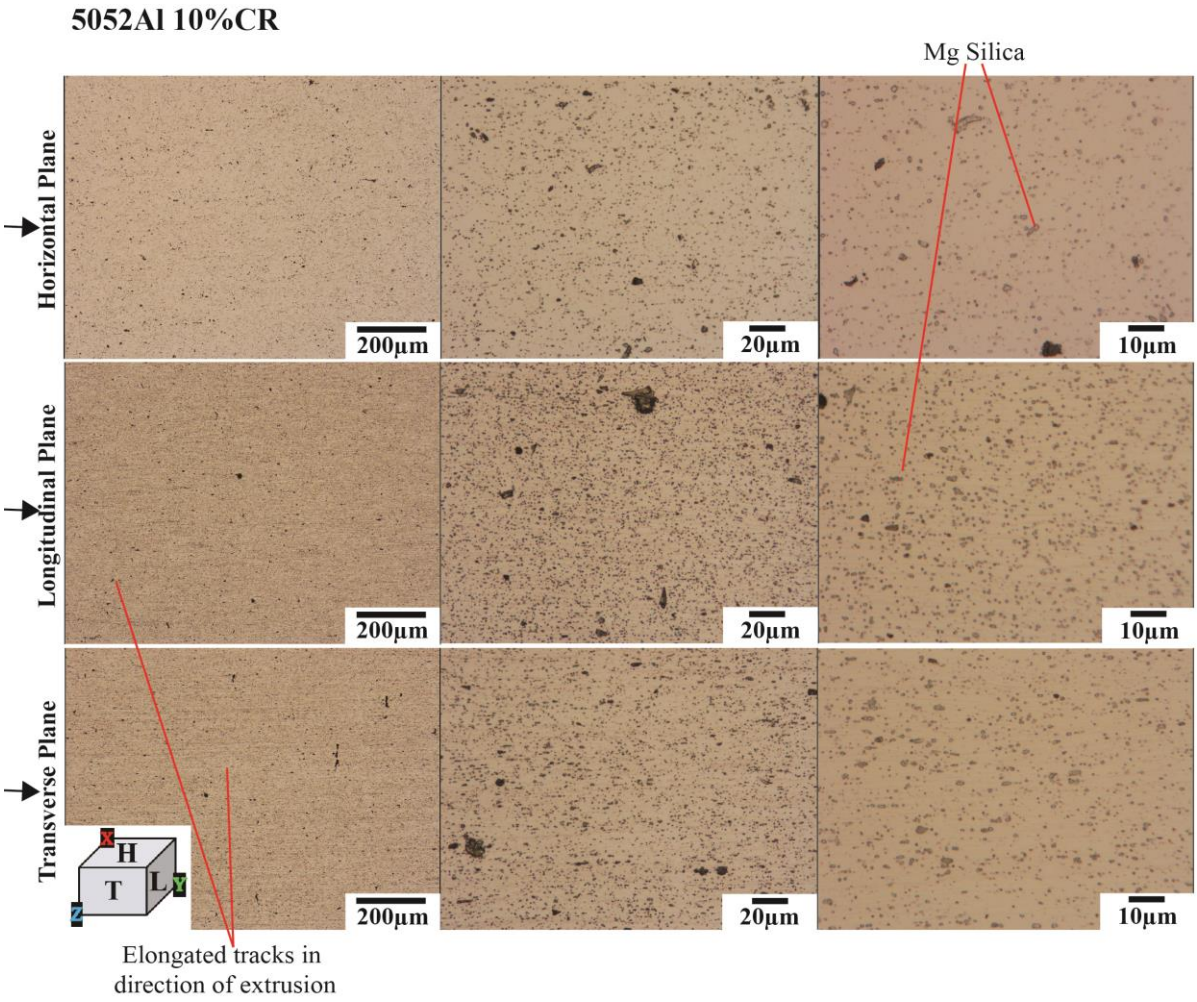

Fig. 5.17 Optical micrograph of the microstructure of 10%CR 5052Al alloy in the horizontal, longitudinal, and transverse planes

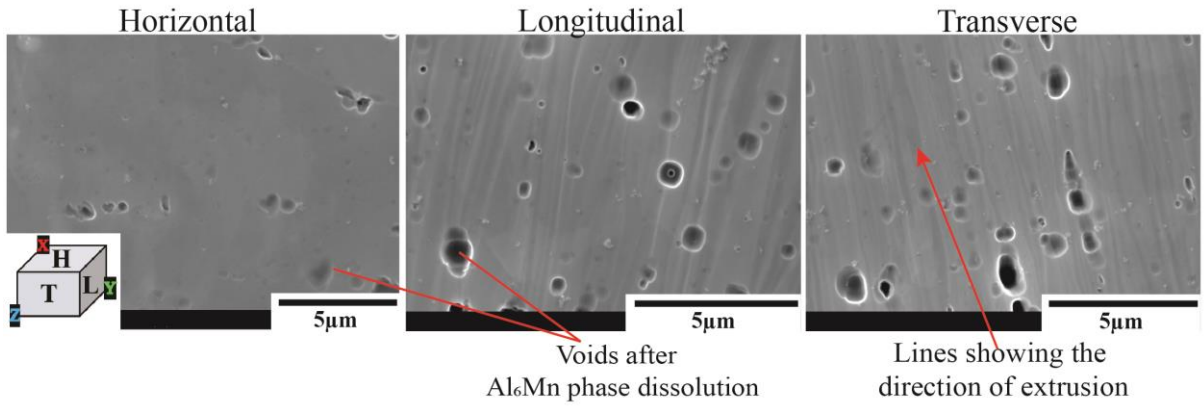

Fig. 5.18 SEM micrograph of the microstructure of 10%CR 5052Al alloy in the horizontal, longitudinal, and transverse planes

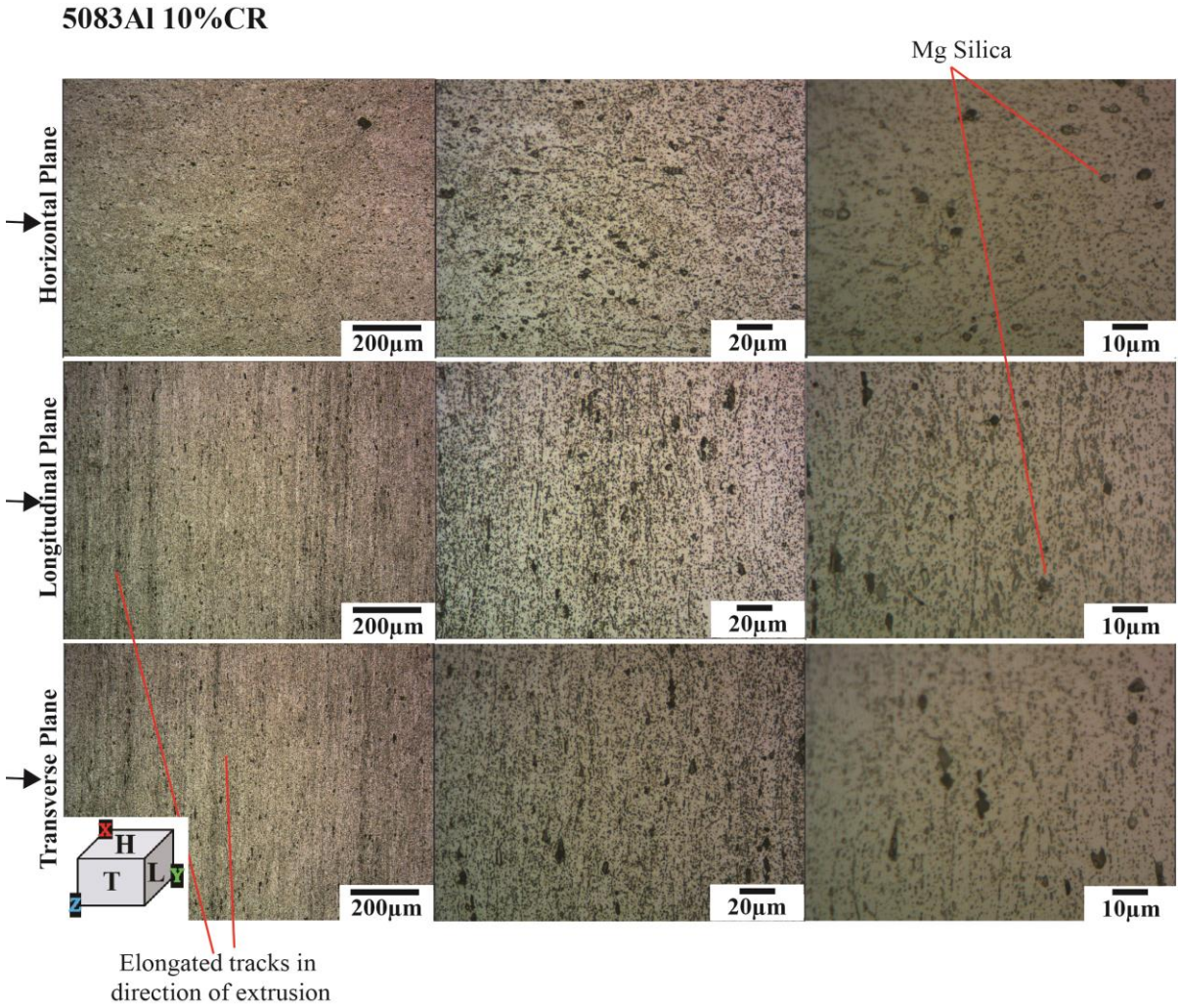

Fig. 5.19 Optical micrograph of the microstructure of 10%CR 5083Al alloy in the horizontal, longitudinal, and transverse planes

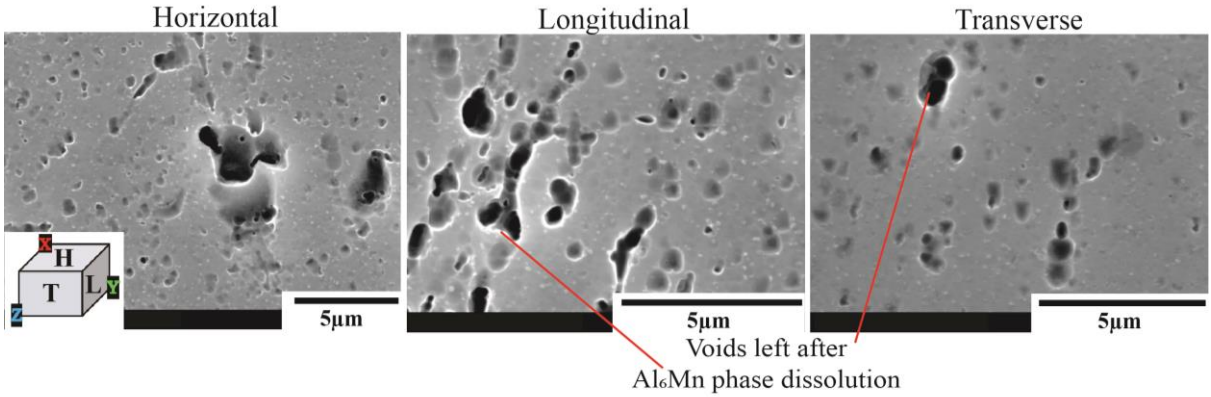

Fig. 5.20 SEM micrograph of the microstructure of 10%CR 5083Al alloy in the horizontal, longitudinal, and transverse planes

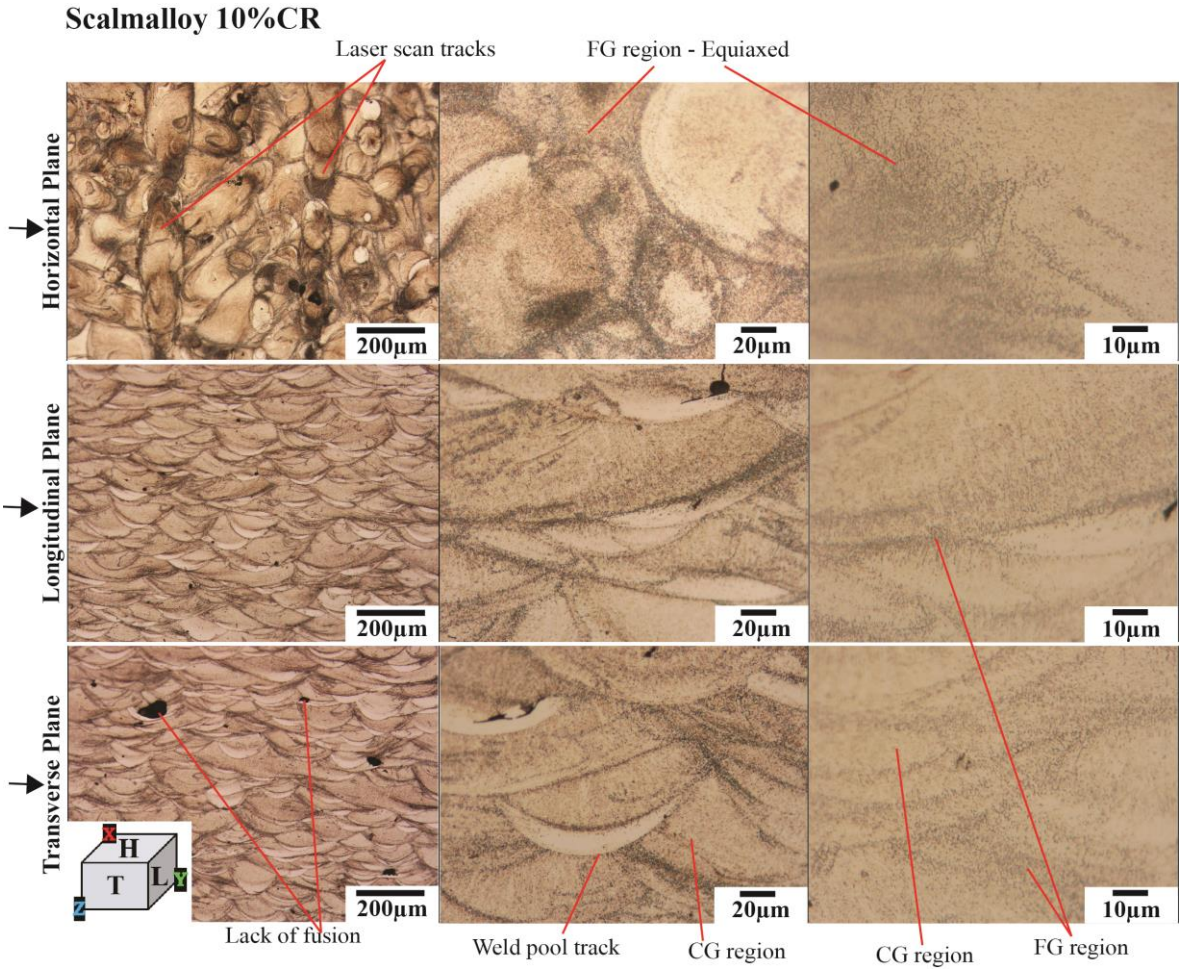

Fig. 5.21 Optical micrograph of the Scalmalloy 10%CR microstructure in horizontal, longitudinal, and transverse planes

Fig. 5.22 shows the EBSD mapping of the 10%CR condition. When compared to the AB condition, the various colours in the EBSD map show there is no preferential grain growth for both FG and CG regions as the reduction in by cold rolling is low, only 10%. The overall grain size distribution of the transverse plane is shown in Fig. 5.23 with an average grain size of ≈ 2.18µm. The FG region consisted of equiaxed grains between 0.4µm and 1µm, and the CG region consisted of elongated columnar grains with sizes up to 12µm. The average and minimum grain sizes are slightly increased as the grains are elongated due to cold rolling. These values are further

confirmed by Fig. 5.24 showing SEM micrographs of the 10% CR condition. The CG and FG region are visible and microporosity still exist and are likely SLM-process induced. It is also apparent that there are a greater number of darker shaded FG regions when compared to the AB condition. As cold rolling is applied, dislocation density is increased and a higher density of second phase particles $Al_3(Sc_xZr_{1-x})$ are precipitated. Hence, the residual stress is increased by the high plastic deformation and fine grain size as reported by Ma et al. (2020a)

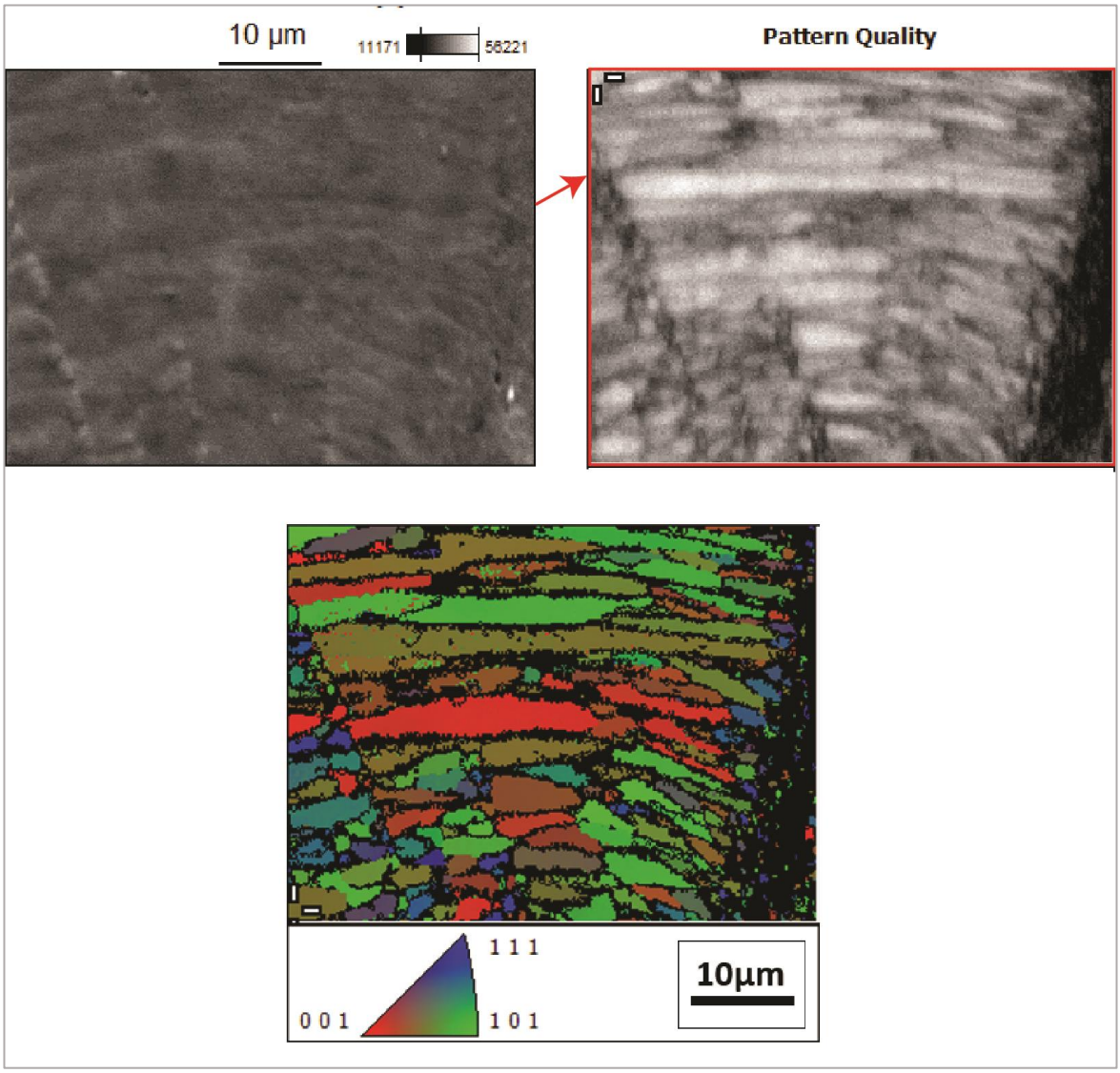

Fig. 5.22 EBSD Mapping of the Scalmalloy 10%CR condition in the transverse direction perpendicular to the build direction. Pattern quality is also shown here

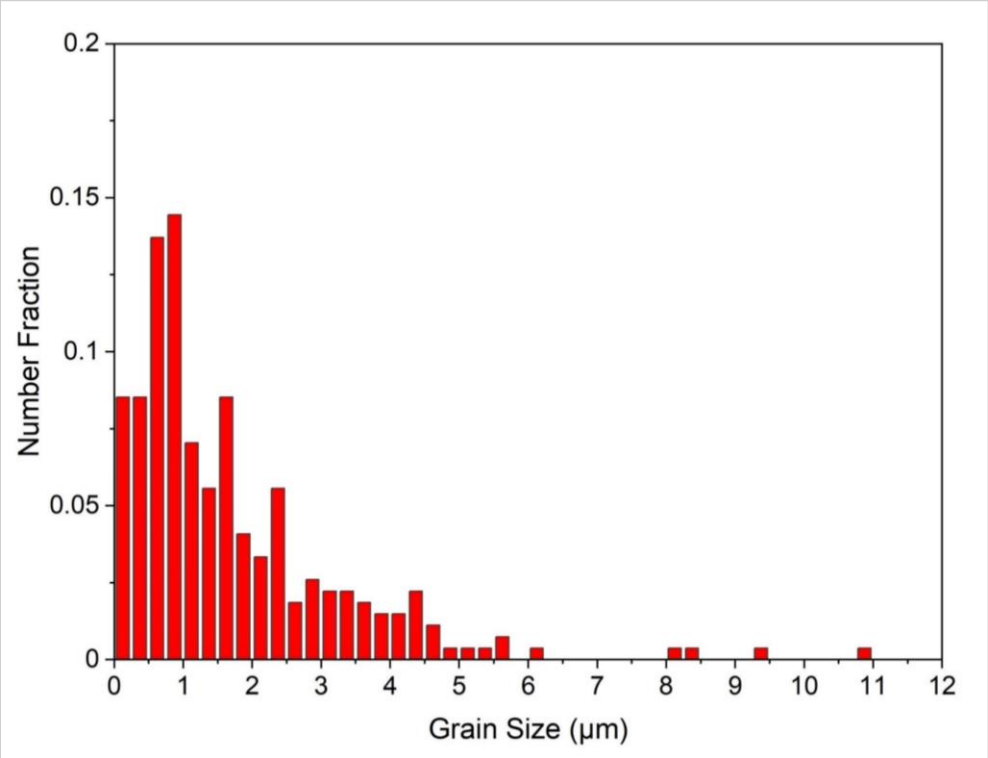

Fig. 5.23 Overall grain size distribution of the 10%CR condition

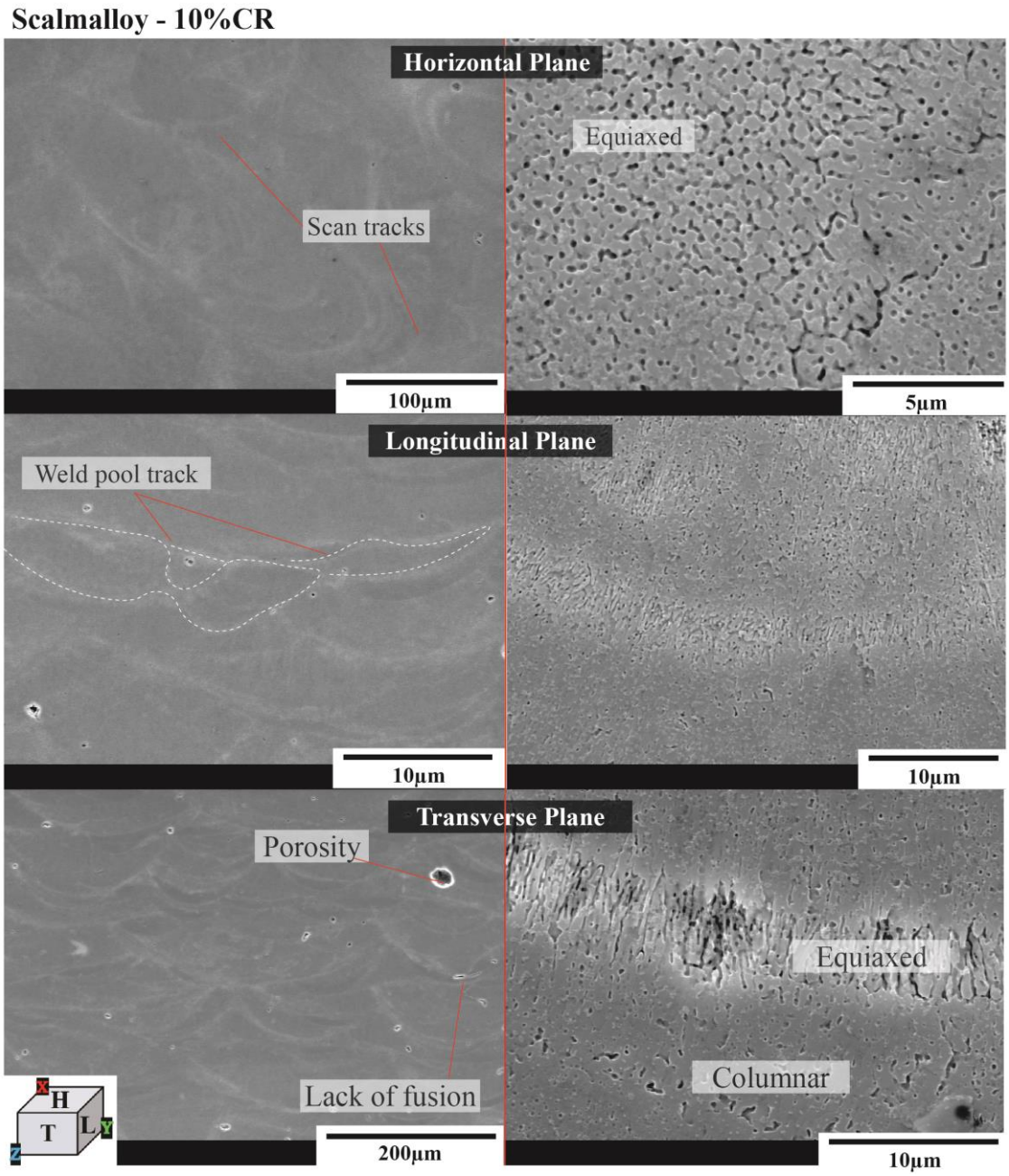

Fig. 5.24 SEM micrographs of the Scalmalloy 10%CR microstructure in the horizontal, longitudinal, and transverse planes

Fig. 5.25 shows the microstructure of the condition cold rolled to a reduction in 10% thickness and heat treated at 450ºC/1h (10%CR+HT1). The microstructure is similar to the 10%CR condition, except there are less darker regions. As heat treatment was applied to the 10%CR condition, the residual stress is eliminated and the alumininium matrix enters the elastic recovery process which is a typical reaction according to Ma et al. (2020a). Hence, dislocations at the grain boundaries of the alloy are less and tend towards regular arrangement of dislocations due to the pinning of $Al_3(Sc_xZr_{1-x})$ second phase particles. Hence, these high density (darker regions) areas become less (Ma et al., 2020a, 2020b). Microporosities and small defects also continue to be visible.

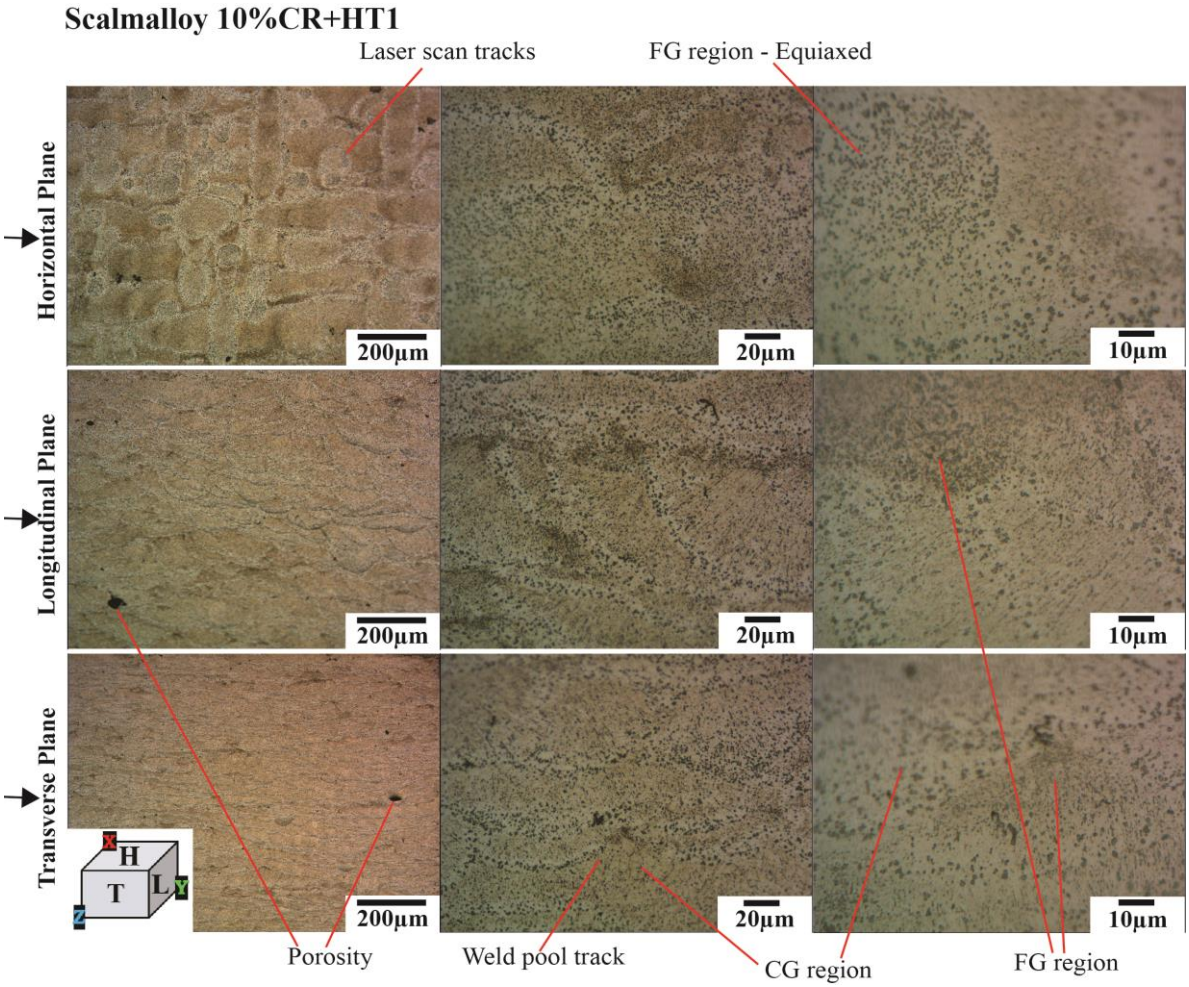

Fig. 5.25 Optical micrograph of 10%CR+HT1 microstructure in horizontal, longitudinal, and transverse planes

The EBSD mapping for the 10%CR+HT1 condition is shown in Fig. 5.26 and shows the CG region has more red grain indicating preferential grain growth in the <100> direction as these were more susceptible to the cold rolling reduction of 10%, however, the FG regions largely exhibits no preferential grain growth consistent with findings reported by Ma et al. (2020a). The overall grain size distribution is shown in Fig 5.27 with an average grain size of ≈1.98µm. The FG region consisted of equiaxed grains between 0.4 and 1µm, and the CG region consisted of elongated columnar grains with sizes up to 12µm. In comparison to the AB condition, the average and minimum grain sizes are slightly increased as the grains are elongated due to cold rolling, however, it is similar to the 10%CR condition. Fig. 5.28 shows the SEM micrographs of the 10%CR+HT1 condition. Porosity and lack of fusion is visible caused during the SLM process, such as gas developing within the melt pool and incomplete melting. CG and FG region also remain like previous conditions.

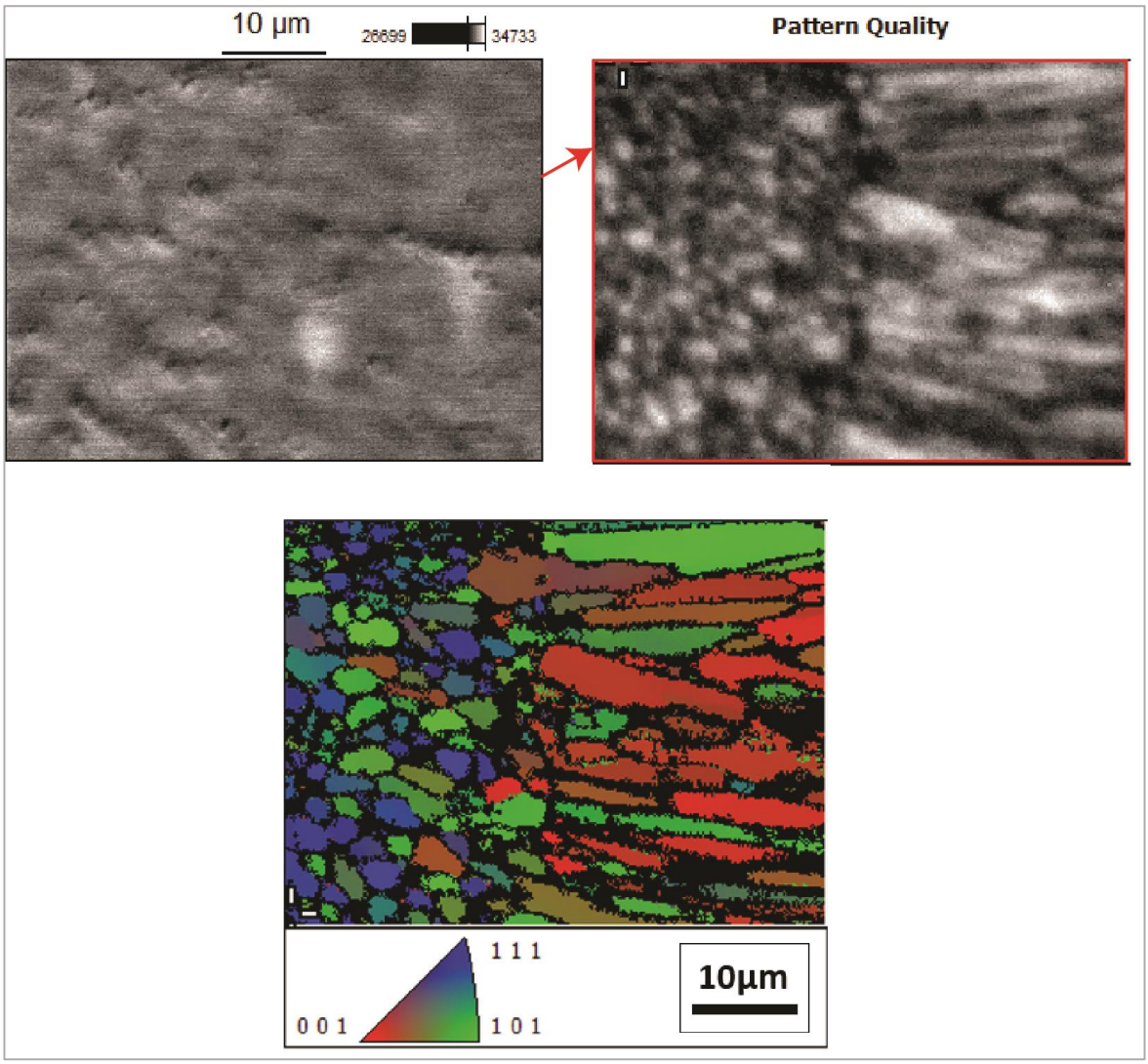

Fig. 5.26 EBSD Mapping of the 10%CR+HT1 condition in the transverse direction perpendicular to the build direction. Pattern quality is also shown here.

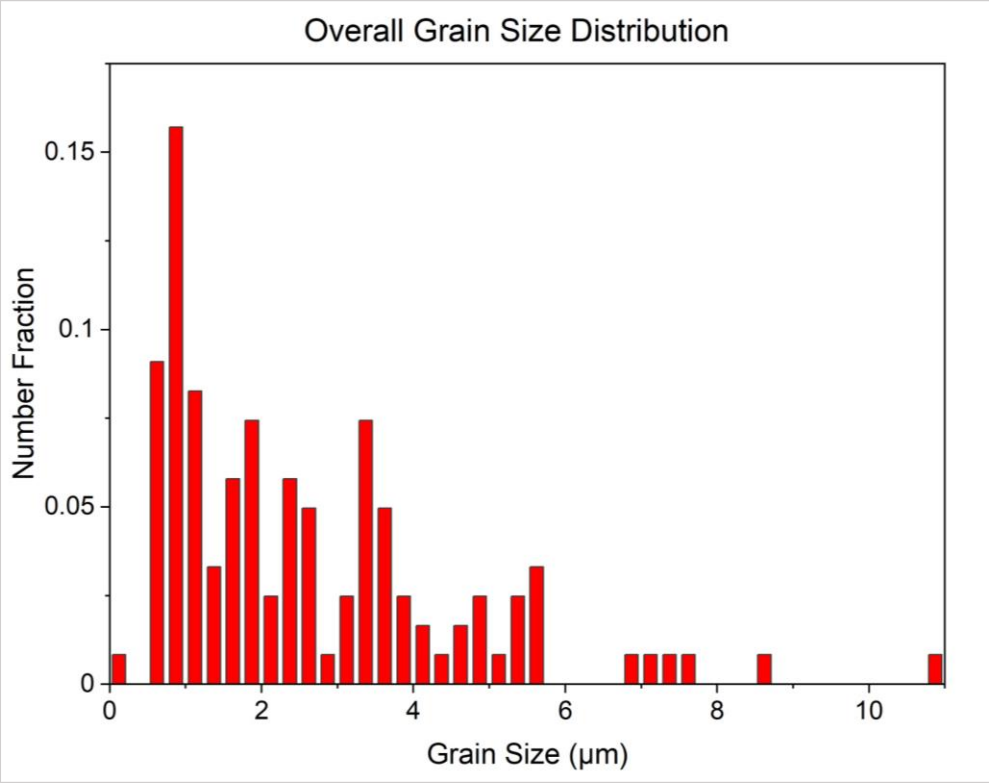

Fig. 5.27 Overall grain size distribution of the 10%CR+HT1 condition

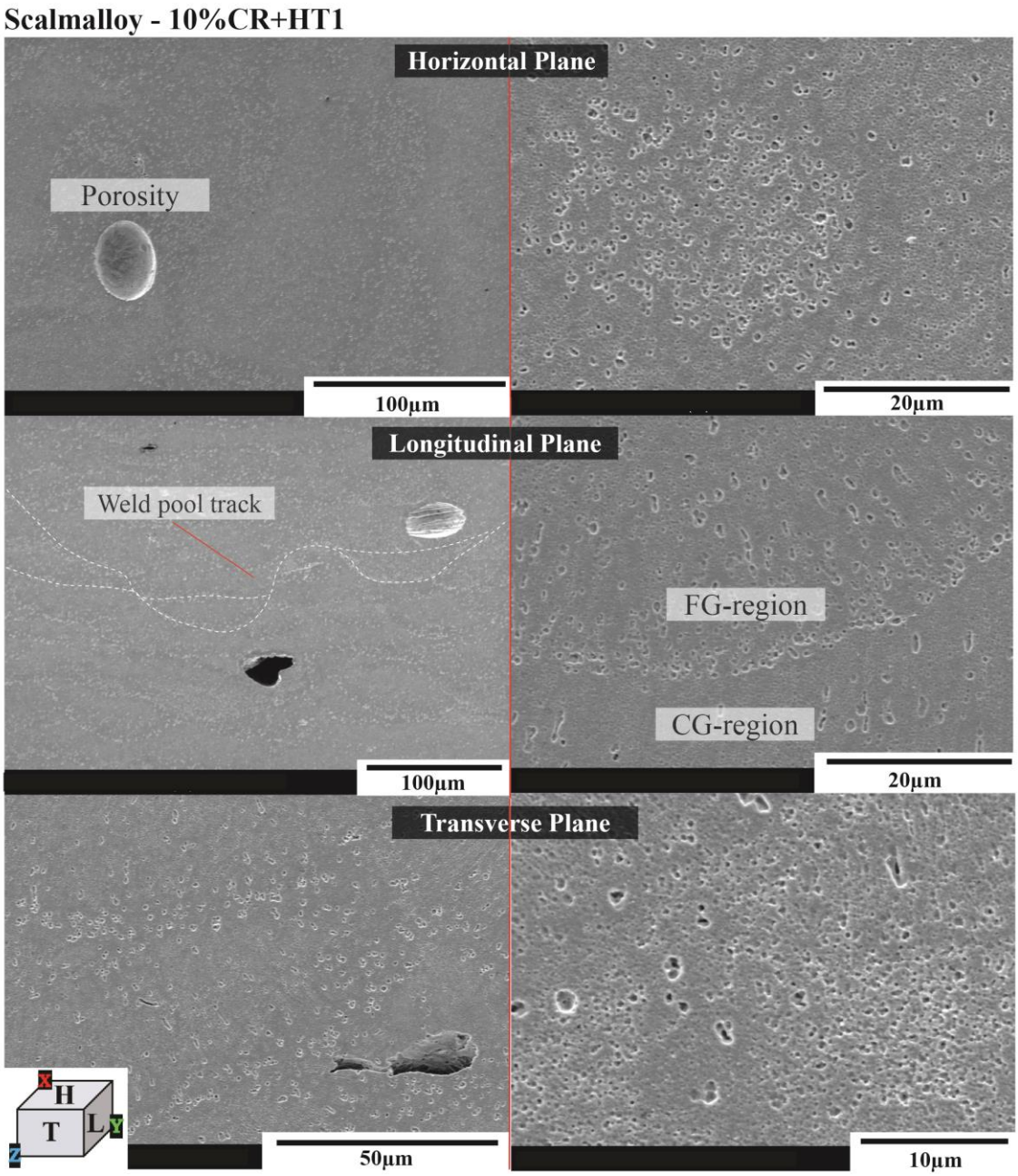

Fig. 5.28 SEM micrographs of the 10%CR+HT1 microstructure in the horizontal, longitudinal, and transverse planes

Fig. 5.29 and Fig 5.31 show optical micrographs of the microstructure of the 10%CR+HT2 and 10%CR+HT3 condition, respectively. Here, the CG and FG regions are visible along with some microporosity, laser scan tracks in the horizontal plane and weld pool tracks defined in the longitudinal and transverse planes. The microstructure resembles the 10%CR+HT1 condition in that there is less darker regions of FG material due to the removal of residual stresses through heat treatment, rearrangement and annihilation of dislocations (Ma et al., 2020a). The Al_3(Sc, Zr) second phase particles also seem to have coarsened assumed to be due to overageing Davydov et al. (2000). Fig. 5.30 and Fig. 5.32 show SEM micrographs of the 10%CR+HT2 and 10%CR+HT3 condition, respectively, where CG and FG regions are prominent. Defects still remain for each condition thought to be process induced and resemble that of previous conditions.

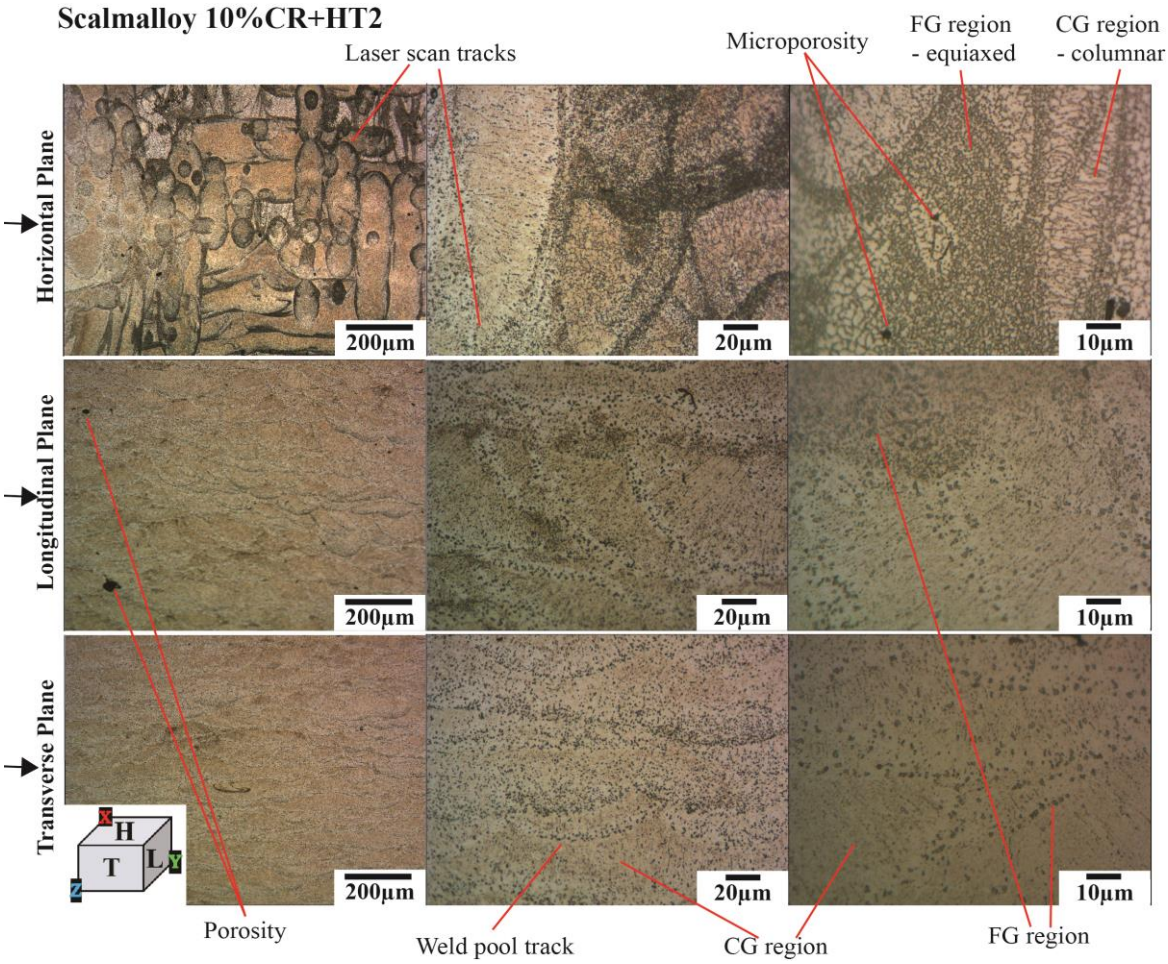

Fig. 5.29 Optical micrograph of 10%CR+HT2 microstructure in horizontal, longitudinal, and transverse planes

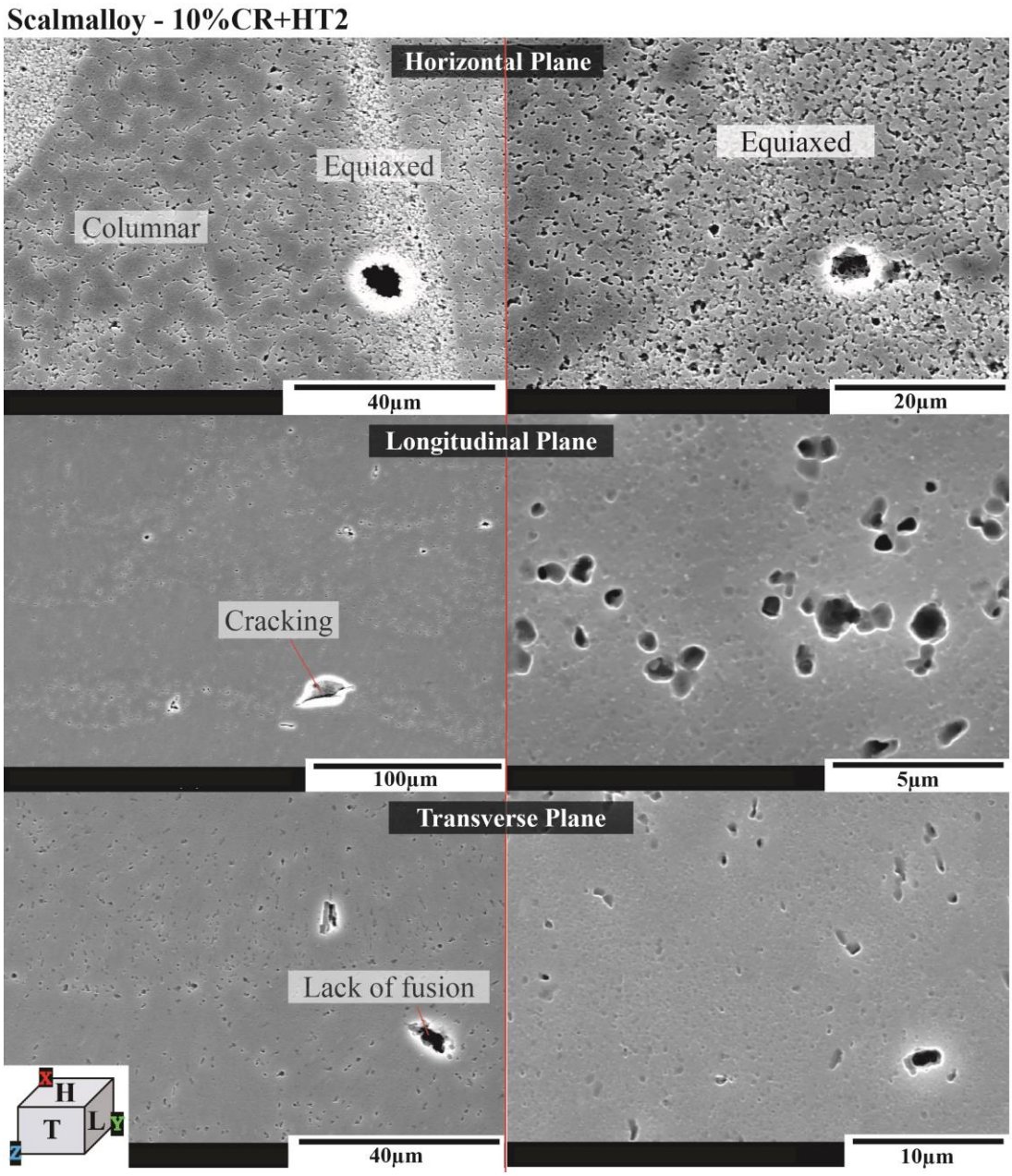

Fig. 5.30 SEM micrographs of the Scalmalloy 10%CR+HT2 microstructure in the horizontal, longitudinal, and transverse planes

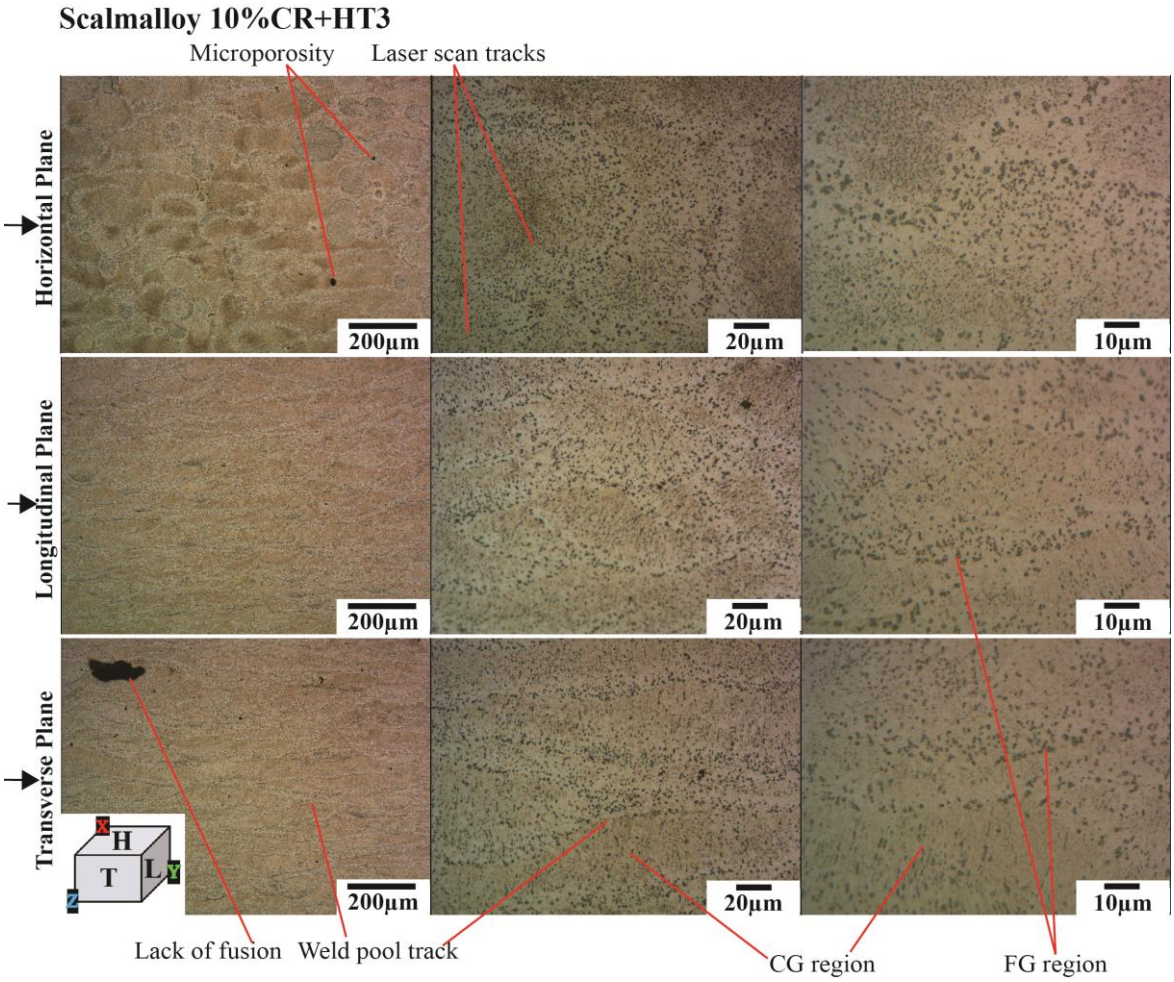

Fig. 5.31 Optical micrograph of 10%CR+HT3 microstructure in horizontal, longitudinal, and transverse planes.

Fig. 5.33 and Fig. 5.34 show optical and SEM micrographs of the 5052Al 30%CR microstructure in the horizontal, longitudinal, and transverse planes, respectively. In a similar manner, Fig. 5.35 and Fig. 5.36 shows optical and SEM micrographs of the 5083Al 30%CR microstructure in the horizontal, longitudinal, and transverse planes, respectively. The microstructure is similar to that of the AR and 10%CR conditions, but the silica is more prominent on the surface due to the induced plastic deformation along with the lines indicating the direction of rolling, which is also in the same direction of extrusion.

Fig. 5.37 shows the microstructure of the 30% cold rolled (30%CR) condition. The inherent AB microstructure still remains, however the higher percentage in roll reduction has greatly compressed the molten pool tracks. The molten pool depth has greatly decreased to a depth of 20-30µm, while the molten pool length is elongated to 120µm to 200 µm. Also, there also seems to be a higher area of darker shaded FG regions than the AB condition and 10%CR condition. Since the roll reduction is increased to 30%, high dislocation density is induced and precipitation of $Al_3(Sc_xZr_{1-x})$ second phase particles along with increased residual stresses as described in the literature (Ma et al., 2020a, 2020b), much like the mechanism for the 10%CR condition. Fig. 5.38 shows SEM micrographs of the microstructure for the 30%CR condition showing higher

magnification of the molten pool and FG and CG regions. There does seem to be some delamination of layers in the transverse plane due to incomplete solidification of the last layers and some porosity due to gas entrapment around the melt pool during SLM process (Galy, Guen, et al., 2018). The FG region seems to contain much finer grains evident in Fig. 5.38 likely due to the high roll reduction increasing dislocation density and precipitation of fine second phase particles. Microporosity is visible and there does not seem to be any large gas porosities most likely due to the high compression from cold rolling to reduce pore size (T. Wang et al., 2021).

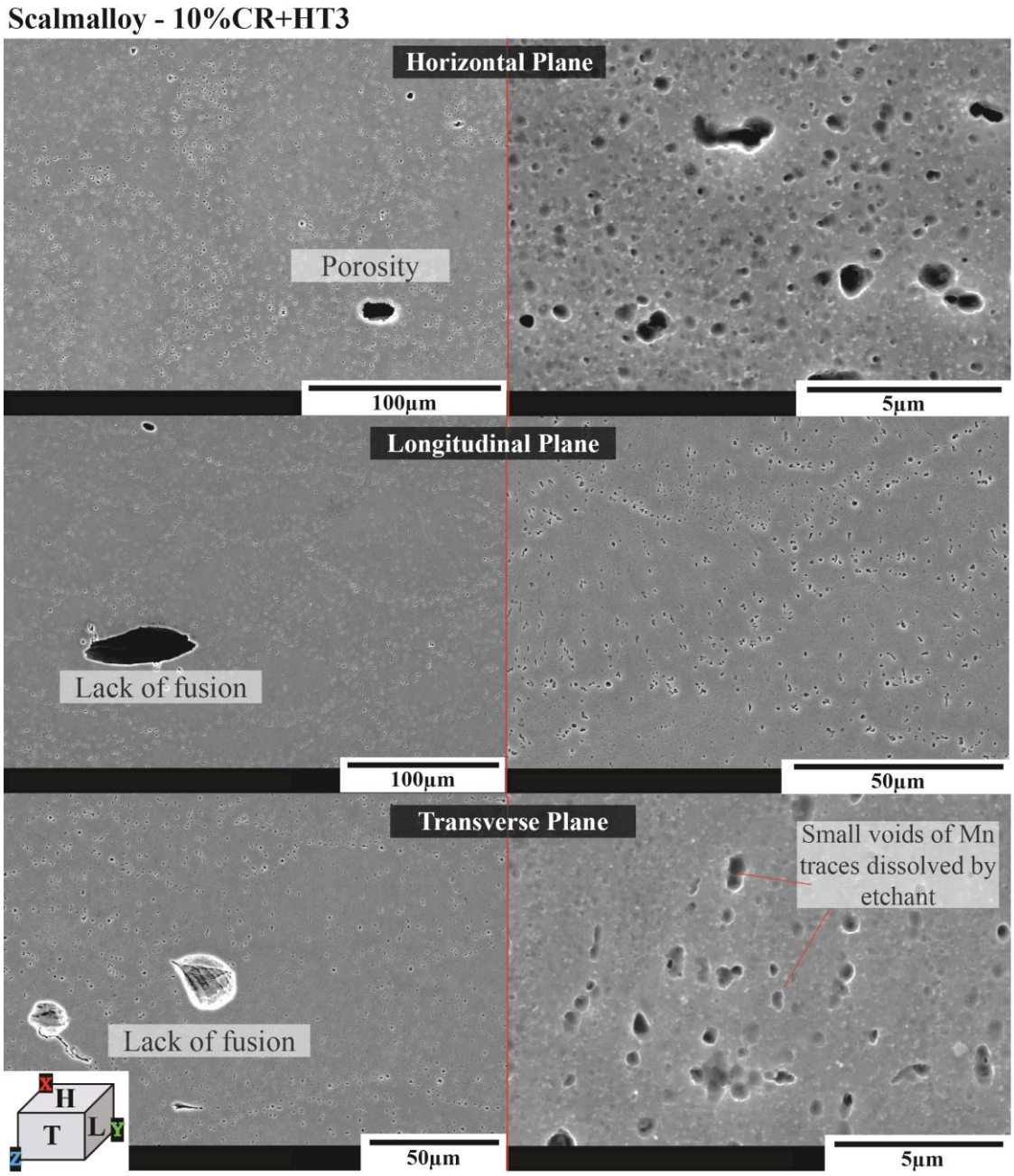

Fig. 5.32 SEM micrographs of the 10%CR+HT3 microstructure in the horizontal, longitudinal, and transverse planes

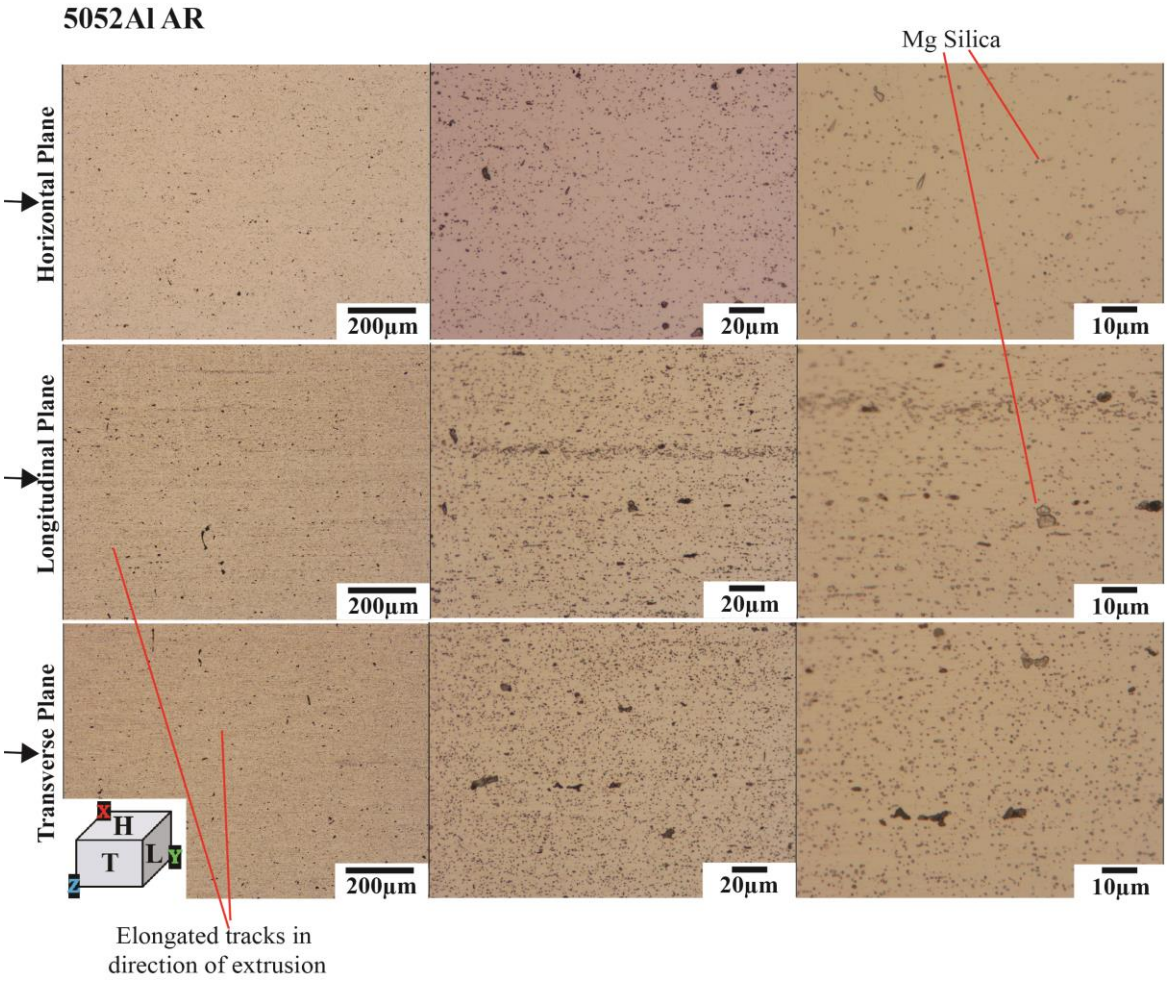

Fig. 5.33 Optical micrograph of the microstructure of 30%CR 5052Al alloy in the horizontal, longitudinal, and transverse planes

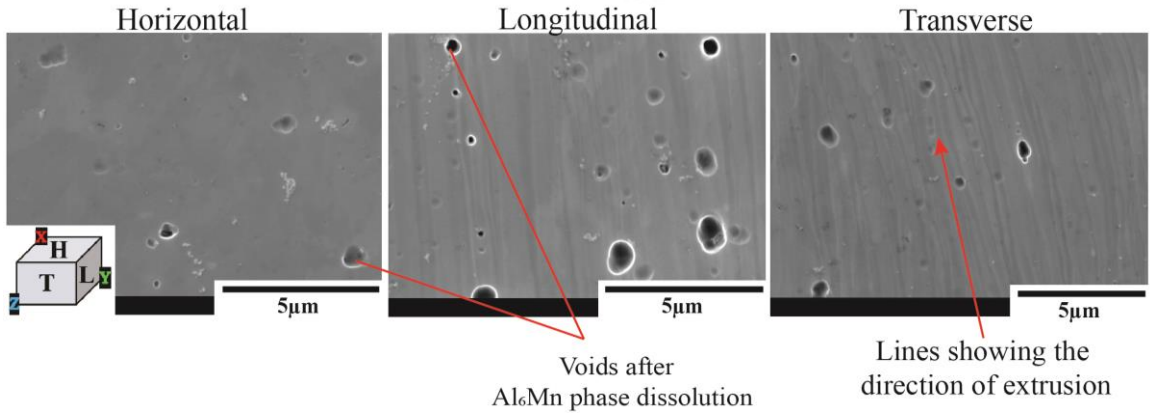

Fig. 5.34 SEM micrograph of the microstructure of 30%CR 5052Al alloy in the horizontal, longitudinal, and transverse planes

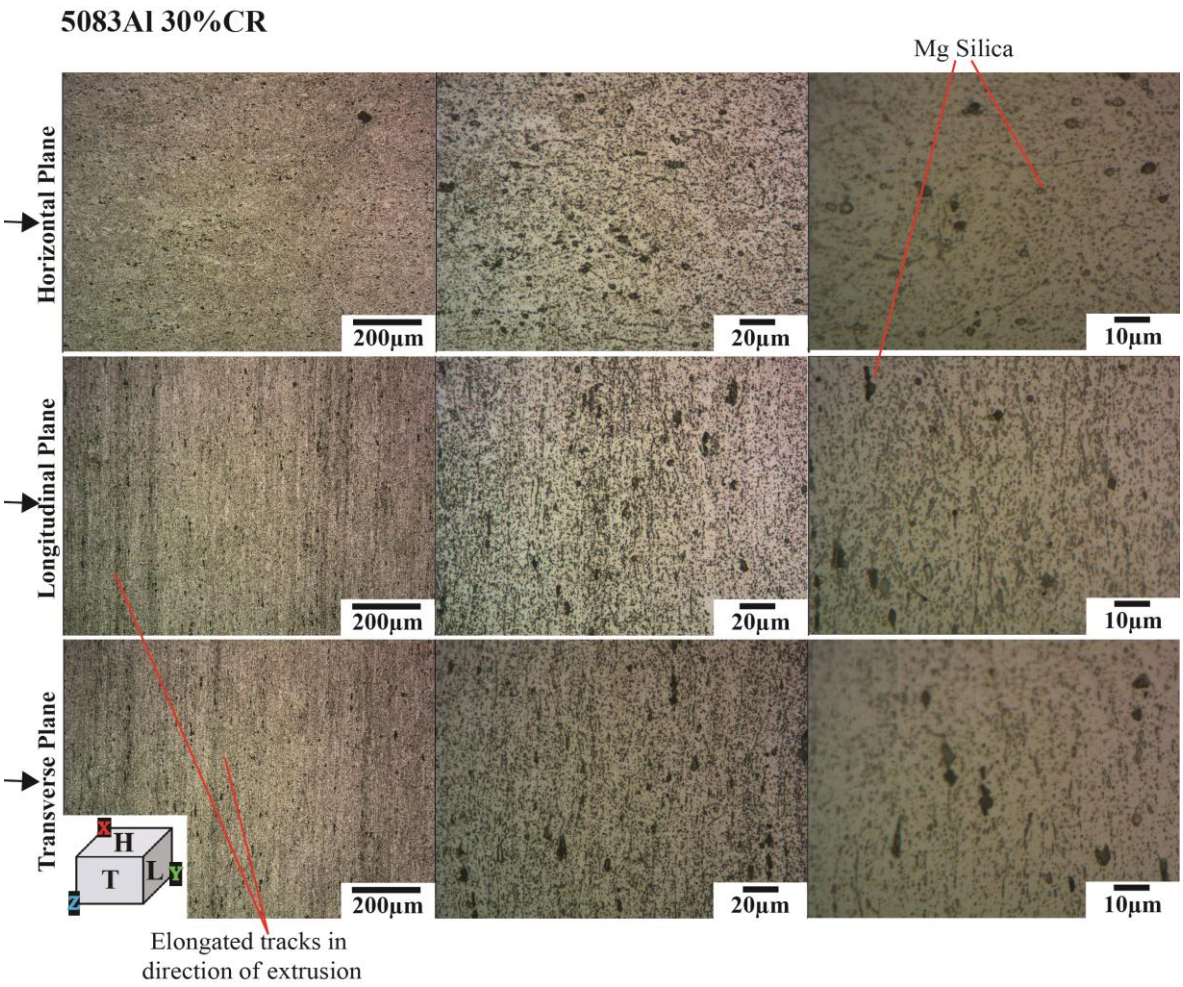

Fig. 5.35 Optical micrograph of the microstructure of 30%CR 5083Al alloy in the horizontal, longitudinal, and transverse planes

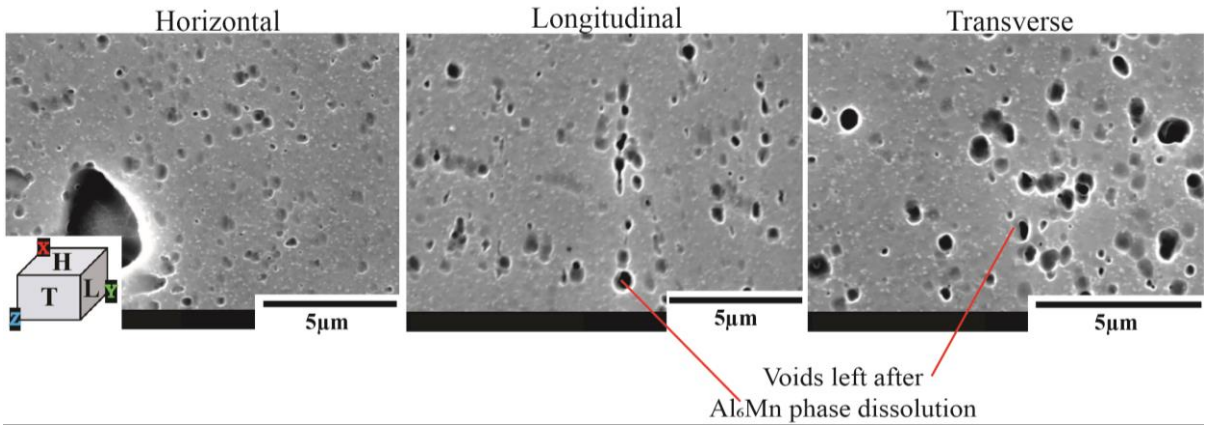

Fig. 5.36 SEM micrograph of the microstructure of 30%CR 5083Al alloy in the horizontal, longitudinal, and transverse planes

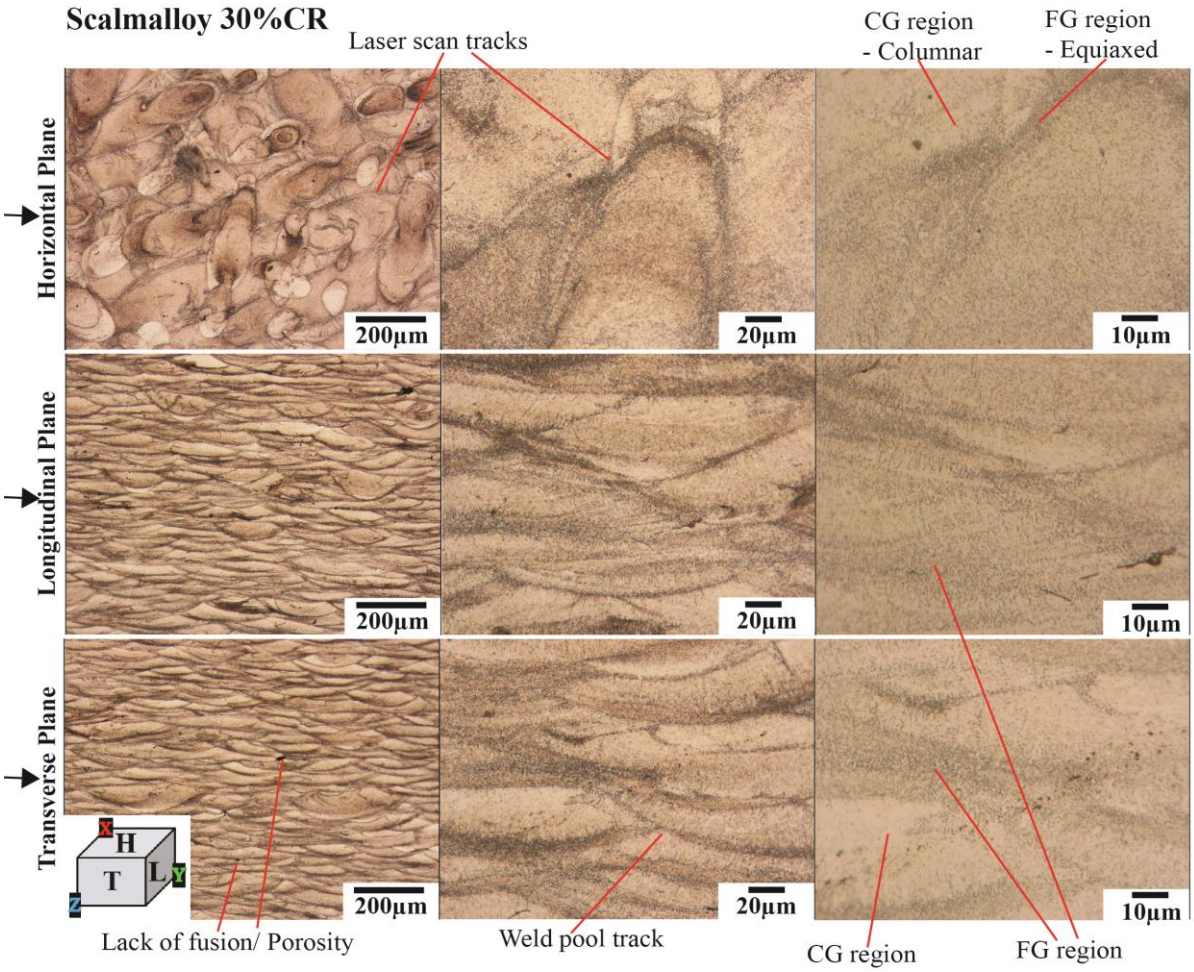

Fig. 5.37 Optical micrograph of the 30%CR+HT1 microstructure in horizontal, longitudinal, and transverse planes

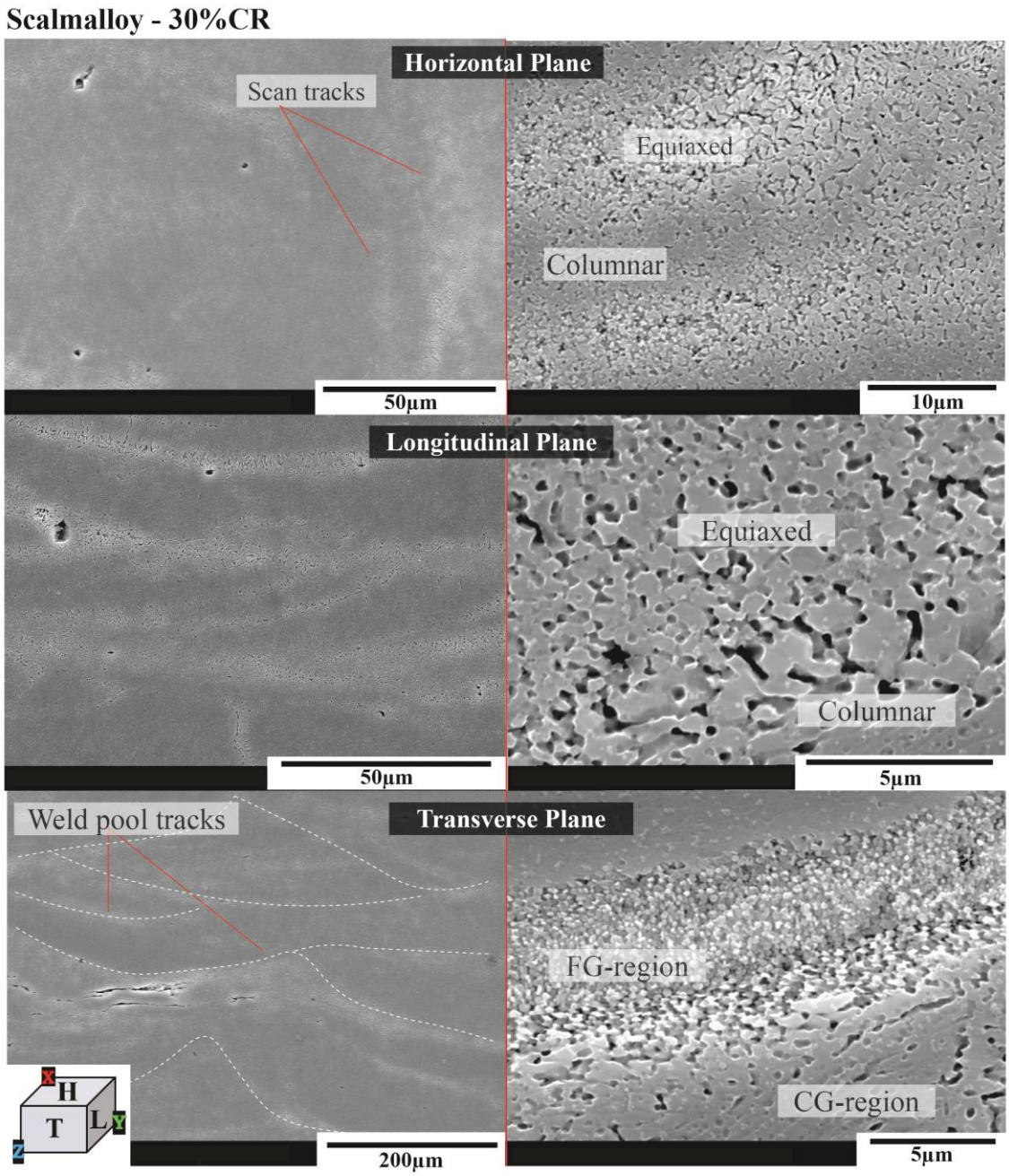

Fig. 5.38 SEM micrographs of the Scalmalloy 30%CR microstructure in the horizontal, longitudinal, and transverse planes

Fig. 5.39 shows optical micrographs of the 30%CR+HT1 condition and the microstructures are similar to the 30%CR microstructure. Laser scan tracks are visible in the horizontal plane consistent with the 67° scanning pattern and FG regions, CG regions and molten pool tracks are visible. The molten pool dimensions are similar to the 30%CR results as expected, yet with less darker FG regions (Fig. 5.38). Similar to the 10%CR+HT1 condition, the 30%CR+HT1 condition has high dislocation density induced by cold rolling and when heat treatement was applied the residual stresses were eliminated and precipitation of $Al_3(Sc_xZr_{1-x})$ second phase particles is consistent with the optical micrographs.

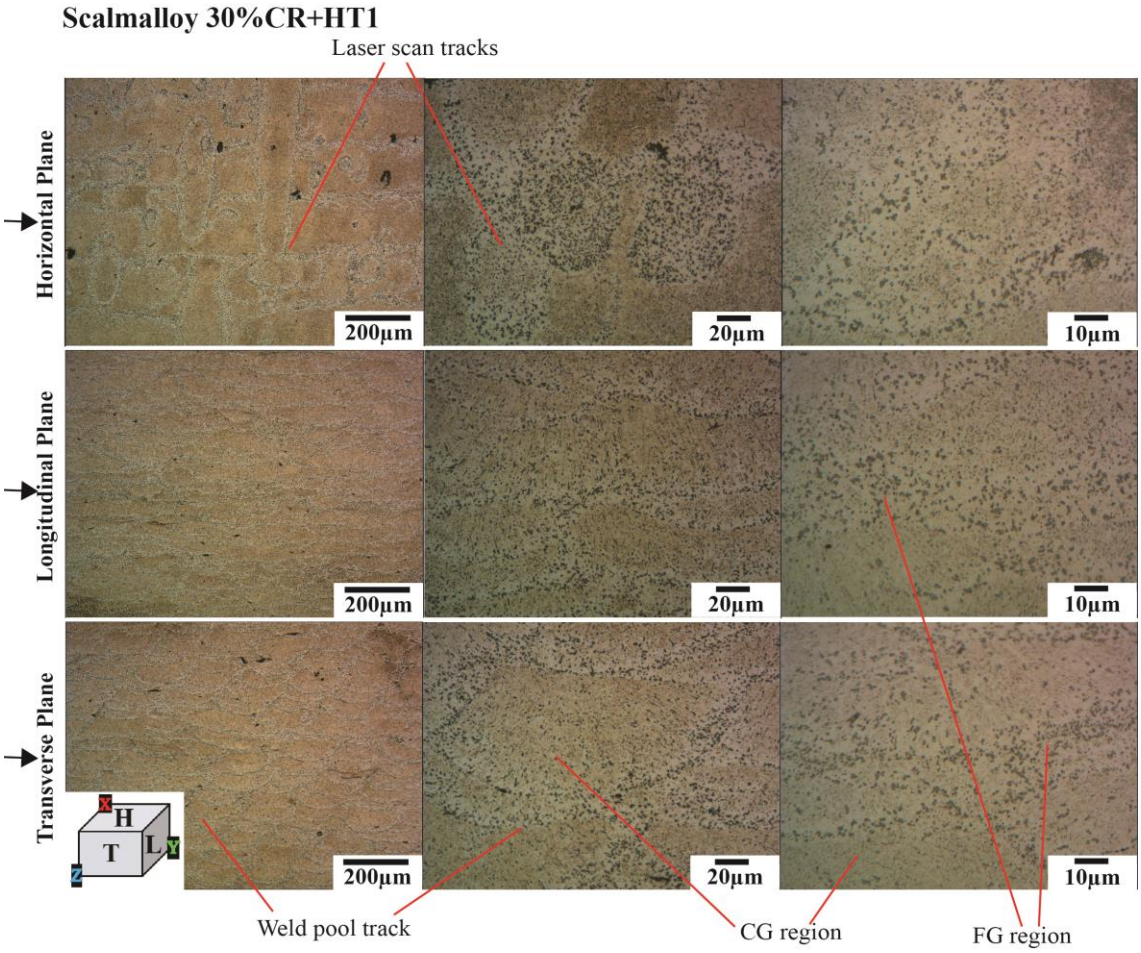

Fig. 5.39 Optical micrograph of 30%CR+HT1 microstructure in horizontal, longitudinal, and transverse planes

Fig. 5.40 shows the EBSD mapping of the 30%CR+HT1 condition. Most of the grains are blue indicating preferential grain growth in the <111> direction for both the FG and CG regions assumed to be due to the higher reduction in cold rolling of 30% which has caused a preferential grain orientation in the direction of rolling, which is consistent with findings reported by Ma et al. (2020a). Fig 5.41 shows the average grain size is ≈1.65µm. The FG region consisted of equiaxed grains between 0.2µm and 1µm, and the CG region consisted of elongated columnar grains with sizes up to 12µm. Fig. 5.40 shows that there are some finer grains in the CG region, indicating that larger grains have been broken due to the cold rolling process similar to that reported by Ma et al. (2020a). Hence, the overall grain size distribution is slightly reduced when compared to the 30%CR condition and compared to the 10%CR and heat-treated conditions. Fig. 5.42 shows SEM micrographs of the 30%CR+HT1 condition where cracking, porosity and lack of fusion are visible within the microstructure; however, slight flattening of the pores due to the compression of the cold rolling is evident. FG equiaxed and CG coarse grain regions are shown clearly and are similar to the 10%CR+HT1 condition but with slightly smaller grain sizes.

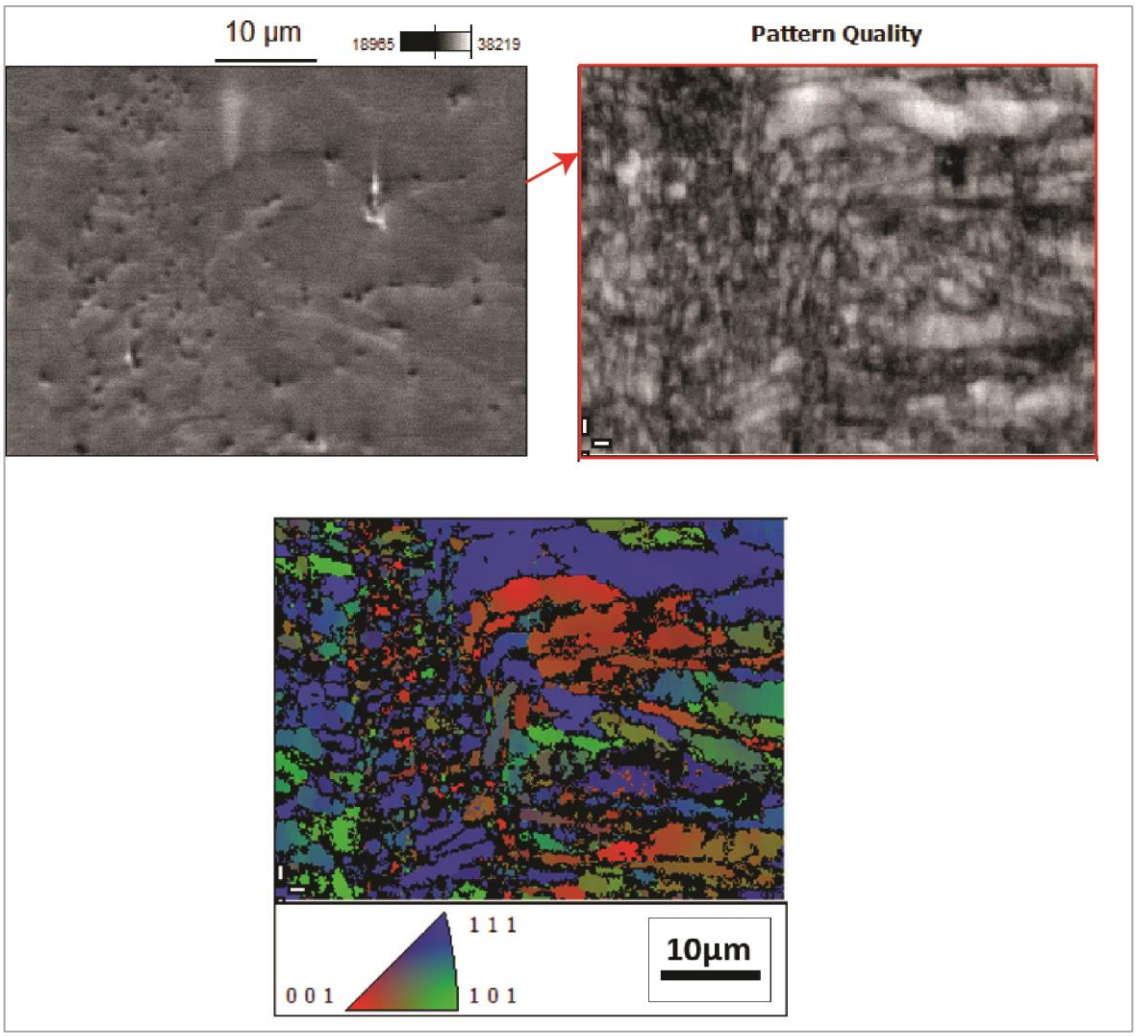

Fig. 5.40 EBSD orientation map of the 30%CR+HT1condition in the transverse direction perpendicular to the build direction. Pattern quality is also shown here.

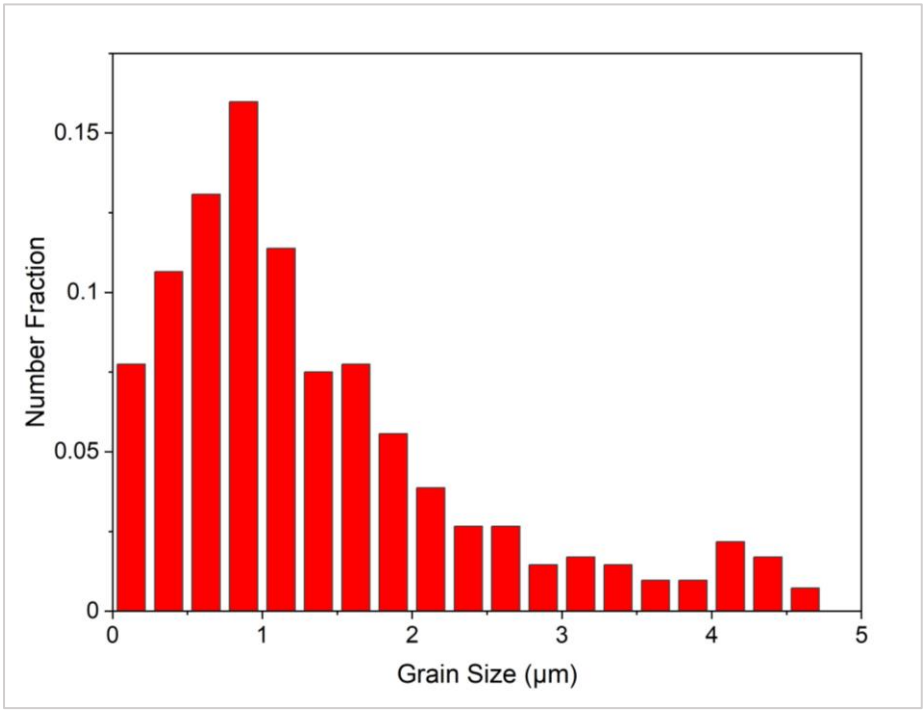

Fig. 5.41 Overall grain size distribution of the 30%CR+HT1 condition

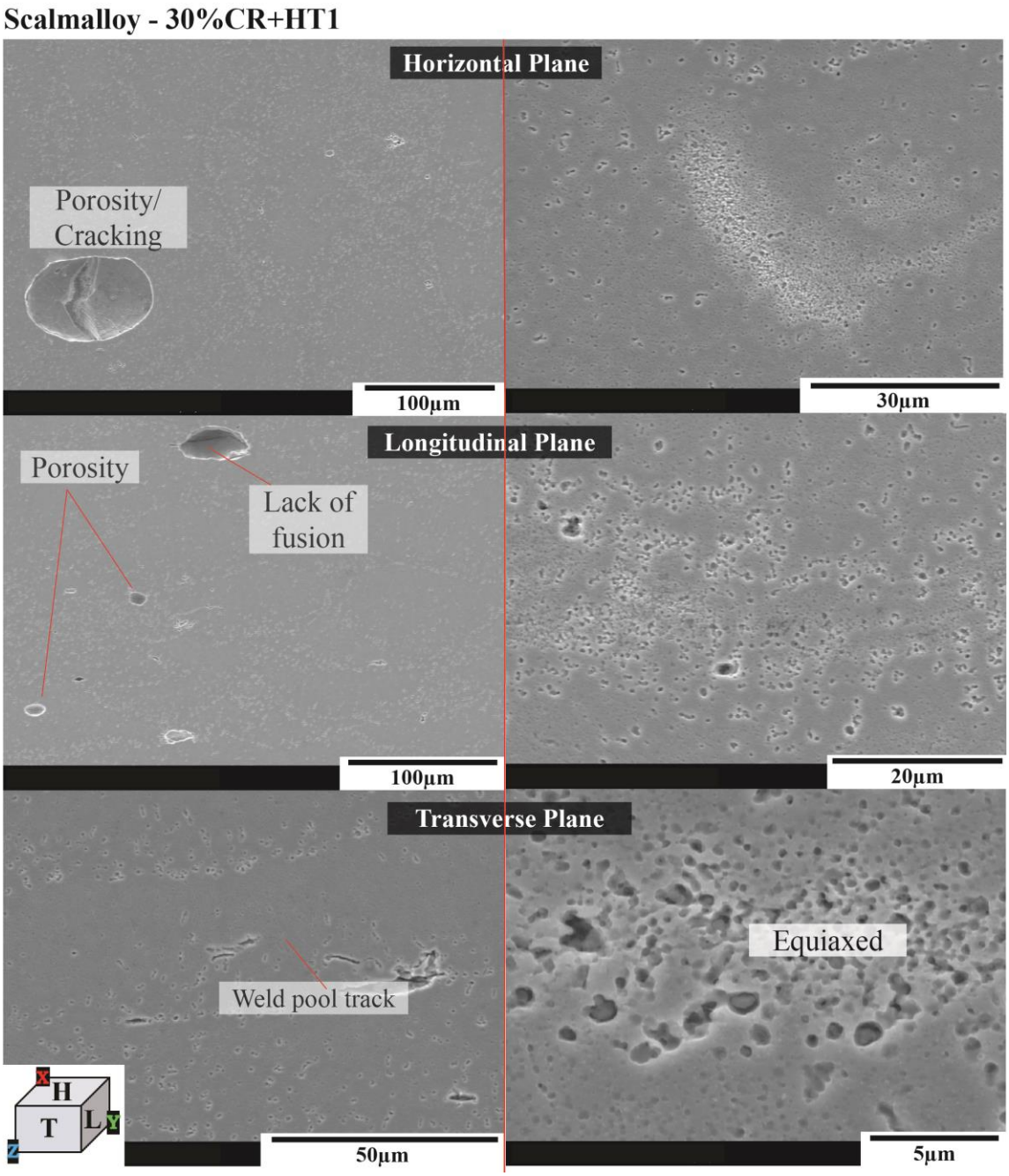

Fig. 5.42 SEM micrographs of the 30%CR+HT1 microstructure in the horizontal, longitudinal, and transverse planes

Fig. 5.43 and 5.45 show optical micrographs for the 30%CR+HT2 and 30%CR+HT3 conditions. They are very similar to one another showing laser scan tracks, FG and CG regions, and molten pool tracks. Fig 5.44 and 5.46 shows SEM micrographs of the 30%CR+HT2 and 30%CR+HT3 cold rolled conditions. These conditions show very similar characteristics to each other and to the 30%CR+HT1 condition, where porosity, cracking and lack of fusion are visible likely induced through the SLM process. Slight growth in $Al_3(Sc_xZr_{1-x})$ second phase particles is also visible, again thought to be due to overageing (Fuller et al., 2003), similar to all conditions subject to HT2 and HT3.

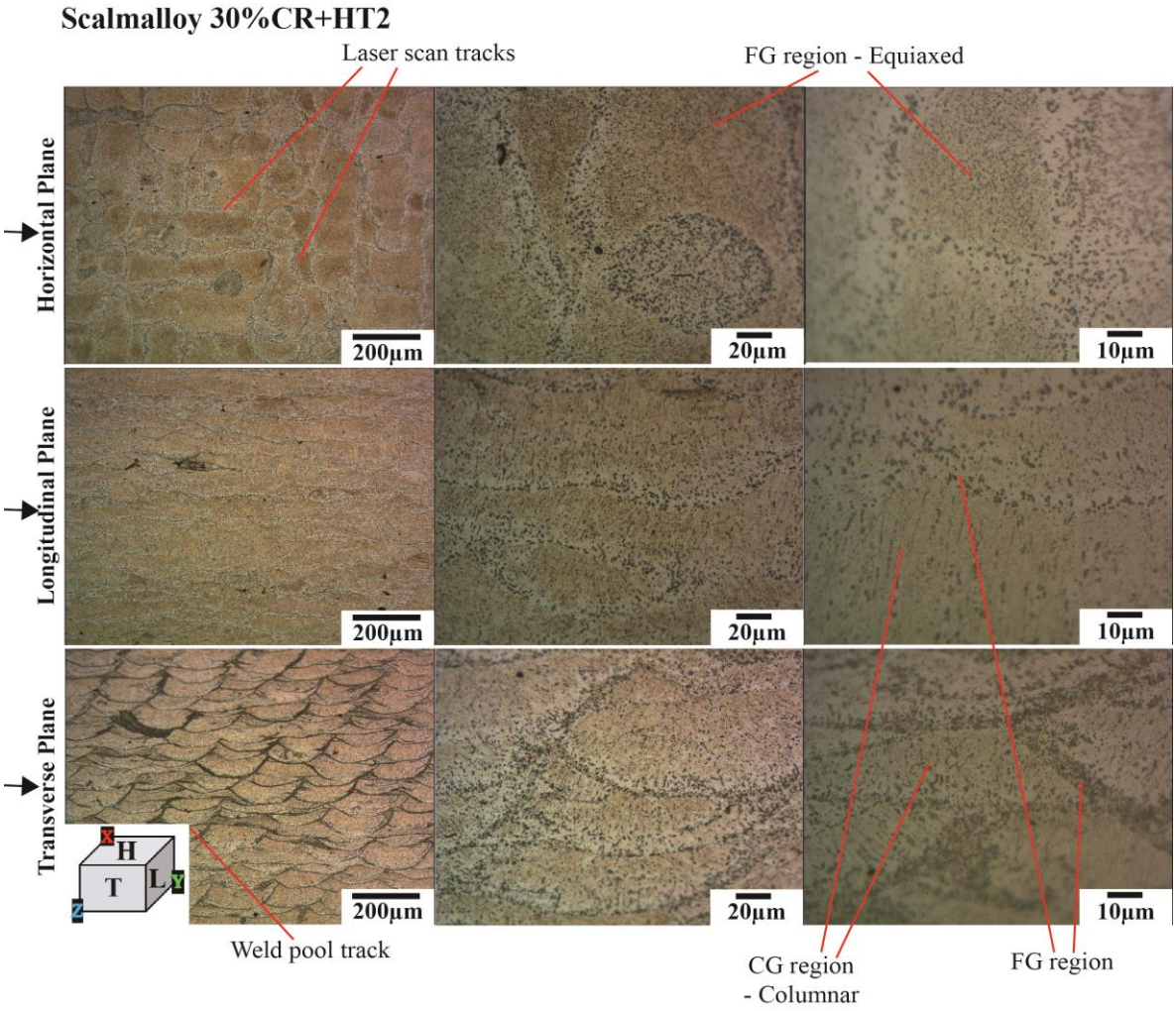

Fig. 5.43 Optical micrographs 30%+HT2 microstructure in horizontal, longitudinal, and transverse planes

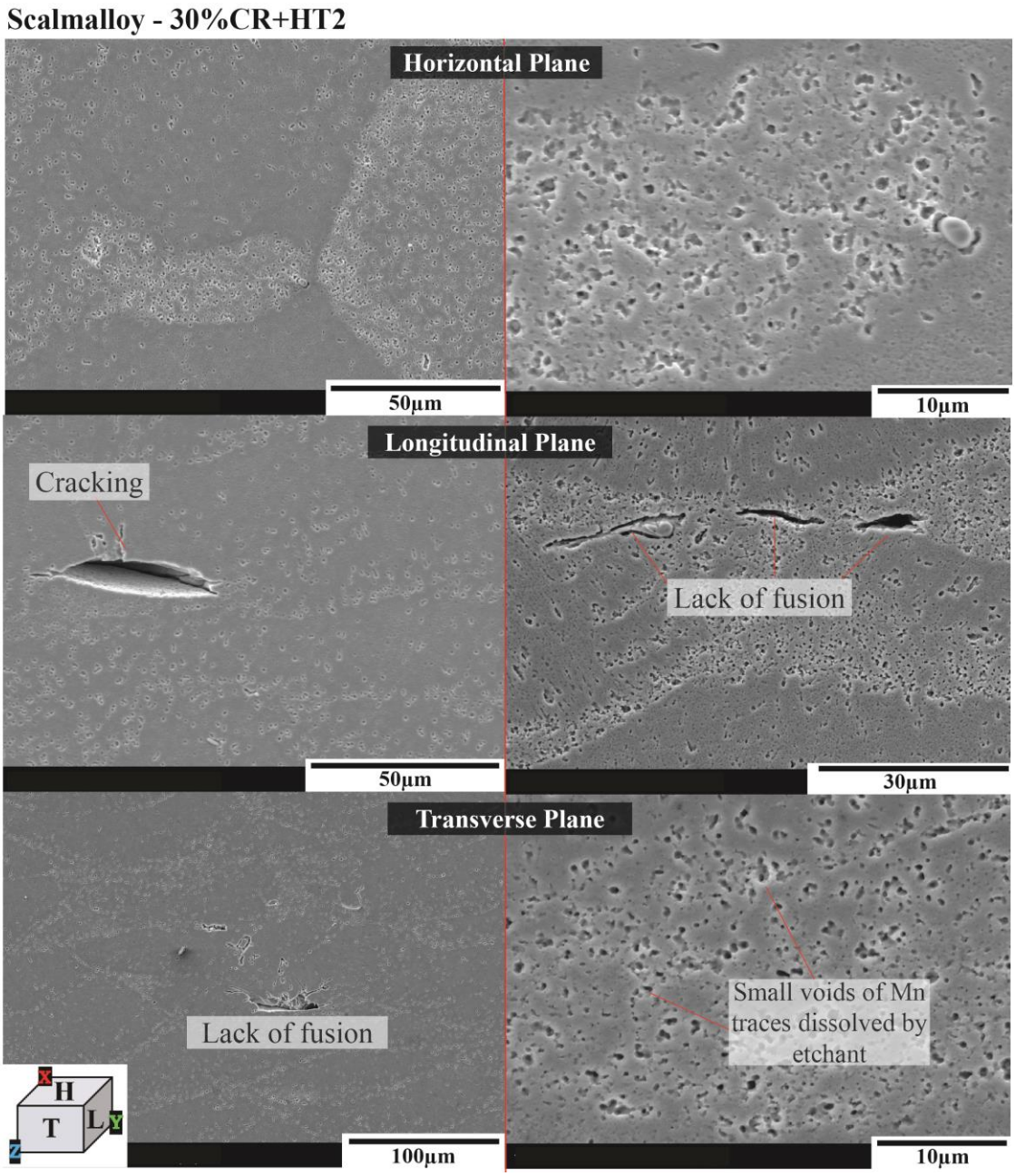

Fig. 5.44 SEM micrographs of the 30%CR+HT2 microstructure in the horizontal, longitudinal, and transverse planes

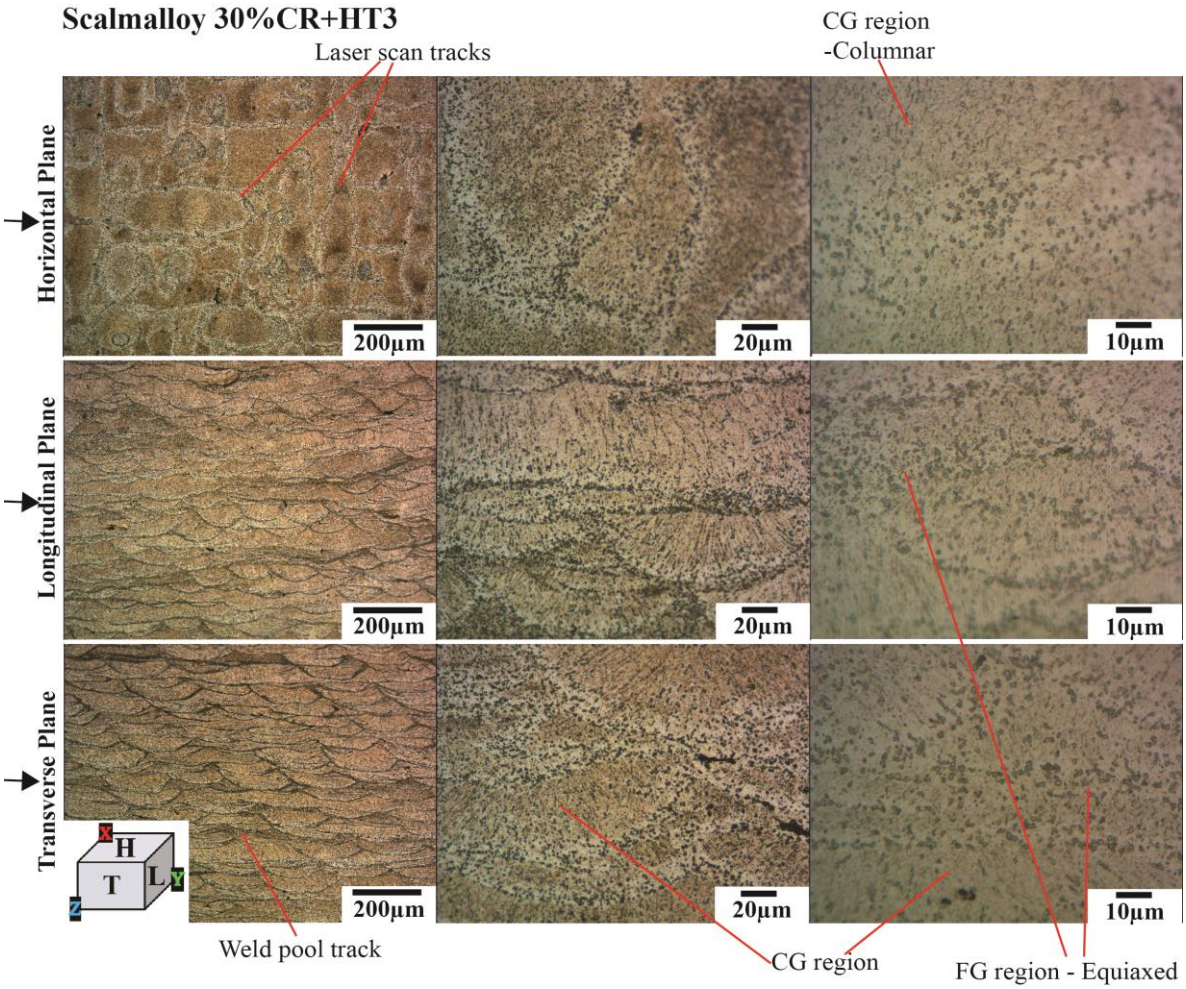

Fig. 5.45 Optical micrograph of 30%CR+HT3 microstructure in horizontal, longitudinal, and transverse planes

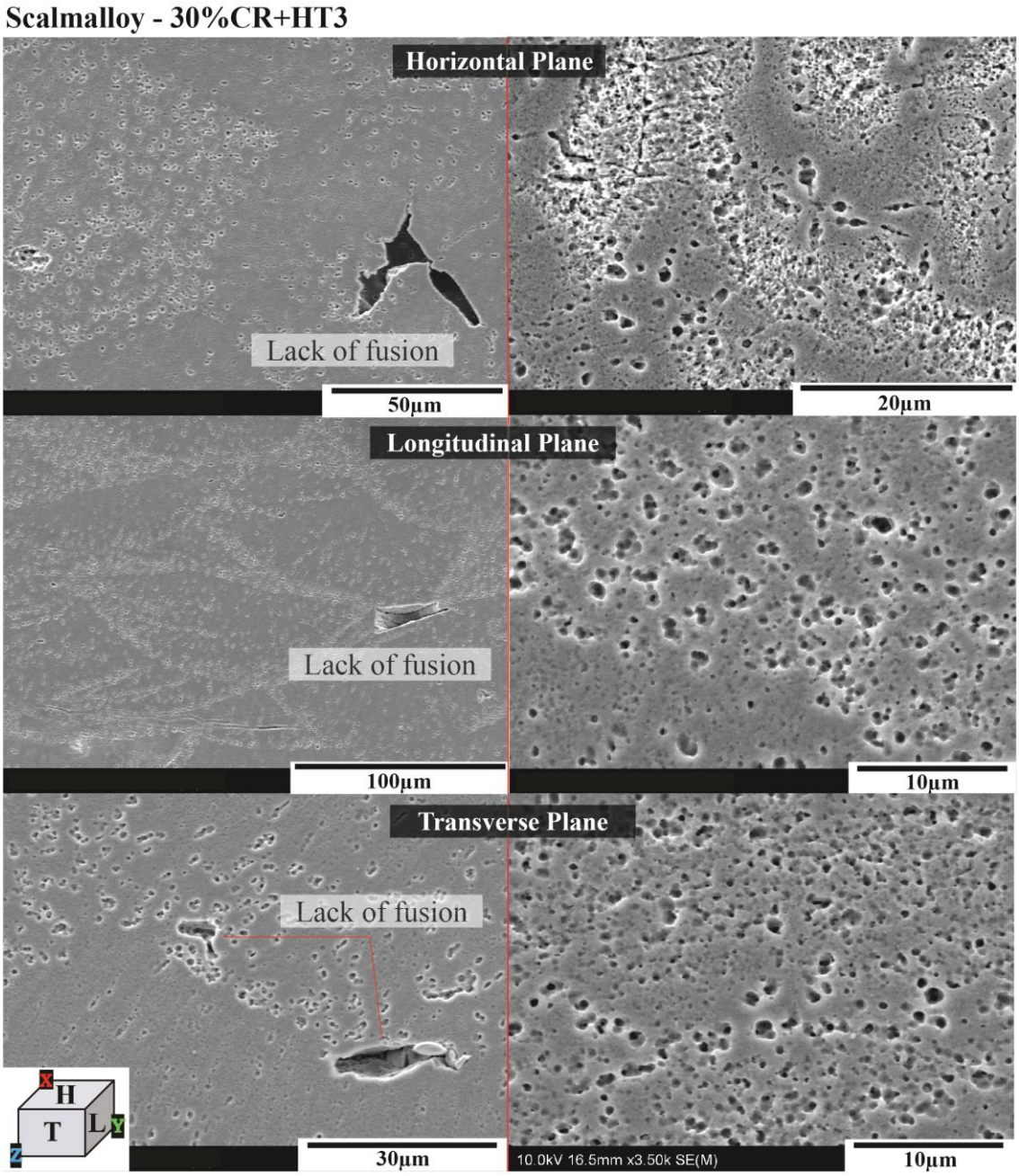

Fig. 5.46 SEM micrographs of the 30%CR+HT3 microstructure in the horizontal, longitudinal, and transverse planes

Fig 5.47 compares the grain size distribution of the AB, AB+HT1, 10%CR, 10%CR+HT1, and 30%CR +HT1 conditions. These findings are consistent with the microstructural analysis of each condition. The AB+HT1 condition has a smaller grain size distribution as heat treatment is found to refine grains (R. Li et al., 2019; A. B. Spierings, Dawson, Dumitraschkewitz, et al., 2018; A. B. Spierings, Dawson, Kern, et al., 2017), however it is not seen to drastically reduce grain size, hence, the reduction is more likely due to the chosen area where the EBSD mapping was taken as this is only a small reflection of the entire surface. The cold rolled and heat-treated conditions have higher grain size distributions due to the elongation of grains occurring during the rolling process (Ma et al., 2020a; Panagopoulos & Georgiou, 2010).

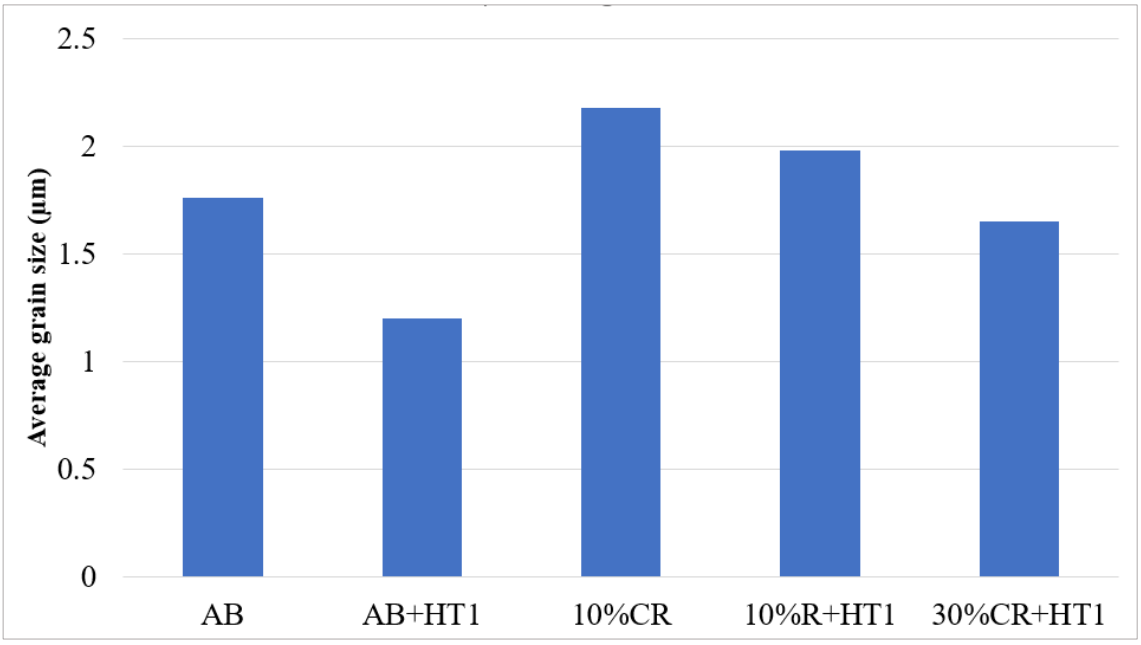

Fig. 5.47 Comparison of grain size distribution for Scalmalloy AB, AB+HT1, 10%CR, 10%CR+HT1, and 30%CR+HT1 conditions

5.2 Tensile properties

Fig. 5.48 - 5.50 shows the stress strain curve comparing each condition, it must be noted that one curve of the three samples tested for each condition are graphed and compared in these figures. Fig. 5.51 - 5.54 show bar graphs comparing average tensile and yield strengths for easy comparison. Please note additional tensile data is provided in Fig. E.1 – E.5 in Appendix E for the reader's information. All conditions show fluctuating wave patterns in the plastic deformation region of the stress-strain curves known as the Portevin-Le Chatelier (PLC) effect. This effect is common in Al-Mg alloys and is caused by magnesium solute atoms diffusing along dislocations. A slightly higher stress is required to tear these solutes off the dislocations causing the rapid increase in stress level. Although, once the solute is released, the stress drops quickly to a lower point until dislocations are blocked again by the solutes. This fluctuation in stress levels form the serrations in the stress-strain curve in the plastic region. For Scalmalloy, $Al_3(Sc_x,Zr_{1-x})$ coherent second phase particles developed after subsequent heat treatment may also act as impedances like the solute atoms and impact the PLC effect (A. B. Spierings, Dawson, Kern, et al., 2017; Z. Wang et al., 2020). Fig 5.48 shows a comparison of the stress strain curves for the AB, AB+HT1, AB+HT2 and AB+HT3 Scalmalloy conditions. The AB condition has an average YS, UTS and strain values of 287MPa, 334MPa and 0.098, respectively (shown in Table 5-1). These are relatively high for the AB condition compared to conventionally manufactured (such as extruded) aluminium alloys as the high cooling rates occurring during the SLM process induced a super fine-grained microstructure and constitutional undercooling of mush constituents (Awd et al., 2017; R. Li et al., 2019). The tensile properties are also higher than similar additively manufactured alloys such as AlSi10Mg as scandium and zirconium are known to increase ambient temperature tensile properties and recrystallisation resistance of Al-Mg-Sc-Zr alloys (Fuller et al.,

2003). However, these values are slightly lower than the AB values from literature (Awd et al., 2017; R. Li et al., 2019) as the SLM process and composition used in this work deferred and the selected SLM process parameters developed in Chapter 4 partially suppressed the precipitation of $Al_3(Sc_{1-x}Zr_x)$ particles so that the AB condition would be more responsive to subsequent heat treatment and ageing.

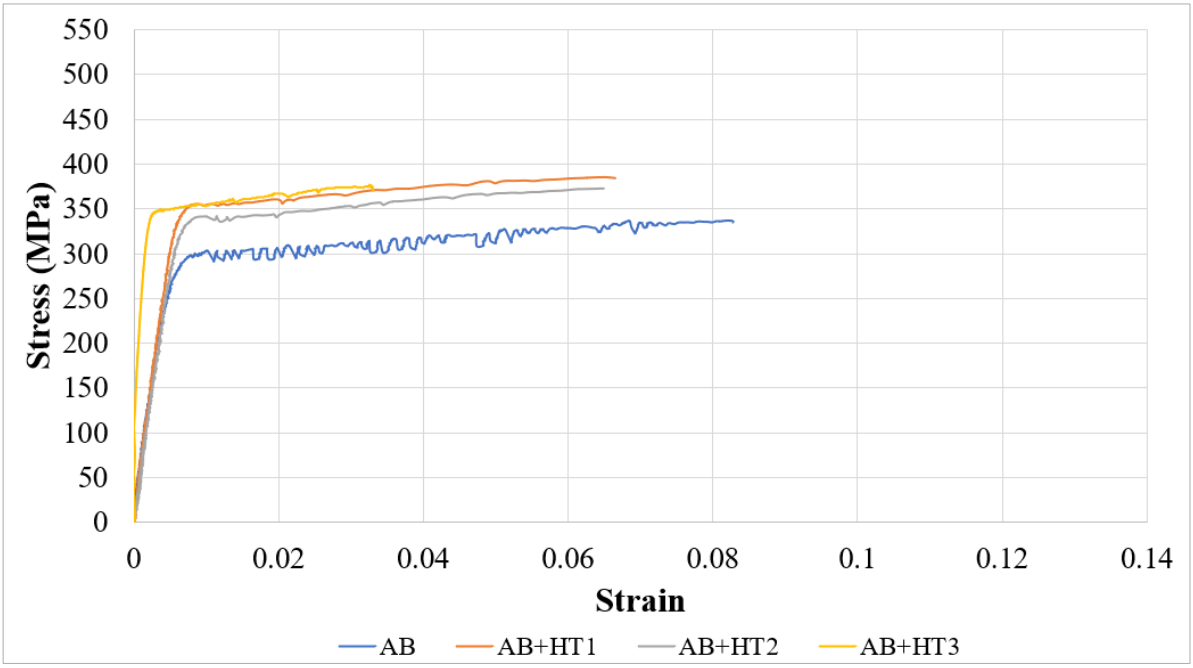

Fig. 5.48 Stress strain curves for AB conditions - a) AB, b) AB+HT1, c) AB+HT2, d) AB+HT3

From Table 5-1, the average YS, UTS and strain at fracture values are 308MPa, 384MPa and 0.07, respectively. The average tensile strength of the AB+HT1 condition has increased compared to the AB condition, while the strain was slightly reduced assumed to be due to the precipitation of $Al_3(Sc_{1-x}Zr_{rx})$ particles during subsequent heat treatment (Z. Wang et al., 2020) and also evident from the many small second phase particles shown in the optical micrographs (Fig 5.9). However, as the tensile strength increased, the plasticity decreased evident from the lower strain values, a typical consequence of increased strength (Rao et al., 2014). According to Ma et al. (2020b), a higher heat treatment temperature causes a faster diffusion rate so as the temperature increases, the rate of the precipitation secondary phase also increases. In turn, the secondary phase coarsening rate increases as well. HT1 starts from a relatively high temperature of 450°C for one hour. During this heat treatment, the precipitation rate increases rapidly for $Al_3(Sc_{1-x,}Zr_x)$ leading to the improvement of tensile strength. A slightly smaller overall grain size distribution (Fig. 5.47) was achieved in comparison to the AB condition, and thicker bands of FG regions were visible in Fig. 5.8, indicating higher particle density consistent with findings reported by R. Li et al. (2019). Similarly, precipitation strengthening has occurred in the AB+HT2 and AB+HT3 conditions since tensile strengths are higher compared to the AB condition. The tensile properties of the AB+HT2 and AB+HT3 showed slightly lower tensile properties compared to the AB+HT1 condition. As reported by Fuller et al. (2003), the subtle decline was assumed to be caused by the

prolonged heat treatment times (overageing) leading to the growth of second phase particles further confirmed by the small second phase particles visible in Fig. 5.13 and Fig. 5.15, where they are slightly larger compared to AB+HT1 condition (Fig. 5.9).

Fig. 5.49 shows the stress strain curves for the 10%CR, 10%CR+HT1, 10%CR+HT2 and 10%CR+HT3 Scalmalloy conditions. The tensile properties of the 10%CR condition was comparable to the AB condition where the YS was 285MPa and the UTS was 321MPa (shown in Table 5-1) thought to be due to the low cold rolling reduction. The strain was 0.058, lower than the AB condition, as ductility was reduced as a result of the work hardening effect induced by cold rolling (Kaiser et al., 2014). The 10%CR+HT1 condition showed a large increase in tensile strengths when compared to both the AB and 10%CR conditions with YS and UTS values of 331MPa and 430MPa, respectively. The point defects and dislocations introduced during the cold rolling process acted as nucleation sites during the application of HT1 for the random nucleation of second phase particles. Hence, it is expected that the density of second phase particles is much higher than in the 10%CR and AB conditions leading to higher tensile strengths (Ma et al., 2020a). Strain for the 10%CR+HT1 was 0.082, comparable to the AB and 10%CR Scalmalloy conditions, showing that it has recovered slightly assumed to be due to recrystallisation induced by the annealing effect and removal of residual stresses from HT1 (Rao et al., 2014). The tensile properties of the 10%CR+HT2 and 10%CR+HT3 Scalmalloy conditions were slightly lower than the 10%CR+HT1 Scalmalloy condition due to overageing. This is consistent with the optical micrographs, shown in Fig. 5.29 and 5.31.

Fig. 5.50 compares the stress-strain curves for the 30%CR, 30%CR+HT1, 30%CR+HT2 and 30%CR+HT3 conditions. The 30%CR condition showed increased tensile strengths compared to the AB condition and 10%CR condition, where Table 5-1 shows the average YS, UTS and strain as 304MPa, 415MPa and 0.046, respectively. The increase in tensile properties compared to the 10%CR condition was assumed to be the difference in cold rolling percentage 30% reduction in thickness can cause a much higher increase in dislocation density than lower reduction percentages (Ma et al., 2020a). With the increase in tensile strength, the ductility was reduced as expected likely due to the work hardening effect introduced through the cold rolling process (Kaiser et al., 2014) and although grain size was increased according to Fig. 5.47, judging by the increase in tensile properties compared to other conditions, it was assumed that point defects had been introduced into the microstructure and dislocation density had increased significantly (Malopheyev, Kulitskiy, & Kaibyshev, 2017). The 30%CR+HT1 conditions displayed further increased tensile strengths when compared to the AB condition and the 10%CR+HT1 conditions with YS, UTS and strain values of 335MPa, 465MPa and 0.0116, respectively (shown in Table 5-1). As with the tensile properties for the 10%CR+HT1 condition, the tensile properties of the 30%CR+HT1 condition has the same strengthening mechanism of increased dislocation density

and work hardening effect, while the strain is increased due to recrystallisation from heat treatment (Kaiser et al., 2014; Ma et al., 2020a, 2020b). The 30%CR+HT2 and 30%CR+HT3 tensile properties are also similar to the 10%CR+HT2 and 10%CR+HT3 conditions, as these are slightly lower than the tensile properties of 30%CR+HT1 condition, due to overageing induced by HT2 and HT3 as outlined by Fuller et al. (2003). Fig. 5.51 compares the stress-strain curves of all the Scalmalloy conditions with the largest increase being almost 40% higher than the AB condition, and where almost all conditions exceeded the maximum average tensile strength of the AB condition. This was assumed to be due to the cold rolling and heat treatment processes that induced precipitation hardening and increased dislocation density within the samples while also eliminating residual stresses as these are consistent with findings reported by Ma et al. (2020a). Cold rolled samples increased in strength, but the elongation suffered as a result of work hardening effect. Fig. E.5 in Appendix E summarises all stress strain curves for each condition, where the extruded aluminium alloys display much higher elongations, but much lower max tensile strengths. This is likely due to the Scalmalloy composition, manufacturing method, and post processing treatments that can produce superior mechanical properties compared to convention manufacturing methods.

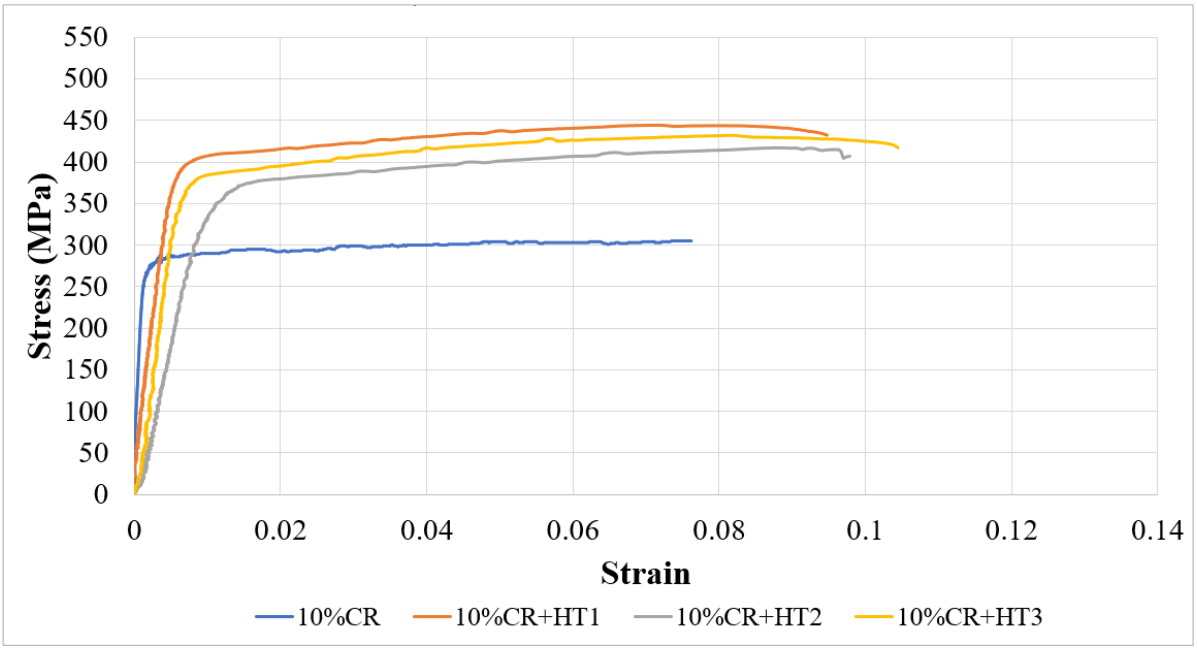

Fig. 5.49 Stress strain curves for AB conditions - a) 10%CR, b) 10%CR+HT1, c) 10%CR+HT2, d) 10%CR+HT3

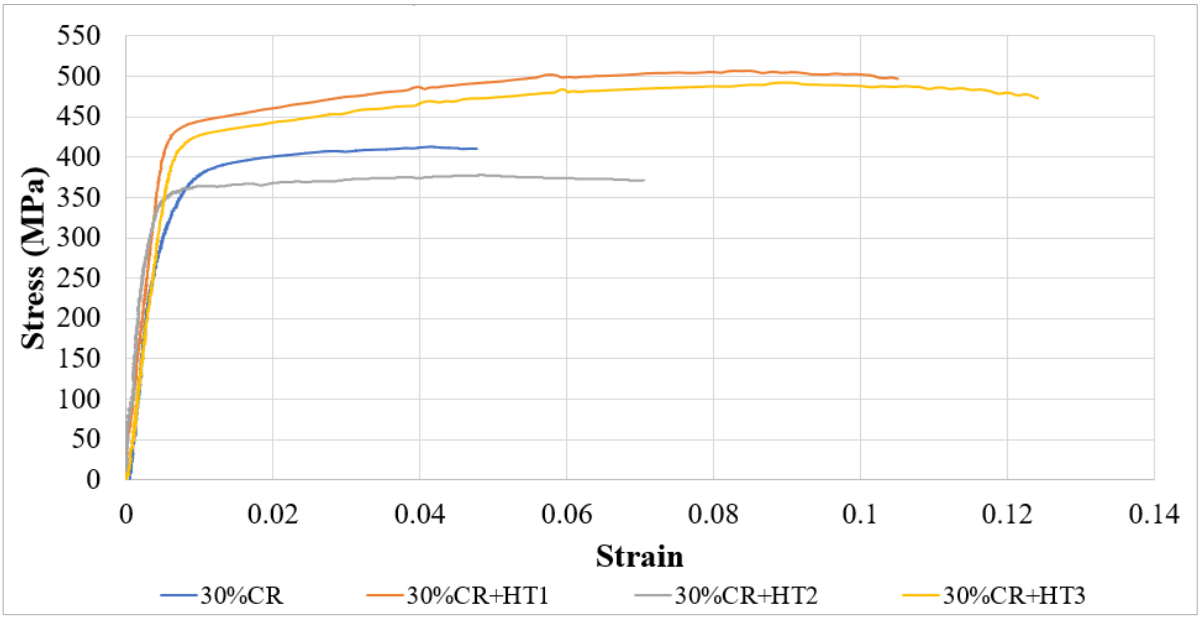

Fig. 5.50 Stress strain curves for AB conditions - a) 30%CR, b) 30%CR+HT1, c) 30%CR+HT2, d) 30%CR+HT3

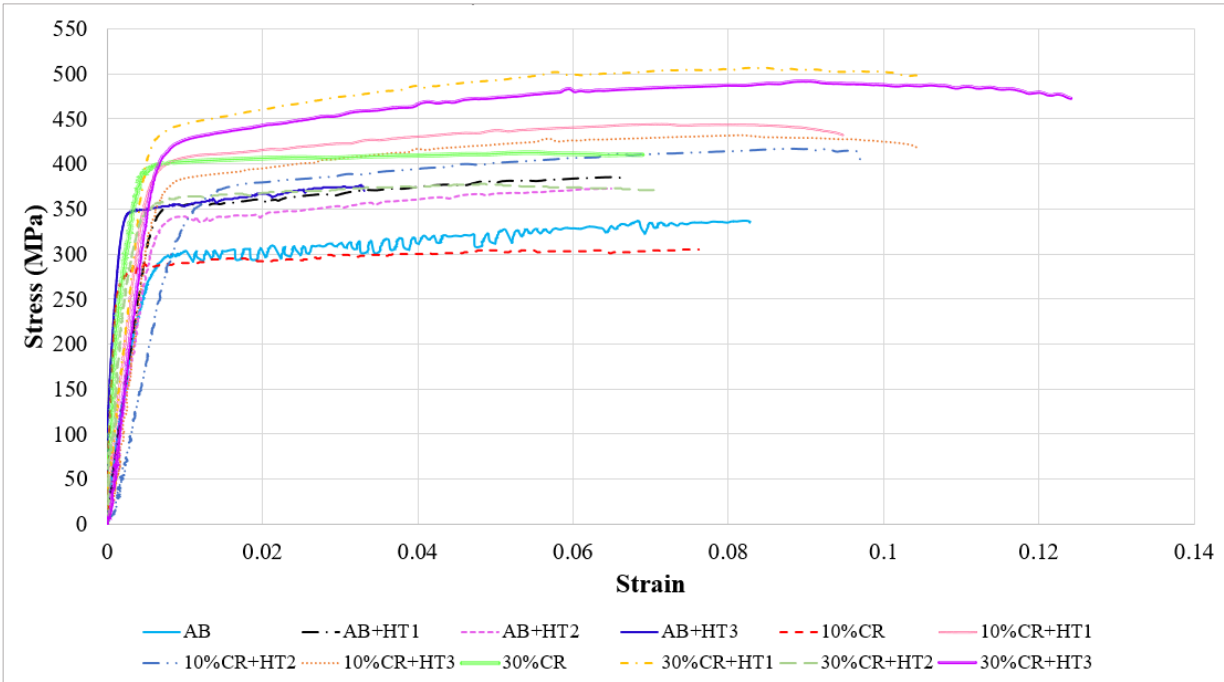

Fig. 5.51 Stress- strain curves comparing average tensile strength for all Scalmalloy conditions

Table 5-1 Tensile data for all conditions – (refer to Table 3-4 in Chapter 3 for a review of the abbreviated terms in the Table below)

Sample Condition	YS (MPa)	UTS (MPa)	Strain at Fracture	Young's Modulus (GPa)
AB	287.3	334.7	0.098	56.67
AB+ HT1	308.3	384.3	0.070	60.33
AB+HT2	285.7	356.9	0.064	60.00
AB+HT3	268.3	367.6	0.055	59.67
10% CR	285.3	321.3	0.068	64.33
10% CR +HT1	331.7	430.0	0.082	71.00
10% CR +HT2	296.7	430.4	0.091	65.33
10% CR +HT3	311.7	412.5	0.073	65.33
30% CR	304.0	410.7	0.048	86.00
30% CR +HT1	335.0	465.8	0.116	74.33
30% CR +HT2	303.5	416.3	0.086	61.50
5052Al AR	160.3	228.3	0.286	66975
5052Al 10%CR	196.0	236.7	0.177	62417
5052Al 30%CR	216.3	270.0	0.145	60043
5083Al AR	231.7	333.7	0.183	68314
5083Al 10%CR	278.3	343.0	0.196	60659
5083Al 30%CR	318.3	364.3	0.098	72673

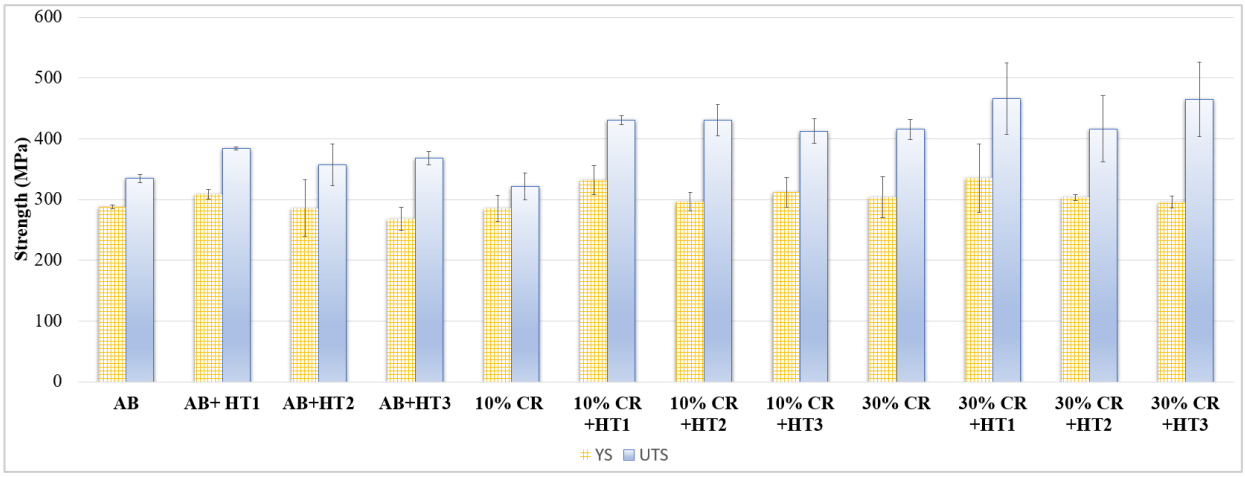

Fig. 5.52 Average yield and tensile strengths for all Scalmalloy conditions

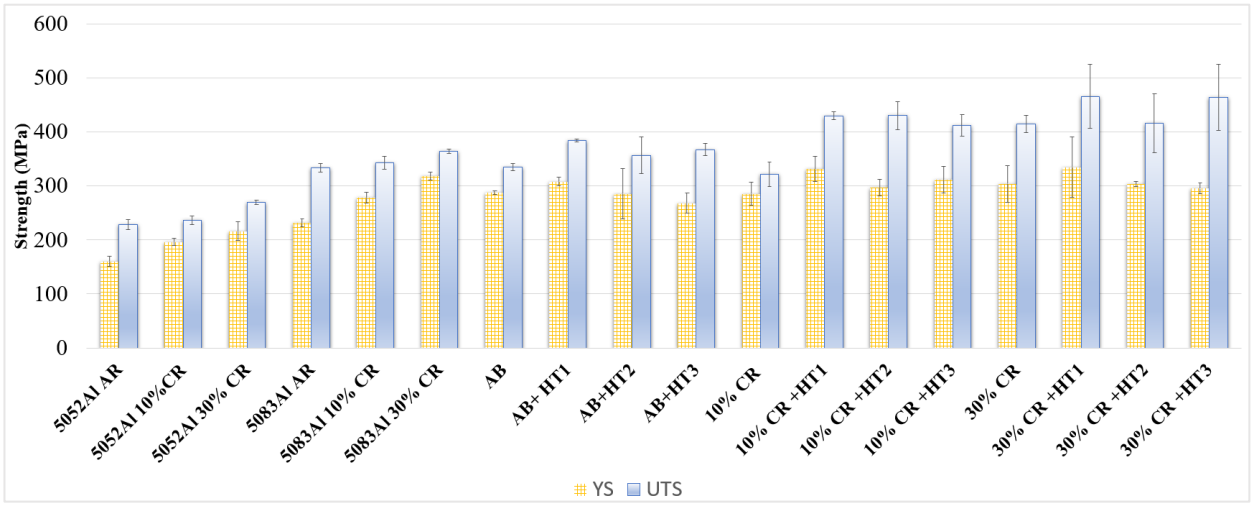

Fig. 5.53 Average yield and tensile strengths for all conditions

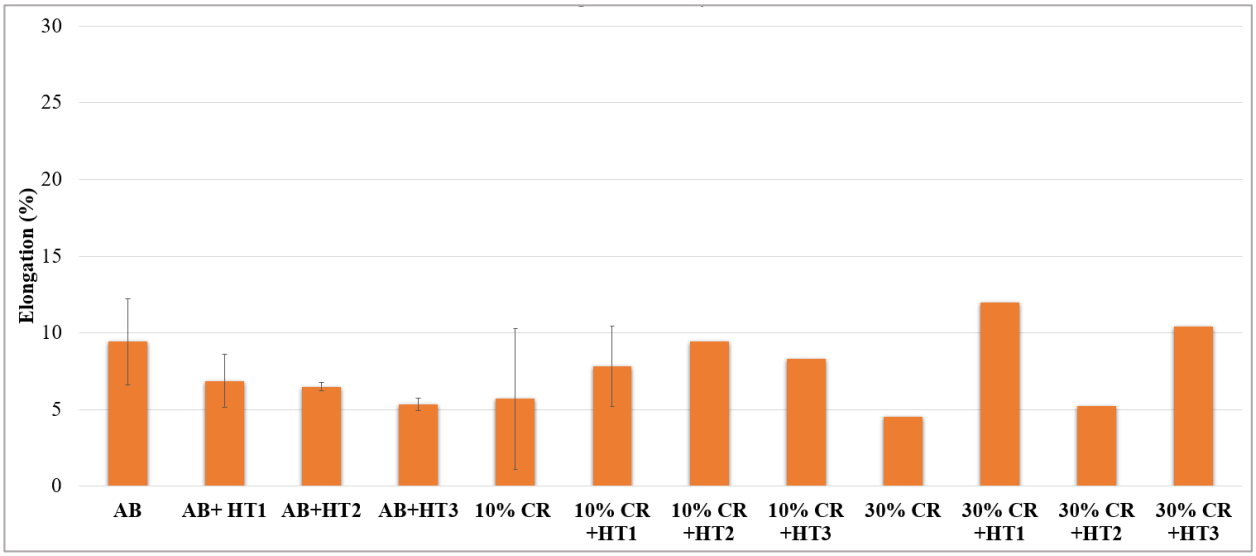

Fig. 5.54 Average elongation values for all Scalmalloy conditions

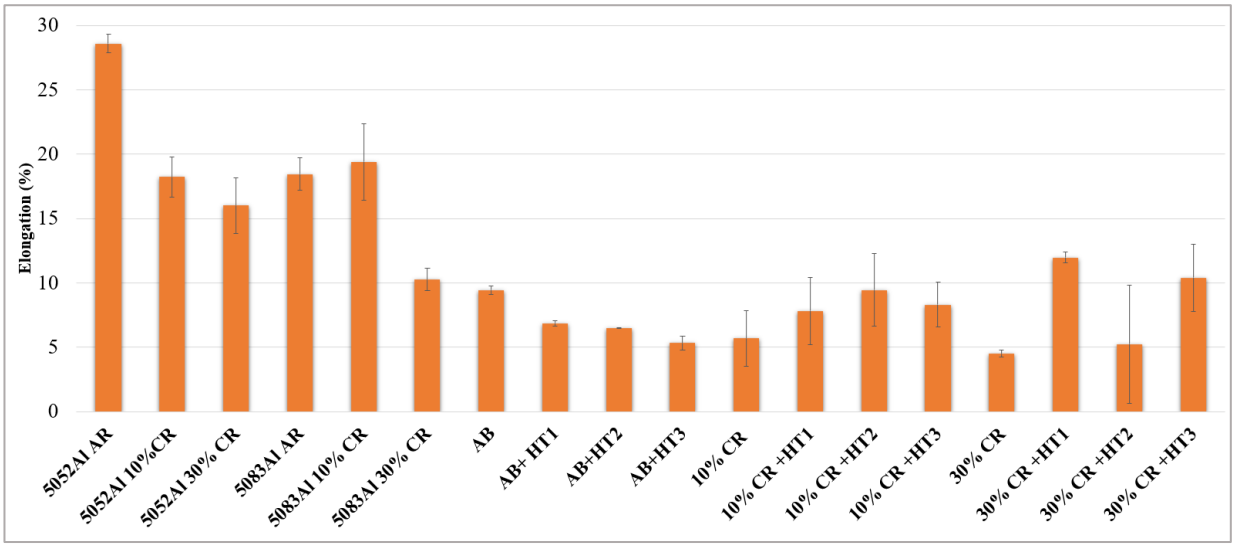

Fig. 5.55 Average elongation values for all conditions

5.3 Strain distribution through digital image correlation

Fig. 5.57 shows the strain distribution during tensile testing using digital image correlation (DIC) of the 5052Al in the AR, 10%CR, and 30%CR conditions. The average highest local strain occurred in the AB sample and lower values occur in the cold rolled condition due to the plastic deformation where the strength has been increased at the expense of strain. This is a typical reaction and findings for extruded aluminium alloys according to (Ashkenazi, 2019; Santos Junior et al., 2016)

Fig. 5.58 - 5.60 show the strain distribution during tensile testing of each Scalmalloy condition. The various colours on the samples correspond to the amount of strain given on the scale on the right of the figures. For the AB and AB+HT samples shown in Fig. 5.58, no obvious necking is visible indicating low ductility. The average highest local strains for the AB, AB+HT1, AB+HT2 and AB+HT3 conditions were 25%, 8.1%, 7.5% and 7.4%, respectively. As the tensile strength increased, assumed to be due to precipitation hardening occurring during heat treatment as reported by A. B. Spierings, Dawson, Dumitraschkewitz, et al. (2018), ductility decreased. Hence, the AB+HT conditions had lower local strains compared to the AB condition. The highest strains were also recorded in the reduced section of the tensile samples consistent with the fracture locations. Fig 5.59 shows the 10%CR, 10%CR+HT1, 10%CR+HT2 and 10%CR+HT3 conditions with highest average local strains of 16%, 13%, 9.5% and 8.5%. Fig. 5.60 show the 30%CR, 30%CR+HT1, 30%CR+HT2 and 30%CR+HT3 conditions with highest average local strains of 60%, 15.5%, 10% and 15.5%, respectively. These also show very slight necking.These local strains are likely due to the work hardening effect and increase in dislocation density, as is common in alloys that undergo plastic deformation and heat treatment (Ma et al., 2020a; C Turangi et al., 2022; B. Wang et al., 2015) as they are all slighlty lower than the AB condition. Unlike the other conditions, the 30%CR condition shows a high local strain before fracture thought to be due to the elongated even grain size and a denser structure (less pores) due to cold rolling (Ning, Liu, & Zeng, 2006; Pasang et al., 2021).

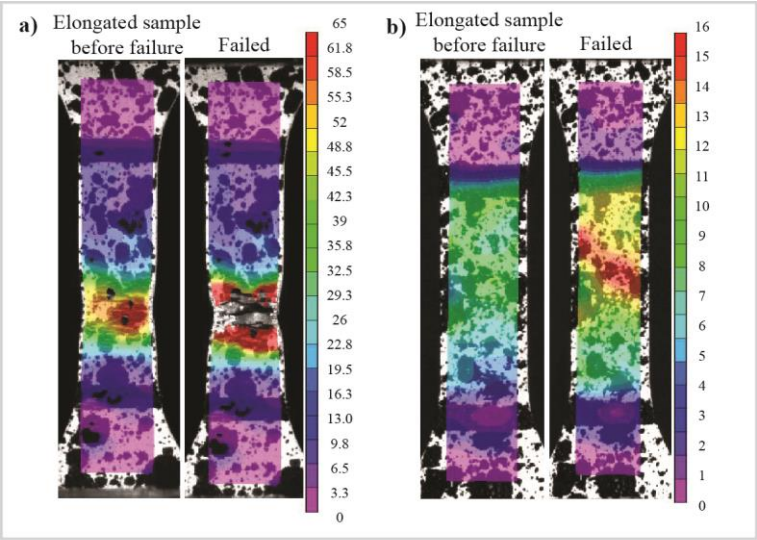

Fig. 5.56 Digital image correlation images for all conditions - a) 5052Al AR, b)5052Al 10%CR

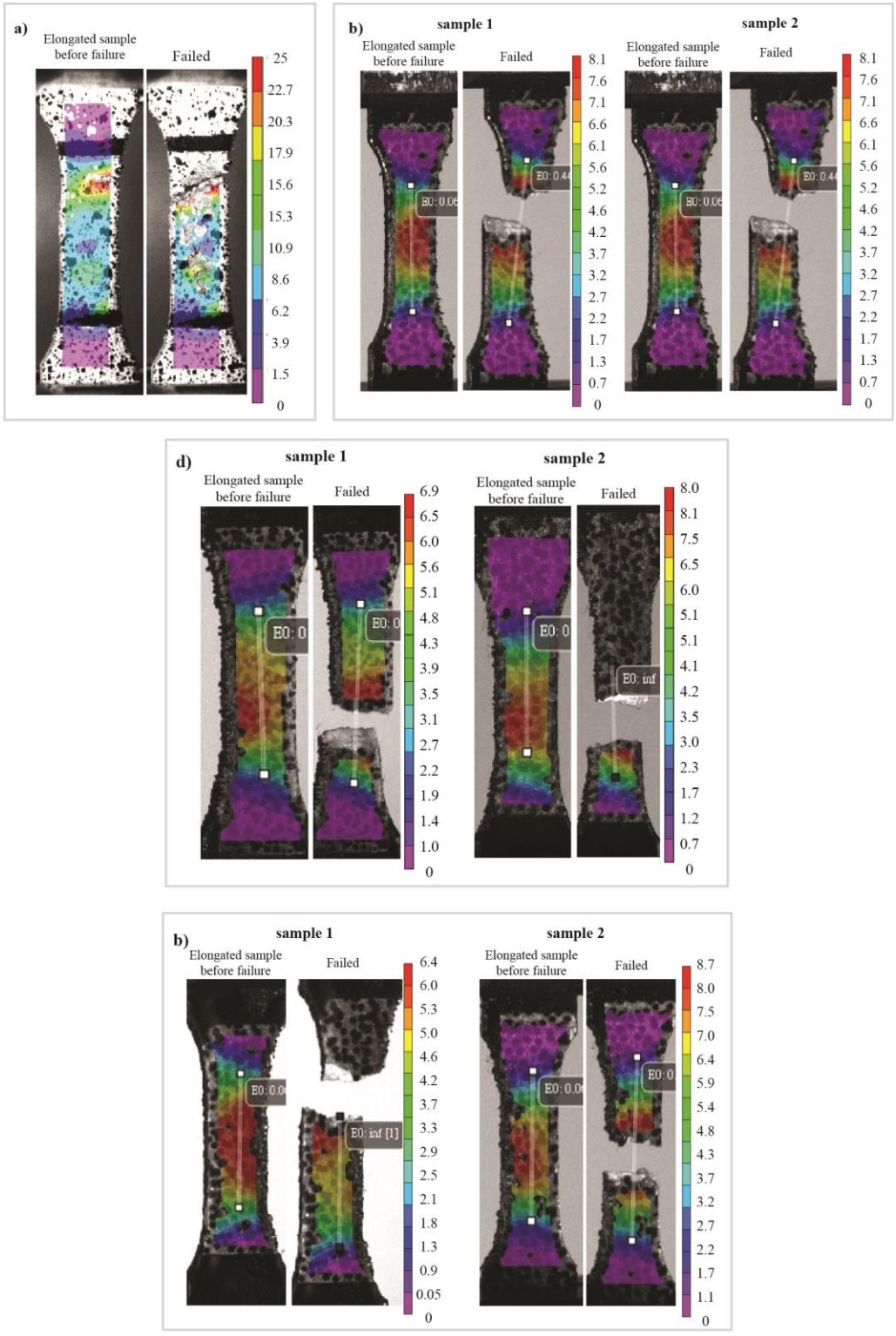

Fig. 5.57 Digital image correlation images for all conditions - a)AB, b) AB+HT1, c) AB+HT2, d) AB+HT3

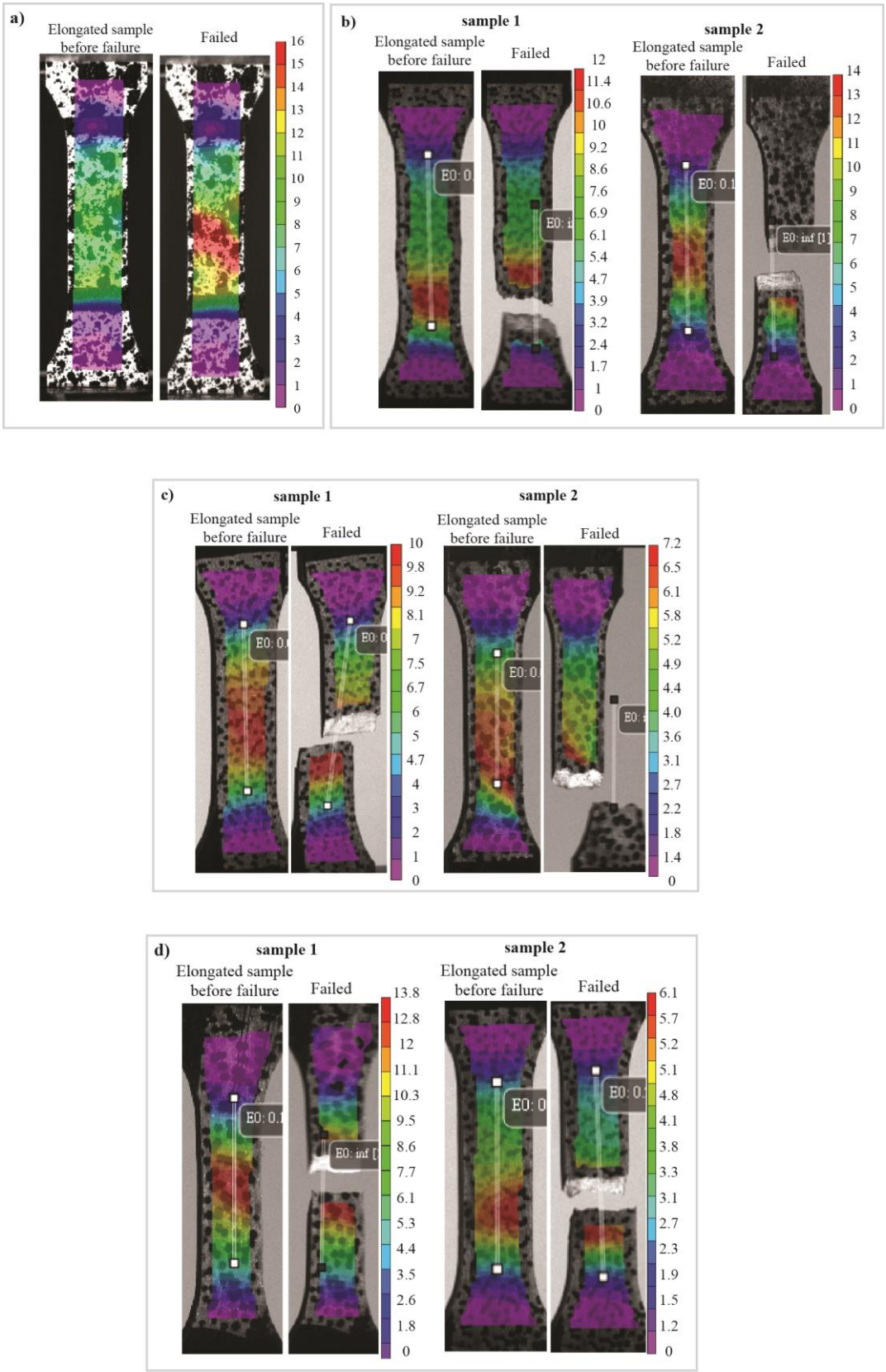

Fig. 5.58 Digital image correlation images for all conditions - a) 10%CR, b) 10%CR+HT1, c) 10%CR+HT2, d) 10%CR+HT3

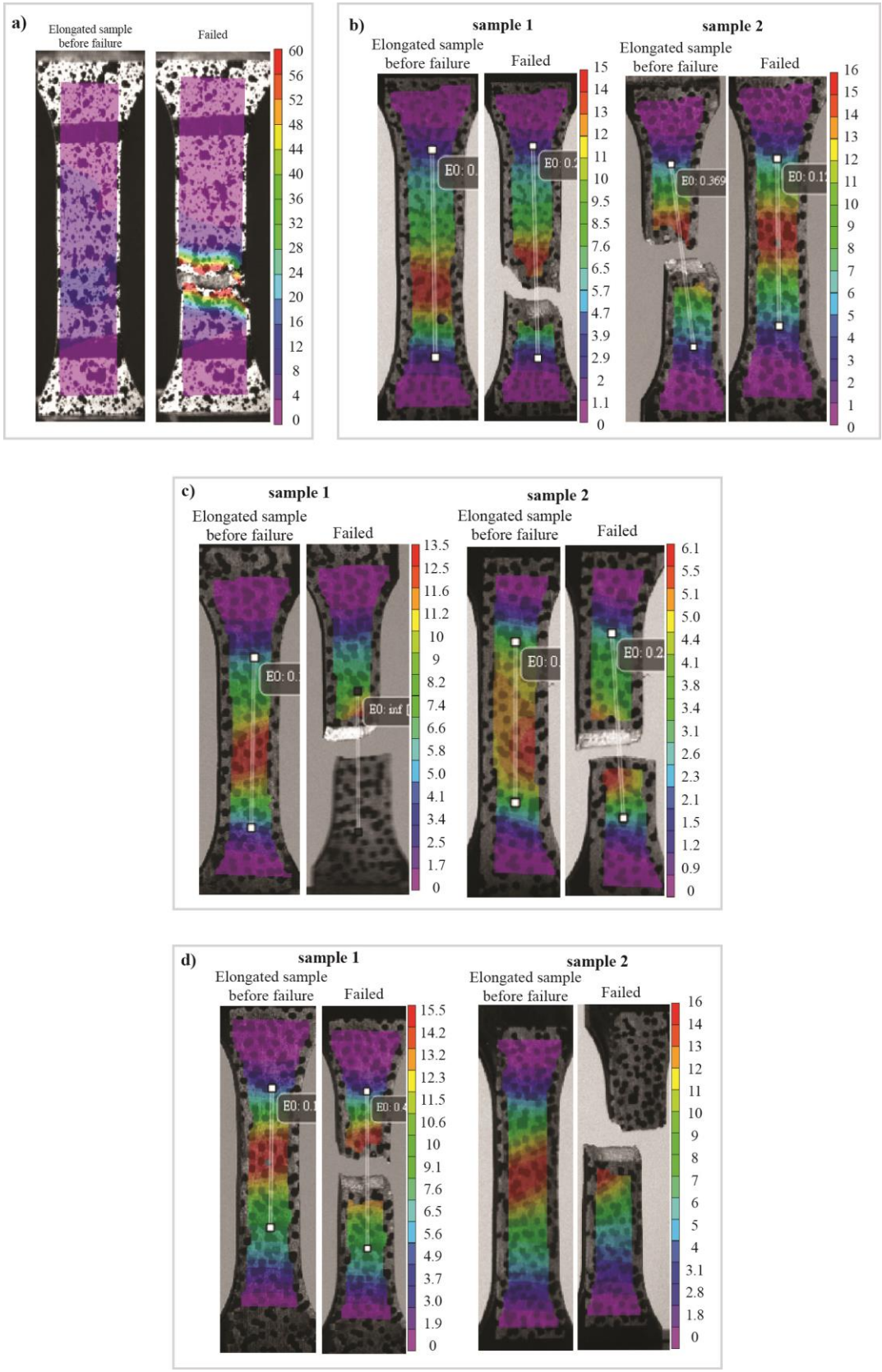

Fig. 5.59 Digital image correlation images for all conditions - a) 30%CR, b) 30%CR+HT1, c) 30%CR+HT2, d) 30%CR+HT3

5.4 Hardness Properties

Vickers hardness results for all Scalmalloy conditions in the horizontal, longitudinal, and transverse planes are given in Fig. 5.61. Fig. 5.62 shows the hardness results of all conditions, where the extruded aluminium alloys show much lower hardness results when compared to Scalmalloy due to the Scalmalloy composition, manufacturing method, and post processing treatments. The hardness values in the AB condition are consistent with findings reported by literature as the fine grain microstructure gives rise to its high hardness (R. Li et al., 2019; Adriaan B. Spierings et al., 2016). The hardness value of the AB+HT1 condition increased by a range of 40% compared to the AB condition. Subsequent ageing of the AB+HT2 and AB+HT3 conditions has resulted in slightly lower values than the AB+HT1 condition, but higher values than the AB condition by 13% to 15%. The 10%CR condition shows higher hardness values than the AB condition and the 10%CR+HT1 shows much higher values than the 10%CR condition with an increase of 23%. The 10%CR+HT2 and the 10%CR+HT3 conditions showed slightly lower hardness values compared to the 10%CR+HT1 condition, yet still higher than the AB condition. The 30%CR condition showed higher hardness values than the AB condition by about 24% similar to the 10%CR condition. Likewise, the 30%CR+HT1 showed much higher values than the AB condition by 40%. The remaining conditions showed slightly lower hardness values compared to the 30%CR+HT1 condition but remained higher than the AB condition. The AB condition compared to the 10%CR and 30%CR condition has shown an increase of approximately 12% and 24%, respectively. As cold rolling is applied, the dislocation density was increased through work hardening of the material by plastic deformation.

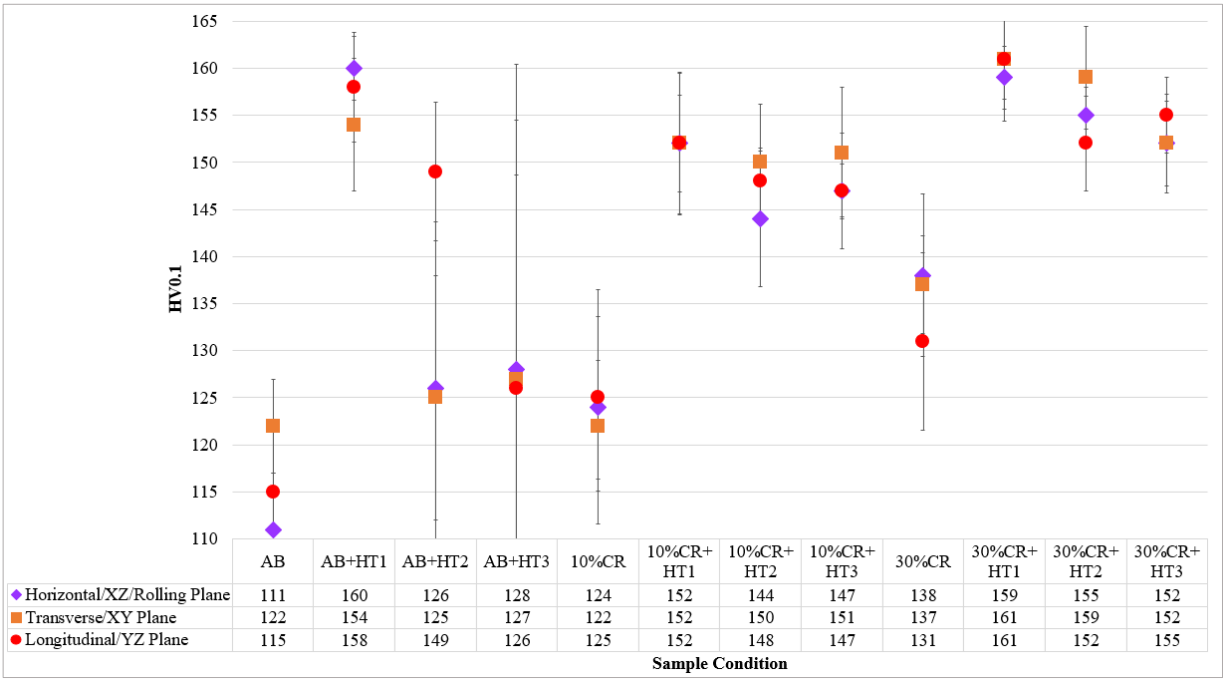

	AB	AB+HT1	AB+HT2	AB+HT3	10%CR	10%CR+ HT1	10%CR+ HT2	10%CR+ HT3	30%CR	30%CR+ HT1	30%CR+ HT2	30%CR+ HT3
Horizontal/XZ/Rolling Plane	111	160	126	128	124	152	144	147	138	159	155	152
Transverse/XY Plane	122	154	125	127	122	152	150	151	137	161	159	152
Longitudinal/YZ Plane	115	158	149	126	125	152	148	147	131	161	152	155

Fig. 5.60 Vickers Hardness results for all conditions showing standard deviations in the horizontal, longitudinal, and transverse planes

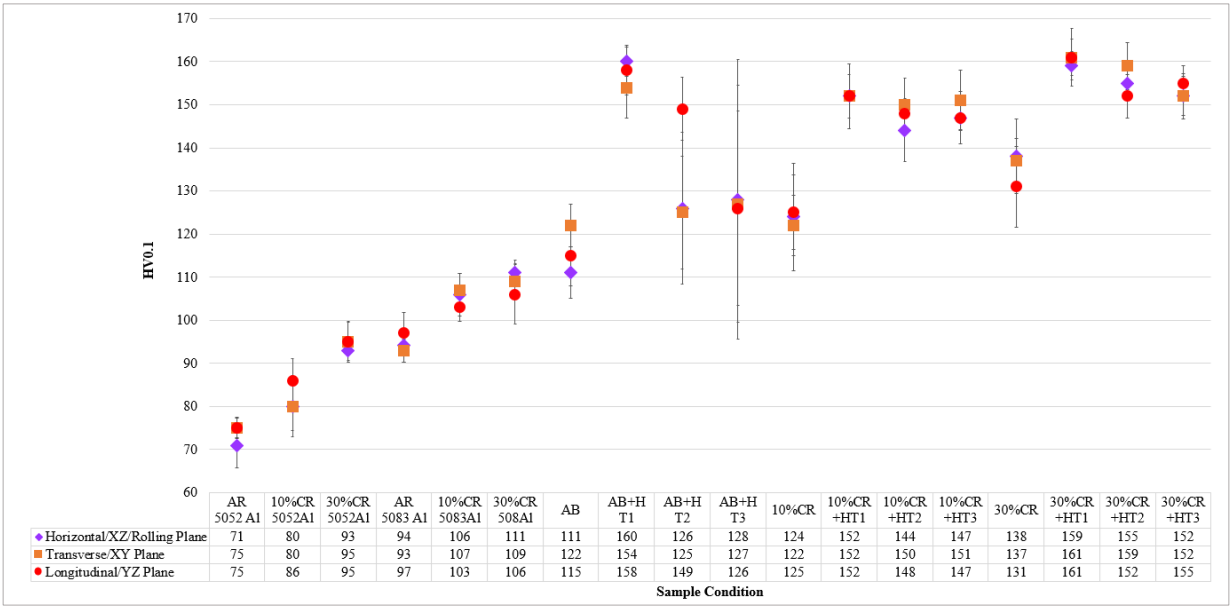

	AR 5052 A1	10%CR 5052A1	30%CR 5052A1	AR 5083 A1	10%CR 5083A1	30%CR 508A1	AB	AB+HT1	AB+HT2	AB+HT3	10%CR	10%CR +HT1	10%CR +HT2	10%CR +HT3	30%CR	30%CR +HT1	30%CR +HT2	30%CR +HT3
Horizontal/XZ/Rolling Plane	71	80	93	94	106	111	111	160	126	128	124	152	144	147	138	159	155	152
Transverse/XY Plane	75	80	95	93	107	109	122	154	125	127	122	152	150	151	137	161	159	152
Longitudinal/YZ Plane	75	86	95	97	103	106	115	158	149	126	125	152	148	147	131	161	152	155

Fig. 5.61 Vickers Hardness results for all conditions showing standard deviations in the horizontal, longitudinal, and transverse planes

As the cold rolling reduction is increased, dislocation density is increased causing the progressive increase of hardness for Scalmalloy (Ma et al., 2020a; B. Wang et al., 2015; T. Wang et al., 2021) The AB+HT1, 10%CR+HT1 and 30%CR+HT1 conditions have much higher hardness values than their non heat treated (and non-cold rolled) conditions (e.g., AB, 10%CR, 30%CR) due to the precipitation of tiny coherent Al_3(Sc, Zr) particles from the Al supersaturated solid solution after heat treatment. Although according to Jostein Røyset and Nils Ryum (2005) and A. B. Spierings, Dawson, Kern, et al. (2017), the maximal hardness were achieved at temperatures between 375ºC to 400ºC. The higher temperature limit of HT1 (450ºC/1h), compared to the lower temperature range of 375ºC to 400ºC might be due to the slightly less Mg content compared to A. B. Spierings, Dawson, Kern, et al. (2017) where there is higher solubility of scandium. Additionally, suppression of Al_3 (Sc, Zr) particles was achieved during the SLM process to allow heat treatment to have a greater effect. When the AB+HT1 condition is compared to the AB+HT2 and AB+HT3 conditions, there is either a plateau in hardness or a steady decline. Likewise, this trend occurs for the 10%CR+HT1 condition when compared to the 10%CR+HT2 and 10%CR+HT3 conditions and when the 30%CR+HT1 is compared to the 30%CR+HT2 and 30%CR+HT3 conditions. This plateau and decline in hardness are evident of overageing where particle growth has occurred. This is assumed to be due to Ostwald ripening leading to the slight loss of coherency of the earlier precipitated Al_3(Sc, Zr) particles as reported by and A. B. Spierings, Dawson, Heeling, et al. (2017) (R. Li et al., 2019; A. B. Spierings, Dawson, Kern, et al., 2017). Nevertheless, each condition compared to the AB condition has higher hardness values. Cold rolling, heat treatment and a combination of these has resulted in the improvement of hardness since dislocation density is increased by cold rolling and heat treatment causes precipitation hardening within the material. A combination of these further increases the material's hardness.

Additionally, the surface roughness of each condition was measured as new heat treatments and cold rolling processes were used. It was found that the surface roughness of the CR Scalmalloy samples was significantly lower than the AB and AB+HT conditions and comparable to the extruded aluminium alloys' surface roughness. This was expected as cold rolling processes are known to significantly smooth the surfaces of metals as reported by Jeng, Lee, Hwu, Liu, and Lu (2020). Additionally, the surface roughness measured on the AB condition of Scalmalloy was comparable to those reported in the literature (Koutny et al., 2018; Strano et al., 2013) . A more detailed explanation for surface roughness is given in Appendix F for further information.

5.5 Fracture analysis

Fig. 5.63 shows the fractured surfaces and photographs of fractured tensile samples for the 5052Al alloys in the AR, 10%CR, and 30%CR conditions. Similarly, Fig. 5.64 shows the fractured surfaces and photographs of the fractured tensile samples for the 5083Al alloys in the AR, 10%CR, and 30%CR conditions. The 5052Al tensile samples all fractured in the narrowest part of the tensile specimen and showed numerous dimples evenly distributed on the entire fracture surface, shown in Fig, 5.63, indicative of a very ductile fracture that is consistent with the tensile results recorded in Table 5-1. Fig. 5.64 shows that some tensile samples have fractured at 45^{o} angles due to the shear strain induced by the tensile load. The 5083Al conditions are also not as ductile as the 5052Al condition as they show slightly less deformation than the 5052Al alloy. However, dimples are evenly distributed over the entire surface where a ductile fracture has occurred. These findings are typical of the extruded 5000 series alloy as they possess medium strength and high elongation.

Fig. 5.65 - 5.67 show the fractured tensile specimens for each Scalmalloy condition. Some samples showed a fracture at 45^{o} due to the shear stress that occurred during maximum tensile load with a very slight reduction in area resulting in a ductile fracture mechanism. Other samples showed an uneven or generally flat fracture surface indicative of a less ductile fracture mode and also could be due to defects such as cracking and gas porosity. It must also be noted that fracture locations occurred in the reduced area sections as expected.

Fig. 5.68 - 5.79 show the fracture surfaces of all sample conditions. They are predominantly covered with dimples, pores, and inclusions distributed evenly throughout the surface along with some cleavage facets and flat areas. The visible pores are consistent with the inherent porous microstructure of additively manufactured components, especially the presence of microporosities which agrees with findings reported by DebRoy et al. (2018). Some larger spherical pores and irregular shaped pores are consistent with the gas porosity and lack of fusion identified earlier in the optical micrographs. Additionally, the dimple structure of each sample varied dependent on the area being observed which are characteristic of the ductile behaviour of aluminium alloys (Musekamp et al., 2021).

The fracture surface of the AB condition shown in Fig. 5.68 shows fine porosity and a large number of spherical pores evenly distributed among the surface consistent with the gas porosity and microporosity identified in Fig 5.5. These tend to favour crack formation caused by local stress concentrations originating from the porosity. A mixture of tearing edges, some cleavage planes and dimpled areas denote a local ductile fracture mode (R. Li et al., 2019). This is in line with the reasonable strength and ductility reported in Table 5-1. The fracture surfaces of the 10%CR and 30%CR Scalmalloy conditions are shown in Fig. 5.72 and Fig. 5.76, respectively. These conditions possessed the lowest overall strain, a result of the work hardening effect induced by cold rolling. The fracture surface of these samples consisted of flat surfaces, striations and visible cleavage planes and facets. Dimples are also visible, so it has a ductile fracture mechanism, however, it is not as ductile as the other conditions (Ma et al., 2020a).

The AB+HT1 condition (Fig. 5.69) showed a dimple covered fracture surface with a dimple size range between 3µm to 5µm and visible cleavage facets showing a local ductile fracture (Schmidtke et al., 2011). The AB+HT2 (Fig. 5.70) and AB+HT3 (Fig. 5.71) conditions showed similar fracture characteristics as the AB+HT1 condition, which agrees with the similar tensile properties reported in Table 5-1. The 10%CR+HT1 condition, shown in Fig. 5.73, displays a ductile fracture mode evident by the many small evenly distributed dimples on the surface. Similarly, the 10%CR+HT2 and 10%CR+HT3 conditions display the same characteristics as the 10%CR condition indicative by the similar tensile properties (Table 5-1) and fracture micrographs shown in Fig. 5.74 and 5.75, respectively. The 30%CR+HT1 condition shown in Fig. 5.77 shows a dimple covered surface and microporosities with sizes between 1-5µm indicative of a ductile fracture. The 30%CR+HT2 and 30%CR+HT3 (shown in Fig. 5.78 and 5.79, respectively) conditions show similar features and fracture characteristics as the 30%CR+HT1 condition. The increased ductility of the heat-treated conditions compared to the non-heat-treated conditions was a result of the heat treatment removing residual stresses and allowing the material elastic recovery process. It also allows the microstructure to be more homogenous with uniform grains, hence, a more ductile material was produced but retained the high strength from the high dislocation density induced by cold rolling (Ma et al., 2020a, 2020b). It is also worth noting that the fracture modes of each condition are consistent with findings reported by various authors (Cui et al., 2022; R. Li et al., 2019; Musekamp et al., 2021; A. B. Spierings, Dawson, Heeling, et al., 2017). Please note that additional fracture micrographs of each sample are provided in Fig. G.1 – G.7 in Appendix G.

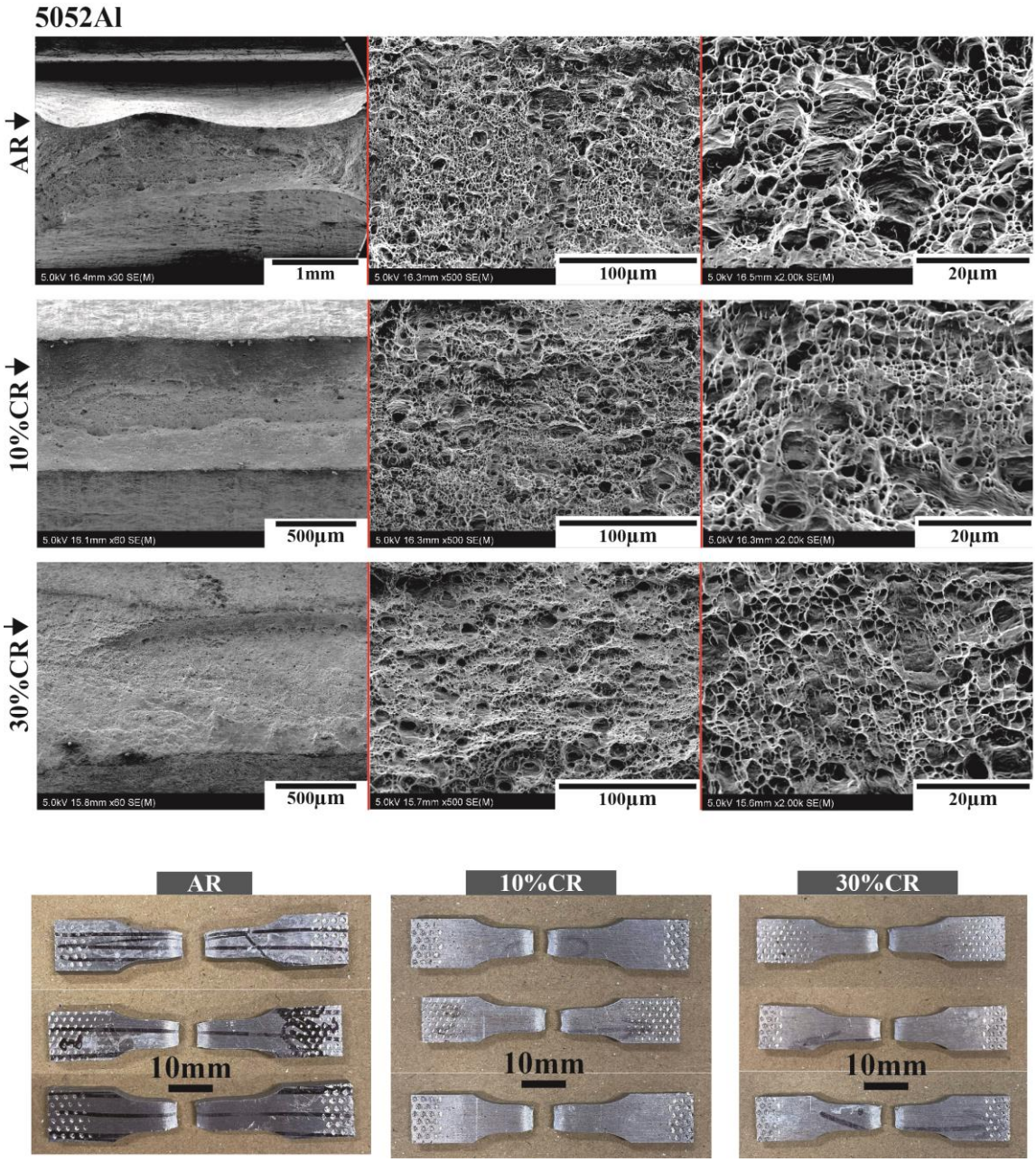

Fig. 5.62 SEM micrographs of the fracture microstructure for AR, 10%CR, and 30%CR 5052Al and photographs of the fractured tensile samples

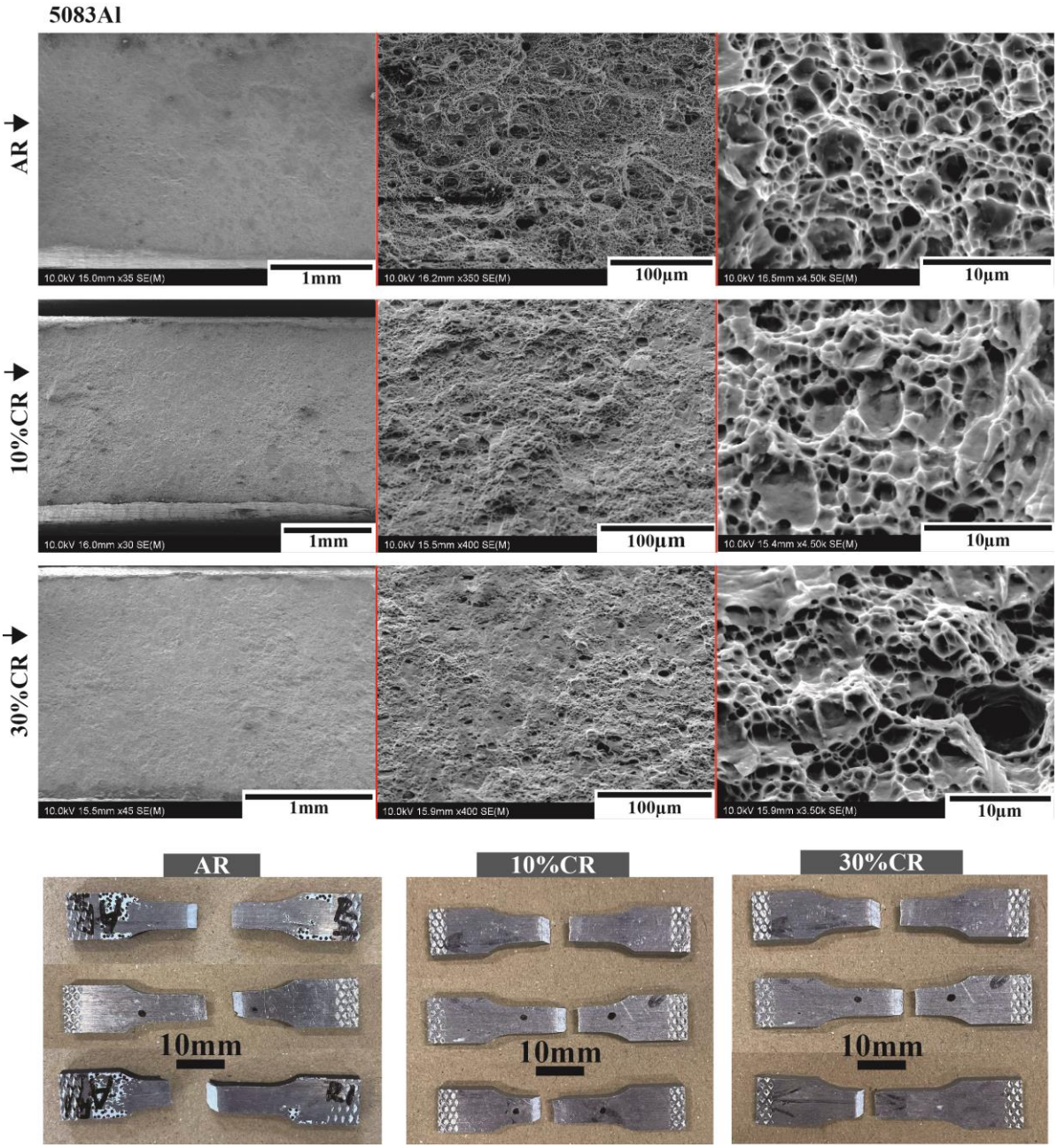

Fig. 5.63 SEM micrographs of the fracture microstructure for AR, 10%CR, and 30%CR 5083Al and photographs of the fractured tensile samples

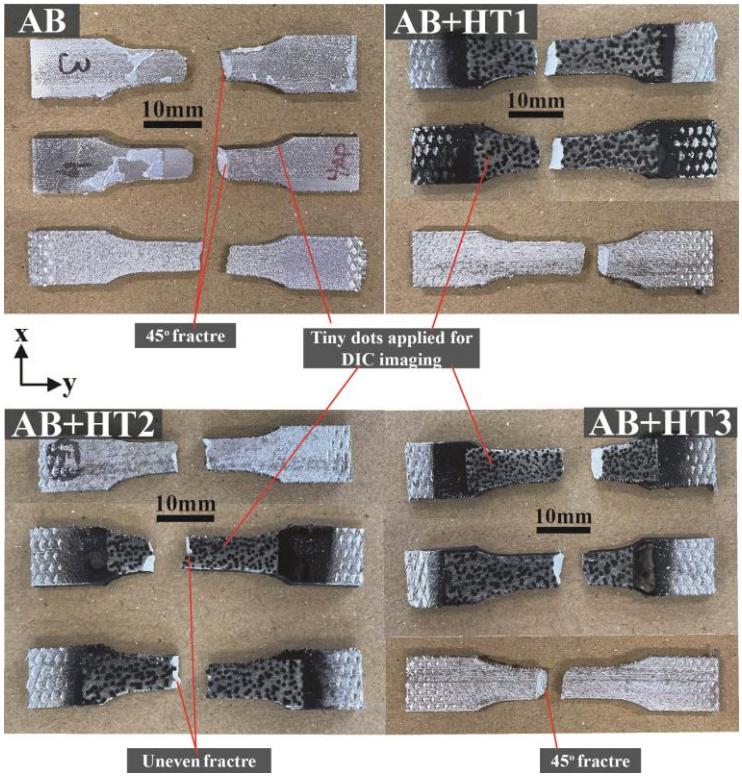

Fig. 5.64 Photograph of fractured tensile specimens for the AB, AB+HT1, AB+HT2 and AB+HT3 conditions

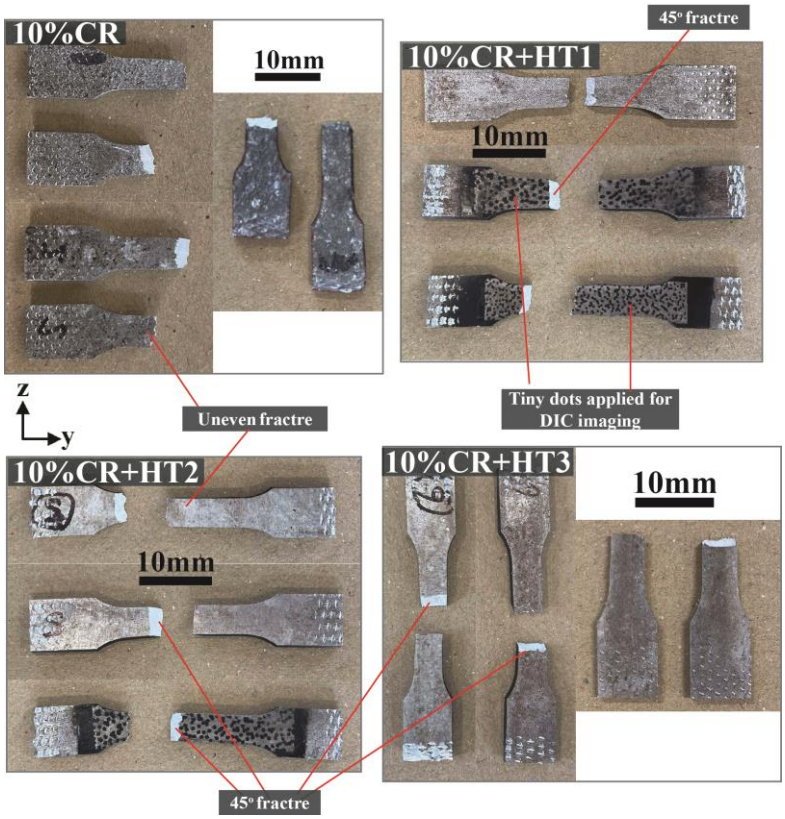

Fig. 5.65 Photograph of fractured tensile specimens for the 10%CR, 10%CR+HT1, 10%CR+HT2 and 10%CR+HT3 conditions

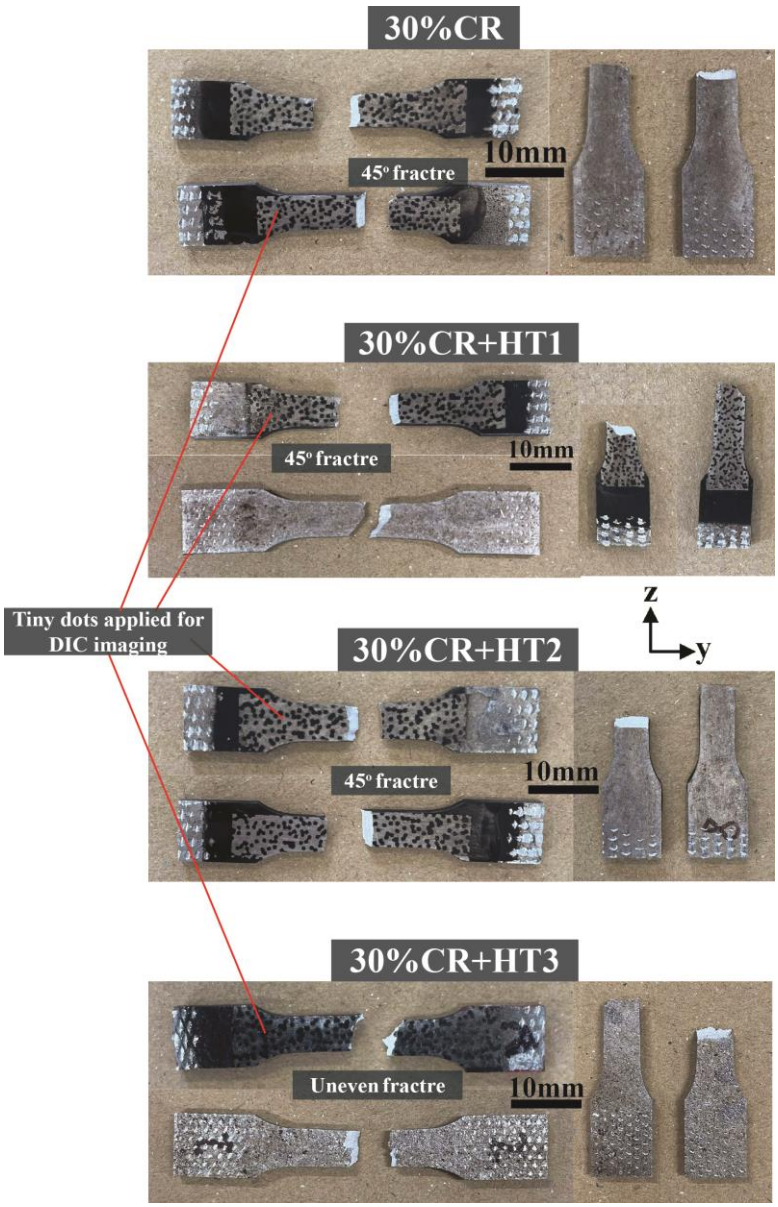

Fig. 5.66 Photograph of fractured tensile specimens for the 30%CR, 30%CR+HT1, 30%CR+HT2 and 30%CR+HT3 conditions

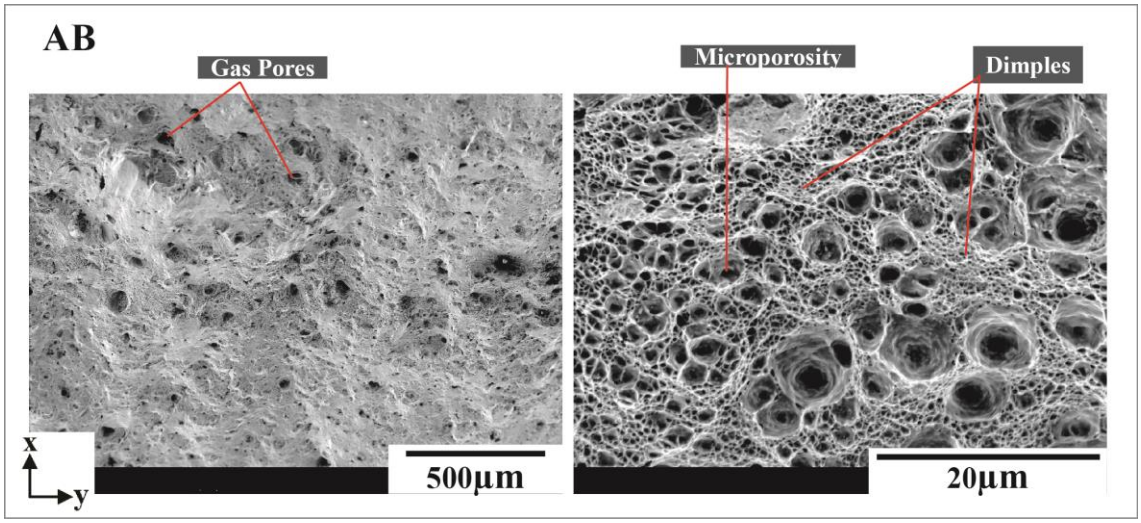

Fig. 5.67 SEM micrographs of the fracture surface for the AB condition

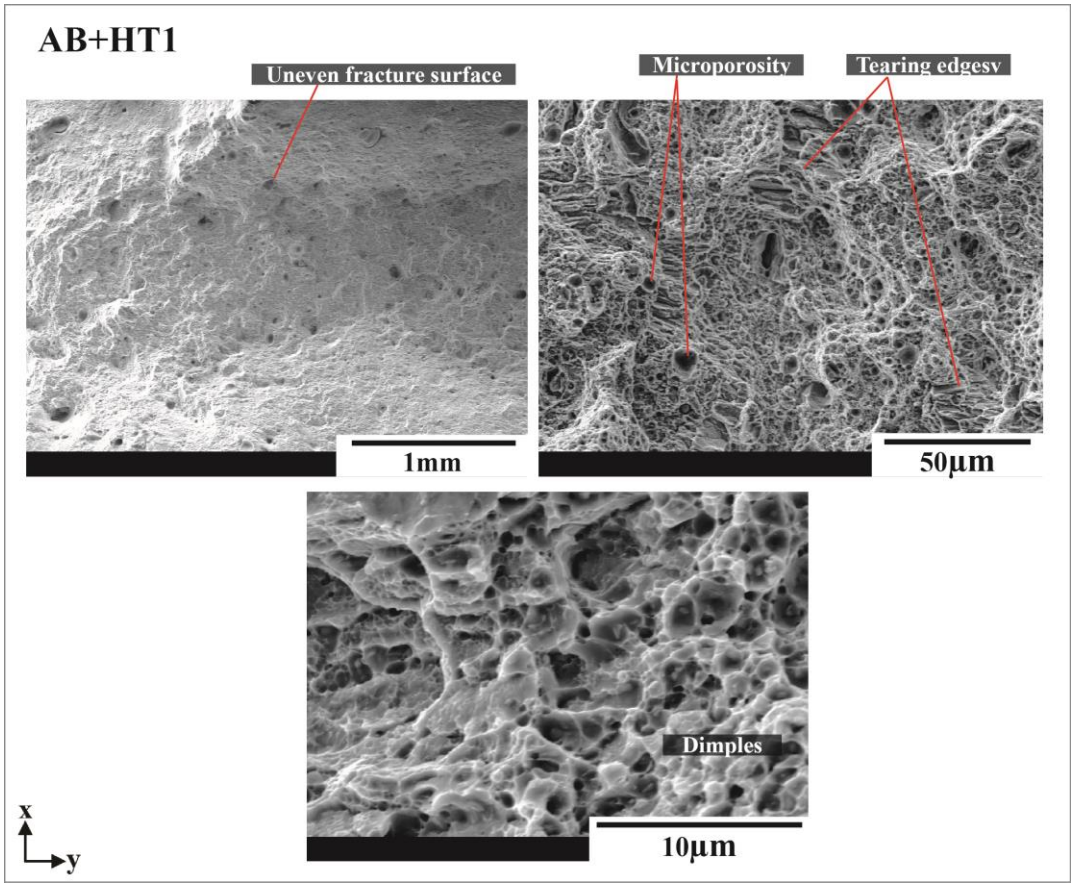

Fig. 5.68 SEM micrographs of the fracture surface for the AB+HT1 condition

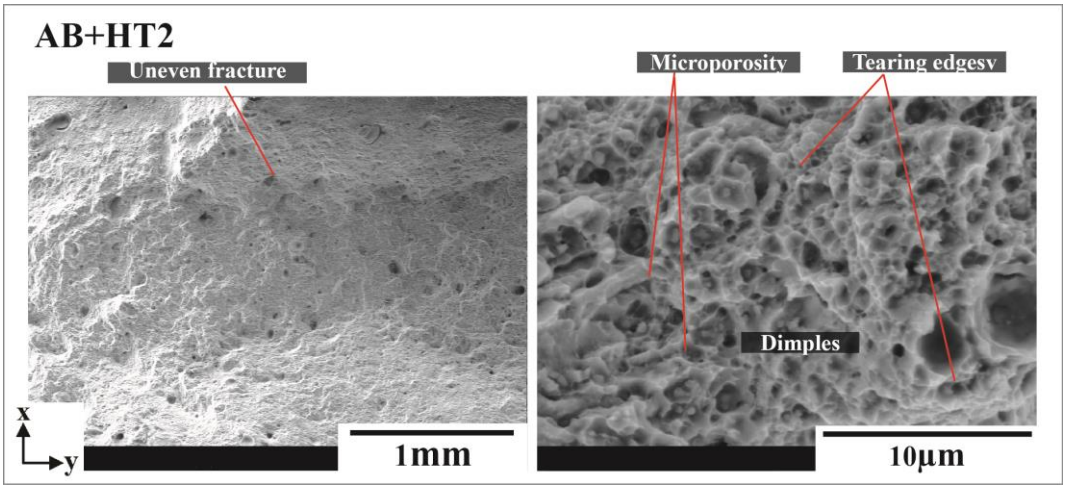

Fig. 5.69 SEM micrographs of the fracture surface for the AB+HT2 condition

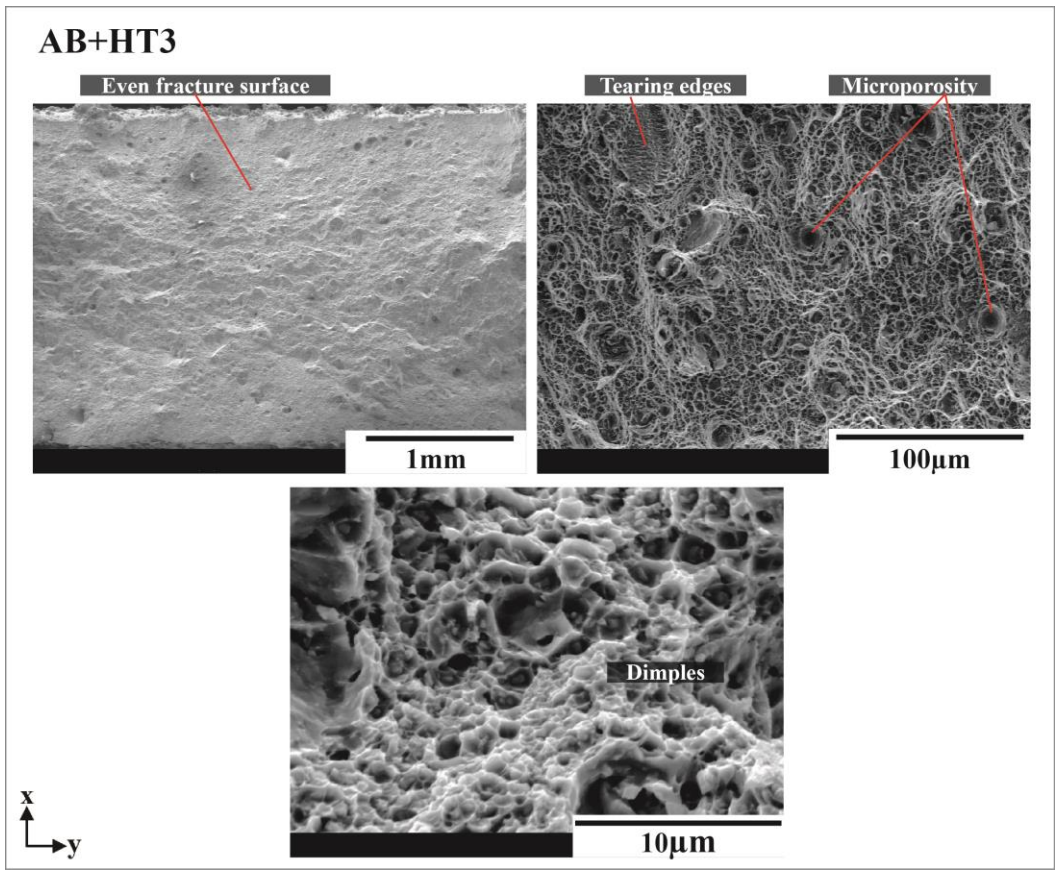

Fig. 5.70 SEM micrographs of the fracture surface for the AB+HT3 condition

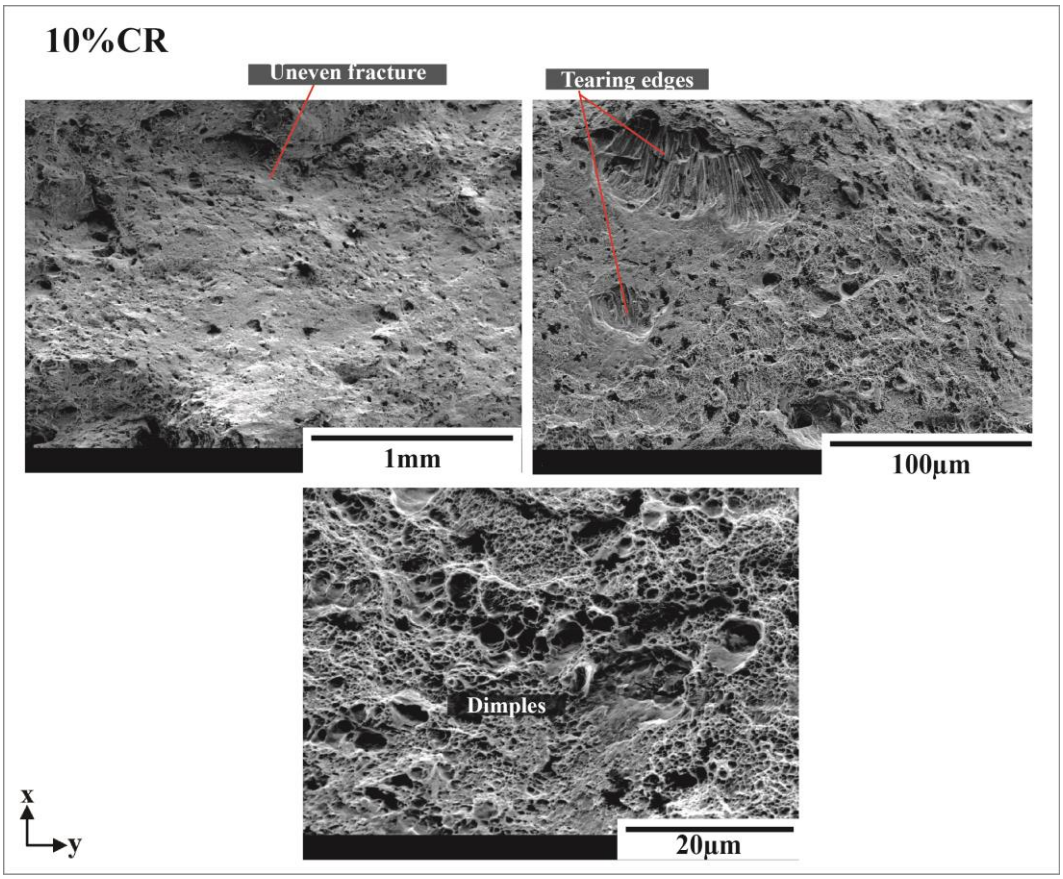

Fig. 5.71 SEM micrographs of the fracture surface for the 10% CR condition

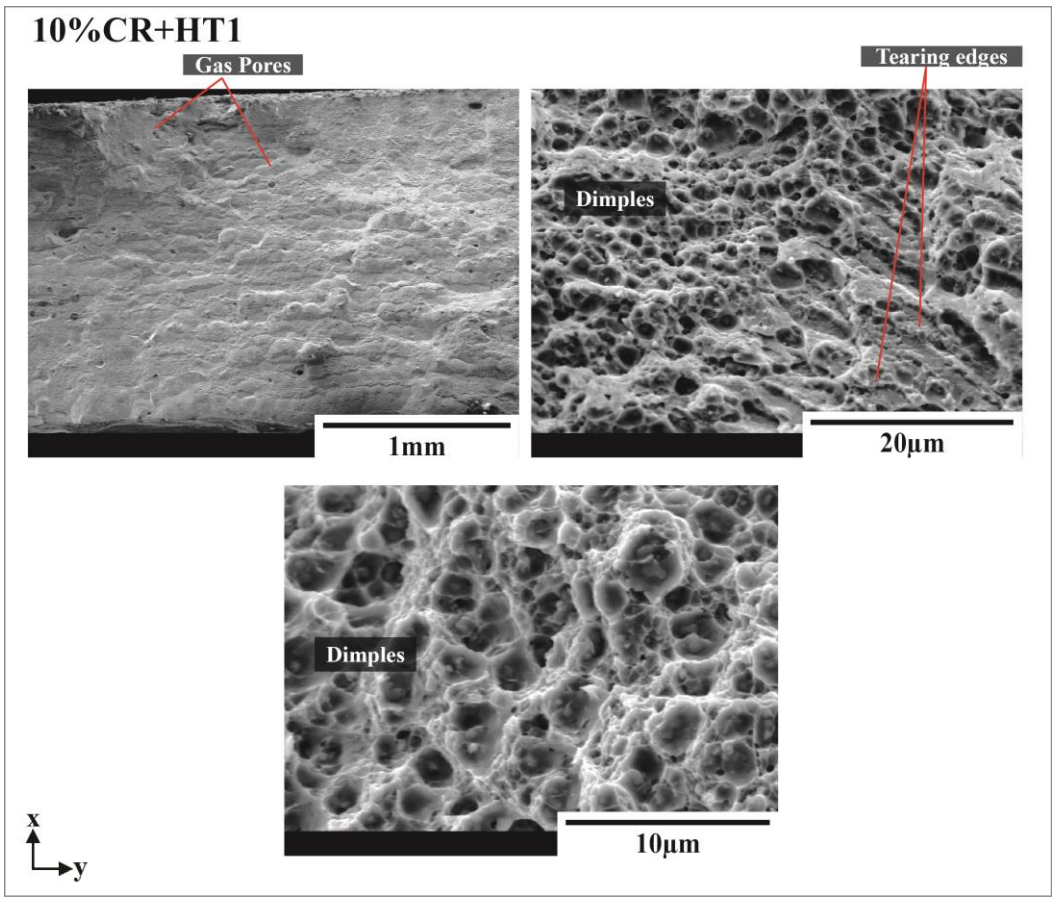

Fig. 5.72 SEM micrographs of the fracture surface for the 10%CR+HT1 condition

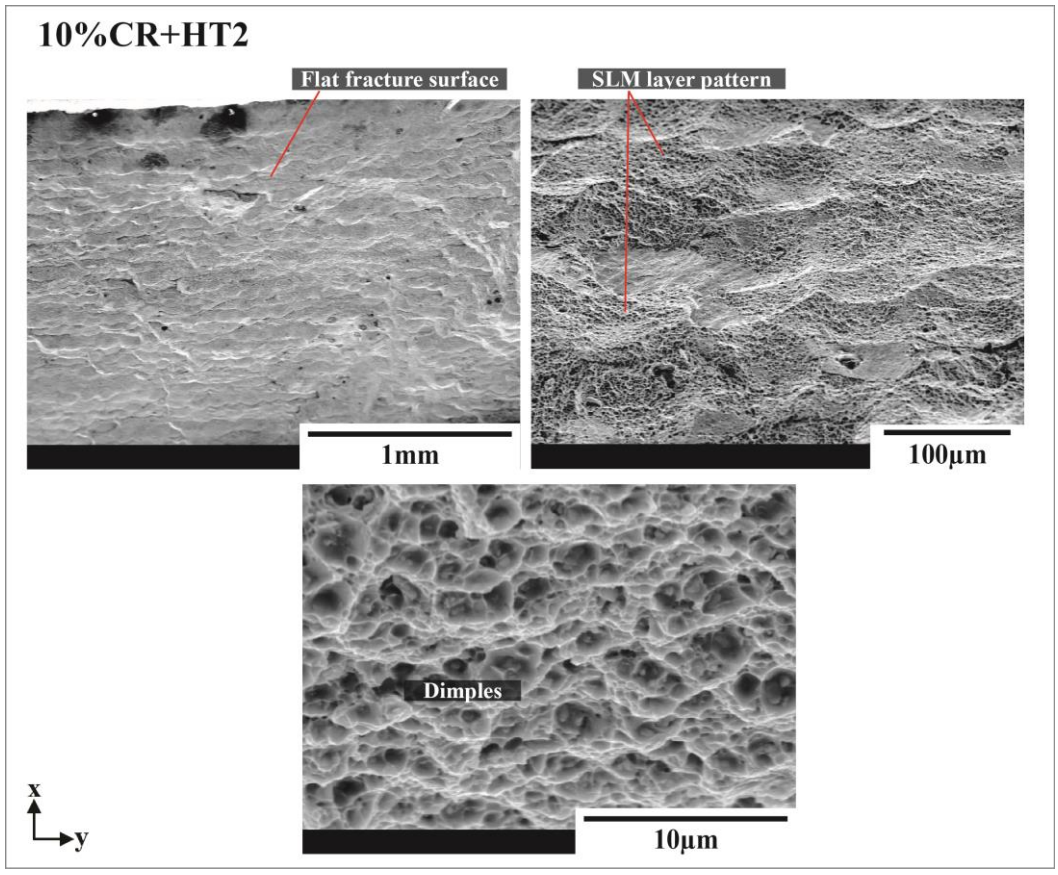

Fig. 5.73 SEM micrographs of the fracture surface for the 10%CR+HT2 condition

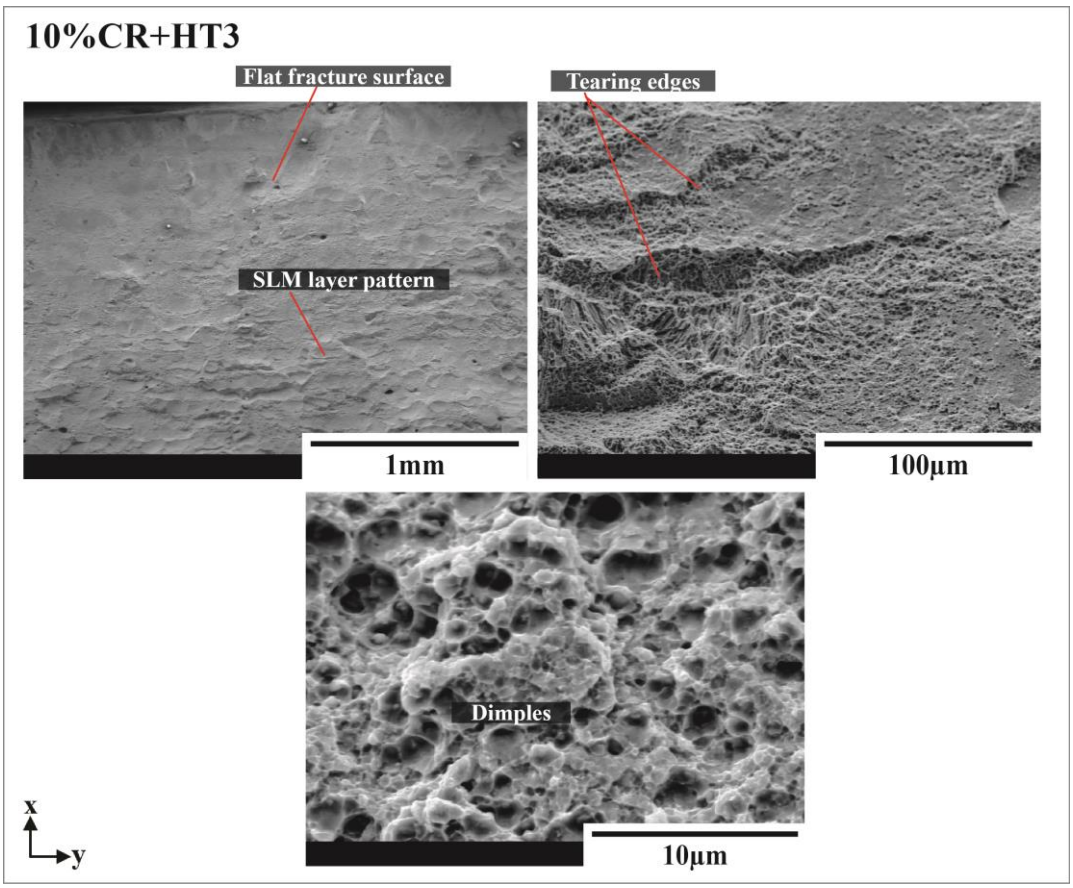

Fig. 5.74 SEM micrographs of the fracture surface for the 10%CR+HT3 condition

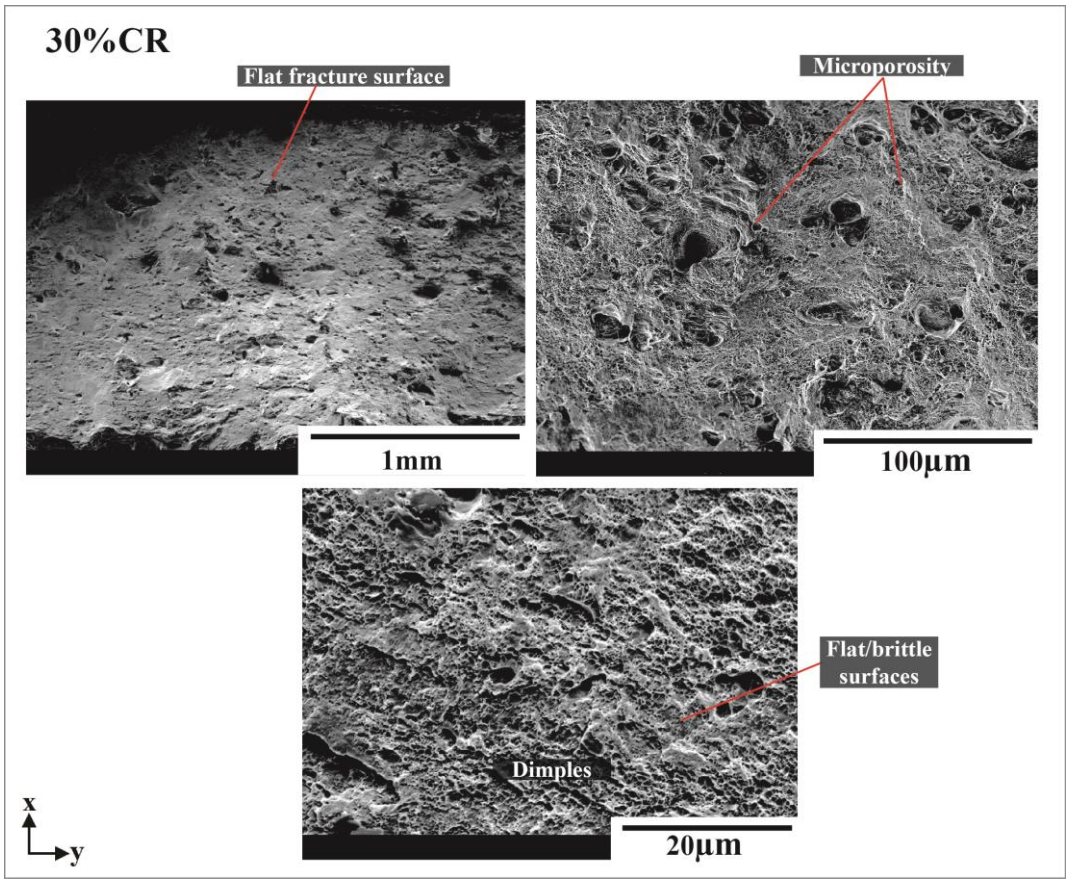

Fig. 5.75 SEM micrographs of the fracture surface for the 30%CR condition

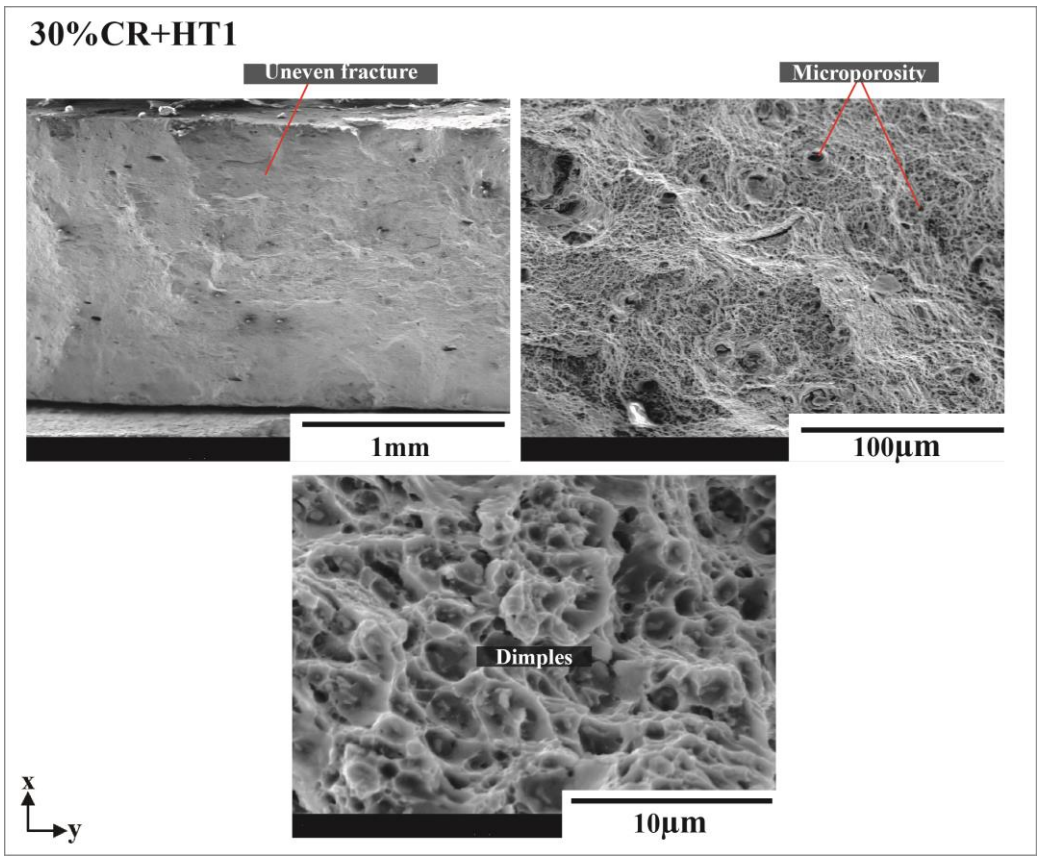

Fig. 5.76 SEM micrographs of the fracture surface for the 30%CR+HT1 condition

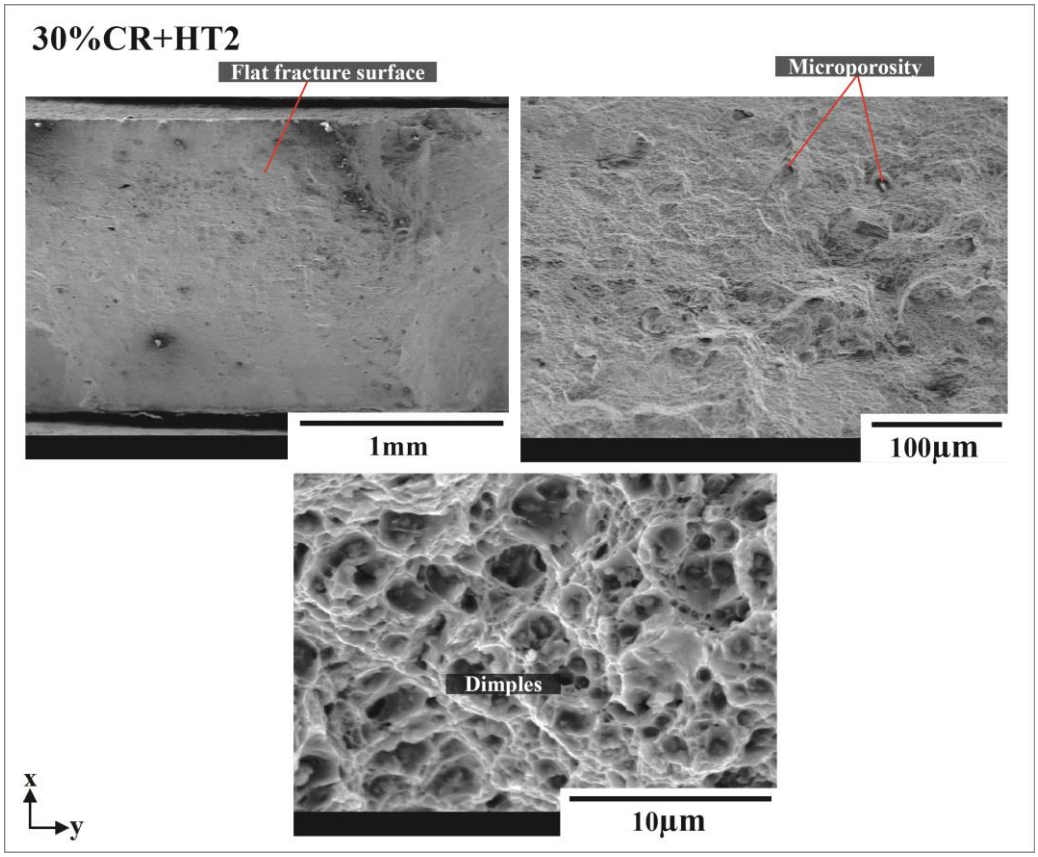

Fig. 5.77 SEM micrographs of the fracture surface for the 30%CR+HT2 condition

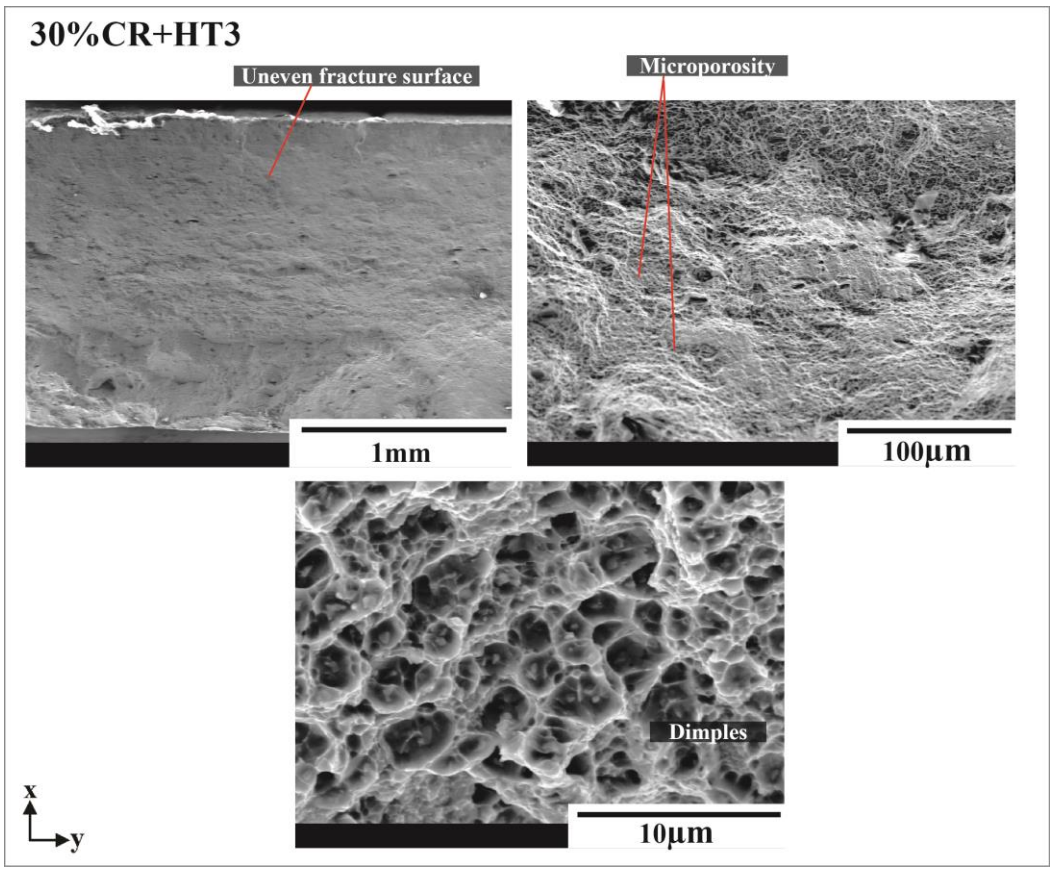

Fig. 5.78 SEM micrographs of the fracture surface for the 30%CR+HT3 condition

5.6 Summary

In this chapter, Scalmalloy samples were subjected to post processing treatments of cold rolling and heat treatment, while 5052Al and 5083Al samples were subjected to cold rolling. The effect on microstructure, mechanical properties and fracture was observed. Generally, the extruded aluminium alloys (5052Al and 5083Al) had much lower mechanical properties than Scalmalloy due to the difference in composition, manufacturing method and post processing treatments, however this was important to establish a baseline for the work on hand. For the Scalmalloy samples, it was found that the AB condition responded favourably to HT1 as this promoted the precipitation of second phase particles as seen in the optical and SEM micrographs (section 5.1), where tensile strength and hardness showed an immediate increase by approximately 15% and 28%. The effect of HT2 and HT3 on the AB condition showed approximately 7% increase in tensile strength, half that of HT1. The lower increase was thought to be due to overageing. All samples in the cold rolled condition showed an increase in mechanical properties when compared to the AB condition assumed to be due to the increase of dislocation density through plastic deformation. The cold rolled samples after application of HT1, HT2 and HT3 experienced increase in tensile strength between 6% and 40% and an increase in hardness of up to 45% thought to be due to the combination of cold rolling increasing dislocation density and the application of heat treatment removing any residual stresses and inducing precipitation of second phase particles. Surface roughness was also observed and showed Scalmalloy AB condition had high

surface roughness compared to the cold rolled conditions and extruded aluminium alloys as the cold rolling process smoothed surface imperfections. Fracture analysis showed all samples had a either a very ductile or ductile fracture consistent with the reported tensile properties.

Typically, the literature has highlighted that the optimum heat treatment for Scalmalloy is 325^{o}C/4h and there is very little literature on the cold rolling of Scalmalloy to improve its mechanical properties. The work on hand has shown that a low reduction in thickness by cold rolling and a shorter heat treatment condition of 450^{o}C/1h, than the standard 325^{o}C/4h, can significantly improve Scalmalloy mechanical properties, each in isolation and in combination with one another. Hence, Scalmalloy has responded favourably to modified heat treatments, cold rolling and a combination of cold rolling and modified heat treatments.

Chapter 6 Results and discussion of the weldability of Scalmalloy

This chapter will include mechanical properties, microstructural characterisation, fracture, and defect analysis for all GTAW samples – Scalmalloy to Scalmalloy, Scalmalloy to 5052Al, Scalmalloy to 5083Al - in the as welded (AW) and post machined (PM) conditions.

6.1 Microstructural characterisation

The macrostructures of the Scalmalloy-Scalmalloy, Scalmalloy-5052Al, and Scalmalloy-5083Al welded joints are shown in Fig. 6.1a, 6.2a and 6.3a. The fusion zone (FZ), heat affected zone (HAZ) and base metals (BM) are indicated in these figures. Please note that additional optical micrographs of each welded joint are shown in Appendix B from Fig. B.18 – B.20.

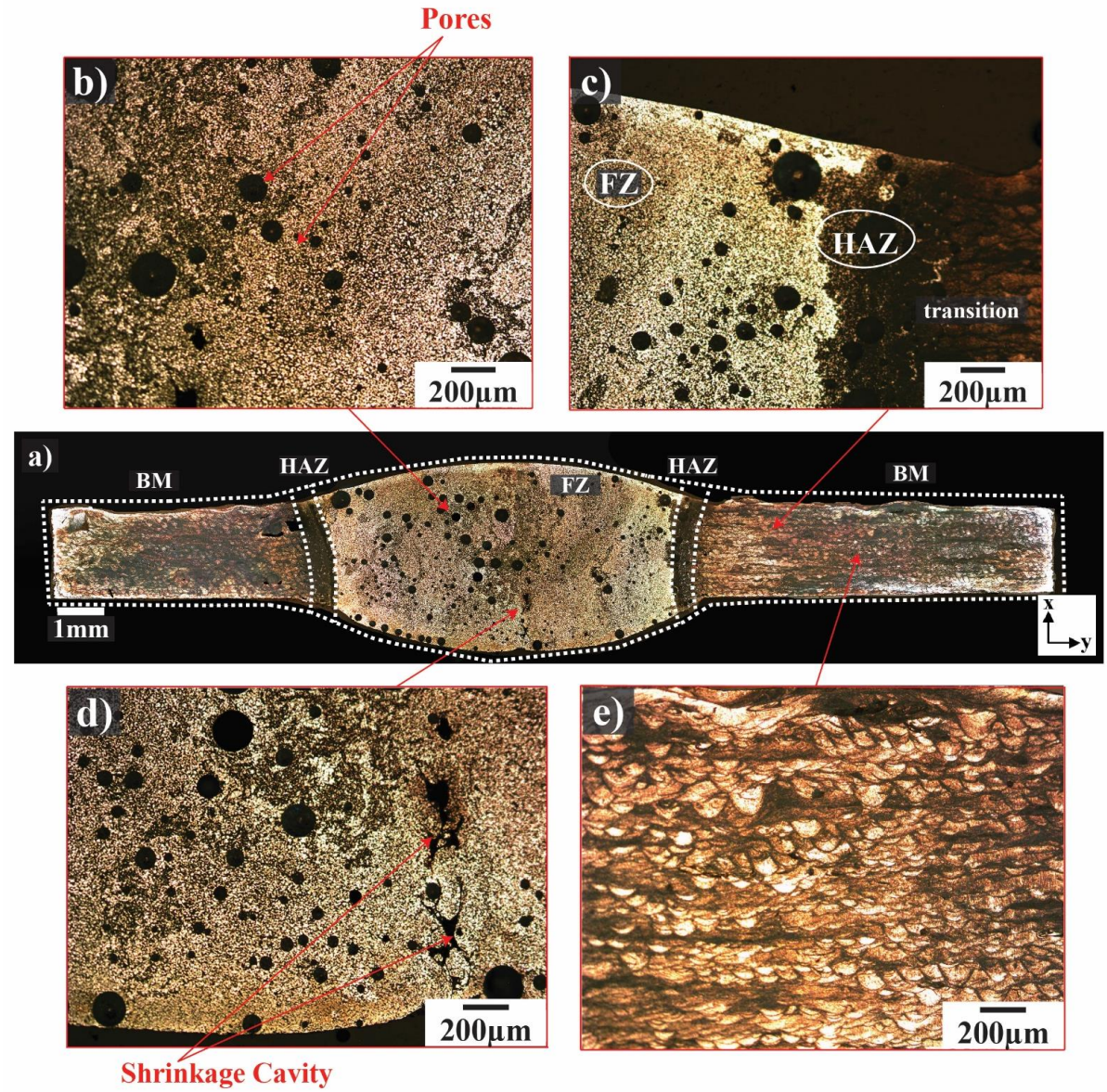

Fig. 6.1 Optical micrographs of Scalmalloy-Scalmalloy welded joint - a) macrostructure of welded joint, b&d) fusion zone, c) heat affected zone, e) base metal

The size and shape of each weld was consistent between samples. The HAZ of the Scalmalloy welded joint and the Scalmalloy sides of the other two joints showed porosity with pore size ranges were optically evaluated using *ImageJ* software and were between 1µm and 200µm, while the HAZ on the extruded aluminium alloy sides exhibited no pores or defects. The FZ of the Scalmalloy welded joint showed porosity with pore sizes ranging between 0.5µm to 200µm, while the FZ of the Scalmalloy-5052Al and Scalmalloy-5083Al welded joints showed only a few pores with a smaller pore size range of 1µm to 40µm. Additive manufactured aluminium alloys are susceptible to gas porosity by the introduction of hydrogen into the base metal from the external environment, as reported by Weingarten et al. (2015), Michler, Hollmann, Zenker, and Buchwalder (2021) and Cui et al. (2022). Hydrogen is introduced into the base metal, mainly from the pre-existing oxide films harbouring dissolved hydrogen and commonly associated with aluminium alloys. The amount of exposure to the external environment is directly related to the amount of oxide film (hydrogen) formed on an aluminium alloy. Beckmann and Emmelmann (2019) reported that additive manufactured aluminium alloys contained seven times more hydrogen than traditionally manufactured aluminium alloys, as Scalmalloy is exposed to the outside environment for a longer period of time through powder atomisation and the SLM process. The dissolved hydrogen originating from the oxide film recombines into the base metal during the welding process giving rise to porosity. Additionally, entrapped hydrogen within the pores of the Scalmalloy base metal occurring during the SLM process can also be a factor in the overall porosity, however this is thought to only have a small influence as reported by Cui et al. (2022). It should be noted that hydrogen content was not measured in this work, however, the circular profile detected porosity, corresponding number and distribution of pores along with supporting literature (Beckmann & Emmelmann, 2019; Cui et al., 2022; Galy, Guen, et al., 2018; Michler et al., 2021; Weingarten et al., 2015) suggest the porosity in the HAZ and FZ of the Scalmalloy welded joints, and the Scalmalloy sides of the other two welded joints is due to hydrogen induced porosity. In contrast, the Scalmalloy-5052Al and Scalmalloy-5083Al welded joints showed less porosity than the Scalmalloy-Scalmalloy welded joint thought to be due to less hydrogen in the extruded aluminium alloys, and the welding parameters, especially the filler rod material, being more suited to the extruded aluminium alloys as these were based upon those used for extruded aluminium alloys (Arunkumar & Subbaiah, 2019; Hakem et al., 2012; Y. Liu et al., 2012; Shanavas & Dhas, 2017; Ye et al., 2017)

The HAZ for the Scalmalloy sides of each welded joint are shown in Fig. 6.1c, 6.2b and 6.3b where hydrogen induced pores as large as 100µm in size can be seen here. Fig. 6.5 show high magnification SEM micrographs of the Scalmalloy HAZ microstructures for all welded joints, where there is a clear transition between BM, HAZ and FZ indicated by the different microstructures. The typical Scalmalloy BM structure can be observed where it transitioned into coarse columnar grains in the HAZ and eventually into smaller, equiaxed, recrystallised grains in the FZ.

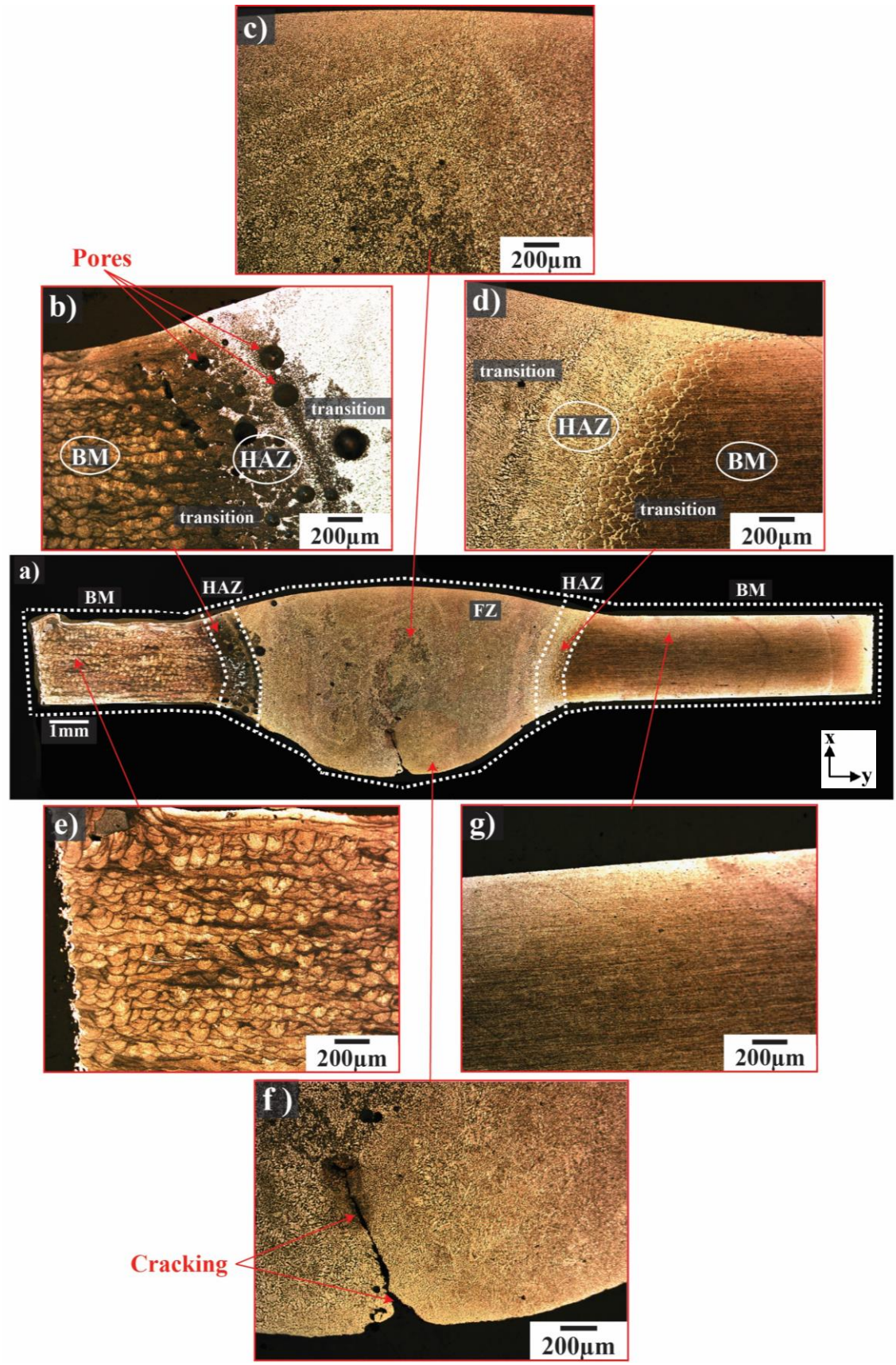

Fig. 6.2 Optical micrographs of Scalmalloy-5052Al welded joint - a) macrostructure of welded joint, b) Scalmalloy heat affected zone, d) 5052Al heat affected zone, c&f) fusion zone, e) Scalmalloy base metal, g) 5052Al base metal

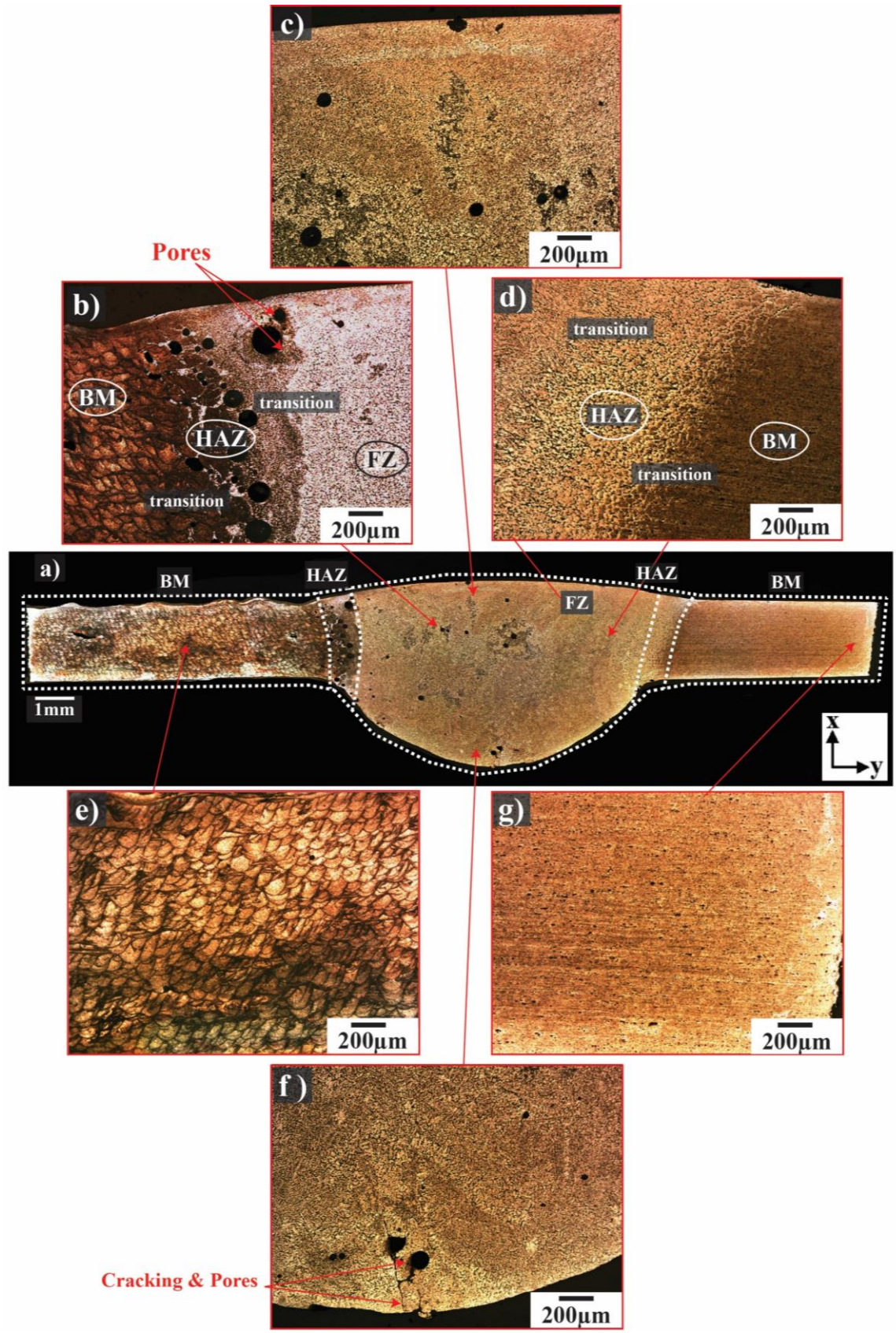

Fig. 6.3 Optical micrographs of Scalmalloy-5083Al welded joint a) macrostructure of welded joint, b) Scalmalloy heat affected zone, d)5083Al heat affected zone, c&f) fusion zone, e) Scalmalloy base metal, g) 5083Al base metal

This microstructure is common in the HAZ of welded joints as exposure to the high welding heat coarsens grains and causes porosity, and the recrystallised equiaxed grains in the FZ is due to the melting and solidification process occurring during welding.

The HAZ on the extruded aluminium alloy sides for the Scalmalloy-5052Al and Scalmalloy-5083Al welded joints are shown in Fig. 6.2d and Fig.6.3d, respectively. These retained the same characteristics as the Scalmalloy HAZ. However, the extruded aluminium alloy HAZ structure does not contain any pores or defects as standard welding parameters suitable for extruded aluminium alloys were used and these alloys are less prone to porosity than additive manufactured components (Michler et al., 2021).

The Scalmalloy BM structure for each welded joint was characterised by layered molten pool tracks 100 to 200µm in size evident in Fig. 6.1e, Fig. 6.2e and Fig. 6.3e. This unique structure is a result of the SLM process of layering, melting and solidifying material in a layer-by-layer fashion. Al_3(Sc, Zr) secondary particles and precipitates have been reported to reside in the Scalmalloy BM structure pinning grain boundaries (Koutny et al., 2018; A. B. Spierings, Dawson, Dumitraschkewitz, et al., 2018; A. B. Spierings, Dawson, Heeling, et al., 2017). SEM micrographs, shown in Fig. 6.4a, reveal the unique bi-modal microstructure of the Scalmalloy BM with a fine equiaxed grain region (FG) and a coarse columnar grain (CG) region consistent with findings reported by A. B. Spierings, Dawson, Heeling, et al. (2017). Each of these characteristics give rise to Scalmalloy high strength and hardness.

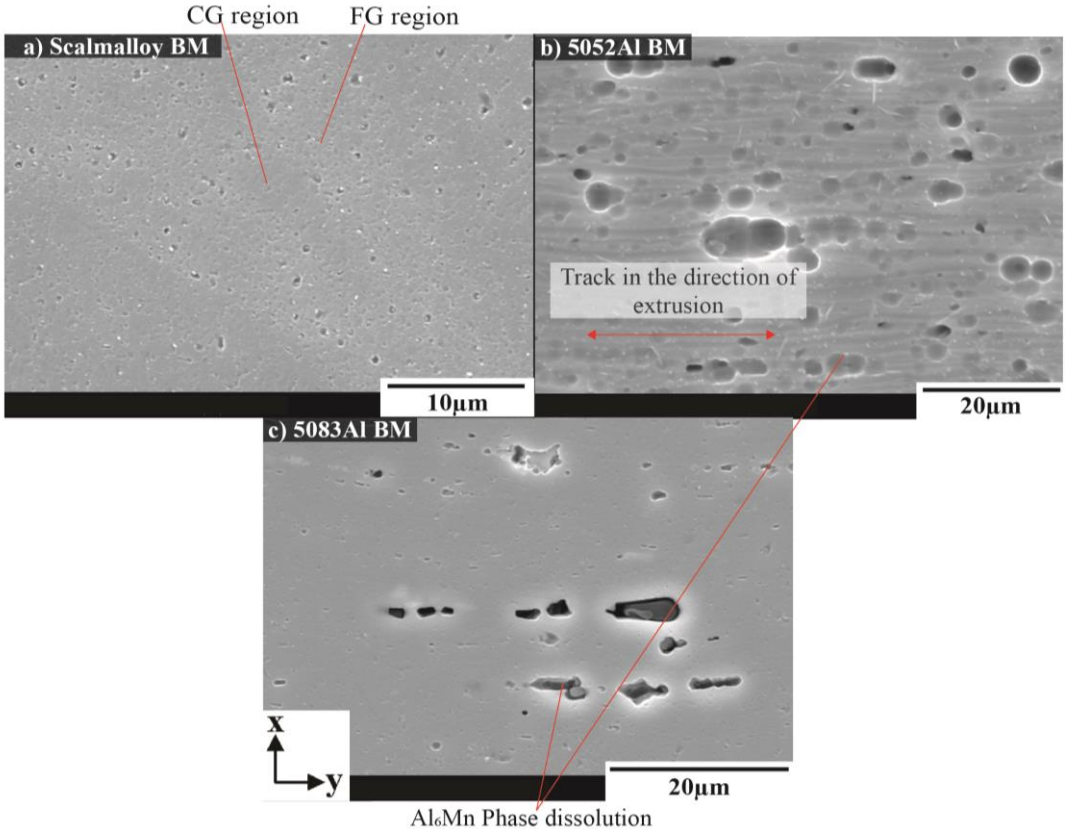

Fig. 6.4 SEM micrographs of base metal microstructure of a) Scalmalloy, b) 5052Al and c) 5083Al

Fig 6.2g and 6.3g show the microstructure of the extruded aluminium alloys of the welded joints, where parallel lines are visible indicating the rolling direction. Un-recrystalised elongated parallel grains in the rolling direction are visible in Fig. 6.4b and 6.4c, along with voids caused by phase dissolution of Al_6Mn. Al_6Mn is a common phase that can develop in aluminium alloys containing 3% to 5% Manganese content (like the aluminium alloys used in the welded joint) and the dissolution is an artifact of material preparation due to its reaction to the etchant (Algendy, Liu, & Chen, 2020).

Fig. 6.1b and 6.1d show the FZ of the Scalmalloy welded joint. It has a homogenous microstructure with pore size range from 5µm to 200µm in size. Some lack of fusion towards the bottom centre of the weld is also visible. The FZ of the Scalmalloy-5052Al welded joint (shown in Fig. 6.2c & 6.2f) and the FZ of the Scalmalloy-5083Al welded joint (shown in Fig. 6.3c and 6.3f) are similar to the FZ of the Scalmalloy welded joint but have less visible pores, less defects, and a smaller pore size range of 10µm to 50µm. Fig.6.2f and Fig. 6.3f show the lower half of the FZ for the Scalmalloy-5052Al and Scalmalloy-5083Al welded joints, respectively, where lack of fusion and shrinkage has occurred in the centre of the FZ due to low energy input and a large weld pool (Çetkin et al., 2019). The microstructure consists of fine recrystallised dendritic and equiaxed grains occurring due to the high welding heat (Cui et al., 2022; G. Xu et al., 2016). Fig. 6.6 shows SEM micrographs of the FZ for each welded joint, but grains are not obvious and only phase dissolution can be seen. However, weld pool tracks (Fig. 6.6b) from the GTAW welding are visible upon high magnification.

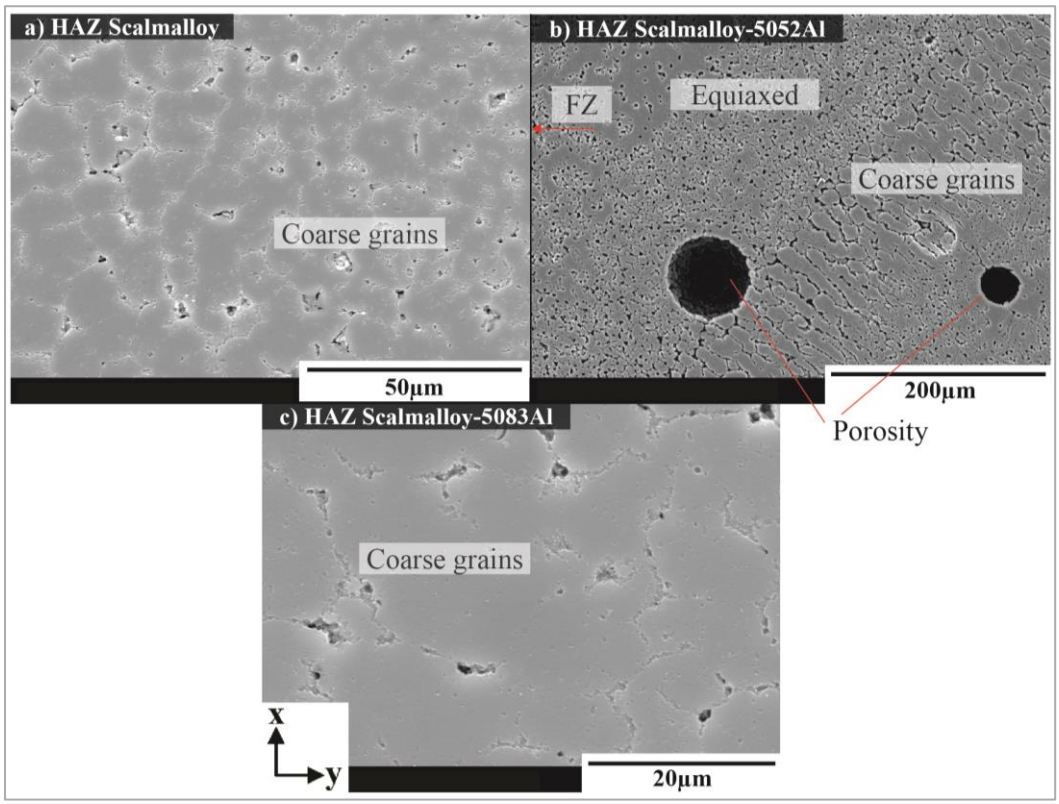

Fig. 6.5 SEM micrographs of heat affected zone microstructure for Scalmalloy side of the welded joint for a)Scalmalloy, b) Scalmalloy-5052Al and c) Scalmalloy-5083Al welded joints

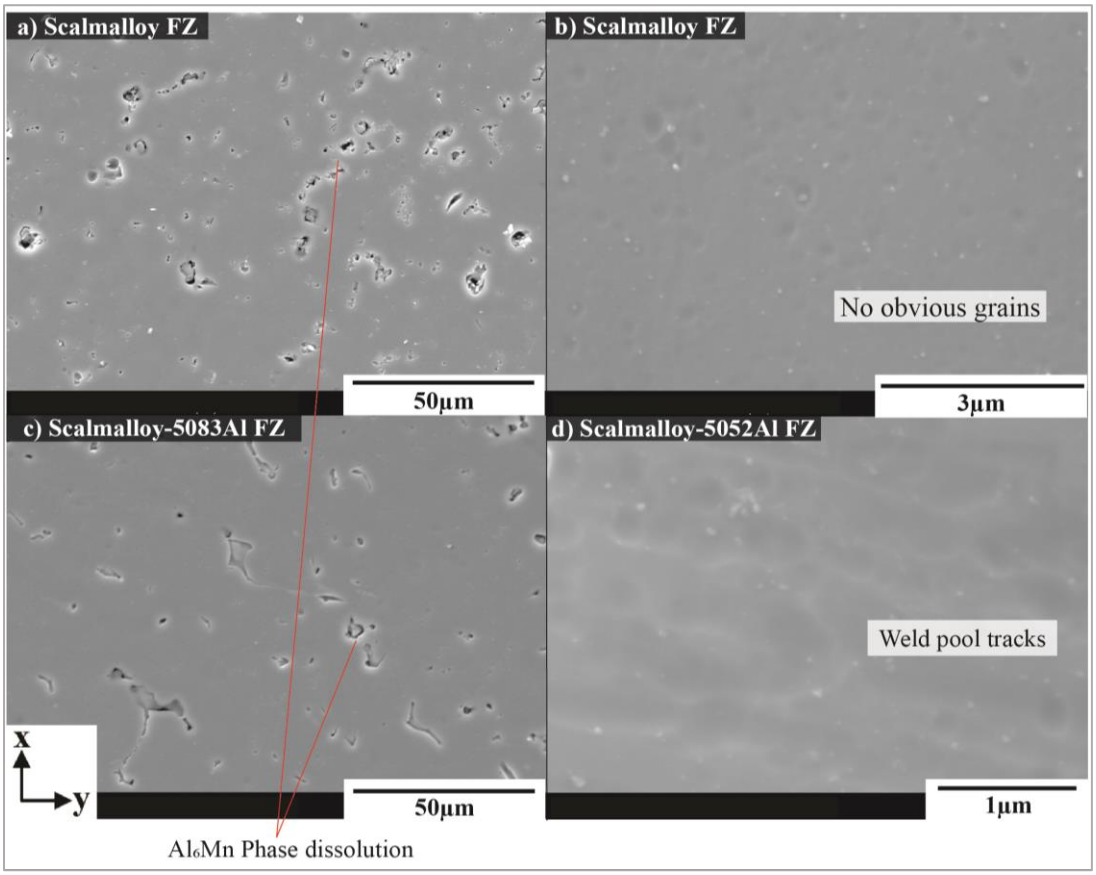

Fig. 6.6 SEM micrographs of fusion zone microstructure for a)Scalmalloy, b) Scalmalloy-5052Al and c) Scalmalloy-5083Al welded joints

Table 6-1, 6-2 and 6-3 show energy dispersive spectroscopy (EDS) composition results detected in various regions of the weld. Please note that additional EDS information of the welded joints are shown in Appendix D. The EDS scans for the Scalmalloy HAZ of each welded joints are similar with high aluminium content, medium magnesium content and traces of scandium and low traces of manganese. The scandium content detected was comparable to the base metal content of Scalmalloy (0.66wt% Sc) confirming that scandium does not dissolve here. The EDS results of the FZ for each welded joint are similar to the HAZ results, but little to no traces of scandium and zirconium were detected or localised here, and as with the HAZ results, the manganese content here is low due to some phase dissolution by the etchant (Algendy et al., 2020). Although welding temperature was not measured in this work, it was reported by G. Xu et al. (2016) that the HAZ experiences temperatures of up to 500^{o}C and the FZ reaches temperatures well above 550^{o}C. Hence, scandium is still present in the HAZ as the welding heat for GTAW within the HAZ reaches up to temperatures of 500^{o}C, which is not high enough for Al_3(Sc, Zr) particles to lose coherency with the aluminium matrix. As the welding heat in the FZ exceeds 550^{o}C, the traces of scandium and zirconium almost vanished and Al_3(Sc, Zr) particles are no longer coherent and dissolve in the solid solution. Hence, from the EDS scans, an aluminium solid solution has formed in the FZ with fine recrystallised grains due to the high heat and the welding process of melting and solidification, consistent with findings reported by G. Xu et al. (2016), P. Xu et al. (2018), Lei et al. (2013) and Subbaiah (2019).

Table 6-1 Energy dispersive spectroscopy scan results of Scalmalloy welded joint of the heat affected zone and the fusion zone

Welded joint/Element	**Mg**	**Al**	**Sc**	**Mn**
Scalmalloy-Scalmalloy HAZ	3.03	95.63	0.69	0.65
Scalmalloy-Scalmalloy FZ	4.50	95.03	0.14	0.34

Table 6-2 Energy dispersive spectroscopy scan results of Scalmalloy-5052Al welded joint of the heat affected zone on Scalmalloy side, and the fusion zone

Welded joint/Element	**Mg**	**Al**	**Sc**	**Mn**
Scalmalloy-5052Al FZ	3.34	96.35	0.13	0.19
Scalmalloy-5052Al HAZ	2.93	95.89	0.54	0.64
Scalmalloy-5052Al FZ	2.98	96.47	0.22	0.34

Table 6-3 Energy dispersive spectroscopy scan results of Scalmalloy-5083Al welded joint showing composition in the fusion zone of the weld

Welded joint/Element	**Mg**	**Al**	**Sc**	**Mn**
Scalmalloy-5083Al FZ	4.10	95.28	0.22	0.4
Scalmalloy-5083Al FZ pt1	4.64	94.90	0.14	0.32
Scalmalloy-5083Al FZ pt2	8.28	90.89	0.18	0.29
Scalmalloy-5083Al FZ pt3	5.01	94.46	0.22	0.32
Scalmalloy-5083Al FZ p4	4.36	92.37	0.12	3.14

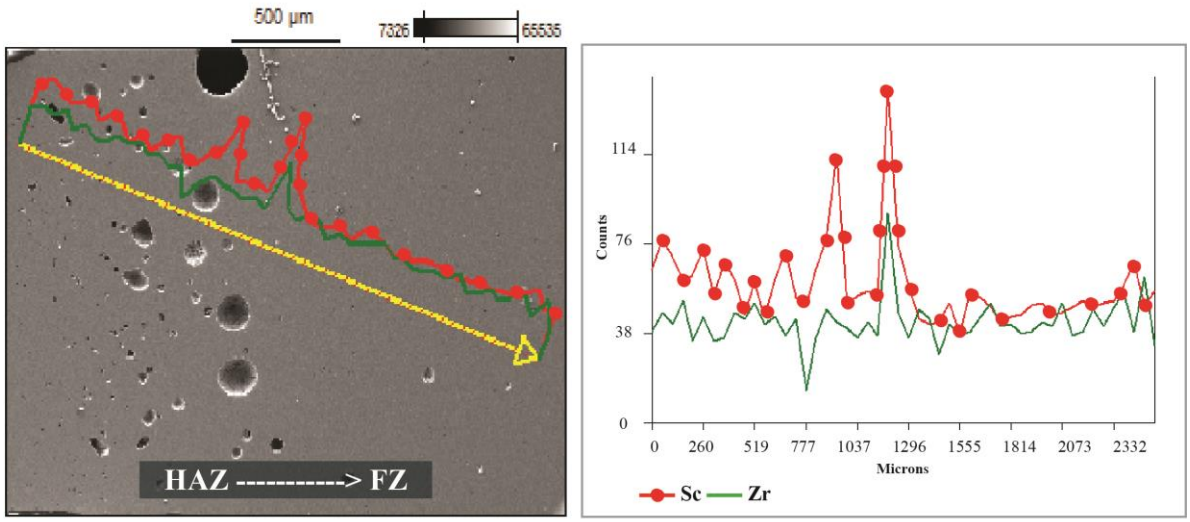

Fig. 6.7 Line scan detecting elements of scandium and zirconium from heat affected zone to fusion zone of Scalmalloy welded joint

In Fig. 6.7, a line scan is shown detecting traces of scandium and zirconium from the HAZ through to the FZ of the Scalmalloy welded joint. It was found that higher levels of scandium and zirconium seemed to have localised through the HAZ, and lower levels were evident moving into the FZ. This is consistent with the traces of scandium and zirconium dissolving into the solid

solution in the FZ due to the high welding heat. A build up of scandium and zirconium was also visible at the transition from HAZ to FZ showing the transition between zones.

6.2 Effect of microstructural evolution on mechanical properties

This section discusses the effect that the microstructure has on the mechanical properties such as tensile strength, strain, and hardness.

6.2.1 Effect of microstructural evolution on hardness

Hardness indentations across the weld perpendicular to the welding direction are shown in Fig. 6.8. The distinct regions of the BM, HAZ FZ, and a yellow dashed line showing the average hardness as a reference are also shown here. In Fig. 6.8a, the lowest average hardness of 77HV for the Scalmalloy welded joint was recorded in the FZ, and the highest average hardness of 129HV resided in the Scalmalloy BM, a difference of almost 50%. The Scalmalloy BM hardness remained consistent up to the HAZ and then steadily declined. A sharp drop in hardness occurred at the FZ and remained consistent until reaching the HAZ where the hardness rose steadily as the distance from the FZ increased until achieving the original hardness of the Scalmalloy BM. Fig. 6.8b showed the Scalmalloy-5052Al welded joint with the highest average hardness of 128HV achieved in the Scalmalloy BM and the lowest hardness of 68HV occurring in the FZ. Beginning from the Scalmalloy side, the trend is similar to the Scalmalloy welded joint as the Scalmalloy BM average hardness remained consistent in the BM zone and then slowly declined approaching and moving through the HAZ. The hardness dropped to an average of 68HV in the FZ, and was maintained through to the 5052Al BM. The Scalmalloy-5083Al welded joint, shown in Fig. 6.8c, was similar to the Scalmalloy-5052Al welded joint as they both followed the same hardness trend, where the highest average hardness of 123HV was achieved in the Scalmalloy BM and the lowest average hardness of 69HV was recorded in the FZ.

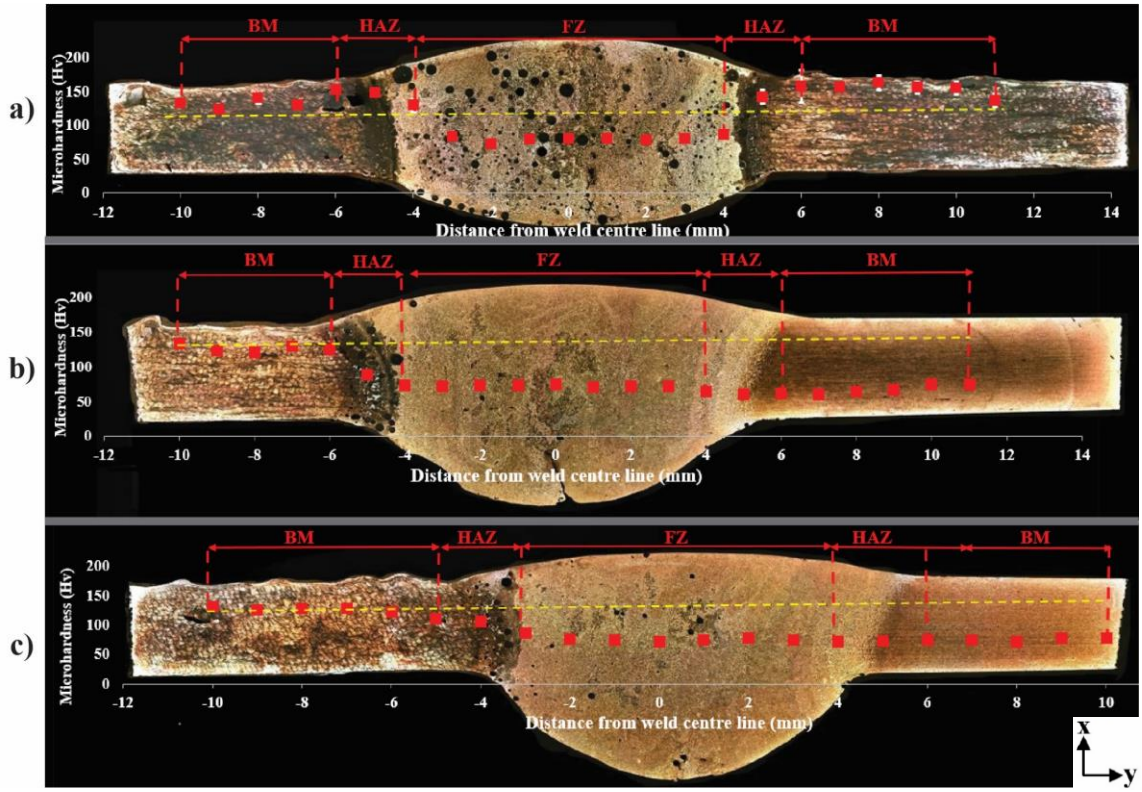

Fig. 6.8 Hardness values of each welded joint a) Scalmalloy, b) Scalmalloy-5052Al, c) Scalmalloy-5083Al

The BM structure of Scalmalloy consisted of fine Al_3(Sc, Zr) second phase particles, fine grains and grain boundary strengthening as reported by A. B. Spierings, Dawson, Heeling, et al. (2017). As the BM zone was unaffected by welding, the hardness remained at an average of 129HV, 128HV, 123HV for the Scalmalloy, Scalmalloy-5052Al and Sclamalloy-5083Al welded joints, respectively. These hardness readings are consistent with findings from current literature (Awd et al., 2017; R. Li et al., 2017; Adriaan B. Spierings et al., 2016). The decline in hardness in the Scalmalloy HAZ was caused by exposure to the high welding temperature resulting in grain growth, dislocation movement and hydrogen induced pores. However, the hardness readings here were higher than those recorded in the FZ as temperatures only reached up to 500^{o}C, where second phase particles, and pinning of dislocations can be maintained (G. Xu et al., 2016; P. Xu et al., 2018). The FZ of each welded joint consisted of a supersaturated aluminium solid solution induced by the high welding heat (>550^{o}C). At this temperature, Al_3(Sc, Zr) particles tend to lose their coherency within the aluminium matrix and scandium and zirconium particles are almost completely dissolved into the aluminium solid solution. Hence, any strengthening effect from the Al_3(Sc, Zr) particles was lost and the hardness was equal to that of the filler rod material of 5356Al. Hence, the hardness trend for the Scalmalloy-extruded aluminium welded joints stabilized at an average of 68HV and 69HV from FZ to extruded aluminium alloy BM due to the standard welding parameters for extruded aluminium alloys being used, where the filler rod material and extruded aluminium alloys had similar hardness'(Santos Junior et al., 2016). For the Scalmalloy welded joint, hardness increased to the original Scalmalloy BM hardness as the

distance away from the FZ and HAZ increased thought to be due to Orowan strengthening from second phase particles as welding heat did not affect the BM (G. Xu et al., 2016)

6.2.2 Effect of microstructural evolution on tensile properties

Stress strain curves for the AW and PM samples for all welded conditions are shown in Fig. 6.9. The AW samples observed a much lower yield strength (YS) and ultimate tensile strength (UTS), and a greater elongation compared to the PM samples. Table 6-4 lists the measured YS, UTS, elongation and Young's modulus for each condition along with the tensile properties for the respective BMs to show comparison between welded and BM values. The correlation between tensile strength and porosity of the samples appear to be directly related. Fig 6.10 shows the average porosity of each welded joint in both the PM and AW conditions. The AW samples contained a higher porosity than PM samples since they contained a larger cross-sectional area. The lack of fusion and cracking at the bottom of the weld bead for some of the welded joints also caused local stress concentration evident from the strain distribution graphs (Fig. 6.11 – 6.12). However, the main cause of the difference in tensile strength was likely change in geometry of the cross section between the PM and AW samples. As the PM samples had a uniform cross section, often recommended when performing a standard tensile test, the sample undergoes normal stress during tensile testing allowing the load to be evenly distributed through the sample . However, the AW samples left the weld bead intact acting as a surface defect leading to non-uniform stress being applied to the sample, hence lower tensile and yield strengths. Consequently, these factors led to lowered tensile strength in the AW samples. The PM samples had a uniform cross section, contained less porosity (Fig. 6.10), and defects on the bottom of some of the welded joints were eliminated during wire cutting of the weld bead. These factors have resulted in higher tensile strengths than the AW samples.

The PM samples for the Scalmalloy-5083Al welded joint displayed the highest average tensile strength of the PM samples as the percentage of porosity present in this sample was much lower than the Scalmalloy welded joint and slightly lower than the Scalmalloy-5052Al welded joint. Scalmalloy PM samples had the second highest average tensile strengths, it was assumed that the Al_3(Sc, Zr) particles were still coherent to pin grain boundaries in the HAZ since the welding temperature was not expected to exceed 500^{o}C in this zone as reported by G. Xu et al. (2016); P. Xu et al. (2018). Scalmalloy-5052Al welded joint had the lowest tensile strength and the fracture occurred on the 5052Al HAZ side. 5052Al has the lowest tensile strength (Table 6-4) when compared to Scalmalloy and 5083Al BM, hence, lower tensile strengths. The PM samples showed very similar elongations when compared to each other, each being very low (less than 8%).

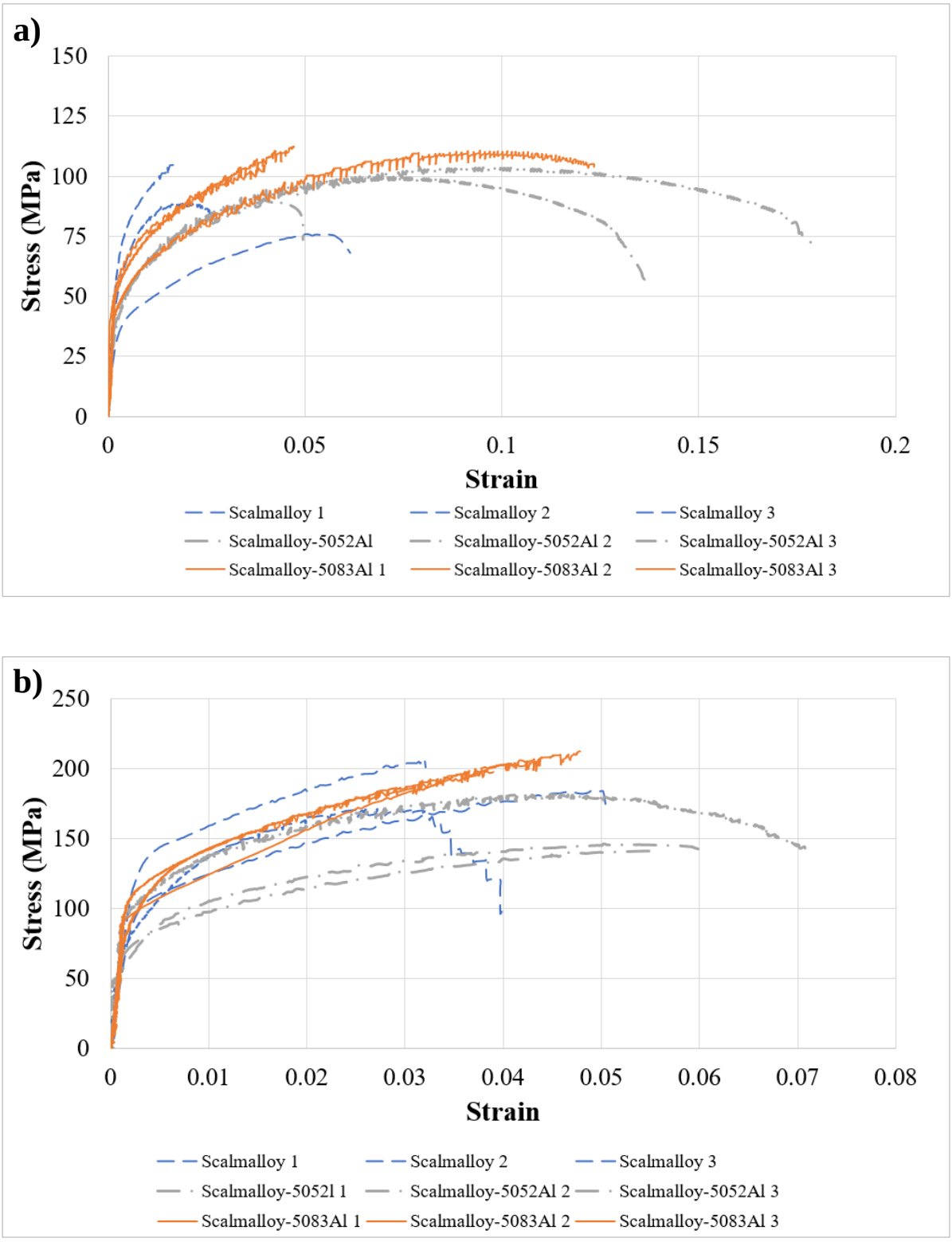

Fig. 6.9 Stress-strain curves of welded samples a) As welded condition, b) Post machined condition

Table 6-4 Average tensile data values

Sample Condition	Yield Stress (MPa)	UTS (MPa)	Strain at fracture	Young's Modulus (GPa)
Scalmalloy AW	36.7	90.4	0.035	25.3
Scalmalloy PM	101.0	187.4	0.045	56
5052Al - Scalmalloy AW	30.0	97.8	0.132	29.7
5052Al - Scalmalloy PM	60.0	118.4	0.056	45.3
5083Al - Scalmalloy AW	44.7	109.3	0.097	38
5083 Al - Scalmalloy PM	73.2	212.2	0.046	66.4
Scalmalloy Base Metal	288	335	0.098	-
5052Al Base Metal	161	229	0.29	-
5083Al Base Metal	232	329	0.18	-

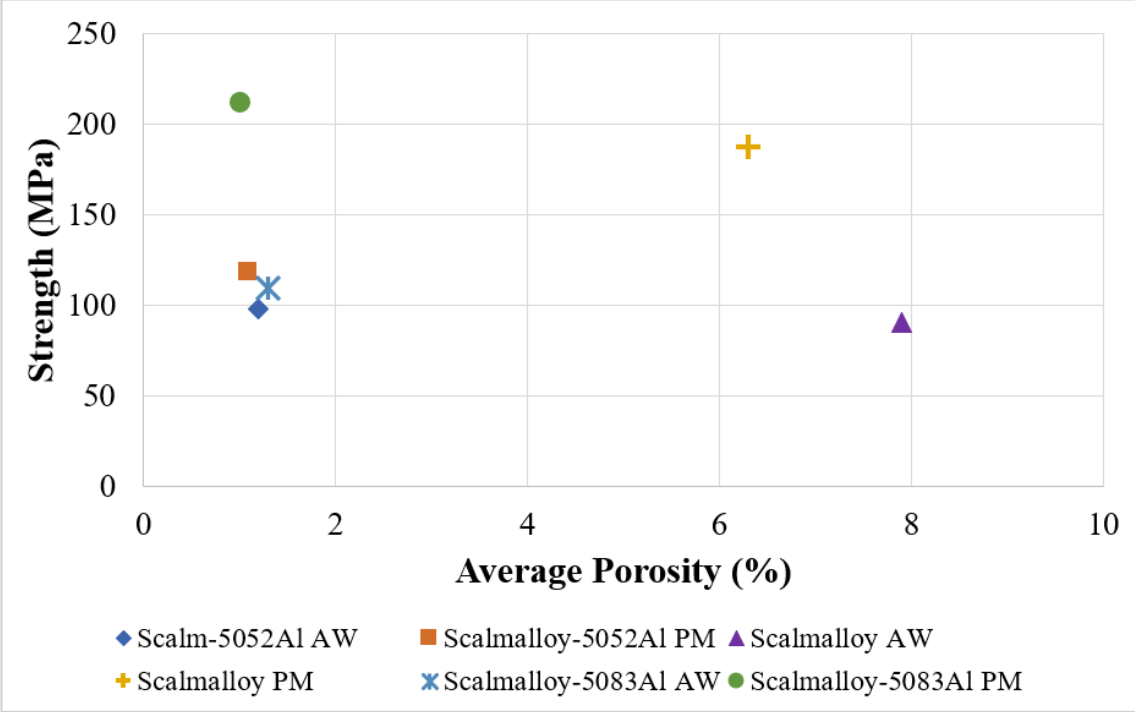

Fig. 6.10 Ultimate tensile strength vs. porosity percentage for welded samples

Again, the porosity and defects developed in the FZ and HAZ caused the low elongations especially when compared to their BM substrates. On the other hand, the AW samples showed larger elongations of the Scalmalloy-5052Al and Scalmalloy-5083Al joints when compared to the PM samples as they had a larger cross-sectional area where early fracture was delayed. Although, the Scalmalloy AW joint also had a larger cross-sectional area than its PM condition, elongations were similar as the porosity percentage was similar where this has led to early fracture for both conditions.

The UTS, YS and elongation of the welded joints in both conditions are almost 50% lower than their respective BM substrates. Key factors that have caused such low tensile and yield strengths are the prevalent microstructures in the HAZ and FZ. Grain growth occurred in the HAZ resulting in coarse columnar grains, large hydrogen induced pores and therefore a weaker structure. The

FZ also has no strengthening effects from Al_3(Sc, Zr) particles originating from the Scalmalloy BM so that only an aluminium solid solution exists in the fusion zone with low hardness when compared to the Scalmalloy BM. Additionally, the interconnected porosity, high porosity percentage and defects such as cracking and lack of fusion in these areas have detrimentally affected the tensile properties (Lei et al., 2013; G. Xu et al., 2016).

6.2.3 Strain distribution under plastic failure

Fig. 6.11 and 6.12 show the welded samples' strain distribution before and after failure measured by DIC technology during tensile testing. The local strain where fracture took place is in red (highest strain). Fig. 6.11 shows the AW samples for each welded joint. The Scalmalloy-Scalmalloy and Scalmalloy-5083Al AW samples showed no obvious necking and average local strains at fracture were 3.3% and 5.8%, respectively. The Scalmalloy-5052Al AW welded joint showed obvious necking with an average local strain at fracture of 40%. The high local strains were thought to be due to the sample fracturing on the 5052Al alloy HAZ side, where coarse columnar grains were present (see Fig. 6.5) and as 5052Al has a higher ductility than Scalmalloy (Santos Junior et al., 2016). Fig. 6.12 shows the PM samples of each welded joint. The Scalmalloy PM samples showed an average local strain at fracture of 3.3%. The Scalmalloy-5052Al PM sample showed an average local strain at fracture of 8% with one sample showing slight necking. The Scalmalloy-5083Al PM samples had an average local strain of 5.6%. The coarse grains and large gas pores in the Scalmalloy HAZ are the primary cause of the low local strains in both the AW and PM samples for those that fractured on the Scalmalloy HAZ side. The two PM samples that fractured in the FZ showed localised strain in the centre of each sample suggesting that stress concentration emanating from defects may have caused the sample to fail here.

Fig. 6.11 Digital image correlation of each welded joint in the As Welded condition- a)Scalmalloy, b) Scalmalloy-5052Al and c) Scalmalloy-5083Al

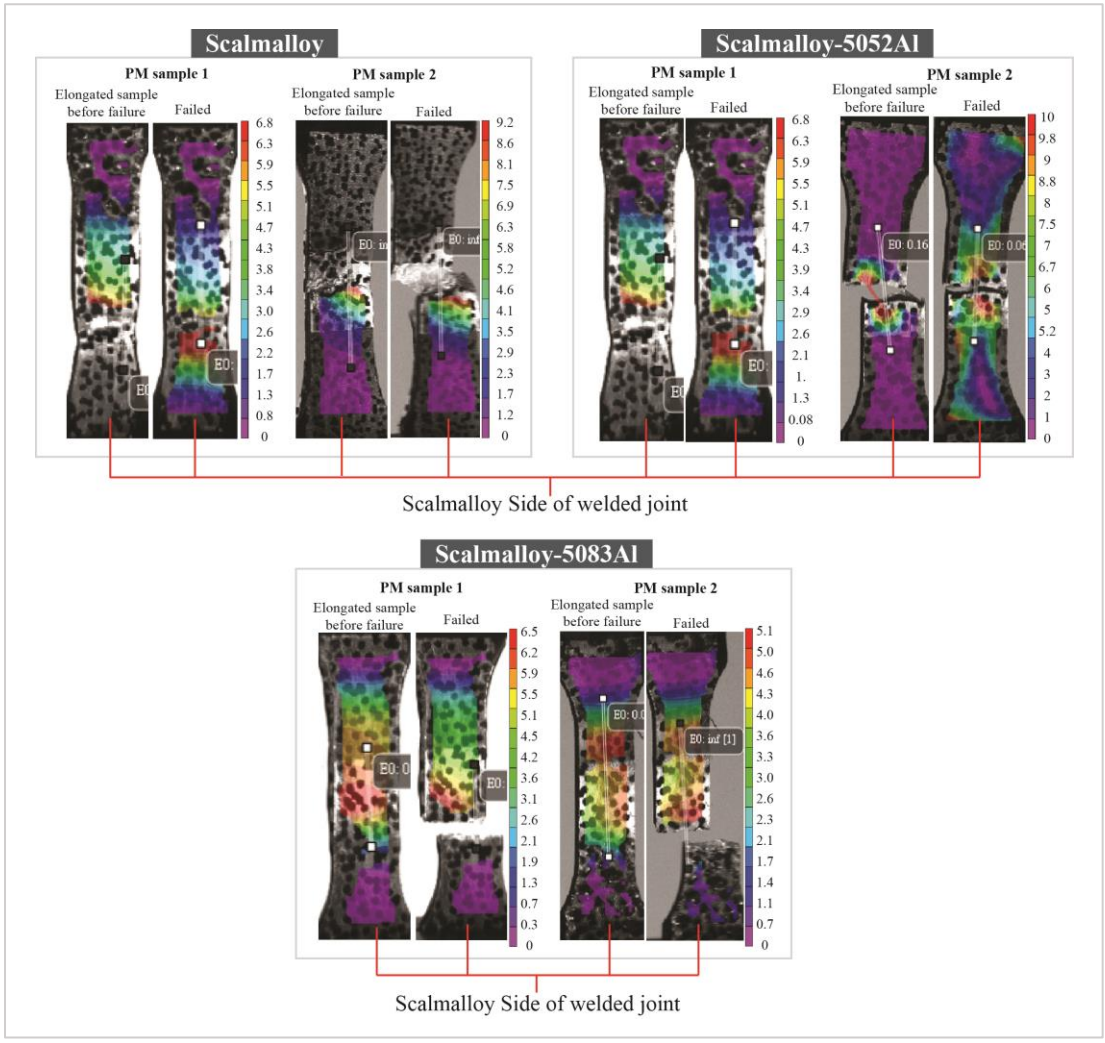

Fig. 6.12 Digital image correlation of each welded joint in the Post Machined condition - a)Scalmalloy, b) Scalmalloy-5052Al and c) Scalmalloy-5083Al

6.3 Analysis of fracture mechanism for welded joints

Fig. 6.13 and 6.14 shows most samples fractured in the HAZ region, indicating this region as the weakest part of the weld due to grain growth, coarse columnar grains and hydrogen induced pores (mainly for the Scalmalloy HAZ) as shown in Fig. 6.1 - 6.3. Softening of the metal in the HAZ as a result of exposure to the welding heat is a common occurrence in aluminium alloys (Cheng et al., 2022), evident here and confirmed by the decline in measured hardness (see Fig. 6.8). Stress concentrations originating from the cross-sectional changes in the AW samples increased the likelihood of fracture occurring in the HAZ. This is further confirmed by DIC (Fig. 6.11 - 6.12), where the highest strains for the AW conditions occurred at the top of the weld near or at the weld bead. For the Scalmalloy-5083Al welded joint in both the PM and AW conditions, failure occurred in the Scalmalloy HAZ due to coarse grains and visible porosity. Scalmalloy and 5083Al also have similar tensile strengths, hence, failure was likely to occur where more defects were present. Scalmalloy-5052Al welded joint fractured on the 5052Al HAZ side as this zone exhibited coarse columnar and equiaxed grains and the tensile strength of 5052Al is much lower than that of Scalmalloy . It should also be noted that one sample of the Scalmalloy PM samples

and one of the Scalmalloy-5052Al PM samples fractured in the FZ, rather than in the HAZ, as the cross-sectional area was smaller and exposed pores and defects has move the fracture location.

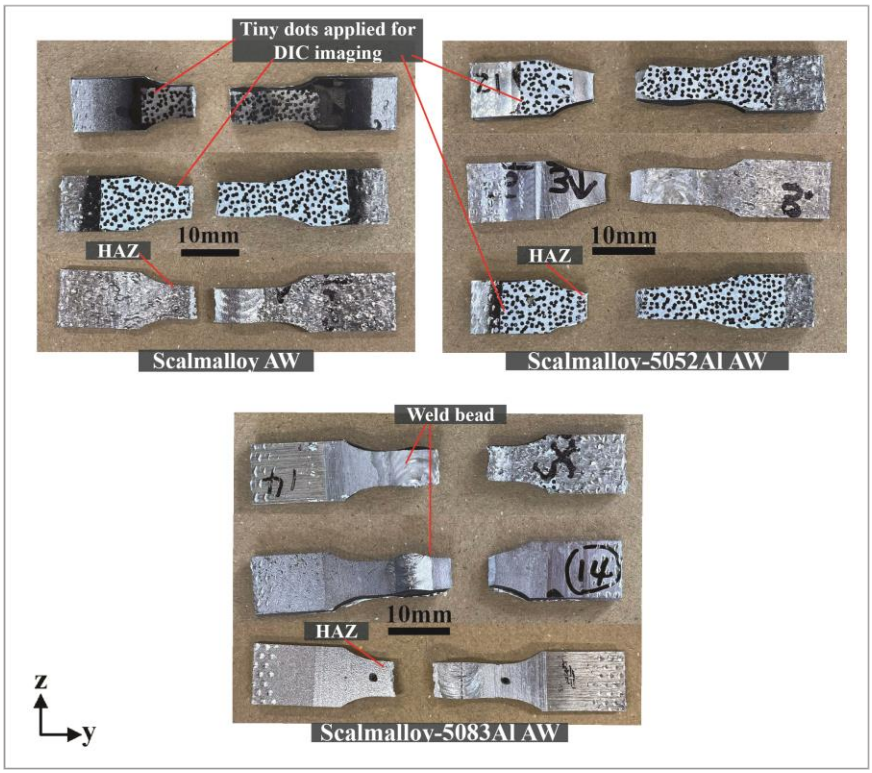

Fig. 6.13 Macrostructures of As Welded tensile samples

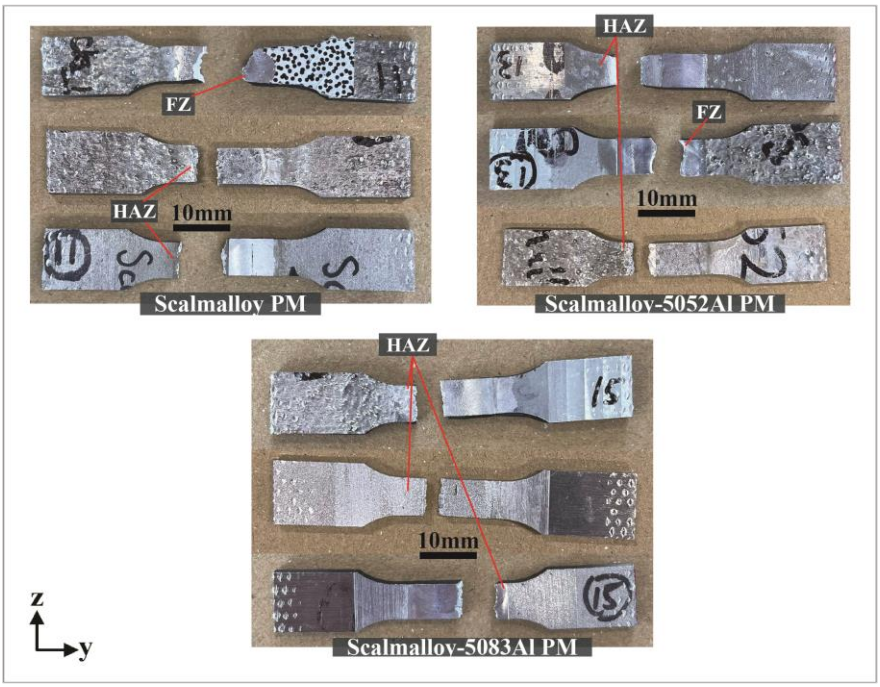

Fig. 6.14 Macrostructures of Post Machined tensile samples

Many pores, lack of fusion and shrinkage exist in the FZ, hence, the likelihood of fracture occurring in the FZ was increased for the PM samples as the excess material from the weld bead was removed and could no longer compensate for the defects present here.

Fig. 6.15 – 6.19 show the fracture micrographs of the welded joints. A large number of spherical pores are evenly distributed on the surface of the samples that fractured on the Scalmalloy HAZ side (Fig. 6.15, 6.17, and 6.18), further confirming the high porosity seen in the optical micrographs of the welded joints, shown in Fig 6.1 - 6.3. Porosity and some cracking and lack of fusion are also observed. The microporosity (<2µm) observed are common in additively manufactured samples as it can develop during the additive manufacturing process by gas entrapment around the melt pool and from incomplete melting and solidification due to insufficient energy input during the SLM process (Aboulkhair et al., 2019; Galy, Le Guen, et al., 2018; Olakanmi et al., 2015; B. Zhang et al., 2017). However, the larger pores (>5µm) are most likely due to hydrogen induced porosity as each pore, at higher magnification, has a smooth internal surface indicative of gas entrapment and would be consistent with findings from Weingarten et al. (2015). Fig. 6.15 and 6.17 show local ductile fracture mechanism as stress raisers occurred at each pore when the tensile load was applied. Cracking was preferentially formed at the pores under maximum stress and propagated to adjacent pores(C. Zhang et al., 2019). Higher magnifications of the fracture surfaces show numerous elongated dimples suggesting that the tensile load does not travel through the pores, but rather through the aluminium matrix and the grain boundaries. Tearing edges are not evident on the fracture surface as well. Hence, a mixture of both ductile and brittle fracture mode was observed.

Fig. 6.16 shows the fracture surface of the Scalmalloy-5052Al AW welded joint. This fracture occurred on the 5052l HAZ side and shows no obvious pores in line with the Fig. 6.2. The fracture surface is also deformed and is slightly protruded outwards. At higher magnification, numerous dimples are observed and are less than 5µm in size and are fairly round. These characteristics are indicative of a ductile fracture consistent with 5052Al alloy reported to possess low to medium tensile strength and high ductility (Santos Junior et al., 2016).

The micrographs of the PM samples that fractured in the HAZ are shown in Fig. G.8 and G.9 in Appendix G and displayed similar fracture characteristics as the AW samples (Fig. 6.15 - 6.17) as the only difference between these samples was a smaller cross-sectional, no stress concentrations due to the weld bead, and exposed pores that could move the failure location. Examples of a change in failure location can be seen in two PM samples that fractured in the FZ shown in Fig. 6.18 and 6.19. In these figures, incomplete melting and lack of fusion are observed in the centre (FZ) of the weld for both the Scalmalloy and Scalmalloy-5052Al PM samples causing local stress concentrations due to the defects consistent with the DIC analysis shown in Fig. 6.12. These defects are most likely the result of low heat input during the welding process and a slow welding speed. Furthermore, the fracture surfaces of the Scalmalloy PM and the Scalmalloy-5052Al PM sample were deformed with evenly distributed pores. Some dimples were visible on both PM samples indicative of a local ductile fracture mechanism (Cui et al., 2022),

similar to the samples described earlier (Fig. 6.15 and 6.17). The fracture analysis of each condition is consistent with the corresponding tensile results. It appears the low elongation in the PM samples would result in a brittle fracture, but in reality, it is a ductile fracture that has prematurely fractured due to the many defects within the FZ and HAZ. The AW samples also show ductile fracture consistent with the higher elongations at fracture, however, it is clear that the increased elongation is due to the excess material at the cross section of the tensile sample (weld bead). Please note that additional fracture micrographs of each sample are provided in Appendix G from Fig. G.8 – G.9.

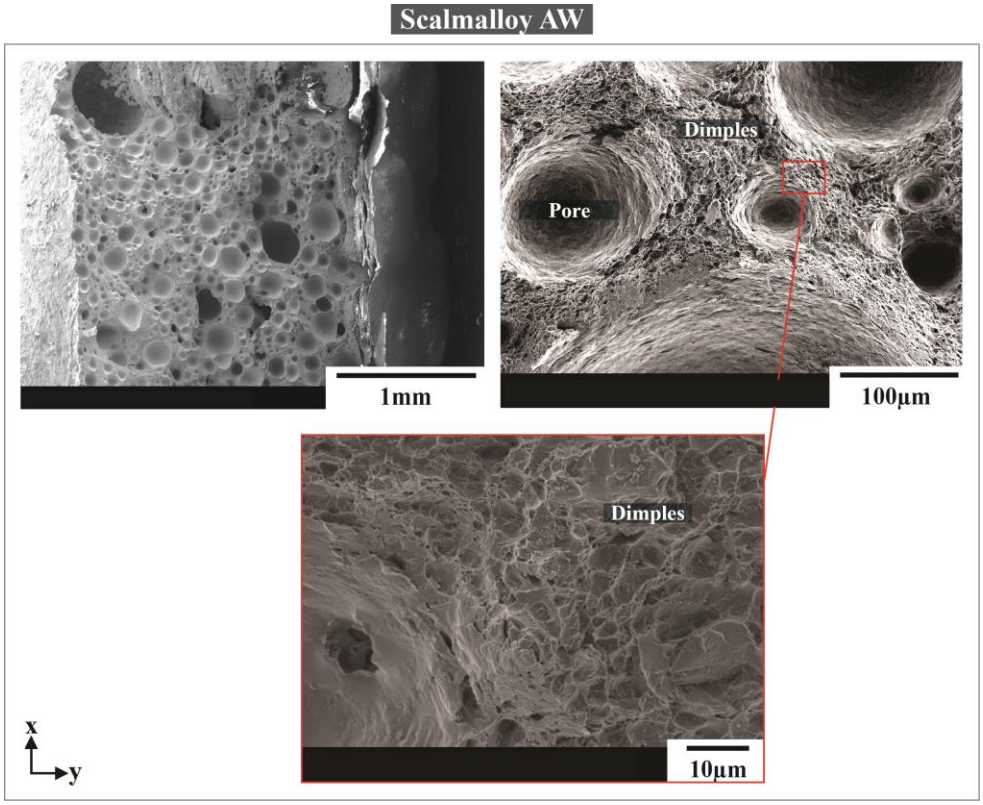

Fig. 6.15 Fracture surfaces and fractured samples for Scalmalloy as welded joint

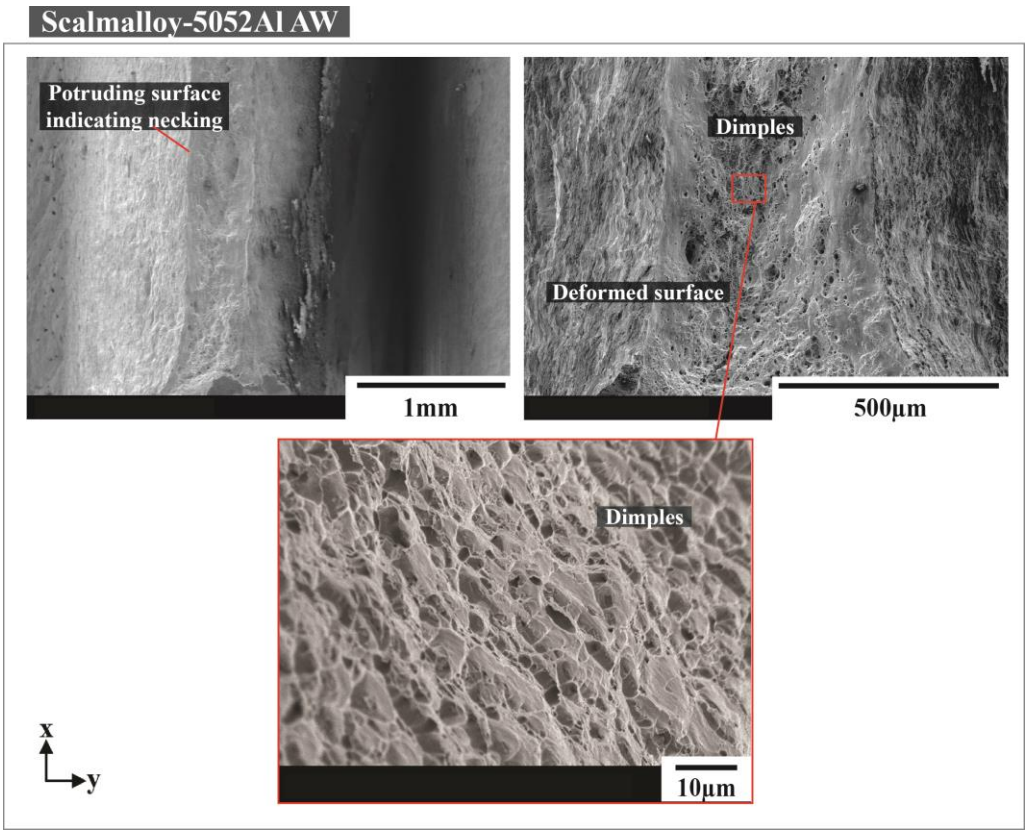

Fig. 6.16 Fracture surfaces and fractured samples for Scalmalloy-5052Al as welded joint

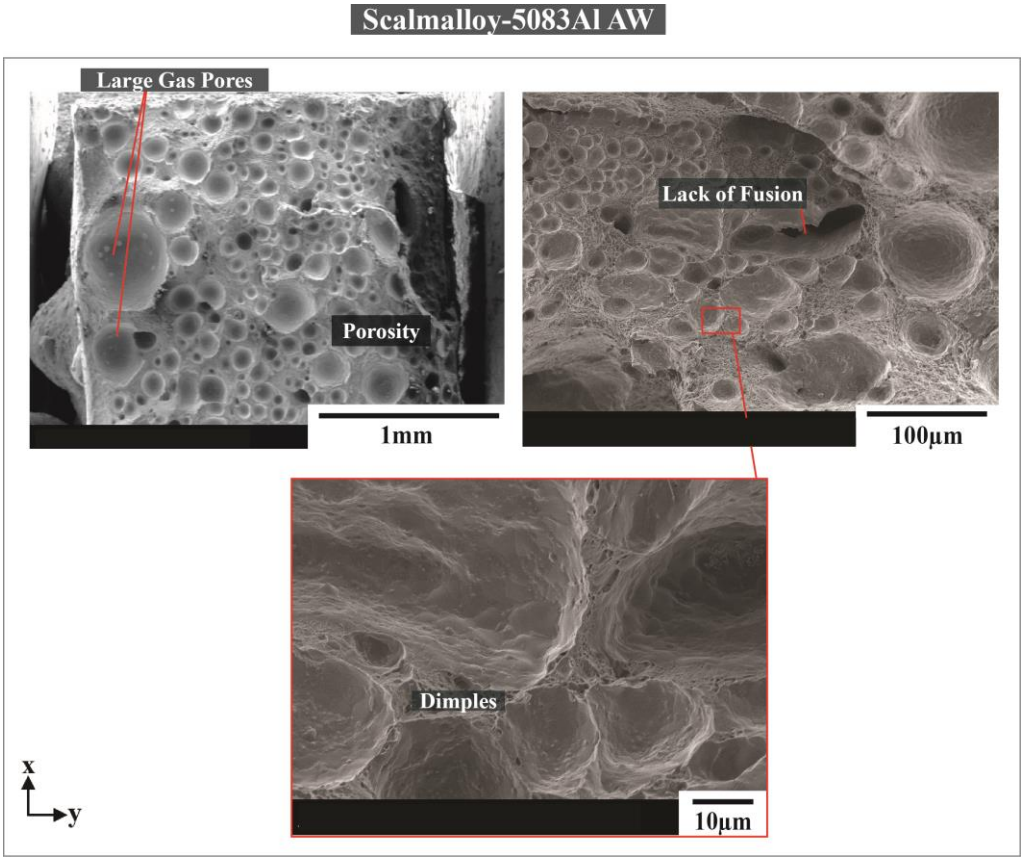

Fig. 6.17 Fracture surfaces and fractured samples for Scalmalloy-5083Al as welded joint

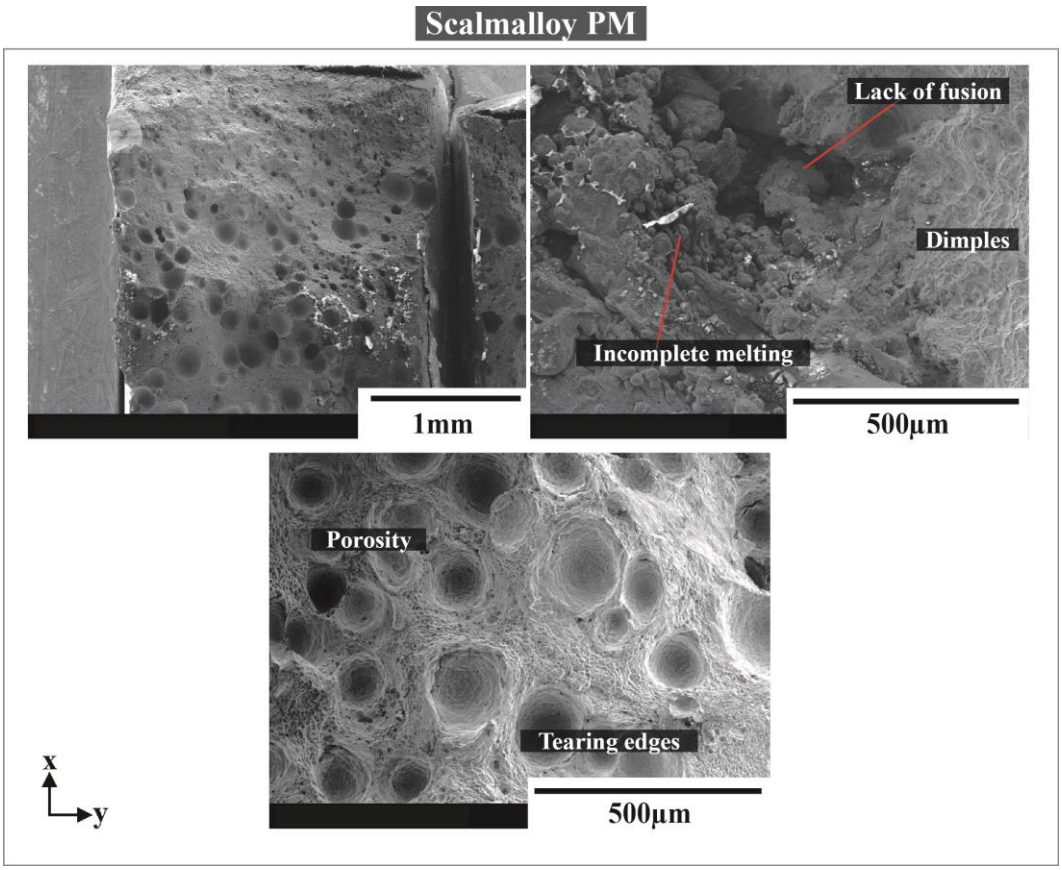

Fig. 6.18 Fracture surfaces and fractured samples for Scalmalloy post machined welded joint

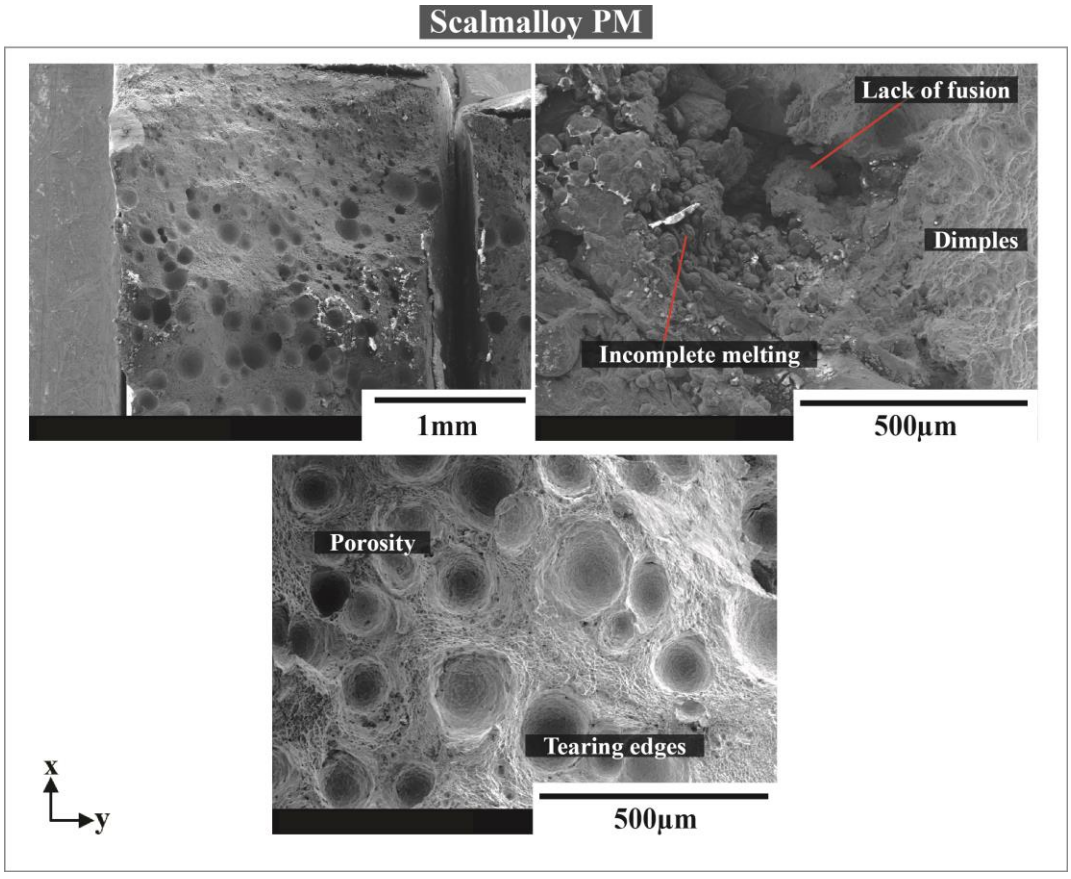

Fig. 6.19 Fracture surfaces and fractured samples for Scalmalloy-5052Al post machined welded joint

6.4 Summary

In this chapter, Scalmalloy samples were welded to extruded aluminium alloys and Scalmalloy samples using GTAW employing standard welding parameters used for conventionally manufactured aluminium alloys. The reported mechanical properties were poor compared to their BM counterparts. Microhardness was inconsistent compared to Scalmalloy BM hardness and the tensile properties (e.g., UTS, YS) of all the welded joints were very low compared to their BM substrates due to high porosity and process induced defects. Furthermore, for a weld to be considered successful, fracture must occur in the BM, but oftentimes occurs in the HAZ. For the work on hand, each either fractured in the HAZ or the FZ. These were primarily due to high porosity and defects evident in both the FZ and HAZ of the welded joints, hence, the structural integrity is compromised. It can be concluded that GTAW welded parameters for conventionally manufactured aluminium alloys cannot simply be transferred and used to weld Scalmalloy. However, the work on hand has proven it is feasible to use GTAW to join Scalmalloy to itself and extruded aluminum alloys, but further work should be done to prioritise minimising defects in order to yield a welded joint with mechanical properties better than or equal to its BM substrates.

Chapter 7 Conclusion and future recommendations

In this thesis, extensive work was carried out in the processing of Scalmalloy, and the effect that post processing treatments and gas tungsten arc welding had on its mechanical properties and microstructure. The following sections give a brief summary, conclusion, and future recommendations for each research topic presented in this thesis.

7.1 SLM process parameter study (Chapter 4)

The SLM process parameter study investigated the manufacturing of high relative density Scalmalloy samples in an *AM Renishaw 400 LBM* Machine using a high laser power of 400W, as opposed to the usual 200W commonly used according to the literature. Powder characterisation showed the powder used in this work had good processability characteristics. Three build jobs were carried out to ensure a full SLM parameter window was explored to be compared to findings reported by A. B. Spierings, Dawson, Dumitraschkewitz, et al. (2018). Archimedes density testing was used to measure relative density of each sample along with the calculation of the metallographic density and microhardness testing was carried out to compare hardness between samples using different SLM process parameters. It was found that the behaviour of the relative density compared to energy volume density differed to expected findings from A. B. Spierings, Dawson, Dumitraschkewitz, et al. (2018), where the density decreased as the energy volume density increased. This discrepancy was thought to be due to differences in Scalmalloy powder composition, LBM machine, laser focus diameter and laser power. However, an optimal range for energy volume density was established as approximately 70J/mm^3 to 110J/mm^3 for an *AM Renishaw 400 LBM* Machine resulting in densities of up to or more than 99% with a productivity rate of double compared to the more commonly used laser power of 200W. Microhardness results for these samples also revealed the high potential for effective subsequent heat treatment and potential for good mechanical properties. Additionally, relative density did not appear to be influenced by the position or layout on the build platform resulting in high reproducibility characteristics. Future recommendations are as follows:

- modifying SLM process parameters to minimize surface roughness, while also measuring its influence on mechanical properties
- investigating the shielding gas flow to determine whether this has an effect on relative densities.

The above future recommendations were not undertaken due to time constraints, software issues and material and manufacturing limitations.

7.2 Cold rolling and heat treatment study (Chapter 5)

Optimal SLM parameters developed in the SLM parameter study were employed to manufacture Scalmalloy samples. These samples were subject to cold rolling and heat treatment and a combination of both (where the abbreviations for each heat treatment condition are given in Table 3-5). Microstructural analysis showed that process induced porosity occurred on all samples as expected for additively manufactured materials and the layer-by-layer microstructural pattern occurring from the additive manufacturing process was prominent in all samples. Additionally, other process induced defects, such as lack of fusion and cracking, were present on some samples. The heat-treated conditions showed the precipitation of many second phase particles, especially for the AB+HT1 condition, where the second phase particles appeared to grow slightly when heat treated using HT2 and HT3 assumed to be due to overageing. This is confirmed by the tensile and hardness properties that showed a large increase for the HT1 condition and a slight increase for HT2 and HT3 when compared to the AB condition. When the AB condition was cold rolled, the layer-by-layer microstructural pattern appeared flattened, and the weld pool was elongated in the direction of rolling. It also appeared that second phase particles were present after rolling assumed to be due to the high dislocation density induced through plastic deformation confirmed by the increased tensile and hardness properties compared to the AB condition. The combination of heat treatment and cold rolling showed precipitation of second phase particles and the removal of residual stresses from the plastic deformation confirmed through the high tensile strength and high (or equal) elongation to the AB condition. EBSD revealed smallest average grain size appeared in the AB+HT1 condition, while the largest average grain sizes appeared in the heat treated and cold rolled conditions due to the cold rolling causing elongated grains. Overall, cold rolling and heat treatment had a favorable effect on Scalmalloy by increasing mechanical properties and improving its microstructure when compared to the AB condition. The heat treatment of 450^{o}C/1h (HT1) yielded optimum results for the work on hand and shows a different heat treatment can be used other than the standard 325^{o}C/4h as stated in the literature. Additionally, the work on hand has shown low reductions in thickness can produce higher mechanical properties than the AB condition and even better mechanical properties when the heat treatment of 450^{o}C/1h is applied after cold rolling. A comparison has also been reported between the microstructure and mechanical properties of extruded aluminium alloys to that of Scalmalloy to establish a baseline. However, further work may include the following:

- carrying out fatigue testing to determine the effect of cyclic stresses on the as built, heat treated and cold rolled conditions
- investigating the effect of shot peening on the mechanical and microstructural properties of Scalmalloy
- performing further testing such as transmission electron microscopy and further EBSD mapping on all conditions to acquire more raw data for further analysis

The above future recommendations were not undertaken in the wok on hand due to time constraints and no access to the appropriate equipment and unavailable technologies and software.

7.3 Gas tungsten arc welding of Scalmalloy study (Chapter 6)

Gas tungsten arc welding was carried out to weld Scalmalloy to itself, Scalmalloy to 5052Al and Scalmalloy to 5083Al using standard welding parameters for conventionally manufactured aluminium alloys. Each sample was tensile tested with DIC in the as welded (AW; weld bead was left intact) and the post machined (PM; weld bead was removed) conditions. Microhardness was also carried out perpendicular to the weld surface to determine and compare the hardness from the base metal (BM) to heat affected zone (HAZ) and finally to the fusion zone (FZ). The microstructure showed that all samples had high porosity in the FZ, little to no porosity in the extruded aluminum alloys BM and HAZ, and high porosity in the Scalmalloy FZ and HAZ with visible cracking and lack of fusion likely due to the hydrogen content present within the Scalmalloy powder being released during the welding process as the welding temperatures was assumed to be higher than 550^{o}C. Tensile testing results showed that AW samples generally had higher elongation and lower tensile strengths, while PM samples had higher tensile strengths and lower elongations. The low tensile strengths in the AW sample was assumed to be due to the non-normal stress occurring due to its abnormal geometry, and the high elongations were thought to be due to the excess material from the weld bead causing fracture to be delayed. Vice versa, normal stress occurred in the PM sample as it had uniform geometry leading to much higher tensile strengths, however lower elongations are assumed to be due to a higher porosity-percentage compared to the AW samples and the removal of excess material (weld bead). Microhardness testing showed the lowest hardness values occurred in the FZ and the highest values occurred in the BM due to the supersaturated solid solution occurring in the FZ along with defects such as cracking and high porosity. The resulting welded joints has poor structural integrity showing that it is a challenge to weld additively manufactured components together, and to conventionally manufactured components, where standard welding parameters cannot be simply transferred from a conventionally manufactured aluminium alloy to an additively manufactured one. However, this work has proven that it is feasible to weld Scalmalloy to itself and other conventionally manufactured aluminium alloys and would be very beneficial to reduce manufacturing costs and size limitations in additive manufacturing and further work should be conducted to produce a better welded joint. Future recommendations include the following:

- modification of welding parameters to minimise porosity and increase mechanical properties such as using a different filler wire closer to Scalmalloy composition or having traces of scandium and zirconium
- investigating whether autogenous welding performs better than using a filler metal
- investigating the effect heat treatment may have on the welded joints
- ensuring the weld pool is kept as small as possible to minimise the release of hydrogen gas within the fusion zone minimising porosity

The above future recommendations were not undertaken in the work on hand due to time constraints, resource constraints, no access to necessary technologies and welding equipment.

References

Aboulkhair, N. T., Simonelli, M., Parry, L., Ashcroft, I., Tuck, C., & Hague, R. (2019). 3D printing of Aluminium alloys: Additive Manufacturing of Aluminium alloys using selective laser melting. *Progress in Materials Science, 106*, 100578. doi:https://doi.org/10.1016/j.pmatsci.2019.100578

Aiura, T., Sugawara, N., & Miura, Y. (2000). The effect of scandium on the as-homogenized microstructure of 5083 alloy for extrusion. *Materials Science and Engineering: A, 280*(1), 139-145. doi:https://doi.org/10.1016/S0921-5093(99)00680-2

Akhtar, N., Afzal, M., Khan, M. A., Hussain, M., & Ali, M. N. (2017, 10-14 Jan. 2017). *Assessment of cold deformation effects on yield-to-tensile ratio and dimensional stability of an aluminium alloy extruded tube.* Paper presented at the 2017 14th International Bhurban Conference on Applied Sciences and Technology (IBCAST).

Algendy, A. Y., Liu, K., & Chen, X. (2020). *Formation of intermetallic phases during solidification in Al-Mg-Mn 5xxx alloys with various Mg levels.* Paper presented at the MATEC Web of Conferences.

Arunkumar, D., & Subbaiah, K. (2019, 2019). *Effect of Continuous and Pulsed Current Tungsten Inert Gas Welding of Cast Al–Mg–Sc Alloy.* Paper presented at the Advances in Manufacturing Processes, Singapore.

Ashkenazi, D. (2019). How aluminum changed the world: A metallurgical revolution through technological and cultural perspectives. *Technological Forecasting and Social Change, 143*, 101-113. doi:https://doi.org/10.1016/j.techfore.2019.03.011

Aversa, A., Marchese, G., Saboori, A., Bassini, E., Manfredi, D., Biamino, S., . . . Lombardi, M. (2019). New Aluminum Alloys Specifically Designed for Laser Powder Bed Fusion: A Review. *Materials (Basel), 12*(7). doi:10.3390/ma12071007

Awd, M., Tenkamp, J., Hirtler, M., Siddique, S., Bambach, M., & Walther, F. (2017). Comparison of Microstructure and Mechanical Properties of Scalmalloy((R)) Produced by Selective Laser Melting and Laser Metal Deposition. *Materials (Basel), 11*(1). doi:10.3390/ma11010017

Azlin, M., Ilyas, R., Zuhri, M., Sapuan, S., Harussani, M., Sharma, S., . . . Afiqah, A. (2022). 3D printing and shaping polymers, composites, and nanocomposites: a review. *Polymers, 14*(1), 180.

Beckmann, F., & Emmelmann, C. (2019). *Optimization of the weldability of laser additive manufactured aluminum by means of hydrogen minimization in the component and welding parameter optimization.* Paper presented at the Lasers in Manufacturing Conference.

Best, J., Maeder, X., Michler, J., & Spierings, A. (2018). Mechanical Anisotropy Investigated in the Complex SLM-Processed Sc- and Zr-Modified Al–Mg Alloy Microstructure. *Advanced Engineering Materials, 21*. doi:10.1002/adem.201801113

Błachnio, J., Kułaszka, A., Chalimoniuk, M., & Woźny, P. (2016). Exemplification of Tomographic Method to Evaluate the Quality of Welded Joints Made from EN 5754-H22 Alloy. *Research Works of Air Force Institute of Technology, 39*(1), 65-78. doi:10.1515/afit-2016-0018

Braun, M., Schubnell, J., Sarmast, A., Subramanian, H., Reissig, L., Altenhöner, F., . . . Ehlers, S. (2023). Mechanical behavior of additively and conventionally manufactured 316L stainless steel plates joined by gas metal arc welding. *Journal of Materials Research and Technology, 24*, 1692-1705. doi:https://doi.org/10.1016/j.jmrt.2023.03.080

Callister, W. D. (2014). *Materials Science and Engineering : An Introduction* (Vol. 9th edition William D. Callister, Jr. Department Of Metallurgical Engineering, the University Of Uta). Hoboken, NJ: Wiley.

Çetkin, E., Çelik, Y. H., & Temiz, Ş. (2019). Effect of welding parameters on microstructure and mechanical properties of AA7075/AA5182 alloys joined by TIG and MIG welding methods. *Journal of the Brazilian Society of Mechanical Sciences and Engineering, 42*(1), 34. doi:10.1007/s40430-019-2119-7

Chaudhury, Z., Hailat, M., Liu, Y., & Newaz, G. (2010). Aluminum-based composites reinforced with SiC particles and NiTi fibers: influence of fiber dimensions and aging time on mechanical properties. *Journal of Materials Science, 46*(6), 1945-1955. doi:10.1007/s10853-010-5030-2

Cheng, J., Song, G., Zhang, Z., Khan, M. S., Liu, Z., & Liu, L. (2022). Improving heat-affected zone softening of aluminum alloys by in-situ cooling and post-weld rolling. *Journal of Materials Processing Technology, 306*, 117639. doi:https://doi.org/10.1016/j.jmatprotec.2022.117639

Chernyshova, P., Guraya, T., Singamneni, S., Zhu, T., & Chen, Z. W. (2021). Fatigue Crack Growth Behavior of Al-4.5Mg-0.6Sc-0.3Zr Alloy Processed by Laser Powder Bed Fusion. *Journal of Materials Engineering and Performance, 30*(9), 6743-6751. doi:10.1007/s11665-021-05989-6

Cherry, J. A., Davies, H. M., Mehmood, S., Lavery, N. P., Brown, S. G. R., & Sienz, J. (2014). Investigation into the effect of process parameters on microstructural and physical properties of 316L stainless steel parts by selective laser melting. *The International Journal of Advanced Manufacturing Technology, 76*(5-8), 869-879. doi:10.1007/s00170-014-6297-2

Chituc, C.-M. (2017). XML interoperability standards for seamless communication: An analysis of industry-neutral and domain-specific initiatives. *Computers in Industry, 92-93*, 118-136. doi:https://doi.org/10.1016/j.compind.2017.06.010

Cui, L., Peng, Z., Chang, Y., He, D., Cao, Q., Guo, X., & Zeng, Y. (2022). Porosity, microstructure and mechanical property of welded joints produced by different laser welding processes in selective laser melting AlSi10Mg alloys. *Optics & Laser Technology, 150*, 107952. doi:https://doi.org/10.1016/j.optlastec.2022.107952

Curtis, S., de los Rios, E. R., Rodopoulos, C. A., & Levers, A. (2003). Analysis of the effects of controlled shot peening on fatigue damage of high strength aluminium alloys. *International Journal of Fatigue, 25*(1), 59-66. doi:https://doi.org/10.1016/S0142-1123(02)00049-X

Davydov, V. G., Rostova, T. D., Zakharov, V. V., Filatov, Y. A., & Yelagin, V. I. (2000). Scientific principles of making an alloying addition of scandium to aluminium alloys. *Materials Science and Engineering: A, 280*(1), 30-36. doi:https://doi.org/10.1016/S0921-5093(99)00652-8

DebRoy, T., Wei, H. L., Zuback, J. S., Mukherjee, T., Elmer, J. W., Milewski, J. O., . . . Zhang, W. (2018). Additive manufacturing of metallic components – Process, structure and properties. *Progress in Materials Science, 92*, 112-224. doi:10.1016/j.pmatsci.2017.10.001

Fuller, C. B., Seidman, D. N., & Dunand, D. C. (2003). Mechanical properties of Al(Sc,Zr) alloys at ambient and elevated temperatures. *Acta Materialia, 51*(16), 4803-4814. doi:https://doi.org/10.1016/S1359-6454(03)00320-3

Galy, C., Guen, E., Lacoste, E., & Arvieu, C. (2018). Main defects observed in aluminum alloy parts produced by SLM: From causes to consequences. *Additive Manufacturing, 22*. doi:10.1016/j.addma.2018.05.005

Galy, C., Le Guen, E., Lacoste, E., & Arvieu, C. (2018). Main defects observed in aluminum alloy parts produced by SLM: From causes to consequences. *Additive Manufacturing, 22*, 165-175. doi:10.1016/j.addma.2018.05.005

Gibson, I., Rosen, D. W., & Stucker, B. (2010). Powder Bed Fusion Processes. In I. Gibson, D. W. Rosen, & B. Stucker (Eds.), *Additive Manufacturing Technologies: Rapid Prototyping to Direct Digital Manufacturing* (pp. 120-159). Boston, MA: Springer US.

Glazoff, M. V., Khvan, A. V., Zolotorevsky, V. S., Belov, N. A., & Dinsdale, A. T. (2019a). Chapter 1 - Phase Diagrams for Binary and Multicomponent Aluminum Systems. In M. V. Glazoff, A. V. Khvan, V. S. Zolotorevsky, N. A. Belov, & A. T. Dinsdale (Eds.), *Casting Aluminum Alloys (Second Edition)* (pp. 1-131): Butterworth-Heinemann.

Glazoff, M. V., Khvan, A. V., Zolotorevsky, V. S., Belov, N. A., & Dinsdale, A. T. (2019b). Chapter 2 - Structure and Microstructure of Aluminum Alloys in As-Cast State. In M. V. Glazoff, A. V. Khvan, V. S. Zolotorevsky, N. A. Belov, & A. T. Dinsdale (Eds.), *Casting Aluminum Alloys (Second Edition)* (pp. 133-234): Butterworth-Heinemann.

Griffiths, V., Scanlan, J. P., Eres, M. H., Martinez-Sykora, A., & Chinchapatnam, P. (2019). Cost-driven build orientation and bin packing of parts in Selective Laser Melting (SLM). *European Journal of Operational Research, 273*(1), 334-352. doi:https://doi.org/10.1016/j.ejor.2018.07.053

Hakem, M., Lebaili, S., Miroud, J., Bentaleb, A., & Toukali, S. (2012). Welding and characterization of 5083 aluminum alloy. *Metallofizika, 5*, 23-25.

Hanzl, P., Zetek, M., Bakša, T., & Kroupa, T. (2015). The Influence of Processing Parameters on the Mechanical Properties of SLM Parts. *Procedia Engineering, 100*, 1405-1413. doi:10.1016/j.proeng.2015.01.510

Hitzler, L., Hirsch, J., Merkel, M., & Hall, W. (2017). Position dependent surface quality in Selective Laser Melting. *Materialwissenschaft und Werkstofftechnik, 48*, 327-334. doi:10.1002/mawe.201600742

Hornbogen, E., & Starkejr, E. (1993). *Overview no. 102 Theory assisted design of high strength low alloy aluminum* (Vol. 41).

Jägle, E. A., Sheng, Z., Wu, L., Lu, L., Risse, J., Weisheit, A., & Raabe, D. (2016). Precipitation Reactions in Age-Hardenable Alloys During Laser Additive Manufacturing. *JOM, 68*(3), 943-949. doi:10.1007/s11837-015-1764-2

Jaya Prasad, V., Rao, N. M., Kamaluddin, S., & Surya, K. V. P. (2018). A Study of Microstructure and Tribological Properties of Al 5083 MMC Processed by Direct Extrusion. *Materials Today: Proceedings, 5*(2, Part 2), 8232-8240. doi:https://doi.org/10.1016/j.matpr.2017.11.513

Jeng, Y.-R., Lee, J.-T., Hwu, Y.-J., Liu, L.-C., & Lu, C.-Y. (2020). Effects of operation parameters of cold rolling on surface finish of aluminum. *Tribology International, 148*, 106321. doi:https://doi.org/10.1016/j.triboint.2020.106321

Kaiser, M. S., Datta, S., Roychowdhury, A., & Banerjee, M. K. (2014). Effect of prior cold work on tensile properties of Al-6Mg alloy with minor scandium additions. *Canadian Metallurgical Quarterly, 53*(4), 486-493. doi:10.1179/1879139514y.0000000142

Kogtenkova, O., Straumal, B. B., Mazilkin, A., Czeppe, T., & Zieba, P. Phase Transformations in the Al-Mg Alloys Driven by High-Pressure Torsion. *PHYSICA STATUS SOLIDI B-BASIC SOLID STATE PHYSICS*. doi:10.1002/pssb.202100210

Kou, S. (2003). Welding metallurgy. *New Jersey, USA, 431*(446), 223-225.

Koutny, D., Skulina, D., Pantělejev, L., Paloušek, D., Lenczowski, B., Palm, F., & Nick, A. (2018). Processing of Al-Sc aluminum alloy using SLM technology. *Procedia CIRP, 74*, 44-48. doi:https://doi.org/10.1016/j.procir.2018.08.027

Kvande, H. (2008). Two hundred years of aluminum ... or is it aluminium? *JOM, 60*(8), 23-24. doi:10.1007/s11837-008-0102-3

Lei, X., Deng, Y., Peng, Y., Yin, Z., & Xu, G. (2013). Microstructure and Properties of TIG/FSW Welded Joints of a New Al-Zn-Mg-Sc-Zr Alloy. *Journal of Materials Engineering and Performance, 22*(9), 2723-2729. doi:10.1007/s11665-013-0577-0

Li, H., Zou, J., Yao, J., & Peng, H. (2017). The effect of TIG welding techniques on microstructure, properties and porosity of the welded joint of 2219 aluminum alloy. *Journal of Alloys and Compounds, 727*, 531-539. doi:https://doi.org/10.1016/j.jallcom.2017.08.157

Li, N., Huang, S., Zhang, G., Qin, R., Liu, W., Xiong, H., . . . Blackburn, J. (2019). Progress in additive manufacturing on new materials: A review. *Journal of Materials Science & Technology, 35*(2), 242-269. doi:10.1016/j.jmst.2018.09.002

Li, R., Chen, H., Zhu, H., Wang, M., Chen, C., & Yuan, T. (2019). Effect of aging treatment on the microstructure and mechanical properties of Al-3.02Mg-0.2Sc-0.1Zr alloy printed by selective laser melting. *Materials & Design, 168*, 107668. doi:10.1016/j.matdes.2019.107668

Li, R., Wang, M., Yuan, T., Song, B., Chen, C., Zhou, K., & Cao, P. (2017). Selective laser melting of a novel Sc and Zr modified Al-6.2 Mg alloy: Processing, microstructure, and properties. *Powder Technology, 319*, 117-128. doi:10.1016/j.powtec.2017.06.050

Liu, S., Zhu, H., Peng, G., Yin, J., & Zeng, X. (2018). Microstructure prediction of selective laser melting AlSi10Mg using finite element analysis. *Materials & Design, 142*, 319-328. doi:https://doi.org/10.1016/j.matdes.2018.01.022

Liu, Y., Wang, W., Xie, J., Sun, S., Wang, L., Qian, Y., . . . Wei, Y. (2012). Microstructure and mechanical properties of aluminum 5083 weldments by gas tungsten arc and gas metal arc welding. *Materials Science and Engineering: A, 549*, 7-13. doi:https://doi.org/10.1016/j.msea.2012.03.108

Ma, R., Peng, C., Cai, Z., Wang, R., Zhou, Z., Li, X., & Cao, X. (2020a). Enhanced strength of the selective laser melted Al-Mg-Sc-Zr alloy by cold rolling. *Materials Science and Engineering: A, 775*, 138975. doi:https://doi.org/10.1016/j.msea.2020.138975

Ma, R., Peng, C., Cai, Z., Wang, R., Zhou, Z., Li, X., & Cao, X. (2020b). Manipulating the microstructure and tensile properties of selective laser melted Al–Mg-Sc-Zr alloy through heat treatment. *Journal of Alloys and Compounds, 831*, 154773. doi:https://doi.org/10.1016/j.jallcom.2020.154773

Maamoun, A. H., Xue, Y. F., Elbestawi, M. A., & Veldhuis, S. C. (2018). Effect of Selective Laser Melting Process Parameters on the Quality of Al Alloy Parts: Powder Characterization, Density, Surface Roughness, and Dimensional Accuracy. *Materials (Basel, Switzerland), 11*(12), 2343. doi:10.3390/ma11122343

Mäkikangas, J., Rautio, T., Mustakangas, A., & Mäntyjärvi, K. (2019). Laser welding of AlSi10Mg aluminium-based alloy produced by Selective Laser Melting (SLM). *Procedia Manufacturing, 36*, 88-94. doi:https://doi.org/10.1016/j.promfg.2019.08.013

Malopheyev, S., Kulitskiy, V., & Kaibyshev, R. (2017). Deformation structures and strengthening mechanisms in an AlMgScZr alloy. *Journal of Alloys and Compounds, 698*, 957-966. doi:https://doi.org/10.1016/j.jallcom.2016.12.289

Mansourinejad, M., & Mirzakhani, B. (2012). Influence of sequence of cold working and aging treatment on mechanical behaviour of 6061 aluminum alloy. *Transactions of Nonferrous Metals Society of China, 22*(9), 2072-2079. doi:10.1016/s1003-6326(11)61430-1

Marquis, E. A., & Seidman, D. N. (2001). Nanoscale structural evolution of Al3Sc precipitates in Al(Sc) alloys. *Acta Materialia, 49*(11), 1909-1919. doi:https://doi.org/10.1016/S1359-6454(01)00116-1

Matilainen, V.-P., Pekkarinen, J., & Salminen, A. (2016). Weldability of Additive Manufactured Stainless Steel. *Physics Procedia, 83*, 808-817. doi:10.1016/j.phpro.2016.08.083

Messler Jr, R. W. (2008). *Principles of welding: processes, physics, chemistry, and metallurgy*: John Wiley & Sons.

Michler, M., Hollmann, P., Zenker, R., & Buchwalder, A. (2021). Investigation of Pore Reduction in Hybrid Joints of Conventionally and Additively Manufactured AlSi10Mg Using Electron Beam Welding. *Advanced Engineering Materials, 23*(6), 2001325. doi:https://doi.org/10.1002/adem.202001325

Murray, J. L. (1998). The Al-Sc (aluminum-scandium) system. *Journal of Phase Equilibria, 19*(4), 380. doi:10.1361/105497198770342120

Musekamp, J., Reiber, T., Hoche, H. C., Oechsner, M., Weigold, M., & Abele, E. (2021). Influence of LPBF-Surface Characteristics on Fatigue Properties of Scalmalloy®. *Metals, 11*(12), 1961.

Natali, S., Brotzu, A., & Pilone, D. (2019). Comparison between Mechanical Properties and Structures of a Rolled and a 3D-Printed Stainless Steel. *Materials (Basel), 12*(23). doi:10.3390/ma12233867

Ning, A.-l., Liu, Z.-y., & Zeng, S.-m. (2006). Effect of large cold deformation on characteristics of age-strengthening of 2024 aluminum alloys. *Transactions of Nonferrous Metals Society of China, 16*(5), 1121-1128. doi:https://doi.org/10.1016/S1003-6326(06)60388-9

Olakanmi, E. O., Cochrane, R. F., & Dalgarno, K. W. (2015). A review on selective laser sintering/melting (SLS/SLM) of aluminium alloy powders: Processing, microstructure, and properties. *Progress in Materials Science, 74*, 401-477. doi:https://doi.org/10.1016/j.pmatsci.2015.03.002

Olaru, P. (2011). *Metallurgical aspects regarding wire welding / cladding of leveler hot rolling-rolls for performant working*.

Palm, F., Leuschner, R., Schubert, T., & Kieback, B. (2010). *Scalmalloy® = A Unique High Strength AlMgSc Type Material Concept Processed by Innovative Technologies for Aerospace Applications*.

Panagopoulos, C. N., & Georgiou, E. P. (2010). Cold rolling and lubricated wear of 5083 aluminium alloy. *Materials & Design, 31*(3), 1050-1055. doi:https://doi.org/10.1016/j.matdes.2009.09.056

Pasang, T., Kirchner, A., Jehring, U., Aziziderouei, M., Tao, Y., Jiang, C. P., . . . Aisyah, I. S. (2019). Microstructure and Mechanical Properties of Welded Additively Manufactured Stainless Steels SS316L. *Metals and Materials International, 25*(5), 1278-1286. doi:10.1007/s12540-019-00264-9

Pasang, T., Tavlovich, B., Yannay, O., Jackson, B., Fry, M., Tao, Y., . . . Misiolek, W. Z. (2021). Directionally-Dependent Mechanical Properties of Ti6Al4V Manufactured by Electron Beam Melting (EBM) and Selective Laser Melting (SLM). *Materials (Basel), 14*(13). doi:10.3390/ma14133603

Polmear, I., Qian, M., StJohn, D., & Nie, J.-F. (2017). *Light Alloys : Metallurgy of the Light Metals*. Oxford, UNITED KINGDOM: Elsevier Science & Technology.

Qin, Z., Kang, N., Zhang, F., Wang, Z., Wang, Q., Chen, J., . . . Huang, W. (2021). Role of defects on the high cycle fatigue behavior of selective laser melted Al–Mg–Sc–Zr alloy. *International Journal of Fracture*. doi:10.1007/s10704-021-00593-0

Rabinovich, D. (2013). The allure of aluminium. *Nature Chemistry, 5*(1), 76-76. doi:10.1038/nchem.1535

Rao, A. C. U., Vasu, V., Govindaraju, M., & Srinadh, K. V. S. (2014). Influence of Cold Rolling and Annealing on the Tensile Properties of Aluminum 7075 Alloy. *Procedia Materials Science, 5*, 86-95. doi:10.1016/j.mspro.2014.07.245

Røyset, J., & Ryum, N. (2005). Kinetics and mechanisms of precipitation in an Al–0.2wt.% Sc alloy. *Materials Science and Engineering: A, 396*(1), 409-422. doi:https://doi.org/10.1016/j.msea.2005.02.015

Røyset, J., & Ryum, N. (2005). Scandium in aluminum alloys. *International Materials Reviews, 50*, 19-44. doi:10.1179/174328005X14311

Salvati, E., & Korsunsky, A. M. (2020). Micro-scale measurement & FEM modelling of residual stresses in AA6082-T6 Al alloy generated by wire EDM cutting. *Journal of Materials Processing Technology, 275*, 116373. doi:https://doi.org/10.1016/j.jmatprotec.2019.116373

Santos Junior, M., Machado, A., Falco Sales, W., Barrozo, M., & Ezugwu, E. (2016). Machining of aluminum alloys: a review. *The International Journal of Advanced Manufacturing Technology, 86*. doi:10.1007/s00170-016-8431-9

Schmidtke, K., Palm, F., Hawkins, A., & Emmelmann, C. (2011). Process and Mechanical Properties: Applicability of a Scandium modified Al-alloy for Laser Additive Manufacturing. *Physics Procedia, 12*, 369-374. doi:10.1016/j.phpro.2011.03.047

Schneller, W., Leitner, M., Leuders, S., Sprauel, J. M., Grün, F., Pfeifer, T., & Jantschner, O. (2021). Fatigue strength estimation methodology of additively manufactured metallic bulk material. *Additive Manufacturing, 39*, 101688. doi:https://doi.org/10.1016/j.addma.2020.101688

Shanavas, S., & Dhas, J. (2017). *Weldability of AA 5052 H32 aluminium alloy by TIG welding and FSW process: A comparative study.* Paper presented at the IOP Conf. Ser.: Mater. Sci. Eng.

Shankar, K., & Wu, W. (2002). Effect of welding and weld repair on crack propagation behaviour in aluminium alloy 5083 plates. *Materials & Design, 23*(2), 201-208. doi:https://doi.org/10.1016/S0261-3069(01)00059-0

Singh, M., & Singh, A. K. (2019). Performance investigation of magnetorheological finishing of rolls surface in cold rolling process. *Journal of Manufacturing Processes, 41*, 315-329. doi:https://doi.org/10.1016/j.jmapro.2019.04.007

Singh, S., Ramakrishna, S., & Singh, R. (2017). Material issues in additive manufacturing: A review. *Journal of Manufacturing Processes, 25*, 185-200. doi:10.1016/j.jmapro.2016.11.006

Sivaramakrishnan, C. (1995). Physical Metallurgy of Aluminium.

Spierings, A. B., Dawson, K., Dumitraschkewitz, P., Pogatscher, S., & Wegener, K. (2018). Microstructure characterization of SLM-processed Al-Mg-Sc-Zr alloy in the heat treated and HIPed condition. *Additive Manufacturing, 20*, 173-181. doi:https://doi.org/10.1016/j.addma.2017.12.011

Spierings, A. B., Dawson, K., Heeling, T., Uggowitzer, P. J., Schäublin, R., Palm, F., & Wegener, K. (2017). Microstructural features of Sc- and Zr-modified Al-Mg alloys processed by selective laser melting. *Materials & Design, 115*, 52-63. doi:https://doi.org/10.1016/j.matdes.2016.11.040

Spierings, A. B., Dawson, K., Kern, K., Palm, F., & Wegener, K. (2017). SLM-processed Sc- and Zr- modified Al-Mg alloy: Mechanical properties and microstructural effects of heat treatment. *Materials Science and Engineering: A, 701*, 264-273. doi:10.1016/j.msea.2017.06.089

Spierings, A. B., Dawson, K., Uggowitzer, P. J., & Wegener, K. (2018). Influence of SLM scan-speed on microstructure, precipitation of Al3Sc particles and mechanical properties in Sc- and Zr-modified Al-Mg alloys. *Materials & Design, 140*, 134-143. doi:10.1016/j.matdes.2017.11.053

Spierings, A. B., Dawson, K., Voegtlin, M., Palm, F., & Uggowitzer, P. J. (2016). Microstructure and mechanical properties of as-processed scandium-modified aluminium using selective laser melting. *CIRP Annals, 65*(1), 213-216. doi:10.1016/j.cirp.2016.04.057

Spierings, A. B., Schneider, M., & Eggenberger, R. (2011). Comparison of density measurement techniques for additive manufactured metallic parts. *Rapid Prototyping Journal, 17*(5), 380-386. doi:10.1108/13552541111156504

Strano, G., Hao, L., Everson, R. M., & Evans, K. E. (2013). Surface roughness analysis, modelling and prediction in selective laser melting. *Journal of Materials Processing Technology, 213*, 589-597.

Subbaiah, K. (2019, 2019). *Comparative Evaluation TIG and FS Welding of Cast Al–Mg–Sc Alloy.* Paper presented at the Advances in Manufacturing Processes, Singapore.

Sufiiarov, V. S., Popovich, A. A., Borisov, E. V., Polozov, I. A., Masaylo, D. V., & Orlov, A. V. (2017). The Effect of Layer Thickness at Selective Laser Melting. *Procedia Engineering, 174*, 126-134. doi:https://doi.org/10.1016/j.proeng.2017.01.179

Turangi, C., Haslich, F., & Pasang, T. (2020). *An Investigation of the Influence of Changing Energy Volume Densities to Produce a Complete Process Parameter Window for Selective Laser Melting of Scalmalloy*.

Turangi, C., Häslich, F., Schaefer, M., Nomani, J., Pasang, T., Jehring, U., & Weißgärber, T. (2022). *Mechanical properties and microstructure of cold-rolled Scalmalloy®(Al-4.5 Mg-0.6 Sc-0.3 Zr alloy) at a low reduction in thickness.* Paper presented at the Journal of Physics: Conference Series.

Varshney, D., & Kumar, K. (2021). Application and use of different aluminium alloys with respect to workability, strength and welding parameter optimization. *Ain Shams Engineering Journal, 12*(1), 1143-1152. doi:https://doi.org/10.1016/j.asej.2020.05.013

VDI. (2014). Additive Manufacturing Processes, Rapid Manufacturing—Basics, Definitions, Processes.

Vock, S., Klöden, B., Kirchner, A., Weißgärber, T., & Kieback, B. (2019). Powders for powder bed fusion: a review. *Progress in Additive Manufacturing*. doi:10.1007/s40964-019-00078-6

Waeselmann, N. (2012). *Structural transformations in complex perovskite-type relaxor and relaxor-based ferroelectrics at high pressures and temperatures.*

Wang, B., Chen, X.-h., Pan, F.-s., Mao, J.-j., & Fang, Y. (2015). Effects of cold rolling and heat treatment on microstructure and mechanical properties of AA 5052 aluminum alloy. *Transactions of Nonferrous Metals Society of China, 25*(8), 2481-2489. doi:https://doi.org/10.1016/S1003-6326(15)63866-3

Wang, B. B., Xie, G. M., Wu, L. H., Xue, P., Ni, D. R., Xiao, B. L., . . . Ma, Z. Y. (2021). Grain size effect on tensile deformation behaviors of pure aluminum. *Materials Science and Engineering: A, 820*, 141504. doi:https://doi.org/10.1016/j.msea.2021.141504

Wang, T., Huang, Y., Ma, Y., Wu, L., Yan, H., Liu, C., . . . Liu, W. (2021). Microstructure and mechanical properties of powder metallurgy 2024 aluminum alloy during cold rolling. *Journal of Materials Research and Technology, 15*, 3337-3348. doi:https://doi.org/10.1016/j.jmrt.2021.09.120

Wang, W., Cao, Z., Liu, K., Zhang, X., Zhou, K., & Ou, P. (2018). Fabrication and Mechanical Properties of Tungsten Inert Gas Welding Ring Welded Joint of 7A05-T6/5A06-O Dissimilar Aluminum Alloy. *Materials (Basel), 11*(7). doi:10.3390/ma11071156

Wang, Z., Lin, X., Kang, N., Hu, Y., Chen, J., & Huang, W. (2020). Strength-ductility synergy of selective laser melted Al-Mg-Sc-Zr alloy with a heterogeneous grain structure. *Additive Manufacturing, 34*, 101260. doi:https://doi.org/10.1016/j.addma.2020.101260

Weingarten, C., Buchbinder, D., Pirch, N., Meiners, W., Wissenbach, K., & Poprawe, R. (2015). Formation and reduction of hydrogen porosity during selective laser melting of AlSi10Mg. *Journal of Materials Processing Technology, 221*, 112-120. doi:https://doi.org/10.1016/j.jmatprotec.2015.02.013

Westermann, I., Pedersen, K. O., Furu, T., Børvik, T., & Hopperstad, O. S. (2014). Effects of particles and solutes on strength, work-hardening and ductile fracture of aluminium alloys. *Mechanics of Materials, 79*, 58-72. doi:10.1016/j.mechmat.2014.08.006

Wilkinson, A. J., & Britton, T. B. (2012). Strains, planes, and EBSD in materials science. *Materials Today, 15*(9), 366-376. doi:https://doi.org/10.1016/S1369-7021(12)70163-3

Wits, W. W., & Becker, J. M. J. (2015). Laser Beam Welding of Titanium Additive Manufactured Parts. *Procedia CIRP, 28*, 70-75. doi:https://doi.org/10.1016/j.procir.2015.04.013

Wong, K. V., & Hernandez, A. (2012). A Review of Additive Manufacturing. *ISRN Mechanical Engineering, 2012*, 1-10. doi:10.5402/2012/208760

Xu, G., Qian, J., Xiao, D., Deng, Y., Lu, L., & Yin, Z. (2016). Mechanical Properties and Microstructure of TIG and FSW Joints of a New Al-Mg-Mn-Sc-Zr Alloy. *Journal of Materials Engineering and Performance, 25*(4), 1249-1256. doi:10.1007/s11665-016-1942-6

Xu, P., Jiang, F., Meng, S., Yi, K., Jiang, J., Cao, Q., & Peng, Y. (2018). Microstructure and Mechanical Properties of Al-Mg-Sc-Zr Alloy Variable Polarity Plasma Arc Welding Joint. *Journal of Materials Engineering and Performance, 27*, 4783. doi:10.1007/s11665-018-3549-6

Yadroitsev, I., Gusarov, A., Yadroitsava, I., & Smurov, I. (2010). Single track formation in selective laser melting of metal powders. *Journal of Materials Processing Technology, 210*(12), 1624-1631. doi:https://doi.org/10.1016/j.jmatprotec.2010.05.010

Yap, C. Y., K. Chua, C., L. Dong, Z., H. Liu, Z., Q. Zhang, D., Loh, L. E., & Sing, S. L. (2015). *Review of selective laser melting: Materials and applications* (Vol. 2).

Ye, Z., Huang, J., Gao, W., Zhang, Y., Cheng, Z., Chen, S., & Yang, J. (2017). Microstructure and mechanical properties of 5052 aluminum alloy/mild steel butt joint achieved by MIG-TIG double-sided arc welding-brazing. *Materials & Design, 123*, 69-79. doi:https://doi.org/10.1016/j.matdes.2017.03.039

Yu, X., & Wang, L. (2018). T6 heat-treated AlSi10Mg alloys additive-manufactured by selective laser melting. *Procedia Manufacturing, 15*, 1701-1707.

Zahner, L. W. (2019). *Aluminum Surfaces : A Guide to Alloys, Finishes, Fabrication and Maintenance in Architecture and Art*. Newark, UNITED STATES: John Wiley & Sons, Incorporated.

Zakharov, V. V. (2003). Effect of Scandium on the Structure and Properties of Aluminum Alloys. *Metal Science and Heat Treatment, 45*(7), 246-253. doi:10.1023/A:1027368032062

Zhang, B., Li, Y., & Bai, Q. (2017). Defect Formation Mechanisms in Selective Laser Melting: A Review. *Chinese Journal of Mechanical Engineering, 30*(3), 515-527. doi:10.1007/s10033-017-0121-5

Zhang, C., Bao, Y., Zhu, H., Nie, X., Zhang, W., Zhang, S., & Zeng, X. (2019). A comparison between laser and TIG welding of selective laser melted AlSi10Mg. *Optics & Laser Technology, 120*, 105696. doi:https://doi.org/10.1016/j.optlastec.2019.105696

Zhang, D.-k., Zhao, Y., Dong, M.-y., Wang, G.-q., Wu, A.-p., Shan, J.-g., . . . Zhang, Z.-p. (2019). Effects of weld penetration on tensile properties of 2219 aluminum alloy TIG-welded joints. *Transactions of Nonferrous Metals Society of China, 29*(6), 1161-1168. doi:https://doi.org/10.1016/S1003-6326(19)65024-7

Zhang, D., Wang, G., Wu, A., Zhao, Y., Li, Q., Liu, X., . . . Zhang, Z. (2019). Study on the inconsistency in mechanical properties of 2219 aluminium alloy TIG-welded joints. *Journal of Alloys and Compounds, 777*, 1044-1053. doi:https://doi.org/10.1016/j.jallcom.2018.10.182

Zhang, J., Song, B., Wei, Q., Bourell, D., & Shi, Y. (2019). A review of selective laser melting of aluminum alloys: Processing, microstructure, property and developing trends. *Journal of Materials Science & Technology, 35*(2), 270-284. doi:10.1016/j.jmst.2018.09.004

Zhao, J., Luo, L., Xue, X., Liu, T., Luo, L., Wang, B., . . . Fu, H. (2021). The evolution and characterizations of Al3(ScxZr1-x) phase in Al–Mg-based alloys proceeded by SLM. *Materials Science and Engineering: A, 824*, 141863. doi:https://doi.org/10.1016/j.msea.2021.141863

Appendix

A. Scalmalloy powder composition and influence of layout position

LPW

Test Certificate

Customer :	Auckland University of Technology			
Sales Order Nº :	002331			
Customer PO Nº :	AUT029485			
Customer Reference :	N/A			
Product Code :	LPW-ALMGSC-ANYM	**Product Rev :**	00	
Batch Nº :	UK82828	**Quantity :**	20	Kg

CHEMICAL ANALYSIS

		Units	Min	Max	Result	Approved
Al	Aluminium	weight %	-	Bal	Bal	y
Mg	Magnesium	weight %	4.00	4.90	4.55	y
Sc	Scandium	weight %	0.60	0.80	0.65	y
Zr	Zirconium	weight %	0.20	0.50	0.30	y
Mn	Manganese	weight %	0.30	0.80	0.51	y
Si	Silicon	weight %	-	0.40	0.16	y
Fe	Iron	weight %	-	0.40	0.14	y
Zn	Zinc	weight %	-	0.25	0.02	y
Cu	Copper	weight %	-	0.10	0.01	y
Ti	Titanium	weight %	-	0.15	<0.01	y
V	Vanadium	weight %	-	0.05	0.01	y
O	Oxygen	weight %	-	0.05	0.04	y

SIEVE ANALYSIS

	Units	Min	Max	Result	Approved
+63µm	weight %	Info Only	-	0	y

LASER SIZE DIFFRACTION - ASTM B822

	Units	Min	Max	Result	Approved
-20 µm	volume %	Info Only	-	6	y

LPW

Test Certificate

Customer :	Auckland University of Technology			
Sales Order Nº :	002331			
Customer PO Nº :	AUT029485			
Customer Reference :	N/A			
Product Code :	LPW-ALMGSC-ANYM	**Product Rev :**	00	
Batch Nº :	UK82828	**Quantity :**	20	Kg

NOTES

LPW Technology Certifies that the material on this document conforms to the specification above.

*This document is validated by suppliers authorised inspection representative in accordance with EN 10204 type 3.1 Inspection Document

Generated By	Validated By*
LPW 43	LPW 41
Date	Date
11/05/2018	11/05/2018

Fig. A.1 Scalmalloy composition data sheet supplied from LPW Technologies

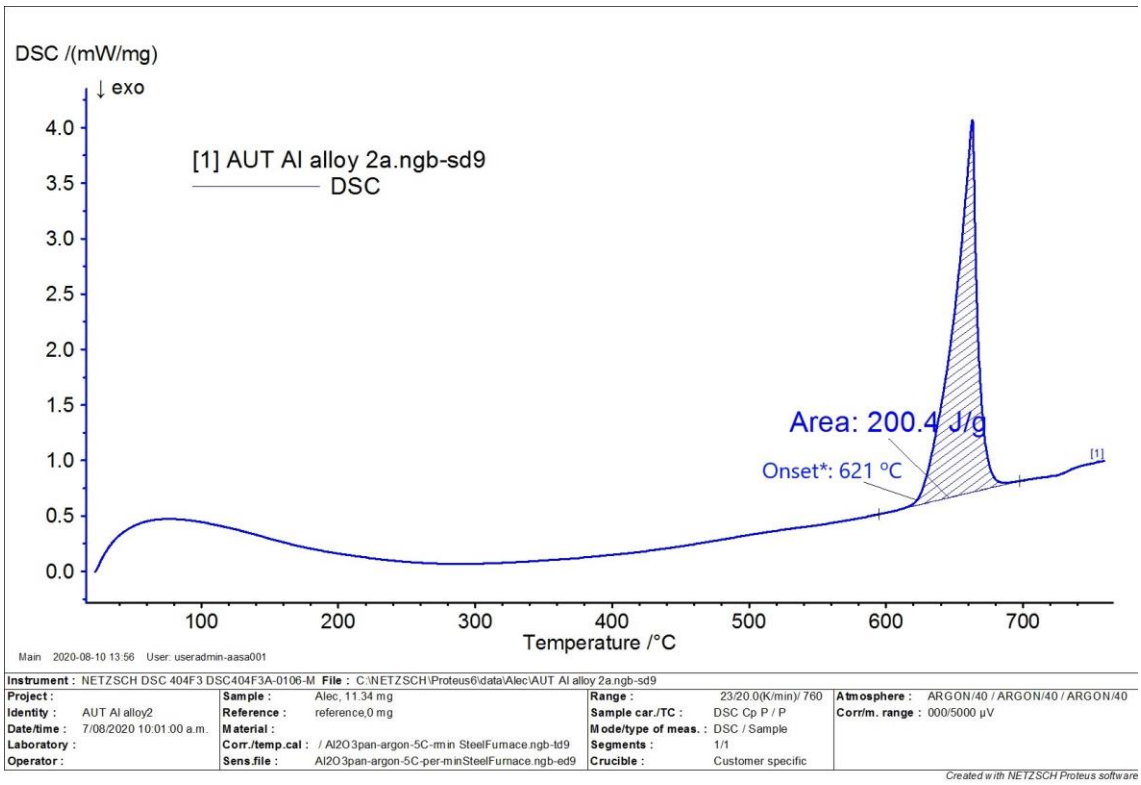

Fig. A.2 Thermogavimetric graph showing the actual melting temperature of a second sample of Scalmalloy used in this work

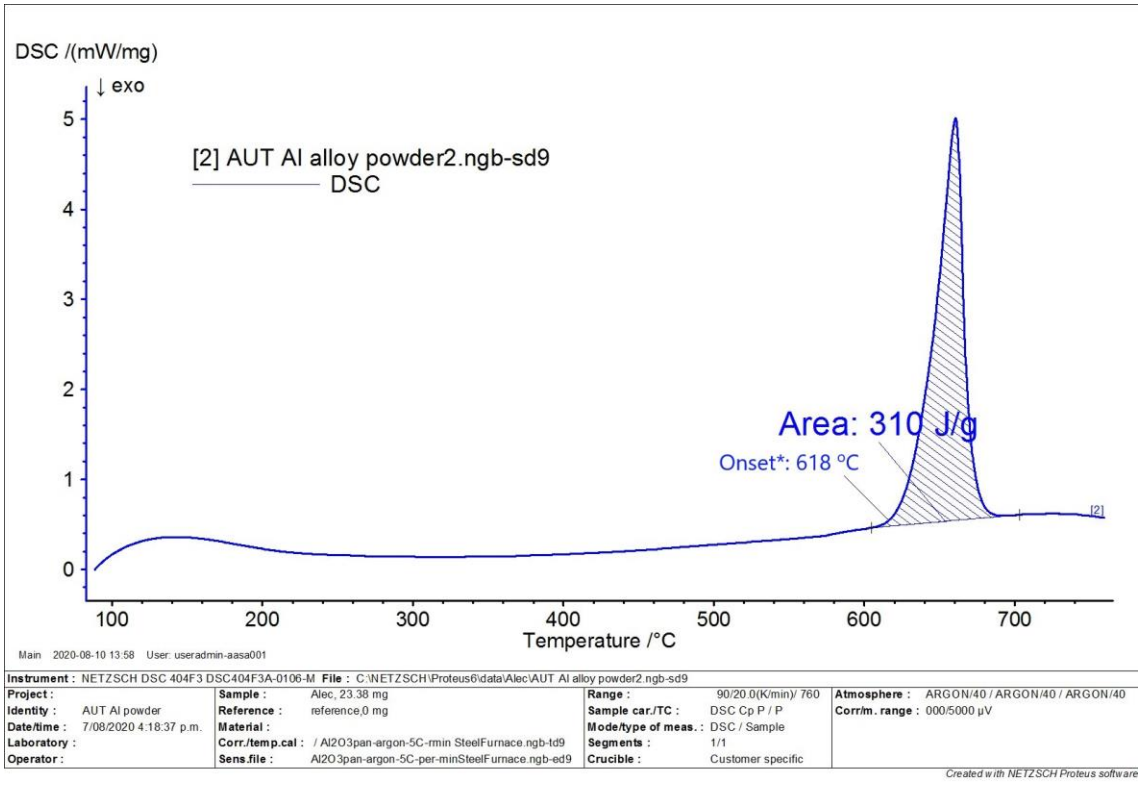

Fig. A.3 Thermogavimetric graph showing the actual melting temperature of Scalmalloy in its powder form used in this work

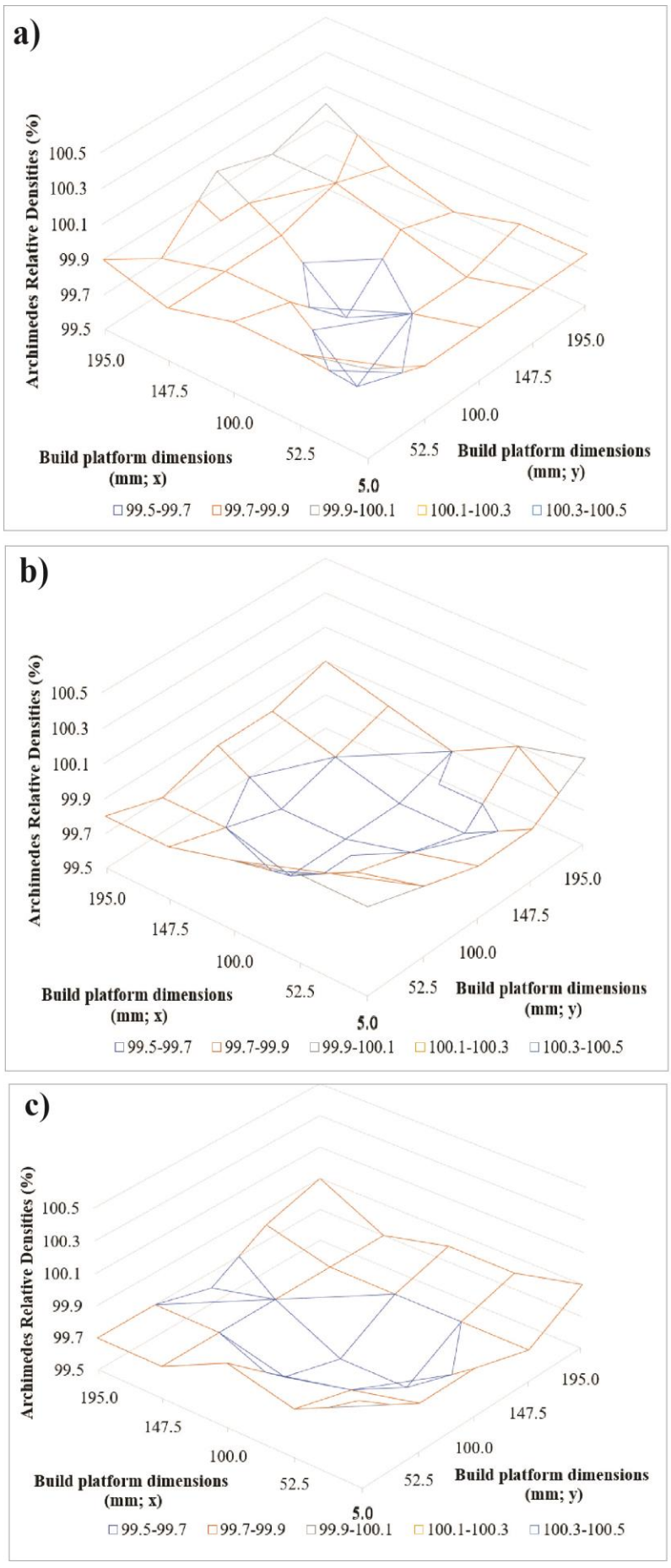

Fig. A.4 Contour plots for each build job to determine the influence of the layout position on the build platform - a) build Job 1, b) build Job 2, c) build Job 3

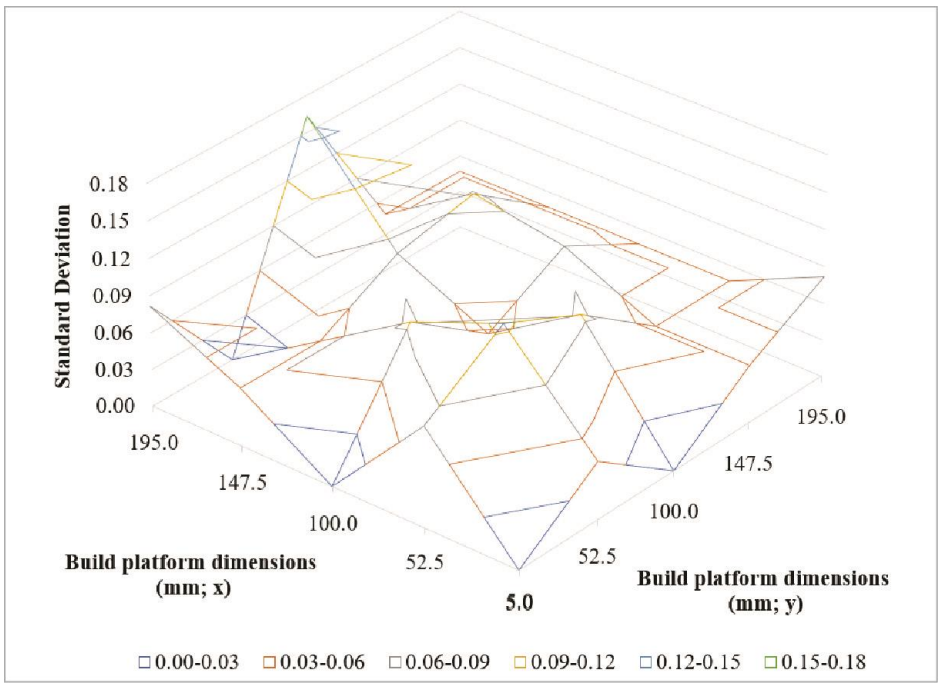

Fig. A.5 Contour plot showing the standard deviations for each sample position on the build platform

B. Additional optical micrograph

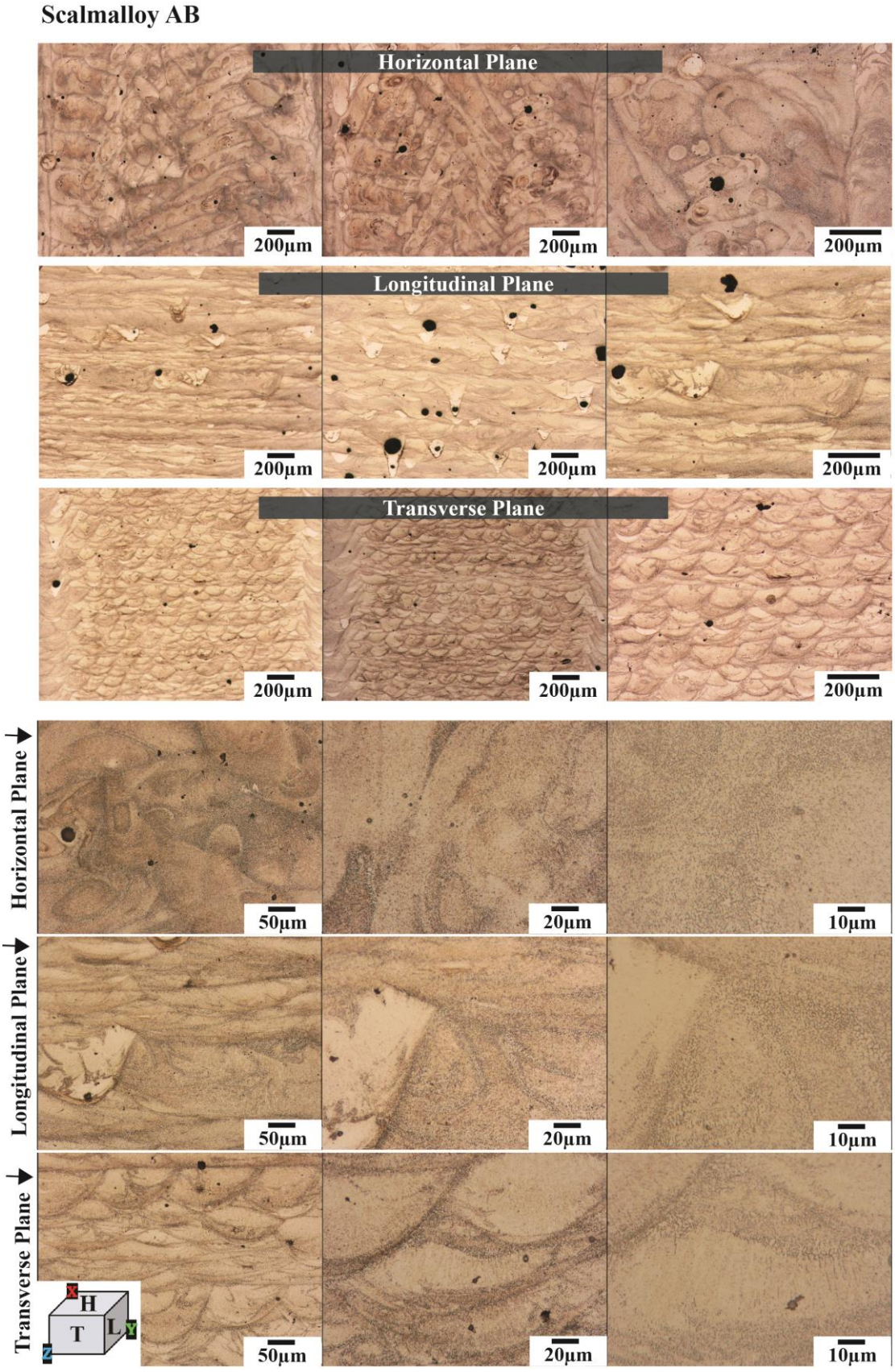

Fig. B.1 Optical micrographs of Scalmalloy AB microstructure in the horizontal, longitudinal, and transverse planes

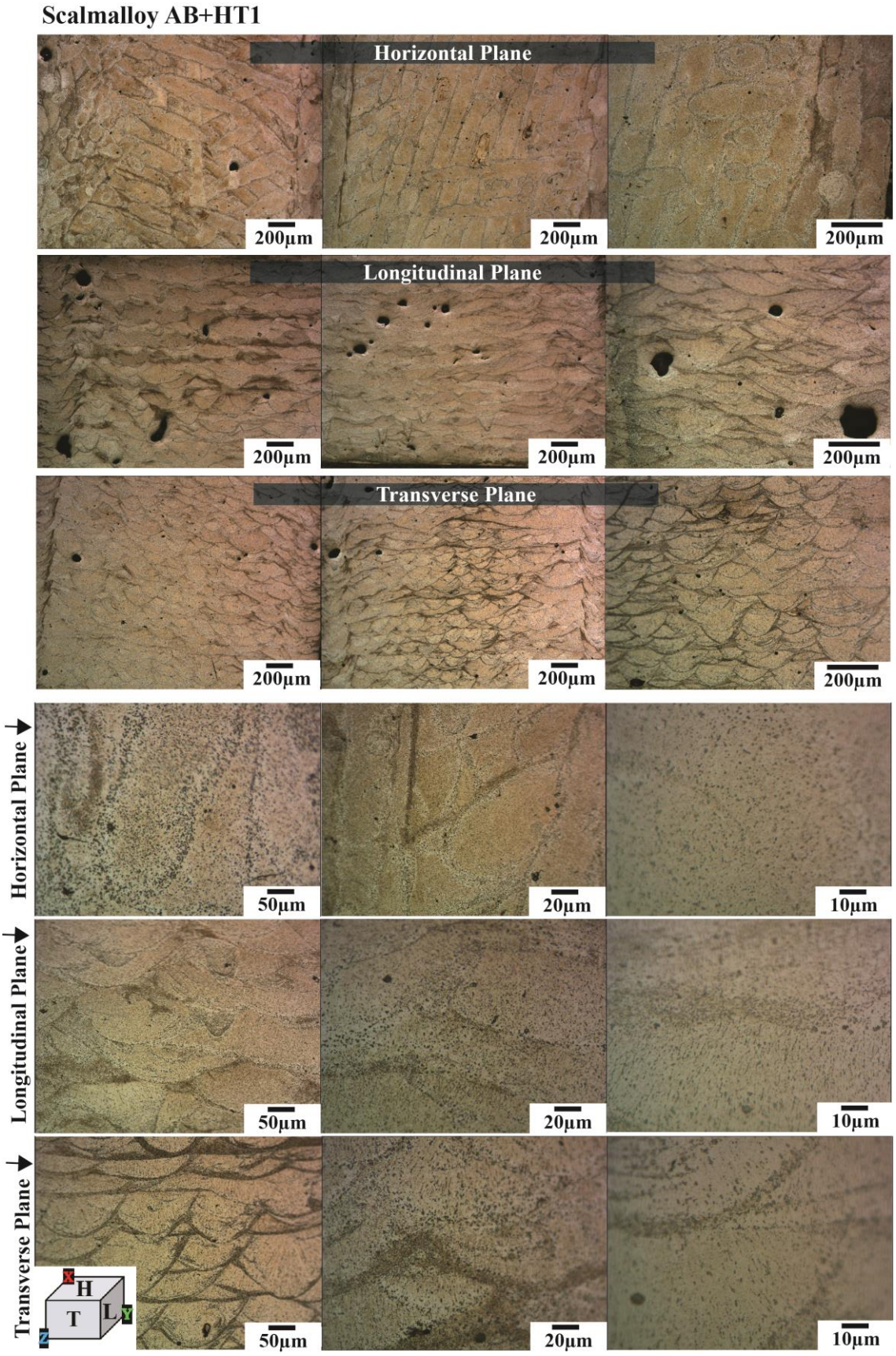

Fig. B.2 Optical micrographs of Scalmalloy AB+HT1 microstructure in the horizontal, longitudinal, and transverse planes

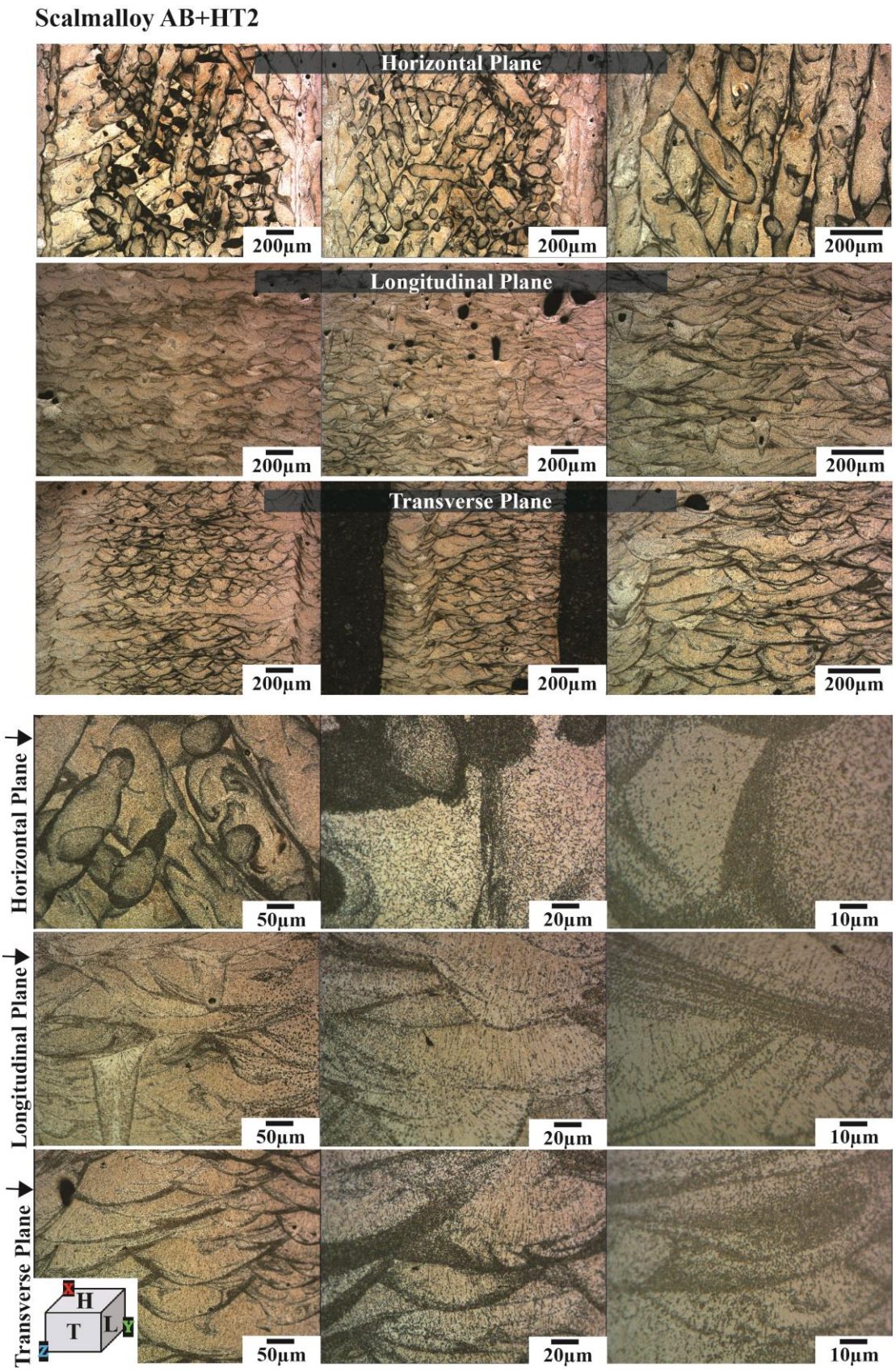

Fig. B.3 Optical micrographs of Scalmalloy AB+HT2 microstructure in the horizontal, longitudinal, and transverse planes

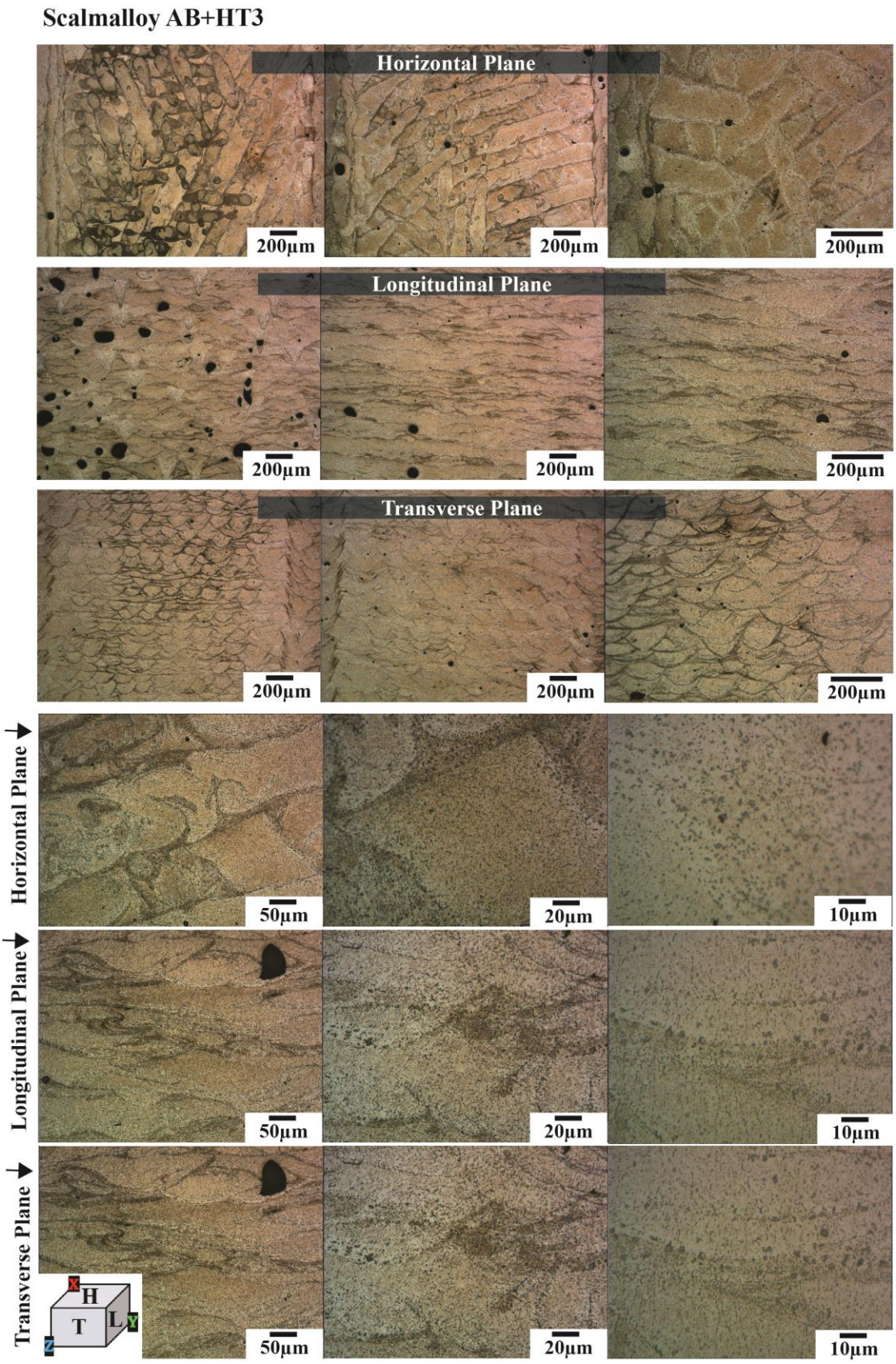

Fig. B.4 Optical micrographs of Scalmalloy AB+HT3 microstructure in the horizontal, longitudinal, and transverse planes

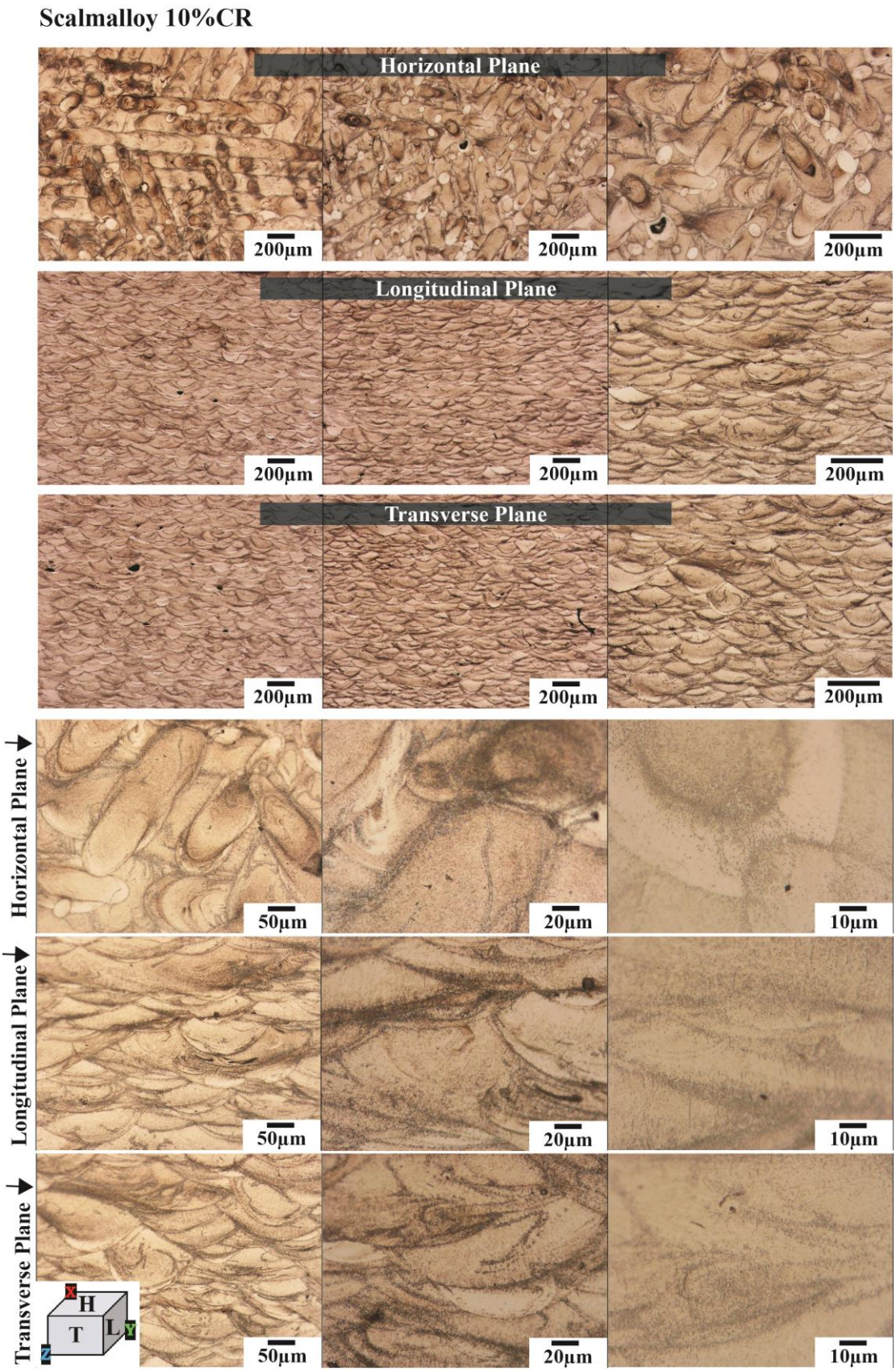

Fig. B.5 Optical micrographs of Scalmalloy 10%CR microstructure in the horizontal, longitudinal, and transverse planes

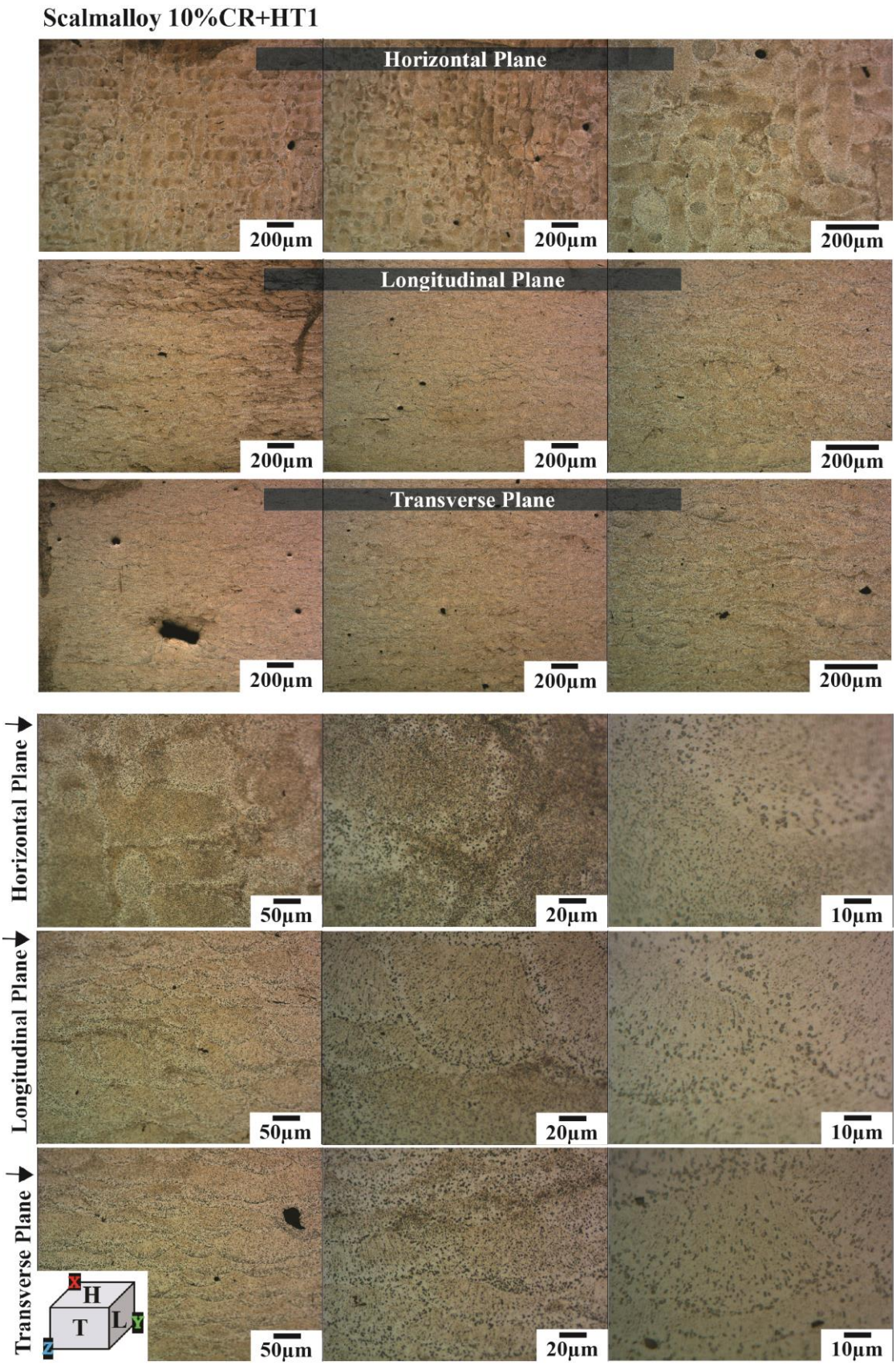

Fig. B.6 Optical micrographs of Scalmalloy 10%CR+HT1 microstructure in the horizontal, longitudinal, and transverse planes

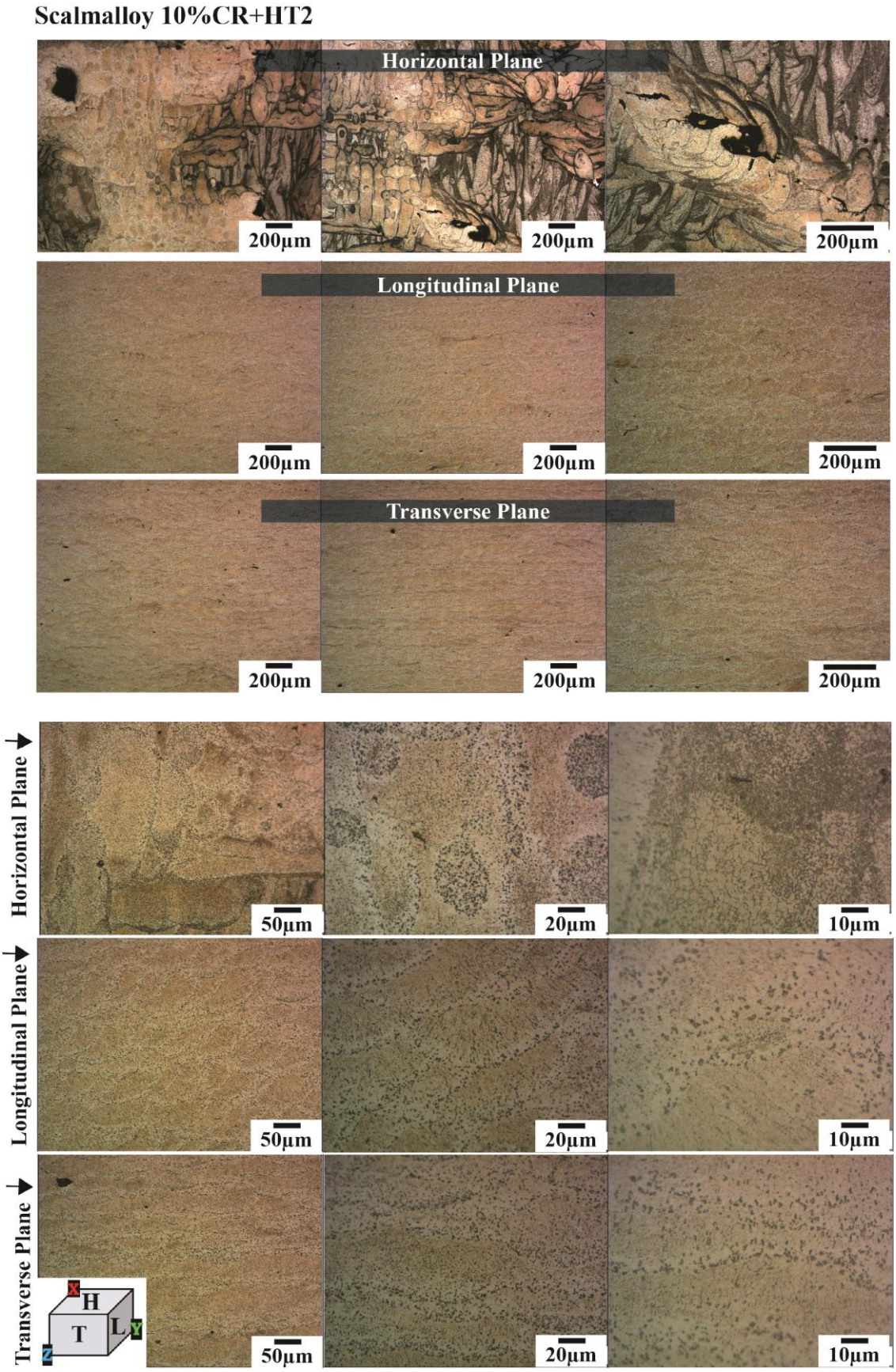

Fig. B.7 Optical micrographs of Scalmalloy 10%CR+HT2 microstructure in the horizontal, longitudinal, and transverse planes

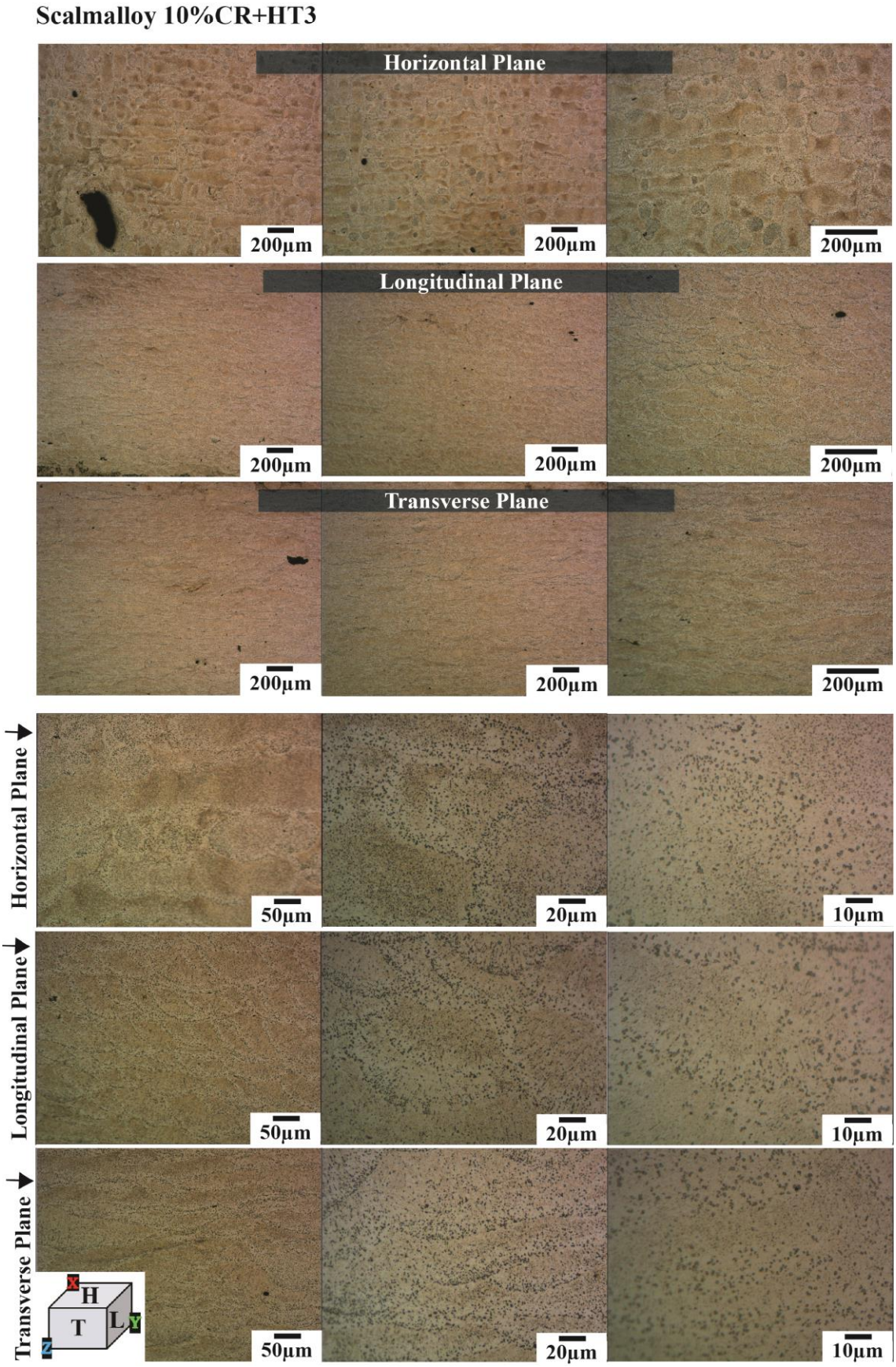

Fig. B.8 Optical micrographs of Scalmalloy 10%CR+HT3 microstructure in the horizontal, longitudinal, and transverse planes

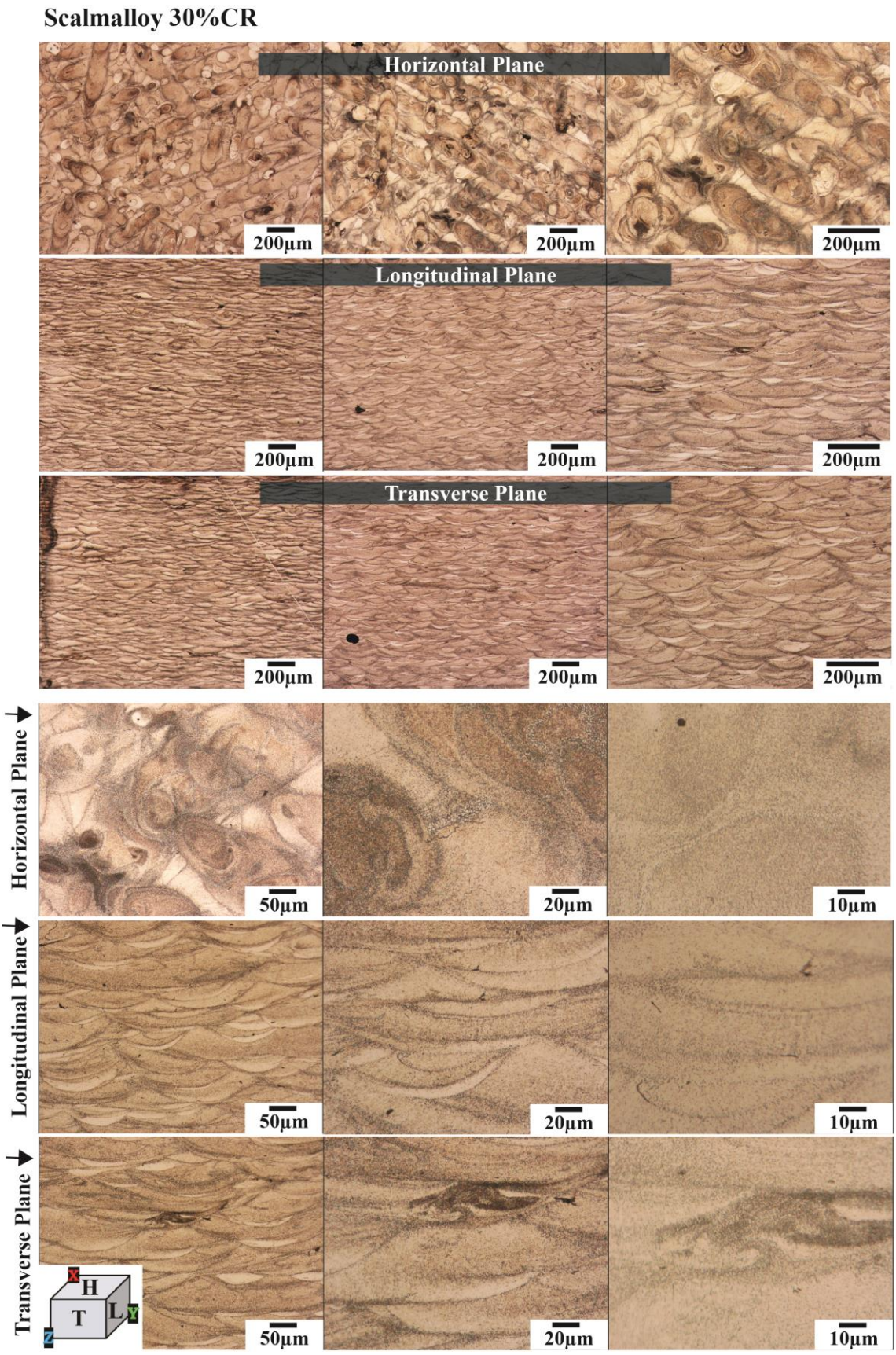

Fig. B.9 Optical micrographs of Scalmalloy 30%CR microstructure in the horizontal, longitudinal, and transverse planes

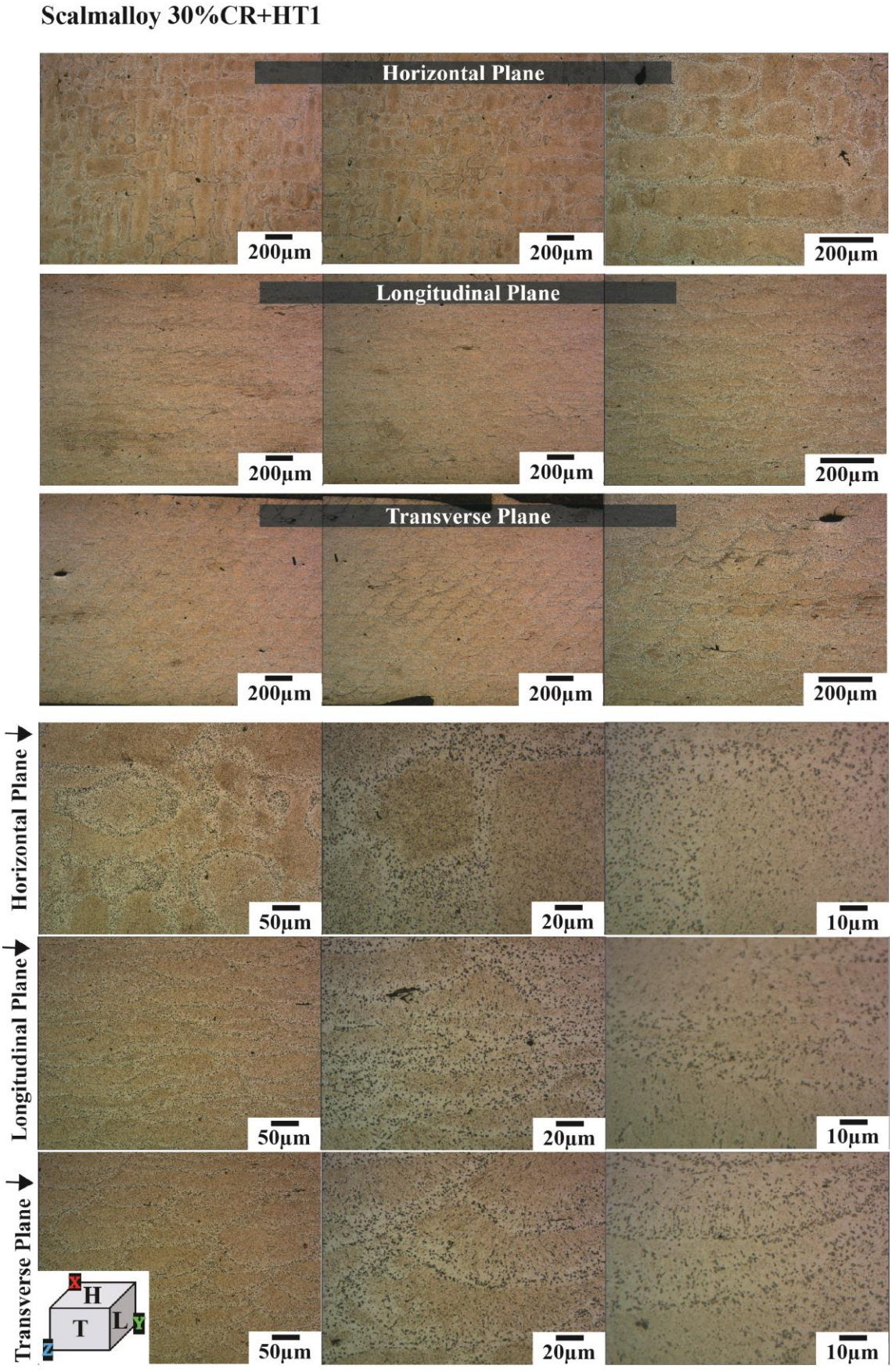

Fig. B.10 Optical micrographs of Scalmalloy 30%CR+HT1 microstructure in the horizontal, longitudinal, and transverse planes

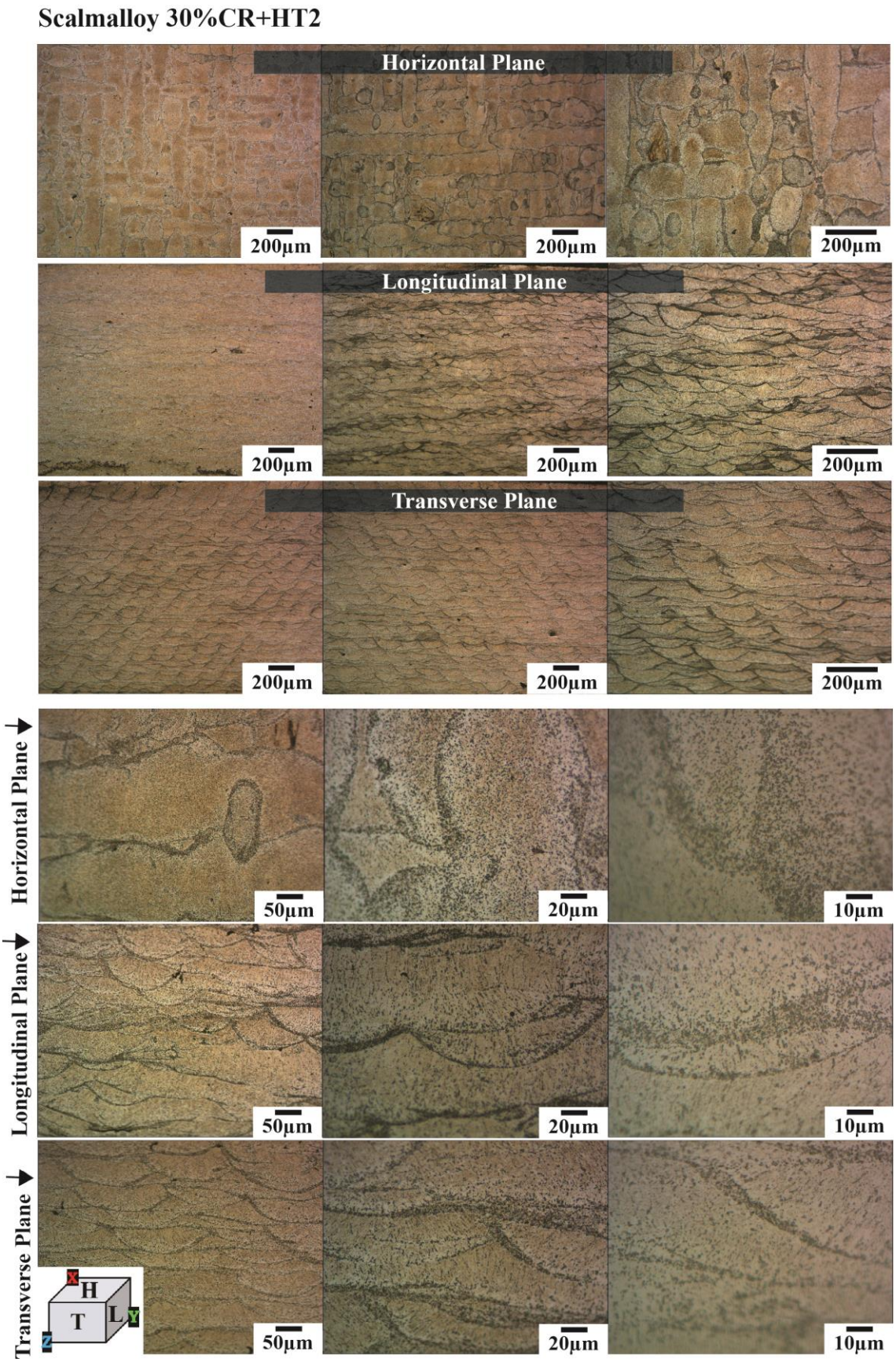

Fig. B.11 Optical micrographs of Scalmalloy 30%CR+HT2 microstructure in the horizontal, longitudinal, and transverse planes

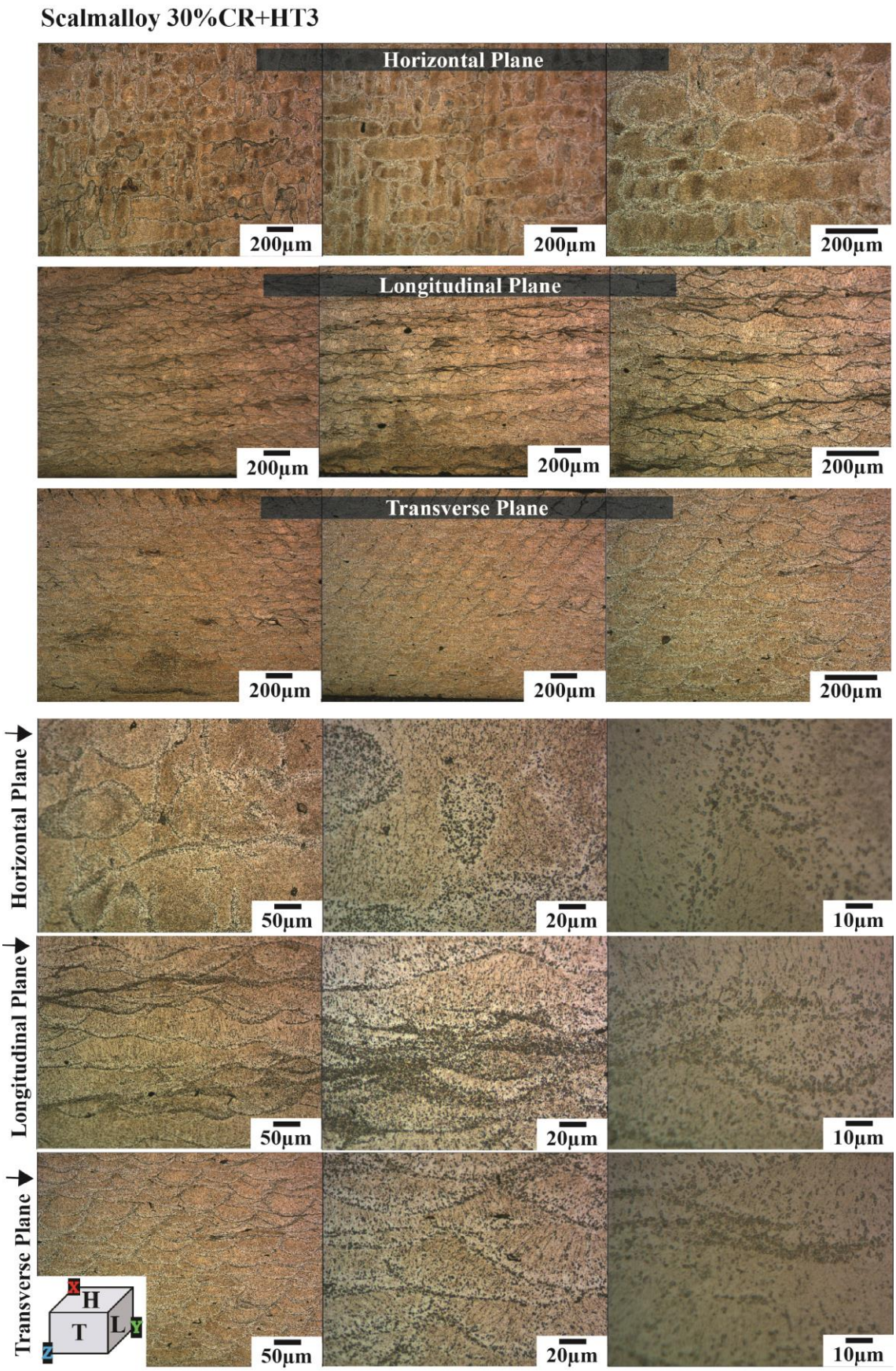

Fig. B.12 Optical micrographs of Scalmalloy 30%CR+HT3 microstructure in the horizontal, longitudinal, and transverse planes

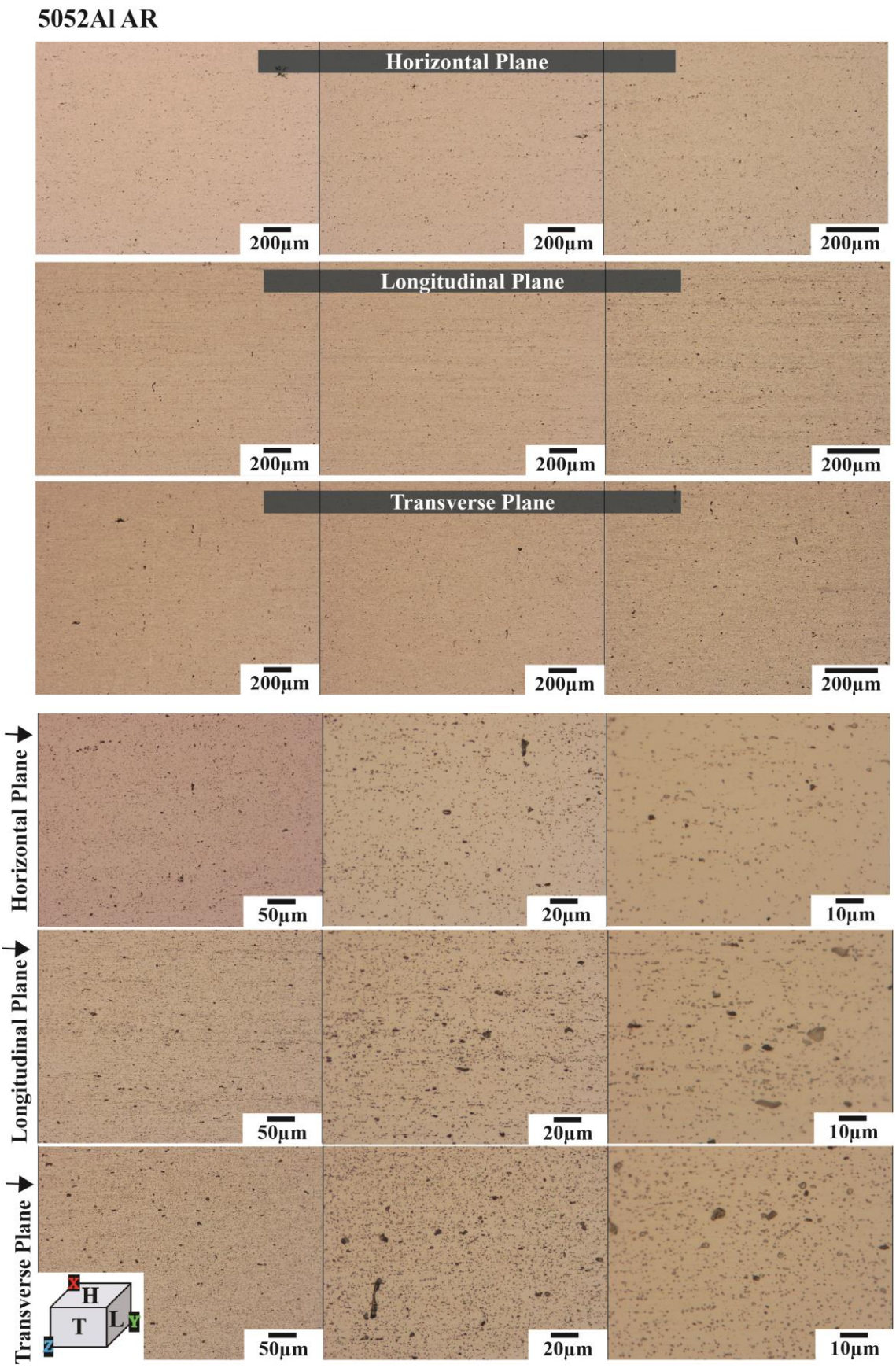

Fig. B.13 Optical micrographs of 5052Al AR microstructure in the horizontal, longitudinal, and transverse planes

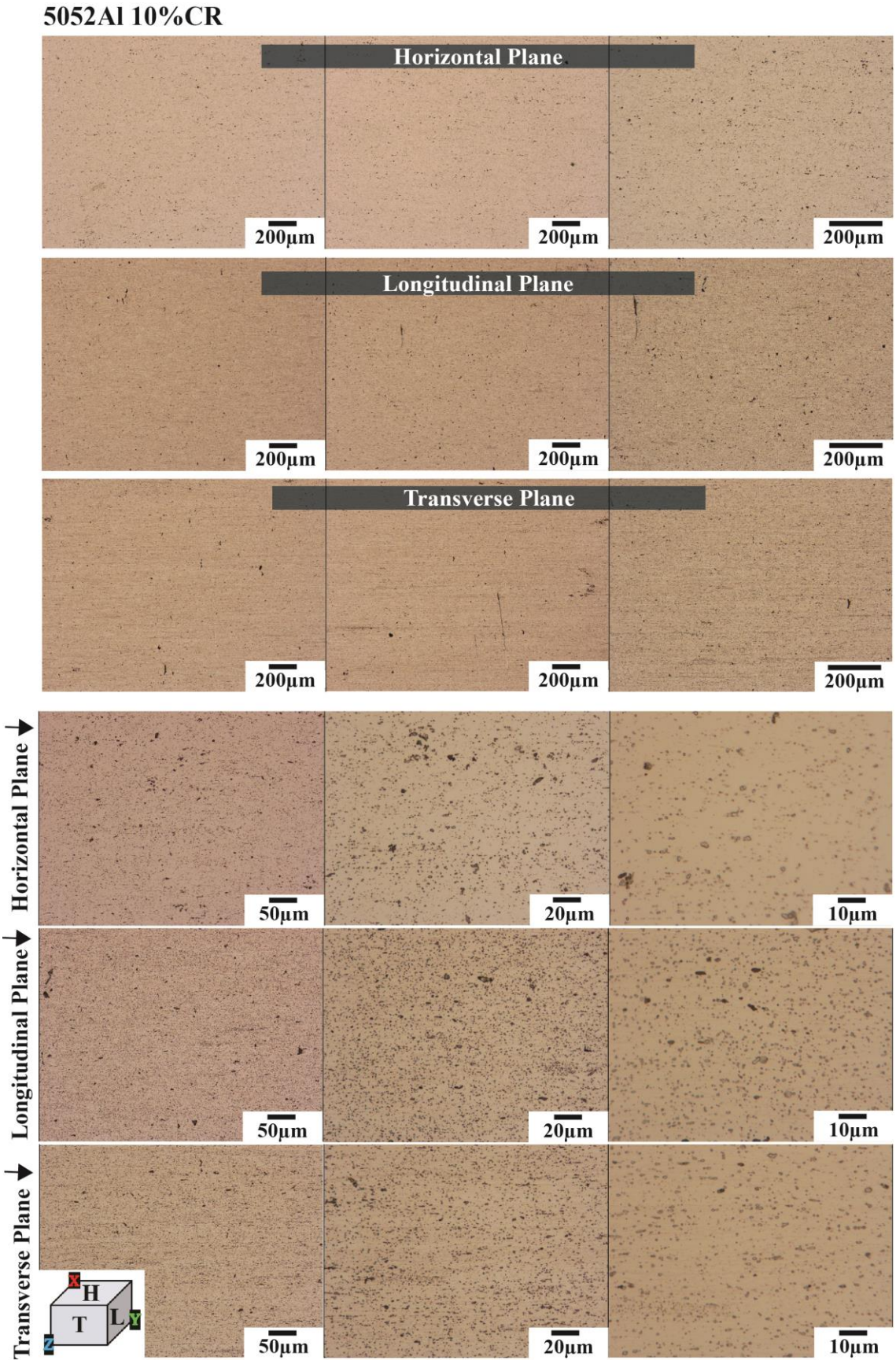

Fig. B.14 Optical micrographs of 5052Al 10%CR microstructure in the horizontal, longitudinal, and transverse planes

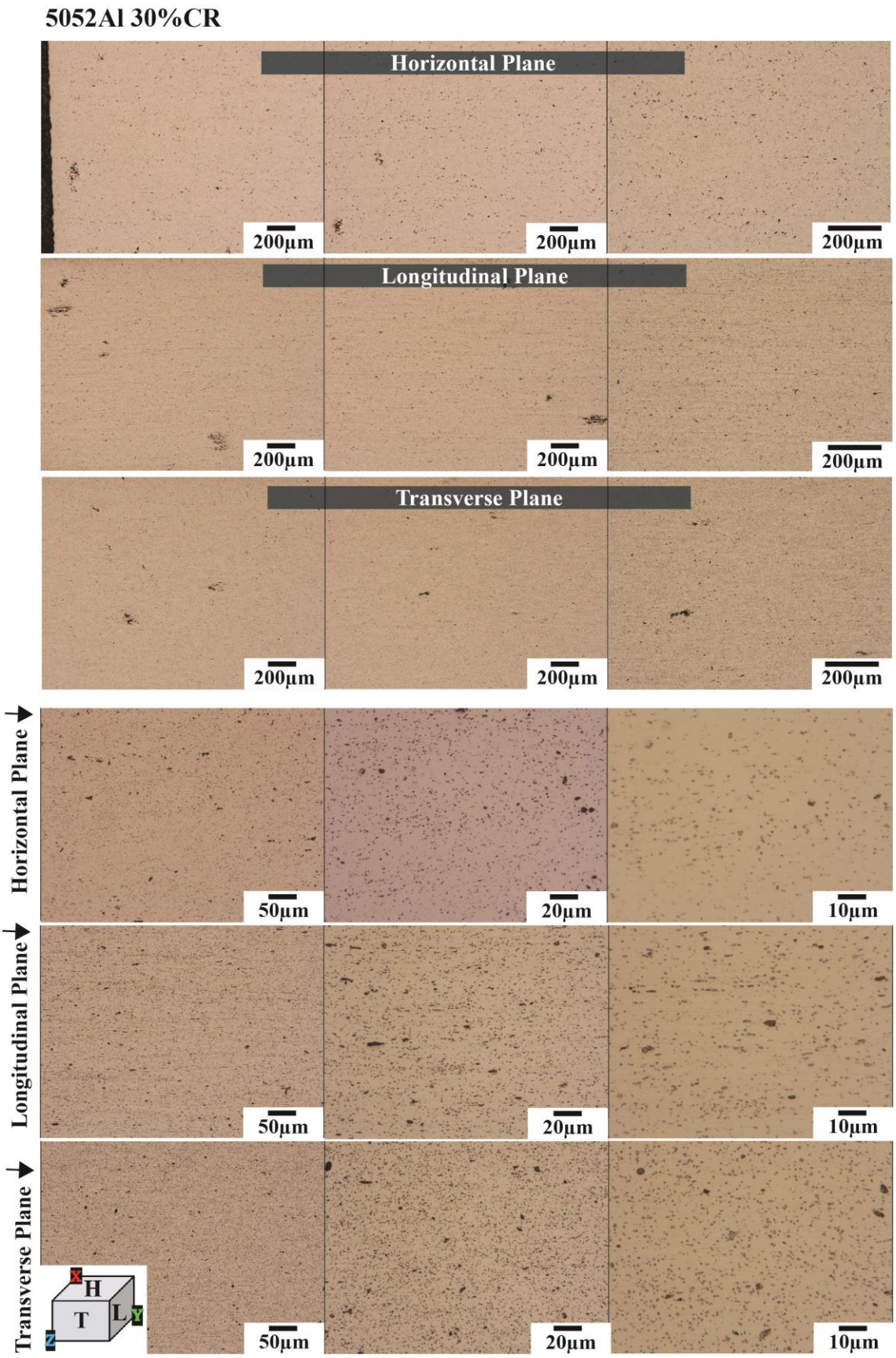

Fig. B.15 Optical micrographs of 5052Al 30%CR microstructure in the horizontal, longitudinal, and transverse planes

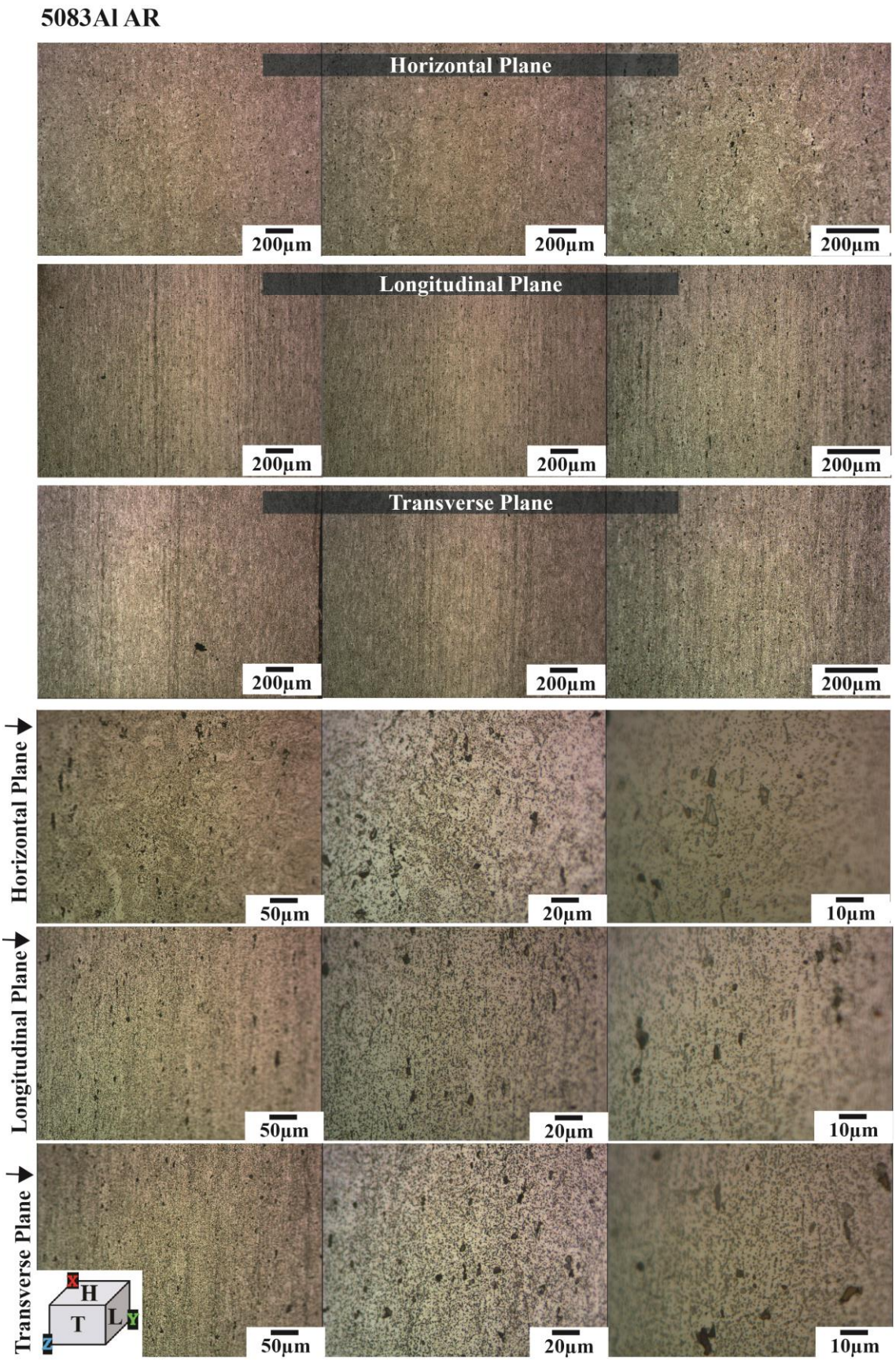

Fig. B.16 Optical micrographs of 5083Al AR microstructure in the horizontal, longitudinal, and transverse planes

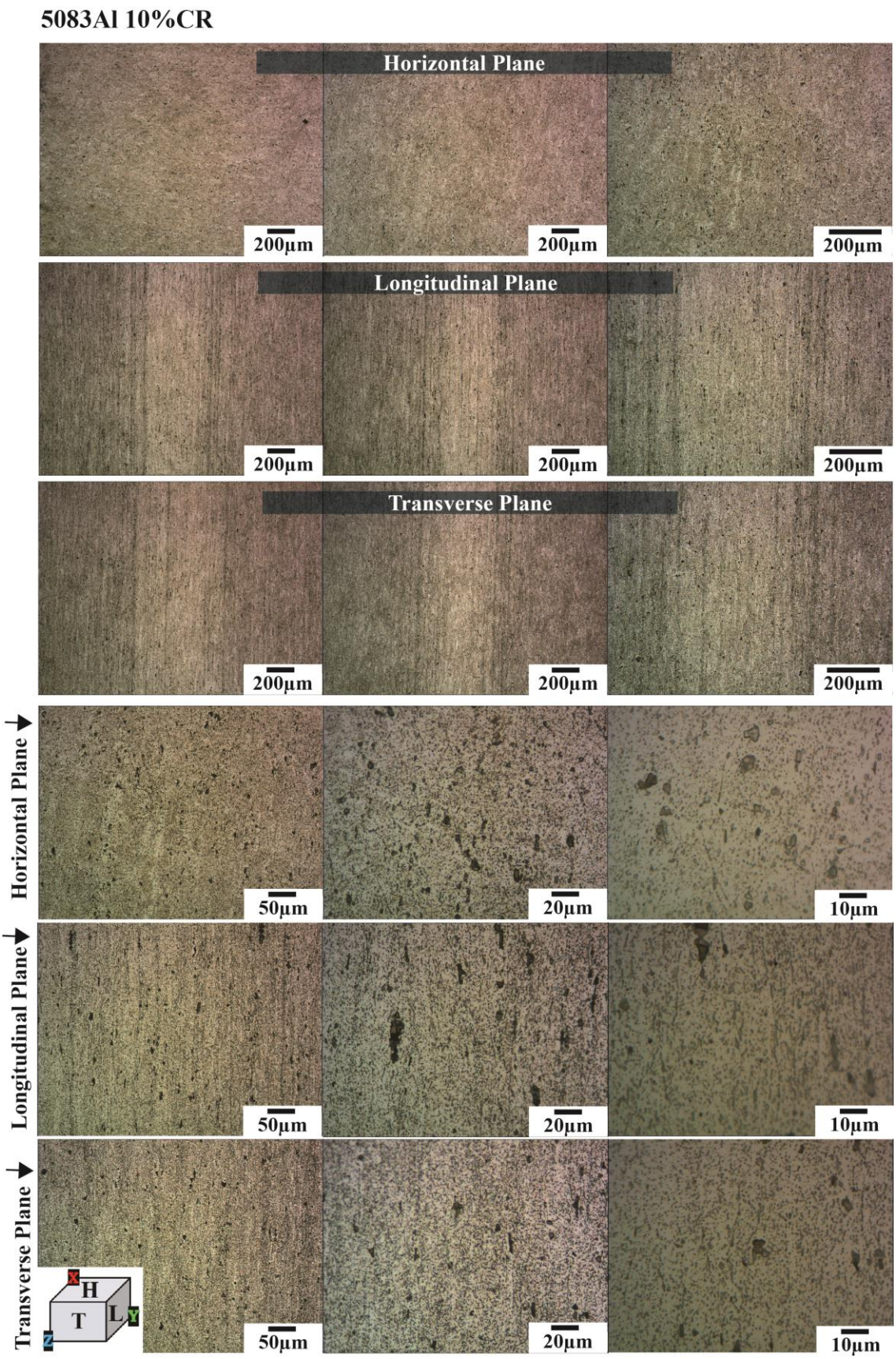

Fig. B.17 Optical micrographs of 5083Al 10%CR microstructure in the horizontal, longitudinal, and transverse planes

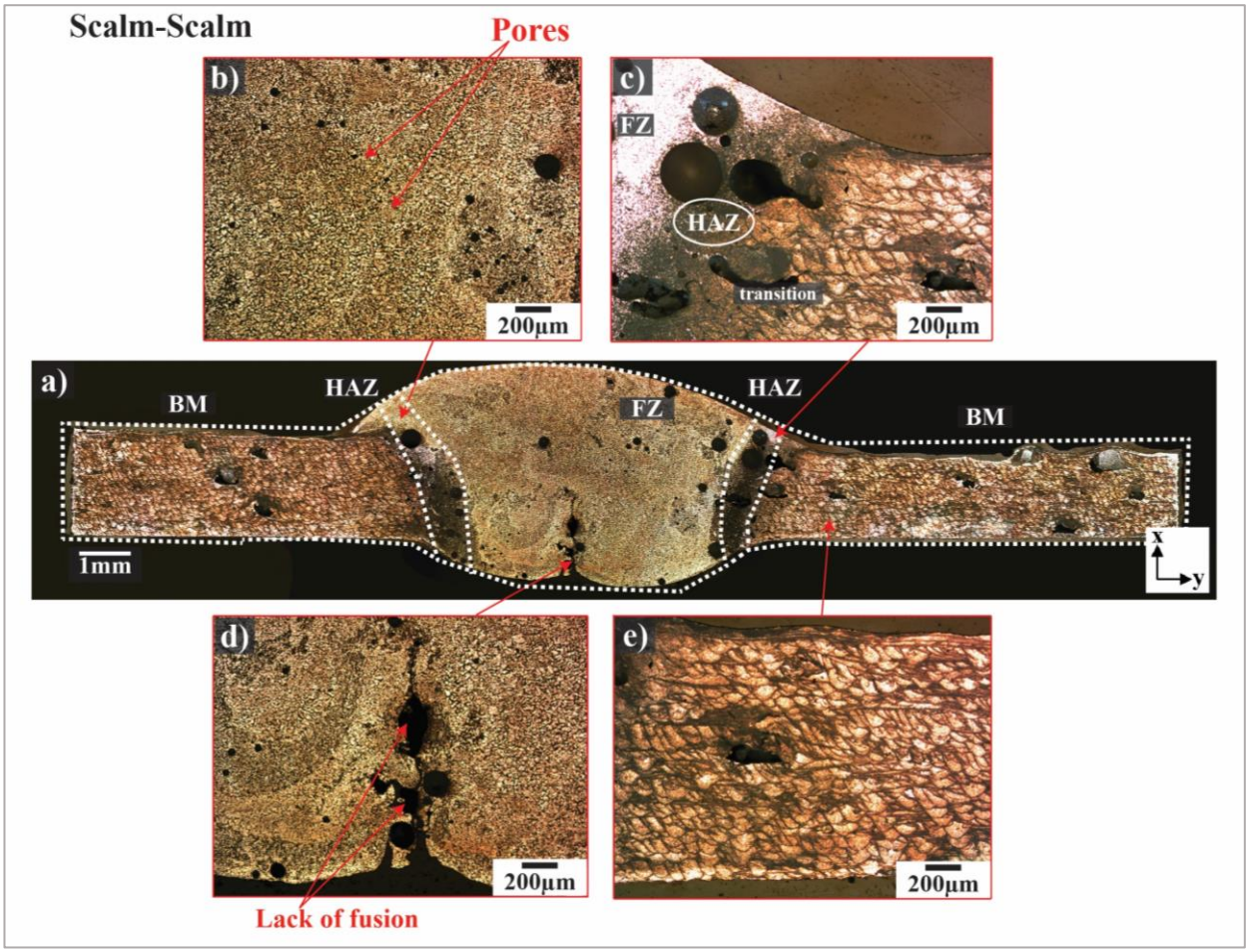

Fig. B.18 Optical micrographs of Scalmalloy to Scalmalloy welded microstructure in the perpendicular to the weld direction – heat affected zone (HAZ)\, base metal (BM) and fusion zone (FZ)

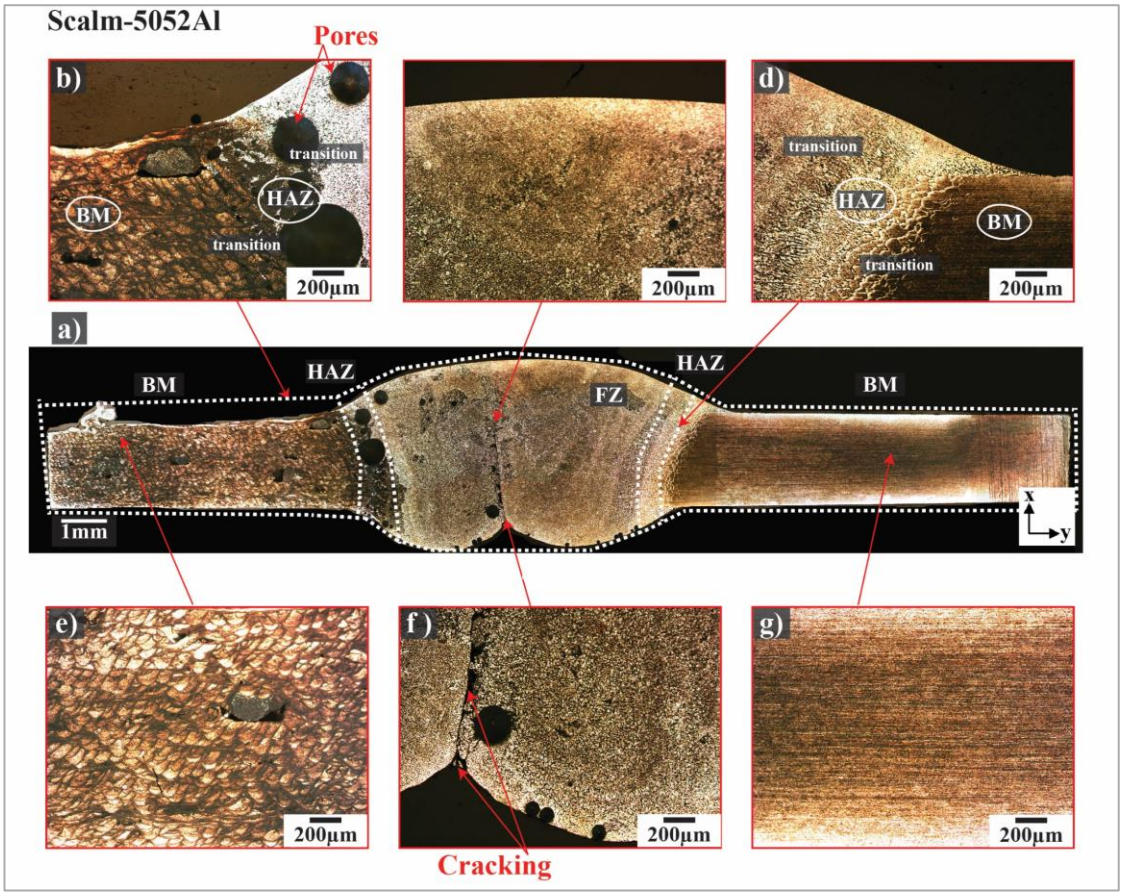

Fig. B.19- Optical micrographs of Scalmalloy to 5052Al welded microstructure in the perpendicular to the weld direction – heat affected zone (HAZ)\, base metal (BM) and fusion zone (FZ)

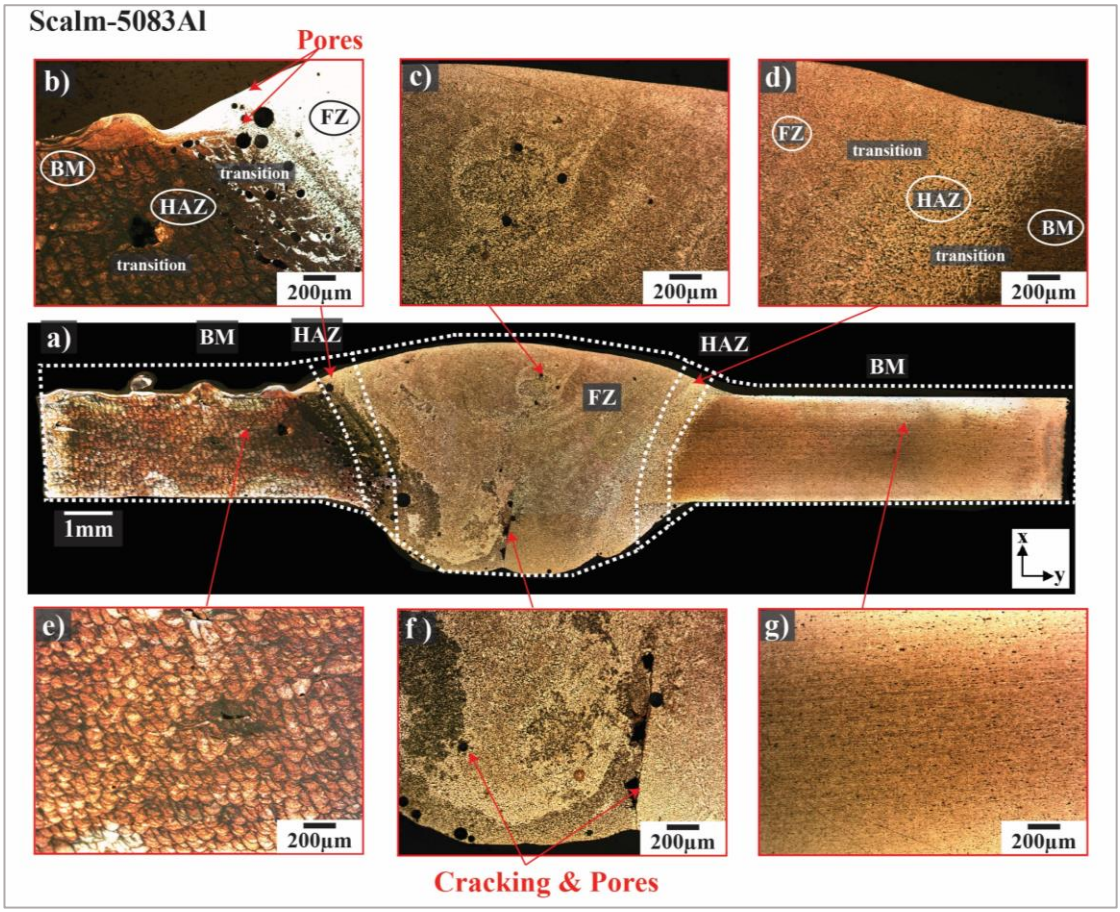

Fig. B.20 Optical micrographs of Scalmalloy to 5083Al welded microstructure in the perpendicular to the weld direction – heat affected zone (HAZ), base metal (BM) and fusion zone (FZ)

C. Additional SEM micrographs of microstructure

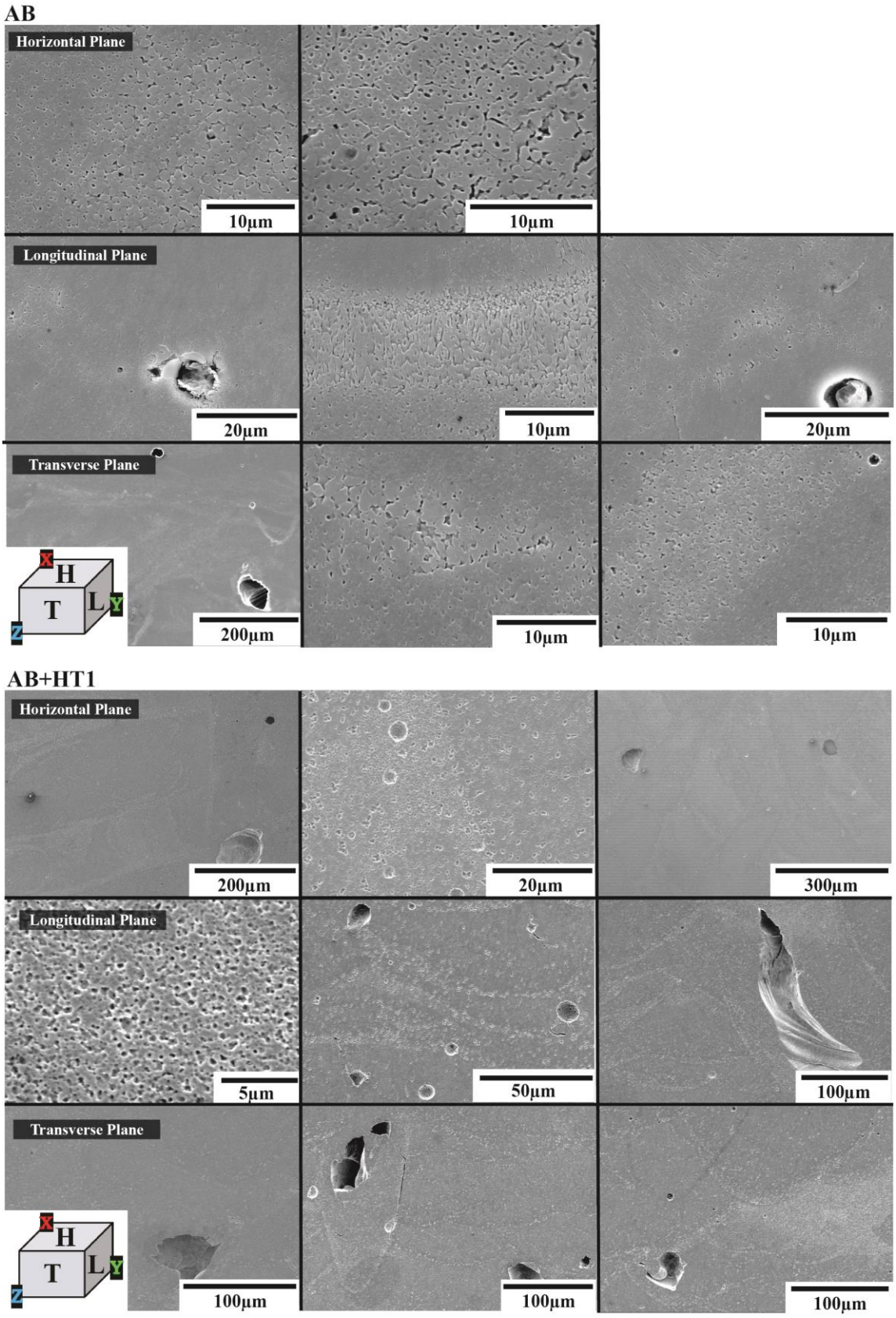

Fig. C.1 SEM micrographs of Scalmalloy AB and AB+HT1 microstructure in the horizontal, longitudinal, and transverse planes

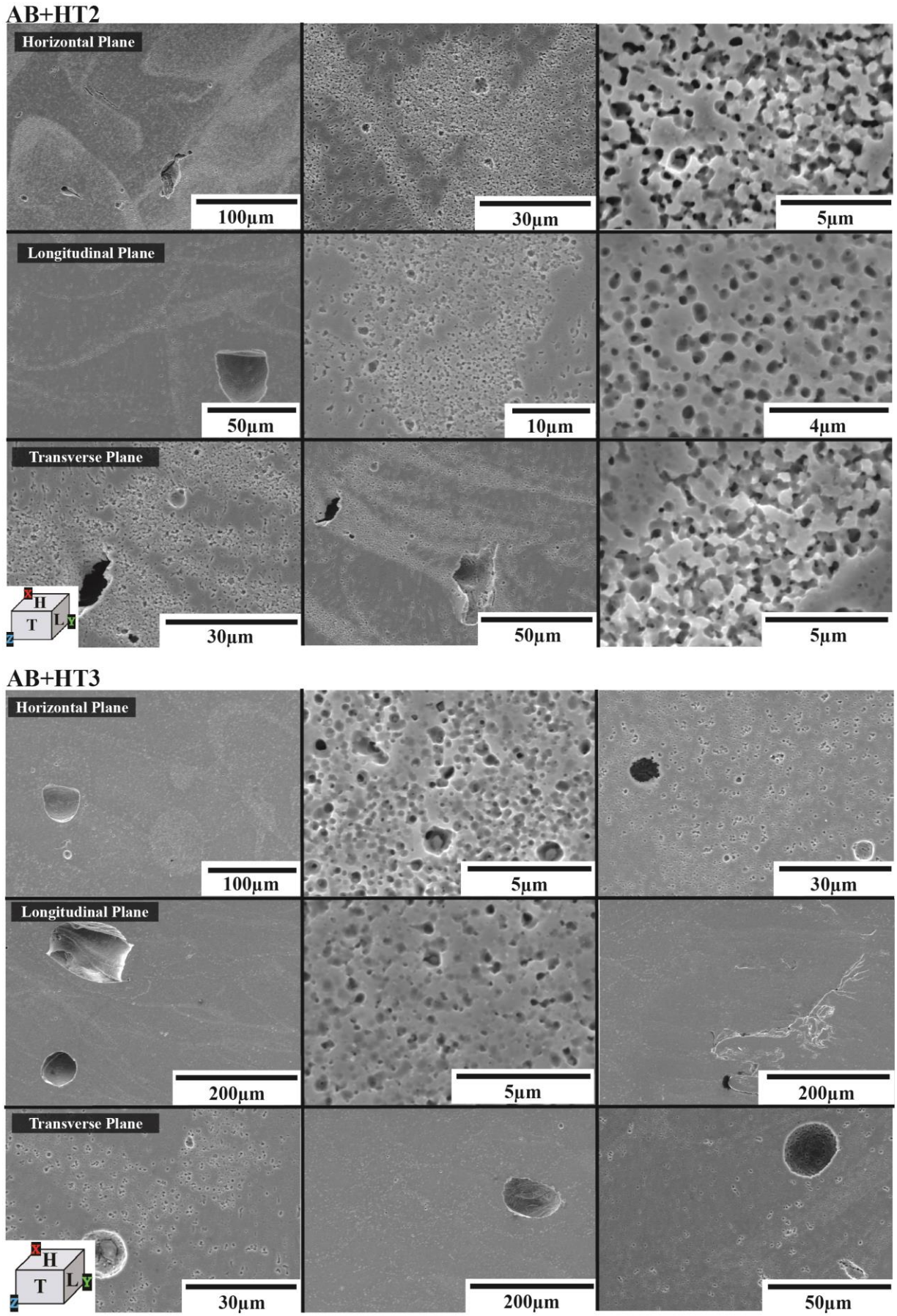

Fig. C.2 SEM micrographs of Scalmalloy AB+HT2 and AB+HT3 microstructure in the horizontal, longitudinal, and transverse planes

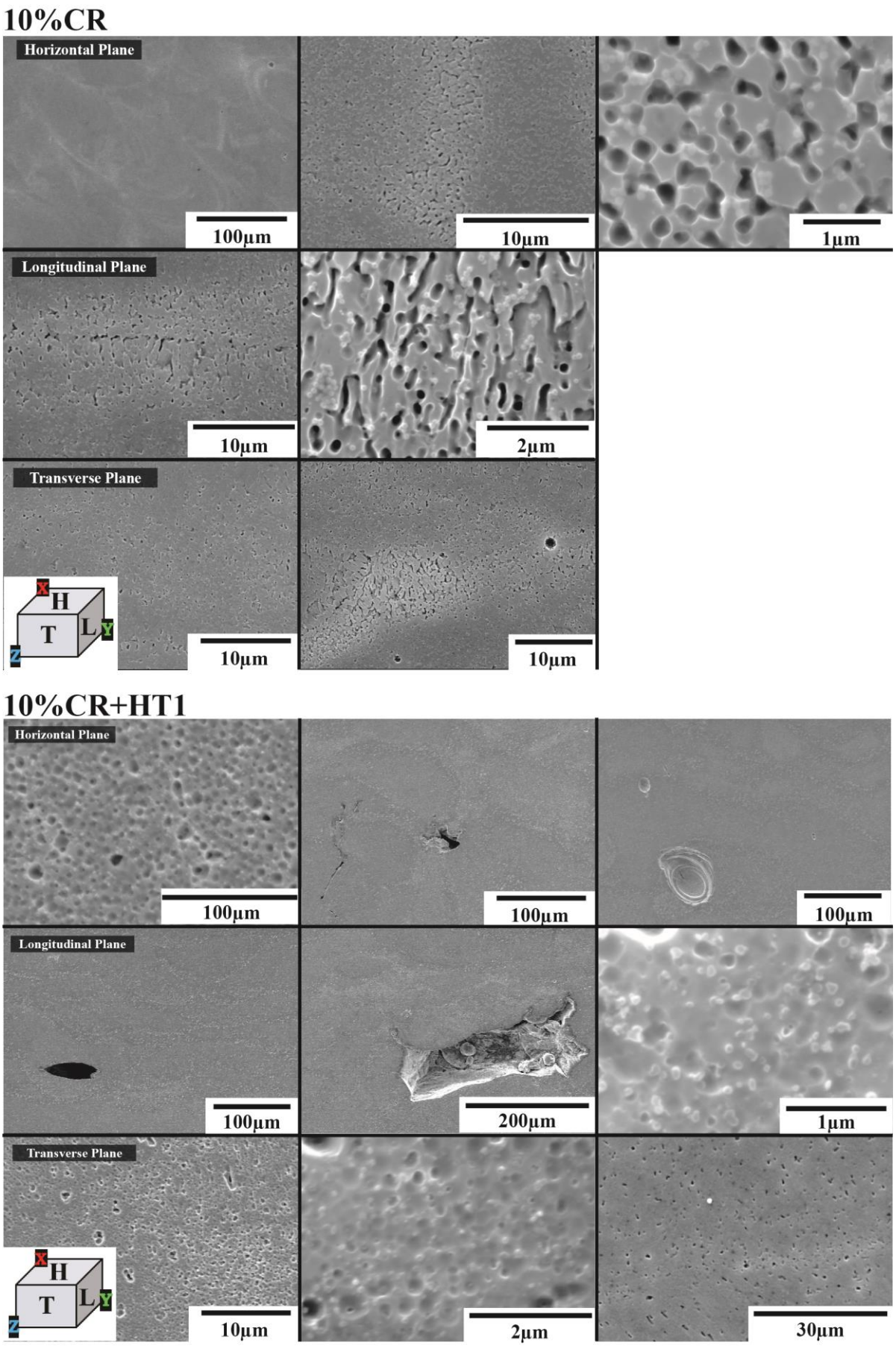

Fig. C.3 SEM micrographs of Scalmalloy 10%CR and 10%CR+HT1 microstructure in the horizontal, longitudinal, and transverse planes

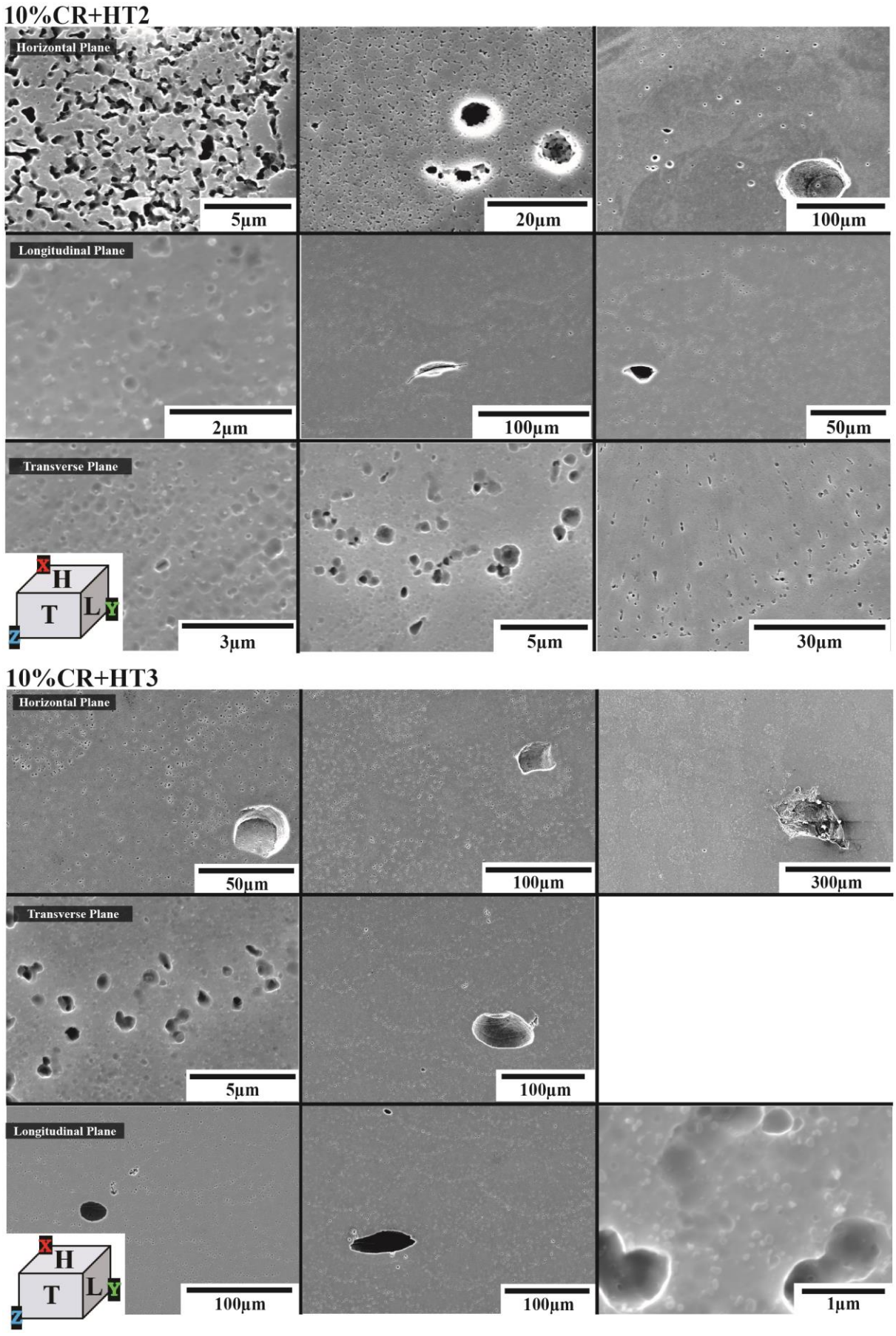

Fig. C.4 micrographs of Scalmalloy 10%CR+HT2 and 10%CR+HT3 microstructure in the horizontal, longitudinal, and transverse planes

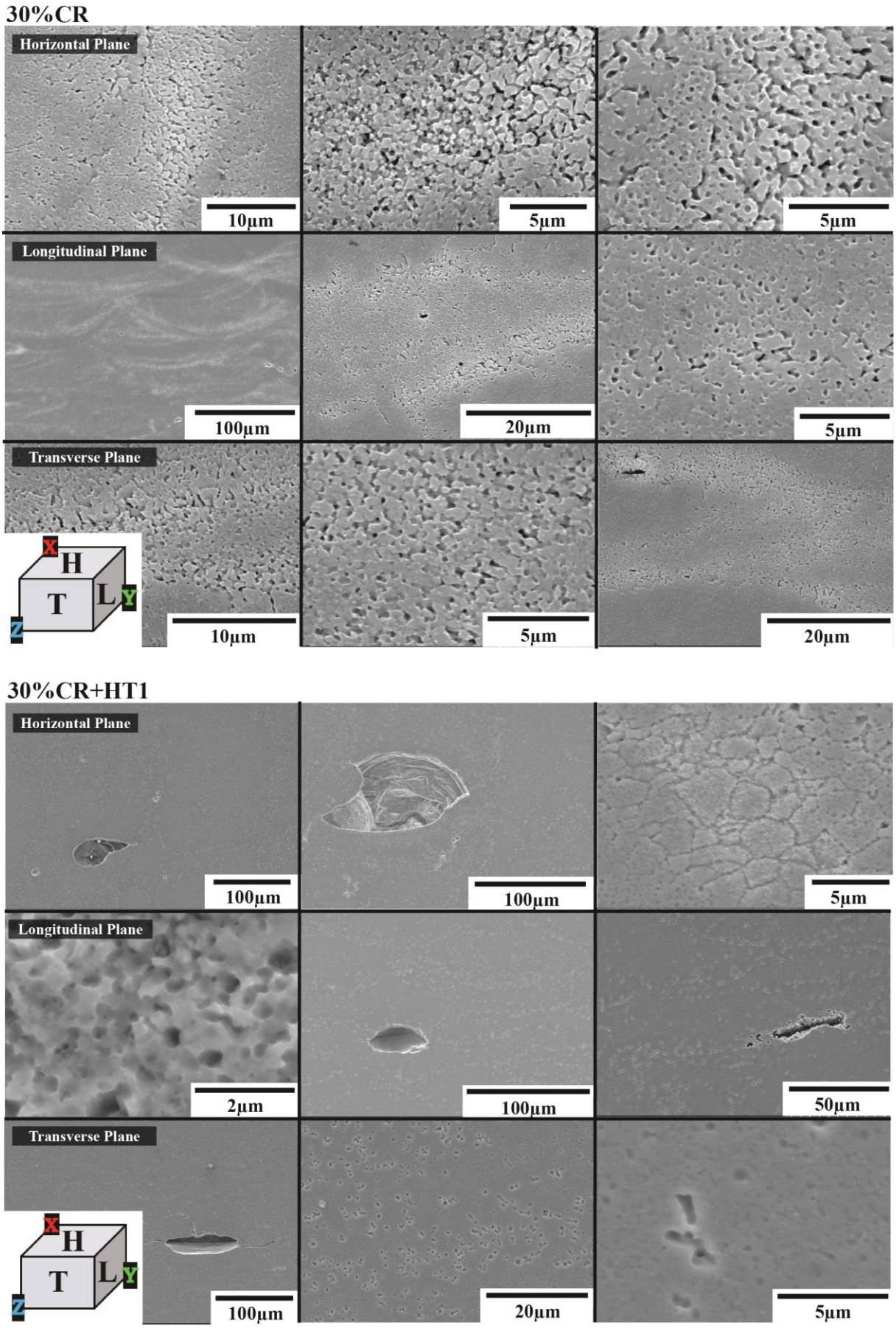

Fig. C.5 SEM micrographs of Scalmalloy 30%CR and 30%+HT1 microstructure in the horizontal, longitudinal, and transverse planes

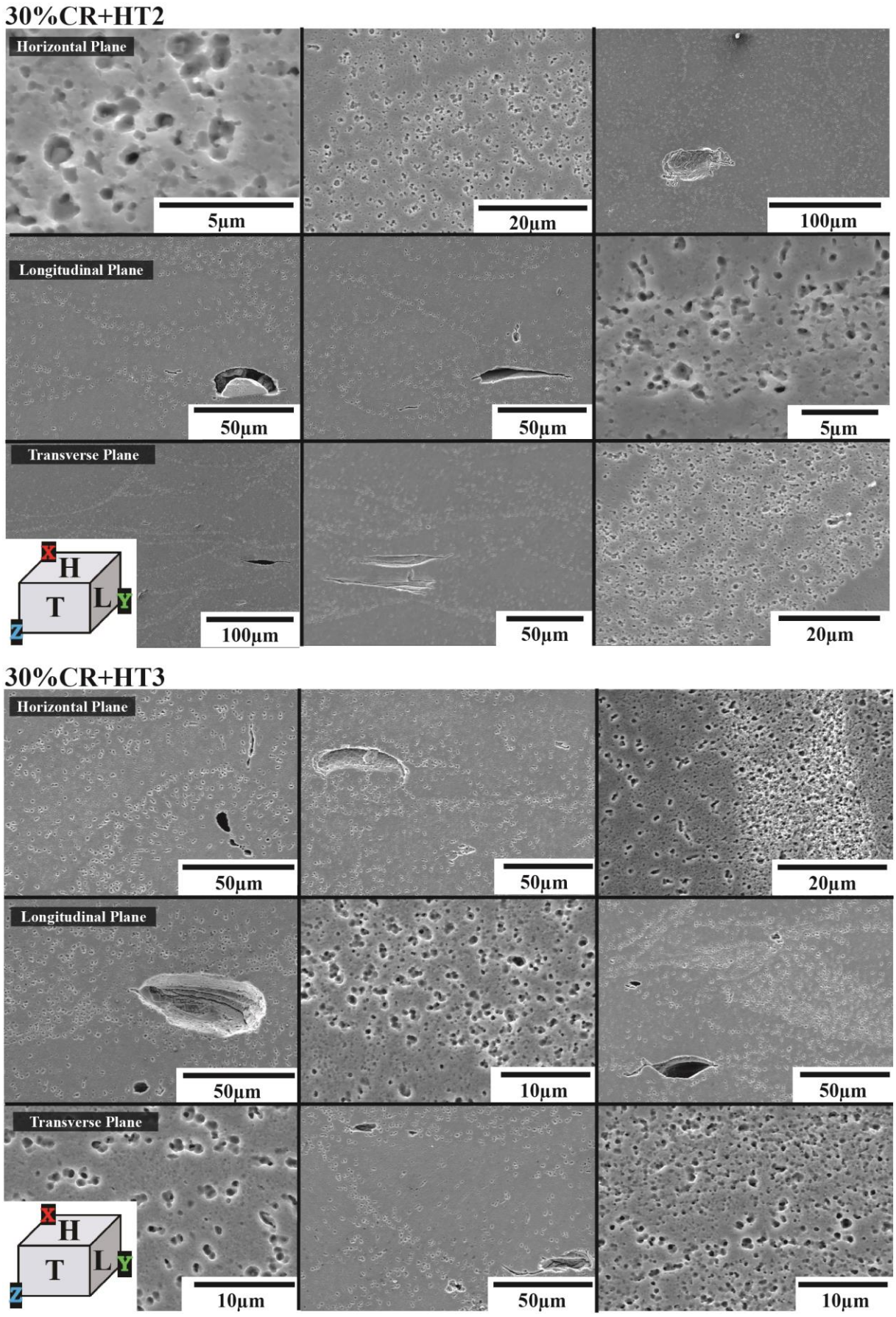

Fig. C.6 SEM micrographs of Scalmalloy 30%CR+HT2 and 30%CR+HT3 microstructure in the horizontal, longitudinal, and transverse plane

D. EDS investigation for welded samples

Scalmalloy Welded

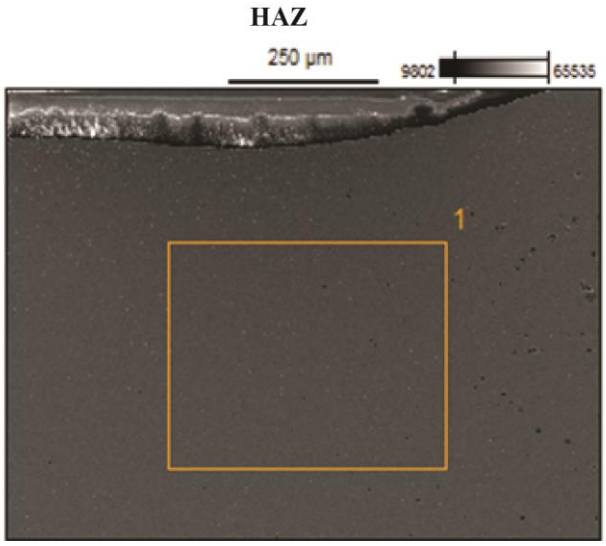

	Mg	Al	Sc	Mn
Scalmalloy to Scalmalloy HAZ	3.30	95.34	0.67	0.68

Fig. D.1 SEM micrograph showing the section where EDS was used to determine the composition of the area for the Scalmalloy welded joint

Scalmalloy-5052Al Welded

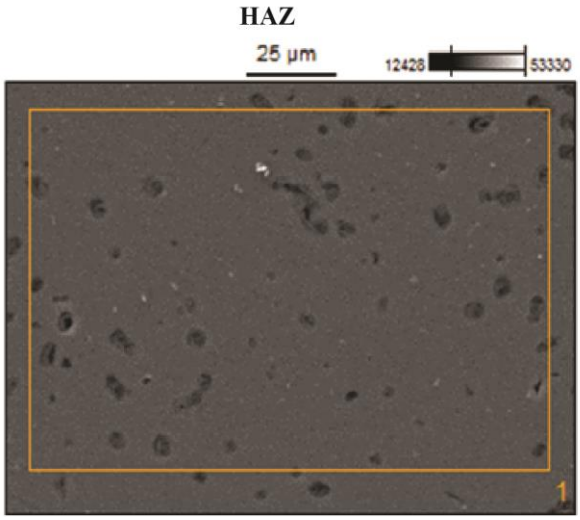

	Mg	Al	Sc	Mn
Scalmalloy to 5052Al FZ - pt1	3.60	96.03	0.15	0.22

Fig. D.2 SEM micrograph showing the section where EDS was used to determine the composition of the area for the Scalmalloy-5052Al welded joint

Scalmalloy-5083Al Welded

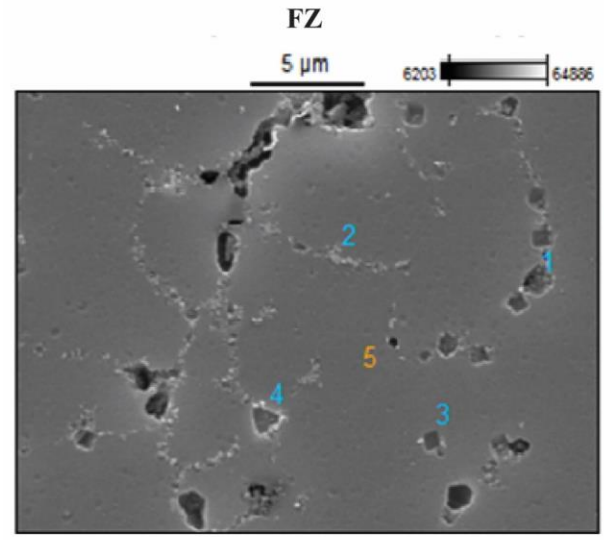

	Mg	Al	Sc	Mn
Scalmalloy to 5083 FZ - pt1	4.19	95.12	0.31	0.38
Scalmalloy to 5083 FZ - pt2	4.66	94.53	0.42	0.40
Scalmalloy to 5083 FZ - pt3	4.37	94.91	0.26	0.47
Scalmalloy to 5083 FZ - pt4	3.66	87.61	8.42	
Scalmalloy to 5083 FZ - pt5	4.38	94.86	0.35	0.40

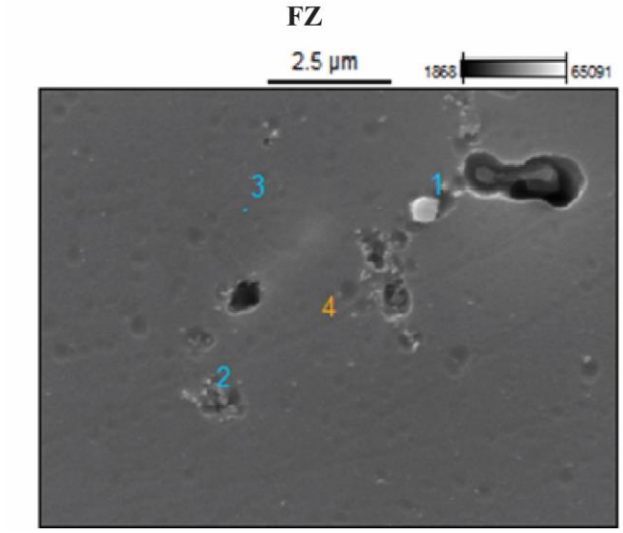

	Mg	Al	Sc	Mn
Scalmalloy to 5083 FZ - pt1	5.76	93.38	0.54	0.32
Scalmalloy to 5083 FZ - pt2	3.88	95.11	0.60	0.41
Scalmalloy to 5083 FZ - pt3	3.92	94.55	0.41	1.11
Scalmalloy to 5083 FZ - pt4	3.99	95.23	0.32	0.45

Fig. D.3 SEM micrograph showing the points where EDS was used to determine the composition for the Scalmalloy-5083Al welded joint

E. Additional tensile data

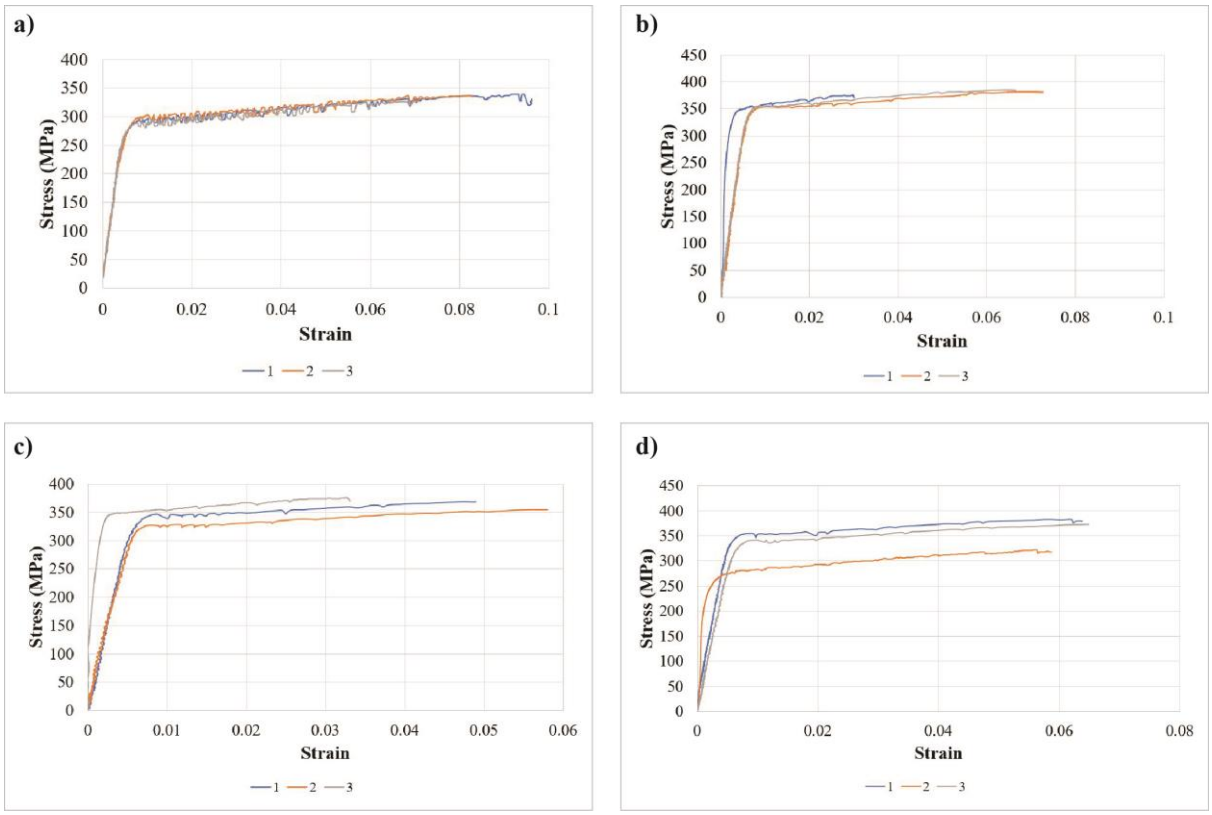

Fig. E.1 Stress-strain curves for the a) Scalmalloy AB, b) Scalmalloy AB+HT1, c) Scalmalloy AB+HT2, and d) Scalmalloy AB+HT3 condition

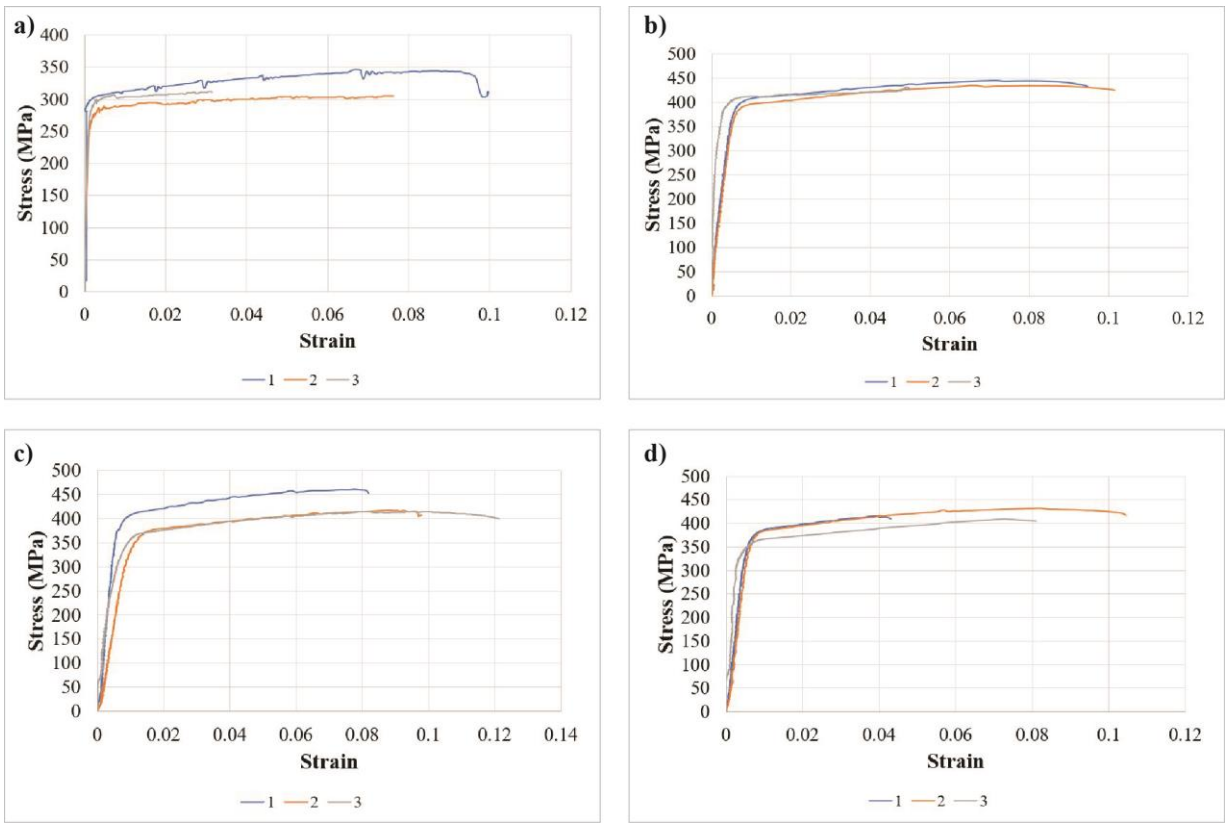

Fig. E.2 Stress-strain curves for the a) Scalmalloy 10%CR, b) Scalmalloy 10%CR+HT1, c) Scalmalloy 10%CR+HT2, and d) Scalmalloy 10%CR+HT3 condition

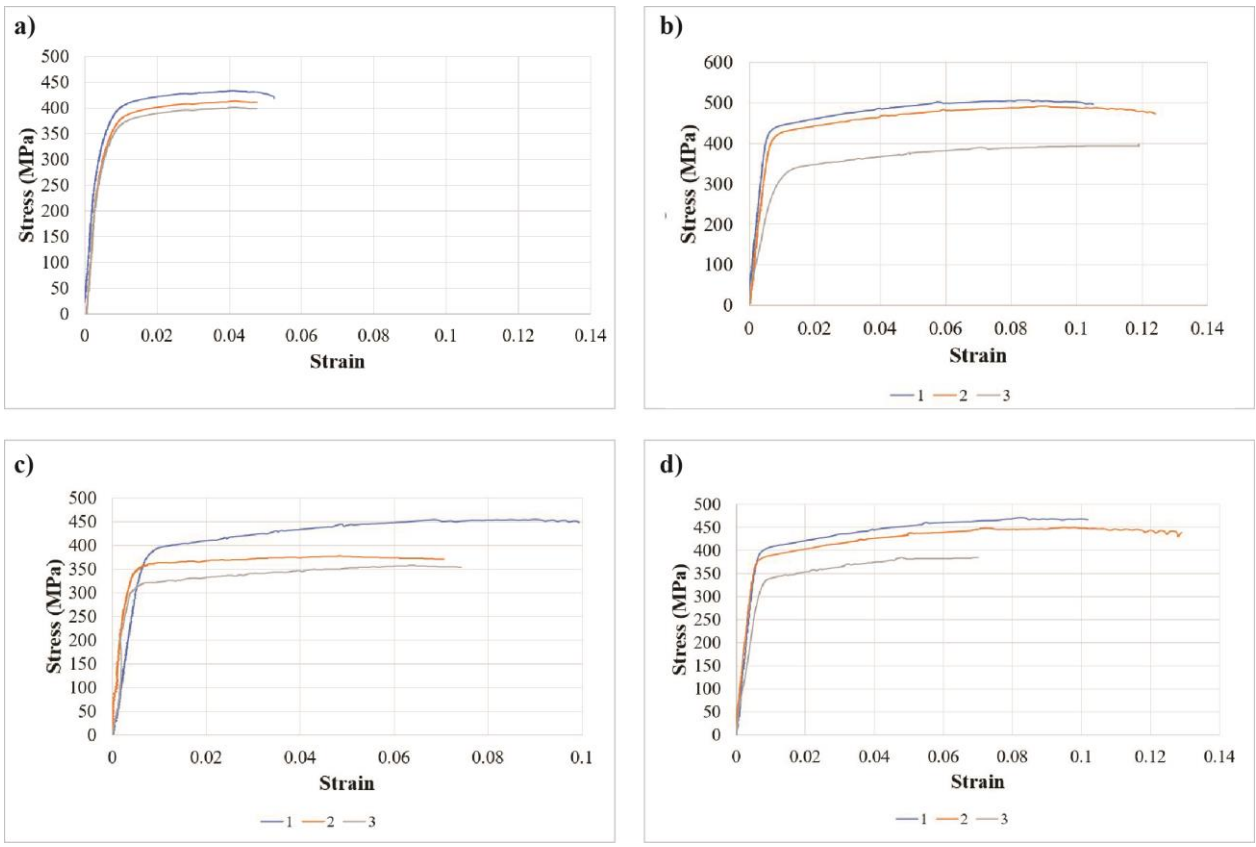

Fig. E.3 Stress-strain curves for the a) Scalmalloy 30%CR, b) Scalmalloy 30%CR+HT1, c) Scalmalloy 30%CR+HT2, and d) Scalmalloy 30%CR+HT3 condition

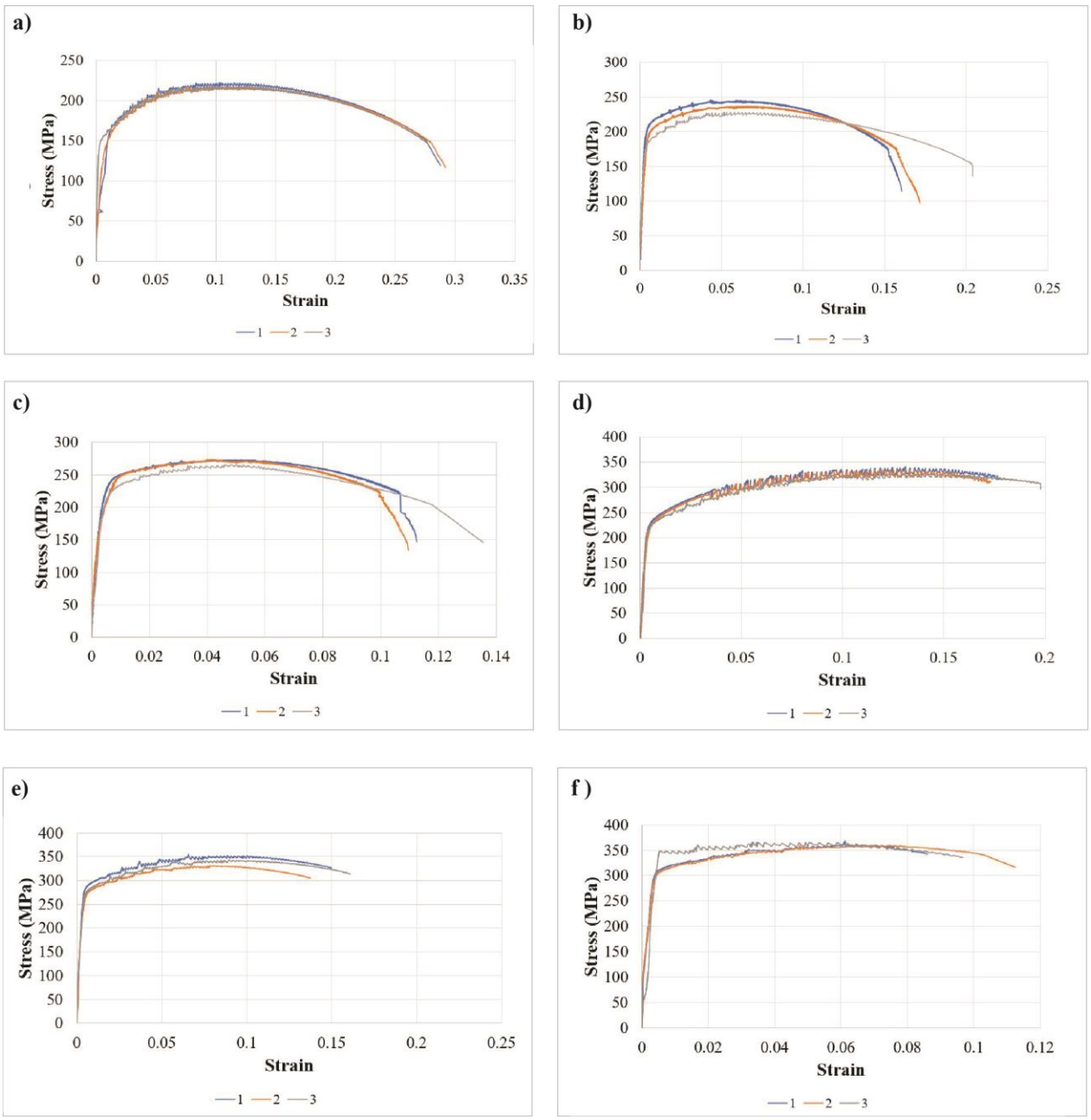

Fig. E.4 Stress-strain curves for the extruded aluminium alloys – a) 5052Al AR, b) 5052Al 10%CR, c) 5052Al 30%CR, d) 5083Al AR, e) 5083Al 10%CR, f) 5083Al 30%CR condition

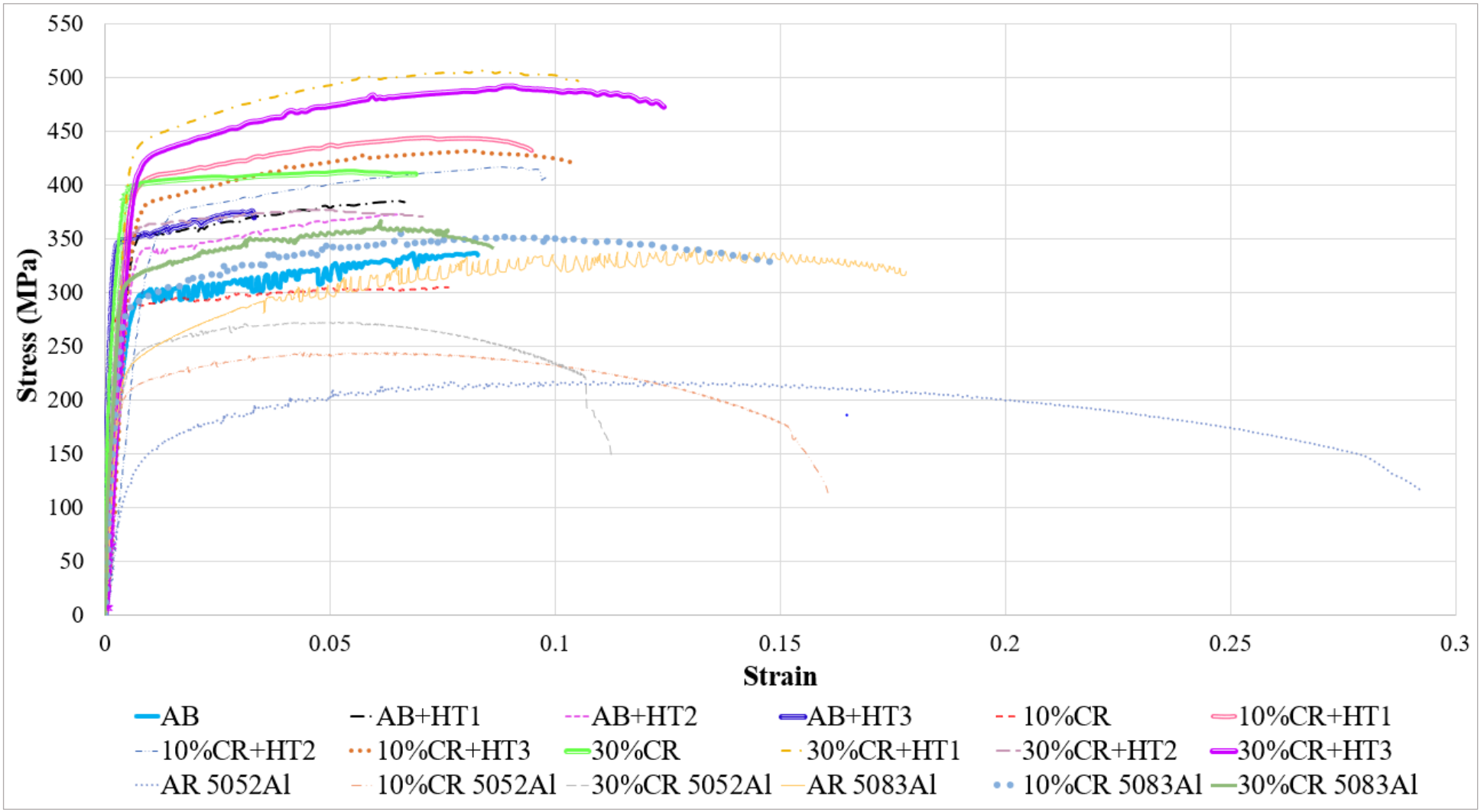

Fig. E.5 Stress-strain curves comparing average tensile strength of all conditions for Scalmalloy, 5052Al and 5083Al

F. Surface roughness data

Surface roughness of each condition is compared in Fig. F.1. The highest surface roughness (Ra) was found in the AB condition with an average of 22.38µm in the horizontal plane. The longitudinal and transverse planes show SR of 12.40µm and 8.13µm, respectively. These are lower than results reported by Koutny et al. (2018) of 17µm ±2 for the Scalmalloy AB conditions produced by SLM assumed to be related to the higher laser power used in their work. It was also reported that the SLM processed components have ≈ 4-5 times higher surface roughness than conventionally processed parts (Koutny et al., 2018; Strano et al., 2013), consistent with the findings in this work. The high SR can be attributed to balling effect producing small satellites on the surface, adhering powder particles, and near surface irregularities. The process parameters such as laser power and scan speed were identified as having the greatest effect on the SR, hence, process parameters may need to be adjusted to minimise surface roughness (Maamoun et al., 2018; Musekamp et al., 2021). The longitudinal plane for the AB and AB+HT conditions experienced the lowest average SR as this was the upward facing surface of the samples on the build platform as they were being built during the SLM process (horizontal build direction). According to Hitzler, Hirsch, Merkel, and Hall (2017), the orientation of the surfaces on the build plate directly correlate to the level of surface roughness. The vertical side surfaces parallel to the build direction typically experiences greater surface roughness than the upward facing surface due to the movement of loose powder particles and weld (laser) splatter within the chamber. For this reason, the AB condition of most additively manufactured components have a high surface roughness and require post processing to smooth the surface (Maamoun et al., 2018). The average surface roughness for the AB+HT1, AB+HT2 and AB+HT3 conditions displayed similar values to the AB condition as heat treatment was not expected to have an effect on SR. However, once cold rolling was applied, the surface roughness for all samples reduced by approximately 60% to 80% indicated as in Fig. F.1. This reduction in SR for the CR and CR+HT conditions in the horizontal plane is typical and expected from the cold rolling process as it smooths by removing surface irregularities and satellites (Jeng et al., 2020). The low surface roughness in the longitudinal and transverse planes of the cold rolled and cold rolled the heat treated conditions were due to wire cutting as the tensile sample was wire cut from the larger section of cold rolled Scalmalloy sheet which produces a smooth and refined surface topology (Salvati & Korsunsky, 2020). Furthermore, the surface roughness for the CR and CR+HT conditions are comparable to those produced by conventional processes (such as extrusion) as shown in Fig. F.2 and F.3 from extruded aluminium alloys tested for SR in this work.

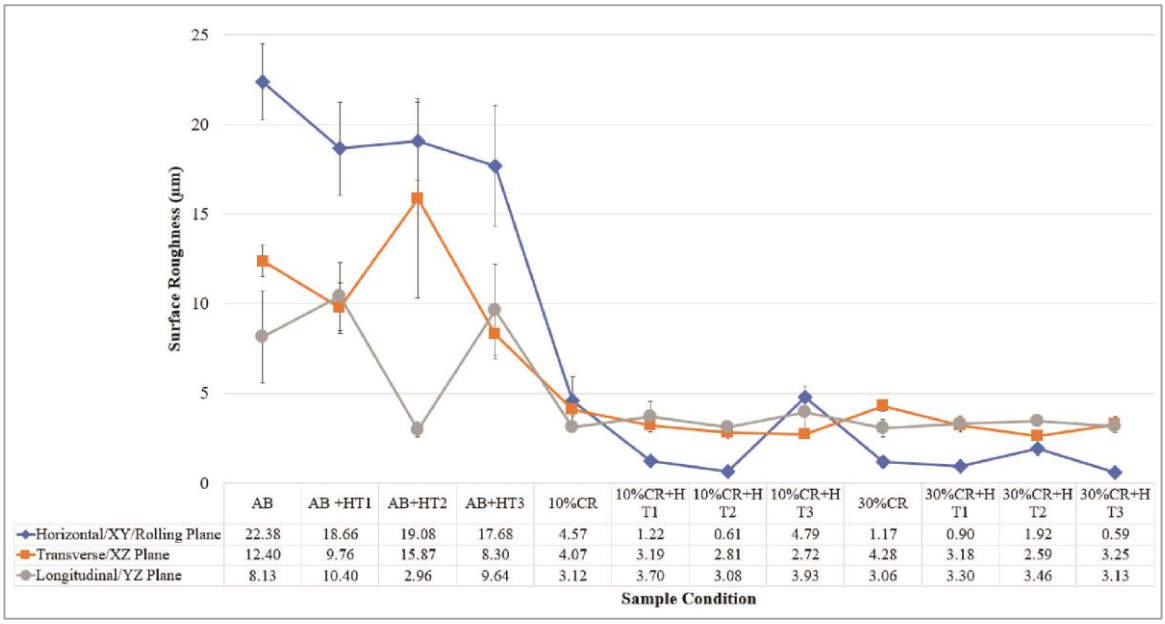

	AB	AB +HT1	AB+HT2	AB+HT3	10%CR	10%CR+HT1	10%CR+HT2	10%CR+HT3	30%CR	30%CR+HT1	30%CR+HT2	30%CR+HT3
Horizontal/XY/Rolling Plane	22.38	18.66	19.08	17.68	4.57	1.22	0.61	4.79	1.17	0.90	1.92	0.59
Transverse/XZ Plane	12.40	9.76	15.87	8.30	4.07	3.19	2.81	2.72	4.28	3.18	2.59	3.25
Longitudinal/YZ Plane	8.13	10.40	2.96	9.64	3.12	3.70	3.08	3.93	3.06	3.30	3.46	3.13

Fig. F.1 Surface Roughness results for all Scalmalloy conditions showing standard deviations in the horizontal, longitudinal, and transverse planes

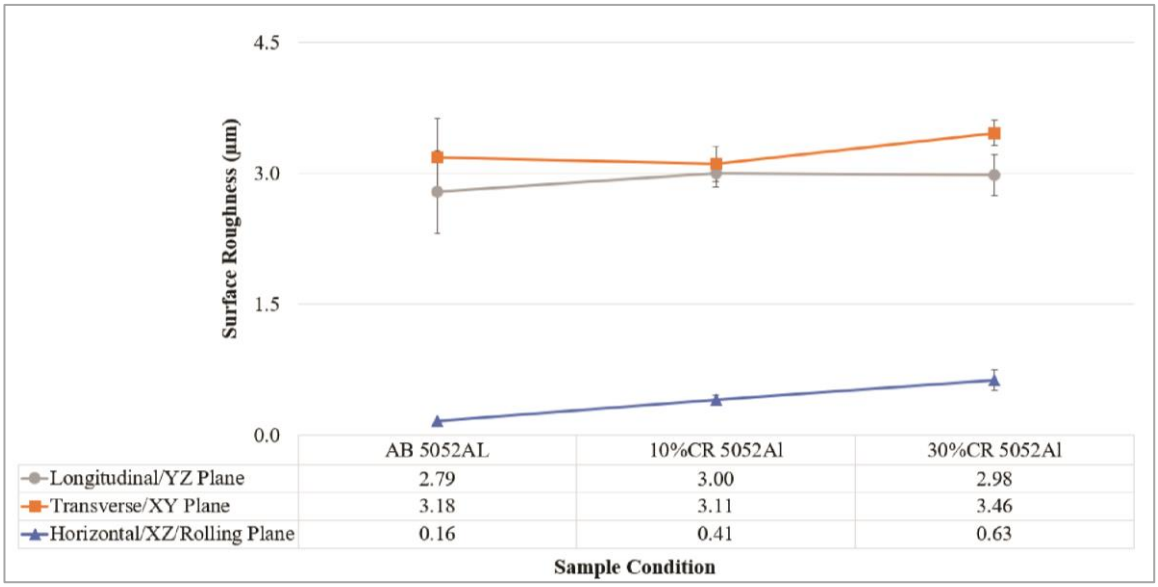

	AB 5052AL	10%CR 5052Al	30%CR 5052Al
Longitudinal/YZ Plane	2.79	3.00	2.98
Transverse/XY Plane	3.18	3.11	3.46
Horizontal/XZ/Rolling Plane	0.16	0.41	0.63

Fig. F.2 Surface roughness results for the as received, 10% cold rolled, and 30% cold rolled conditions for 5052Al with standard deviations in the horizontal, longitudinal, and transverse planes

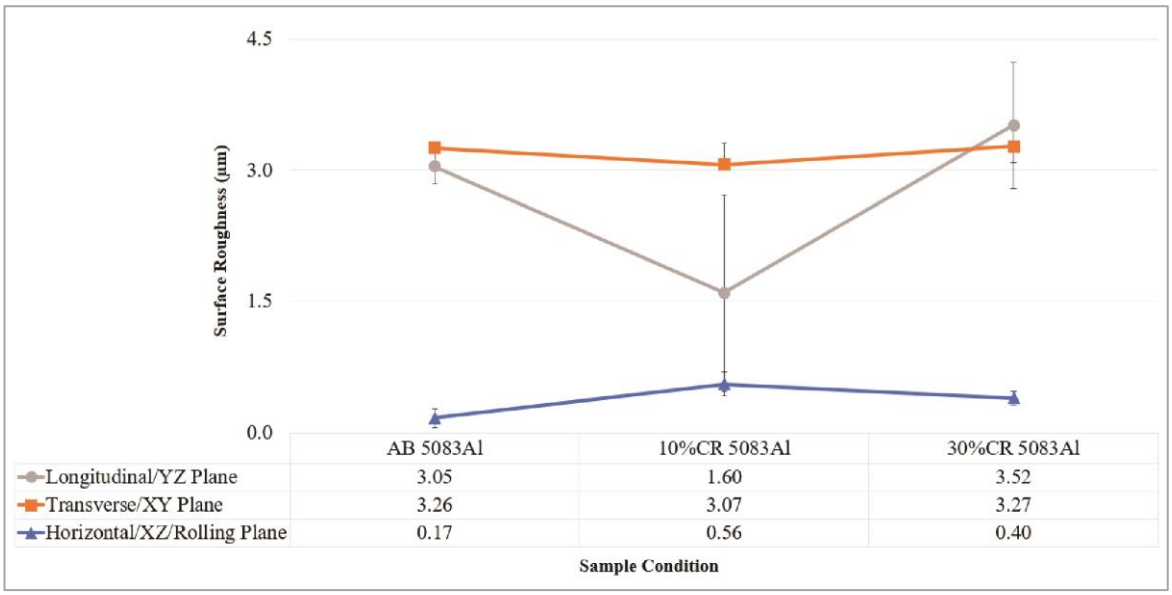

	AB 5083Al	10%CR 5083Al	30%CR 5083Al
Longitudinal/YZ Plane	3.05	1.60	3.52
Transverse/XY Plane	3.26	3.07	3.27
Horizontal/XZ/Rolling Plane	0.17	0.56	0.40

Fig. F.3 Surface roughness results for the as received, 10% cold rolled, and 30% cold rolled conditions for 5083Al with standard deviations in the horizontal, longitudinal, and transverse plane

G. Additional SEM micrographs of fracture surfaces

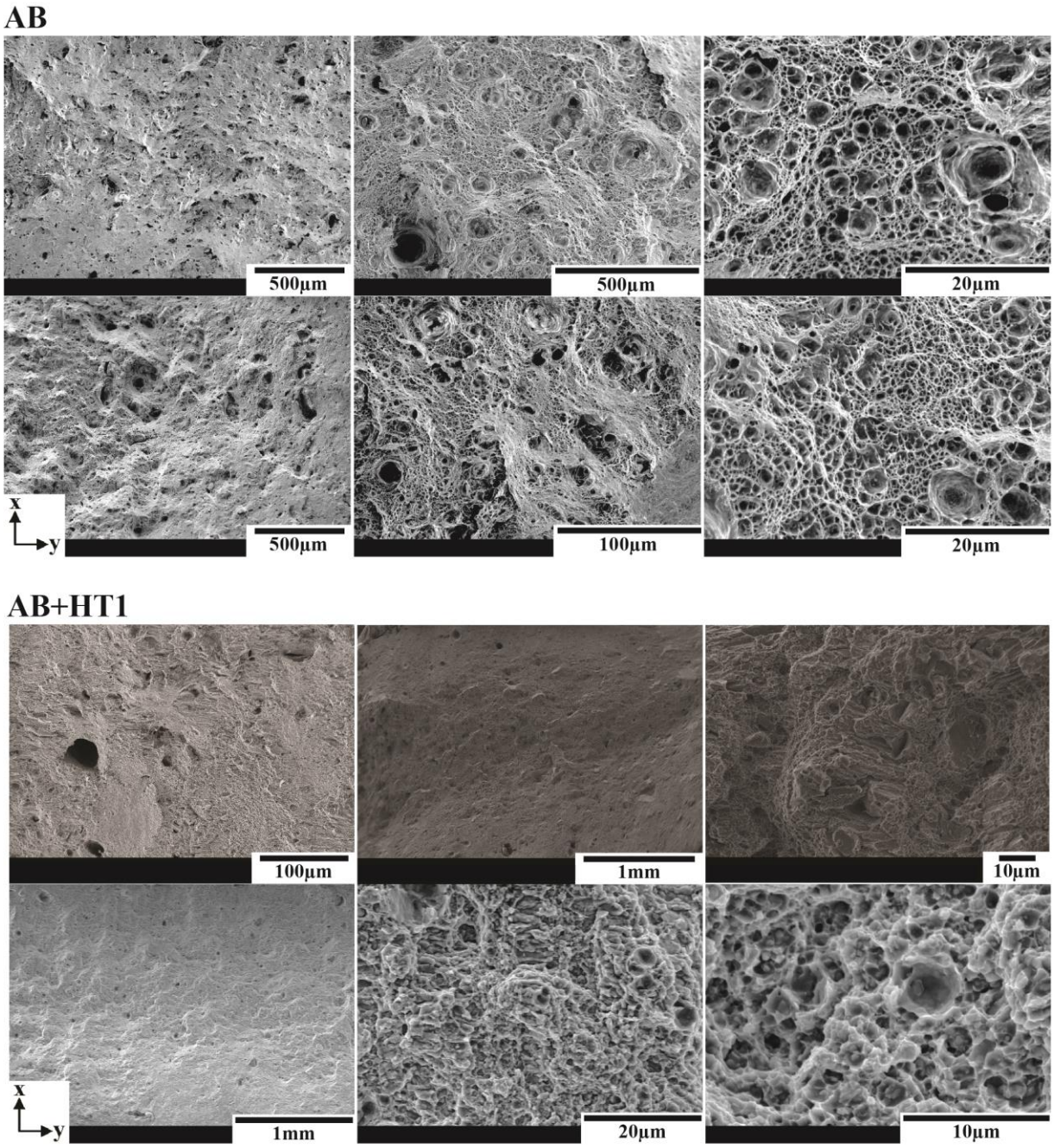

Fig. G.1 SEM micrographs of the fracture surface perpendicular to the fracture for the Scalmalloy AB and AB+HT1 conditions

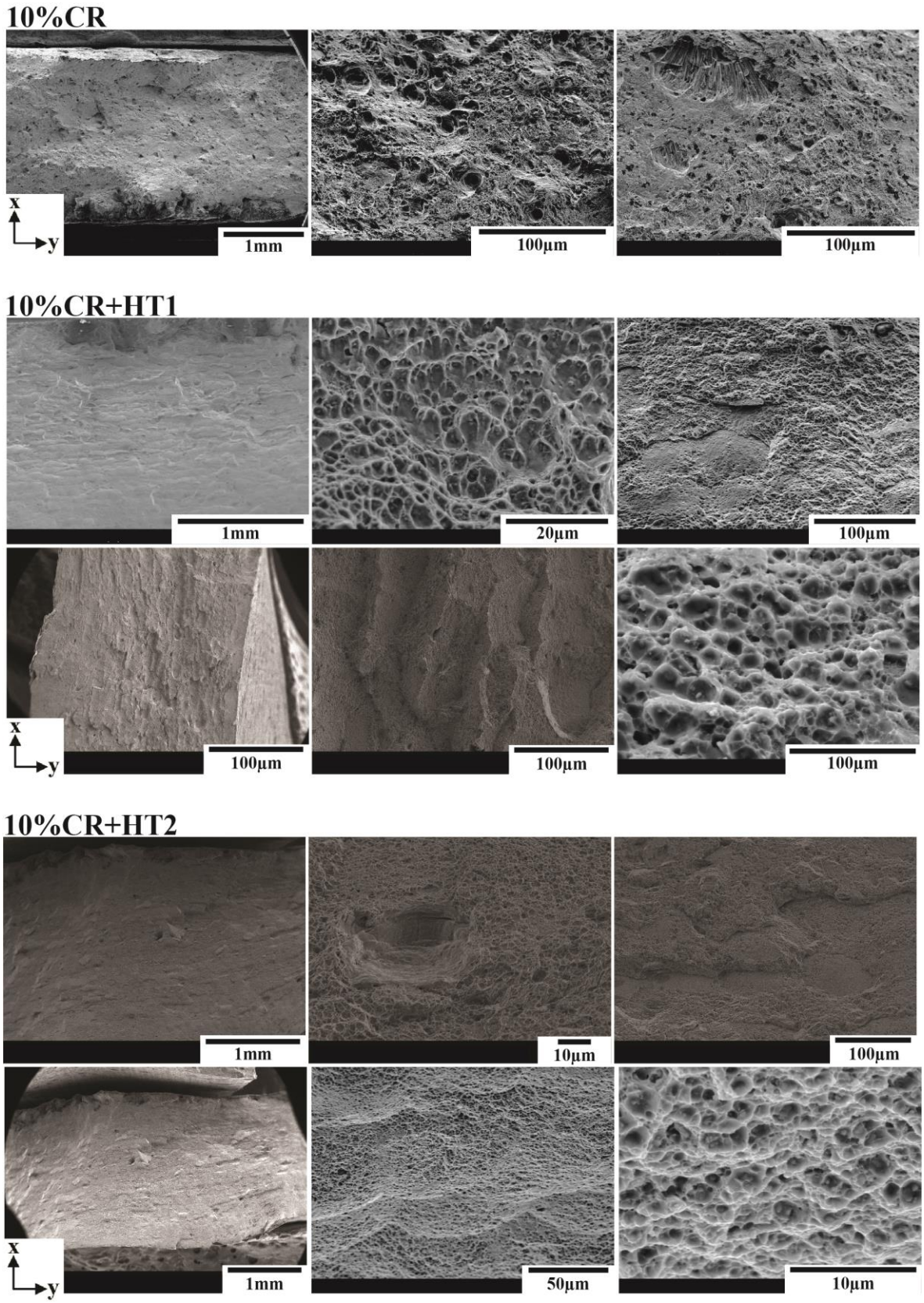

Fig. G.2 SEM micrographs of the fracture surface perpendicular to the fracture for the Scalmalloy 10%CR, 10%CR+HT1 and 10%CR/+HT2 conditions

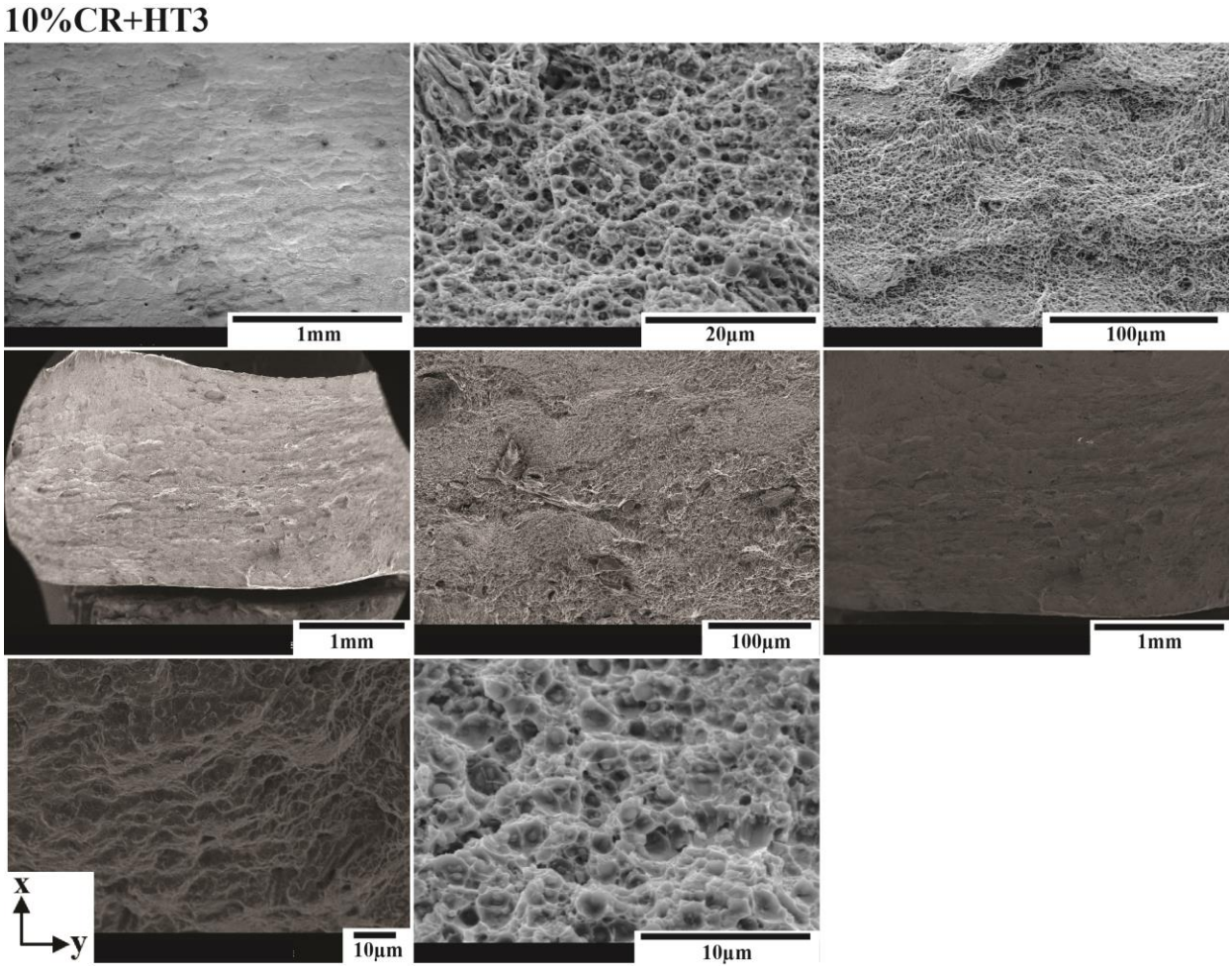

Fig. G.3 SEM micrographs of the fracture surface perpendicular to the fracture for the Scalmalloy 10%CR+HT3 condition

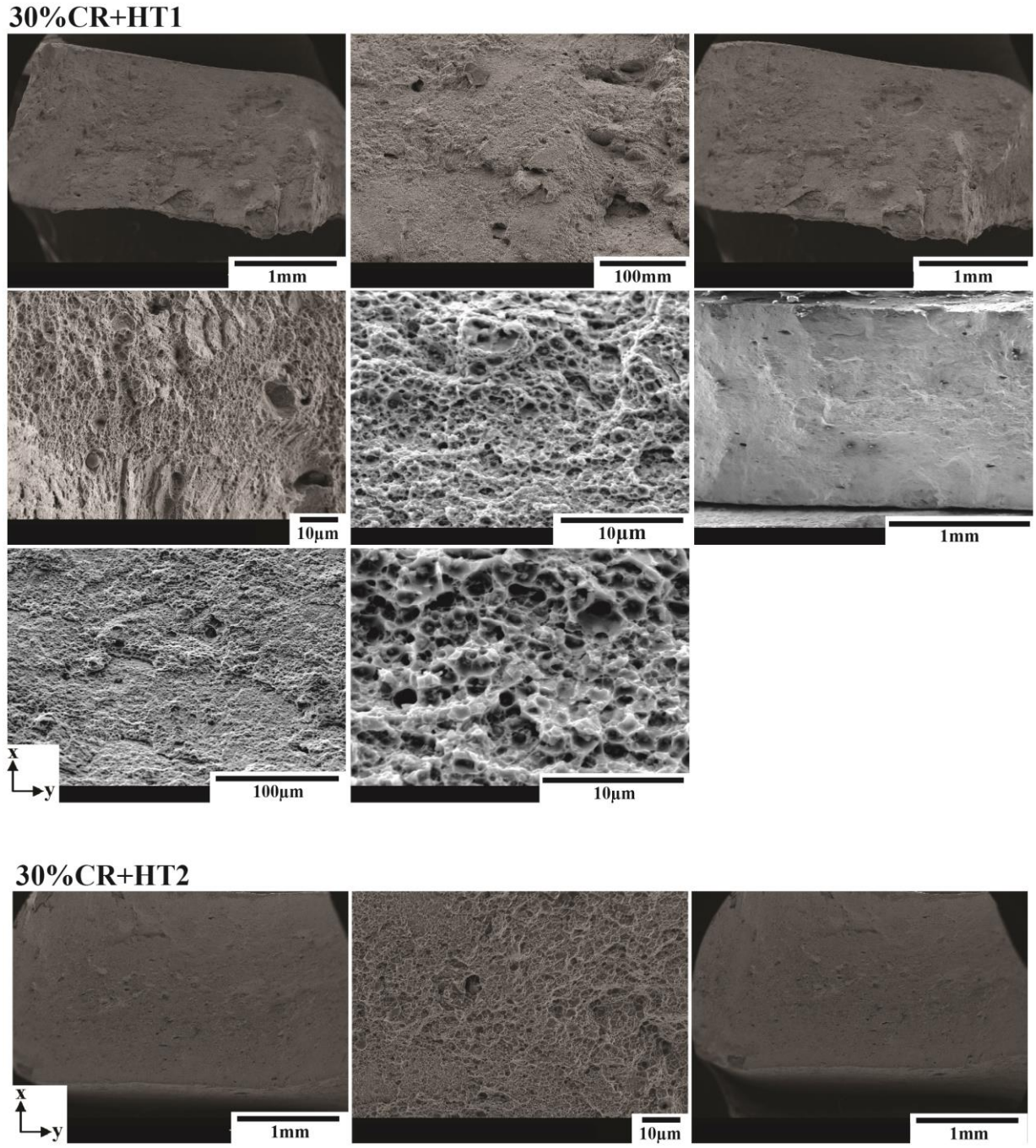

Fig. G.4 SEM micrographs of the fracture surface perpendicular to the fracture for the Scalmalloy 30%CR+HT1 and 30%CR+HT2 conditions

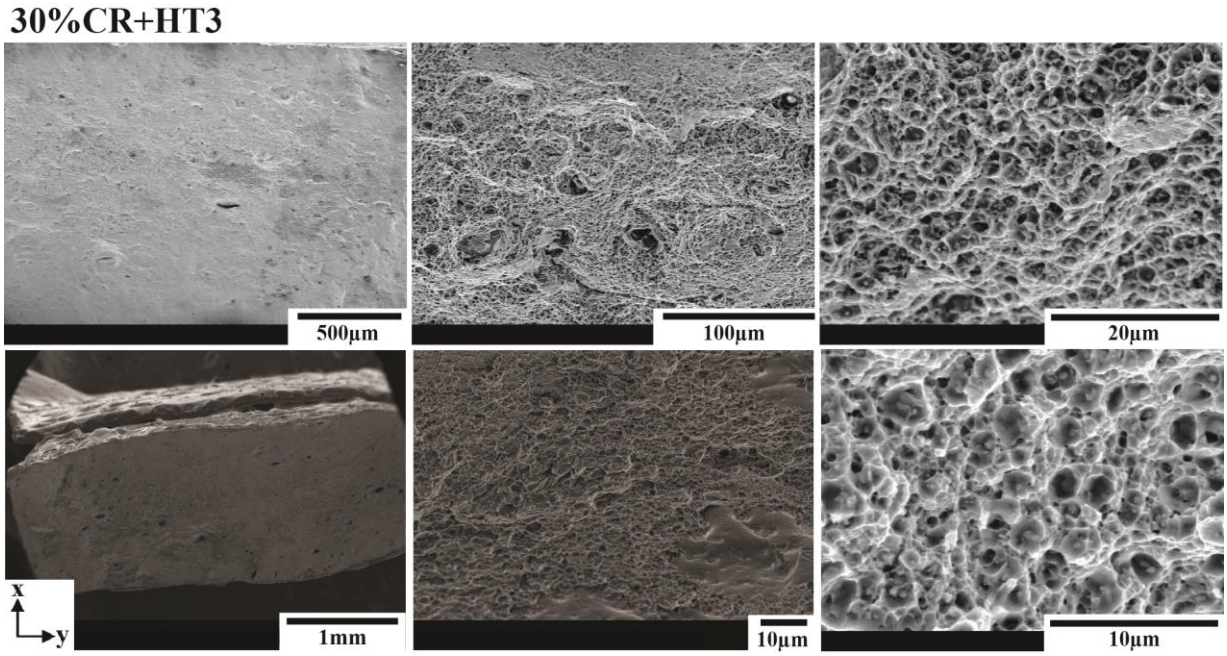

Fig. G.5 SEM micrographs of the fracture surface perpendicular to the fracture for the Scalmalloy 30%CR+HT3 condition

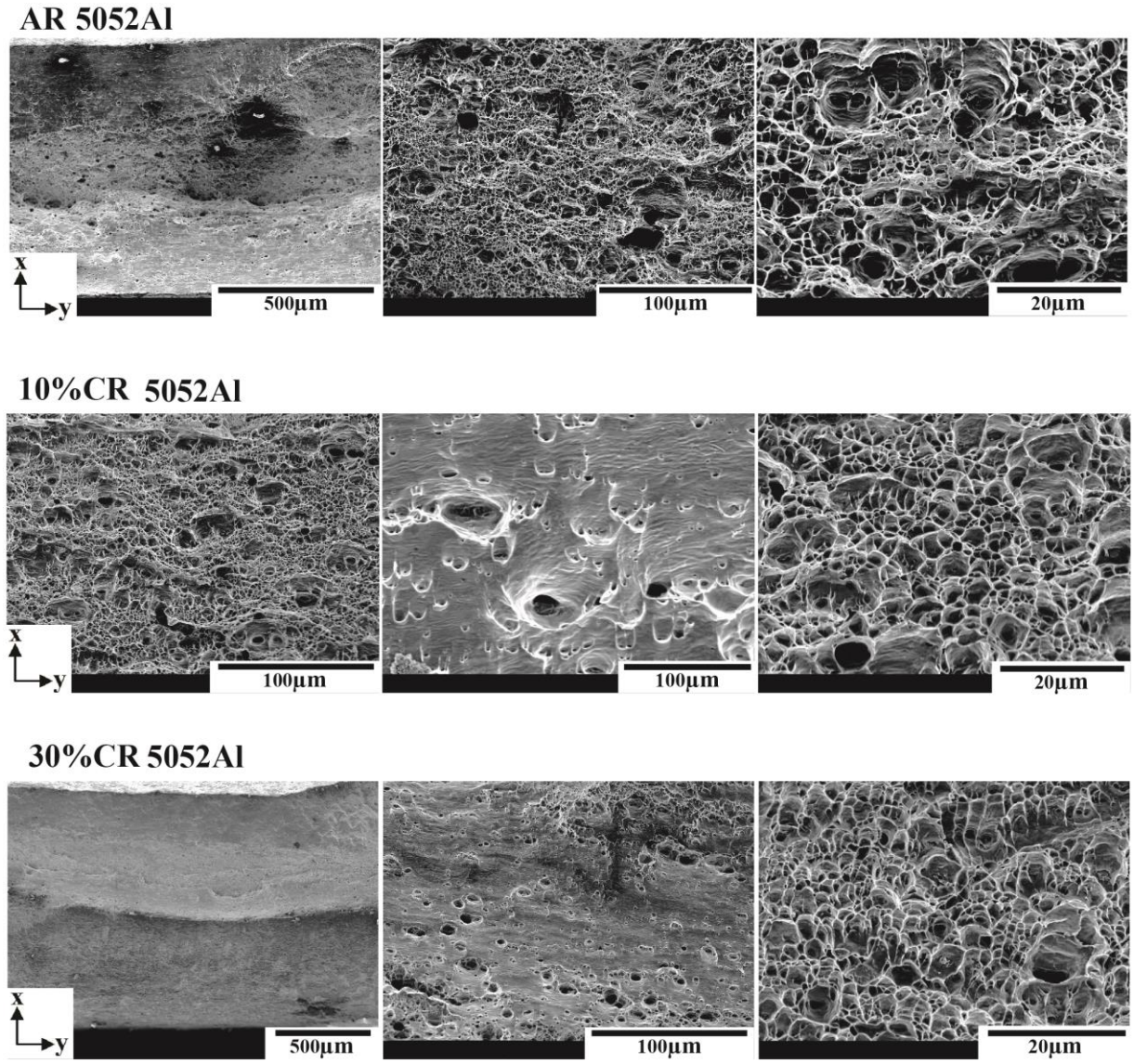

Fig. G.6 SEM micrographs of the fracture surface perpendicular to the fracture for the 5052Al AR, 10%CR and 30%CR conditions

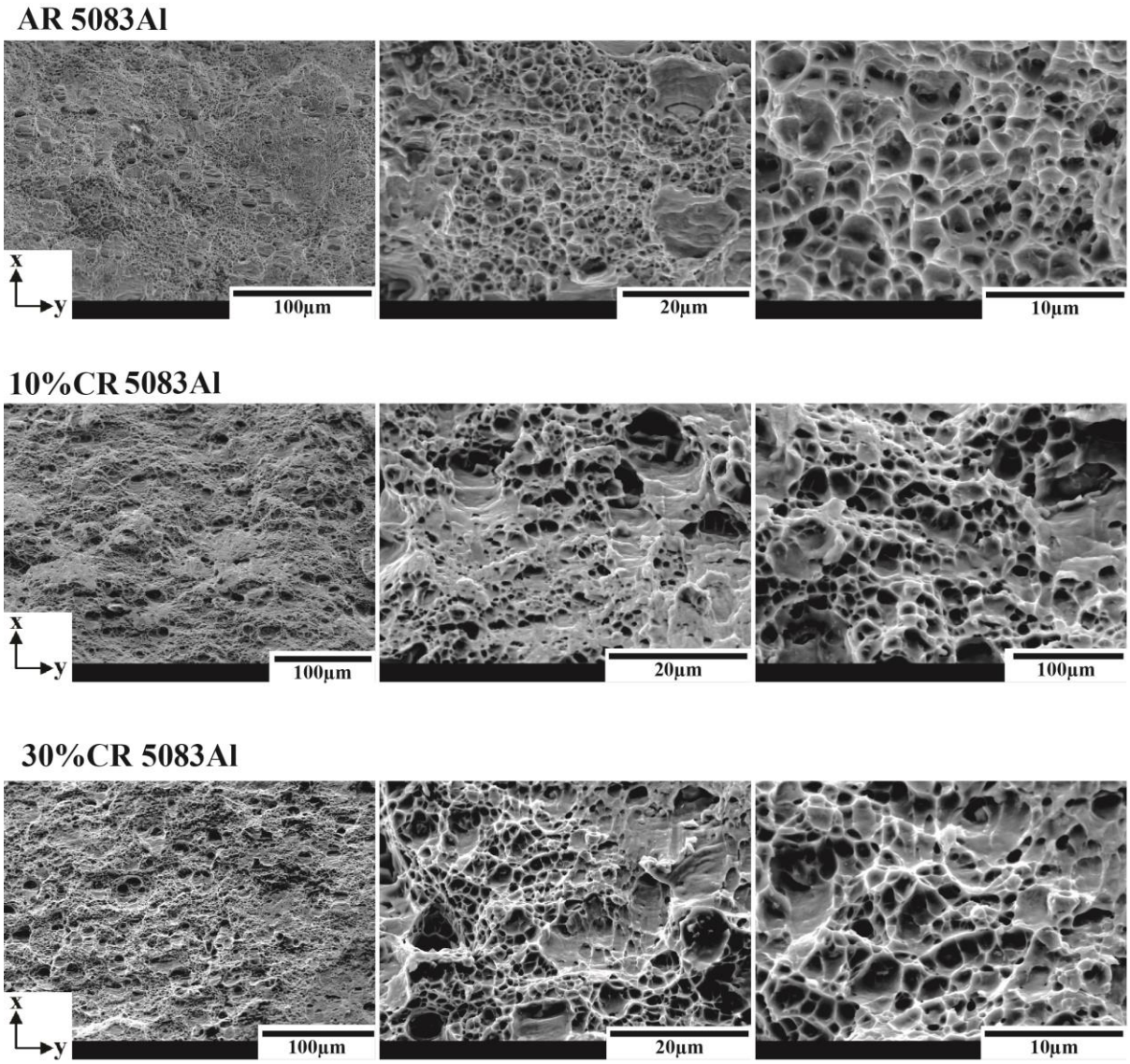

Fig. G.7 SEM micrographs of the fracture surface perpendicular to the fracture for the 5083Al AR, 10%CR and 30%CR conditions

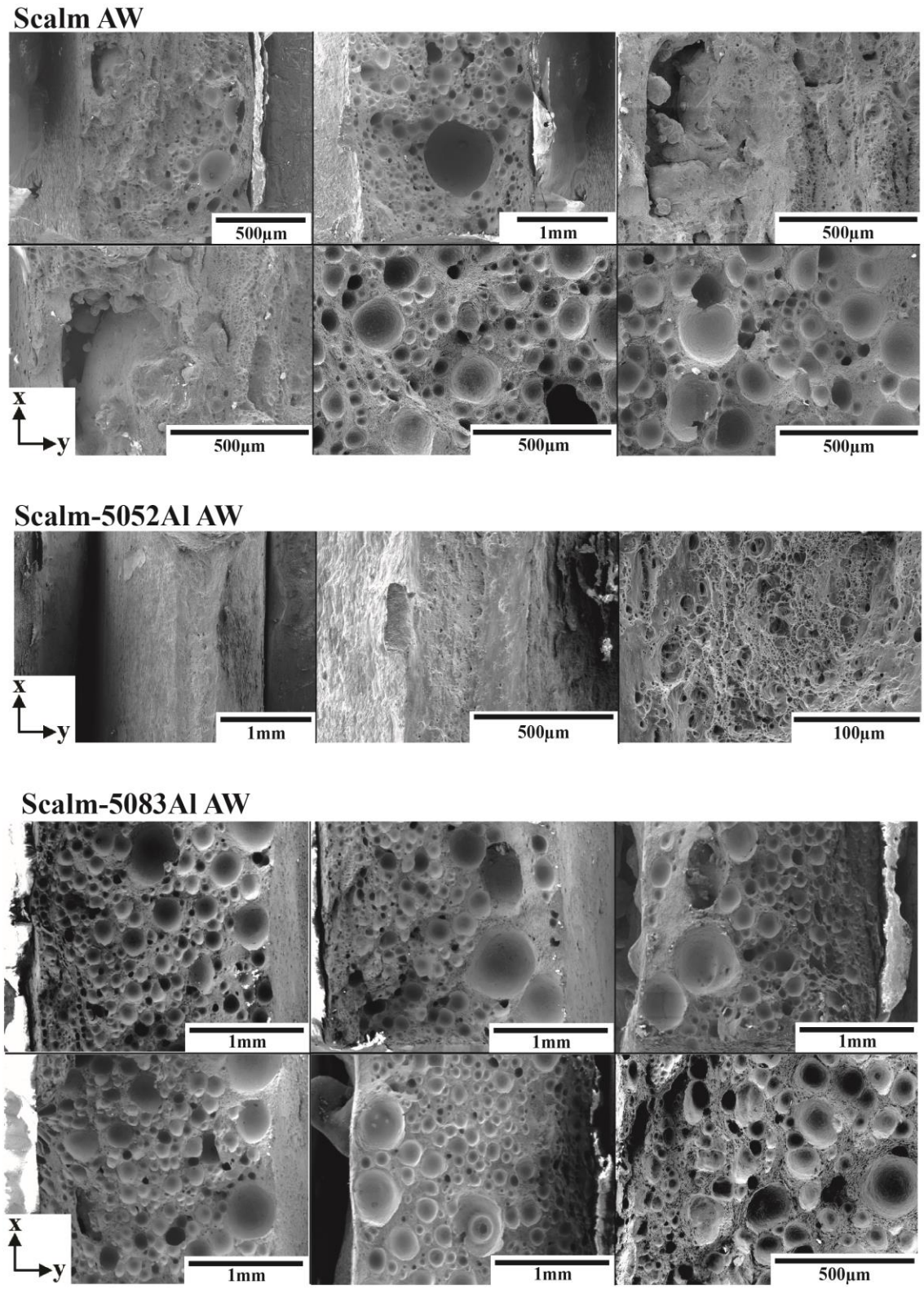

Fig. G.8 SEM micrographs of the fracture surface perpendicular to the fracture for the welded Scalmalloy-Scalmalloy, Scalmalloy-5052Al and Scalmalloy-5083Al samples in the as welded (AW) condition

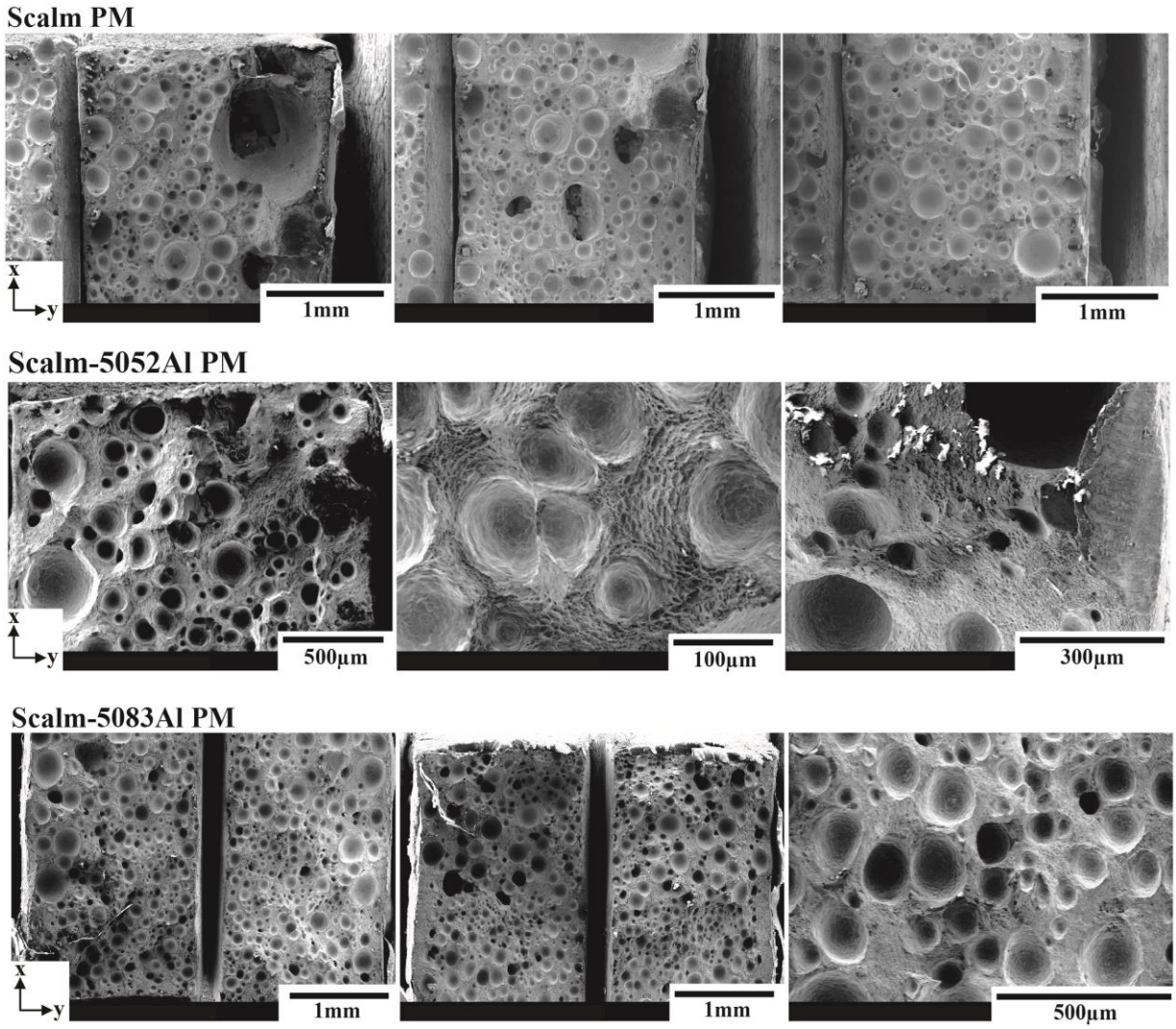

Fig. G.9 SEM micrographs of the fracture surface perpendicular to the fracture for the welded Scalmalloy-Scalmalloy, Scalmalloy-5052Al and Scalmalloy-5083Al samples in the post machined (PM) condition